Development, simulation, and characterisation of a novel multi-PMT optical module for IceCube Upgrade with emphasis on detailed understanding of photomultiplier performance parameters

Martin Antonio Unland Elorrieta
Dissertation 2023

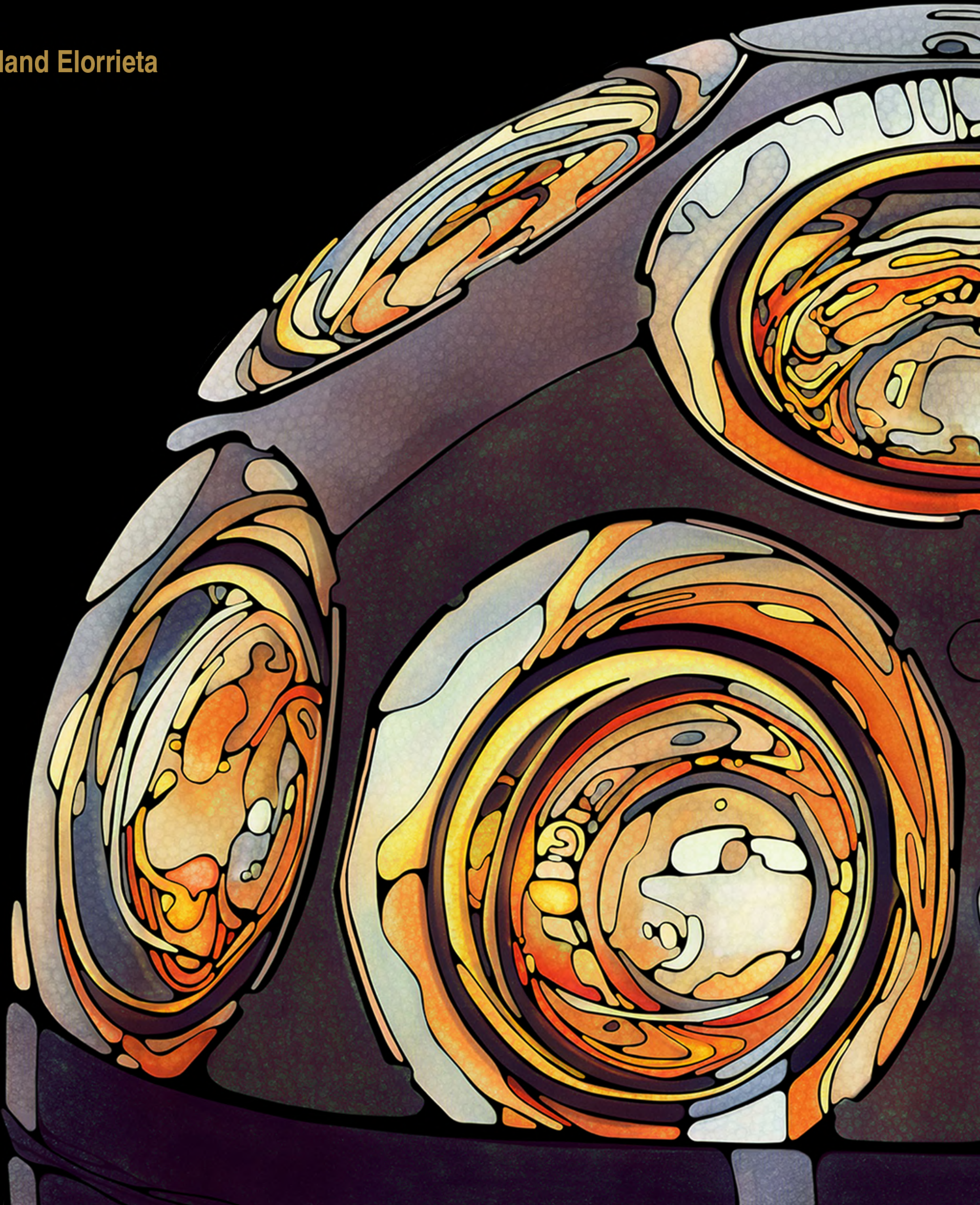

Institut für Kernphysik
Westfälische Wilhelms-
Universität Münster

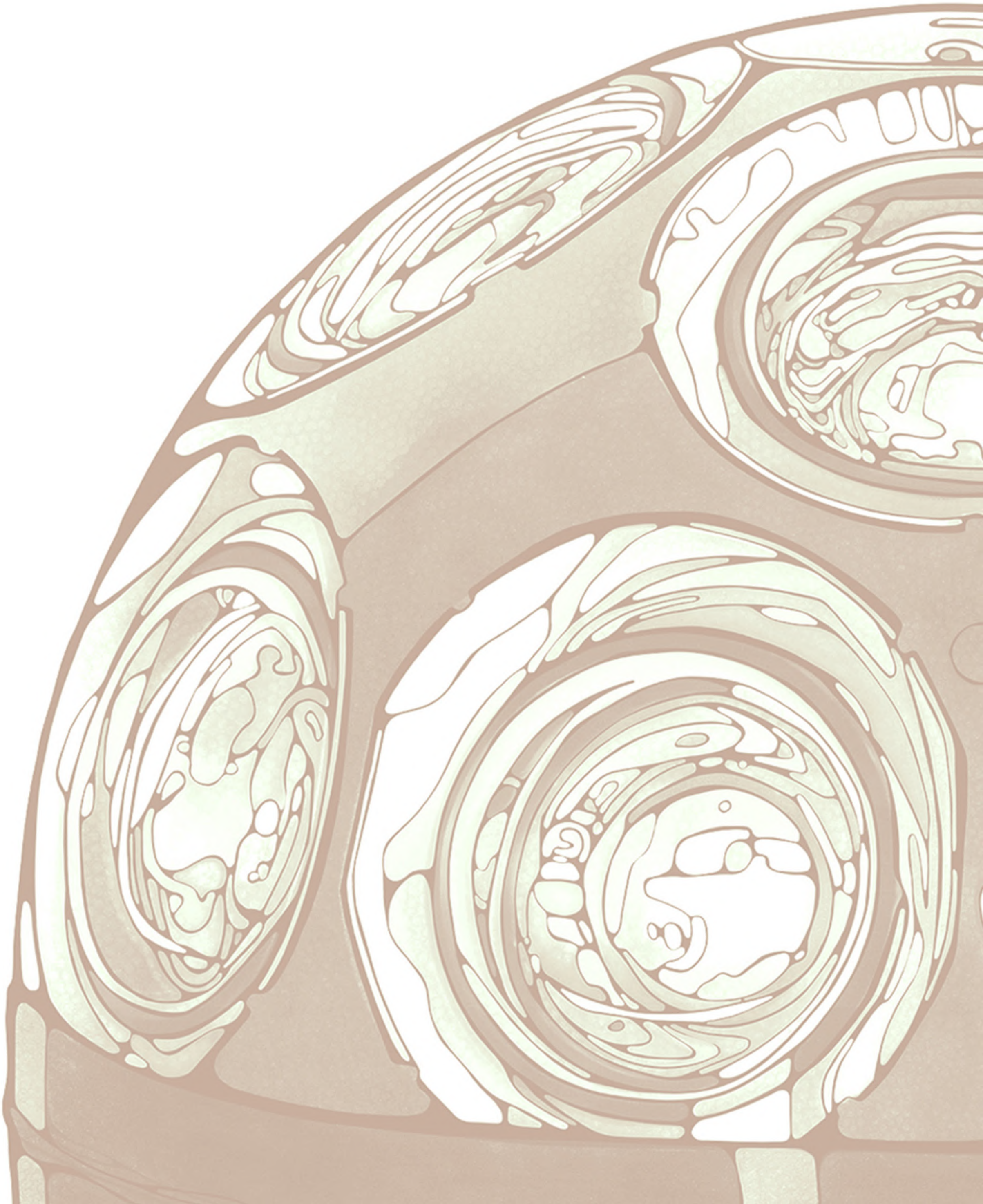

Title page illustration by
Tania Unland Elorrieta
(@tanneland)

Experimentelle Physik

Development, simulation, and characterisation of a novel multi-PMT optical module for IceCube Upgrade with emphasis on detailed understanding of photomultiplier performance parameters

Inaugural-Dissertation
zur Erlangung des Doktorgrades Dr. rer. nat.
der Naturwissenschaften im Fachbereich Physik
der Mathematisch-Naturwissenschaftlichen
Fakultät der Westfälischen Wilhelms-Universität Münster

vorgelegt von

Martin Antonio Unland Elorrieta

aus Osnabrück

—2023—

Dekan:	**Prof. Dr. Michael Rohlfing**
Erster Gutachter:	**Prof. Dr. Alexander Kappes**
Zweiter Gutachter:	**Apl. Prof. Dr. Alfons Khoukaz**
Tag der mündlichen Prüfung:	
Tag der Promotion:	

Abstract

The IceCube observatory at the South Pole is currently the world's largest neutrino detector, with roughly one cubic kilometre of instrumented ice volume. The observatory has detected high-energy astrophysical neutrinos and has provided evidence for the first neutrino point sources. To extend its energy range and sensitivity, plans are in place for the IceCube Upgrade, which will include the deployment of seven additional strings in the 2025/26 Antarctic summer season. This will pave the way for the next-generation detector, IceCube-Gen2, which will increase the volume to eight cubic kilometres and the detection rate of cosmic neutrinos by a factor of ten. This thesis presents studies on the characterisation of the novel multi-PMT Digital Optical Module (mDOMs) that will be one of the primary devices of IceCube Upgrade. These studies are based on simulations, measurements on bare mDOM photomultiplier tubes, and tests with the first built mDOMs.

Zusammenfassung

Das IceCube-Observatorium am Südpol ist derzeit der größte Neutrinodetektor der Welt mit einem Volumen von etwa einem Kubikkilometer instrumentierten Eises. Das Observatorium hat hochenergetische astrophysikalische Neutrinos detektiert und den Nachweis für die ersten Neutrino-Punktquellen erbracht. Um den Energiebereich und die Empfindlichkeit des Observatoriums zu erweitern, ist das IceCube-Upgrade geplant, wofür in der antarktischen Sommersaison 2025/26 sieben zusätzliche Strings installiert werden sollen. Dies wird den Weg für die nächste Generation des Detektors, IceCube-Gen2, ebnen, die das Volumen auf acht Kubikkilometer und die Nachweisrate kosmischer Neutrinos um den Faktor zehn erhöhen wird. In dieser Arbeit werden Studien zur Charakterisierung der neuartigen digitalen optischen Multi-PMT-Module (mDOMs) vorgestellt, die eine der Hauptkomponenten von IceCube Upgrade sein werden. Diese Studien beruhen auf Simulationen, Messungen an nackten mDOM-Photomultipliern und Tests mit den ersten gebauten mDOMs.

Contents

Glossary

AC Alternating current.
ADC Analogue-to-digital converter.
AFE Analogue front-end. In this work, AFE always refers to the circuit that handles the signal from the mDOM PMTs (see Section 4.1.3).
AGN Active galactic nucleus.
AP1 Afterpulting type 1. Signal-induced background of a PMT measured shortly after an initial pulse. See Section 5.4.2.
AP2 Afterpulting type 2. Signal-induced background of a PMT in the microsecond regime produced by ions. See Section 5.4.2.

CAD Computer aided design.
CC Charged current, weak interaction mediated by the W boson.
CCD Charge-coupled device. CCD imaging sensors consist of pixels built from semiconductor capacitors.
CCDF Complementary cumulative distribution.
CR Cosmic ray.

DAC Digital-to-analogue Converter.
DAQ Data acquisition / Data acquisition system.
DC Direct current.
DDR3 Short for Double Data Rate 3 Synchronous Dynamic Random-Access Memory (DDR3 SDRAM).
DE Detection efficiency. Probability that a PMT detects a photon (producing a signal at the anode). It is the product between the QE and the collection efficiency of the PMT.
DOM Digital optical module. In this work it refers to the time to the optical module used in IceCube.
DVT Design verification test.

FAT Final acceptance tests. In this work refers to the series of measurements performed after a module is built to evaluate their performance..
FC Functional Check-out. Test performed on DVT modules, see Section 4.2.
FEA Finite Element Analysis.
FPGA Field-programmable gate array.
FWHM Full width at half maximum.

HA coating Insulating coating which is wrapped around a PMT to avoid dark rate instabilities. 'HA' is the name given by Hamamatsu. See Section 5.4.1.
HV High voltage.

LAP Late afterpulse. Rare type of afterpulse investigated in Section 8.2.4.
LED Light-emitting diode.
LMP Linear Motion Potentiometer.

MC Monte-Carlo. Refers to Monte Carlo simulations, which are based on repeated random sampling.
mDOM Multi-PMT optical module. See Chapter 4.
MPA Multi-pulse analysis. Waveform analysis used in case several pulses should be analysed in a PMT waveform. See Section 6.1.2.
MPE Multiple Photoelectrons.
Multiplicity If a events produces a signal in *n* PMTs of a single mDOM within a predefined time window, this is called a *n* multiplicity event.

NC Neutral current, weak interaction mediated by the Z boson.
ND filter Neutral-density filter. It reduces the intensity of a light beam.

OM Optical module.

PA12 Nylon 12, common material used in SLS printing.
PC Personal computer.
PCA Penetrator Cable Assembly. Cable that connects the internal components of an optical module to the exterior.
PDE Partial Differential Equation.

PE Photoelectron. Often used as a charge unit. In this case, it is the average charge produced by a single photoelectron released in the photocathode after PMT multiplication, e.g. at a gain of 5×10^6, $1\,\mathrm{PE} = 5 \times 10^6 e \approx 0.8\,\mathrm{pC}$.
PMT Photomultiplier tube.
PR Photocurrent response. Is the current produced by the photocathode normalised by the amount of light. If there were no internal reflections in the PMT, PR is the same as the QE. Defined in Section 7.2.

QE Quantum efficiency. Probability for a photon to free an SPE from the photocathode. See Section 5.2.

R12199-01 HA MOD Early version of the Hamamatsu PMT type used in the mDOM.
R12199-02 Hamamatsu PMT type used in KM3NeT.
R15458-02/20 Hamamatsu PMT type used in the mDOMs. The ending -02 refers to PMT only, -20 the PMT + base system.
R16293-01 Hamamatsu PMT type candidate for the LOM.
R5912-100-70 Hamamatsu PMT type used in the D-Egg.
R7081-02 Hamamatsu PMT type used in the DOM.
RAPCal Reciprocal Active Pulsing Calibration. Calibration method to synchronise the mainboards of the DOMs.
rDE Relative detection efficiency.
RMS Root mean square.
ROI Region of interest.

SLS Selective Laser Sintering, a 3D printing technique.
SN Serial number.
SPA Single-pulse analysis. Waveform analysis used in case only a single pulse is analysed per PMT waveform. See Section 6.1.2.
SPE Single Photoelectron.

TT Transit time. The time between a photon hits the photocathode of a PMT and the arrival of a signal at the PMT anode.
TTS Transit time spread. Generally defined as the standard deviation of the transit time.

UV Ultra Violet, photons with wavelengths from 10 nm to 400 nm.

VITROVEX Borosilicate glass type used for the mDOM pressure vessels.

1

Introduction

The Earth's atmosphere is constantly bombarded by cosmic rays (CRs), charged particles with some of the highest energy ever measured. Although this radiation was discovered over a century ago, its source and how cosmic rays acquire such extreme energy largely remain a mystery to this day. Because of their charge, these particles are deflected by magnetic fields, hindering their effectiveness as astronomical messengers. Astronomy through telescopes that detect photons across the electromagnetic spectrum has proven to be a valuable tool for studying astronomical objects and the early universe. However, high-energy photons, which are also expected to be produced in the vicinity of cosmic-ray accelerators, have not answered the open questions in the CR field. This is where neutrino astronomy comes in, since neutrinos are also expected to be released from astronomical accelerators, providing a new potential messenger for study [1].

[1]: Spurio (2018), *Probes of Multimessenger Astrophysics*

Neutrinos are an ideal messenger of (extra)galactic events, as they can travel almost freely through the universe and are a 'smoking gun' signature for the production of cosmic rays. However, their low interaction probability makes their detection a challenging task. Despite this, various large-volume neutrino detectors have been built across the Earth, with IceCube currently being the largest. Located deep in the glacial ice at the South Pole, it consists of about 1 km^3 of instrumented volume with 5160 optical sensors to register the Cherenkov light produced after neutrino interactions [2].

[2]: Aartsen et al. (2017), *The IceCube Neutrino Observatory: Instrumentation and Online Systems*

IceCube has been in operation in full configuration since 2011 and has already made significant discoveries, including detecting a flux of high-energy neutrinos of cosmic origin [3] and providing evidence for the first point sources outside the solar system since the supernova SN1987A [4]. Due to its success, IceCube is planning to expand, improving its energy range (currently from 6 GeV to tens of PeV), both toward lower and higher energies. The first step in this expansion is the IceCube Upgrade [5], set to be deployed during the 2025/26 Antarctic summer season. The Upgrade will involve the addition of 700 highly sensitive optical sensors in a dense configuration. These devices will increase the sensitivity of IceCube to neutrinos in the range of 1 GeV to 100 GeV, significantly enhancing its ability to measure neutrino oscillation parameters, improving its already competitive results. Additionally, advanced calibration devices will be deployed to improve the accuracy of IceCube's current ice calibration. IceCube Upgrade is only the first step for the next-generation detector, IceCube-Gen2 [6], which will increase the detector volume to eight cubic kilometres. This is expected to enhance the sensitivity to cosmic neutrino sources fivefold and amplify the observable volume for transient events by a factor of at least ten.

[3]: Aartsen et al. (2013), *First observation of PeV-energy neutrinos with IceCube*

[4]: Abbasi et al. (2022), *Evidence for neutrino emission from the nearby active galaxy NGC 1068*

[5]: Ishihara et al. (2019), *The IceCube Upgrade - Design and Science Goals*

[6]: Aartsen et al. (2021), *IceCube-Gen2: the window to the extreme Universe*

New sensors with improved sensitivity were developed for these extensions. About 400 of the 700 modules to be installed in the IceCube Upgrade are multi-PMT Digital Optical Modules (mDOMs) that feature 24 photomultipliers (PMTs) arranged isotropically inside a pressure vessel. This design offers several benefits, including a near-uniform angular sensitivity that is more than twice that of the current optical sensors used in IceCube and the ability to measure local coincidences between PMTs within the same module. This thesis focuses on the characterisation of this module with particular emphasis on a detailed understanding of the performance of the photomultiplier type it uses (Hamamatsu R15458-20). The work at hand is structured in three parts:

First, an overview of neutrino astronomy and its technology is given. Here, the properties of neutrinos and their connection to cosmic rays are explained, to then summarise the current neutrino telescope landscape. This is followed by a detailed description of the design and operation of the mDOM and photomultipliers.

In the second part, the characterisation of the mDOM PMTs is presented. This includes a thorough examination of the PMT performance parameters, their sensitivity to magnetic fields, temperature, and wavelength, and the uniformity of the PMT response across the sensitive area. The knowledge gained from these PMT measurements is integrated into a simulation toolkit. Since the deep ice at the South Pole is relatively free of optical activity, the module noise is the primary background source. Therefore, understanding all mDOM background sources is crucial. This part provides a detailed characterisation of the contribution of the PMTs to the total background.

The last part of the study characterises the mDOM, starting with examining the module's mechanical design, including pressure testing and thermal stress analysis. In addition, this part presents a thorough characterisation of the background caused by photons emitted in radioactive decays within the pressure vessel, utilising laboratory measurements and simulations. The thesis concludes by evaluating a calibration method for use in situ after the mDOM deployment, measuring one of the first built mDOM as a test case.

FOUNDATION

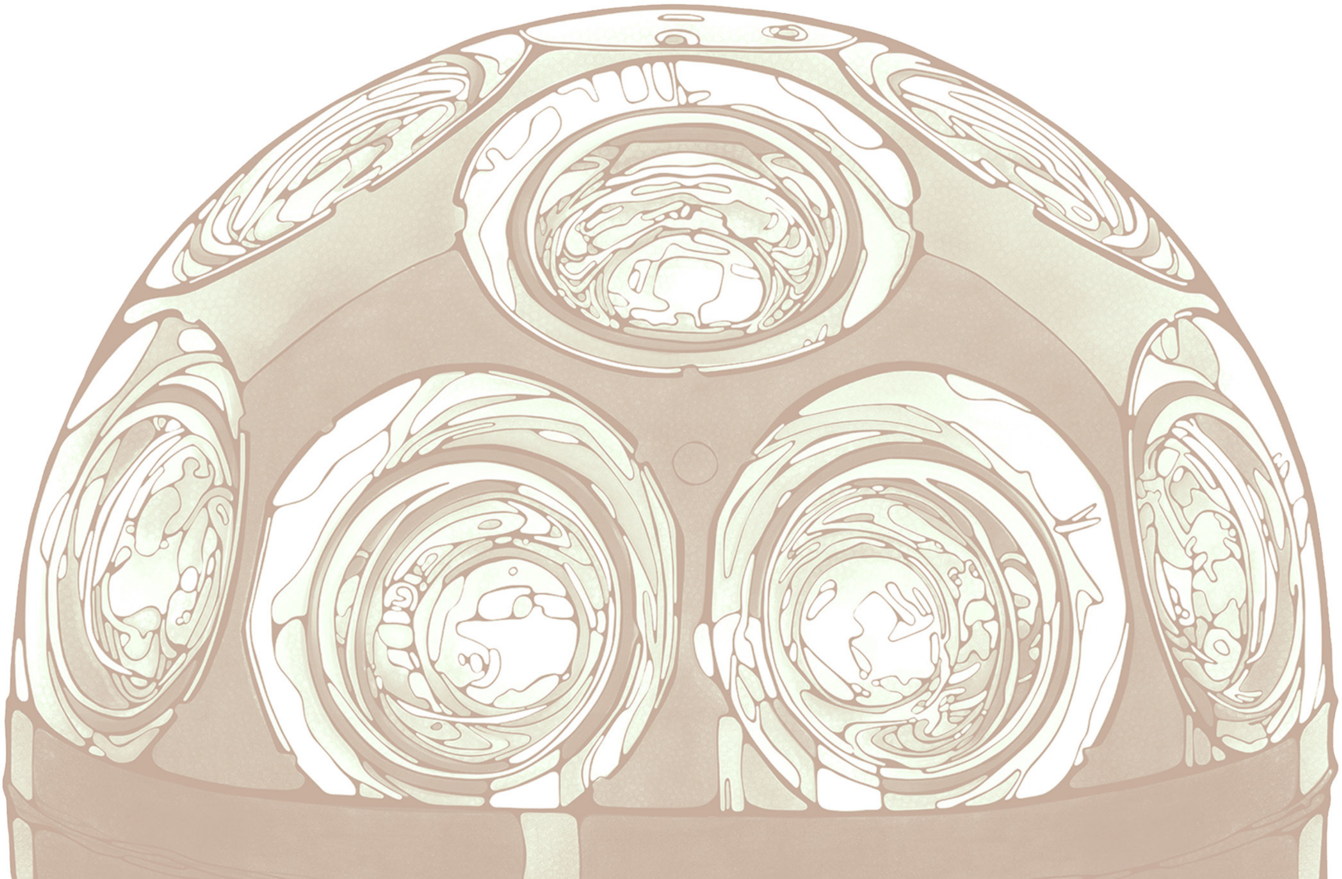

2

Neutrino Astronomy

Over the last century, astronomy across the electromagnetic spectrum — from gamma-ray satellites to radio observatories — has established itself as a robust tool for studying objects in our universe. Nevertheless, in recent years, new observatories have been flourishing, with the detection of the first cosmic high-energy neutrino in 2013 by IceCube [7], and 2015 the first detection of the merging of two black holes at LIGO and VIRGO via gravitational waves [8]. These detections have opened up a new field of astronomy known as multi-messenger astronomy. This field uses the combination of several types of messengers, such as electromagnetic waves, gravitational waves and neutrinos, to study astronomical objects and phenomena in our universe. This is especially relevant for studies of cosmic rays as they do not trace back to their origin.

[7]: Aartsen et al. (2013), *Evidence for High-Energy Extraterrestrial Neutrinos at the IceCube Detector*

[8]: Abbott et al. (2016), *Observation of Gravitational Waves from a Binary Black Hole Merger*

This chapter discusses neutrinos' properties and their role in multi-messenger astronomy, including their oscillations and interactions with matter (Section 2.1). Section 2.2 introduces cosmic rays, exploring their acceleration mechanisms and sources, as well as their relation to other messengers such as neutrinos and gamma rays.

2.1 Neutrino Properties

Neutrinos are elementary subatomic particles in the Standard Model of particle physics and are grouped as part of the lepton family. They can only interact through the weak force [1], since they are neutral and, having no colour, do not undergo strong interactions [9, Ch. 1].

[1] Neutrinos can also interact via gravitational interactions, but it can be neglected in the framework of particle physics.

[9]: Thomson (2013), *Modern Particle Physics*

Neutrinos come in three flavours, one for each of their charged lepton counterparts: electron- ν_e, muon- ν_μ and tau-neutrino ν_τ. Various experiments conducted over the last few decades have shown that neutrinos created with a specific flavour can be measured with a different flavour after they have propagated through vacuum or matter. This process is called neutrino oscillation and is discussed in Section 2.1.1.

As neutrinos feel only the weak force, they rarely interact with matter. This makes them challenging to detect but ideal astronomical messengers since they directly point to their sources. The high-energy neutrino interactions with matter of interest for neutrino astronomy are presented in Section 2.1.2.

2.1.1 Neutrino Oscillations

The process of neutrino oscillation refers to the periodical change in the probability that a neutrino, which is initially produced as a flavour eigenstate ν_α, to be identified as a different flavour ν_β upon detection. This property was first discovered in the Super-Kamiokande experiment for atmospheric neutrinos [10], the SNO experiment for solar neutrinos [11], and the KamLAND experiment for reactor neutrinos [12]. This led to the 2015 Nobel Prize in Physics award to T. Kajita and A. McDonald [13]. As it will be shown in the following, for oscillation to occur, it is essential for neutrinos to possess different masses. This section provides a brief introduction to the oscillation mechanism. A historical introduction to this phenomenon is presented in [14], while the contents of this section are primarily based on [9, Ch. 13].

[10]: Fukuda et al. (1998), *Evidence for oscillation of atmospheric neutrinos*

[11]: Bellerive et al. (2016), *The Sudbury Neutrino Observatory*

[12]: Abe et al. (2008), *Precision Measurement of Neutrino Oscillation Parameters with KamLAND*

[14]: Bilenky (2016), *Neutrino oscillations: From a historical perspective to the present status*

[9]: Thomson (2013), *Modern Particle Physics*

The neutrino flavour eigenstates $|\nu_\alpha\rangle$, with $\alpha = e, \mu, \tau$, are the eigenstates of the weak interaction that are produced with the respective lepton e, μ or τ after a charge-current interaction [9, Sec. 13.1]. Thus, neutrinos are produced as a flavour eigenstate and are projected onto one when they interact. On the other hand, the mass eigenstates of a particle are the stationary eigenstates of the free particle Hamiltonian H. The time evolution of the eigenstates is given by the Schrödinger equation

$$H\,|\psi\rangle = i\frac{\partial\,|\psi\rangle}{\partial t} = E\,|\psi\rangle\,, \tag{2.1}$$

where ψ is the eigenstate of the Hamiltonian and the eigenvalue E is the energy of the particle. In the case of the neutrino, the basis of mass eigenstates is often labelled as ν_1, ν_2 and ν_3. The flavour and mass eigenstates can be related via a unitary matrix [9, Sec. 13.3]

$$\begin{pmatrix}\nu_e\\ \nu_\mu\\ \nu_\tau\end{pmatrix} = \begin{pmatrix}U_{e1} & U_{e2} & U_{e3}\\ U_{\mu1} & U_{\mu2} & U_{\mu3}\\ U_{\tau1} & U_{\tau2} & U_{\tau3}\end{pmatrix}\begin{pmatrix}\nu_1\\ \nu_2\\ \nu_3\end{pmatrix}. \tag{2.2}$$

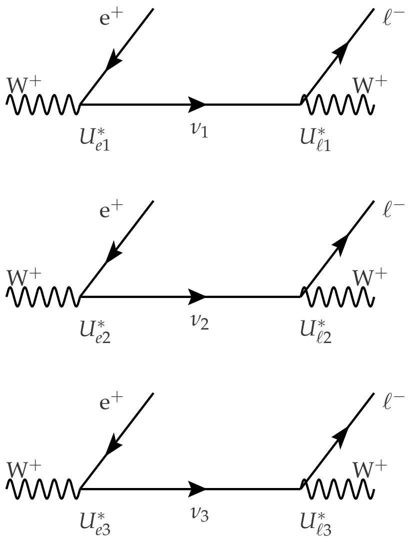

Figure 2.1: Visualisation of the superposition $|\psi\rangle = \sum_{i=1}^{3} U^*_{ei}\,|\nu_i\rangle$ at the W$^+$-e$^+$-ν_e vertex in terms of mass eigenstates. Upon interaction after propagation, it oscillates to ν_ℓ, producing a lepton ℓ^-. Based on [9, p. 344].

The distinction between mass and flavour eigenstates can be visualised in Figure 2.1. After the weak interaction, any of the mass eigenstates can be produced in conjunction with the electron, as the system is described by a superposition of the mass eigenstates. If a free neutrino of flavour α is created at $t = 0$, its wavefunction $|\psi(t,x)\rangle$ can be expressed as the linear combination of the mass eigenstates $|\psi(0)\rangle = |\alpha\rangle = \sum_{i=1}^{3} U^*_{\alpha i}\,|\nu_i\rangle$. The time evolution is given by the solution of the differential Equation 2.1:

$$|\psi(t,x)\rangle = \sum_{i=1}^{3} U^*_{\alpha i}\,|\nu_i(t,x)\rangle = \sum_{i=1}^{3} U^*_{\alpha i}\,|\nu_i\rangle \exp\left[-i(\vec{p}_i\vec{x} - E_i t)\right]. \tag{2.3}$$

Therefore, if the neutrino interacts after a time T and a distance L along its path, the probability of producing a lepton of flavour β is [9, Sec. 13.5]

$$P_{\alpha\to\beta}(T,L) = |\,\langle\nu_\beta|\psi(T,L)\rangle\,|^2 = |\sum_{i=1}^{3} U^*_{\alpha i}U_{\beta i}\exp\left(-i\phi_i\right)|^2, \tag{2.4}$$

with the phases $\phi_i = E_i T - p_i L$.

As neutrinos are very relativistic, $E_i = \sqrt{p_i^2 + m_i^2} \approx p + m_i^2/(2E)$, and Equation 2.4 can be expressed as [15, p. 288]

[15]: Particle Data Group et al. (2022), *Review of Particle Physics*

$$\begin{aligned} P_{\alpha\to\beta}(T,L) =& \delta_{\alpha\beta} - 4\sum_{i<j}^{n} \Re(U_{\alpha i}U^*_{\beta i}U^*_{\alpha j}U_{\beta j})\sin^2(X_{ij}) + \\ &+ 2\sum_{i<j}^{n} \Im(U_{\alpha i}U^*_{\beta i}U^*_{\alpha j}U_{\beta j})\sin(2X_{ij}), \end{aligned} \tag{2.5}$$

with $X_{ij} = L(m_i^2 - m_j^2)/(4E) = L \cdot \Delta m_{ij}^2/(4E)$ (see a standard textbook for complete derivation, e.g. [9, pp. 342–346]). The parameters Δm_{ij}^2 are called *mass splitting*. From here, it can be seen that if the different mass eigenstates are the same —which ultimately means that the three eigenstates have the same mass and $\Delta m_{ij}^2 = 0$ — the collapse of the wavefunction $|\psi(t)\rangle$ will always deliver the same initial flavour state α, since $P_{\alpha\to\beta}(t) = 0$. This means that the observation of oscillations implies that at least two mass eigenstates *are* massive and that they have *unequal* masses.

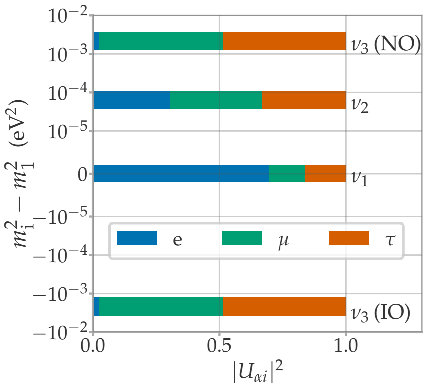

Figure 2.2: Neutrino mass hierarchy with the normal (NO) and inverted ordering (IO) relative to m_1^2. The colours indicate the amount of each flavour state using the current best values of the PMNS matrix (averaging over complex phase). Plot based on [16, Fig. 2.7]. Data from [17].

The Equation 2.5 is only valid for neutrino oscillations in vacuum. However, when neutrinos propagate through matter, they experience an additional effective potential due to their interaction with electrons and nucleons through coherent forward elastic scattering [18, p. 322]. This potential modifies the mixing of neutrinos and can result in a resonant enhancement of the mixing, known as the MSW effect. This effect is named after Mikheyev, Smirnov, and Wolfenstein and occurs in media with variable density, such as the Sun or Earth.

[9]: Thomson (2013), *Modern Particle Physics*

[18]: Giunti et al. (2007), *Fundamentals of Neutrino Physics and Astrophysics*

The MSW mechanism depends on the sign of Δm_{ij}^2. Solar neutrino experiments, which are particularly sensitive to matter effects within the Sun, have shown that $\Delta m_{21}^2 > 0$ [19]. Nevertheless, current oscillation experiments cannot distinguish the sign of Δm_{31}^2, leading to two possible *hierarchies* or *ordering* for the neutrino masses. In the *normal* mass ordering $m_3 > m_1$ and in the *inverted* mass hierarchy $m_3 < m_1$. Current analyses favour the normal mass ordering, although with a low significance [17]. Figure 2.2 shows a visualisation of the hierarchy using the current best values for Δm_{ij}^2.

[19]: Qian et al. (2015), *Neutrino mass hierarchy*

[17]: Esteban et al. (2020), *The fate of hints: updated global analysis of three-flavor neutrino oscillations*

The unitary matrix is called the Pontecorvo-Maki-Nakagawa-Sakata (PMNS) matrix. In a 3×3 complex matrix there are $2N^2 = 18$ independent parameters, but after applying the constraints of unitarity and furthermore, since fermion fields are left unchanged after rotations, the number of degrees of freedom is reduced to three real numbers and one complex phase. The usually advocated parameterisation is [1, p. 460]

[1]: Spurio (2018), *Probes of Multimessenger Astrophysics*

$$U = U_{23}U_{13}U_{12} = \begin{pmatrix} 1 & 0 & 0 \\ 0 & c_{23} & s_{23} \\ 0 & -s_{23} & c_{23} \end{pmatrix} \begin{pmatrix} c_{13} & 0 & s_{13}e^{-i\delta} \\ 0 & 1 & 0 \\ -s_{13}e^{-i\delta} & 0 & c_{13} \end{pmatrix} \begin{pmatrix} c_{12} & s_{12} & 0 \\ -s_{12} & c_{12} & 0 \\ 0 & 0 & 1 \end{pmatrix}, \tag{2.6}$$

where $s_{ij} = \sin\theta_{ij}$ and $c_{ij} = \cos\theta_{ij}$, with the mixing angles θ_{ij}.

Neutrino oscillation experiments measure the oscillation probability 2.5 usually in either of two modes: *appearance* $P_{\alpha\to\beta}$, for example, the observation of an electron or a tau from an initially pure ν_μ-beam, or *disappearance*, where the change of intensity of the same flavour beam is measured $P_{\alpha\to\alpha}$ [9, p. 351]. A single oscillation experiment is sensitive to only a few of the free parameters (the mixing angles θ_{ij}, the complex phase δ and the mass splitting Δm_{ij}^2), and the best fits are provided using all available data of atmospheric, solar, reactor and accelerator neutrinos (see, for example, [17]). It should be noted that these experiments are sensitive to the mass splitting but not to the absolute mass m_i. The KATRIN experiment [20] intends to directly measure the effective electron antineutrino mass $m_\nu = \sum_i |U_{ei}|^2 m_i^2$ and provides the current best upper limit $m_\nu < 0.8\,\mathrm{eVc}^{-2}$ [21].

[20]: Aker et al. (2021), *The design, construction, and commissioning of the KATRIN experiment*

[21]: Aker et al. (2022), *Direct neutrino-mass measurement with sub-electronvolt sensitivity*

2.1.2 High energy neutrino interactions with matter

At energies relevant to neutrino astronomy, the primary interaction is the deep-inelastic scattering of neutrinos with nucleons on the order of GeV or higher. However, there are other subdominant interactions, especially at energies of a few GeV, which will not be covered in this work. For a comprehensive overview of the different neutrino interactions throughout the entire energy range from eV to EeV, including their corresponding cross sections, please refer to [22].

In a scattering process, neutrinos can interact through two different mechanisms: *neutral current*, mediated by a Z boson, or *charged current*, mediated by a $W^\pm$ boson. A visualisation for these interactions in the case of deep inelastic scattering with a nucleon N is shown in Figure 2.3 a) for charged current and b) for neutral current. In this interaction, a neutrino scatters off a quark inside a nucleon, resulting in the breakup of the nucleon and the creation of a hadronic shower, labelled as 'X' in Figure 2.3.

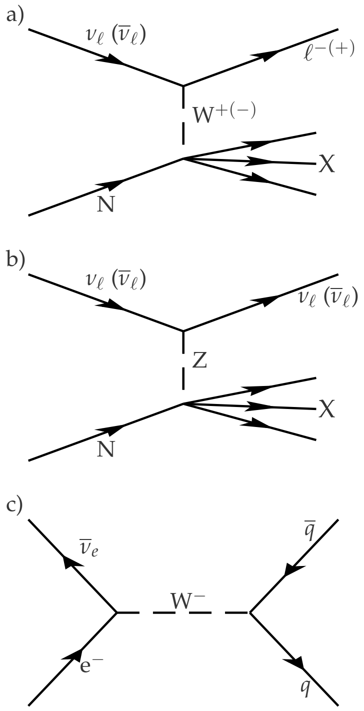

Figure 2.3: Diagrams (time from left to right) of three kinds of high-energy neutrino interactions with an atom. The deep inelastic scattering of a neutrino with a nucleon via charged current is displayed in (a) and via neutral current in (b). The diagrams are valid for antineutrinos, after changing to the corresponding values in the brackets and flipping the direction of the antifermion's arrows. (c) shows the Glashow resonance.

The standard model predicts the s-channel production of a W^- boson in the interaction of an electron antineutrino with an electron. At a centre-of-mass energy $\sqrt{s}$ equal to the mass of W^- (80.38 GeV), the cross section of this process becomes resonantly enhanced, a phenomenon known as the Glashow resonance [23]. In the electron rest frame, this results in a resonant neutrino energy of $E_R \approx M_W^2/(2m_e) \sim 6.32\,\mathrm{PeV}$ [24]. As can be observed in Figure 2.4, the cross section for this process is several orders of magnitude larger than that for the inelastic scattering. The Feynman diagram of this process is illustrated in Figure 2.3 c), where the W boson decays into a quark-antiquark pair (branching ratio ~67 %), but it also commonly decays into a lepton and antineutrino pair (branching ratio ~11 % for each lepton generation).

[22]: Formaggio et al. (2012), *From eV to EeV: Neutrino cross sections across energy scales*

[23]: Glashow (1960), *Resonant Scattering of Antineutrinos*

[24]: Aartsen et al. (2021), *Detection of a particle shower at the Glashow resonance with IceCube*

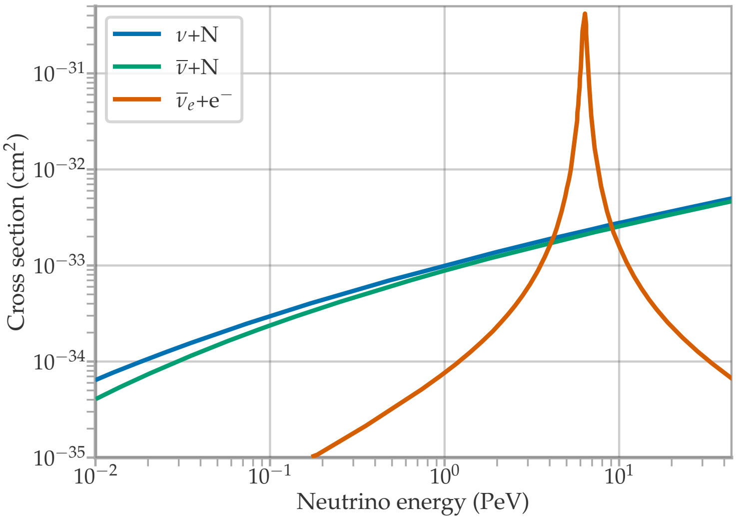

Figure 2.4: Total neutrino-nucleon, antineutrino-nucleon and $\overline{\nu}_e$+e$^-$ cross sections. Data from [25].

2.2 Cosmic Rays and multi-messenger Astronomy

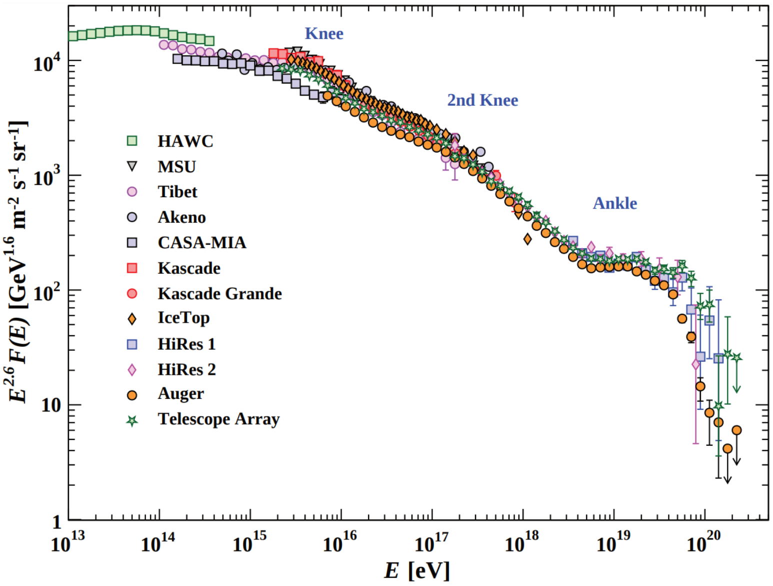

Figure 2.5: Cosmic ray spectrum as a function of energy-per-nucleus from air shower measurements of several experiments. The differential energy spectrum was multiplied by $E^{2.6}$ to display characteristics of the spectrum that would otherwise be difficult to notice. Image from [15].

Cosmic rays (CRs) are high-energy charged particles that travel through space and can impact Earth's atmosphere. They consist primarily of ionised nuclei — about ~90 % protons, ~9 % alpha particles and ~1 % heavier nuclei — and a small electron component [26, p. 1].

[26]: Gaisser et al. (2016), *Cosmic Rays and Particle Physics*

Figure 2.5 shows the flux of CRs as a function of energy. The non-thermal particle spectrum can be approximated by power laws of the form $A \cdot E^{-\alpha}$, which is represented by a straight line in a double-logarithmic representation. If the flux is very steep, the y-axis is usually weighed with a power of the energy E^{β}, which changes the slope of the line in a double-logarithmic figure (if $\alpha = \beta$, the flux would be represented as a horizontal line) [1, p. 11].

[1]: Spurio (2018), *Probes of Multimessenger Astrophysics*

From ~1 GeV to ~1 PeV the spectral index is $\alpha \approx 2.7$ up to the so-called 'knee', where the flux softness to $\alpha \approx 3.1$. A second steepening occurs at around 10^{17} eV — the second knee — with $\alpha \approx 3.3$. The feature around $10^{18.5}$ eV is called 'ankle', where the flux hardens again to $\alpha \approx 2.6$. The softening at the knee is often attributed to galactic accelerators reaching their maximal energy for proton acceleration [15, p. 525]. The second knee is interpreted similarly but corresponding to heavier nuclei, particularly iron; thus, it is also often called the 'iron knee' [27]. The flattening at the ankle is usually associated with the emergence of particles from extra-galactic sources [26, p. 12].

[15]: Particle Data Group et al. (2022), *Review of Particle Physics*

[27]: Abu-Zayyad et al. (2018), *The Knee and the Second Knee of the Cosmic-Ray Energy Spectrum*

[26]: Gaisser et al. (2016), *Cosmic Rays and Particle Physics*

At energies above $\sim 10^{19.7}$ eV, the propagation of the CRs over extra-galactic distances is expected to be suppressed due to the onset of inelastic interactions of CRs with the cosmic microwave background (called the GZK effect) [1, p. 239].

Although Victor Hess discovered this radiation over a century ago, and since then, a fleet of experiments have studied its characteristics, the origin and exact acceleration mechanism of these particles still need to be understood [1]. This task is hindered by the fact that the localisation of cosmic objects with charged particles is inhibited by intergalactic magnetic fields, which randomise the direction of the CRs.[2] Therefore, the identification of these sources is only open to neutral messengers (photons and neutrinos). The connection between these astronomy probes is introduced in Section 2.2.2.

[2] Only protons at energies above 10^{19} eV travel along approximately straight lines [1, p. 5].

2.2.1 Acceleration mechanisms and CRs sources

The acceleration mechanisms that bring CRs to such high energies still need to be fully understood, but several theories have been proposed. A robust and reliable model is the *diffusive shock acceleration*, based on the repeated scattering of charged particles at magnetic field irregularities of a moving shock front [1, Sec. 6]. In this context, the leading candidate source for galactic CRs is the environment provided by the shock wave from core-collapse supernovae, so-called *SNRs*[3](see Figure 2.6) [28].

[1]: Spurio (2018), *Probes of Multimessenger Astrophysics*

[3] **S**uper**n**ova **r**emnant.

[28]: Liu et al. (2022), *The origin of galactic cosmic rays*

Static magnetic fields cannot transfer energy to charged particles, and in astrophysical environments, large-scale electric fields are disrupted by the presence of plasma. However, magnetic field variations can act as elastic scattering centres for charged particles. These magnetic irregularities can be realised, for example, at magnetic boundary surfaces from colliding plasma fields [1, Sec. 6.1.1]. Charged particles crossing strong shock waves gain energy as they suffer a head-on collision with the magnetic turbulence of the front. After a single crossing, the particle energy is increased by a factor $(1 + v_s/c)$, where v_s is the speed of the shock front [1, p. 195]. However, since the value of v_s/c is typically small, multiple collisions are required to produce a significant energy gain. As there is an escape probability after each crossing, the diffusive shock acceleration model results in an energy spectrum of the accelerated particles of the form E^{-2}, close to the measurements (the mathematical derivation of the model and its predicted spectrum can be found in [1, Sec. 6]).

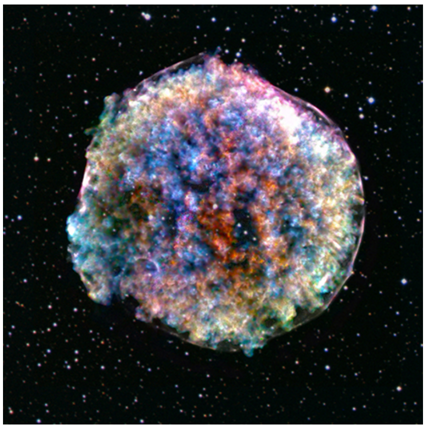

Figure 2.6: Composite image of the Tycho Brahe supernova remnant. Created by combining X-ray (Chandra X-ray Observatory) and optical observations (DSS). Image sourced from [29].

If a particle escapes the region where it was being accelerated, it cannot gain additional energy. The maximum energy $E_{\max}$ that a CR of charge Ze can attain depends on the strength of the magnetic field B and the

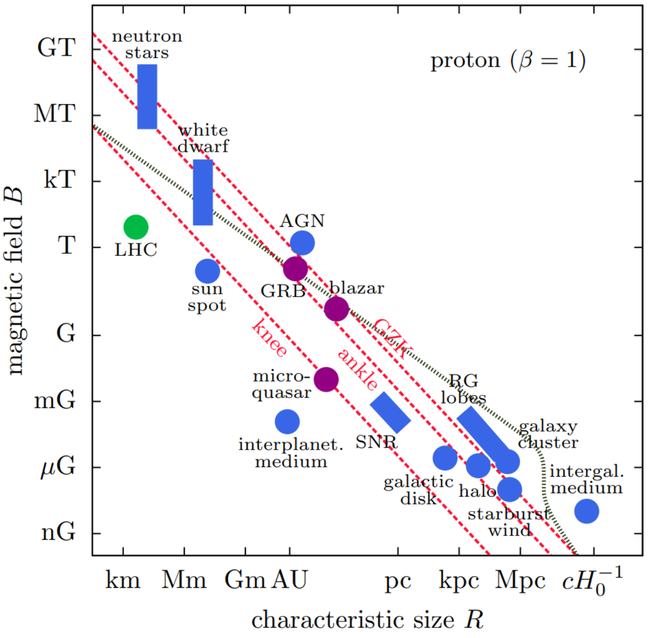

Figure 2.7: *Hillas diagram* displaying the possible astronomical accelerators according to their size and magnetic field strength. Red dashed lines mark the maximal energy a proton can be accelerated to at the energies of the knee, ankle and GZK (cf. Figure 2.5) as determined by the Hillas criterion 2.7. Picture from [30, Fig. 1].

size of the region R in which it accelerates, and it is given by the *Hillas criterion* [1, p. 235]:

$$E_{\text{max}} \simeq Z \cdot \frac{v}{c} \cdot \frac{B}{\mu\text{G}} \cdot \frac{R}{\text{kpc}} [\text{EeV}], \tag{2.7}$$

where v is the characteristic velocity of magnetic scattering centres and c the light speed. The Hillas criterion is derived by requiring that the particle's Larmor radius should not exceed the size of the acceleration region. Therefore, it only sets the minimal conditions for a potential CR source, which will be further constrained by additional requirements. Equation 2.7 is usually represented as a *Hillas plot* with possible known sources that can provide the energies observed from the CRs. Figure 2.7 presents such a diagram considering only protons ($Z = 1$). Here, the red dashed lines show the E_{max} corresponding to the energies of the knee, ankle, and GZK limit (compare Figure 2.5). If objects lie on the left side of the line, the source cannot accelerate the protons to the corresponding energy.

CRs with energies above the ankle are expected to be extragalactic, as their Larmor radius cannot be contained by the galaxy. One of the most luminous astronomical objects are active galactic nuclei (AGNs), which are considered a primary candidate for the acceleration of high-energy CRs [1, Sec. 9.10]. The nucleus of a galaxy consists of a supermassive black hole that attracts nearby matter, producing energy from the release of the gravitational potential energy. When the rate of accumulation of matter is high, the galactic nucleus is considered active. These objects are referred to as AGNs or sometimes as quasars (quasi-stellar objects). As the accretion rate stabilises, a disc of accreting material develops, and energy is released in the form of jets perpendicular to the spin axis. If the jet is pointing towards Earth, the AGN is known as a *blazar*. Blazars are among the most potent objects in the universe, and the primary component of extragalactic objects observed in high-energy gamma rays. They may also emit strong radio radiation, where the AGN is said to be *radio loud*,

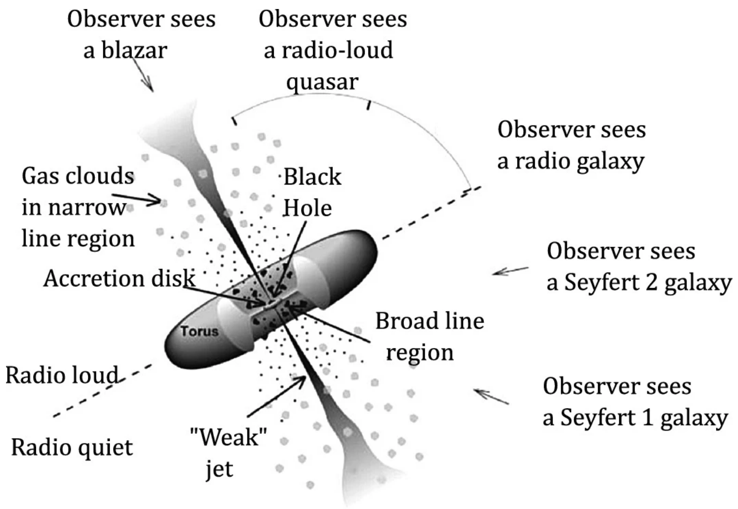

Figure 2.8: Sketch of different features of an active galactic nucleus (AGN). Our view angle determines what type of AGN is observed. Picture reused with publisher permission from [31, Fig. 8.5].

otherwise *radio quiet*. Under the *Unified AGN model*, several astronomical phenomena are classified as AGNs being viewed from different angles, such as Seyfert galaxies and radio galaxies (see Figure 2.8) [31, Sec. 8.2].

[31]: Horvath (2022), *Active Galactic Nuclei (AGNs)*

The IceCube neutrino observatory has provided evidence of two AGNs (one of them a blazar) being sources of high-energy neutrinos (see Section 3.3), supporting the hypothesis that AGNs are a significant source of high-energy CRs. The next section summarises the connection between CRs and other messengers, such as neutrinos.

2.2.2 Messenger relations and production mechanisms

CRs are believed to initiate the production of other messenger particles, such as gammas and neutrinos. This section summarises the mechanisms by which neutrinos and photons are produced from CR interactions. Because these particles are neutral, they can be traced back to their origin, making them useful for astronomical observations.

Production in astrophysical sources

In γ-astronomy, there are production models purely based on electron acceleration (*leptonic models*), which cannot solve the origin of CRs. Nevertheless, γ-particles can also be explained by proton acceleration (the *Hadronic model*), which is of interest for CR investigations and is a mechanism through which neutrinos can also be produced [32]. Figure 2.9 sketches the possible production mechanisms inside a jet.

Electrons in the presence of astrophysical magnetic fields will emit photons via synchroton radiation with a spectrum peaked at energies ranging from radio to X-rays. Leptonic models, such as the Synchroton Self-Compton (SSC) mechanism, describe the production of photons of higher energies. Here, the low-energy photons from the synchroton radiation gain energy through inverse Compton scattering with high-energy electrons. The spectrum of the produced γ-rays can peak at the range of GeV to TeV [1, Sec. 8.3].

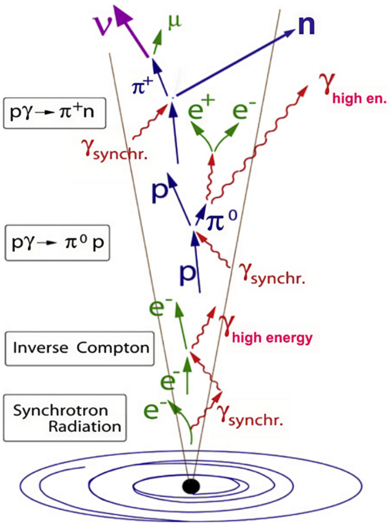

Figure 2.9: Production of γ-rays and neutrinos in a jet with electron and hadronic acceleration. Sketch from [32, p. 656].

[32]: Katz et al. (2012), *High-energy neutrino astrophysics: Status and perspectives*

In the hadronic model, the γ-particles are produced by accelerated protons or heavier nuclei. Proton-proton collisions can produce mesons via

$$p + p \longrightarrow \pi^{\pm}, \pi^{0}, K^{\pm}, \ldots \tag{2.8}$$

where higher mass mesons and baryons are also possible [1, Sec. 8.4]. In these high energy 'astrophysical beam-dump processes', almost the same amount of π^0, π^- and π^+ are produced.

[1]: Spurio (2018), *Probes of Multimessenger Astrophysics*

Another mechanism for the production of mesons is with 'photoproduction processes'. Here, CR protons interact with low-energy photons γ_ϵ produced by e.g. synchroton radiation of electrons. In this case, the mesons are products of the decay of a Δ^+ resonance:

$$\begin{aligned} p + \gamma_\epsilon \longrightarrow \Delta^+ &\longrightarrow \pi^0 + p\,, \\ &\longrightarrow \pi^+ + n\,, \end{aligned} \tag{2.9}$$

where the branching ratio for the decay to π^0 is approximately twice as large as π^+ [1, p. 357]. The kinematic threshold for this process is determined by the energy of the photon γ_ϵ, e.g. the proton needs several PeV to interact with photons in the UV region [32].

[32]: Katz et al. (2012), *High-energy neutrino astrophysics: Status and perspectives*

Neutral pions decay into γ-rays via

$$\pi^0 \longrightarrow \gamma + \gamma\,, \tag{2.10}$$

whereas the charged pions initiate the decay chain leading to neutrino emission

$$\begin{aligned} \pi^+ &\longrightarrow \nu_\mu + \mu^+ \\ &\qquad\qquad \hookrightarrow \mu^+ \longrightarrow e^+ + \nu_e + \overline{\nu}_\mu\,, \\ \pi^- &\longrightarrow \overline{\nu}_\mu + \mu^- \\ &\qquad\qquad \hookrightarrow \mu^- \longrightarrow e^- + \overline{\nu}_e + \nu_\mu\,. \end{aligned} \tag{2.11}$$

Thus, in beam-dump mechanisms there are six neutrinos for every two γ particles, while in photoproduction processes there are three neutrinos every four γ [1, p. 357]. As observed in Equation 2.11, the flavour composition $\nu_e : \nu_\mu : \nu_\tau$ of the produced neutrinos at the source is $1 : 2 : 0$ (without distinguishing between neutrino and antineutrinos). Since the size of astronomical sources is very large compared to the oscillation lengths, the terms with the X_{ij} in Equation 2.5 are averaged ($\sin^2 X_{ij} \longrightarrow 0.5$ and $\sin X_{ij} \longrightarrow 0$) leaving only the mixings. Thus, after the neutrino flux composition should become close to $1 : 1 : 1$ when it reaches Earth [33].

[33]: Pisanti (2019), *Astrophysical neutrinos: theory*

Cosmic ray interactions in the atmosphere

When CR particles collide with the upper layer of Earth's atmosphere, they interact with the nuclei of air molecules, initiating an air shower. This process can be seen in Figure 2.10. The air shower has a hadronic core, and the short-lived hadrons produced in this interaction decay and generate electromagnetic sub-showers made of photons, electrons, and positrons.

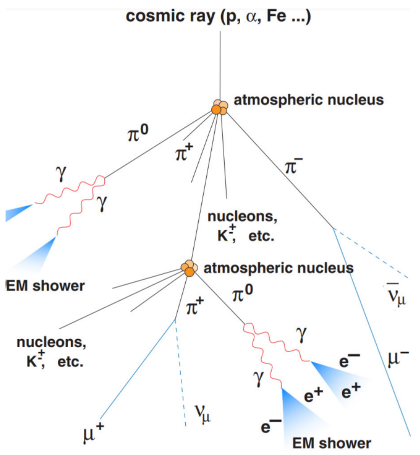

Figure 2.10: Sketch of an air shower produced by a CR interaction with the atmosphere. The blue cones represent electromagnetic showers. Image from [34, p. 44].

These sub-showers are primarily generated by the decay of $\pi^0 \longrightarrow 2\gamma$, where photons with energies above 20 MeV interact mainly through pair production, $\gamma \longrightarrow e^- + e^+$. Additionally, the charged mesons produced in the interaction lead to the production of muons and neutrinos (as described in Equation 2.11), which are the most penetrating components of the air shower [1].

In the two-body decays of $\pi^\pm$ and kaons, muons carry a larger fraction of the meson energy due to kinematics. The neutrinos produced in these decays, known as the *conventional atmospheric neutrino flux*, have energies ranging from a fraction of a GeV to approximately ~100 TeV and follow an approximate power law of $E^{-2.7}$ (see Figure 2.11) [1, p. 412].

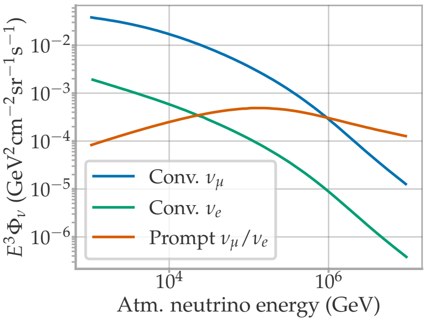

Figure 2.11: The predicted zenith-averaged neutrino flux, including both the conventional flux from π/K decays and the prompt flux from charmed meson decays. The data for this graph is taken from [35, Fig. 1], and the flux models used can be found in [36, 37].

At high energies, the decay of heavy and unstable charmed mesons, such as the $D^\pm$, is expected to occur. Due to the short lifetime of these particles, on the order of a picosecond, it is unlikely that they will reinteract before decaying. As a result, the energy spectrum of the prompt neutrinos produced in these decays is expected to follow that of the CRs up to an energy of 50 PeV. However, due to the small production cross section of charmed mesons in proton-nucleon interactions, it is expected that the contribution of D decays to the so-called *prompt flux* of neutrinos or muons will only be significant at very high energies. To date, the prompt flux of these particles has not been measured, and models that predict the normalisation of this flux vary widely [35].

[35]: van Santen (2015), *Probing Extraterrestrial Neutrino Fluxes and Atmospheric Charm with Contained Neutrino Events above 1 TeV in IceCube*

Cosmogenic neutrinos and gamma rays

As mentioned above, protons with ultra-high energy (UHE) above ~50 EeV are expected to interact with the cosmic microwave background (CMB), suppressing the observed CR flux [39]. This is a photoproduction process, the same as described in Equation 2.9, but with a higher threshold due to the small energy of CMB photons. Analogously as before, the pions from the Δ resonance will decay, producing neutrinos and γ-rays, which are called *cosmogenic*.

The theoretical scenarios that predict the flux of cosmogenic neutrinos and γ's depend on the composition and propagation of the UHE-CRs (see Figure 2.12). The production of cosmogenic particles is only efficient in the case of UHE protons, as UHE nuclei are expected to photo-disintegrate, losing one or more nucleons N via $A + \gamma \longrightarrow (A - nN) + nN$, where A is the atomic number of the UHE nucleus, γ a CMB photon or extragalactic background light. These interactions contribute negligently to the cosmogenic flux of neutrinos and γ-rays [40].

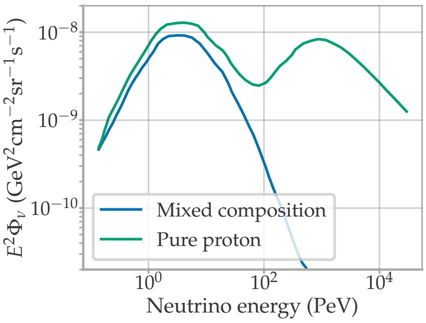

Figure 2.12: Predicted all-flavour cosmogenic neutrino flux for the case of mixed composition of UHE CR and UHE proton only. The data for this graph is taken from [38, Fig. 28].

[39]: Stanev (2014), *Cosmogenic neutrinos and gamma rays*

[40]: Ahlers et al. (2011), *Cosmogenic gamma-rays and the composition of cosmic rays*

The case for Neutrino Astronomy

Summarising this section, one of the main goals of neutrino and γ-ray astronomy is to understand the sources and mechanisms of CR acceleration. Being neutral messengers, they point back towards their sources, unlike CRs, which are deflected by magnetic fields.

Gamma rays are easier to detect due to their larger interaction cross section, but they can be produced through both hadronic processes, such as pion decay, and leptonic processes. On the other hand, neutrinos can only be produced through hadronic processes. Thus, they are a 'smoking gun' for hadronic acceleration and the source of CRs.

Moreover, the universe becomes opaque to γ-particles at high energies (see Figure 2.13). Here, the γ's interact with a low-energy photon (from the extragalactic background light, CMB or radio background) through the pair production process $\gamma\,\gamma \longrightarrow e^+\,e^-$, leading to a strong suppression of the high-energy γ flux [41].

This makes neutrinos, which can escape dense environments, a unique probe for studying the most powerful hadronic accelerators in the universe. However, it is important to note that neutrino and gamma-ray astronomy should not be viewed as competing fields. Instead, they have a complementary relationship. Following [42, Sec. 4.2], astronomical sources that are observed with high-energy gamma rays must be transparent to $\gamma\gamma$ absorption, making them unlikely to also produce neutrinos (opacity for $\gamma\gamma$ interaction is typically two orders of magnitude larger than for $p\gamma$ interaction, necessary for pion production). Conversely, sources of neutrinos are unlikely to be transparent to high-energy photons. Therefore, both high-energy gamma-ray and neutrino astronomy are crucial for understanding the nature of CR sources.

The next chapter delves into the methods and technology used in the study of neutrino astronomy, including the detection mechanism and current neutrino telescopes.

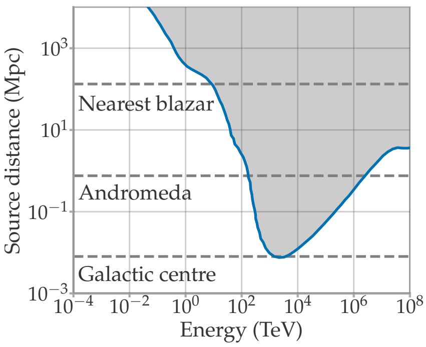

Figure 2.13: Opacity of the universe for γ-ray sources at varying energy levels. The blue line indicates a 1 % survival probability for γ rays, and sources that emit γ rays from the shaded region can be considered invisible (survival probability less than 1 %). Data sourced from [41, Fig. 1].

[41]: Angelis et al. (2013), *Transparency of the Universe to gamma rays*

[42]: Halzen (2022), *The observation of high-energy neutrinos from the cosmos: Lessons learned for multimessenger astronomy*

3

Large Volume Neutrino Telescopes

Early neutrino detectors, such as Kamiokande [43], used large shells containing the target volume (in the case of Kamiokande, with a target mass of 3 kiloton). This allowed, for example, the detection of a neutrino flux in the MeV energy regime from the sun [44] and supernova SN1987a [45]. Nevertheless, for higher neutrino energies, much larger volumes are necessary to measure a significant rate of these particles. For neutrinos in the GeV energy regime, a target mass of around one Megaton is necessary, while a Gigaton is needed for the TeV neutrino energies [46]. Since building such large artificial volumes is not feasible, neutrino telescopes use natural accumulations of water or ice. The operation principle of such detectors is introduced in Section 3.1.

[43]: Ikeda et al. (1982), *The Kamioka Proton Decay Experiment*

[44]: Hirata et al. (1989), *Observation of* ^{8}B *solar neutrinos in the Kamiokande-II detector*

[45]: Hirata et al. (1987), *Observation of a neutrino burst from the supernova SN1987A*

[46]: Anton (2020), *Neutrino Telescopes*

The pioneering project for a neutrino telescope was **DUMAND**[1] [47]. It started in 1975 as a series of workshops culminating in 1978 in a design envisioning a cubic kilometre instrumented volume close to Hawaii. Due to financial and technical issues, the project was officially terminated in 1996 [48]. Nevertheless, deployment tests and expertise gained in this period laid the groundwork for the first generation of neutrino telescopes in Russia, the Mediterranean Sea and at the South Pole. These are introduced in Section 3.2, including their expansion to the second generation of neutrino telescopes. Since this thesis focuses on IceCube, this experiment is explained in more detail in Section 3.3.

[1] **D**eep **U**nderwater **M**uon **A**nd **N**eutrino **D**etector

[47]: Roberts (1979), *Weak-interaction studies with the DUMAND detector*

[48]: Spiering (2012), *Towards high-energy neutrino astronomy*

This chapter provides only a partial overview of the dynamic and rapidly expanding field of neutrino research. Currently, several projects are underway, such as P-ONE, a km^3-scale neutrino telescope planned for the Pacific Ocean, with already two successful pathfinder missions completed [49]. Also worth mentioning is TRIDENT [50], envisioned as a ~7.5 km^3 instrumented volume in the South China Sea.

[49]: Resconi (2021), *The Pacific Ocean Neutrino Experiment*

[50]: Ye et al. (2022), *Proposal for a neutrino telescope in South China Sea*

3.1 OPERATION PRINCIPLE

Neutrinos cannot be detected directly because they only interact through the weak and gravitational force. However, as introduced in Section 2.1.2, when high-energy neutrinos interact with matter, they can produce charged particles that can be detected through various techniques. The most widespread method is the detection of photons emitted by these secondaries via the Cherenkov effect. This process is the basis for detecting neutrinos in large-volume neutrino telescopes introduced in Section 3.2 and Section 3.3.

When charged particles move through a dielectric medium, their electric field causes the medium to become polarised. Electromagnetic wavelets are produced as the electrons return to their normal position. If the charged particle is slower than the phase velocity of this radiation, the emission interferes destructively. However, if the particle is faster than the light in the medium, the wavelets overlap constructively in phase forming a wavefront, causing coherent photon emission. This effect is called the Cherenkov effect, after Pavel Cherenkov, the first to detect the radiation experimentally in 1934 [51]. A schematic of this process is illustrated in Figure 3.1.

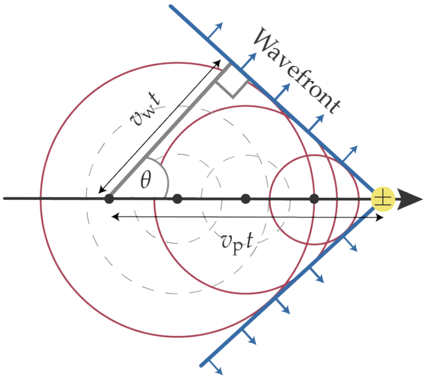

Figure 3.1: Schematic of the production of a Cherenkov wavefront. During the time interval t, photons move a distance $v_{\mathrm{w}}t$ while the charged particle (±) travels further, with $v_{\mathrm{p}} > v_{\mathrm{w}}$.

[51]: Jennings (1962), *Čerenkov Radiation*

The Cherenkov radiation is released in the form of a cone with an opening angle θ with respect to the particle trajectory. As shown in Figure 3.1, this angle can be calculated with simple trigonometry. With the velocity of the wavefront $v_{\mathrm{w}} = c/n$, which depends on the refractive index of the medium n, and the velocity of the charged particle v_{p}, it follows that:

$$\cos(\theta) = \frac{v_{\mathrm{w}}t}{v_{\mathrm{p}}t} = \frac{1}{\beta n},$$

with $\beta = \frac{v_{\mathrm{p}}}{c}$ [51].

The first theoretical description based on Maxwell's equations was derived 1937 by I. Tamm and I. Frank [52]. The number of photons of a certain wavelength λ can be approximated by the Frank-Tamm formula [52]

[52]: Frank et al. (1991), *Coherent Visible Radiation of Fast Electrons Passing Through Matter*

$$\frac{dN}{d\lambda} = \frac{2\pi\alpha}{\lambda^2}\left(1 - \frac{1}{\beta^2 n(\lambda)^2}\right)\Delta x,$$

where $\alpha \approx 1/137$ is the fine structure constant and Δx the distance travelled by the charged particle. The emission spectrum is, in first order, proportional to λ^{-2} with a further small dependence on λ from the variation of the refractive index of the medium $n(\lambda)$.

In large neutrino telescopes, the emitted Cherenkov photons are measured by optical modules (OMs); pressure vessel housings containing one or several photomultipliers (PMTs). PMTs are optical detectors capable of measuring down to single photons with a time resolution of a few nanoseconds. These devices are introduced in detail in Chapter 5. Hundreds of modules are deployed in several vertical strings, forming an optical array. The instrumentation density is optimised depending on the neutrino energy range to be measured.

The reconstruction of neutrino interactions is based exclusively on the number of photons detected in different modules along the path of the secondary charged particles and their time distribution. In contrast to smaller but densely instrumented neutrino detectors, such as Kamiokande, the Cherenkov cone cannot be resolved in neutrino observatories and the neutrino flavour, direction and energy have to be deduced by other means. Nonetheless, light patterns across the detector can be identified and used to reconstruct the charged particles' properties, such as energy and direction, and also determine the neutrino flavour of some of the events. The three (high-energy) neutrino interaction signatures that can be identified are presented in Figure 3.2.

In both NC and CC interactions, the light signatures start as a spherical pattern at the vertex of the interaction, where a hadronic shower takes place, originating from the remnants of the nucleon the neutrino interacted with. The released electron (positron) in ν_e ($\overline{\nu}_e$) CC-interactions induce an electromagnetic shower comprising bremsstrahlung photons and secondary electron-positron pairs over a short distance (a few metres). In the large scale of a neutrino telescope, the light signature will resemble a point-source and cannot be distinguished from the signature of the initial hadronic shower. Such light signatures are called **cascades** (see the top picture of Figure 3.2).

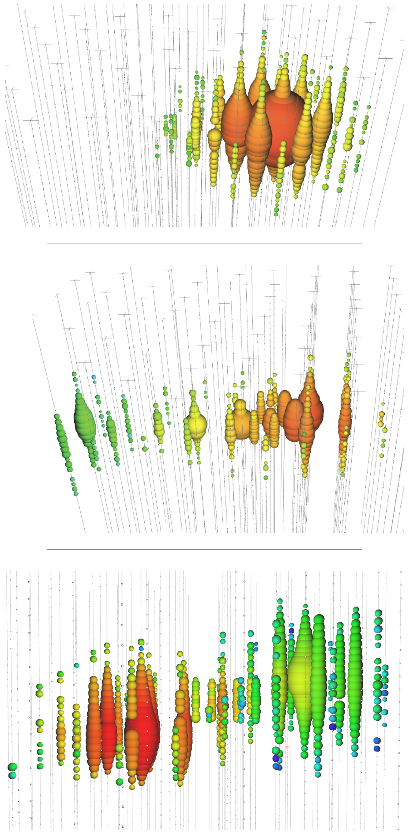

Figure 3.2: Light deposition signatures of cascades (top), tracks (middle) and double-bang events (bottom). The colour indicates the light detection time from early to late in red to blue. The size of the spheres illustrates the number of detected photons in a module. Figures courtesy of the IceCube collaboration.

The deposited energy in cascades can be well reconstructed, particularly in those events that are completely contained within the instrumented volume. However, as interactions through NC, CC of ν_e ($\overline{\nu}_e$) and, as will be explained later, most CC of ν_τ ($\overline{\nu}_\tau$) cannot be distinguished, the neutrino energy can only be estimated assuming a particle hypothesis from an expected flux. Moreover, due to its quasi-spherical shape, the angular resolution for such events can be very limited, depending on the energy and medium [53].

[53]: Katori et al. (2021), *Neutrino interaction physics in neutrino telescopes*

Muons from ν_μ ($\overline{\nu}_\mu$) CC-interactions with energies E_μ above tens of GeVs can travel very long distances before stopping, and thus produce a signature similar to a **track** (see the central picture of Figure 3.2). This allows for a very precise directional reconstruction with a sub-1° resolution for energies above 1 TeV [53]. Thus, this signature is key for searches of astrophysical neutrino point-sources.

The interaction vertex must be fully contained inside the detector to derive the initial muon energy accurately. Since this is usually not the case, a lower limit of the energy is calculated based on the differential energy loss of the muon dE_μ/dx. The average dE_μ/dx of muons in ice is shown in Figure 3.3. At energies E_μ >1 TeV, muons lose their energy mainly through stochastic processes (pair production, bremsstrahlung, and photonuclear effects), producing electromagnetic showers along its path. As in this energy range, dE_μ/dx increases linearly with E_μ, the energy can be calculated directly from the measured dE_μ/dx [54]. Muons in the GeV range lose their energy primarily by ionisation and dE_μ/dx is nearly constant, making an energy reconstruction of such unconfined muons impossible [55].

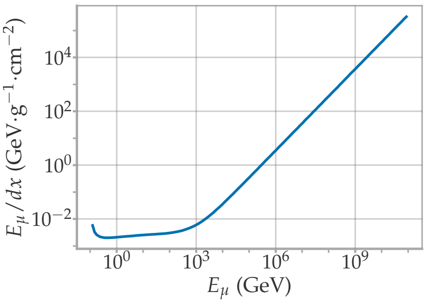

Figure 3.3: Average total energy loss of muons in ice. Data from [54].

[55]: Abbasi et al. (2013), *An improved method for measuring muon energy using the truncated mean of dE/dx*

Tau neutrinos in a charged current interaction emit a tau together with a hadronic shower. Taus have a short lifetime (~0.3 ps [46]) and will travel a small distance before decaying. In 83 % of the cases [56], it decays into an electron or quark-antiquark pair, producing a second cascade. As the spherical light emission is produced in both, the hadronic cascade at the vertex of the interaction and the one originating from the electrons/mesons, the signature can be understood as a superposition of two cascades. As the average decay length of the tau scales roughly as 5 cm/TeV, the two cascades can only be separated if the tau has a large initial energy (above few hundred TeV) [56]. Such a signature is called a **double-bang** (see the bottom picture of Figure 3.2). There is a 17 % chance that the tau will decay into a muon, producing a track and not the double-bang signature.

[56]: Aartsen et al. (2016), *Search for Astrophysical Tau Neutrinos in Three Years of IceCube Data*

Radio neutrino detection

Characterising the extremely low flux of neutrinos at the highest energies (EeV) using optical arrays would require a detector volume that is orders of magnitude larger than the largest current detector, IceCube. However, radio detectors, such as ANITA [57], RICE [58], ARA [59] and ARIANNA [60], are capable of detecting electromagnetic showers emerging from these interactions. Next-generation neutrino telescopes, such as IceCube-Gen2 [61], are planned to be based on both approaches, measuring radio and optical signatures.

Radio neutrino detection is founded on the Askaryan effect. It was postulated by Gurgen Askaryan in [62] and it is based on the Cherenkov effect. It describes the coherent emission of radiowaves from hadronic or electromagnetic showers in a dielectric medium. This is caused by an excess of electrons in the cascade. In high-energy cascades, additional electrons are released from the medium due to Compton scattering, whereas positrons from the shower annihilate during propagation. This leads to a surplus in net negative charge of 20%-30% for the particles that carry most of the shower energy [63]. The wavelength range for coherent emission depends on the dimensions of the excess charge cluster, following a proportionality of λ^2 for wavelengths λ larger than the cluster size [62]. For shorter wavelengths, the radiation interferes destructively. This effect was first observed in 2000 at a SLAC experiment [63], and in 2006, the first measurement of the effect in ice was reported [64].

The coherent emission produces a broad-band bipolar radio signal with a duration in the nanosecond range. The signal is the strongest at the Cherenkov angle but loses coherence at departing angles. The amplitude of the signal scales linearly with the energy of the shower. The signal from shower energies above a few PeV can surpass the thermal noise floor, but the exact threshold depends on the trigger and gain of the antenna. To reconstruct the energy of the shower, it is important to calculate the location of the shower vertex, as the amplitude of the radio signal drops following $1/r$, with r the distance to the vertex. Therefore, analogous to the optical array, several radio antennas are necessary in order to triangulate the neutrino interaction [65]. The resolution to the neutrino direction is of a few degrees and systematically depends on the uncertainty of the reconstructed signal direction, view angle and polarisation [66].

Since the radio emission is generated by electromagnetic showers and the electromagnetic component of hadronic showers, a radio detector is sensitive to all neutrino flavours.

[57]: Gorham et al. (2009), *The Antarctic Impulsive Transient Antenna ultra-high energy neutrino detector: Design, performance, and sensitivity for the 2006–2007 balloon flight*

[58]: Kravchenko et al. (2012), *Updated Results from the RICE Experiment and Future Prospects for Ultra-High Energy Neutrino Detection at the South Pole*

[59]: Allison et al. (2016), *Performance of two Askaryan Radio Array stations and first results in the search for ultrahigh energy neutrinos*

[60]: Barwick et al. (2015), *A first search for cosmogenic neutrinos with the ARIANNA Hexagonal Radio Array*

[61]: Aartsen et al. (2014), *IceCube-Gen2: A Vision for the Future of Neutrino Astronomy in Antarctica*

[62]: Askaryan (1961), *Excess Negative Charge of an Electron-Photon Shower and Its Coherent Radio Emission*

[63]: Saltzberg et al. (2001), *Observation of the Askaryan Effect: Coherent Microwave Cherenkov Emission from Charge Asymmetry in High-Energy Particle Cascades*

[64]: Gorham et al. (2007), *Observations of the Askaryan effect in ice*

[65]: Aguilar et al. (2021), *Design and Sensitivity of the Radio Neutrino Observatory in Greenland (RNO-G)*

[66]: Glaser (2019), *Neutrino direction and energy resolution of Askaryan detectors*

3.2 LANDSCAPE OF LARGE NEUTRINO TELESCOPES

In this section, the first successful neutrino telescopes are briefly described together with their successors. These are located at three different sites: in the Baikal lake in Russia, in the Mediterranean Sea and at the South Pole, and are introduced in Section 3.2.1, 3.2.2 and 3.2.3, respectively.

3.2.1 NT200+ and Baikal-GVD

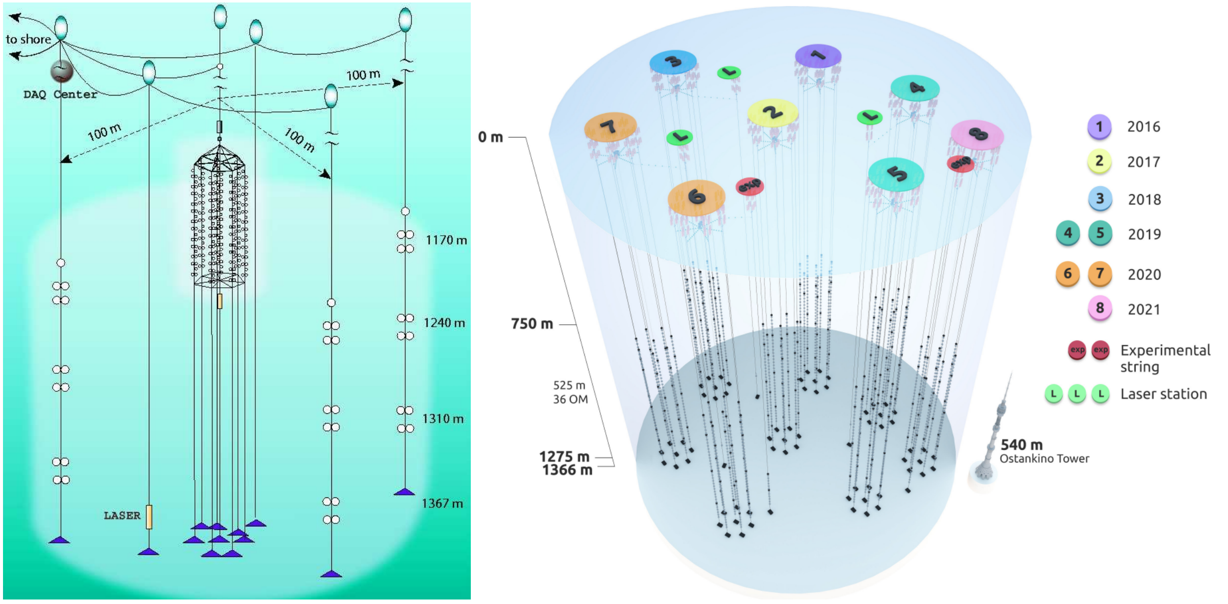

Figure 3.4: *Left:* Schematic view of the Baikal Telescope NT200+. Figure from [67]. *Right:* The current layout of Baikal-GVD. The deployment year of each cluster is given in the legend. The Ostankino Tower is depicted as scale. Taken from [68].

The Baikal **NT200** detector [67], completed in 1998, was the first neutrino observatory to be put into operation. It was located 3.6 km offshore the southern basin of Lake Baikal, Russia, and it consisted of a heptagonal array of 8 strings with 24 optical modules anchored at a depth of ~1367 m. The optical modules contained a QUASAR-370 PMT of 37 cm photocathode diameter and were positioned and operated in pairs in order to reduce the background caused by bioluminescence[2] [69]. With a vertical distance of 6.25 m between OM pairs, the spacing led to a comparably low energy threshold of ~15 GeV. The detector was upgraded to NT200+ in 2005 with three new strings [67] with a larger but sparser instrumentation in order to increase the sensitivity to high-energy neutrinos. The layout of NT200+ is shown on the left side of Figure 3.4.

[67]: Aynutdinov et al. (2006), *The BAIKAL neutrino experiment: From NT200 to NT200+*

[2] From a per PMT signal rate of ~ $10^5\,\mathrm{s}^{-1}$, the coincidence condition reduces the rate to 100-300 s^{-1} per OM pair.

[69]: Bagduev et al. (1999), *The Optical module of the Baikal deep underwater neutrino telescope*

The NT200 detector reported the first atmospheric neutrinos detected underwater [70] and served as a proof of concept for the neutrino observatories. With the expertise gained, the Baikal Collaboration started 2016 the construction of a km^3 scale observatory, **Baikal-GVD**[3] [68]. It consists of several clusters of 8 strings, each string equipped with 36 OMs with a vertical spacing of 15 m. The strings in a cluster are grouped forming a heptagon with an average horizontal inter-string distance of 60 m. The optical modules contain a single 24 cm PMT with enhanced sensitivity[4] [71]. Since Baikal-GVD aims to detect high-energy neutrinos, the instrumentation is sparser than in NT200 and the OM pair design was dropped.

[70]: Balkanov et al. (1998), *The Baikal deep Underwater Neutrino Experiment: Results, status, future*

[3] **G**igaton **V**olume **D**etector

[68]: Belolaptikov et al. (2021), *Neutrino Telescope in Lake Baikal: Present and Nearest Future*

[4] Hamamatsu R7081-100 with peak quantum efficiency of 35 %.

[71]: Avrorin et al. (2016), *The optical module of Baikal-GVD*

Each cluster is routed to the shore station independently and can be considered as a stand-alone detector. The effective volume of a GVD cluster for shower signatures is $0.05\,\mathrm{km}^3$. As of December 2021, the detector consists of eight clusters, amounting to a total effective volume of $0.4\,\mathrm{km}^3$, making the Baikal GVD detector the second-largest neutrino observatory and the largest in the Northern Hemisphere [68]. The current layout is presented on the right side of Figure 3.4. The second stage, GVD-II, anticipates six additional clusters between the years 2023 to 2024. With the current detector arrangement, upgoing track-like neutrino events have been observed [72] as well as several high-energy cascades neutrino candidates, including a 1.2 PeV event [73].

[72]: Zaborov et al. (2021), *Observations of track-like neutrino events with Baikal-GVD*

[73]: Dzhilkibaev et al. (2021), *The Baikal-GVD neutrino telescope: search for high-energy cascades*

3.2.2 ANTARES and KM3NeT

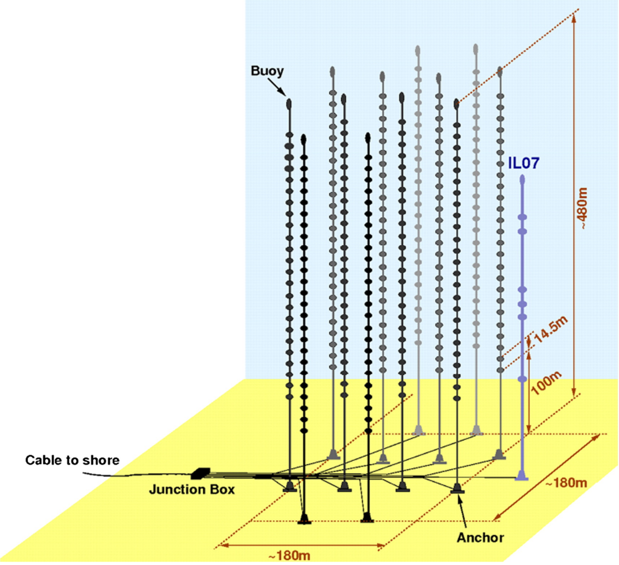

Figure 3.5: Layout of the ANTARES detector. Black lines represent the strings and the dots the location of the storeys. IL07 stands for instrumented line, which supports sensors for environmental measurements. Figure taken from [74].

The first successfully built deep-sea neutrino detector was **ANTARES**[5]. Completed in May 2008, the observatory was located 40 km offshore the city of Toulon, France, at a depth of 2475 m. It consisted of 12 strings, each with 25 *storeys* spaced vertically in 14.5 m intervals (see Figure 3.5). A storey was a frame supporting three optical modules, as illustrated in Figure 3.6. Each optical module was instrumented with a 24 cm hemispherical PMT[6]. The digitised data from all strings were sent to the shore station via optical fibres. The total instrumented volume amounted to ~0.1 km^3 [74].

Due to the sea currents, the position of the OMs constantly changed and it was monitored using triangulation with an acoustic positioning system, whereas their orientation was calibrated with a compass and tiltmeter inside the stories.

The ANTARES detector provided data for a large number of scientific publications, such as setting upper limits on the diffuse neutrino flux from galactic and cosmic origin, as well as measuring neutrino mixing parameters compatible with other experiments [76–78]. The success of this detector, being the first operational neutrino telescope in saltwater, produced the required expertise and grounded the first steps for its successor, **KM3NeT**[7].

The KM3NeT observatory is currently being built in two different sites and in its final form will comprise three *building blocks* of 115 strings (also known as detection units, DU), each DU instrumented with 18 optical modules. In the site located 100 km offshore Portopalo di Capo

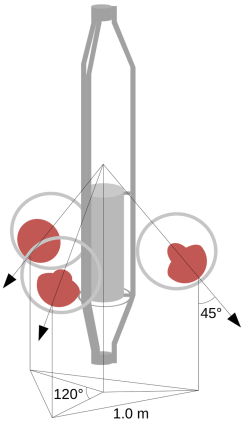

Figure 3.6: Schematic of a single storey in the ANTARES detector. Three optical modules (gray circles) containing a PMT each (red), facing 45° downward. Image from [75].

[5] **A**stronomy with a **N**eutrino **T**elescope and **A**byss environmental **RES**earch

[6] Hamamatsu R7081-20.

[74]: Ageron et al. (2011), *ANTARES: The first undersea neutrino telescope*

[7] Cubic Kilometre Neutrino Telescope

[8] **A**stroparticle **R**esearch with **C**osmics in the **A**byss

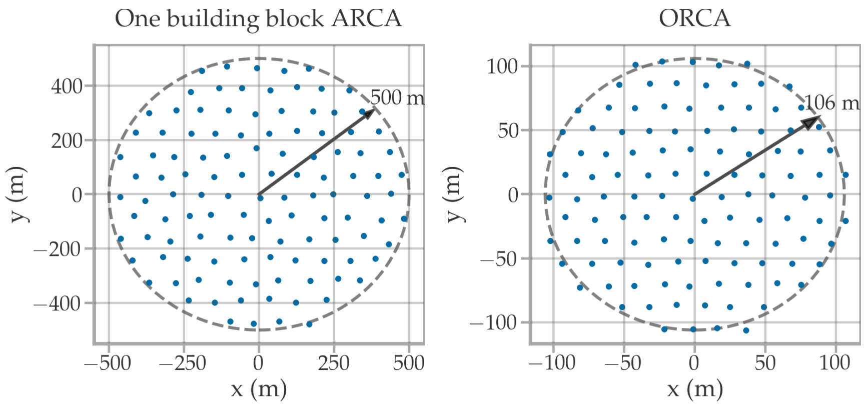

Figure 3.7: Footprint of one building block of the ARCA detector (left) and the ORCA detector (right). Layout from [79].

Passero, Sicily, Italy, the **ARCA**[8] detector will be anchored at a depth of 3500 m. It comprises two building blocks with a vertical inter-module distance of 36 m and an average horizontal inter-string spacing of 95 m (see left side of Figure 3.7). This geometry is intended to measure the high-energy neutrino spectrum from GeV to PeV. As of January 2023, ARCA is operational with 21 such DUs. After completion, each block will instrument a cylindrical volume of radius of ~500 m, yielding a total instrumented volume of ~1 km^3 [79].

At the French installation site, 10 km west of the ANTARES detector, the **ORCA**[9] array is being deployed. This will be the low-energy detector intended for oscillation studies with atmospheric neutrinos. It will consist of a single detector block of 115 strings, but with dense instrumentation optimised for the detection of GeV neutrinos. The inter-module vertical spacing is 9 m and the average inter-string distance 20 m [79] (see right side of Figure 3.7). Currently, 15 ORCA-DUs have been installed and are operating.

Both detectors are based on the same technology. One of its novelties is the optical module, with a *multi-PMT* design. It consists of a 43 cm spherical pressure vessel containing 31 PMTs of 80 mm diameter[10] and respective electronics [81]. A picture of the KM3NeT OM is presented in Figure 3.8. This pioneering design inspired several multi-PMT designs, such as the module covered in this thesis (see Chapter 4).

[79]: Adrian-Martinez et al. (2016), *Letter of intent for KM3NeT 2.0*

Figure 3.8: Side-view of an optical module of KM3NeT. Picture from [80].

[9] **O**scillation **R**esearch with **C**osmics in the **A**byss

[10] Hamamatsu PMT R12199-02 [81].

[81]: Aiello et al. (2022), *The KM3NeT multi-PMT optical module*

3.2.3 AMANDA

Located at the South Pole, **AMANDA**[11] was completed in 2000. The first installation consisted of four strings with 20 OMs each at depths between 800 and 1000 m. The high content on bubbles of the ice resulted in a very short scattering length, making track reconstruction impossible [48]. The detector was upgraded consecutively deploying in deeper ice, which is bubble-free, resulting in a total of 19 strings with 677 OMs, most at depths between 1.5 and 2 km [82]. Figure 3.9 shows the layout of the completed AMANDA detector.

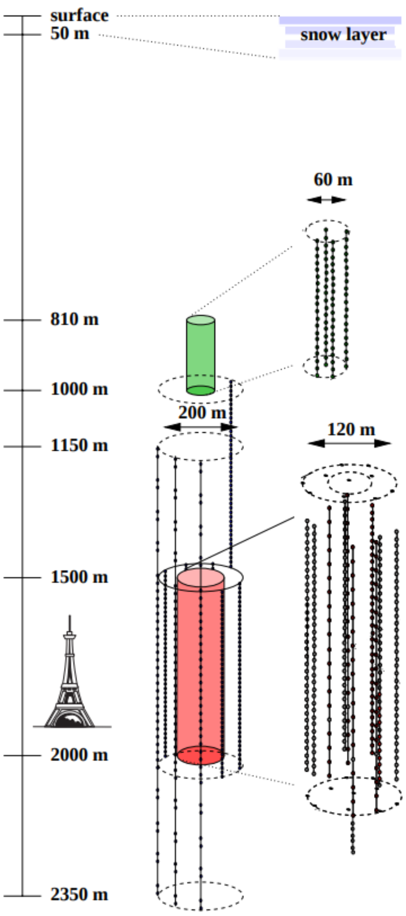

Figure 3.9: Schematic view of the AMANDA detector. The Eiffel Tower is depicted as scale. Image taken from [82] and modified.

Each optical module contains a single 20 cm PMT,[12] which were capable of producing signals of large amplitudes.[13] This was necessary since the analogue signal from the modules was directly sent to the surface without in-situ digitisation. Using analogue signals was only possible due to the short length of the cables, 2 km, compared to the much longer site-to-shore distances required in water-based observatories.

AMANDA was switched off in 2009 after a large portion of its successor, IceCube, was deployed. Nevertheless, during its running years it measured over 6500 high-energy neutrinos from the Northern Hemisphere [83], providing the best limits on the cosmic neutrino flux at the time [84] and extending the measured atmospheric neutrino spectrum by almost two orders of magnitudes [85]. This and the pioneering work from the technical point of view made the construction of IceCube possible, which is described in the following section.

3.3 IceCube Neutrino Observatory

IceCube was completed in 2011 and is the first kilometre-scale neutrino detector. It is located at the South Pole at 1 km distance from the Amundsen-Scott Station. It consists of an in-ice detector for measuring astrophysical neutrinos and an air shower array, *IceTop*. A sketch of the observatory is shown in Figure 3.10.

The interaction medium for neutrinos is the glacial ice and the Cherenkov radiation is measured by 5160 digital optical modules (DOMs) placed between 1450 m and 2450 m below the surface. These are distributed over 86 strings, 78 of which are spaced 125 m apart in a hexagonal pattern, resulting in a detector area of ~1 km^2. The vertical spacing between the optical modules in these strings is 17 m. This geometry is optimised for the study of neutrinos in the energy range from 100 GeV to $\mathcal{O}$(PeV). At the centre of the detector there are eight additional strings, spaced on average about 72 m apart (horizontally). The modules are deployed at depths ranging from 2100 m to 2450 m with a vertical separation between sensors of only 7 m. This subdetector is called *DeepCore* and extends the lower energy threshold down to ~6 GeV. This allows the study of oscillations with atmospheric neutrinos [2].

An image of a DOM is presented in Figure 3.11. It consists of a 24 cm Hamamatsu photomultiplier tube and electronics in a glass pressure vessel of 33 cm diameter. A gel layer acts as an optical coupler and holds

[11] **A**ntarctic **M**uon **A**nd **N**eutrino **D**etection **A**rray.

[82]: Kowalski et al. (2001), *Physics results from the AMANDA neutrino detector*

[12] Hamamatsu R5912-2.

[13] PMTs were driven at a gain of 10^9, three orders of magnitude larger than currently used in most neutrino telescopes.

[83]: Abbasi et al. (2009), *Search for point sources of high energy neutrinos with final data from AMANDA-II*

[84]: Bernardini (2006), *AMANDA: Selected physics results*

[85]: Abbasi et al. (2009), *Determination of the atmospheric neutrino flux and searches for new physics with AMANDA-II*

[2]: Aartsen et al. (2017), *The IceCube Neutrino Observatory: Instrumentation and Online Systems*

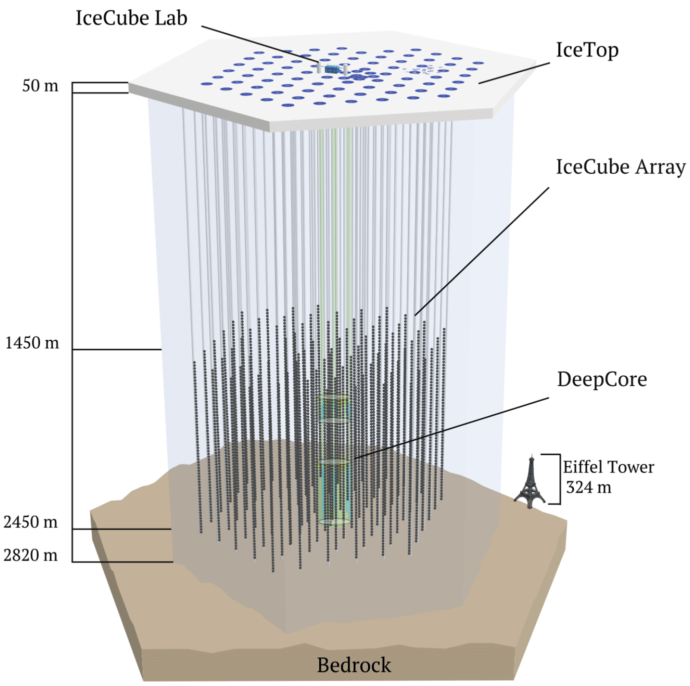

Figure 3.10: Layout of the IceCube observatory infrastructure at South Pole. The lines represent the strings and the dots represent the optical modules. The circles on the surface mark the position of the strings, which correspond to the position of the IceTop stations. The Eiffel Tower is shown to scale. Illustration courtesy of the IceCube Collaboration.

the PMT in position. Surrounding the PMT is a mu-metal grid that shields the PMT from the Earth's magnetic field. Data acquisition, digitisation, and triggering are done individually inside each DOM and sent via copper wire pairs to the surface to the IceCube Central Laboratory (ICL). All these functions are controlled by a Field Programmable Gate Array (FPGA) on the DOM mainboard. The timing is controlled by the mainboard oscillator that is calibrated with the ICL master clock regularly. Furthermore, each DOM is equipped with a flasher board comprising 12 LEDs. They are used to calibrate neighbouring DOMs, investigate ice properties, and simulate physical events [86].

[86]: Abbasi et al. (2009), *The IceCube Data Acquisition System: Signal Capture, Digitization, and Timestamping*

IceTop consists of 81 water stations near the location of each string [87]. Each station features two tanks filled with ice and equipped with two standard IceCube DOMs. It is capable of measuring cosmic rays in the energy region of 300 TeV to 1 EeV. It is also used as a veto against atmospheric neutrinos.

Figure 3.11: Photo of an assembled IceCube DOM. Picture courtesy of the IceCube Collaboration.

[87]: Abbasi et al. (2013), *IceTop: The surface component of IceCube*

Ice as interaction and propagation medium

Because event reconstructions are based on the measurement of Cherenkov photons produced from secondary particles, knowledge of the optical properties of glacial ice through which they propagate is crucial.

Glacial ice has several unique properties, resulting in advantages and drawbacks compared to other mediums, such as marine water. Whereas in water-based observatories the optical noise is significant, due to bioluminescence and K^{40} decays in saltwater, the deep ice is basically free of optical background. This makes for 'cleaner' neutrino events and allows for a lower detection threshold for rate-bursts expected after near Supernovae. Furthermore, the ice is very transparent but features a larger scattering cross section for photons due to the dust and bubbles frozen in the glacier [46]. In this context, one of the major sources of

[46]: Anton (2020), *Neutrino Telescopes*

systematic uncertainties for reconstructing high-energy cascades has been the modelling of optical properties of the bulk ice, which change with depth [5].

Over the years, the optical properties of the natural glacier were studied thoroughly with different calibration methods. The first studies in AMANDA and further calibration with IceCube LED calibration system allowed the determination of the average optical properties in 10 m-thick ice layers, in the form of a table of absorption and effective scattering coefficients for the entire instrumented depth, as described in [88] and [89]. The absorption and scattering lengths are strongly depth-dependent due to the cyclic change in climate conditions which directly affects the dust concentration in the ice. An introduction to the connection between the climate cycle changes, ice impurities and ice sheet dynamics in IceCube can be found in [90].

In the LED calibration runs, a DOM is operated in *flasher* mode, which emits light from its built-in LEDs. The neighbouring DOMs act as *observers*, measuring the light intensity over a period of time. In such calibration runs it was noticed that the ice at the South Pole exhibits an anisotropy in light propagation, where observer DOMs along the *flow* axis measure about twice as much light than on the *orthogonal* axis. The flow axis is the direction in which the ice flows[14].

The anisotropy could be modelled by simulations assuming a birefringent polycrystalline microstructure of the ice. This model can be optimised by adjusting the average orientation, size, and shape of ice crystals, achieving a relatively good agreement between data and Monte Carlo (MC) simulations [91].

An extra absorption anisotropy was added to this ice model, with which a near-perfect data-MC agreement was obtained, as can be seen in Figure 3.12. Nevertheless, adding this absorption anisotropy meant a departure from the first-principle model of birefringence alone [91] and this term still needs to be fully understood.

Another ice feature worth mentioning is the so-called *bubble column*. During deployment, when the boreholes refreeze (from the outside to the inside of the hole), bubbles and dust particles are grouped in the centre, forming the ‘bubble column’. This is a source of photon scattering, but the scattering length of the column remains unknown. In the reconstruction of low-energy events, this produces a significant systematic uncertainty [5].

Selected latest IceCube results

IceCube has been a very successful detector with publications on a wide range of research topics. In less than two years of effective live time with the full detector, IceCube detected the first high-energy astrophysical neutrinos [3] and since then characterised the astrophysical ν_μ-flux [92] and ν_e-ν_τ-flux [93]. In the following, a handful of the latest IceCube results are highlighted.

[5]: Ishihara et al. (2019), *The IceCube Upgrade - Design and Science Goals*

[88]: Ackermann et al. (2006), *Optical properties of deep glacial ice at the South Pole*

[89]: Aartsen et al. (2013), *Measurement of South Pole ice transparency with the IceCube LED calibration system*

[90]: Rongen (2019), *Calibration of the IceCube neutrino observatory*

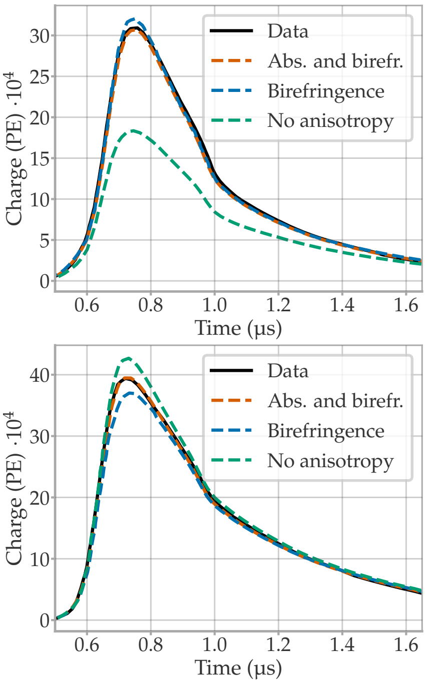

Figure 3.12: Comparison between the simulation results of different ice models and data. The curves are the combined photon detection time distribution for DOM pairs in a string along the flow axis (*top*) and perpendicular to the flow axis (*bottom*). Data taken from [91].

[91]: Rongen et al. (2021), *A novel microstructure based model to explain the IceCube ice anisotropy*

[3]: Aartsen et al. (2013), *First observation of PeV-energy neutrinos with IceCube*

[92]: Abbasi et al. (2022), *Improved Characterization of the Astrophysical Muon–neutrino Flux with 9.5 Years of IceCube Data*

[93]: Aartsen et al. (2020), *Characteristics of the diffuse astrophysical electron and tau neutrino flux with six years of IceCube high energy cascade data*

[14] The ice moves at a rate of ~10 m/year in the direction grid NW [90].

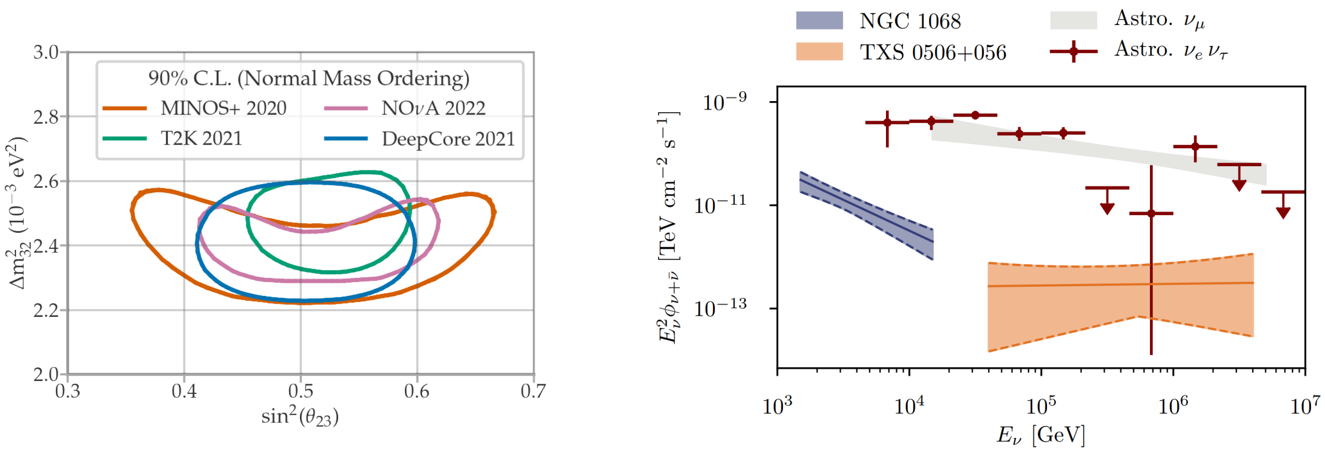

Figure 3.13: *Left:* The 90 % allowed region in the Δm^2_{32}-$\sin^2(\theta_{23})$-space compared to results of dedicated long-baseline accelerator experiments. Data from [94–97]. *Right:* Neutrino flux of TXS 0506+056, NGC 1068 and total flux measured by IceCube. The shaded regions indicate the 68 % confidence interval and the downward arrows are 68 % upper limits. Figure from [4].

Neutrino oscillations: Analyses using ν_μ-disappearance in DeepCore's atmospheric neutrino data have measured oscillation parameters with high precision. The last published best fits are $\Delta m^2_{32} = 2.31^{+0.11}_{-0.13} 10^{-3}\,\mathrm{eV}^2$ and $\sin^2(\theta_{23}) = 0.51^{+0.07}_{-0.09}$ (assuming normal neutrino mass ordering) [98]. Nevertheless, with the neutrino data set continuously expanding and new analysis techniques, the sensitivity to these parameters is constantly improving. The current allowed region in the Δm^2_{32}-$\sin^2(\theta_{23})$-space is presented on the left side of Figure 3.13, which is similar in size to those from dedicated experiments [99]. However, DeepCore probes neutrinos from longer distances and higher energies than those generated in accelerator experiments. Thus, the results are subject to different systematic uncertainties and provide a complementary measurement [98].

[98]: Aartsen et al. (2018), *Measurement of Atmospheric Neutrino Oscillations at 6–56 GeV with IceCube DeepCore*

[99]: Leonard DeHolton (2022), *Atmospheric Neutrino Oscillations with 8 years of data from IceCube DeepCore*

First cosmic ν_τ candidates: As introduced in Section 3.1, a double-bang signature produced by tau neutrino is difficult to distinguish from the other signatures, due to the prompt decay of the tau close to the initial neutrino interaction. This leads to a significant degeneracy in neutrino flavour studies between the ν_e and ν_τ flavours, as only the charged-current ν_μ contribution can be separated. Improved analysis techniques allowed identifying two double-cascades candidates in IceCube's high-energy data set (7.5 yr *HESE* sample, 60 events with neutrino energies from 60 TeV to 10 PeV and the neutrino interaction taking place inside the detector) [100]. The best fit for the flavour composition in this data set was found to be $\mu_e : \mu_\mu : \mu_\tau = 0.20 : 0.39 : 0.42$, which is consistent with previous IceCube results.

[100]: Abbasi et al. (2022), *Detection of astrophysical tau neutrino candidates in IceCube*

Astrophysical neutrino sources: In 2017, a high-energy muon neutrino was detected by IceCube, with its sky-coordinates consistent with the blazar TXS 0506+056, observed to be in a flaring state [101]. This triggered an extensive multi-wavelength campaign with measurements from radio to γ-particles, and thus this event is regarded as a milestone of multimessenger astronomy. After this event, the IceCube archival data were investigated and a neutrino flare was identified in a 5-month period in 2014-2015, which resulted in a 3.5σ evidence for the blazar TXS 0506+056 being a high-energy neutrino source [102]. In a recent publication [4], the position of 110 known gamma-ray sources in the northern

[101]: Aartsen et al. (2018), *Multimessenger observations of a flaring blazar coincident with high-energy neutrino IceCube-170922A*

[102]: Aartsen et al. (2018), *Neutrino emission from the direction of the blazar TXS 0506+056 prior to the IceCube-170922A alert*

[4]: Abbasi et al. (2022), *Evidence for neutrino emission from the nearby active galaxy NGC 1068*

sky was searched for neutrino detections. The source NGC 1068, an AGN, showed an excess of 79^{+22}_{-20} ν_μ with a significance of 4.2σ. The right side of Figure 3.13 shows the neutrino flux of both sources and the total flux measured by IceCube. The blazar TXS 0506+056 is $\sim$ 100 times farther away than NGC 1068. Given the differences in distance and spectra, the data suggest that there are at least two populations of neutrino sources with different density and luminosity [4].

The association of these sources has been an essential step for neutrino astronomy. However, both contribute ~1 % of the total measured flux in the observed energy range [4], so the bulk of the neutrino flux remains unresolved. This makes evident the need for a larger detector to boost the neutrino collection rate. In the coming years, IceCube will be extended with several new strings, starting with IceCube Upgrade, a low-energy extension, which will be introduced in the next section. Following the Upgrade, the detector will increase in volume eightfold with IceCube-Gen2, which is the topic of Section 3.3.2.

[4]: Abbasi et al. (2022), *Evidence for neutrino emission from the nearby active galaxy NGC 1068*

3.3.1 The IceCube Upgrade

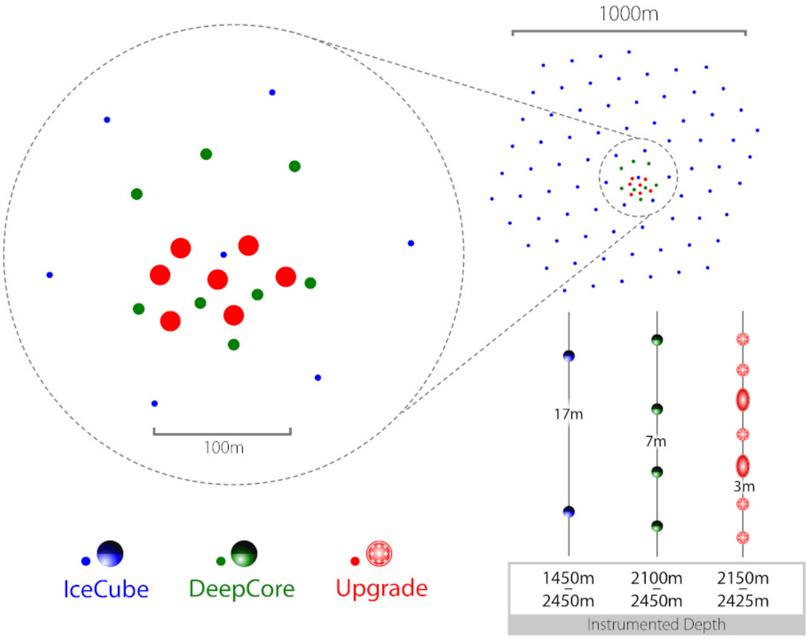

Figure 3.14: The IceCube Upgrade array layout. The seven Upgrade strings (red) are placed surrounded by DeepCore (green) in the centre of IceCube (blue dots). Deployment depths given in the lower right box consider only the *physics region* (see text). Figure courtesy of the IceCube collaboration.

The IceCube Upgrade is planned to be deployed in the summer season of 2025/2026 and consists of seven densely instrumented strings inside DeepCore. The string footprint is illustrated in Figure 3.14. The horizontal string spacing is approximately ~20 m. In the region at depths from 2150 m to 2425 m, referred to as *physics region*, the vertical distance between the sensors on a string is 3 m. At these depths, the ice has the largest scattering length and the background from atmospheric muons is low. For calibration and veto purposes, the seven strings will also be sparsely instrumented outside the physics region at depths from 1450 m to 1850 m with a vertical distance between sensors of ~25 m (so-called *special calibration region*) [5].

[5]: Ishihara et al. (2019), *The IceCube Upgrade - Design and Science Goals*

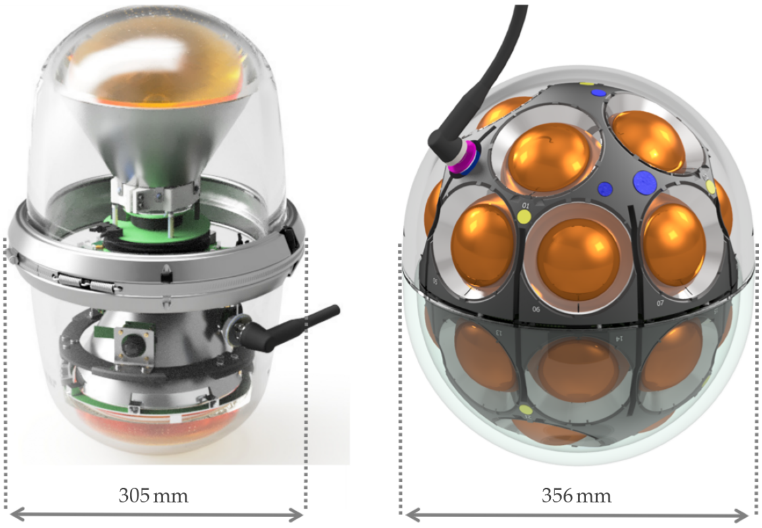

Figure 3.15: Rendering of the main two optical modules to be deployed in the IceCube Upgrade together with their diameter. *Left:* D-Egg, *right:* mDOM. Pictures courtesy of the IceCube Collaboration.

Several novel optical sensors were designed and developed for the IceCube Upgrade. Of all the proposed modules, two designs were selected as main sensors, both featuring a segmented sensitive area. On the one hand, 277 D-Egg are to be deployed, each with two 20 cm-diameter PMTs[15] vertically aligned, pointing in opposite directions. The PMTs, together with their high voltage supply bases, mainboard, magnetic shielding, and calibration devices, are housed inside an ellipsoidal pressure vessel with increased optical transmittance in the UV region compared to the current IceCube DOM [103]. A rendering of the D-Egg can be seen on the left side of Figure 3.15.

[15] Hamamatsu Photonics R5912-100-70

[103]: Hill et al. (2021), *Performance of the D-Egg optical sensor for the IceCube-Upgrade*

On the other hand, 402 mDOM (multi-PMT optical module) will be deployed, with an even larger segmentation featuring 24 PMTs of 80 mm diameter. The PMTs are surrounded by reflectors to increase the sensitivity and are fixed in place by a 3D printed support structure and a layer of gel. A picture of the mDOM is found on the right side of Figure 3.15. The mDOM design is based on the optical module of KM3NeT (see Section 3.2.2) but with a reduced total diameter of 356 mm. This module is introduced in detail in Chapter 4.

Besides the mDOM and D-Egg modules, the strings will be instrumented with 117 other devices. Several of these are calibration devices, such as Precision Optical Calibration Modules (POCAM) [104], which produce self-monitored isotropic light pulses, and Pencil Beam Modules (PB), which provide collimated beams steerable in all directions. Also, R&D devices are to be deployed, such as the Wavelength-shifting Optical Module (WOM) [105], the Fibre-optic Optical Module (FOM) and the elongated optical module (LOM) [106], all under development for further IceCube expansions.

[104]: Khera et al. (2021), *POCAM in the IceCube Upgrade*

[105]: Rack-Helleis et al. (2021), *The Wavelength-shifting Optical Module (WOM) for the IceCube Upgrade*

[106]: Basu et al. (2021), *A next-generation optical sensor for IceCube-Gen2*

The most important science capabilities of IceCube Upgrade can be separated into two categories [5]:

[5]: Ishihara et al. (2019), *The IceCube Upgrade - Design and Science Goals*

Neutrino physics: As introduced in Section 2.1.1, the neutrino oscillation probability depends on the flight path length and the neutrino energy. The reconstructed neutrino incident angle is translated into a path length through the Earth. Therefore, an accurate reconstruction of the zenith angle and energy of incident neutrinos is essential for any oscillation analysis.

The higher sensitivity of the modules and the dense instrumentation of the Upgrade will reduce IceCube's low-energy neutrino threshold from ~6 GeV to ~1 GeV, enabling access to new regions of the atmospheric neutrino oscillogram (see Figure 3.16). Furthermore, the energy and zenith resolution are expected to increase at least twofold and threefold, respectively, compared to the current DeepCore [97]. Studies of ν_μ disappearance in IceCube Upgrade are expected to results in tighter constraints on the atmospheric oscillation Δm^2_{32}-$\sin^2(\theta_{23})$-space, competitive with long-baseline accelerator experiments. The improved reconstruction of cascades should also allow for better ν_τ-appearance studies, with which the unitarity of the PMNS matrix will be tested with a precision of at least 6 % (a 4-fold improvement on current world best).

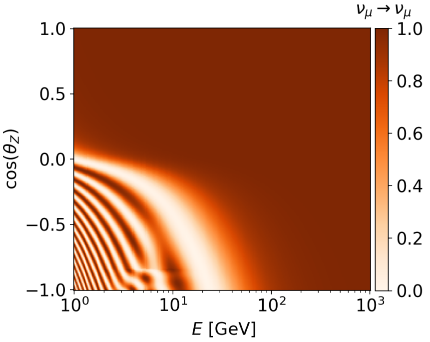

Figure 3.16: Oscillogram of survival probability of atmospheric ν_μ (assuming normal mass ordering). The length of the neutrino path through the Earth is parameterised in terms of its zenith angle θ_Z. Figure courtesy of the IceCube collaboration.

[97]: Mead (2022), *IceCube Upgrade: ν-oscillations' high-statistics era*

Ice calibration and neutrino astrophysics: As introduced in Section 3.3 one important systematic for the reconstruction of neutrino events originates from the optical properties of the ice. With the Pencil Beam's light, which can be directed in arbitrary directions, it is expected to disentangle the absorption and birefringence contributions to the anisotropy model and also improve the current scattering function [107]. Furthermore, calibration devices inside the mDOM and D-Egg, such as cameras and flashers, are intended to calibrate the currently unknown properties of the *bubble column* (see Section 3.3).

[107]: Rongen et al. (2021), *Advances in IceCube ice modelling & what to expect from the Upgrade*

The improved ice calibration should enhance the reconstruction of future and archival data and achieve an angular reconstruction of cascades closer to the statistical limit, which leads to more opportunities for neutrino point-source searches (as currently only tracks are used) [5].

[5]: Ishihara et al. (2019), *The IceCube Upgrade - Design and Science Goals*

3.3.2 IceCube-Gen2

Given the success of the IceCube observatory, the next step is to substantially increase the sensitive volume of the detector. The concept for a high-energy expansion was announced by the collaboration in 2014 in [61], and the deployment of the first strings is expected to be in the summer of 2027/2028.

[61]: Aartsen et al. (2014), *IceCube-Gen2: A Vision for the Future of Neutrino Astronomy in Antarctica*

As introduced in [6], the main goals of IceCube-Gen2 are

[6]: Aartsen et al. (2021), *IceCube-Gen2: the window to the extreme Universe*

- Increase the detector's sensitivity for high-energy neutrinos from TeV to EeV energies.
- Investigate the acceleration mechanism of cosmic particles through multi-messenger observations.
- Reveal the sources of these high-energy particles.
- Probe fundamental physics with neutrinos in this energy scale.

In order to accomplish these endeavours, the design considers the extension of the optical array, a surface air shower array, and an extended radio detector array. The top view of these extensions is depicted in Figure 3.17.

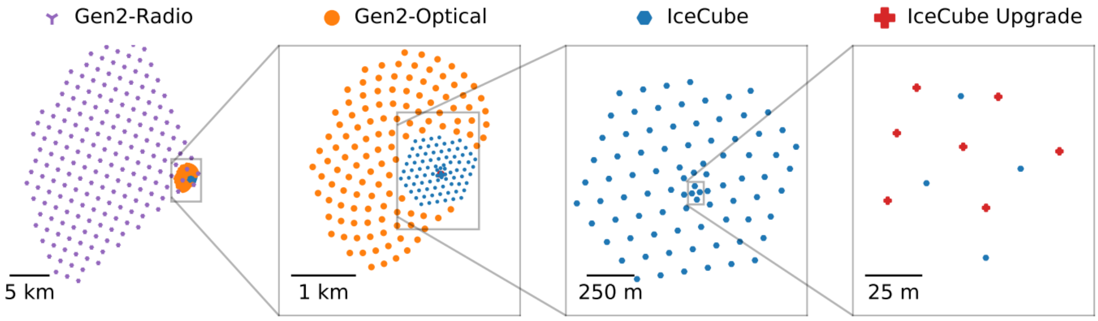

Figure 3.17: Footprint of the envisioned IceCube-Gen2 radio array (left) and optical array (mid left) compared to the current IceCube footprint (mid right). On the right is IceCube Upgrade, considered as the first phase of IceCube-Gen2. Image from [6].

The radio array is a cost-effective way to explore the neutrino EeV energy range. Antennas measure the radio pulses generated in cascades after neutrino interactions via the Askaryan effect (see Section 3.1). The preliminary baseline design for Gen2 is based on the experiences gained with the ARA and ARIANNA arrays. Two hundred stations are planned over an area of 500 km^2 (see Figure 3.17). Each station consists of three 100 m-deep strings with radio antennas and calibration pulses to triangulate the antenna position inside the ice. On the surface, each station has nine antennas that work as an air-shower veto and provide additional reconstruction information [6].

[6]: Aartsen et al. (2021), *IceCube-Gen2: the window to the extreme Universe*

The design of the optical array builds on the experience gained in the IceCube experiment. The optical properties of glacial ice dictate the maximal distance between strings without impacting the physic goals. These properties are now known in detail over a wide depth range from the in-site ice calibrations. The absorption length for Cherenkov light is larger than initially assumed and, depending on depth, it ranges from 100 to over 200 m. In addition, the measurements show that 125 m above and below the current instrumented volume the ice also has a scattering length that is large enough for neutrino detection. This means that future expansions can cover considerably larger volumes with lower string densities than the ones used in IceCube. Thus, the preliminary design considers strings with an average horizontal separation of 240 m. Each of these strings hosts 80 modules (9600 in total) arranged with a vertical separation of 16 m at depths 1325 m to 2575 m below the surface. This equates to an instrumented volume of 7.9 km^2 [6]. The larger spacing between strings results in a higher energy threshold for through-going muons —in the range of 10 to 30 TeV—, suppressing the atmospheric contribution, which vastly dominates the neutrino flux below 10 TeV. This comes with no significant cost to astrophysical neutrino signal since the bright events of high-energy neutrinos can still be reconstructed well with the envisioned detector geometry [6].

Since the cost and time of the drilling of the boreholes scale rapidly with their diameter, the IceCube collaboration has initiated efforts to combine the smaller diameter of the D-Egg with the highly segmented, large sensitive area of the mDOM. This design is referred to as LOM (eLongated Optical Module)[16]. Currently, there are two designs being developed in parallel. The distinction between these two models lies

[16] Initially, the module was envisioned to be much thinner, only the width needed for a single PMT placed horizontally, and longer, stacking PMTs vertically. The name was kept, also after remodelling to a more mDOM-like design.

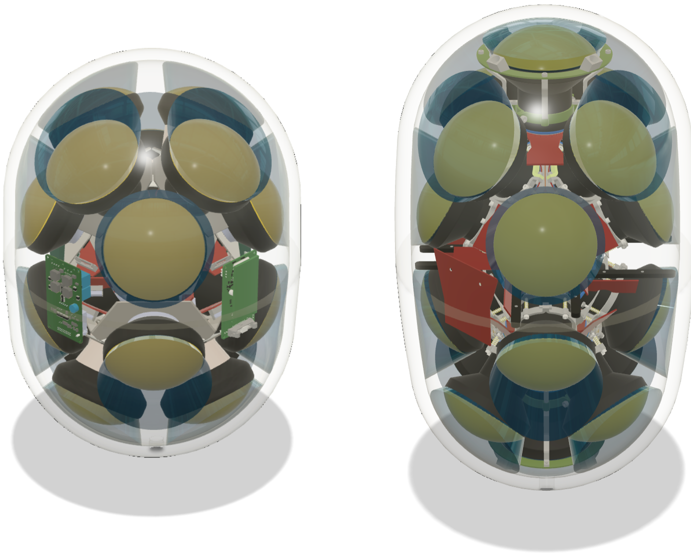

Figure 3.18: Rendering of LOM-16 (*left*) and LOM-18 (*right*). Figure courtesy of the IceCube-Gen2 collaboration.

primarily in the number of PMTs and the shape of the pressure vessel, rather than in the electronics and type of PMT used. One features 18 PMTs of 10 cm diameter inside a pressure vessel of 305 mm diameter (LOM-18), while the other design (LOM-16) features 16 PMTs inside a 313 mm diameter vessel. Figure 3.18 shows a rendering of both designs.

A novel technique that is being investigated is the use of *gel pads*. These are conical gel pieces between the PMTs and the pressure vessel. Reflectors, as featured in the mDOM, are not necessary, since total internal reflection at the conical surface concentrates the light with similar efficiency. This has the benefit that the 3D-printed support structure of the mDOM is no longer necessary, which is a substantial portion of the total cost of that module.

4

The mDOM — a multi-PMT optical module for IceCube Upgrade

Until recently, all the optical modules of deployed neutrino telescopes featured a single PMT (see Section 3.2). The first multi-PMT module was developed for KM3NeT and is currently being successfully deployed. However, the optical module concept — many small PMTs enclosed in a pressure vessel — was already proposed in the early stages of neutrino astronomy by S. O. Flyckt for the DUMAND project.

The development of a multi-PMT Optical Module for IceCube extensions began in 2012 based on the KM3NeT design, in the context of a dissertation [108], which laid the foundation of the concept of the mDOM. The design had to comply with several conditions imposed by the deep ice environment, such as the temperature rating down to $-45\,^{\circ}\mathrm{C}$, a limited module diameter up to $\sim 36\,\mathrm{cm}$ and a high pressure rating up to 700 bar. This high pressure rating is necessary, as after installation, the drilled water columns start to freeze at the surface and then downward, producing the excess maximum pressure [2].

The segmentation of the sensitive area results in a number of advantages compared to the conventional single PMT design:

- A **large sensitive area** covering a near homogeneous 4π angular acceptance.
- Intrinsic **directional sensitivity**, as the orientation of the PMT provides information about the direction of the detected light.
- Better **photon counting**, since photons are detected in different PMTs, each with its own dedicated data acquisition (DAQ). The number and arrival time of photons can be more easily reconstructed, unlike a multi-photon waveform from a single large photomultiplier.
- Moreover, as the detected photons are distributed over several PMTs, each DAQ is **less prone to saturation**.
- The development of reconstruction algorithms based on **local coincidences** is possible, i.e. correlated signals in several PMTs from a single module. This enables novel methods for background suppression, such as those shown in supernova neutrino sensitivity studies [109].

In the following sections, the design and general functioning of the mDOM are introduced.

[108]: Classen (2017), *The mDOM - a multi-PMT digital optical module for the IceCube-Gen2 neutrino telescope*

[2]: Aartsen et al. (2017), *The IceCube Neutrino Observatory: Instrumentation and Online Systems*

[109]: Lozano Mariscal et al. (2021), *Sensitivity of multi-PMT optical modules in Antarctic ice to supernova neutrinos of MeV energy*

4.1 Design

The mDOM consists of 24 PMTs of 80 mm diameter orientated in multiple directions. A schematic image of the module and its internal parts is illustrated in Figure 4.1. PMTs, calibration devices, and other electronic components are mounted on a 3D printed support structure made of nylon 12 (PA12). Due to the loss of sensitivity caused by the shadowing of the structure, the PMTs are surrounded by a reflector. This recovers the lost sensitive area by redistributing the angular sensitivity of each PMT [108]. The PMTs are soldered directly to a circuit board (µBase), which provides the PMT with high voltage and connects the signal from the anode to the mainboard, located in the equatorial plane at the centre of the mDOM.

A two-component silicon-based gel layer acts as an optical and mechanical coupling between the vessel, PMTs, and the support structure. This reduces light reflections as a result of the different refractive indices of glass and air and provides cushioning for the internal components against transport vibrations. Both materials, glass and gel, feature high transparency down to wavelengths of ∼ 300 nm [108]. The left side of Figure 4.2 shows a cross section of the assembly in the PMT region. Because the gel is initially in liquid state, an o-ring is placed inside a groove in the support structure, which is pressed against the PMT. Once the gel is cured, it becomes a more rubbery material, and all components are fixed in place.

All these components are enclosed in a pressure vessel of borosilicate glass of 356 mm diameter and 13.5 mm thickness, produced by Nautilus GmbH. The design of the pressure vessel is shown on the right side of Figure 4.2. It consists of two half-vessels with a bipartite design: a half-vessel is a half-sphere of 176.5 mm outer radius and 13.5 mm wall thickness, which terminates in a cone of 27.5 mm height and 2.8° wall

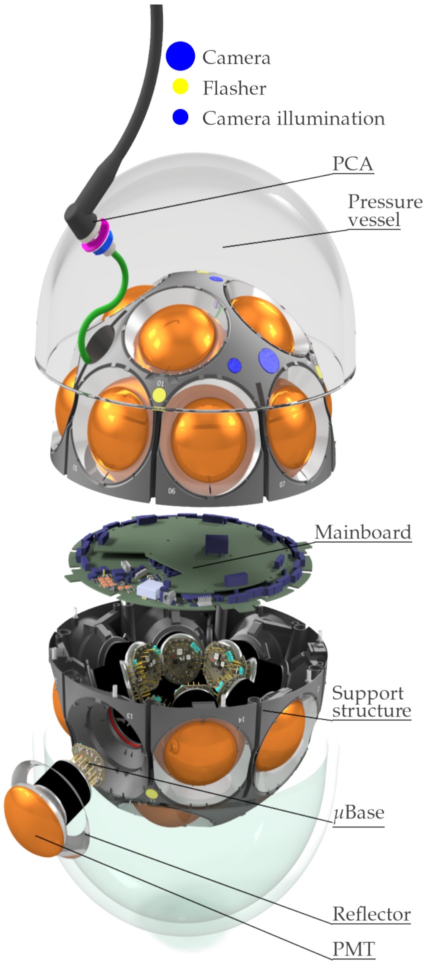

Figure 4.1: Exploded view of the mDOM.

[108]: Classen (2017), *The mDOM - a multi-PMT digital optical module for the IceCube-Gen2 neutrino telescope*

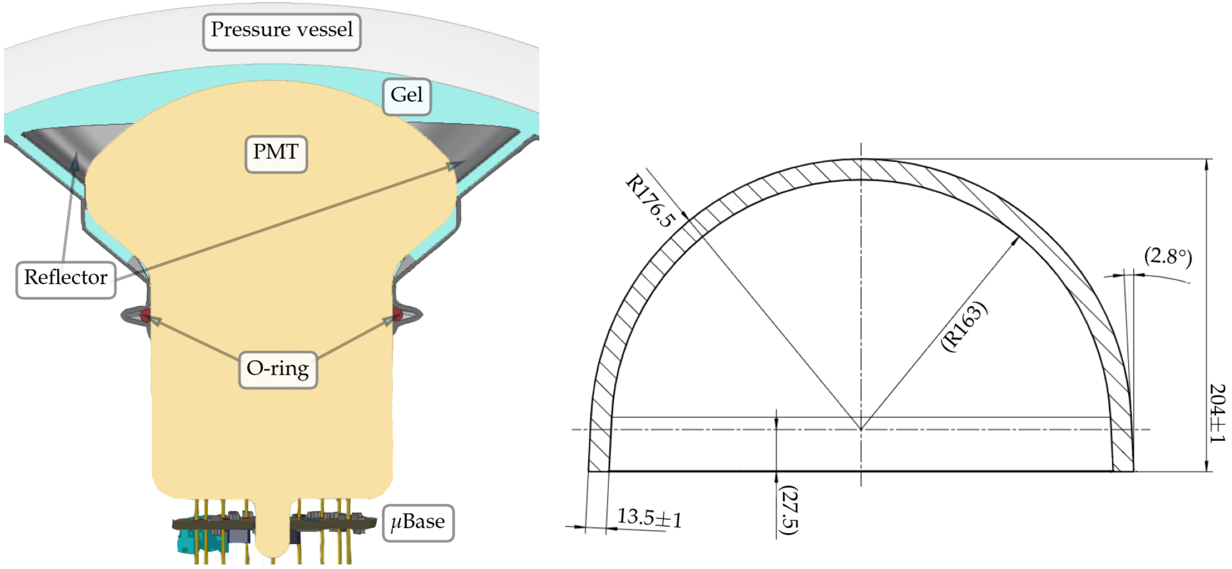

Figure 4.2: *Left:* Cross section of the PMT assembly inside the mDOM. The cyan colour represents the regions filled with optical gel, which is transparent in reality. *Right:* Technical drawing of the mDOM pressure vessel. All dimensions, except the angle, are in millimetres. Provided by Nautilus GmbH and modified.

inclination. The outer diameter of the vessel at the end of the cone is 356 mm. The cone region was included to increase the volume of the module and allow for the inclusion of more PMTs without the need to increase the module width, as would be necessary with a spherical design. A structural stability simulation of the manufacturer resulted in a pressure rating of 1050 bar [108].

For further details on the mechanical components, see Chapter 10, which is dedicated to the testing of the pressure vessel, gel, and support structure.

4.1.1 Hamamatsu R15458-02/20 PMT

The PMT model used in the mDOM — R15458-02 from Hamamatsu — was developed for the special conditions of IceCube. In Figure 4.3 a photography of this PMT is presented. It is the successor to the PMT type R12199-01 HA MOD, with the only difference being the reduced PMT length from 93 mm to 91 mm. Excluding the total length and an insulating coating around the tube, the design of the PMT is the same as that of the PMT type R12199-02, which is 98 mm in length, developed for the KM3NeT experiment from the flat-window PMT type R6233. The insulating coating, *HA coating*, was introduced to reduce and stabilise the intrinsic background of PMTs. Hamamatsu solders the µBases directly, and the PMT-µBase system is managed under the name R15458-20. A general introduction to photomultipliers is provided in Chapter 5. A large portion of this thesis (Chapters 6 to 8) involves the characterisation of this PMT model, since they are the most important component for understanding the mDOM response.

Figure 4.3: Picture of the Hamamatsu R15458-02 PMT. Published in [110].

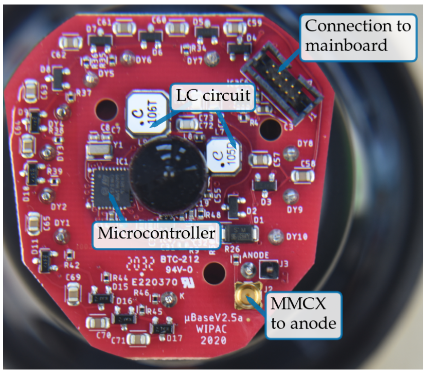

Figure 4.4: Back view of a PMT with the µBase attached to the PMT pins.

4.1.2 µBase — PMT high-voltage control

Figure 4.4 shows the front view of the µBase attached to the back of a Hamamatsu R15458-20. The main function of the base is to supply a stable and controlled high voltage to the PMT and provide an interface for the PMT signal. It is mainly composed of a Cockcroft-Walton multiplier combined with a resonant circuit and was inspired by the PMT base used in COUPP [111]. In this design, a microcontroller produces a square wave signal with an adjustable frequency on the order of 100 kHz [112]. This is fed to an LC resonator producing a sine wave that is routed to the Cockcroft-Walton multiplier. A simplified block diagram of the high voltage control of the µBase is shown in Figure 4.5.

[111]: Crisler et al. (2010), *The Chicagoland Observatory Underground for Particle Physics cosmic ray veto system*

[112]: Classen et al. (2021), *Design and performance of the multi-PMT optical module for IceCube Upgrade*

A Cockcroft-Walton multiplier consists of a chain of diodes and capacitors that produce a high DC voltage from a low AC voltage input. The output voltage is proportional to the amplitude of the AC. In the case of the µBase, the AC input is the sine wave produced by the LC resonator.

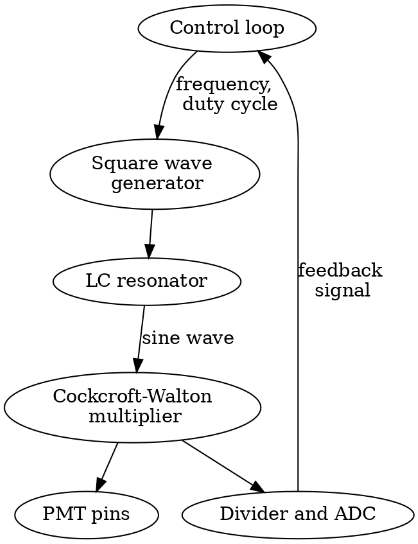

Figure 4.5: Simplified block diagram of the µBase high voltage control.

The amplitude given by the LC circuit depends mainly on two factors: the frequency of the square waves and their duty cycle. The former is programmed at or near the resonant frequency of the LC circuit and sets the maximum achievable output voltage. As the resonance position varies from base to base and is temperature dependent, the microcontroller performs a frequency scan before setting the high voltage, measuring the output voltage at different frequencies, and determining the approximate location of the resonance.

Fine tuning of the output voltage V_{out} can be done by changing the duty cycle D of the square wave since the LC resonator responds mostly to the lowest sine wave of the Fourier decomposition of the square pulses, thus following $V_{\text{out}} \propto \sin(\pi D)$ [1]. The µBase has an HV feedback control loop, which measures the output voltage in 10 SPS and adjusts the frequency of the square wave and the duty cycle to maintain the set voltage.

[1] Here the duty cycle is expressed as the ratio of the square pulse width to the period of the signal

4.1.3 Communication and data acquisition

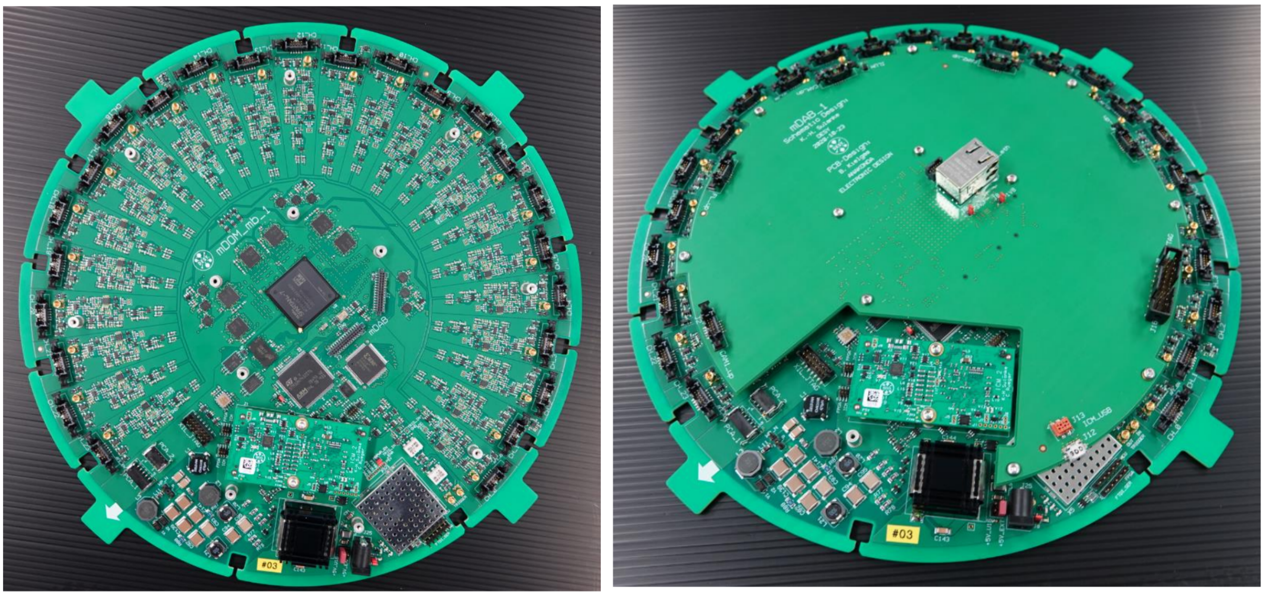

Figure 4.6: Picture of the mainboard (*left*) and assembled with the mDAB auxiliary board (*right*). Pictures courtesy of IceCube group DESY.

A picture of the mDOM mainboard is shown in Figure 4.6. The modules are connected to the exterior via the ICM (IceCube Communication Module) as an interface to the penetrator cable assembly (PCA), which provides communication and DC power to the mainboard by a single wire pair [112]. The primary DC voltage is reduced with two DC/DC converters. The ICM is a standardised communication interface to the electronics on the surface. It provides the timestamps to the in-ice devices, including the optical modules, and it also provides an interlock. This is especially important for devices or subsystems that can generate light.

The heart of the DAQ is its field-programmable gate array (FPGA), which controls the analogue front-end channels (AFE) and the analogue-to-digital converters (ADCs). There is an AFE for each PMT. A simplified block diagram of the AFEs is shown in Figure 4.7. Here, the signal is routed in two paths, once towards a discriminator and once to a signal shaper. The discriminator is sampled by the FPGA with 960 MHz and provides a precise leading-edge time (~ 1 ns resolution) for PMT pulses. The shaper consists of a pre-amplifier, a low-pass filter, an amplifier, and finally a second low-pass filter. This chain amplifies and lengthens the signal by

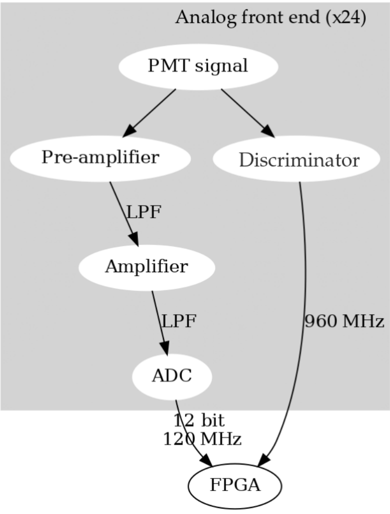

Figure 4.7: Simplified block diagram of the analogue front end (AFE) of each PMT. LPF means that between the two stages there is a low-pass filter.

a factor of ~11 and ~10, respectively. Afterwards, the signal is routed towards one of the six ADCs. Each ADC has four channels and operates at 120 MHz with 12-bit resolution. The PMT signal is terminated at 0.95 V to avoid any ADC baseline variations (*droop* effects). Therefore, two DAC channels are used to adjust the ADC baseline and the discriminator threshold [112].

[112]: Classen et al. (2021), *Design and performance of the multi-PMT optical module for IceCube Upgrade*

Data containing the ADC waveforms and discriminator samples can be transferred from the FPGA buffers to the 2 gigabit DDR3 memory. This is enough space for several seconds or minutes of PMT data [112].[2]

A **M**icro**C**ontroller **U**nit (MCU) controls and monitors the operating modes, task execution, and parameter setting of the FPGA. It also initialises the AFEs of each PMT and controls the mDAB board, an auxiliary board for the calibration devices.

4.1.4 Calibration devices

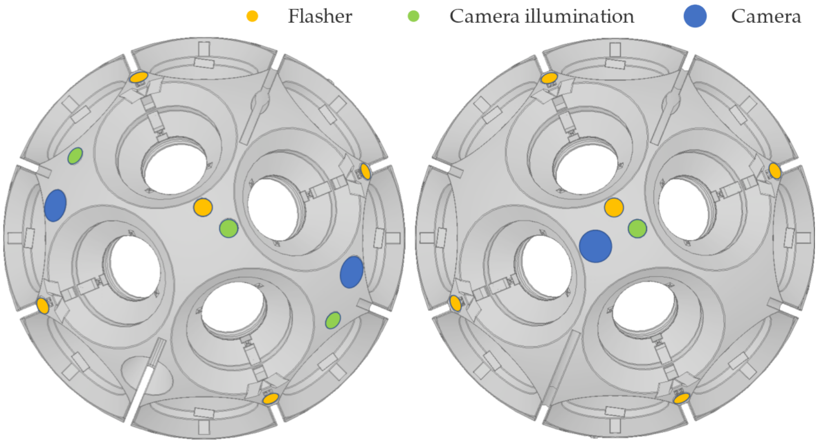

Figure 4.8: Top view of the support structures marking the location of flashers (yellow), cameras (blue), and illumination LEDs of the camera system (green). Left for the upper hemisphere and right for the lower hemisphere.

Each mDOM is equipped with ten flasher LEDs, three cameras [113], and four illumination LEDs, which are mounted on the support structure. The flasher LEDs, positioned along the equatorial region (see Figure 4.8), are of type Roithner XRL-400-5O and emit light of a wavelength of (405 ± 10) nm [114]. The maximum intensity of a LED pulse is 10^9 photons with a pulse width of 7.5 ns (FWHM) at high intensity and is shorter at lower brightness [112]. A picture of a flasher and camera mounted in the support structure is shown in Figure 4.9.

[113]: Kang et al. (2021), *Camera Calibration for the IceCube Upgrade and Gen2*

[114]: Roithner LaserTechnik GmbH (2012), *XRL-400-5O Technical Data Sheet*

The camera system consists of a board containing a Sony IMX225LQR-C CMOS image sensor and a second board with an illumination LED. The latter is an SSL 80 GB CS8PM1.13 LED from Oslon, which emits light at (470 ± 25) nm with an angular profile of 80° width. Two of the cameras are installed in the upper hemisphere pointing at an angle of 45°, intended for bulk ice studies, and one at the bottom pole of the module pointing downward. At the top pole, there is a fourth illumination LED, which is used in measurements where the downward-facing camera of one module measures the upward-pointing illumination LED from the mDOM below. This is intended for studies of the refrozen ice and the bubble column [113] (see Section 3.3).

---

[2] The buffer time available for data storage depends on the amount of information being saved. If only the charge, time, and channel number of each pulse is conserved, one can buffer over 10^3 s of data. However, if the complete PMT waveforms are saved, the buffer time is drastically reduced.

4.2 DVT modules — towards the mDOM production

Before starting the production of the modules, a design verification is required. This involves the construction of ten *DVT*[3] modules, which must undergo various tests that simulate the conditions the modules must endure during transport and deployment. The mechanical tests are:

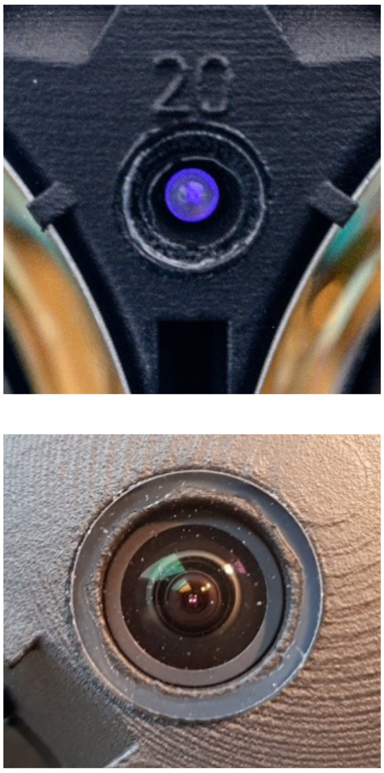

Figure 4.9: Flasher (turned on, *top picture*) and camera (*bottom*) placed in an mDOM support structure.

- Thermal shock test: The modules must withstand a sudden temperature change from −40 °C in the air to 20 °C in water. This simulates the change in temperature at the submersion of the modules during deployment.
- Vibration test: It consists of vibrating the DVT modules with different frequency spectra for several minutes, simulating vibration during ground and air transport.
- Mechanical shock test: Simulates the forces on the module if it falls from a height of 1 m. During the test, the module must withstand an acceleration of 30 g for 11 ms.
- Pressure test: The modules have to endure a pressure of up to 700 bar, simulating the maximum pressure during the refreezing of the boreholes.

Before and after each test, a *Functional Check-Out* (FC) has to be performed to make sure that all components are working correctly. An FC is a series of tests performed at least once before and after a DVT and, if conditions permit, during the test. Its purpose is to perform a basic functionality test of different units of the module with simple pass/fail criteria and is therefore not a verification of engineering requirements. In the scope of this thesis, the pressure test on DVT module 04 is presented in Chapter 10, together with a brief description of all the tests performed during the FCs.

Figure 4.10: mDOM DVT 03, *Dornröschen*. Photograph courtesy of IceCube group DESY.

At the time of writing this thesis, all DVT modules were built (see Figure 4.10), and the tests were completed successfully. The pre-production of mDOMs is currently underway at DESY Zeuthen in Germany, with the first 20 modules being produced since September 2022. Meanwhile, the pre-production at MSU in the US is anticipated to begin shortly.

---

[3] **D**esign **V**erification **T**est

5

Photomultiplier tubes

Photomultiplier tubes (PMTs) are the primary sensitive component of optical modules and thus a rigorous understanding of these devices is key for the accurate analysis and interpretation of their signal. PMTs are able to convert even single photons into a measurable charge via the photoelectric effect and electron multiplication. The construction and operation principle is briefly discussed in Section 5.1. The sections thereafter explain the key features of these devices in more detail. A general introduction to PMTs, their construction, and their applications can be found in [115], while a detailed and comprehensive description of PMT parameters and characterisation methods is given in [116].

[115]: Hamamatsu Photonics K.K. (2017), *Photomultiplier tubes - Basics and Applications*

[116]: Wright (2017), *The Photomultiplier Handbook*

5.1 Operation principle

The detection of single photons in a PMT is done in two stages: the conversion of the photon to an electron, via the photoelectric effect, and the multiplication of this **single photoelectron** (SPE) into a measurable signal. This process happens in different components of a photomultiplier, which are depicted in Figure 5.1.

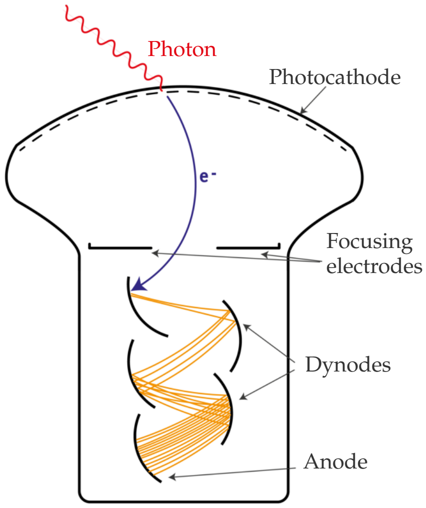

Figure 5.1: Schematic of a photomultiplier tube with its main components. The red sinusoidal line represents a photon emitting a photoelectron (blue curve) at the photocathode. The secondary electrons emitted by the dynodes are represented by yellow lines.

The photosensitive area of a PMT is a thin semitransparent layer, called **photocathode**. It can be made from different materials depending on the operation requirements. The photocathode and the relevant performance parameters are discussed in Section 5.2.

The photoelectrons are focused and accelerated towards the electron multiplier, which is on a higher electric potential than the photocathode. The electric field between the cathode and multiplier is often shaped with focusing electrodes for better collection efficiency of the photoelectrons. The electron multiplier consists of a series of electrodes, called **dynodes**, which release secondary electrons after they are hit by an incident electron. Since the intensity of the electric potential increases stepwise with each dynode, the secondary electrons are accelerated toward the next dynode, multiplying their total number at each stage. The final electrode is the anode, which delivers the output signal. Section 5.3 goes into more detail on the electron multiplier and the parameters that derive from it.

The signal of the anode can be read out as a charge or as a voltage signal. In **pulse** or **photon-counting mode**, the analogue signal is supplied to a resistor, which results in a voltage drop (e.g. using an oscilloscope). At low light levels, the output pulses can be discretely resolved, as depicted on the top of Figure 5.2, and information such as the detection time and charge of single-photon events can be extracted. However, if the light intensity increases, the pulses overlap and cannot be discriminated from each other (like in Figure 5.2, bottom). In this case, reading out the charge directly is more appropriate, integrating the signal within a certain time window by a current measuring device (e.g. picoammeter). This operation mode is called **current** or **analogue mode**.

In the case of working in pulse mode, there are several variables that characterise the PMT performance. On the one hand, there are the timing-related parameters. The **transit time** of the PMT is the time elapsed between the absorption of a photon in the photocathode and the recording of the pulse at the anode. This time varies due to the fact that photoelectrons take different paths from the photocathode to the first dynode and also by secondary electrons in the subsequent dynodes. This **transit time spread** (TTS) is commonly measured as the standard deviation or the FWHM of the transit time distribution. Therefore, the TTS defines the intrinsic uncertainty of the photon detection time of a PMT.

On the other hand, there are the pulse shape-related parameters. These are shown in Figure 5.3. The voltage drop can be characterised by its **width** (FWHM) and by its **rise** and **fall times**. The latter two are defined by the times required for the signal to cross two successive voltage thresholds. The most common definition is to use the 10% and 90% of the pulse height. However, in cases where the pulse amplitude is low with respect to the noise floor, the 20% and 80% thresholds are also often used.

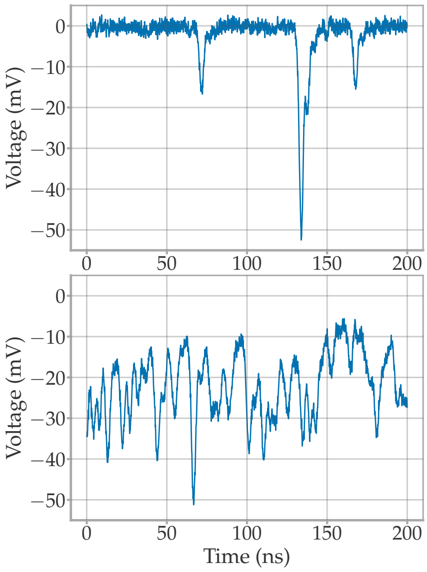

Figure 5.2: PMT signal measured by an oscilloscope using a low intensity light source (top) and a high intensity light source (bottom).

5.2 PHOTOCATHODE

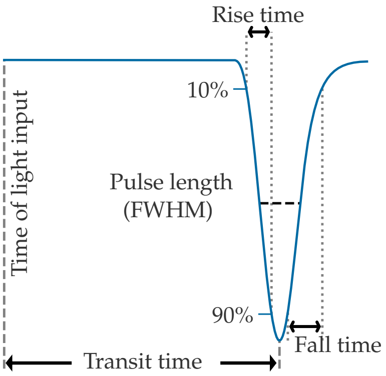

Figure 5.3: Schematic representation of the shape and timing parameters of PMT pulses.

Most photocathodes are semiconductors with a low work function. There are several types currently available, each with different compounds of alkali metals resulting in different spectral range responses. For the detection of photons in the visible region, usually bialkali (K_2CsSb or Rb_2CsSb) or multialkali (Na_2KSbCs) compounds are used [115, p. 36].

The photocathode sensitivity (conversion efficiency of photons to photoelectrons) is wavelength dependent and it is normally described by the **quantum efficiency** (QE) or the radiant sensitivity.

The QE is the fraction of photons that release a photoelectron and it is usually expressed as a percentage. The radiant sensitivity S is the fraction between the photocathode current I and the incident radiant flux Φ, conventionally in units of Ampere per Watts. Both quantities are directly proportional following the ratio [115, p. 40]

[115]: Hamamatsu Photonics K.K. (2017), *Photomultiplier tubes - Basics and Applications*

$$\mathrm{QE}(\lambda) = \frac{I/e}{\Phi/E_\lambda} = S \cdot \frac{h \cdot c}{\lambda \cdot e}, \tag{5.1}$$

where $E_\lambda = \frac{h \cdot c}{\lambda}$ is the energy of a photon of wavelength λ and e the elementary charge.

The response of the photocathode does not exclusively depend on the compound of alkali metals, but also on several parameters which can be adjusted, such as the ratio between alkali metals, activating temperature[1], crystallisation quality, etc. In this regard, a high crystalline structure of the

[1] Temperature at which the alkali metals are evaporated to the glass surface

Sb film in bialkali photocathodes results in a higher QE [117]. A standard bialkali, without enhanced crystallinity, exhibits a maximal QE of ~25 % for wavelengths around 400 nm. Hamamatsu offers these as *Ultra Bialkali* (UBA), and an intermediate, featuring a maximal QE of ~35 %, as *Super Bialkali* (SBA). Typical QE curves for standard bialkali, SBA and UBA photocathodes are shown in Figure 5.4.

Bilalkali photocathodes are also sensitive to UV light, but this sensitivity is lost or limited by the transmission of the window material. Windows made of borosilicate glass, for example, are no longer transparent for wavelengths shorter than ~300 nm. Detection of UV light requires windows made from, e.g. silica glass (cutoff at ~160 nm), sapphire (cutoff at ~150 nm) or magnesium fluoride (MgF_2) (cutoff at ~115 nm) [115, p. 38].

The photomultipliers used in the mDOMs, D-Eggs and IceCube DOMs all have a bialkali photocathode with borosilicate glass as the window material. However, the PMTs in the D-Eggs and DeepCore DOMs feature an SBA photocathode, with higher QE [2, 103].

The current drawn from a photocathode is limited due to its own resistivity, which depends on the alkali compound and the thickness of the photocathode. For the correct functioning of a PMT, the photocathode surface should be equipotential. This is not the case if a very high current is drawn. After illuminating the centre of the PMT, the voltage drop ΔV produced between the centre and the periphery of a photocathode can be approximated as $\Delta V = R_\square \cdot I/(4\pi)$, with $R_\square$ the sheet resistance of the photocathode[2] and I the photocurrent [116, p. 63]. This means that, assuming that the SPE is released with a starting kinetic energy of ~1 eV and for a typical bialkali sheet resistance of $R_\square \approx 10^{10}\,\Omega/\square$, the photocurrent is limited to ~0.1 nA before the voltage drop starts to impede further electron emissions [116, pp. 62–64]. This is not relevant for PMTs used under normal working conditions in neutrino telescopes, since the dynode system is the limiting factor, having a much lower saturation level than the photocathode. However, the photocathode resistivity has to be taken into consideration during calibration of the PMTs, if they are being used as photodiodes.[3]

[117]: Nakamura et al. (2010), *Latest bialkali photocathode with ultra high sensitivity*

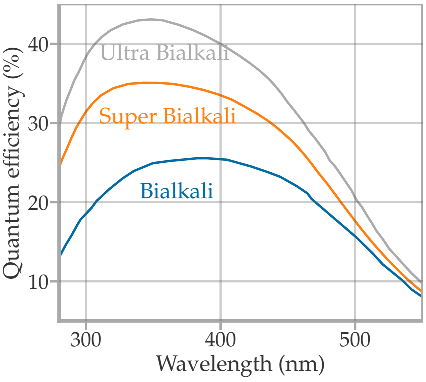

Figure 5.4: Quantum efficiency of standard bialkali, SBA and UBA with a borosilicate glass entrance window. Data from [117].

[115]: Hamamatsu Photonics K.K. (2017), *Photomultiplier tubes - Basics and Applications*

[2]: Aartsen et al. (2017), *The IceCube Neutrino Observatory: Instrumentation and Online Systems*

[103]: Hill et al. (2021), *Performance of the D-Egg optical sensor for the IceCube-Upgrade*

[116]: Wright (2017), *The Photomultiplier Handbook*

5.3 ELECTRON MULTIPLICATION SYSTEM

Dynodes consist of a substrate electrode made of nickel, stainless steel, or a copper-beryllium alloy, coated with an emissive material. This material is usually alkali antimonide (Sb), beryllium oxide (BeO) or magnesium oxide (MgO) [115, p. 19].

The secondary emission yield δ, or dynode gain, is the fraction between outgoing and incoming electrons from the dynode. It depends on the energy of the incoming electron and thus on the inter-dynode voltage ν. Both magnitudes follow the semi-empirical equation [116, p. 205]

$$\delta = \frac{N_\text{out}}{N_\text{in}} = \alpha \cdot \nu^\beta, \tag{5.2}$$

[2] Measured in Ohm per square, describes the resistance of a thin film regardless of its size. See `en.wikipedia.org/wiki/Sheet_resistance` for a short introduction.

[3] This means, with all the dynodes shortcut, measuring directly the photocurrent. In this case, a high light intensity is necessary to obtain a measurable signal.

with $\beta < 1$. In a system without losses, a direct proportionality $\delta = \alpha \cdot v$ would be expected, but there is normally a fraction of electrons undergoing inelastic scattering, losing part of their energy, or leaving the dynode stage without producing secondaries. The gain of the PMT G is the product of all stage gains

$$G = \prod_{k=1}^{n} \delta_k = \prod_{k=1}^{n} \alpha_k \cdot v_k^{\beta_k}, \tag{5.3}$$

where n is the number of dynodes.[4] Thus, the gain is the average total multiplication of a single photoelectron, which is equal to the average charge collected at the anode divided by the elementary charge after a single photoelectron (SPE) is released at the photocathode.

Since the inter-dynode voltages are distributed via a voltage divider, each v_k is a fraction of the total applied voltage V between the photocathode and the anode. The voltage increase between each dynode is given by the *dynode ratios*, normally expressed with the nomenclature

$$r_0 : r_1 : r_2 : \ldots : r_{n-1} : r_n.$$

These are the fractions between the resistances used in the voltage divider supplying each dynode, where $v_k = V \cdot r_k / (\sum_{i=0}^{n} r_i)$. For the mDOM PMT a dynode ratio of $3 : 1 : \ldots : 1$ is recommended by the manufacturer, which means that the voltage difference between cathode and first dynode should be three times the inter-dynode voltage difference.

Since each v_k is a fraction of V, Equation 5.3 can be simplified by a power relationship

$$G = \prod_{k=1}^{n} \alpha_k \cdot \left(\frac{r_k \cdot V}{\sum_{i=0}^{n} r_i} \right)^{\beta_k} = a \cdot V^b. \tag{5.4}$$

Every PMT has to be calibrated to its **nominal gain**, which is a user-defined gain level necessary for the experiment.[5] A gain calibration consists of varying the applied voltage and fitting the obtained gains with Equation 5.4.

In some cases, especially when PMTs are driven only in current mode, the gain is defined as the ratio between the anode current I_a and the cathode current I_k,

$$g = \frac{I_a}{I_k}.$$

In an idealised photomultiplier, both definitions G and g would be equal. Nevertheless, not all emitted photoelectrons are measured at the anode. The fraction depends on the **collection efficiency** F, which is defined as the ratio of SPEs leading to a signal at the anode to the total amount of SPEs released at the photocathode. F depends mostly on the probability of an SPE hitting the first dynode. Since G derives from only the SPEs that have been multiplied, it follows that [116, p. 414]

$$F = \frac{g}{G}. \tag{5.5}$$

The **detection efficiency** DE of a PMT directly depends on the collection efficiency of the PMT. The detection efficiency at a certain wavelength is

[4] The collection efficiency between dynodes is near 100 % at normal operating voltages but may decrease at low voltages. This would introduce a v dependency in α of Equation 5.3, which is, nevertheless, ignored in the following.

[5] For the mDOM PMT it is $5 \cdot 10^6$, and for the DOM and D-Egg $10 \cdot 10^6$.

[116]: Wright (2017), *The Photomultiplier Handbook*

$\mathrm{DE}(\lambda) = F \cdot \mathrm{QE}(\lambda)$, and thus the optimisation of the collection efficiency is important.[6] Although Equation 5.5 seems to provide a straightforward method for calculating the collection efficiency of the PMT, the determination of an unbiased G is not trivial. The latter requires a good understanding of the charge distribution of the PMT, the **SPE spectrum**, which will be the topic of Section 5.5. An alternative method for the determination of F is through the DE and QE, although this also carries several systematics, making reliable measurements of the collection efficiency difficult [116, p. 429].

[116]: Wright (2017), *The Photomultiplier Handbook*

There are many types of multiplier structures with a different number of dynode stages. Their design is key for the resulting timing properties, linearity, and collection efficiency of a photomultiplier. The photomultipliers covered in this thesis use modified *linear focused dynodes*. The cross section of a linear focused multiplication system is a series of arcs facing each other as shown in Figure 5.5 a). The dynodes are terminated on the sides by a tangential segment, preventing secondary electrons from spreading to the outside of the multiplication system [116, p. 232]. This geometry allows for a good time resolution, collection efficiency and linearity [115, p. 46]. A *circular* linear focused dynode system is shown in Figure 5.5 b). It is conceptually the same as a linear system, but the dynodes are curled and curved for larger compactness, as is necessary in the small mDOM PMTs.

[115]: Hamamatsu Photonics K.K. (2017), *Photomultiplier tubes - Basics and Applications*

A *box linear focused* dynode system, as shown in Figure 5.5 c), combines a *box-and-grid* with the linear focused design. Box-and-grid dynode arrays are quadrant-shaped boxes with the entrance of the dynode covered by a fine mesh. This allows for superior collection efficiency, but inferior pulse time characteristics than linear-focused. The combination of both geometries results in a good time response from linear-focused and the superior collection efficiency of box-grid. This design is used in the larger PMTs of the D-Egg and DOM.

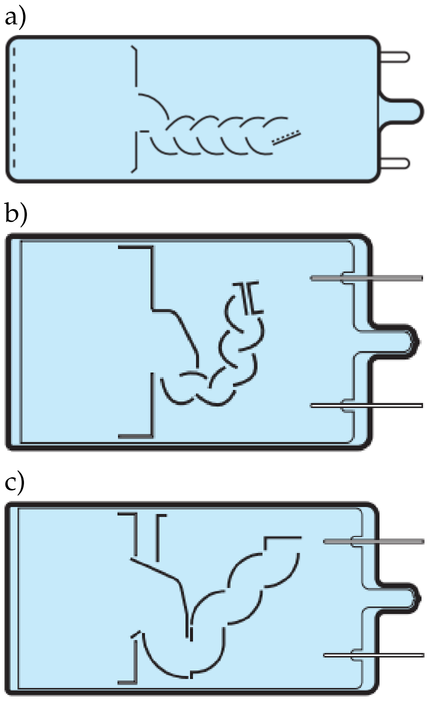

Figure 5.5: Schematic representation of a PMT with **a)** linear focused dynodes, **b)** circular linear focused dynodes and **c)** box linear focused dynodes. Reused with author permission from [115, p. 45].

5.4 Background

The background in a photomultiplier can refer to two unwanted sources of noise. On the one hand, there is always a measurable signal produced even during total darkness. This is called dark rate in the case of a PMT operated in pulse mode and dark current for a PMT in analogue mode. The different sources of this background are introduced in Section 5.4.1. On the other hand, there is signal-induced noise that appears with a certain probability after an initial pulse (whether produced by a photon or not). This is explained in Section 5.4.2.

5.4.1 Background without external light

The following effects produce pulses in a PMT which are indistinguishable from pulses generated by external photons. This noise is random in nature, except for signals from radioactive decays, which can also result in correlated photons if several of them are measured after one decay.

[6] Here, the loss due to a possible detection trigger level is not considered.

Thermionic emission is a major source of the total background at room temperature. It is caused by the spontaneous emission of electrons at the photocathode, which is collected by the multiplier system as a normal pulse. These electrons are released when their thermal energy exceeds the work function of the photocathode. Therefore, this effect is strongly temperature dependent[7], and it can be suppressed by cooling the PMT. At low temperatures, its contribution to the total dark rate is negligible, however, electron emission is in principle always possible, since the energy of the electrons in the photocathode follows a Fermi–Dirac distribution. There is also thermionic emission from dynodes, but its effect is subdominant since they have a smaller area and the electrons released do not multiply through all dynode stages [115, p. 70].

[115]: Hamamatsu Photonics K.K. (2017), *Photomultiplier tubes - Basics and Applications*

Field electron emission is the emission of electrons induced by the strong electrostatic field between dynodes due to quantum tunnelling. This is strongly dependent on the applied voltage[8] and sets the limiting voltage a PMT should be operated since a higher voltage considerably shortens the life of a PMT [115, p. 72].

A (potentially large) contribution stems from **radioactive decays** inside the envelope glass of the PMT. Due to the natural radioactivity of the raw material and contamination during manufacturing, different isotopes can be found inside the glass, such as ^{40}K or from the three natural decay chains ^{238}U, ^{235}U and ^{232}Th. The emitted particles during the decay can produce Cherenkov radiation or scintillation. If several photons are emitted after a decay, they can cause correlated detections. Section 11.2 is dedicated to this type of background since it is the largest contribution to the total background of the mDOM.

Cosmic ray muons passing through the glass envelope produce Cherenkov photons, which can be a noticeable contribution to the total dark rate, especially in PMTs of diameter greater than 50 mm. Since the photons are emitted on a time scale shorter than the time resolution of the PMT, the charge of the pulses can be equivalent to several tens to hundreds of photoelectrons, depending on the thickness of the glass [116, p. 276].

[116]: Wright (2017), *The Photomultiplier Handbook*

Strong **external electric fields** can also increase and destabilise the dark rate since electrons can deviate from their path inside the multiplier system and hit the envelope glass. The energy deposited in the glass results in scintillation, which can later release photoelectrons in the photocathode. This is especially an issue for PMTs driven by negative high voltage since any object at a ground voltage near the PMT is at a higher potential than the photocathode. Grounding the photocathode and applying a positive high voltage to the multiplication stages would solve this problem, but this is not always viable. In this case, a common countermeasure is to apply a conductive carbon layer around the tube, which is directly connected to the lowest potential, the cathode pin (see Figure 5.6) [115, p. 269]. The carbon layer is protected by an insulating cover to avoid discharges with conductors in the environment.

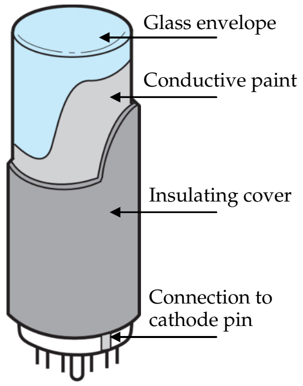

Figure 5.6: Sketch of a "HA treatment" as applied by Hamamatsu to improve the dark rate of PMTs driven in negative high voltage. Reused and modified with author permission from [115, p. 269].

In the case of operating in current mode, the **leakage current** is also of importance. This is a constant Ohmic current caused by the finite resistance of the insulating materials used in the PMT. The insulation resistance is of the order of $\sim 10^{12}\,\Omega$, which leads to a leakage current

---

[7] From the Richardson-Dushman equation, the thermionic emission follows a $(T^2 \cdot \exp{(-W/(k_B \cdot T))})$ dependency with the temperature T, material work function W and Boltzmann constant k_B [118].

[8] The field emission is described by the Fowler-Nordheim equation, which follows a dependency $\propto F^2 \cdot \exp{(-(B/F))}$. with the electric field strength F, and B a material-dependent constant [119].

of the order of nanoamperes for a PMT with an applied voltage of $\sim 10^3$ V [115, p. 72]. This is the limiting background for PMTs operated as photodiodes (without any multiplication from the dynodes).

[115]: Hamamatsu Photonics K.K. (2017), *Photomultiplier tubes - Basics and Applications*

During the operation of a PMT in the dark, the background will generally decrease with time. Manufacturers normally *hot-age* the PMTs to provide the devices in an already *run-in* state, but even so, the dark count can be a factor of up to two less one year after manufacture than the initially measured [116, p. 258]. However, this reduction is limited by all the effects above, which are mostly constant over the lifetime of a PMT.

[116]: Wright (2017), *The Photomultiplier Handbook*

5.4.2 SIGNAL-INDUCED BACKGROUND AND OTHER TIMING EFFECTS

There is a small probability that the PMT response will differ from that expected, detecting a pulse significantly outside the time window allowed by the TTS. In addition, PMTs can generate unwanted background pulses correlated in time with an initial signal. The time scale of this background ranges from a few nanoseconds to days.

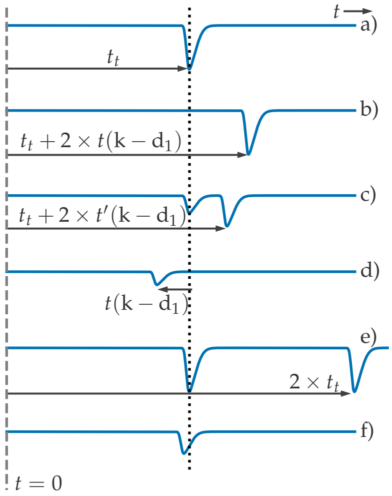

Figure 5.7: Timing effects and correlated background on the nanosecond time scale. The blue lines illustrate the PMT signal as measured in an idealised oscilloscope (pulse mode). $t = 0$ marks the absorption of a photon in the photocathode. t_t is the transit time of the PMT and $0 < t'(\mathrm{k}-\mathrm{d}_1) < t(\mathrm{k}-\mathrm{d}_1)$. Each case is explained in the text. Recreated with publisher's permission from [116, Fig. 11.6, p. 437].

Figure 5.7 shows a schematic of the different PMT responses to a single photon on a nanosecond time scale. In this diagram, the TTS has been ignored. Case **a)** represents the normal PMT behaviour, where a pulse is measured after the transit time t_t,[9] marked by the vertical dotted line. The other effects are produced as follows [116, pp. 436–439]:

- **b)** an SPE may **elastically** backscatter from the first dynode. The electron then decelerates, stopping a short distance from the photocathode, and returns to the first dynode after $2 \times t(\mathrm{k}-\mathrm{d}_1)$, where $t(\mathrm{k}-\mathrm{d}_1)$ is the average time required for an SPE to travel from the photocathode to the first dynode.[10] These pulses are called **delayed pulses** or **late pulses**.
- **c)** the SPE can also backscatter **inelastically**. A fraction of its energy is absorbed by the first dynode, which may release a reduced number of secondaries producing an underamplified pulse at the usual time t_t. The backscattered SPE will take a time $t'(\mathrm{k}-\mathrm{d}_1)$ to return to the multiplication system, with $0 < t'(\mathrm{k}-\mathrm{d}_1) < t(\mathrm{k}-\mathrm{d}_1)$ as the SPE has less kinetic energy. Thus, two pulses are generated, both underamplified. The second pulse is called **afterpulsing type I**. However, as the first pulse may have a charge too low to be detected, this kind of afterpulses are often misclassified as delayed pulses.
- **d)** a **prepulse** is produced when a photon releases an electron directly at the first dynode. These pulses arrive early by an interval equal to the time that the electrons normally need to reach the first dynode $t(\mathrm{k}-\mathrm{d}_1)$, considering that the photon transit time from the photocathode to the first dynode is negligible in comparison. Since the first multiplication stage is missing, the pulse charge is approximately one order of magnitude smaller than that of a typical SPE.
- **e) afterpulsing type I** may also be produced by photons released at the anode and last few dynodes as a result of electron bombardment after an intense signal. This signal appears t_t after an initial pulse.

[9] The mDOM PMT features a typical $t_t = 43$ ns [120].

[10] In the mDOM PMT $t(\mathrm{k}-\mathrm{d}_1) \approx 12$ ns, see Section 8.2.

- **f)** if an SPE scatters at the first dynode and hits directly the second dynode, the total transit time is reduced by a couple of nanoseconds and the pulse is underamplified as a multiplication stage is missing.

Afterpulses type II are pulses that are measured a few microseconds after the initial signal. Photoelectrons on their way to the dynode system can ionise residual gases or release particles from the electrodes. This positively charged ion is accelerated toward the photocathode and releases several photoelectrons upon impact. The arrival time depends on the mass of the ion and the size of the PMT, and ranges from several hundreds of nanoseconds to a few tens of microseconds [115, p. 79].

[115]: Hamamatsu Photonics K.K. (2017), *Photomultiplier tubes - Basics and Applications*

Exposure to intense levels of light leads to a higher dark count for several hours with a signal decay described by an inverse power relationship of the form t^{-k}. The cause of this is not fully understood, although it is partially attributed to fluorescence of the tube glass, where differences of more than a factor of 100 have been measured in the initial count rate between different glass types [116, p. 451]. Therefore, PMTs should be stored in the dark before use and never exposed to daylight during operation [115, p. 70].

[116]: Wright (2017), *The Photomultiplier Handbook*

5.5 CHARGE SPECTRUM

The total number of secondary electrons collected at the anode after the multiplication of an SPE is not constant but follows a statistical distribution. Such a distribution can be obtained by operating the PMT in pulse mode and triggering it in coincidence with a pulsed light source. In the measured waveform, an integration window is defined at the times where the light pulse is expected. The integration of several waveforms and the posterior representation in a histogram results in a SPE spectrum.

This principle is shown in Figure 5.8. The number of photons emitted in a light pulse from an LED follows Poisson statistics and none or a fraction of these photons is detected by the PMT. For the case where no LED photon is detected, only the baseline is integrated resulting in a Gaussian distribution in the histogram which is called a pedestal (see red distribution in Figure 5.8). The charge of the waveforms in which single photons were detected follows a distribution $S_1(q)$ to the right of the pedestal (see blue distribution in Figure 5.8). Events with several photoelectrons result in even broader distributions at higher charges. The distribution for n-PE events $S_\mathrm{n}(q)$ is a convolution of n SPE distributions $S_\mathrm{n}(q) = S_1(q) * S_{\mathrm{n}-1}(q)$.

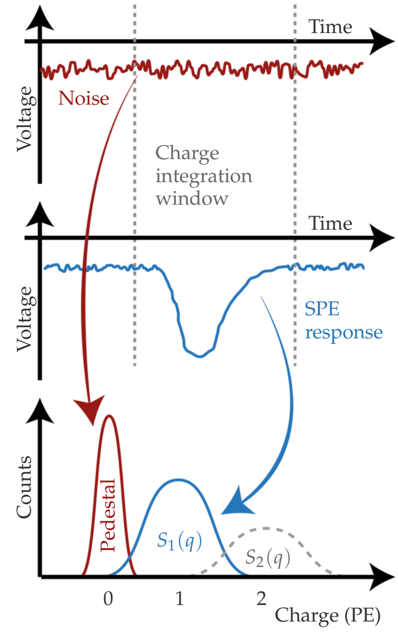

Figure 5.8: Schematic representation of the acquisition of a SPE spectrum. Based on [108, p. 31].

In such a measurement, the charge distribution is distorted by the (partial) integration of background pulses and prepulses. The latter can be avoided using a short integration window, although the measurement of underamplified pulses is still possible, such as in pulses produced by inelastic scattering of the photoelectron at the first dynode.

Thus, the resulting PMT charge spectrum can be described as a convolution between three distributions:

- The distribution modelling the number of released SPE per waveform n. In this case, this is a Poisson distribution $P(n|\mu) = \mu^n \cdot \mathrm{e}^{-\mu}/n!$ with μ the mean number of detected photons per light pulse.
- The ideal PMT response to an SPE $S_1(q)$.
- The background distribution describing the pedestal, dark rate, and under-amplified pulses.

It is common to model $S_1(q)$ as a Gaussian (with free parameters mean Q_1 and width σ_1), like done in [121]. In this paper, the background is described as a sum of a Gaussian (representing the pedestal) of mean Q_0 and width σ_0 and an exponential distribution $\lambda \cdot \mathrm{e}^{-\lambda q}$. The convolution of the three functions results in the probability density function (pdf): [11]

[121]: Bellamy et al. (1994), *Absolute calibration and monitoring of a spectrometric channel using a photomultiplier*

$$f(q) = \sum_{n=0}^{\infty} \frac{\mu^n \cdot \mathrm{e}^{-\mu}}{n!} \Bigg[(1 - P_u) \cdot G(q, Q_n, \sigma_n) + \\ + P_u \cdot \frac{\lambda}{2} \cdot \mathrm{e}^{-\lambda \cdot (q - Q_n - \frac{1}{2}\lambda n \sigma_1^2)} \cdot \left[1 - \mathrm{erf}\left(\frac{Q_n - q + \lambda \cdot n \cdot \sigma_1^2}{\sqrt{2n}\,\sigma_1} \right) \right] \Bigg], \tag{5.6}$$

where P_u the probability of measuring a non-Gaussian charge contribution from background signals and

$$\begin{aligned} Q_n &= Q_0 + n \cdot Q_1, \\ \sigma_n &= \sqrt{\sigma_0^2 + n \cdot \sigma_1^2}, \\ G(x, \mu, \sigma) &= 1/(\sqrt{2\pi}\sigma) \cdot \exp\left(-(x - \mu)^2/2\sigma^2\right). \end{aligned} \tag{5.7}$$

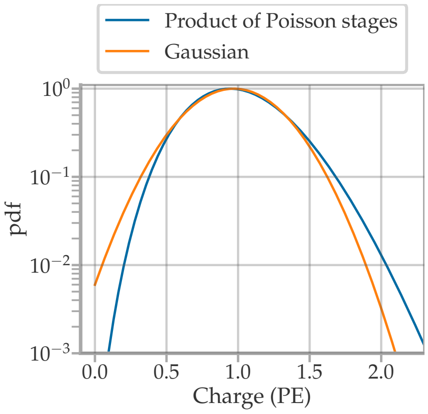

Figure 5.9: Comparison between an SPE spectrum produced assuming Poisson statistics on each dynode stage for a 10 stage PMT and the best fit with a Gaussian.

After fitting an SPE spectrum with function 5.6, the gain of the PMT is derived as $G = \frac{Q_1}{e}$, where e is the elementary charge. This model is used in several analyses of this thesis, although not exclusively.

A Gaussian model for $S_1(q)$ is normally a good approximation, although it has some caveats, such as being symmetric and allowing negative values. A better approximation is to follow Equation 5.3 and assume that the multiplication of an electron at a dynode follows a Poisson distribution with mean δ, with δ the gain of the dynode. This can be done via a simple Monte-Carlo simulation or with numerical algorithms, such as the one introduced in [123]. Figure 5.9 shows the distribution resulting from a numerical calculation following [123] for an exemplary 10-stage PMT and the best-fit Gaussian. Since the numerical distribution is asymmetrical, its maximum does not lie at the average of the distribution (in Figure 5.9 normalised to be 1 PE), and it also extends to higher values than the Gaussian model. This means that fitting with a Gaussian results in a biased measurement of the gain.

[123]: Rademacker (2002), *An exact formula to describe the amplification process in a photomultiplier tube*

This is further complicated by the fact that the gain is not homogeneous along the photocathode [110], and thus even a numerical distribution could result in a poor model and in a biased average charge.

[110]: Unland Elorrieta et al. (2021), *Homogeneity of the photocathode in the Hamamatsu R15458-02 Photomultiplier Tube*

An accurate determination of the gain (the average of the SPE distribution) is important, since the best estimate of the number of photons detected in a large pulse of charge Q is in first order Q/G, and thus any bias on G is propagated to the reconstruction. These biases can be partially

[11] Equation 5.6 results from the convolution of the three functions, as explained in [121], which is solved in Appendix A. However, it is worth noting that the solution presented in Appendix A differs from the one given in [121], which the author considers to be incorrect. The SPE fitter used in this thesis has been implemented in Python and is available at [122].

resolved by calculating the effective detection efficiency by comparing data and MC simulations using the assumed charge spectrum. Thus, any overestimation of the gain would be absorbed by an underestimation of the PMTs detection efficiency, and vice versa.

mDOM Photomultiplier Characterisation and Simulation

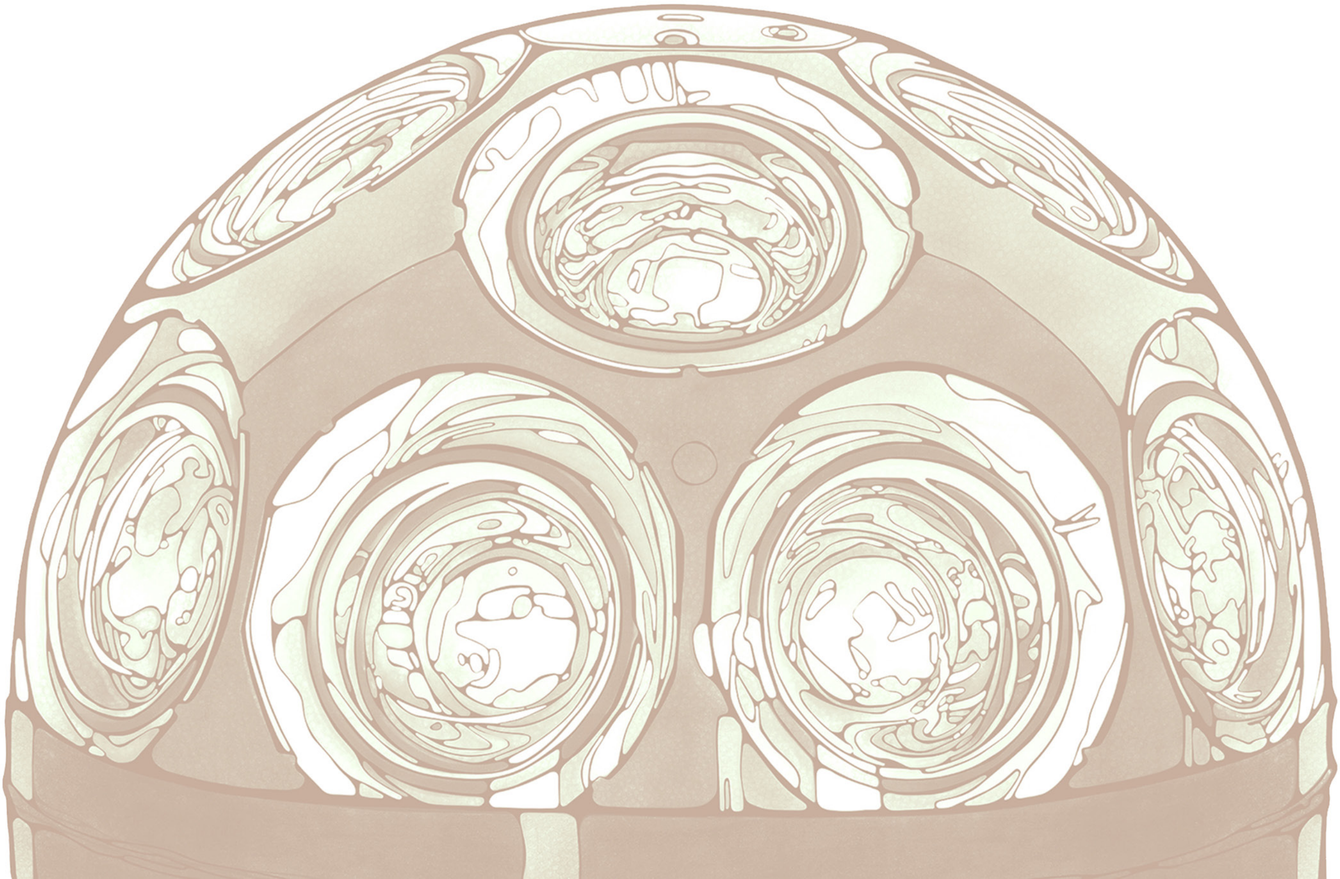

6

General performance parameters

The PMT characteristics are an essential contributor or limiter to the performance of a neutrino telescope, as they are the primary detectors of an optical module. For example, uncertainty in the photon time affects the reconstruction, since their arrival times are the main estimator for the distance between the module and the path of the particle. On the other hand, uncertainties in the charge reconstruction affect photon counting and thus the energy reconstruction of the charged particle that produced the Cherenkov radiation [124].

[124]: Spiering (2020), *Neutrino Detectors Under Water and Ice*

As introduced in Section 4.1.1, the mDOM PMT — the 80 mm R15458 from Hamamatsu — is based on the R12199-02 model used in the optical module of KM3NeT. In this context, the performance of 7000 R12199-02 PMTs was published in [125]. In [126], it was shown that the mDOM PMT performs similarly to its parent model, even at the low temperatures encountered in the IceCube experiment. In the scope of this publication [126], two PMTs were thoroughly measured in temperature dependence. Some of the results measured by the author published in [126] are also shown in this chapter.

[125]: Aiello et al. (2018), *Characterisation of the Hamamatsu photomultipliers for the KM3NeT Neutrino Telescope*

[126]: Unland Elorrieta et al. (2019), *Characterisation of the Hamamatsu R12199-01 HA MOD photomultiplier tube for low temperature applications*

In the following, the performance of the mDOM PMT at different temperatures and for light of various wavelengths is presented. First, Section 6.1 introduces the experimental setup and analysis method used in many studies of this work. Then, the performance parameters related to pulse mode operation are studied. The pulse shape parameters and timing of the mDOM PMT are covered in Section 6.3. This is followed by the gain characteristics in Section 6.2. Section 6.5 examines the magnetic field dependence of the PMT characteristics discussed in previous sections. Finally, the detection, quantum and collection efficiency of the mDOM PMT are studied in Section 6.4.

Generally, the background noise of a PMT is also considered a standard performance parameter. Nevertheless, due to the extension of the background studies, a separate chapter, Chapter 8, is dedicated to the characterisation of the dark rate and signal-induced pulses.

6.1 Experimental setup and analysis of pulses

In the following, the experimental setup used in this chapter with the PMT driven in pulse mode is presented. After that, the analysis method for extracting pulse information from waveforms measured by an oscilloscope is introduced in Section 6.1.2.

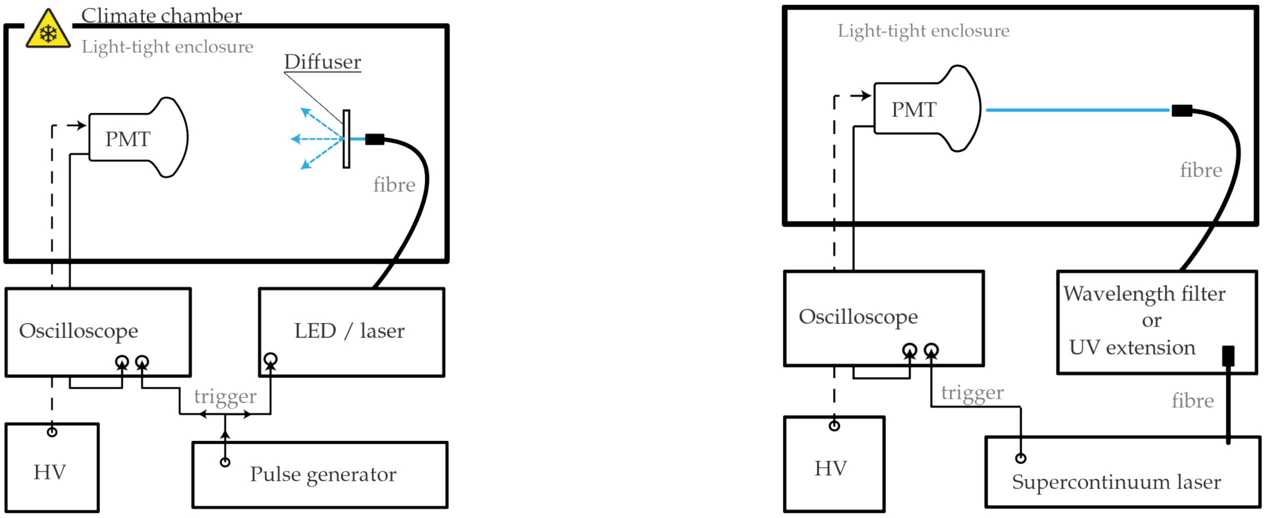

Figure 6.1: *Left:* Experimental setup for the measurement of PMT pulse parameters. The climate chamber was used only in temperature-dependence investigations. In magnetic field studies the PMT is surrounded by Helmholtz coils (not shown in the sketch). *Right:* Experimental setup used for the wavelength dependence investigations of Section 6.3.3, Section 6.2.3 and Section 6.4.2.

The QE of the PMTs is measured in current mode. The setup of that measurement is explained separately in Section 6.4.

6.1.1 Experimental setup

The left side of Figure 6.1 illustrates a generic experimental setup used to measure parameters in pulse mode. The PMT must be in a light-tight enclosure to avoid a high dark rate. In the case of the magnetic field investigation of Section 6.5 this is a 'dark room', due to the size of the Helmholtz coils. For the temperature dependence studies of Section 6.3.2 and Section 6.2.2, a small 'dark box' was used inside a climatic chamber [1]. Both the darkroom and the darkbox have 'photon mazes' on the outside and inside. These are anodised aluminium tunnels through which cables can be routed from the outside to the inside of the enclosure (see Figure 6.2).

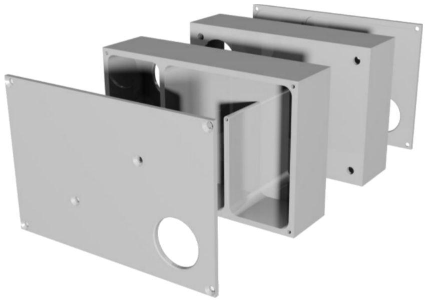

Figure 6.2: Exploded view of a photon maze used to route the cables into a light-tight enclosure. One maze is on the outside of the enclosure, the other on the inside. Picture taken from [108, p. 114] and modified.

The PMT pins are connected via a passive base to a high-voltage supply[2]. The anode signal is measured with an oscilloscope.[3]

Because it is desired to measure mostly SPEs pulses, the PMT is illuminated with an LED[4] of adjustable intensity. The light from the LED is coupled to a fibre optic and pointed towards the PMT. A diffuser is placed at the fibre output to illuminate the entire photocathode. A pulse generator[5] simultaneously triggers the LED and the oscilloscope with a frequency of 20 kHz.

The right side of Figure 6.1 shows the experimental setup used for the wavelength dependency investigations of Section 6.3.3 and Section 6.2.3. A supercontinuum laser[6] was used, which produced a white beam with wavelengths from 450 nm to 2400 nm. The wavelength was selected using either a wavelength filter[7] or a UV extension[8]. In the former case, wavelengths from 460 nm to 1000 nm can be selected with a bandwidth of 2.5 nm. The UV extension unit enables wavelengths between 265 nm to

---

1: CTS C-70/350.

2: Iseg NHQ 226L.

3: Lecroy Waverunner 640Zi in Section 6.3, PicoScope 6404C otherwise.

4: In Section 6.3.1: PicoQuant PDL 800-B with LED head PLS-8-2-719 (centre wavelength 459 nm). In Sections 6.3.2 and 6.2.2: 385 nm LED mrongen – Custom Picosecond light sources [127].

5: RIGOL DG1032Z.

6: SuperK COMPACT from NKT Photonics.

7: LLTF VIS HP8 from NKT Photonics.

8: SuperK EXTEND-UV from NKT Photonics.

480 nm via frequency doubling with a bandwidth from ~2 nm at 265 nm to ~12 nm at 480 nm. Due to the high beam intensity, the output had to be attenuated using ND filters.[9] These acted as a wavelength-shifter in the UV; therefore, only wavelengths between 400 and 650 nm were measured.

The output of the wavelength filter and UV extension is collimated, resulting in a beam with a width of approximately 0.1 mm.[10] As discussed later, the wavelength dependence of PMT parameters is mostly determined by the trajectories of the SPEs from the photocathode to the first dynode. To minimise the number of possible SPE paths, in the wavelength-dependence studies, the beam was directed to the centre of the PMT rather than using a diffuser.

6.1.2 Capture and analysis of PMT pulses

The output signal of a PMT for an SPE exhibits significant variability for most performance parameters. Therefore, to accurately characterise a PMT, a large number of waveforms must be analysed to produce a statistical distribution of the parameters. Additionally, when using an external illumination device, the light intensity is typically set to very low levels to produce pulses at the single photon level, resulting in a large number of triggered PMT waveforms that are empty. These factors make saving the waveforms to memory an inefficient task that requires substantial storage capacity and post-measurement analysis time. As a result, in the majority of measurements in this work, the PMT signal was analysed in real-time, immediately after its transmission from the oscilloscope to the PC.

Two methods were developed to extract pulse properties from a waveform. In the following, the case where only one pulse per waveform is analysed is referred to as a *single-pulse analysis* (SPA). In contrast, a *multi-pulse analysis* (MPA) is applied in measurements in which many pulses of the waveform are analysed.

In the case of a SPA, a region of interest (ROI) is defined as a ±15 ns window around the minimum of the waveform. It is important to note that if the waveform does not contain any pulse, the minimum of the waveform is simply the signal baseline. When using the MPA method, the ROI positions are selected using the Python package *scipy.signal.find_peaks* [128]. This function retrieves a list of the pulse-candidate's arrival times in the waveform that conform to certain peak properties, such as their amplitude and distance between pulses. In an MPA, only pulses that surpass the threshold configured in *scipy.signal.find_peaks* are saved. In contrast, in an SPA, all waveforms have one, and only one, ROI. The MPA results in data that is almost completely free of electronic noise (if the threshold was set high enough), although transients in the baseline could still be captured if they surpass the set threshold. On the other hand, an SPA dataset inherently features a large amount of background which must be considered in post-analysis. However, it is threshold-free, meaning that pulses of small amplitude can also be measured as long as they are larger than the intrinsic baseline peak-to-peak variation.

[9] NE40A, NE30A and NE15A from Thorlabs.

[10] The beam size of this laser is measured in Section 9.2.

[128]: Virtanen et al. (2020), *SciPy 1.0: Fundamental Algorithms for Scientific Computing in Python*

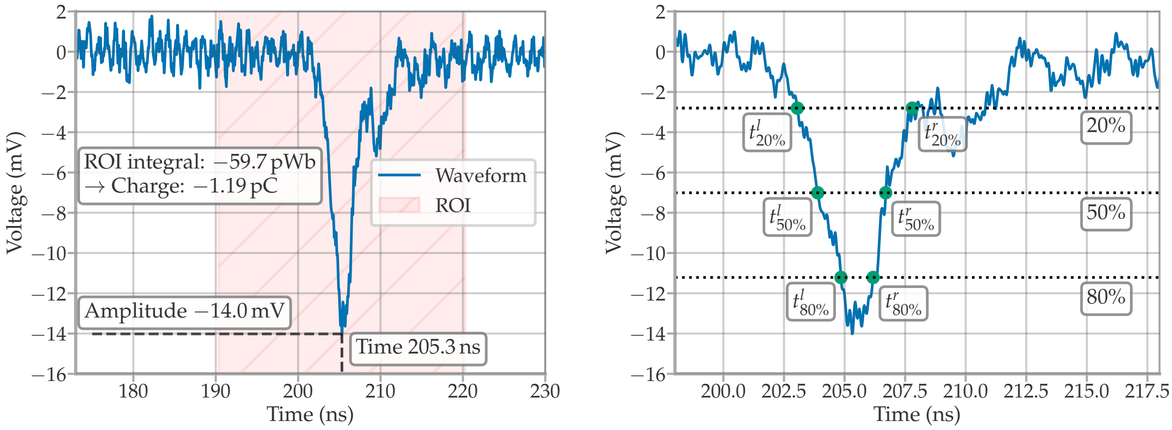

Figure 6.3: Example of extraction of parameters from a single PMT pulse. *Left:* Extraction of amplitude, arrival time, and charge. *Right:* Extraction of pulse shape parameters, rise time, fall time and FWHM. Waveform measured with an oscilloscope directly from an mDOM PMT.

All ROIs are analysed to extract the pulse charge, arrival time, amplitude, and, in some cases, the pulse shape parameters. The arrival time of a pulse is defined at the time of the minimum of the ROI and the pulse amplitude by the voltage level of the minimum. The charge is calculated by integrating the ROI (±15 ns around the extracted arrival time) and dividing this result by the input resistance of the oscilloscope, in this work always 50 Ω. An example of such feature extraction is shown on the left side of Figure 6.3.

For the calculation of shape parameters, it is necessary to obtain the crossing time at 20%, 80% (or 10% and 90%) of the amplitude for the rise and fall time and 50% for its full width at half maximum (FWHM). For this, the following routine is used:

- The ROI is separated into two parts, the waveform to the left of the minimum and its right.
- The time-voltage pairs (t_i,v_i) of each part are tested starting from the minimum of the ROI towards the outer region. This means that the left part starts to be tested from the latest times and the right part from the earliest.
- Once the amplitude v_i of the element pairs (t_i,v_i) inside a part is above a certain desired level, a linear interpolation is performed with the previous pair of elements (t_{i-1},v_{i-1}) to obtain the best estimate of the time of crossing t_v of the sought level v

$$t_v = t_{i-1} + (t_i - t_{i-1}) \cdot \frac{(v - v_{i-1})}{(v_i - v_{i-1})}.$$

- Once all the sought levels are obtained, the pulse shape parameters are calculated as

$$\begin{aligned}\text{Rise time}: t^l_{80\%} - t^l_{20\%}\\ \text{Fall time}: t^r_{20\%} - t^r_{80\%}\\ \text{FWHM}: t^r_{50\%} - t^l_{50\%},\end{aligned}$$

where the superscripts $\{l, r\}$ stand for the time crossings extracted from the left and right parts of the ROI, respectively.

An example of the extraction of the shape parameters of a pulse is shown in Figure 6.3. Only the first threshold crossing after the minimum is counted, ignoring cases where the pulse extends further with secondary peaks, which also cross the threshold levels, such as the case in Figure 6.3. This is done to avoid including noise and transients in the measured parameters. The described routine can fail if there is no pulse inside the ROI, as is possible in a SPA measurement. In this case, default values are saved, which can be easily cleaned out during analysis. Saving a default value is necessary to maintain the array size of all parameters and hence easily correlate a set of parameter results to the same pulse by their position in the arrays.

6.2 GAIN AND SPE RESOLUTION

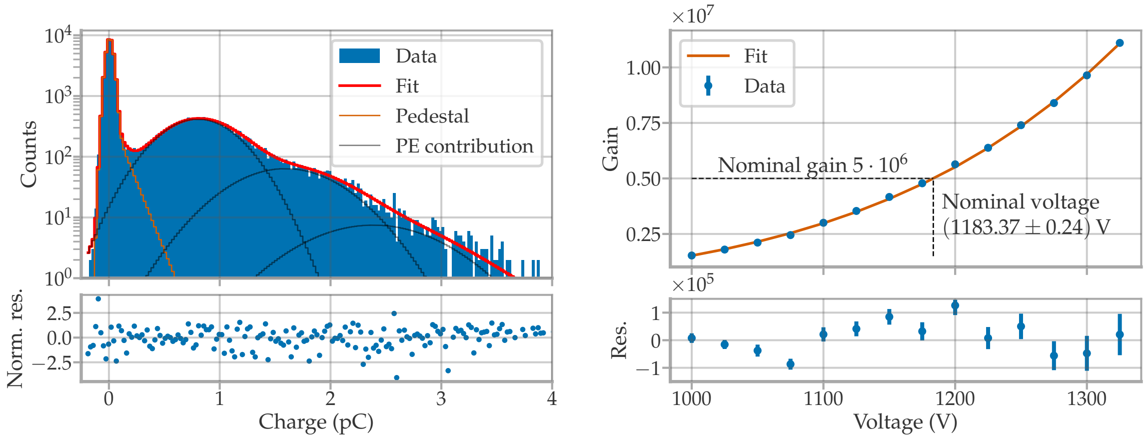

Figure 6.4: *Left:* An SPE charge distribution and its corresponding fit using Equation 5.6 shown in red, used to calculate the gain. The background contribution of the fit model is shown with a yellow line and each PE component is shown in black. The residuals were normalised with the bin uncertainty. *Right:* A complete gain calibration, after calculating the gain at different operating voltages. Fitting with Function 6.1 enables the determination of the nominal voltage of a PMT.

As introduced in Section 5.5, the gain of a PMT is commonly calculated by measuring and fitting its charge spectrum. The mean charge of an SPE is equal to the gain if it is expressed in number of electrons. This means that, after fitting a spectrum with Equation 5.6, the gain is Q_1/e. The SPE resolution is proportional to the variance of the SPE charge distribution, and in the case of Equation 5.6, it is defined as σ_1/Q_1 and often given as a percentage.[11]

The left side of Figure 6.4 depicts the SPE spectrum of an mDOM PMT operated at its nominal gain of $5 \cdot 10^6$. The fit with Equation 5.6 and its individual Gaussian components are shown in red and black, respectively. The SPE resolution in this example is (39.0 ± 0.5) %.

The PMT must be calibrated to calculate its *nominal voltage*, the voltage needed for the nominal gain. This is done by measuring the gain at different applied voltages, resulting in a gain-voltage curve, such as the one shown on the right side of Figure 6.4. This curve is then fitted with Equation 5.4, from which the voltage needed for the nominal gain is calculated. Since a power law can result in numerical problems during

[11] In literature, it can also be found the FWHM of the charge distribution is used as SPE resolution instead of σ_1. The FWHM does not require a fit but is susceptible to the MPE contribution in the spectrum.

fitting, often the double logarithm of this curve is fitted instead. In this case, the relationship is linear

$$\log(G) = \log(a \cdot V^b) = b \cdot \log(V) + \hat{a}, \tag{6.1}$$

with $\hat{a} = \log a$. However, the downside of this is an overestimated uncertainty on the nominal voltage, since the parameters a and b are usually highly correlated. This correlation can be seen in Figure 6.5, which shows the contour of the two fit parameters around the minimum for the data shown in Figure 6.4 left. For the data of the example, the error for the fitting of the nominal voltage with Equation 6.1 is ±0.8 V, while the correct uncertainty is ±0.24 V. Therefore, the best approach was found to first fit the data with Equation 6.1 and use the fit results as initial parameters for a minimisation with Equation 5.4.

Assuming that all stages of the dynodes are identical, with a stage gain of $\alpha \cdot v^\beta$, it follows from Equation 5.4 that $b = n \cdot \beta$, where $n = 10$ is the number of PMT dynodes. Under this assumption, α can also be obtained from a as

$$a = \alpha^n \frac{3^\beta}{13^{n \cdot \beta}}, \tag{6.2}$$

since the used dynode ratio is 3 : 1... : 1. For the calibration shown in Figure 6.5 this results in $\beta = 0.7026 \pm 0.0019$. The value agrees with the expectations of the literature, where the exponent β ranges between 0.65 and 0.75 depending on the dynode material [129]. Equation 6.2 yields $\alpha = 0.1819 \pm 0.0014$. The parameter α is strongly material dependent, as, for example, $\alpha = 0.09$ for BeCu-dynodes and $\alpha = 0.172$ for SbCs-dynodes has been reported [116, p. 205]. Nevertheless, since the dynode material of the mDOM PMT is not public information and reference values are scarce, no further comparison with literature can be made.

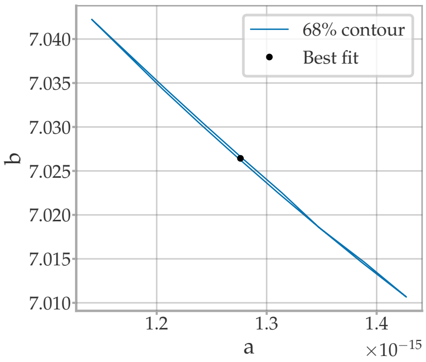

Figure 6.5: Best fit and contour for the 68% certainty region of the fit shown on the right side of Figure 6.4.

[129]: Flyckt et al. (2002), *Photomultiplier tubes - principicles and applications*

[116]: Wright (2017), *The Photomultiplier Handbook*

Figure 6.6 shows the SPE resolution of an mDOM PMT at different gains. As can be noticed, the resolution improves with the gain, especially in the low-gain region. However, the curve is significantly less steep, and working with PMTs at gains higher than the nominal of $5 \cdot 10^6$ would only marginally improve the resolution.

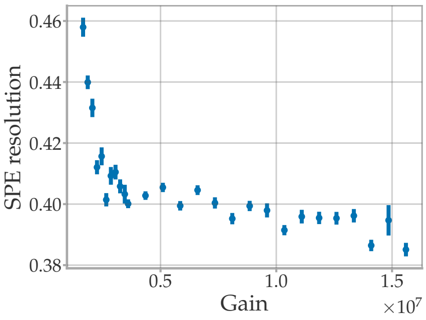

Figure 6.6: SPE resolution against the gain of PMT BA0373 at room temperature.

6.2.1 BIAS OF GAIN FIT MODEL

As introduced in Section 5.5, the gain calculated from the fit with Equation 5.6 is biased, as the model assumes a Gaussian as the SPE response. Since a chain of Poissonian multiplications produces the charge, the distribution has only positive values and is asymmetric (see Figure 5.9). This section estimates the bias of the gains calculated in this work.

For the following analysis, it was assumed that all dynodes work similarly (i.e. their gain are described with the same parameters α and β. Using the algorithm of [123] an SPE distribution can be calculated for arbitrary gains. In this algorithm, the user sets the gain of each dynode as input. The resulting curve is a pdf of the number of electrons that arrive at the anode. The algorithm was verified with a Monte-Carlo simulation sampling from a Poisson distribution at each stage. The results agree for all the tested

[123]: Rademacker (2002), *An exact formula to describe the amplification process in a photomultiplier tube*

dynode gains. However, the algorithm provides results much faster than the Monte-Carlo simulation and without statistical fluctuations.

From the used dynode ratio 3 : 1... : 1 and Equation 5.4 it follows that the gains of the dynodes that produce a total gain G are

$$\delta = G^{1/n} \cdot 3^{-\beta/n}, \text{ and } \delta_1 = G^{1/n} \cdot 3^{\beta \cdot ((n-1)/n)}, \tag{6.3}$$

where $\delta_1 = \alpha \cdot (3 \cdot V/13)^\beta$ is the gain of the first dynode, $\delta = \alpha \cdot (V/13)^\beta$ the gain of each of the rest of the dynodes. A factor $\beta = 0.7026$ was assumed from the results in the last section. The analytical SPE distribution was calculated for gains from 0.5×10^6 to 10×10^6 in steps of 0.5×10^6. Figure 6.7 shows the SPEs distributions calculated with [123] for the gains 0.5×10^6, 5×10^6 and 10×10^6. The x axes of the curves were divided by the gain to be able to compare them. Although the distributions are similar, the resolution improves with the gain in a similar fashion as in the measurement results of the last section (cf. Figure 6.6).

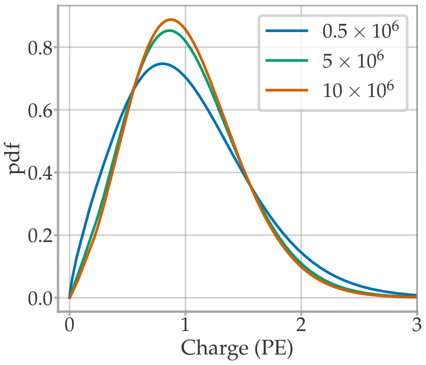

Figure 6.7: SPE distribution in PE for the gains 0.5×10^6, 5×10^6 and 10×10^6. Calculated with the algorithm provided in [123] for the dynode ratios of the mDOM PMT.

[123]: Rademacker (2002), *An exact formula to describe the amplification process in a photomultiplier tube*

The bias was calculated by generating charge distributions sampling from the analytical curves. For a single SPE spectrum of gain G, a set of 250,000 waveforms was simulated, where the charge of each waveform is generated as follows:

- First, the number of measured photons N is sampled from a Poisson of mean μ.
- A value c_i of the analytical SPE curve for gain G is sampled for each measured photon and summed. Thus, the total charge produced by the LED flash is $C = \sum_i c_i$.
- The charge produced by the baseline variation is added to C. In case that C is 0, this step would generate the pedestal. Here, a random value from a Gaussian of $\sigma = 0.3 \times 10^6$ was sampled. This is a typical pedestal width in actual measurements.

Ten charge distributions were generated for each investigated gain with varying light intensity from $\mu = 0.1$ to $\mu = 1.0$. As an example, the spectrum generated with $\mu = 0.7$ and the analytical curve of $G = 5 \times 10^6$ are shown in Figure 6.8.

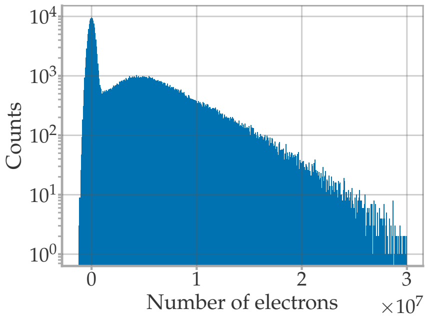

Figure 6.8: SPE distribution sampled randomly using $G = 5 \times 10^6$ and $\mu = 0.7$.

The sampled spectra were fitted using Equation 5.6, from which the gain is again calculated from the fit parameter Q_1. The dependency of the fitted gains on μ is rather small. Therefore, the gains obtained at the different light intensities were averaged. Figure 6.9 presents the ratio between the mean fitted gain and the true gain. In all cases, the fit underestimates the gain, with a larger bias the smaller the gain. At the nominal gain of the mDOM PMT (5×10^6) a bias of (-5.39 ± 0.08) % is observed.

These bias calculations were also performed simulating background from (partial) coincident dark rate pulses and prepulses. In these cases, the ratios of Figure 6.9 are up to 3 % smaller, but only at rather large probabilities for background events.

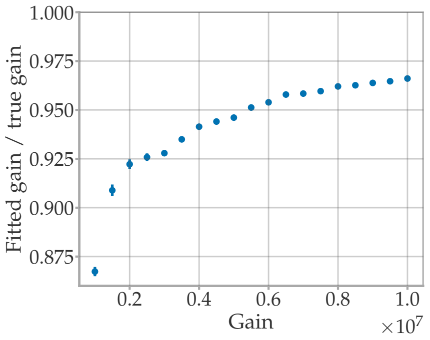

Figure 6.9: Ratio between the mean fitted gain (average between the results at different μ) and the true gain.

This gain bias is irrelevant for the majority of the studies in this work. Most of the time, the gain calibration is used to adjust all PMTs to the same relative performance. However, in cases where the number of photons in MPE pulses is to be estimated directly using the gain, the bias will propagate in the calculated values. In principle, the fits could be performed using the analytical curves provided by the method of [123]. However, calculating a single SPE distribution with the algorithm takes a long time; thus, it would be impractical to implement in a minimisation procedure.

[123]: Rademacker (2002), *An exact formula to describe the amplification process in a photomultiplier tube*

6.2.2 Temperature dependence

The gain of the PMTs was investigated at low temperatures using a climate chamber. The temperature was lowered stepwise in 5 °C steps from 20 °C to −50 °C. Each temperature step included a settling period of 5 h before starting a gain calibration, measuring the gain voltages between 975 V to 1350 V in 25 V steps.

The charge distribution of the PMT with serial number (SN) BA0375 driven at 1200 V at temperatures of 20 °C and −50 °C is shown in Figure 6.10. It can be noticed that the SPE distribution shifts to larger charges at −50 °C compared to room temperature, resulting in a 23.4 % larger average SPE charge Q_1 after fitting both spectra. This implies a decrease in gain with the temperature of ~0.3 %/°C.

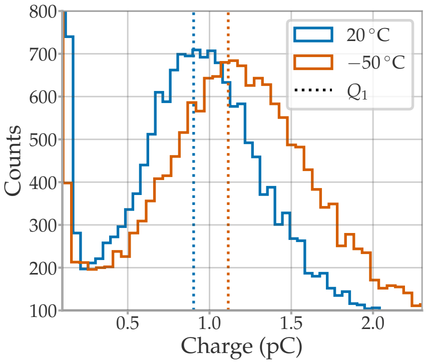

Figure 6.10: Zoomed SPE spectrum of PMT BA0375 driven with 1200 V at 20 °C and −50 °C. The vertical dashed lines represent the position of the one PE Gaussian after fitting the spectra.

Each charge spectrum was fitted with Equation 5.6, from which the gain was calculated at each voltage and temperature step. Figure 6.11 shows the results for two mDOM PMTs. After fitting the gain-voltage curve at each temperature, the nominal voltages were interpolated, which are also shown in Figure 6.11 as orange points marking the contour line for the 5×10^6 gain. The gain consistently increases with lower temperatures independently of the set voltage. This has the consequence that the nominal voltage is lower with descending temperatures, making an in situ calibration of the PMTs after the deployment of the mDOMs mandatory.

These results agree with other studies reporting similar temperature coefficients [116, p. 218][130, 131]. In contrast, [131] also reported the opposite behaviour when measuring at even lower temperatures. They found that the gain decreased by 3 % compared to room temperature after the PMTs were inserted in liquid xenon at −100 °C, despite initially increasing with cooling. In [130, p. 300] it is argued that the mean free path for the scattering of electrons in the dynode material decreases with

[116]: Wright (2017), *The Photomultiplier Handbook*

[130]: Dekker (1958), *Secondary Electron Emission*

[131]: Barrow et al. (2017), *Qualification Tests of the R11410-21 Photomultiplier Tubes for the XENON1T Detector*

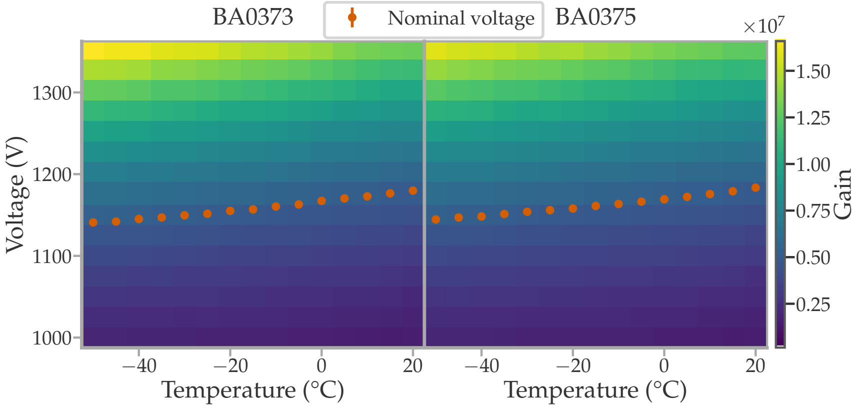

Figure 6.11: Calculated gain for each temperature and voltage step for two mDOM PMTs. At each temperature the gain-voltage curve is fitted and the nominal voltage is interpolated, which is indicated by the orange markers. Error bars are smaller than the marker size.

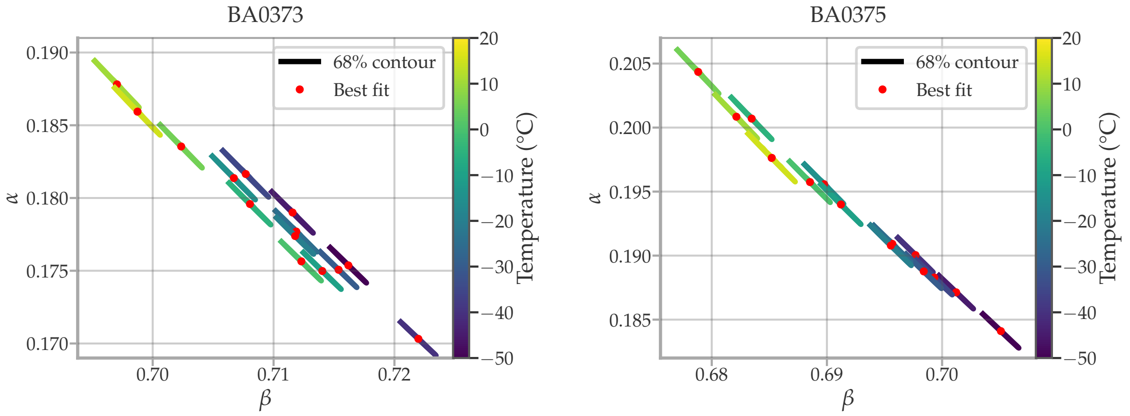

Figure 6.12: Best-fit parameters from the fit calibrations (see Equation 6.4) at all temperature steps of PMT BA0373 (left) and BA0375 (right). The 68 % contour line was drawn around the best-fit values and indicates the corresponding temperature step.

temperature. At each scattering process, the electrons lose energy. If the energy is lower than the electron affinity of the material, the electron is lost for the secondary emission process, reducing the yield of the material. On the other hand, [131] suggested that the increase in gain is artificial and results from a lower electric resistance of the signal cables. But this hypothesis is questionable, as a higher cable resistance would result in a decrease in voltage but not in current, resulting in smaller and wider PMT pulses but retaining the original charge.

[131]: Barrow et al. (2017), *Qualification Tests of the R11410-21 Photomultiplier Tubes for the XENON1T Detector*

To further study this effect, the temperature dependence of the fit parameters of Equation 5.4 was examined. They were first disentangled, assuming that all dynodes are equal (as was done in the last section), and the gain calibration was refitted with

$$G = \alpha^n \frac{3^\beta}{13^{n\cdot\beta}} V^{n\cdot\beta}, \tag{6.4}$$

with $n = 10$ the number of dynodes. The best fit and 68% contour of α and β for the data at each temperature step is presented in Figure 6.12. There is a clear tendency for β to decrease with temperature, while α shows the opposite behaviour. Therefore, the increase in gain at lower temperatures would be solely explained by the rise of the exponent β, which also has to compensate for the decrease of α.

The α and β best-fit positions follow the same correlation as their individual 68 % confidence regions, from which one could postulate that the observed behaviour is a fit artefact due to low statistics. To discard this possibility, a fake data set was sampled from a Gaussian distribution for each temperature step, using as mean the gains measured at 20 °C and as standard deviation their uncertainty, both scaled by a constant factor to achieve the gain change of 0.3 %/°C. The resulting α and β best fit positions after fitting these fake data sets are shown in Figure 6.13. As expected, in this case, the change in gain is completely covered by α, which decreases with temperature, while β remains constant considering its uncertainty.

In Figure 6.14, the α and β best-fit positions of Figure 6.12 are plotted

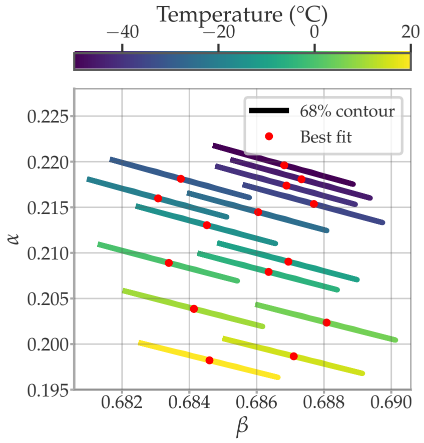

Figure 6.13: Fitted α and β of fake data generated sampling from Gaussian distribution to test statistical artefacts (see text).

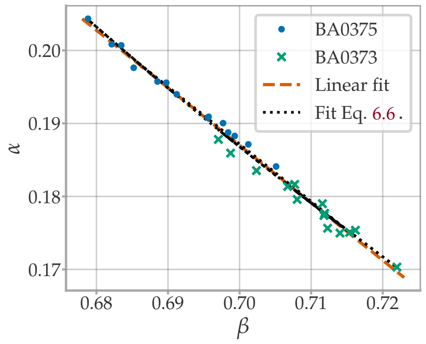

Figure 6.14: All pairs of α and β fitted for PMT BA0373 and BA0375. Data were fitted with a linear function and Equation 6.6.

again, but with both PMTs together. Remarkably, the α and β pairs seem to follow a linear relationship similar for the two PMTs. Fitting a line results in $\alpha = \beta \cdot (-0.79 \pm 0.02) + (0.74 \pm 0.01)$.

One possible explanation for this correlation is that the fit model used is incorrect and that both parameters are not genuinely independent. Indeed, secondary electron emission models, such as [132], are complicated and contain many parameters. The semi-empirical equation assumed for the dynode gain is an approximation for low energies and is probably bound to introduce correlations. However, another explanation for the observed correlation could be constraints for the gain-voltage relationship outside the measured range. For example, if we assume that the gain at a certain voltage V_0 is constant and independent of the temperature,

[132]: Furman et al. (2002), *Probabilistic model for the simulation of secondary electron emission*

$$(\alpha)^{10}\frac{3^{\beta}}{13^{10\cdot\beta}}V_0^{10\cdot\beta} = K, \tag{6.5}$$

solving for α, this constraint would result in the following

$$\alpha = \frac{13^{\beta}\cdot K^{1/10}}{3^{\beta/10}V_0^{\beta}}. \tag{6.6}$$

This is certainly not a linear function, but depending on the set K and V_0, near-linear relationships between α and β can be obtained for the limited range of measured β values. Fitting the measurement data with Equation 6.6 produces a similar agreement as with the linear function (see Figure 6.14) resulting in the fit parameters $K = (3 \pm 2) \cdot 10^5$ and $V_0 = (786 \pm 70)\,\mathrm{V}$.

If one assumes that the near-linear relationship between α and β holds for longer ranges, increasing β will not always translate into a larger gain, since at some point, the decreasing α will dominate. This can be observed in Figure 6.15, where the change of the gain relative to the value at 20 °C is shown for a hypothetical PMT driven at 1300 V, which follows the linear relationship between α and β shown in Figure 6.14 and the linear relationship between β and the temperature shown in Figure 6.12 (linear fit results in $\beta = -3.55 \cdot 10^{-4} T + 0.687$). For this hypothetical case, the gain stops increasing at ~−110 °C and it even starts to be lower than at room temperature below ~−220 °C. These calculations require extrapolation at far distances from the measured relationships between α and β and their temperature dependence, making them very crude. However, this shows how in principle, the contradictory temperature dependence of the PMT gain found in literature could be fully explained by the temperature dependence of α and β.

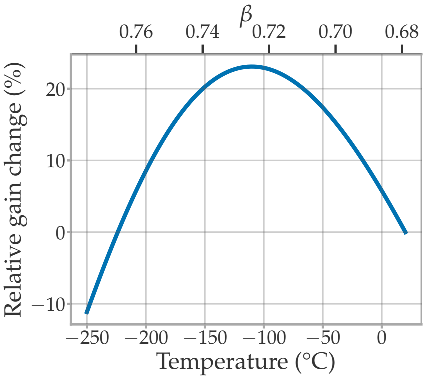

Figure 6.15: Extrapolated gain change with temperature relative to 20 °C.

In Figure 6.16, the SPE resolution against the measured gain at 20 °C and −50 °C is presented. Both PMTs were plotted in the same figure to gather more data points. The temperature dependence of the SPE resolution is difficult to disentangle. On the one hand, as observed in Figure 6.6, the resolution depends on the gain, and since the latter changes with temperature, the resolution will also change accordingly. On the other hand, this parameter is usually less well determined by the fit due to the correlation to other fit parameters, making a specific assertion challenging.

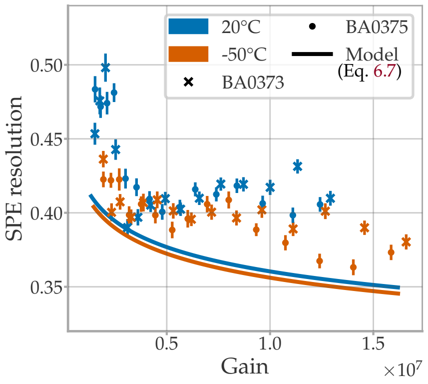

Figure 6.16: SPE resolution against the gain of PMT BA0373 and BA0375 at 20 °C and −50 °C and the expected resolution calculated with Equation 6.7.

Although the uncertainties are relatively large, there is a tendency for a better resolution with lower temperatures. In the gain interval from $3 \cdot 10^6$ to $7 \cdot 10^6$, the average SPE resolution is 0.407 ± 0.003 and 0.400 ± 0.002 at 20 °C and −50 °C, respectively, which translates to a relative improvement of (1.7 ± 0.8) %.

In [116, p. 156], a statistical model is derived that estimates the variance of the number of electrons after the dynode multiplication. In this framework, the expected SPE resolution can be calculated as

[116]: Wright (2017), *The Photomultiplier Handbook*

$$\sqrt{\frac{\delta}{\delta_1 \cdot (\delta - 1)}}, \tag{6.7}$$

where δ_1 is the gain of the first dynode and δ the average gain of the other dynodes. Since the dynode ratios used is 3 : 1 : ... : 1, Equation 6.7 can be calculated using $\delta_1 = \alpha \cdot (3 \cdot V/13)^\beta$ and $\delta = \alpha \cdot (V/13)^\beta$ with the fitted α and β from Figure 6.12. The expected SPE resolution for the fitted parameters of PMT BA0375 at 20 °C and −50 °C is shown in Figure 6.16. Although the model underestimates the measurement, it predicts an improvement in the resolution of around 1.2 % at −50 °C relative to 20 °C, which agrees with the measurement.

Nevertheless, the increase is too small to be significant when compared to the intrinsic variation between PMTs. Therefore, from a practical perspective, this parameter can be considered temperature independent.

6.2.3 Wavelength dependence

Initial studies on the wavelength dependence of the mDOM PMT's gain were conducted as part of a Bachelor's thesis [133, pp. 30–33], which was co-supervised by the author. The study involved measuring the gain of the PMT at different wavelengths while keeping the voltage constant. The results suggested an increase in gain in the wavelength range of 460 to 650 nm, but also revealed inconsistencies and substantial uncertainties. These inconsistencies can be partially attributed to the non-Poisson photon counting statistics of the laser system, which was not taken into account in the fitting model used.

[133]: F. Peters (2020), *Studien zur Wellenlängenabhängigkeit von Performance-Parametern von Photomultipliern des Typs Hamamatsu R12199-01 HA*

A more robust measurement of wavelength dependence is achieved with a complete gain calibration at each wavelength rather than remaining at a constant voltage. Five PMTs were measured in the wavelength range of 460 to 650 nm in 10 nm steps illuminating only the centre of the PMT (see setup introduced in Section 6.1). Three of the PMTs were also calibrated with one UV extension module, covering the wavelength interval from 400 to 450 nm in 10 nm steps. At each wavelength, an SPE spectrum was measured at the voltages from 1000 V to 1300 V in 25 V steps. The spectra were fitted with a modified version of Equation 5.6

$$f(q) = \sum_{n=0}^{3} A_n \left[(1 - P_u) \cdot G(q, Q_n, \sigma_n) + \ldots \right], \tag{6.8}$$

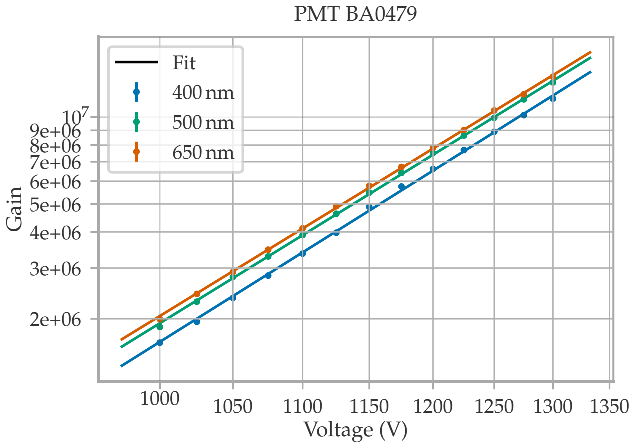

Figure 6.17: Gain calibration of the mDOM PMT BA0789 performed at three different wavelengths. The two axes are on logarithmic scales. The error bars are smaller than the marker size.

where the Gaussian n is weighted by the free parameters A_n instead of a probability from a Poisson distribution and '...' is the second line of Equation 5.6. The sum was truncated to $n = 3$ to avoid introducing too many free variables. This only affects the amplitudes of the Gaussians and the gain is still calculated using Q_1. The resulting gain-voltage curves were fitted with Equation 6.4.

The calibration curves for the wavelengths 400 nm, 500 nm and 650 nm of PMT BA0479 are shown in Figure 6.17. Although the differences are small, there is a clear wavelength dependence of the gain consistent through all measured voltages. From the calibrations, the gain of the PMTs for any voltage within the measured range can be interpolated. Since there is no convention at which wavelength the nominal voltage of a PMT should be measured, without loss of generality, the voltage that leads to a gain of $5 \cdot 10^6$ at 460 nm was chosen as the nominal. This is the smallest wavelength measured with all PMTs.

Figure 6.18 shows the gain at the nominal voltage[12] against the wavelength for all investigated PMTs. In all cases, the gain increases with the wavelength. In the region from 460 nm to 650 nm, the PMTs feature a similar growth in gain of ~6 %. From 400 nm to 460 nm, the curves show a stronger wavelength dependence, with PMT BA0479 increasing by over 10 %.

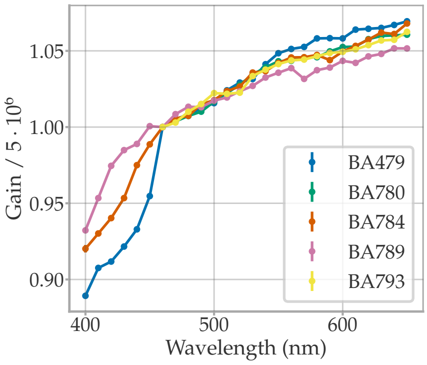

Figure 6.18: Wavelength dependence of the gain of five PMTs. The results are relative to the nominal value arbitrarily set to be at 460 nm.

The wavelength dependence of the gain is not well-researched, and no other studies in this regard could be found in the literature. Therefore, interpreting the results is a difficult task. However, what is known is that the trajectories of photoelectrons released from the same spot on the photocathode vary more for higher-energy photons, since the SPEs have a larger starting velocity in a random direction. Conversely, the longer the wavelength, the lower the starting energy of the SPEs and the more similar their paths are.

Assuming that the SPEs are released without any kinetic energy, all should follow the same trajectory and hit the same spot on the first dynode. This should also be the case for the conditions of this measurement since the laser beam is very thin and illuminates a small spot in the centre of the photocathode. If the electric field lines from the centre of the photocathode terminate at a point in the first dynode where the gain is

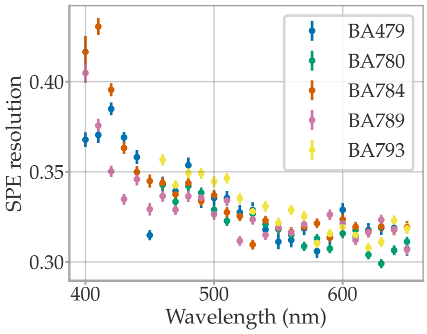

Figure 6.19: SPE resolution against wavelength of all measured PMTs.

---

[12] i.e. the voltage at which the PMT features a gain of $5 \cdot 10^6$ for 460 nm-light.

high, increasing the photon energy (and thus the SPE initial velocity) could lead to a decrease in the average gain, as the SPEs could be deflected to regions of the first dynode of lower multiplication. Furthermore, the secondary emission yield depends on the angle of entry of the impinging electron [132], with the maximum gain for the SPEs hitting perpendicular to the surface. Thus, the increased variance in the SPE trajectories could result in the SPEs arriving at larger angles to the first dynode, producing fewer secondaries.

[132]: Furman et al. (2002), *Probabilistic model for the simulation of secondary electron emission*

Figure 6.19 shows the SPE resolution at the closest measured voltage to the nominal voltage of the PMTs. It is clear that increasing the wavelength results in a better SPE resolution (which is a measure of the SPE charge variance). This resolution improvement cannot be explained by the SPE dependence on the gain, as the change in the resolution in the region between $4.5 \cdot 10^6$ and $5.5 \cdot 10^6$ is marginal (see Figure 6.6). This supports the idea of a more 'collimated' SPE path towards the first dynode and, thus, less variation of the first multiplication stage with longer wavelengths.

Figure 6.20 shows the fitted α and β pairs from all gain calibrations at different wavelengths of each PMT, as was done in the last section in Figure 6.14. Here, a linear behaviour between both parameters can also be observed. The average slope of the linear fits is -0.076 with a standard deviation of 0.002, while the mean intercept is 0.723 with a standard deviation of 0.016. These values are very similar to those calculated for the temperature dependence in Section 6.2.2, supporting the idea of the correlation between α and β stemming from a boundary condition instead of reflecting the temperature/wavelength dependence of a variable that α and β depend on.

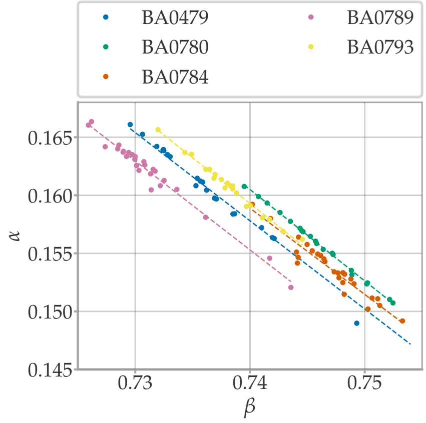

Figure 6.20: All fitted α and β pairs of the gain calibrations performed at different wavelengths. Each PMT is plotted with its own colour including a linear regression.

6.3 Timing and pulse shape parameters

The temporal resolution of the PMT is determined by the shape of the pulse generated by an SPE and the intrinsic transit time difference between pulses. The latter is typically parameterised with the TTS assuming that the transit time distribution follows a Gaussian, although other models are also used. As such, the TTS is the uncertainty of an SPE detection time, whereas the PMT pulse's shape sets the shortest time interval between two pulses that can be resolved.

In the actual mDOM operation, the AFE of the mDOM mainboard lengthens the pulses (see Section 4.1.3). The measurements shown in this section were performed with a PMT directly connected to an oscilloscope. Therefore, the characterisation of the pulse shape is not compatible with waveforms measured with the mDOM mainboard. Due to the AFE signal lengthening, the shortest time interval between two pulses that can be resolved worsens for the ADC waveforms compared to raw PMT pulses, but they can still be distinguished via the discriminator, as this samples the PMT signal directly. This can be observed, for example, in the measurement of Figure 6.21 carried out by IceCube collaborators, where the input for the mainboard AFE was a signal from a pulse generator with two pulses approximately 10 ns apart [134]. Thus, the PMT pulse shape characterisation is still needed to understand the mDOM response.

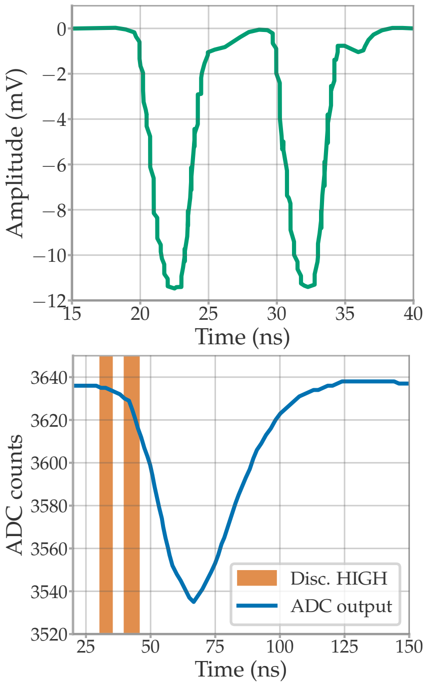

Figure 6.21: *Top:* Double pulse produced by a pulse generator used as input for the mainboard AFE. *Bottom:* Output of the discriminator and ADC for the double pulse. x-axes are independent from each other. Data taken by IceCube collaborators [134].

[134]: Sulanke (2022), *mDOM Mainboard Final Design Review (presentation)*

Figure 6.22 shows the average of 5000 pulses of an mDOM PMT operated at nominal gain with a passive base. Signal ringing is observed at ∼ 4 ns on the trailing edge of the pulse. These oscillations are caused by the circuit design of the voltage divider and could be avoided by adding *damping* resistors in series with the last dynodes [116, p. 513]. In principle, a discriminator could be triggered twice from a single pulse if the ringing is large enough, but this does not have consequences for the measurements shown in this work and has not been observed with the mDOM circuitry.

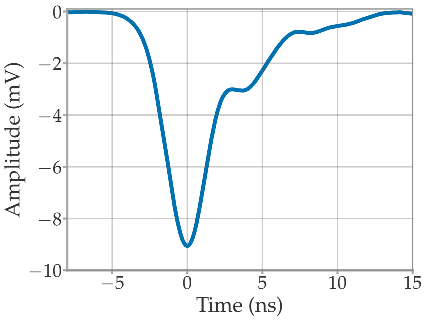

Figure 6.22: Average pulse of PMT BA0373 driven at nominal gain with a passive base.

Five PMTs were tested by illuminating with diffuse light covering the entire photocathode following the SPA method introduced in Section 6.1.2. As SPE pulses are of interest, only the data of pulses with charge in the interval of [0.5,1.5] PE are considered. The upper side of Figure 6.23 shows the resulting distributions of each pulse shape parameter of PMT BA0794. It should be noted that they vary significantly between different pulses, since the distributions are very broad. As discussed in Section 6.1.2, only the first amplitude crossing from the left and right of the pulse's minimum is saved. Since there is ringing on the right side of the pulse and the pulse shape parameters vary significantly, on some of the pulses, the ringing is larger than 20 % of the pulse amplitude, and on others, they are lower. Consequently, two peaks can be identified in the fall time distribution at ∼1.3 ns and ∼4.3 ns.

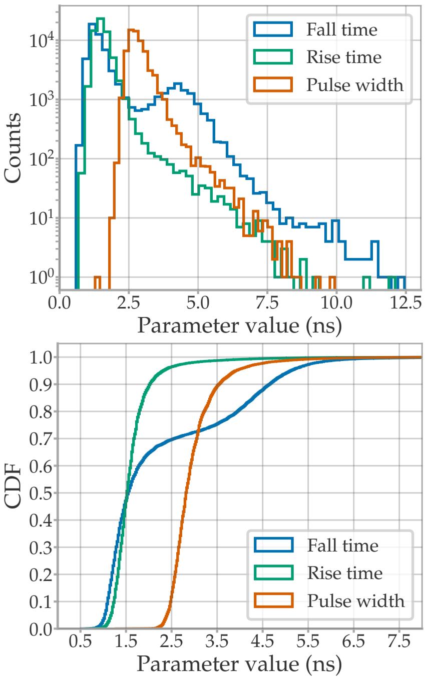

Figure 6.23: *Top:* Distribution of measured shape parameters for single SPEs of charge [0.5,1.5] PE produced by PMT BA0794. *Bottom:* Cumulative distribution of the shape parameters for single SPEs of charge [0.5,1.5] PE of the five measured PMTs combined.

All measured PMTs show a similar distribution with an average [median/ 68% range] of [(1.57 ± 0.04) ns/(3.03 ± 0.14) ns], [(1.54 ± 0.02) ns/(0.58 ± 0.02) ns] and [(2.83 ± 0.03) ns/(0.78 ± 0.04) ns] for the fall time, rise time and pulse width, respectively. Due to the similarity between PMTs, the data of all measured PMTs were grouped and represented as a cumulative distribution in Figure 6.23, bottom.

As mentioned above, the TTS represents the intrinsic statistical uncertainty on the detection time of photons and is calculated from the arrival-time distribution measured from many pulses. Figure 6.24 shows a time distribution of PMT pulses for a PMT illuminated with diffuse light. Regular pulses form a Gaussian-like distribution, in the following called the *main peak*, while prepulses form the distribution to the left of this region, and late and afterpulses appear to the right of the main peak.

There are different conventions on which pulse feature marks its arrival time. As explained in Section 6.1.2, the arrival time of the pulse is defined as its minimum in this work. This is a straightforward definition in terms of data extraction, as it is independent of the pulse amplitude. However, often the time of a certain amplitude level of the leading edge is chosen, for example, at the trigger voltage level that is going to be used in an experiment. Figure 6.24 shows the transit time distribution measured with both definitions in the same data with an mDOM PMT operated at nominal gain. In this case, for the second method, the time was taken at −2 mV of the leading edge of the pulse. The results shown in Figure 6.24 were shifted to match, as the leading edge is on average 2.7 ns earlier than the pulse minimum. Except for this systematic shift in times, there is practically no difference between both methods, providing similar standard deviations of the data inside the main peak, (1.98 ± 0.01) ns for the time taken at the minimum of the pulses and (1.95 ± 0.01) ns for the times taken at the −2 mV amplitude of the leading edge.

[116]: Wright (2017), *The Photomultiplier Handbook*

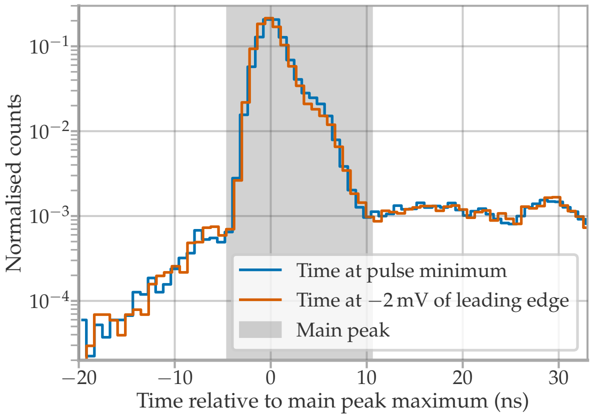

Figure 6.24: Arrival time distribution of pulses of the mDOM PMT BA0780 measured with two different definitions for the arrival time of a pulse. In blue the time extracted at the pulse minimum and in orange the time extracted at the -2 mV crossing of the leading edge. The latter is shifted by ~−2.7 ns relative to the former, but was matched for better clarity. Grey marks the region of *main peak*, which is populated by regular SPE pulses. The pulses to the left of this area are prepulses and to the right are late and afterpulses.

As shown in Figure 6.24, when the PMT is illuminated with frontal plane waves covering the entire photocathode, the distribution is asymmetric with a "shoulder" toward later times. A symmetric distribution is obtained only if a small area of the photocathode is illuminated, as can be seen in Figure 6.25. This points to a photocathode inhomogeneity for the transit time of the SPEs, which will be explored in Chapter 7.

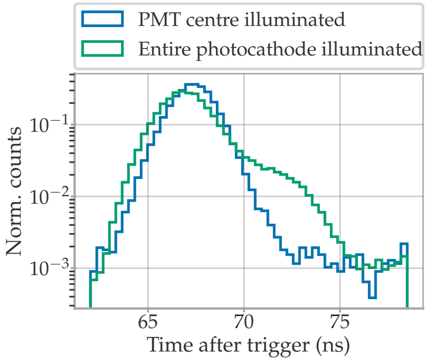

Figure 6.25: Arrival time distribution produced illuminating only the centre of the PMT and by means of a plane wave, covering the entire photocathode.

From the arrival time distributions, the TTS is conventionally calculated using the standard deviation of a Gaussian model fit σ_G on the main peak or by calculating its FWHM. Five PMTs were measured with low-intensity frontal light, so only 10% or fewer of the measured waveforms contained a pulse (also referred to as *occupancy of* < 0.1) to avoid multiphoton events. Table 6.1 lists the results for both methods for the five PMTs. Here, to be able to compare values, the FWHM was divided by $2\sqrt{2\ln 2} \approx 2.355$, which is the relationship between the FWHM and the standard deviation of a Gaussian distribution.

The fourth column of Table 6.1 lists the standard deviation (labelled SD) of the times within the main peak of the time distribution. The latter was defined as the pulses in the range of −5 ns to 10 ns relative to the peak maximum. Due to the asymmetry of the distribution when the entire photocathode is illuminated, both metrics, the FWHM and the Gaussian fit, could be a somewhat questionable parameterisation for the TTS. On the one hand, the Gaussian fit results strongly depend on the fitted time range. In the measurements of this section, the entire main peak was used for the fit, but if the shoulder is only partially included,[13] the fitted σ_G is ~ 40% smaller. However, using the entire time range of the main peak, σ_G overestimates the standard estimation on average only by 2%.

PMT SN	σ_G (ns)	$\frac{\text{FWHM}}{2.355}$ (ns)	SD (ns)	$\sqrt{\sigma_F^2 \frac{\pi^2}{6}}$ (ns)
BA0780	1.95 ± 0.01	1.22 ± 0.01	1.98 ± 0.01	2.05 ± 0.01
BA0784	1.85 ± 0.01	1.19 ± 0.01	1.82 ± 0.01	1.90 ± 0.01
BA0789	1.85 ± 0.01	1.31 ± 0.01	1.82 ± 0.01	1.95 ± 0.01
BA0793	1.79 ± 0.01	1.23 ± 0.01	1.75 ± 0.01	1.94 ± 0.01
BA0794	1.83 ± 0.01	1.18 ± 0.01	1.80 ± 0.01	1.88 ± 0.01

Table 6.1: The standard deviation of the main peak of pulse arrival time calculated by four different methods for five mDOM PMTs. The second and third columns list the results for the conventional methods, with σ_G of a Gaussian fit and the FWHM of the peak, respectively. The fourth column is the standard deviation of the data inside the main peak. The last column is the standard deviation of a fit with the Fisher-Tippett function (Equation 6.9).

[13] Which is easy to miss if working in a linear scale.

On the other hand, the FWHM completely ignores the shoulder toward later times, as it usually peaks at counts less than 50% of the main peak maximum. This results in a 34% average underestimation of the actual standard deviation of the data.

In IceCube software, the arrival time of the IceCube DOM pulses is modelled with a Fisher-Tippett function, since the 10″ PMTs also feature an asymmetric time response distribution. This is of the form

$$\frac{z(t)}{\mid \sigma_F \mid} \cdot \exp\left(-z(t)\right), \text{ with } z(t) = \exp\left(-\frac{(t-\mu)}{\sigma_F}\right), \tag{6.9}$$

where μ is a location parameter and σ is a scale parameter. The standard deviation of this distribution is given by $\sqrt{\sigma_F^2 \pi^2/6}$.

Figure 6.26 shows the Fisher-Tippett function fit on the data from one of the PMTs, together with the Gaussian fit. It can be observed that Equation 6.9 provides a much better model for the data compared to a Gaussian. However, the standard deviation of the fit $\sqrt{\sigma_F^2 \pi^2/6}$ (see the last column of Table 6.1) overestimates the one measured on average by 6%, while the Gaussian overestimates it only by 2% on average. Notwithstanding, if the PMT response is to be simulated with an analytical function, the current model used in the IceCube software is compatible with the behaviour of the mDOM PMT. In principle, a better fit-data agreement could be gained by using compound functions, such as two Gaussian, but no further improvement was sought as this is neither conventional in literature nor used in current IceCube modelling.

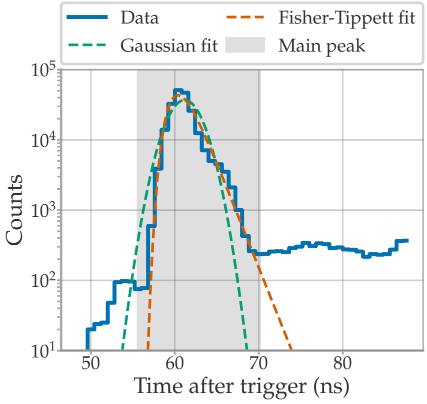

Figure 6.26: Pulse arrival time distribution of PMT BA0793 with the Gaussian and Fisher-Tippett distributions fitting the main peak (grey shaded area).

The hereby calculated standard deviation of the arrival times does not equal the TTS, as the variance of the data is increased by the time distribution of the light emitted by the LED and also the electronic jitter. Furthermore, as mentioned above, the time distributions in this section were measured with a low waveform occupancy of < 0.1. This is due to the systematic decrease of the TTS with multiphoton pulses. These effects are the topic of the following section. Following this, the temperature dependence of the timing parameters (Section 6.3.2) and wavelength dependence (Section 6.3.3) are presented.

6.3.1 TTS APPARENT LIGHT INTENSITY DEPENDENCE AND FURTHER CORRECTIONS

The time distributions of MPE pulses from short light pulses[14] are narrower than for SPEs. This is a known effect in the PMT community, but its source is not well known. In this section, a statistical model is derived for the TTS calculation regardless of the light intensity used. This correction function was derived by the author and published in the appendix of [110].

The grouping of SPE pulses into a single pulse is analogous to averaging the transit time of each SPE that forms the MPE pulse. The variance of a mean can be derived from basic rules from statistics: assuming that the variance of the transit times for different SPEs is $\mathrm{Var}(\mathrm{TT}) = \sigma^2$, the

[14] *Short* means in this case a light pulse width negligible compared to the PMT time resolution.

[110]: Unland Elorrieta et al. (2021), *Homogeneity of the photocathode in the Hamamatsu R15458-02 Photomultiplier Tube*

variance of the average transit time $\overline{\mathrm{TT}}$ of n PE-pulses can be calculated as follows

$$\mathrm{Var}\left[\overline{\mathrm{TT}}\right] = \mathrm{Var}\left[\frac{1}{n}\sum_{i=1}^{n}\mathrm{TT}_i\right] = \frac{1}{n^2}\sum_{i=1}^{n}\mathrm{Var}[\mathrm{TT}_i] = \frac{\sigma^2}{n}. \tag{6.10}$$

Thus, the standard deviation of the distribution — the apparent TTS — will decrease as $1/\sqrt{n}$. However, in real data, a time distribution for a fixed number of PEs cannot be measured, and therefore Equation 6.10 cannot be used as a correction function. The measured time distribution is always formed by both SPE and MPE pulses[15], where the number of detected photons n follows a particular statistical distribution, such as Poisson statistics for an ordinary LED.

The time distribution of the SPEs released at the same spot in the photocathode is assumed to be a Gaussian $G(t, TT, \sigma)$ with mean TT and standard deviation σ. Following Equation 6.10, the time distribution for pulses produced by n SPEs is a Gaussian with a standard deviation $\sigma/\sqrt{n}$.

With the number of photons detected per LED pulse following a Poisson statistic $P(n, \mu)$, the probability density function (pdf) of the transit time $f(t)$ can be described as a sum of Gaussians weighted by $P(n, \mu)$

$$f(t) = \frac{1}{N}\cdot\sum_{n=1}^{\infty}P(n,\mu)\cdot G(t, \mathrm{TT}, \sigma/\sqrt{n}), \tag{6.11}$$

with $N = (1 - e^{-\mu})^{-1}$ a normalisation factor. This normalisation is needed for the Poisson distribution since $n = 0$, the case of no photons detected, does not contribute to $f(t)$. The variance of this distribution can be determined analytically with[16]

$$\begin{aligned}\sigma_\mu^2 &= \mathrm{Var}[f(t)] = \mathrm{E}[t^2] - \mathrm{E}[t]^2\\ &= \frac{\sigma^2}{e^\mu - 1}[\mathrm{Ei}(\mu) - \gamma - \log(\mu)],\end{aligned} \tag{6.12}$$

with the expected value $\mathrm{E}[t] = \int t\cdot f(t)dt$, the exponential integral $\mathrm{Ei}(\mu) = \int_{-\infty}^{\mu}\mathrm{e}^x\cdot x^{-1}dx$ and the Euler-Mascheroni constant γ.

The emission profile of the LED usually has a non-negligible width σ_L, which widens the measured time distribution. There is a degeneracy between the real TTS of the PMT σ and σ_L, so the latter must be determined with an independent measurement. Furthermore, there is a constant contribution from the electronic jitter σ_j, which does not scale with n. Therefore, the measured apparent TTS σ_μ follows

$$\sigma_\mu(\mu) = \sqrt{\frac{(\sigma^2 + \sigma_\mathrm{L}^2)}{e^\mu - 1}[\mathrm{Ei}(\mu) - \gamma - \log(\mu)] + \sigma_j^2}. \tag{6.13}$$

[15] The MPE contribution can always be decreased by reducing the light intensity of the LED, but this also results in longer measurements.

[16] Equation 6.12 is derived in Appendix B.

A fit of this model to real data from an mDOM PMT is shown in Figure 6.27. This measurement was performed by illuminating only the centre of the PMT (pinhole in front of the photocathode). In this arrangement, the light intensity was increased by reducing the distance between the PMT and the light source. From the fit, the electronic jitter σ_j of the DAQ and the LED driver was determined to be $\sigma_\mathrm{j} = (136 \pm 6)\,\mathrm{ps}$. The emission profile of the LED in this example[17] was measured with a single-photon avalanche diode (SPAD)[18], and presented in Figure 6.28. Using the standard deviation of the distribution $\sigma_{\mathrm{L,j}}$, the LED contribution σ_L is determined to be $\sigma_\mathrm{L} = \sqrt{\sigma^2_{\mathrm{L,j}} - \sigma^2_\mathrm{j}} = (234 \pm 4)\,\mathrm{ps}$.

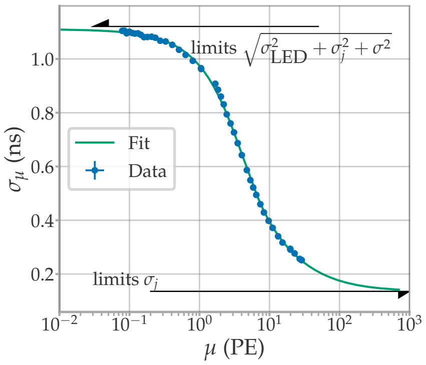

Figure 6.27: Standard deviation of transit time distribution against the mean number of detected photons per waveform. Error bars smaller than marker size. Points were fitted with Equation 6.13. Data published in [110] by the author.

Rearranging Equation 6.13, the intrinsic TTS of a PMT can be calculated with

$$\sigma = \sqrt{\frac{\sigma^2_\mu - \sigma^2_j}{\mathrm{Ei}(\mu) - \gamma - \log(\mu)}[e^\mu - 1] - \sigma^2_\mathrm{L}}. \tag{6.14}$$

One caveat here is that it was assumed that the transit time distribution follows a Gaussian. As seen in Figure 6.25, this is true when a small area of the photocathode is illuminated, but the average transit time can depend on the specific location of the photocathode. Therefore, in measurements in which the entire photocathode is illuminated, as in this chapter, a very low light intensity of ~0.1 PE or less per LED pulse is mandatory. In this case, only the electronic jitter and LED emission profile have to be corrected from the measured TTS, with

$$\sigma = \sqrt{\sigma^2_{\mu<0.1} - \sigma^2_\mathrm{L} - \sigma^2_j}. \tag{6.15}$$

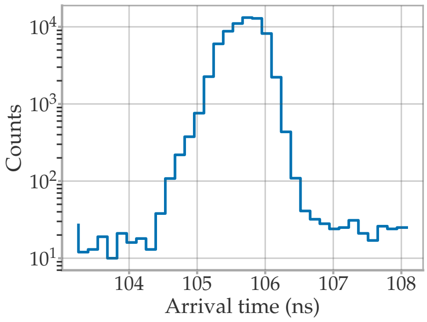

Figure 6.28: Time distribution of the LED emission measured with a fast SPAD. Data published in [110] by the author.

As σ_L and σ_j are small compared to the TTS of the PMT, correcting the measured SD listed in Table 6.1 with Equation 6.15 results in a slightly lower value. For example, BA0793, which has the smallest measured SD $\sigma_{\mu<0.1} = (1.80 \pm 0.01)\,\mathrm{ns}$ (and therefore the impact of σ_L and σ_j is the largest) results in a corrected TTS of $(1.78 \pm 0.01)\,\mathrm{ns}$.

The TTS correction for large occupancy derived in this section (Equation 6.14) is especially useful for measurements where small areas of the photocathode are illuminated and the long measurement time produced by small light intensities should be avoided; this is the case in the measurements of Chapter 7.

6.3.2 TEMPERATURE DEPENDENCE

The temperature dependence of the pulse shape parameters and TTS was investigated and published by the author in [126]. Two PMTs were placed inside a climatic chamber and measured in the temperature range from −50 °C to 20 °C.

There was no evidence that temperature influenced any timing parameters, which remained constant (deviations less than 1 %) throughout the measured temperature range. For details, see [126].

[126]: Unland Elorrieta et al. (2019), *Characterisation of the Hamamatsu R12199-01 HA MOD photomultiplier tube for low temperature applications*

[17] PicoQuant PDL 800-B with LED head PLS-8-2-719.

[18] ID100-20 from IDQ, with a time resolution of <60 ps.

6.3.3 Wavelength dependence

As introduced before, detailed studies on the wavelength dependence of the mDOM PMT timing parameters were performed in the context of [133]. Although no wavelength dependence was found for the pulse-shaped parameters, the measurements revealed a significant relationship between the TTS and the wavelength.

To verify the observations of [133], the TTS of five PMTs was calculated with the data taken for the gain calibration of Section 6.2.3. The arrival time distributions were fitted with a Gaussian, and the standard deviation obtained was corrected with Equation 6.14. The contribution from the timing of the laser σ_L was measured in [133] for the different wavelengths and is presented in Figure 6.29. In contrast to the LED used in the previous sections, the time profile of the laser system is not negligible, especially for measurements with the UV extension.

Since several voltages were measured for the gain calibration, a TTS vs voltage curve was calculated at each wavelength step. Figure 6.30 shows the curve measured at 400 nm and 650 nm of PMT BA0479. As expected from the literature [115], the TTS decreases with voltage. However, the wavelength makes the largest difference, with less than half of the TTS at 650 nm than 400 nm. The curves were fitted with a linear function to interpolate the TTS at the nominal voltage.

The left side of Figure 6.31 shows the TTS at nominal voltage of five PMTs. All show a steady improvement of the TTS with the wavelength, except for PMT BA0784, which features two peaks at 520 nm and 585 nm. The data of this PMT was closely examined to check for systematics. However, these two peaks were found at all measured voltages and also, the light intensity was constant between the measurements of all PMTs. One possible explanation for this deviation could be a different incoming angle of the laser relative to the PMT. As explained in Section 6.1, the beam was pointed directly to the PMT centre. Nevertheless, a deviation in the incoming angle can cause reflections on the internal structures to hit different parts of the photocathode. In Chapter 7, the wavelength

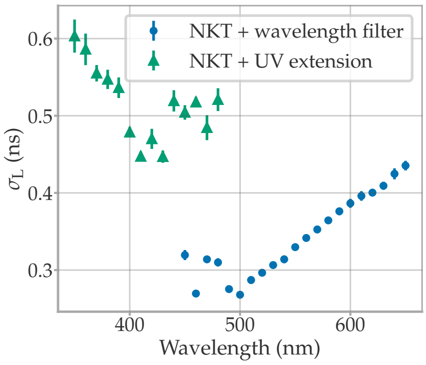

Figure 6.29: Standard deviation of the time distribution of the laser emission using the wavelength filter and the UV extension. Data from [133].

[133]: F. Peters (2020), *Studien zur Wellenlängenabhängigkeit von Performance-Parametern von Photomultipliern des Typs Hamamatsu R12199-01 HA*

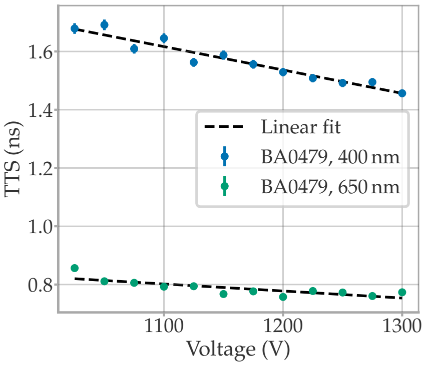

Figure 6.30: TTS against the absolute voltage of the PMT BA0479 at 400 nm and 650 nm. The dashed lines show the linear fit on the data.

[115]: Hamamatsu Photonics K.K. (2017), *Photomultiplier tubes - Basics and Applications*

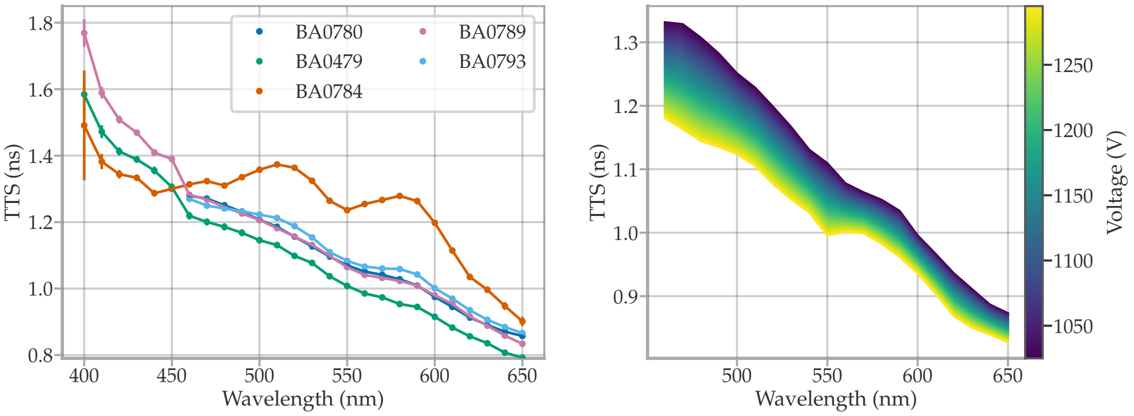

Figure 6.31: *Left:* TTS in wavelength dependence of five mDOM PMTs. The values were calculated for the nominal voltage by interpolating the TTS versus voltage lines (see e.g. Figure 6.30). *Right:* Wavelength dependence of the TTS at different voltages of the mDOM PMT BA0780. The values were calculated by interpolating the TTS vs voltage lines.

dependence of the TTS at different locations of the photocathode is investigated further.

Although this behaviour is not well researched, it has been reported in a few publications [135–137]. This change in TTS could be explained by the different trajectories of the SPEs between the photocathode and the first dynode. The more energy the photon has, the higher the kinetic energy of the released SPE, which is emitted at a random angle with respect to the normal of the surface of the photocathode. Thus, SPEs with higher initial kinetic energies have a larger variety of possible path lengths, resulting in a larger variance of the transit time. This idea is supported by the fact that the PMTs show a smaller wavelength dependence at higher voltages, as presented on the right side of Figure 6.31. Here, the TTS was calculated using the linear fits for voltages between 1000 V and 1300 V. The larger the voltage, the smaller the influence of the initial kinetic energy on the final position of the electron (and thus the less steep the TTS vs wavelength curve). The first studies in the Münster group using particle tracking simulations confirmed this hypothesis [138], although it is still being investigated.

[135]: Sipp et al. (1976), *Wavelength dependence of the time resolution of high-speed photomultipliers used in single-photon timing experiments*

[136]: Moszyński et al. (1977), *Influence of incident light wavelength on time jitter of fast photomultipliers*

[137]: Bebelaar (1986), *Time response of various types of photomultipliers and its wavelength dependence in time-correlated single-photon counting with an ultimate resolution of 47 ps FWHM*

[138]: J. Averbeck (2022), *Nachbau eines Photomultipliers in COMSOL Multiphysics und Untersuchung der Elektronentrajektorien zwischen Photokathode und erster Dynode*

6.4 Sensitivity

The sensitivity is a critical aspect of PMT performance because it refers to the ability of a PMT to convert light into an electrical signal. This section delves into the measurement technique used for the determination of the sensitivity parameters of the mDOM PMT (quantum efficiency, detection efficiency, and collection efficiency).

The measurement of PMT sensitivity is not straightforward. Reflections of light on the internal components of the PMT can lead to overlapping of the response from different regions of the photocathode, making the accuracy of sensitivity measurements challenging. To address this issue, this section is limited to measurements at the centre of the PMT. When a light beam parallel to the tube axis crosses the centre of the photocathode, it reaches the first dynode, which has poor reflectivity due to its curvature and surface finish. Therefore, the parameters calculated in this section provide a close approximation of the PMT's actual performance at the illuminated region. The uniformity of the PMT response across the photocathode is explored further in Chapter 7.

6.4.1 Quantum efficiency

As introduced in Section 5.2, the quantum efficiency (QE) is the probability that a photon releases a photoelectron from the photocathode. In this section, first the method for measuring the QE for different wavelengths is presented. Following this, the results of five PMTs are shown in comparison to other measurements performed within the IceCube Collaboration. The PMTs investigated in this section were measured with higher statistics than usual, as these results are used later to estimate the collection efficiency of these PMTs in Section 6.4.2.

The experimental setup used for these measurements is illustrated in Figure 6.32. The light from a xenon lamp is coupled to the input of a monochromator, with which the wavelength of the output light can be selected. This monochromatic light is guided through an adjustable iris into a dark box, where the PMT and a photodiode (PHD) are located. The PHD is calibrated and used to calculate the absolute light flux.

To eliminate the charge multiplication of the dynode system, the PMT is connected to a base that short-circuits all the dynodes. In this way, only one potential difference is applied between the photocathode and the multiplier system. There are two alternatives here: apply a positive voltage to the dynodes and measure the current from the photocathode pin, or apply a negative voltage to the photocathode and measure the current from the dynodes.

Because the photocathode saturates at a high light flux (see Section 5.2), the monochromator light output must be reduced, closing the monochromator slits until the PMT measures currents at a few nanoampere levels. Since the PHD does not feature multiplication, it also measures currents of the same order of magnitude. These low currents make the use of a picoammeter as a measurement device mandatory.[19]

Electrons released from the photocathode are counted regardless of where they arrive in the multiplication system; thus, the results are independent of the collection efficiency. This is true only if the applied potential difference is large enough to attract the released electrons; otherwise, a fraction of the current is measured. For the mDOM PMT it was found that the photocurrent reaches a plateau and stabilises in the range of 20 V to 50 V, much lower than the normal working voltage between the first dynode and the photocathode of 200 V to 350 V,[20] as can be seen in Figure 6.33.

The leakage current of the PMT also increases linearly with the applied voltage. Nevertheless, it is on the order of picoamperes, and an optimisation of the signal-to-noise ratio was not necessary, since the largest current variations are caused by the picoamperemeter and not the PMT background. The absolute voltage value was chosen as the one found in normal PMT operation, a fraction 3/13 of the nominal voltage.

During a measurement run, the wavelength was changed in the desired step and range. The monochromatic light was measured by the PHD and then by the PMT for each wavelength. The PHD was attached to a 3D scanner to facilitate this process,[21] which can move the PHD into and out of the monochromatic light beam. The currents of both devices were measured in each step. In this way, the background signal of the PMT was obtained while the PHD was in front of the light, and vice versa.

The PHD used as a reference in several of the measurements presented in this work is the model 818-UV from Newport (serial number 3557). Its spectral response ranges from 200 nm to 1100 nm and is linear up to an output current of ~1 mA [140]. The detector was calibrated by the manufacturer with NIST-traceable standards [22], providing the radiant sensitivity of the PHD shown in Figure 6.34. The systematic error depends on the wavelength and ranges from 1 % to 4 %. During calibration, approximately 70 % of the active centre diameter of the detector is illuminated.

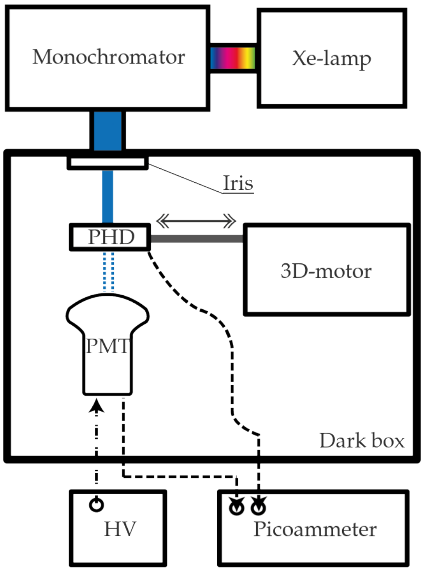

Figure 6.32: Schematic drawing of the QE measurement setup. The photodiode (PHD) is moved by the 3D motor into or out of the light beam.

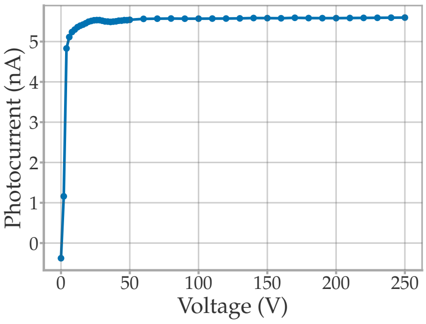

Figure 6.33: Photocurrent of a PMT against the voltage applied between the photocathode and dynode system. The errors are smaller than the markers.

---

[19] Picoammeter Keithley Model 487

[20] The normal operating voltage of the PMT is specified to be in the range of 900 V to 1500 V and the photocathode-first dynode voltage is a fraction 3/13 of the total.

[21] Custom built, commissioned in the framework of a Master thesis [139].

[22] Calibration traceability number 685/281985-12/1.

Therefore, care was taken during the measurements to ensure that the same area was illuminated.

The surface of the PHD reflects a significant portion of the light, because of its high refractive index. Furthermore, the amount of reflected light depends on the angle of incidence and the polarisation of the beam. The values provided from the calibration include the loss due to reflection for incoherent light incident normally on the PHD. To avoid introducing systematic errors, the detector was used at near-normal incidence in all measurements.

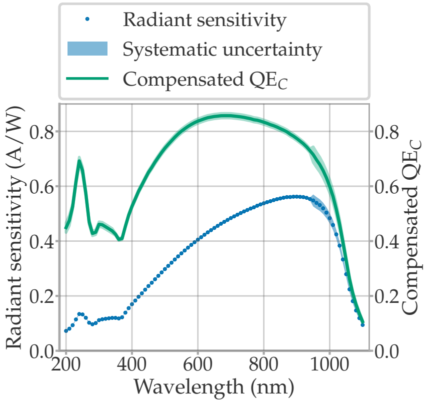

Figure 6.34: Radiant sensitivity of the photodiode provided by the manufacturer and reparameterised as a compensated quantum efficiency using Equation 5.1 from Chapter 5.

A more useful parameterisation of the radiant sensitivity can be calculated using Equation 5.1 from Chapter 5, which is shown in Figure 6.34. Since the sensitivity was corrected for reflections, the obtained value is not directly the quantum efficiency of the PHD. Nevertheless, this *compensated quantum efficiency* QE_C provides the correct factor to calculate the incident light flux Φ_λ of wavelength λ without the need for reflection corrections, as long as the measured light is normal to the PHD surface. The flux is calculated as follows

$$\Phi_\lambda = \frac{I_{\mathrm{PHD}}}{e \cdot QE_C(\lambda)}, \tag{6.16}$$

with I_{PHD} the current measured by the PHD and e the elementary charge.

With the source photon flux Φ_λ, the PMT signal current I_λ and the average background current of the PMT I_{B}, the QE_λ at a certain wavelength is calculated as

$$QE_\lambda = \frac{I_\lambda - I_{\mathrm{B}}}{e \cdot \Phi_\lambda}, \tag{6.17}$$

with e the elementary charge.

Five PMTs were measured in the wavelength range 250 nm to 700 nm in 10 nm step. The resulting QE curves are presented on the left side of Figure 6.35. The highest efficiency is for photons in the range of 360 nm

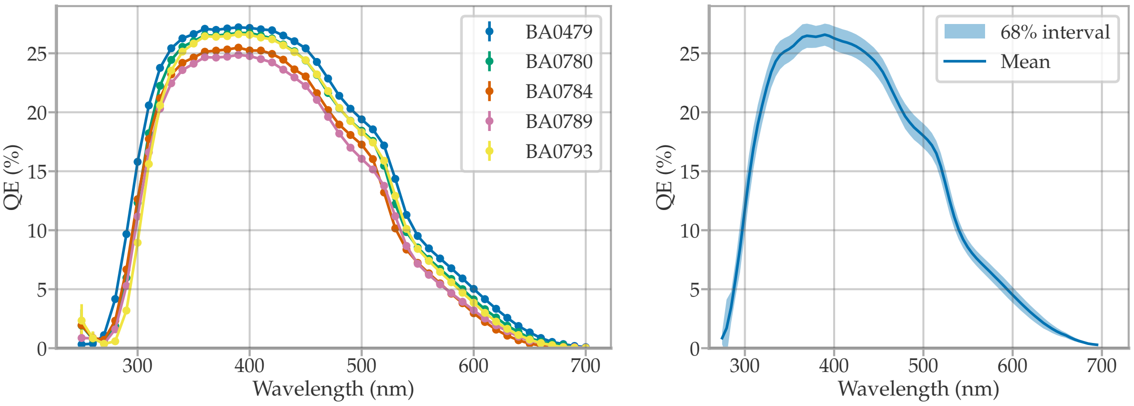

Figure 6.35: *Left:* Absolute quantum efficiency of five mDOM PMTs in dependence of the wavelength. Data markers were joined with lines for clarity. The marker size is larger than the uncertainty for the majority of the points. *Right:* Mean absolute quantum efficiency of 145 mDOM PMTs [141]. The shaded region represents the standard deviation of all QE curves.

to 420 nm, with an average of 26.2 %. For shorter and longer wavelengths, the efficiency drops until it reaches zero.

The UV cutoff point produced by the transparency of the PMT bulb glass is around 270 nm to 280 nm. However, it can be observed that the QE starts rising again for lower wavelengths. This is a known artefact of the setup and does not reflect the real QE. This systematic is not fully understood but could be attributed to, for example, a wavelength shifting effect of the glass absorbing and reemitting scintillation photons of larger wavelengths or scattered photons that escape the monochromator.

Toward longer wavelengths, the photocathode stops being sensitive at approximately 690 nm to 700 nm, as the photons do not have enough energy to promote an electron from the valence to the conduction band in the photocathode.

These PMTs do not deviate from the expected response of the mDOM PMT. The right side of Figure 6.35 shows the average QE curve measured from 145 mDOM PMTs by collaborators [141]. They were measured and tested for compliance with the IceCube requirements during the PMT characterisation campaign in its prototype phase.

6.4.2 DETECTION AND COLLECTION EFFICIENCY

As introduced in Section 5.3, the detection efficiency is the total probability of a photon being detected by a PMT operating with the multiplication system active. Ideally, it should be equal to the QE of the PMT. However, not all of the released photoelectrons reach the first dynode and start a multiplication process. This probability is given by the collection efficiency F, and thus

$$DE(\lambda) = QE(\lambda) \cdot F(\lambda). \tag{6.18}$$

The experimental setup used to measure the detection efficiency is the same as the one shown on the right side of Figure 6.1. The laser beam is always pointed to the centre of the photocathode, perpendicular to its surface. As explained in Section 6.1, the laser output was attenuated with several ND filters. Here, it was sought to obtain MPE pulses of several tens to a few hundred PEs. With such large pulses, a few thousand waveforms are enough to obtain a precise average pulse charge with a relative error on the order of 0.1 %.

At each wavelength λ the mean charge Q_λ of 10,000 pulses was measured, from which the number of detected photons n_λ is calculated as $n_\lambda = Q_\lambda / G_\lambda$, where G_λ is the gain of the PMT at the wavelength λ. The gain wavelength dependence of the investigated PMTs was calculated in Section 6.2.2.

The absolute light flux Φ_λ was measured with the calibrated photodiode connected to a picoammeter. In this case, the laser output is directly pointed to the device without any filters. As the light source is pulsed, the number of photons emitted per pulse is obtained by dividing the photon rate by the laser repetition rate $R = 20\,\text{kHz}$. Thus, the number of photons per laser pulse reaching the photocathode is $N_\lambda = \Phi_\lambda \cdot T_\lambda / R$, where T_λ is the fraction of photons transmitted by the ND filters.

Although the filter manufacturer provides generic transmission data, it was necessary to measure this parameter in situ to avoid introducing extra systematics. In this case, the photodiode was used again, measuring the beam at each wavelength with and without an ND filter. The ratio between the measured photocurrents provides T_λ, which is shown in Figure 6.36 for the ND filters used in this measurement.

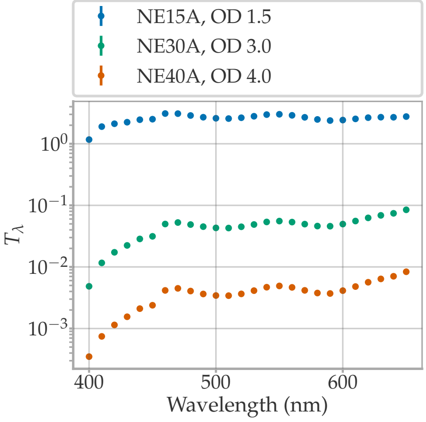

Figure 6.36: Measured transmittance of the ND filters used. The labels indicate the filter model and the optical density (OD). The error bars are smaller than the marker size.

The detection efficiency DE_λ at wavelength λ is thus the fraction of detected photons

$$DE_\lambda = \frac{n_\lambda}{N_\lambda} = \frac{Q_\lambda}{G_\lambda} \frac{R}{\Phi_\lambda \cdot T_\lambda}. \tag{6.19}$$

Figure 6.37 shows the results for all PMTs. The curves are similar to those measured in the QE section, except in the lower wavelength region, where the DE drops while approaching 400 nm, instead of staying on a plateau like the QE (cf. Figure 6.35).

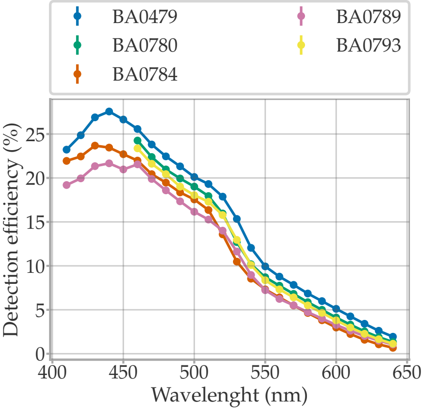

Figure 6.37: Wavelength dependence of the detection efficiency of five mDOM PMTs. Uncertainties are smaller than the data points' marker size.

Having measured the QE and the DE, the collection efficiency F was calculated with Equation 6.18. The results are presented in Figure 6.38. For wavelengths above 450 nm, there is a clear overestimation of the collection efficiency, as it cannot be greater than 100 %. This systematic shift is probably caused by an underestimation of the gain. In Section 6.2.1 it was discussed that the Gaussian model used for the gain determination is expected to produce biased results. At a gain of $5{\times}10^6$ it was estimated that the fit would result in an average underestimation of ~5.4 %. Following Equation 6.19, any bias on the gain results in an indirect proportional systematic shift on the DE. The mean F in the interval from 450 nm to 650 nm ranges from (104.4 ± 0.3) % (BA0479) to (99.4 ± 0.2) % (BA0793). Assuming the gain bias calculated in Section 6.2.1 this would translate to the actual collection efficiency from ~99 % (BA0479) to ~94 % (BA0793).

The drop in F at lower wavelengths is consistent with measurements in the literature [129], but publications in this area are scarce. This reduction in efficiency may be explained with the same reasoning as in discussions of the wavelength dependence of the gain (Section 6.2.3) and TTS (Section 6.3.3). If SPEs start with a higher velocity in a direction different from the electromagnetic field line, the probability of the electron deviating and not reaching the first dynode is higher. In [129, pp. 2–5] it is reported that the efficiency increases again for wavelengths below ~350 nm, although no explanation for this recovery has been provided.

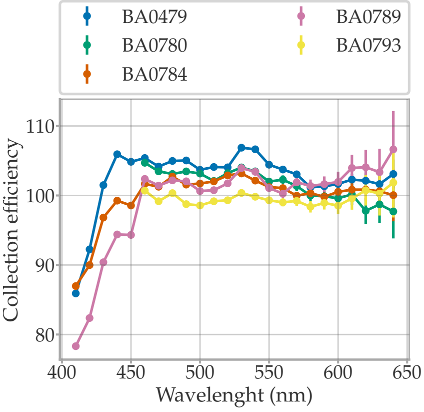

Figure 6.38: Wavelength dependence of the collection efficiency of five mDOM PMTs. Values above 100 % are not possible, so the results indicate that one or several parameters involved in the collection efficiency calculation are biased.

The significant spread observed in Figure 6.38 suggests that the calculated efficiency may be impacted by systematic error. As the calculation of F involves the ratio of two similar numbers, small uncertainties propagate to noticeable variations. There is no universally accepted method for measuring this variable. In [142], a method is proposed where F is calculated by measuring the *true* and *apparent* gain of the first dynode (as described in Equation 5.5). This approach eliminates the need for knowledge of the absolute light flux, but requires the construction of a specialised voltage divider for the PMT. It may be useful to repeat these measurements using alternative methods to reduce uncertainties. However, as will be explored in Chapter 7, determining the detection efficiency for the entire photocathode (instead of only the centre) can be challenging due to reflections on the internal components.

[129]: Flyckt et al. (2002), *Photomultiplier tubes - principicles and applications*

[142]: Wright (2010), *Method for the determination of photomultiplier collection efficiency, F*

6.5 Magnetic field dependence

The Earth's magnetic field at the South Pole is relatively intense at 54.7 µT. After deployment, each PMT will have a unique magnetic field vector $\vec{B}$ relative to its axis, since each PMT within the module points in a different direction. Due to the size limitations inside the mDOM, there is no insulation against magnetic fields, as is the case in the DOM or D-Egg. However, how much the Earth's magnetic field affects the PMT performance is known to depend on the size of the PMT. The effects on Hamamatsu 3" PMTs were already found to be too small to justify any magnetic shielding in the KM3NeT optical module in [143]. Nevertheless, in that study a lower field strength was investigated (~40 µT) than the one at the South Pole.

[143]: Giordano et al. (2016), *The effects of Earth's magnetic field on 3-inch diameter photomultipliers used in KM3NeT neutrino telescope*

To study the magnetic field dependence of mDOM PMTs, a magnetic field test stand was commissioned and built in the context of a Master thesis [144]. It consists of three Helmholtz coils with which a magnetic field of up to 107.28 µT in an arbitrary direction can be created. In the framework of that thesis, the impact of the magnetic field found at the South Pole on the mDOM PMT was also measured and confirmed previous studies.

[144]: K. Ueberholz (2020), *Setup and commission of a magnetic field test stand and studies on the influence of magnetic fields on the performance of the Hamamatsu R12199-02*

In this section, the measurement of another five mDOM PMTs in 192 different magnetic field directions is presented. In each field direction, 250,000 waveforms were analysed following the SPA method (see Section 6.1.2) with the LED illuminating the entire photocathode (setup on the left side of Figure 6.1). The field vectors were chosen using *Healpy*, a HEALPix python wrapper [145], with which a sphere can be separated into pixels of equal area. The software directly provides the position of the pixels through angle pairs (θ, ϕ), the zenith and azimuth, respectively.

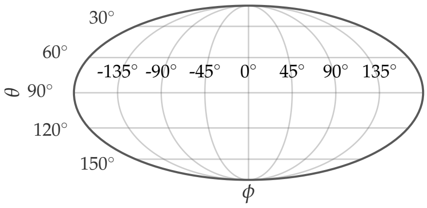

Figure 6.39: Grid of coordinates used in Mollweide projections of data distributed in pairs of angles (θ, ϕ).

[145]: Gorski et al. (2005), *HEALPix: A Framework for High-Resolution Discretization and Fast Analysis of Data Distributed on the Sphere*

A reference data set with the coils compensating the Earth's magnetic field (PMT under $\vec{B}$ =(0,0,0) T) is measured at the beginning, at the end, and every ten field direction steps, also comprising 250,000 waveforms each. This is used to monitor the light intensity of the LED over time and verify the statistical error of the parameters with a single data set.

The parameters illustrated in dependence of the direction angles (θ, ϕ) are presented in Mollweide projections, such as the grid shown in Figure 6.39. For the sake of clarity, the ticks and labels of the axes are removed in the following figures. However, these are the same as in Figure 6.39.

As the Helmholtz coils have their own coordinate system, it is necessary to rotate the directions used to a coordinate system related to the PMT geometry. In the following, the tube axis is chosen as the z-axis, and the front of the PMT corresponds to the x-y-plane. The first dynode is defined to be bent along the y-axis. The entrance to the second dynode is chosen to be in the upper quadrants, as indicated in Figure 6.40. In the following,

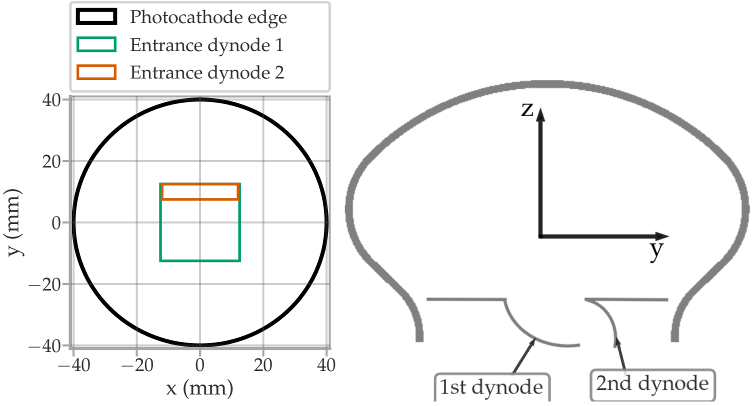

Figure 6.40: Sketch of the defined PMT coordinate system with respect to physical components of the PMTs. *Left:* The x-y-plane on the front of the PMT and *right* the z-axis along the tube axis.

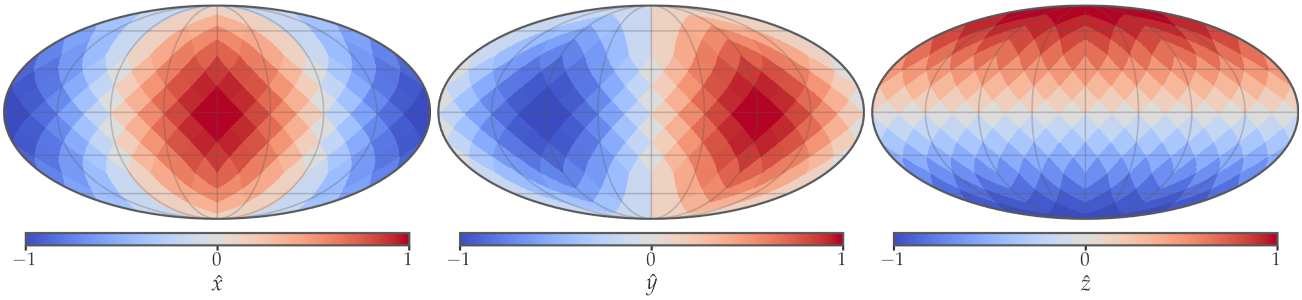

Figure 6.41: The unit vector components of the PMT coordinate system defined in Figure 6.40 as seen in the Mollweide projections used to present the results.

all angle pairs are given in the PMT coordinate system, following the conventional Cartesian to spherical coordinate transformation. Figure 6.41 shows the unit vector components of the PMT coordinate system along the x-, y- and z-axes in the Mollweide projections to guide the interpretation of the results.

The arrival times of the pulses were grouped into a histogram for each measured data set. The mean and standard deviation inside the main peak were calculated, which are a measure of the transit time of the SPEs and the TTS, respectively (see Section 6.3). The absolute transit time is not measurable with this setup, but can be compared in relative terms. In this case, the mean arrival time of a data set t_x is given relative to the mean arrival time of the reference data sets measured at (0,0,0) T, t_R, in the form of $t_x - t_R$. Figure 6.42 shows the average Mollweide projection of the relative transit time of the five PMTs.

Comparing Figure 6.42 with the left projection of Figure 6.41 makes it clear that the most significant deviations appear when the magnetic field is orientated along the x-axis of the PMT, as the patterns are almost a copy of each other. The standard deviation of the values of all pixels is ~0.52 ns. This could be considered as the systematic uncertainty for the transit time of an mDOM PMT after deployment if it cannot be recalibrated in situ. Compared to the results of the PMT without any magnetic field, the pulses arrive on average up to ~0.77 ns later if the magnetic field is parallel to the x-axis and up to ~1.04 ns earlier if it is antiparallel.

Figure 6.43 shows the results of the TTS. Here, the values are the relative difference (in percentage) from the mean TTS of the reference data sets measured with a field of (0,0,0) T. In this case, the dependence also seems

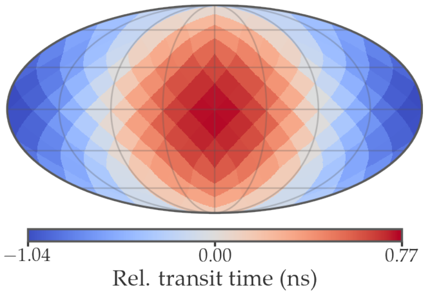

Figure 6.42: Average transit time for different magnetic field orientations relative to the mean transit time for $\vec{B}$ =(0,0,0) T. Each pixel shows the average of five PMTs.

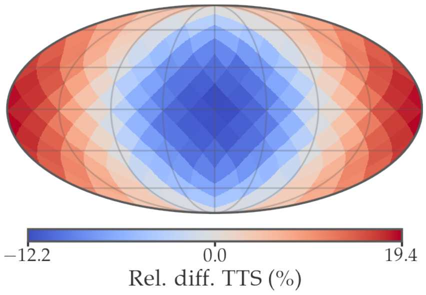

Figure 6.43: TTS for different magnetic field orientations relative to the mean TTS at $\vec{B}$ =(0,0,0) T. Each pixel shows the average of five PMTs.

Table 6.2: The standard deviation and extrema of the transit time, TTS, gain, and rel. detection efficiency, from all directions of the magnetic field. The numbers are given relative to the measurement at $\vec{B} = (0, 0, 0)$ T (see text). Columns three to seven list the values of single mDOM PMTs (the first row indicates their serial number), and the last column presents the mean values calculated from all PMTs.

		BA0780	BA0784	BA0789	BA0793	BA0794	Mean
Rel. transit time (ns)	SD	0.5155(4)	0.5279(3)	0.5175(4)	0.5396(3)	0.5143(4)	0.5230(2)
	Min	−1.015(7)	−1.059(4)	−1.018(7)	−1.079(4)	−1.032(6)	−1.041(3)
	Max	0.744(5)	0.782(3)	0.774(5)	0.801(3)	0.737(5)	0.767(2)
Rel. diff. TTS (%)	SD	9.43(2)	9.47(2)	9.65(2)	8.26(2)	9.29(2)	9.222(8)
	Min	−13.79(24)	−12.36(20)	−12.99(30)	−10.37(20)	−13.56(28)	−12.61(11)
	Max	20.59(27)	19.39(22)	19.41(26)	18.18(22)	19.91(30)	19.5(11)
Rel. diff.gain (%)	SD	4.3(4)	4.6(7)	3.57(7)	4.5(7)	3.87(2)	4.18(20)
	Min	−14.13(22)	−15.33(21)	−14.9(4)	−14.87(18)	−14.5(5)	−14.74(15)
	Max	2.8(3)	1.7(3)	0.6(4)	1.34(22)	1.49(27)	1.59(14)
Rel. diff.efficiency (%)	SD	1.3(4)	1.4(5)	0.91(27)	1.3(7)	1.36(3)	1.25(20)
	Min	−2.6(4)	−2.4(3)	−1.2(5)	−2.22(28)	−1.9(4)	−2.08(18)
	Max	3.3(4)	3.2(3)	3.6(6)	3.33(28)	5.2(4)	3.73(18)

to originate solely from the x component of $\vec{B}$, with average extreme values of(-12.61 ± 0.11) % and (19.50 ± 0.11) % when the field is parallel or antiparallel to the x-axis, respectively. The mean standard deviation between all pixels is (9.222 ± 0.008) %, which is greater than the intrinsic variance of the TTS between different PMTs of ~ 5 % [126].

[126]: Unland Elorrieta et al. (2019), *Characterisation of the Hamamatsu R12199-01 HA MOD photomultiplier tube for low temperature applications*

The first and second rows of Table 6.2 summarise the results of the transit time and TTS of all measured PMTs. As mentioned above, the results are consistent between different PMTs.

For each magnetic field orientation, the gain was obtained after fitting the measured charge spectrum with Equation 5.6. Figure 6.44 shows the average Mollweide projection of the gain results of all PMTs. Gain values are given as the relative difference to the average gain of the reference data sets at (0,0,0) T in percentage. As with the TTS and the transit time, it can be observed that the gain changes depending on the x component of the magnetic field vector. In this case, the gain appears to only decrease compared to the reference, although there are six pixels that have average values slightly larger than 0 %, with the mean maximum value of (1.59 ± 0.14) %. The reference data sets show an average relative uncertainty for the gain of 0.5 %. Therefore, these six pixels with positive numbers may be just statistical fluctuations. However, their correlation in magnetic field direction may indicate a real effect.[23]

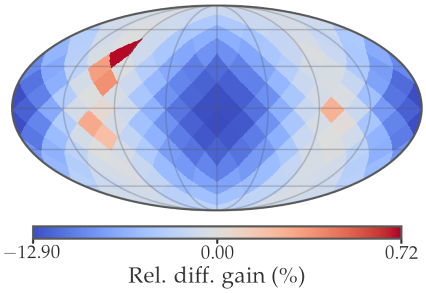

Figure 6.44: Average gain at different magnetic field orientations relative to the gain at $\vec{B}$ =(0,0,0) T. Each pixel shows the average of five PMTs.

The relative detection efficiency ϵ_k of the PMT of the data set k is determined as

$$\epsilon_k = \frac{N_k}{L(t)} \ , \tag{6.20}$$

where N_k is the mean number of photons detected per LED flash during the measurement of the data set k taken at time t and $L(t)$ is a correction function that compensates for changes in the light intensity in relative terms. How this function is derived is explained later. Having determined the gain G_k in each field direction, the average number of detected photons per waveform N_k is calculated with

$$N_k = \frac{\hat{Q}_k}{G_k \cdot e} \ , \tag{6.21}$$

where e is the elementary charge and $\hat{Q}_k$ is the average charge per

[23] This region shows also a higher gain in magnetic field studies made in Chapter 7.

waveform measured in the data set k. In principle, the fitted μ from Equation 5.6 should be equal to N, but due to the correlation with the other fit parameters μ normally has a higher statistical uncertainty than the one resulting from the error propagation of Equation 6.21.

The correction function $L(t)$ is extracted from the reference data sets. As the average charge $\hat{Q}$ is directly proportional to the intensity of the light and the gain can be assumed to be constant during the reference measurements,[24] the relative light intensity of the LED is

$$L(t_i) = \frac{\hat{Q}(t_i)}{< \hat{Q} >}, \tag{6.22}$$

where $\hat{Q}(t_i)$ is the average charge measured for the reference data set i measured at time t_i and $< \hat{Q} >$ is the mean $\hat{Q}$ between all reference data sets of a PMT. Thus, there are a discrete number of $L(t_i)$ (one per reference measurement), which are then interpolated to obtain the correction at all times, as needed by Equation 6.20. Since the light intensity changes very slowly over time, the data are smoothed[25] to avoid introducing the statistical fluctuation of the single $L(t_i)$. Figure 6.45 shows the discrete calculated $L(t_i)$ of the measurement of PMT BA0793 and the interpolation. Although fluctuations are small ($\sim$ 1 % peak to peak in Figure 6.45), there is always a tendency for the light intensity to increase or decrease due to changes in the internal temperature of the LED.

Figure 6.46 shows the average Mollweide projection of the relative detection efficiency ϵ_k. The values are given as the relative difference to the mean ϵ of the reference measurements in percentage. The average standard deviation between all directions is (1.24 ± 0.20) %, and the minimum and maximum values are (-2.63 ± 0.18) % and (3.15 ± 0.18) %. These are quite small differences, and one must be aware of the uncertainties of the calculated values, which after error propagation combine to a relative uncertainty for $\Delta\epsilon/\epsilon$ of 0.7 % to 1 %. As the statistical errors are on the same order of magnitude, the given standard deviation and extreme values should be considered as upper limits. Despite the noisy results, the dependence on the x component of the magnetic field can also be observed in Figure 6.46.

The observed variation in detection efficiency may imply a dependence of the photocathode sensitivity on the magnetic field. However, the quantum efficiency is not expected to change with the applied field strengths because the distances travelled by the electrons inside the bialkali layer are not that large. To verify this, one of the PMTs was measured in current mode with a base short cutting all dynodes (as in Section 6.4.1). The magnetic field was set in the same directions as before, and the same number of reference measurements was taken. Figure 6.47 shows the difference in the photocathode response relative to the reference measurements. The standard deviation between all directions is 0.27 %, and the extreme values are less than 1 %. These are produced by statistical fluctuations without any patterns to be recognised.

As was hypothesised in [144], the fact that the observed magnetic field dependence seems to depend only on the x component of $\vec{B}$ should

[24] One could also use the measured gain and calculate N for the reference data sets, but this would only increase the statistical error.

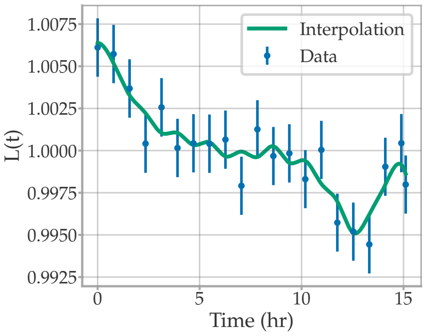

Figure 6.45: Light intensity correction function interpolated from the reference data sets measured at $\vec{B}$ =(0,0,0) T.

[25] With a Savitzky–Golay filter of window length 3 and polynomial order 1 [146].

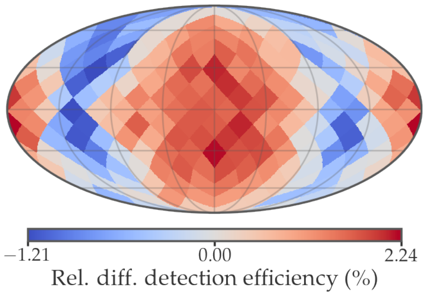

Figure 6.46: Average relative detection efficiency at different magnetic field orientations relative to the values at $\vec{B}$ =(0,0,0) T. Each pixel shows the average of five PMTs.

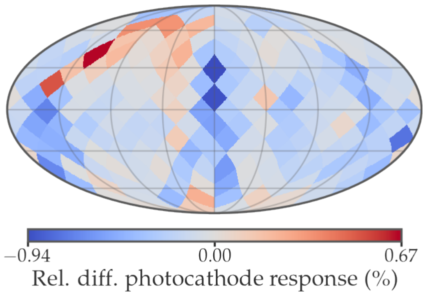

Figure 6.47: Photocathode response of one PMT without electron multiplication at different magnetic field orientations relative to the values at $\vec{B}$ =(0,0,0) T.

originate from the geometrical asymmetry of the first dynode. The SPEs released from the photocathode accelerate towards the multiplication system because of the electric field applied. The velocity of the SPE paths that are collected successfully at the first dynode must have an increasing z component as it approaches the multiplication system. Thus, the magnetic field components that affect these trajectories are either in the x or y direction (following the Lorentz force law), with the most significant force applied at the end of the trajectory as the particle's speed is the greatest. A magnetic field in the x direction will deflect the SPEs along the y-axis, changing the height on the first dynode curvature where they arrive, as depicted in Figure 6.48. Analogously, a magnetic field with a sizeable y component will change the arrival position of the SPE on the first dynode along the x-axis. However, the first dynode has no curvature along the y-axis, and the magnetic field will not change the height of the curvature where the SPEs arrive.

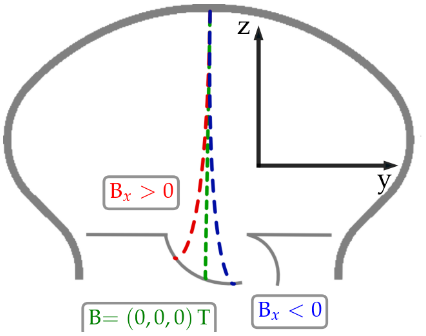

Figure 6.48: Sketch of how the trajectory of an SPE is bent due to a magnetic field with a large component along the x-axis, resulting in the electron hitting the first dynode at different heights and distances to the second dynode.

In this perspective, the results of Figure 6.42 can be understood as a change in arrival time depending on where the SPEs hit the first dynode. Following the example in Figure 6.48, a large x component of the magnetic field will translate into the SPE hitting the first dynode further away from the second dynode, while a negative x component results in SPEs arriving closer to the second dynode. This could lead to the observed transit time difference in Figure 6.42 because the secondary electrons released from the first dynode need to cover a longer ($B_x > 0$) or shorter ($B_x < 0$) path to reach the next dynode stage.

In Figure 6.44 the gain appeared to decrease mainly with a large absolute x component of the magnetic field. Following Figure 6.48 it is possible that the deflection along the y-axis increases the incoming angle of the SPE with respect to the dynode surface, reducing the secondary emission yield, as expected from [132]. However, the gain reduction could also be explained by a worsening of the collection efficiency between the different dynode stages further down in the multiplication system.

[132]: Furman et al. (2002), *Probabilistic model for the simulation of secondary electron emission*

The origin of both the TTS and the relative detection efficiency results is more difficult to pinpoint. The TTS results imply that the paths of the SPEs vary more in a field $\vec{B}$ of negative x component than with the field in the opposite direction. This variation can be produced anywhere, from the photocathode to the first dynode, or further down between the different multiplication stages.

The change in detection efficiency is probably explained by a change in the collection efficiency between the photocathode and the first dynode because the QE is independent of the magnetic field. In Section 6.4.2 it was shown that the collection efficiency in the centre of the photocathode is close to 100 %, therefore the larger efficiency seen in Figure 6.46 must originate from a better performance at the edges of the photocathode, where the collection efficiency is likely to be lower than at the centre.

A more precise understanding of the processes involved to explain the results fully may be obtained with COMSOL simulations or further measurements. In any case, it is clear that the mDOM PMTs may need an in situ calibration after deployment, as the observed deviations, although small, are still significant.

7

Response uniformity across the sensitive area

In the previous chapter, most properties of the PMTs were tested by illuminating the entire photocathode using a plane wave perpendicular to the PMT axis. This results in average performance parameters masking intrinsic inhomogeneities of the sensitive area. However, especially in the single-photon regime, it is essential also to know the systematic variations across the photocathode, which requires measurements with focused light sources illuminating only small regions of the PMT. This chapter presents the uniformity of these parameters over the entire photocathode by employing an elaborate measurement technique, which is explained in Section 7.1.

Section 7.2 presents the results of an mDOM PMT with the multiplication system shorted out, from which the photocurrent response can be extracted without the influence of the dynodes. Nevertheless, the uniformity of a PMT working with full multiplication depends on the homogeneity of both the photocathode and multiplication system. A detailed characterisation of the mDOM PMT response homogeneity while operating in pulse mode is introduced in Section 7.3, studying the gain, transit time, TTS and relative detection efficiency. Section 7.4 and Section 7.5 show the dependence of the uniformity of these pulse parameters on the magnetic field and light wavelength, respectively.

The larger PMTs used in other IceCube optical modules were also investigated. The characterisation of one candidate PMT for the LOM (see Section 3.3.2), of the Hamamatsu R5912-100-70 PMT used in the D-Egg (see Section 3.3.1) and of the Hamamatsu R7081-02 used Gen1-DOMs are presented in Section 7.6.

7.1 SETUP AND METHOD

The setup used for this study is shown in Figure 7.1. Different positions on the photocathode are illuminated by light from an optical fibre[1] attached to a 3D scanner. The latter can move the optical fibre in three directions in a volume of 200 mm×200 mm×200 mm with an accuracy below 50 µm. The commissioning and characterisation of this device is part of a Master thesis of the Münster IceCube group [139].

[139]: R. S. Busse (2017), *Setup and commissioning of a test stand for detailed investigations of quantum efficiency characteristics of photomultiplier tubes, and initial studies for IceCube-Gen2*

The measurement was performed inside three Helmholtz coils that compensate for the Earth's magnetic field in the laboratory. This ensures that the measurements are not affected by the magnetic field strength and direction and makes the results independent of PMT position and orientation. The magnetic field test stand was characterised in [144] and

[144]: K. Ueberholz (2020), *Setup and commission of a magnetic field test stand and studies on the influence of magnetic fields on the performance of the Hamamatsu R12199-02*

[1] Multimode 105 µm

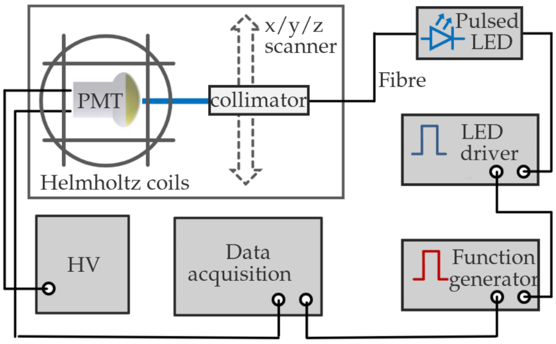

Figure 7.1: Schematic layout of the parameter scan setup. The data acquisition is an oscilloscope (Piscoscope 6404C) for measurements performed in pulse mode and a picoamperemeter (Keithley Model 487) in current mode measurements.

can produce a field with relative deviations of less than 1 % throughout the entire PMT volume.

The photocathode was scanned with the light always parallel to the axis of the tube. Depending on the studies, the PMT is read out in current or pulse mode. More details about the DAQ are introduced in the respective sections. The light source is an LED[2] driven by a function generator[3]. The light output is collimated,[4] resulting in a beam with an FWHM of ∼ 0.9 mm at a distance of 60 mm from the collimator. The characterisation of the beam is the topic of Section 7.1.1.

The curvature of the photocathode was compensated by adjusting the distance between the illuminated surface and the fibre for each measurement. This ensures that the photocathode was always illuminated with the focal point of the beam. The curvature of the characterised PMTs is taken from the technical drawings provided by the manufacturer. The curvature of the 8″ and 10″ PMTs is so large that the fibre can reach distances beyond the plane perpendicular to the PMT tip. In such a case, the distance was limited to a few millimetres ahead of this plane to eliminate any possibility of collision. For this curvature compensation, it is important to know precisely the relative position of the centre of the photocathode and the fibre. This is achieved by a measurement and adjustment performed prior to a scan, explained in Section 7.1.2.

Next to the measured PMT, two reference devices were installed, with which the light was monitored every 30 measured points on the photocathode. In current mode measurements, a calibrated photodiode was used as a reference, with which it is possible to calculate the absolute light flux. In pulse mode, the light intensity was too low for a photodiode; therefore, a second PMT[5] was used as a reference. The fibre was always moved to the same position of the reference device, avoiding systematics from inhomogeneities of the sensitive area of the reference devices.

7.1.1 COLLIMATION AND BEAM DIAMETER

The light output of the fibre was connected to a collimator lens which is designed for a longer wavelength than the one provided by the LED. This mismatch results in a focusing instead of collimation of the beam. A CCD camera[6] was placed in front of the fibre to find the distance from the collimator to the plane of the shortest beam diameter. The camera

[2] PLS-8-2-719 controlled by PicoQuant PDL 800-B, wavelength 459 nm (FWHM 24 nm).

[3] RIGOL DG1032Z with a frequency of 20 kHz in pulse mode measurements. In current mode the high trigger rate of the controller PicoQuant PDL 800-B (20 MHz) is used.

[4] 60FC-SMA-0-A7.5-01 lens collimator by Schäfter & Kirchhoff, collimated at 532 nm.

[5] Hamamatsu R7600.

[6] Andor Solis Newton CCD DU920P-OE.
]

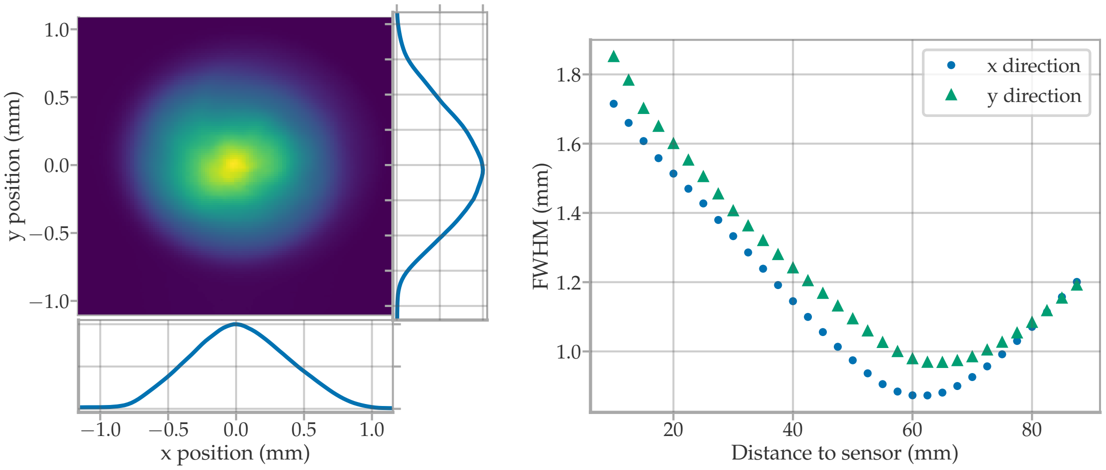

Figure 7.2: *Left:* Picture of the beam at a distance of 60 mm from the collimator. The marginal profiles in the x and y directions are used as a measure of the beam diameter. The colour-bar of the plot is in arbitrary units, linear and omitted for clarity. *Right:* The FWHM of the profiles resulting from the projection of the 2D data in the y and x direction.

has a linear response to the light intensity.[7] The fibre was moved with the scanner perpendicular to the CCD sensor, and a picture of the beam was taken every 2 mm. The picture taken at a distance of 60 mm is shown on the left side of Figure 7.2. The data were marginalised in the y and x directions, resulting in nearly Gaussian distributions. The FWHMs of these profiles are taken as a measure of the beam diameter. This procedure was performed on each image, which resulted in the curve on the right side of Figure 7.2.

The focal points for the x and y axes were found at 61.3 mm and 63.8 mm, with a minimum beam diameter of 0.87 mm and 0.97 mm, respectively. The scanner was configured to be at a distance of 62 mm from the photocathode, although the systematic error on the z-axis is estimated to be at ~3 mm. Since the curvature is relatively shallow, this systematic only translates into a small uncertainty of the beam width of $879^{+11}_{-3}\,\mu\text{m}$ and $976^{+15}_{-4}\,\mu\text{m}$ for the x and y directions, respectively. The smallest grid step used in the following measurements (1.25 mm) was larger than the diameter of the beam. Therefore, there is not much overlap in the measured area between neighbouring points.

The distance along the z axis that must be compensated for when travelling along the curvature of the PMT is shown in Figure 7.3. Toward the edges of the PMTs Hamamatsu R7081-02 and Hamamatsu R5912-100-70 the fibre would have to move more than 62 mm in z relative to the central position to maintain a constant distance. To avoid a collision between the PMT and the fibre, the maximal distance along the z axis is truncated at 60 mm. This means that the illuminated area increases towards the edges for these two PMT models since the photocathode is not located in the focal plane. For the Hamamatsu R7081-02 PMT, the maximum beam diameter is 1.3 mm, but the used grid spacing is 3 mm; therefore, the overlapping illuminated area was also small. This is also the case for the Hamamatsu R5912-100-70 PMT, where the maximum diameter of the beam is 1.0 mm and the grid step 2.75 mm.

[7] 7: This analysis could also be done with a DSLR camera. Nevertheless, in this case, the resulting beam diameter is difficult to be mapped to an intensity fraction (such as with FWHM) since the sensors and processing of commercial cameras try to reproduce the human eye response, which is not linear.

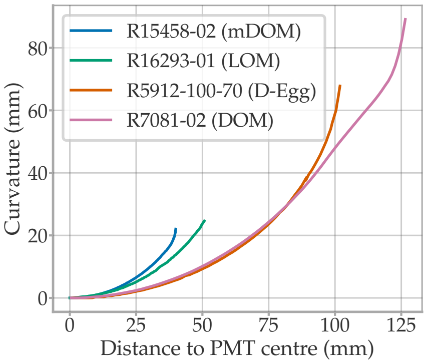

Figure 7.3: Curvature of the photocathode in the z axis, which has to be compensated by the fibre while moving towards the edges of the PMT in order to illuminate with a constant beam size.

7.1.2 Finding the PMT centre

The PMT is fixed by a 3D printed support structure that is mounted on the same aluminium profile as the scanner. The position of the support structure with respect to the scanner does not change between measurements. Nevertheless, the relative position of the PMT centre can vary a few millimetres after the PMT is inserted into the support structure. For the curvature compensation introduced in the last section, it is necessary to know the position of the PMT. Therefore, the PMT centre is determined with the following method before each scan.

In this calibration, the PMT response is measured along the radial coordinate r relative to the assumed PMT centre, starting at $r = R + 5\,\mathrm{mm}$, where R is the PMT radius, moving stepwise toward the centre until $r = R - 5\,\mathrm{mm}$. An example of such an edge profile is shown in Figure 7.4. This is performed along several polar angles ϕ with a 30° increment surrounding the PMT. Assuming that the PMT response at the edges of the PMT is radially symmetric for a certain intensity I, it is possible to fit the centre of the PMT (X_0, Y_0) by minimising

$$\mathscr{L}(X_0, Y_0, R_I|\{{}^I x_\phi, {}^I y_\phi\}) = \sum_\phi \frac{1}{2}\left(R_I^2 - \left({}^I x_\phi - X_0\right)^2 - \left({}^I y_\phi - Y_0\right)^2\right)^2 ,$$

where $({}^I x_\phi, {}^I y_\phi)$ is the position interpolated along a profile curve corresponding to the angle ϕ where the PMT response is I. Therefore, R_I defines the radius of the concentric PMT response with intensity I. Since the complete profile at the edges was measured, several intensity levels $\{I_i\}$ are used summing the log-likelihoods $\sum_i \mathscr{L}(X_0, Y_0, R_i|\{{}^i x_\phi, {}^i y_\phi\})$.

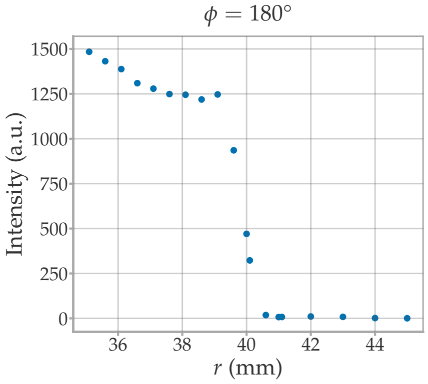

Figure 7.4: PMT response along the edge of the PMT at the angle coordinate 180°. Uncertainties are smaller than data point markers.

The results presented in the following sections are relative to the centre calculated with this minimisation. The relative position between two measurements in a grid has a very low uncertainty since the scanner has a precision of less than 50 µm. Nevertheless, the given positions have a systematic error due to the centre fit. The systematic errors are larger than the uncertainty given by the minimiser (normally between 20 µm and 70 µm) since the assumption that the PMT response is radially symmetric is too simple. Moreover, this fit would not account for a possible rotation of the PMT relative to the z axis (in which case an ellipse would be a better model). However, if a shift between the assumed and actual PMT centre is noticeable, it is still possible to correct the data afterwards since the same fitting procedure presented above can be implemented using the scan data.

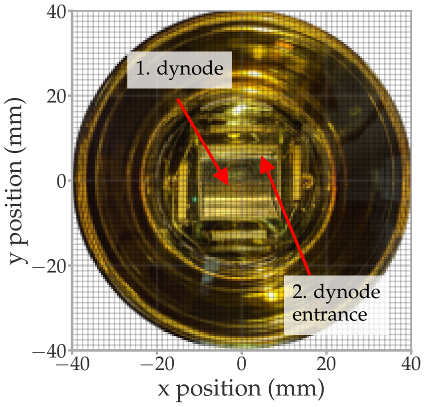

Figure 7.5: Frontal picture of the Hamamatsu R15458-02 PMT with respect to the used coordinate system. The position and scale of the PMT picture is approximated.

The coordinate system used in the following sections is shown in Figure 7.5. The position of the grid corresponds to the location of the measurement on the PMT picture. Therefore, the curvature of the first dynode, where it meets the frontal plate of the multiplication system, is on the negative ordinate region, and the entrance towards the second dynode is on the positive ordinate side.

7.2 Photocurrent response

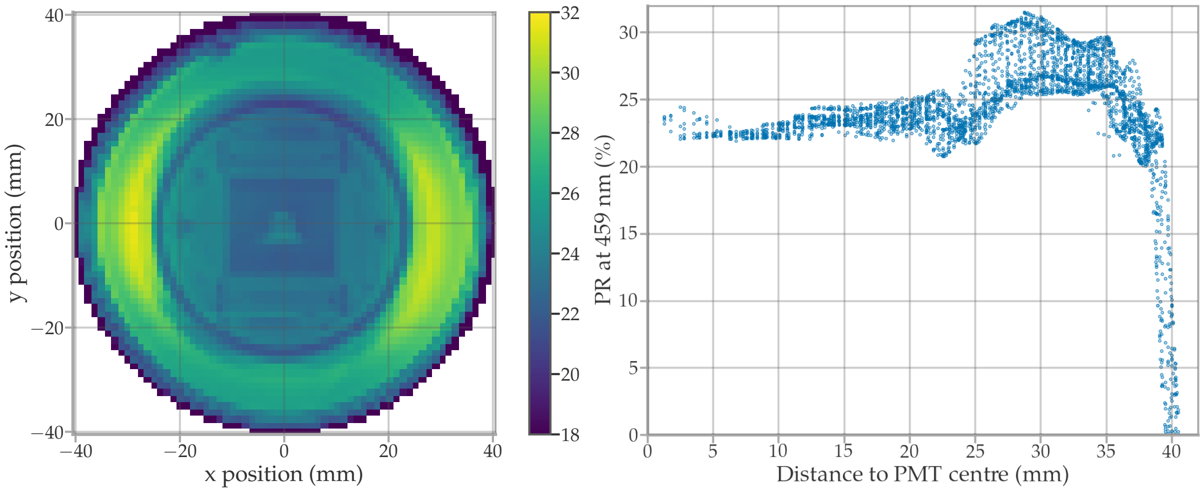

Figure 7.6: *Left:* Photocathode response (PR) scan for light peaking at 459 nm. colour-bar was saturated in the lower values for better contrast. Several internal components are observed in the measurement results due to internal reflections. Label of colour-bar match the label of y-axis of the right plot. *Right:* Photocathode response as a function of the distance to the PMT centre. This is the same data as shown on the left side of the figure, which results from the illumination on different locations of the photocathode following a regular grid (shown in Figure 7.5).

This section presents the response of the photocathode without any amplification of the multiplier system. The method and DAQ for this measurement are the same as that used for the quantum efficiency measurements in Section 6.4.1, with the dynodes of the PMT short-cut and measuring the cathode current directly with a picoamperemeter (Keithley Model 487). The calibrated photodiode is used (Newport 818-UV, see Section 6.4.1) to measure the light intensity. The photocurrent of the PMT is measured at each grid position together with the dark current of the photodiode. Every 30 measured points, the fibre is moved in front of the photodiode, and the reference light intensity is measured, together with the dark current of the PMT. In total, five mDOM PMTs were scanned, but only one is shown in detail in this section, as the results are comparable.

The cathode sensitivity is calculated using Equation 6.17. The calculated values are referred to as photocurrent response (PR) instead of quantum efficiency for reasons that will be explained later. The scan results of the PMT of serial number BA0784 are shown on the left side of Figure 7.6. Several patterns and structures can be observed on this map. These can be compared with Figure 7.7, which shows a photograph of the internal components of the PMT that are revealed in the measurement. For example, the circular frontal plate (C), rectangular entrance to the first dynode (D) and even smaller details such as the entrance holes (F) can be clearly identified in the measurement results. This is due to reflections (or absorption) of the light beam on the inner surfaces of the PMT, giving the possibility of multiple beam crossings with the photocathode.

Since most reflections are neither specular nor parallel to the beam, the results cannot be interpreted as the intrinsic QE of the location directly illuminated on the photocathode. Figure 7.8 summarises the principal

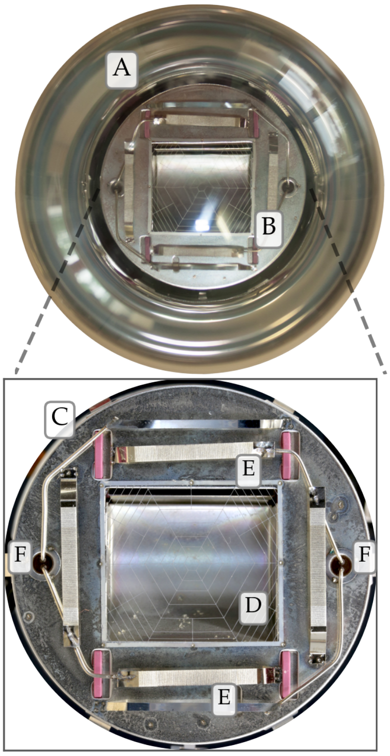

Figure 7.7: *Top:* photograph of frontal view of a PMT, without the photocathode layer for better visibility. A): Inner reflective coating which connects the photocathode to its corresponding pin. B): Electron multiplier system. *Bottom:* Zoomed frontal view of the electron multiplier. C) Circular frontal plate, D) rectangular entrance to the first dynode, E) rectangular plates which are assumed to be part for shaping the electrical field and F) the holes that lead the plate wires to the inside of the multiplication system.

components that are believed to contribute to the measured photocurrent. The photocathode location, which is directly illuminated by the beam, will produce a photocurrent proportional to the QE of that point (number ① in Figure 7.8). A fraction of the beam will be reflected (position ② in the example, at the reflective coating), possibly crossing the photocathode again (in the example, at position ③). Additional measurements are needed to separate multiple parameters for calculating the intrinsic QE at point ①, including the reflectivity of ② and the QE of ③. Moreover, this illustration is very simplified, as it assumes complete specular reflection and disregards secondary reflections from the optical boundaries at points ① and ③.

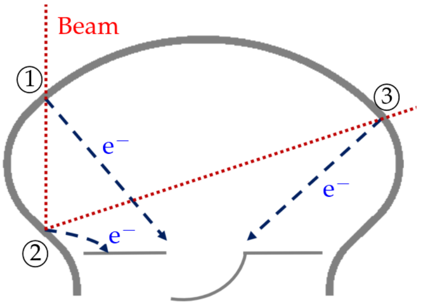

Figure 7.8: Sketch of the cross section of the front portion of a PMT being illuminated with a collimated beam. The numbers mark positions where light could release photoelectrons (see text for explanation).

As seen on the left side of Figure 7.6, there is an inhomogeneous response in the measured photocurrent at the internal reflective coating of the PMT ($r > 25$ mm, (A) in Figure 7.7), where the PR is higher on the horizontal sides of the map, at $y \approx -20$ mm to 20 mm and x in $\pm[25, 30]$ mm, compared to the vertical regions at $x \approx -20$ mm to 20 mm and y in $\pm[25, 30]$ mm. A non-uniform reflectivity of the coating could explain this difference. After visual examination of the PMT, these regions with higher PR seem to have residual photocathode material on the surface of the reflective coating.

During PMT production, the photocathode is evaporated as one of the last steps after the PMT is vacuum-sealed. The photocathode material is released from capsules connected to the multiplication system, allowing for photocathode coating on surfaces other than the frontal glass window. These residues may also be photosensitive and emit photoelectrons. The internal reflective coating is at cathode potential, as is the direct electrical conductor connecting the photocathode to the cathode pin. These photoelectrons are unlikely to arrive at the first dynode and produce a pulse in the normal operation of the PMT. However, in the PR measurement, with a short-cut dynode system, photoelectrons hitting the frontal plate will also contribute to the total measured photocurrent. This possible contribution is sketched at position ② in Figure 7.8.

Summing the sensitivity of all points and multiplying it by the area of the measured pixels (1.56 mm^2) results in the effective area of the PMT for frontal light. However, in this calculation, the effective area has to be understood as just for the generation of a photocurrent and not for the generation of PMT pulses, which will be smaller. For the measurement shown in Figure 7.6, the resulting area is 12.79 cm^2. The average of the five measured PMTs is 12.66 cm^2 with a small standard deviation of 0.11 cm^2 (less than 1 % relative to the average).

On the right side of Figure 7.6, the same data is plotted against the distance to the PMT centre. At $r \approx 23$ mm, there is a gap between the frontal plate of the dynode system and the envelope glass, allowing the beam to escape through the back of the PMT. Therefore, one can expect that the PR will be equal to the QE in this region as it is least influenced by internal reflections. The average value is (22.46 ± 0.02) %, which is similar to the values in the region in front of the first dynode (mean (22.52 ± 0.03) % for $r < 10$ mm). The first dynode should be a bad reflector because of its curvature and matte finish. Thus, the method taken in

Section 6.17 for the measurement of the QE, where a ~1 cm spot at the PMT centre was used, is relatively free of systematics from reflections.

The patterns observed in the scans are similar for all PMTs. Figure 7.9 shows the data for each measured PMT grouped in steps of 1 mm from the PMT centre and averaged. For all PMTs, the increase in PR at $r > 25$ mm is found. Furthermore, PMTs feature sensitivity until the edges of the photocathode (radius of PMT glass bulb 40 mm), although the manufacturer guarantees sensitivity only until $r = 36$ mm (guaranteed photocathode size of 72 mm diameter). According to the Fresnel equations [147], a larger angle of incidence causes an increasing fraction of the beam to reflect at the glass window, leading to less light transmission to the photocathode. Thus, the drop in PR for $r > 35$ mm can be partially explained by the PMT's frontal curvature (see Figure 7.3).

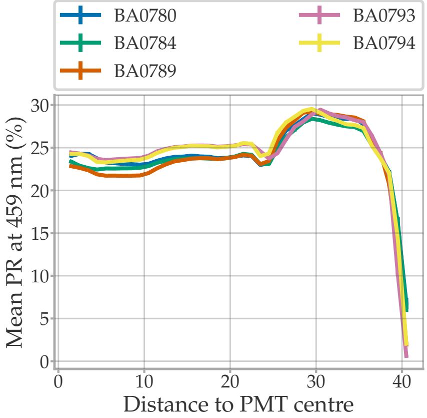

Figure 7.9: Mean PR against distance to PMT centre of all measured PMTs (legend corresponds to the serial number of PMT).

[147]: Miyazaki (2014), *Fresnel Equations*

7.3 Uniformity of pulse characteristics

In this section, the photocathode uniformity for different parameters of the PMTs operated in pulse mode is discussed. These parameters are obtained by measuring each grid position on the photocathode with the method introduced in Section 6.1.2. As DAQ the oscilloscope PicoScope 6404C was used.

The intensity of the LED output was adjusted so that a waveform occupancy of ~50 % ($\mu \sim 0.7$) was reached when the fibre illuminated the centre of the PMT. During the scan, 45,000 waveforms were measured at each grid position. Because the calculation of the pulse parameters is based on the fit of histograms, locations on the photocathode with low detection efficiency will produce failed fits due to a lack of statistics. A cut was applied to reduce these "noisy" data-points, and only those locations on the photocathode are shown that measure at least 5 % of the average number of photoelectrons of the central region ($r < 30$ mm) of the PMT. The number of photoelectrons is calculated by counting the pulses of amplitude of at least 3 mV that arrive at the expected arrival time.

In the following sections, the standard deviation σ_A between the results at the different points is provided as a measure of photocathode homogeneity. This σ_A was calculated for points within concentric circles of radius r and centred around $x = y = 0$ mm of the photocathode. These circles cover a fractional area A_f relative to the total area scanned. An illustration of this process is shown in Figure 7.10. The parameter σ_A will always be given in terms of A_f.

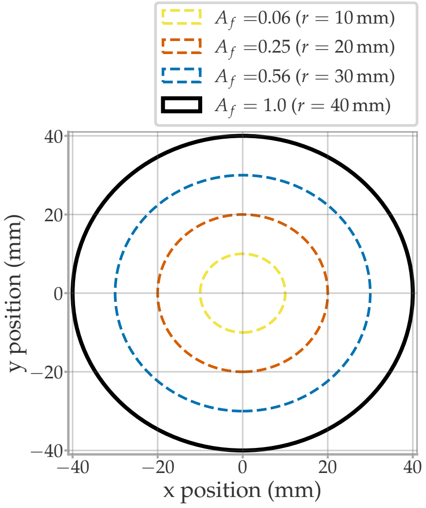

Figure 7.10: Sketch for clarification of the parameter A_f, which is the fraction of area to the total projected photocathode area.

The results of this section were produced by the author and partially published in [110], where most of the figures are from measurements on PMT BA0794. In this section, the images show the results from a different PMT, BA0784, for diversification. However, any data shown in this section that were also published in [110] are explicitly cited. Altogether, five PMTs were measured (the same as in Section 7.2), all offering very similar results.

[110]: Unland Elorrieta et al. (2021), *Homogeneity of the photocathode in the Hamamatsu R15458-02 Photomultiplier Tube*

7.3.1 Gain

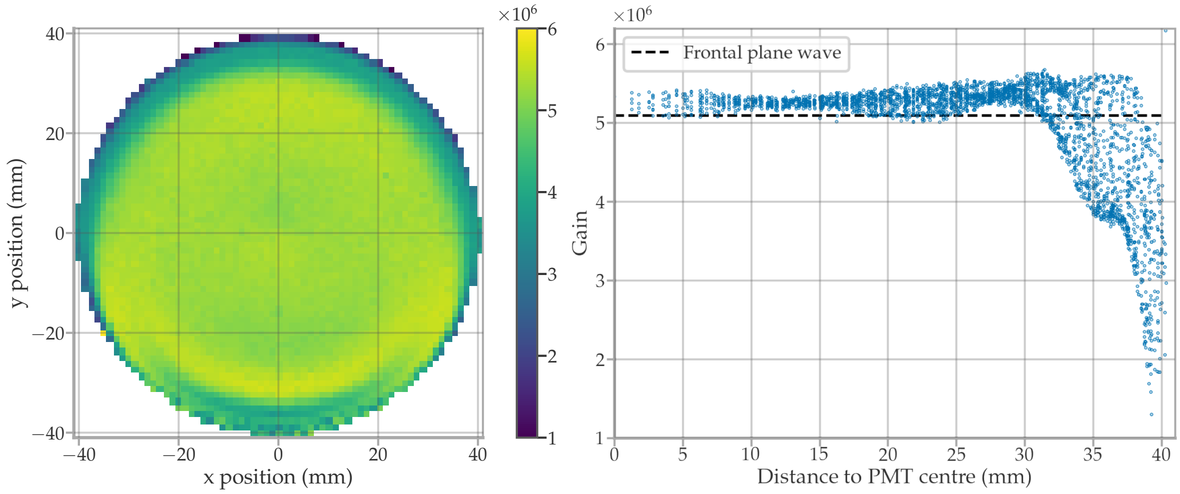

Figure 7.11: *Left:* Gain scan. Label of colour-bar match the label of y-axis of the right plot. Data of PMT BA0784. *Right:* Gain as a function of the distance to the PMT centre. This is the same data as shown on the left side of the figure, which results from the illumination on different locations of the photocathode following a regular grid (shown in Figure 7.5). The dashed-line marks the gain measured with a plane wave illuminating the entire photocathode.

The gain of each measured grid point is calculated by constructing and fitting the charge spectra. The method and the model used for the adjustment are explained in Section 6.2. In Figure 7.12, the spectrum of three locations on the photocathode is shown. It's apparent that the position of the 1 PE peak is not constant, which implies that the PMT has different *local* gains on the photocathode.

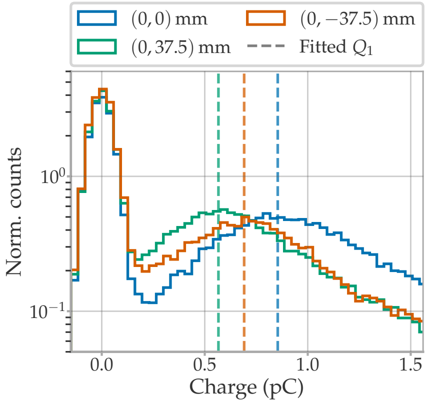

Figure 7.12: Charge distribution of three different positions (cf. Figure 7.5) on the photocathode.

The resulting gain map is shown on the left side of Figure 7.11. For points less than 30 mm from the centre of the PMT, the gain remains relatively constant at values around 5.3×10^6 and a standard deviation of 0.1×10^6. This can also be seen on the right-hand side of Figure 7.11, where the data is plotted against the distance to the PMT centre. The local gains tend to decrease toward the edges of the photocathode, although there is also a slight increase in the region of $y{\sim}{-30}$ mm and x from −20 mm to 20 mm. The shape of the inhomogeneity seems to depend on the orientation of the first and second dynodes (see Figure 7.5), this being the only asymmetry in geometrical terms of the PMT's internal structures when looking at the PMT head-on. Measuring the gain with frontal illumination covering the entire photocathode results in a gain of $(5.09 \pm 0.01) \times 10^6$ (marked with a dashed line on the right side of Figure 7.11), which is lower than the local gain for most of the photocathode due to the drop at the edges.

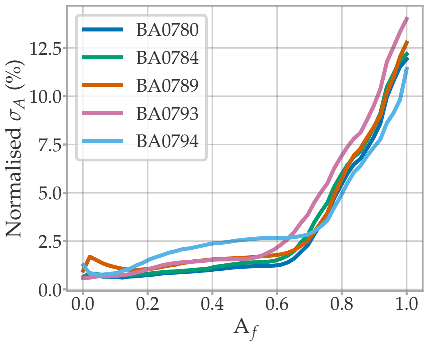

Figure 7.13: Normalised standard deviation σ_A of the gain against the fraction of area A_f to which the points used correspond. σ_A is normalised to the mean gain of the central region (r < 30 mm) and is presented as a percentage. Data published by the author in [110].

As a measure of homogeneity, the standard deviation σ_A of local gains was calculated and normalised to the average gain of the central region r < 30 mm of the photocathode. The results are presented as a percentage in Figure 7.13.

The homogeneity is similar for all PMTs, with $\sigma_A{\sim}12$ % when considering the entire scan area. However, most of the variation is caused by the edges of the photocathode since σ_A remains below 2.5% and relatively constant up to $A_f \approx 0.6$. As the charge resolution of this PMT type is around 40 %, the effects of these gain inhomogeneities cannot be distinguished for pulses at the SPE charge levels from the intrinsic pulse-to-pulse charge variation.

The SPE resolution calculated from the SPE charge spectra fits is shown against the distance to the PMT centre in Figure 7.14. The resolution is the same for almost the entire photocathode area, increasing only at the very edge of the PMT ($r > 36\,\text{mm}$). It should be noted that the average SPE resolution $(37.9 \pm 0.1)\,\%$ is lower than the one measured, illuminating the entire photocathode of this PMT using frontal plane waves $(40.1 \pm 0.3)\,\%$. This increase is probably caused by the gain non-uniformity as the results agree with a (naive) sum of variances $\sqrt{0.38^2 + 0.12^2} \approx 0.40$, taking into account the calculated gain inhomogeneity $\sigma_A \approx 12\,\%$.

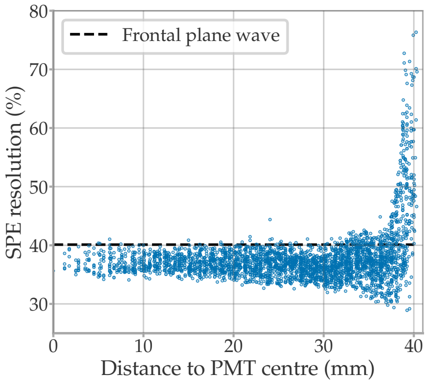

Figure 7.14: Fitted SPE resolution as a function of the distance to the PMT centre. The dashed-line marks the resolution measured with a plane wave illuminating the entire photocathode.

7.3.2 Relative transit time and TTS

The arrival times measured in each position on the photocathode were grouped into a histogram. As an example, three locations on the photocathode are shown in Figure 7.15. There is a clear difference in the detection time suggesting that there is also an inhomogeneity in the PMT's response for this parameter. To quantify this variation, the histograms were fitted with a Gaussian. The Gaussian mean is the average arrival time of the PMT pulse relative to the trigger signal of the function generator. It is important to note that the absolute transit time of the PMT cannot be determined using the current experimental setup, and therefore must be expressed in relative terms. In the following, the arrival time is always relative to the mean arrival time of the central region of the PMT ($r < 30\,\text{mm}$). The standard deviation of the Gaussian fit is then used to calculate the TTS, as outlined in Equation 6.14.

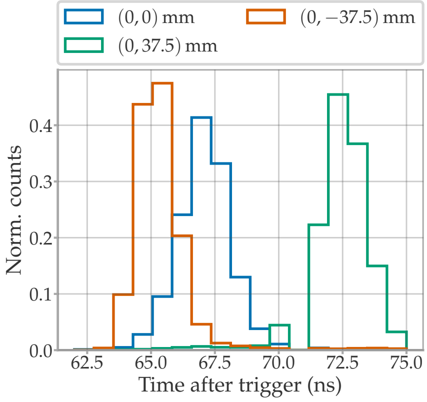

Figure 7.15: Arrival time distribution of three positions (cf. Figure 7.5) on the photocathode.

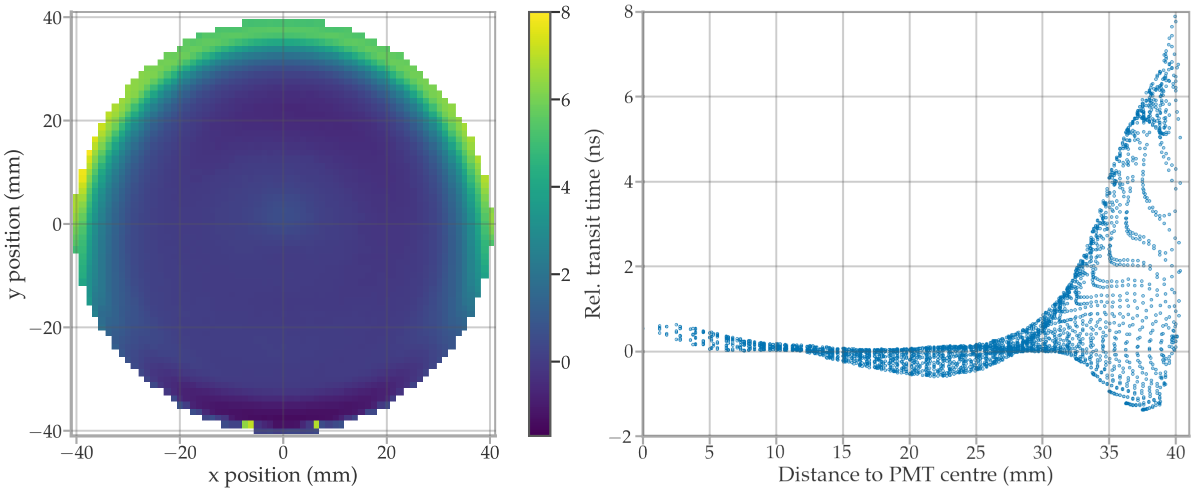

Figure 7.16: *Left:* Average transit time scan relative to the mean of the central region ($r < 30\,\text{mm}$) of the photocathode. Label of colour-bar matches the label of y-axis of the right plot. Data of PMT BA0784. *Right:* The relative transit time data against the distance to the PMT centre. This is the same data as shown on the left side of the figure, which results from the illumination on different locations of the photocathode following a regular grid (shown in Figure 7.5).

The results for the relative transit time are shown in Figure 7.16. As was the case with the gain map, also in the transit time map (left side of Figure 7.16) the y axis is a symmetry axis. The largest deviations were found at the edge of the photocathode with values down to -1.7 ns and up to 8 ns relative to the central mean. For locations up to 30 mm from the photocathode centre, the response is relatively homogeneous with a standard deviation of just 0.23 ns, as seen on the right side of Figure 7.16.

The standard deviation σ_A of the relative transit time as a function of the fractional area A_f is shown in Figure 7.17. As was with the gain, the σ_A is relatively constant until $A_f \approx 60\,\%$. σ_A increases for larger fractional areas, with a maximum between 1.6 ns to 1.9 ns, depending on the PMT.

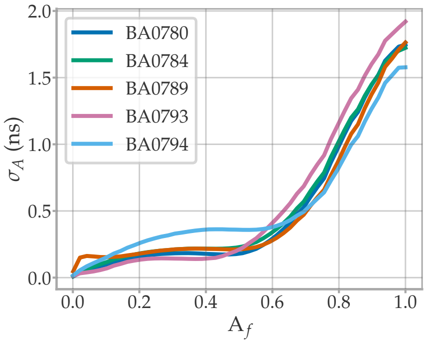

Figure 7.17: Standard deviation σ_A of local transit times inside concentric circles of area fraction A_f with respect to total area. Data published by the author in [110].

The results of the TTS are shown in Figure 7.19. Like with the gain and relative transit time, the TTS deteriorates toward the edges of the PMT (see the right part of Figure 7.19). It should be remarked that the TTS measurement does not reflect the intrinsic variation of the transit time at a specific location on the photocathode but is a convolution of several positions. The internal structures of the PMT reflect the light beam. If the reflected light arrives at a photocathode point with a transit time different from the input position, the time distribution is broadened. At the edges of the PMT, where the transit time deviations are largest (see the left side of Figure 7.16), one can even find transit time distributions with two distinct peaks, as shown in Figure 7.18. Each peak is produced by the response at two different points on the photocathode, one for the entry location of the beam and a second for the exit position after the reflection of the beam.[8] Nevertheless, as can be seen from the low counts, these positions have a low detection efficiency and do not normally pass the cut applied to the data used for Figure 7.19.

It is also worth noting that the TTS is much lower across most of the PMT photocathode than that measured by illuminating the photocathode with

[8] In such distributions, only the largest peak was fitted.

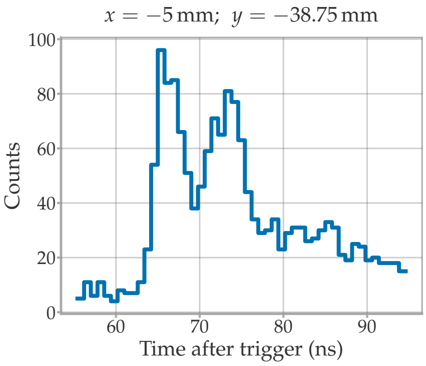

Figure 7.18: Arrival time distribution at $(-5, -38.75)$ mm. The beam is reflected inside the PMT, and two points of the photocathode are illuminated, producing two distinct peaks in the time distribution.

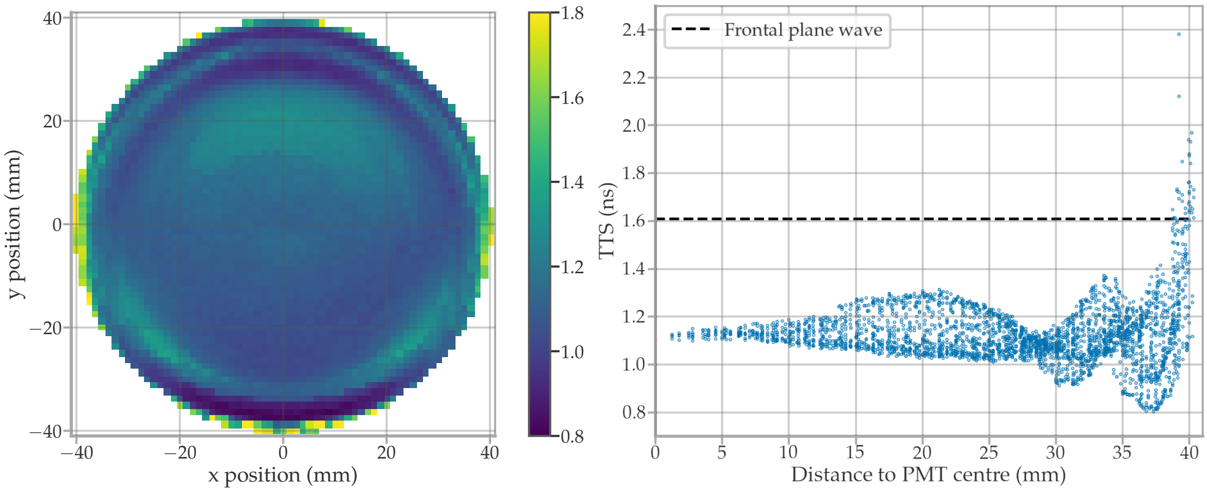

Figure 7.19: *Left:* TTS scan. Label of colour-bar match the label of y-axis of the right plot. Data of PMT BA0784. *Right:* TTS against the distance to the PMT centre. The dashed-line marks the TTS measured with a plane wave illuminating the entire photocathode. This is the same data as shown on the left side of the figure, which results from the illumination on different locations of the photocathode following a regular grid (shown in Figure 7.5).

a frontal plane wave. This is because of the broadening effect of the transit time inhomogeneities on the overall time distribution, similar to the case of the SPE resolution mentioned in the last subsection.

The relative transit time for pulses produced on the edge of the photocathode ($r > 30\,\mathrm{mm}$) (see Figure 7.16 right) deviates from the central mean more than statistically expected from a Gaussian with a standard deviation equal to the TTS. This means that in measurements where the entire photocathode is illuminated, the arrival times will form a non-Gaussian distribution.

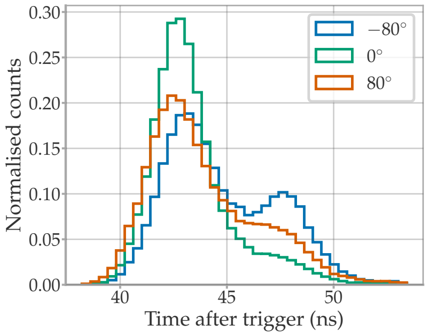

Figure 7.20: Arrival time distribution from plane waves illuminating the entire photocathode at three different incidence angles with respect to the tube axis. An angle of 0° corresponds to a plane wave perpendicular to the tube axis. Data published by the author in [110].

Furthermore, the transit time distribution will also depend on the photon distribution on the photocathode surface. For example, the time distribution changes depending on the angle of incidence of a plane wave. To investigate this effect, one of the PMTs was measured while illuminating its photocathode with a plane wave with an incidence angle of 0°, 80° and −80° with respect to the tube axis. The resulting transit time distributions are shown in Figure 7.20. Incident angles that illuminate the edges of the photocathode more, produce transit time distributions with larger shoulders at later times due to the inhomogeneities in this region.

7.3.3 Correlation between SPE transit time and charge

Comparing Figure 7.15 with Figure 7.12, it can be observed that photocathode locations with larger transit time deviations from the centre also produce pulses with lower charge. This is also true for most of the measured grid points on the photocathode. Figure 7.21 shows the transit time scan data of all PMTs against the corresponding gain scan data normalised to the average gain of the photocathode's central region ($r < 30\,\mathrm{mm}$).

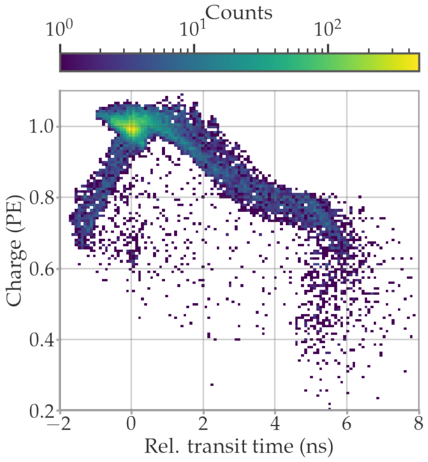

Figure 7.21: Relative transit time of all measured PMTs against the gain on the same photocathode location. The gain was normalised with the mean gain of the central region ($r < 30\,\mathrm{mm}$) of the PMT. Data published by the author in [110].

Although in Figure 7.21 the correlation is apparent, it should be noted that the shown values are the averages of broad distributions (the relative transit time as mean of a Gaussian of standard deviation in the order of 1.5 ns and the gain as mean of an SPE spectrum of width of $\sim 40\,\%$). Therefore, one cannot make a "transit time correction" through the pulse charge.

Nevertheless, the pdf of the transit time for any given SPE pulse could be constrained with its charge. To study this possibility, a dataset was generated via the following procedure:

- For each point (x, y) on the photocathode, $N_{x,y}$ charges and corresponding transit times were sampled from Gaussian distributions.
- The charge was sampled from a Gaussian distribution with a mean equal to the local gain G at the position (x, y) and a standard deviation of $G \cdot R$, where R is the SPE resolution at (x, y).
- Similarly, the transit time was sampled from a Gaussian distribution with a mean and standard deviation equal to the relative transit time and TTS measured at the point (x, y), respectively.
- The number of sampling points is $N_{x,y} = 10000 \cdot \mathrm{DE}_{x,y}$, where $\mathrm{DE}_{x,y}$ is the relative detection efficiency at (x, y) (see Section 7.3.4 for the relative detection efficiency scans).

- The sampled charges are normalised to the average gain of the central region of the PMT ($r < 30\,\mathrm{mm}$).

Figure 7.22 shows the transit time distributions for the sampled data within certain charge intervals. It is apparent that the probability of finding pulses at later transit times is higher the lower the charge is. Conversely, the larger the charge of an SPE, the more Gaussian-like its expected transit time distribution and the less likely the possibility of it arriving at later times.

It might be worth investigating whether this correlation can be used in pulse reconstruction algorithms since the pdf of each pulse's transit time can be limited by its charge. This is especially interesting for water-deployed detectors, as the prompt light time distributions are very narrow due to the large scattering length in this medium [79]. Ice has a shorter scattering length and the direction of the detected photons is more isotropic, resulting in a more extended time distribution. Nevertheless, the inter-spacing between strings and modules in IceCube Upgrade is smaller than in IceCube or DeepCore, so the fraction of detected unscattered photons should be larger than with the current detector configuration.

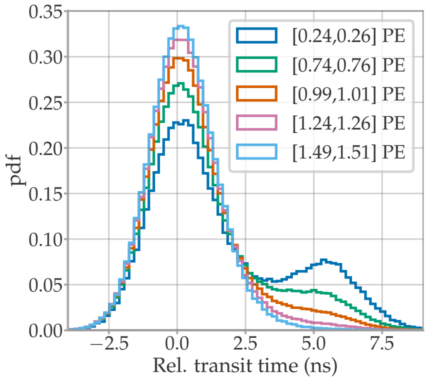

Figure 7.22: Relative transit time distributions for pulses within different charge intervals. Data sampled using the scan data (see text).

[79]: Adrian-Martinez et al. (2016), *Letter of intent for KM3NeT 2.0*

7.3.4 Relative detection and collection efficiency

A third scan is performed with brighter LED pulses of ~50 PE per waveform to measure the homogeneity for the detection efficiency. From such a measurement, it is possible to get a very precise average charge $Q(x, y)$ at each position (x, y) on the photocathode. With the local gain $G(x, y)$ measured with the light intensity at the SPE level in Section 7.3.1, the average number of photoelectrons is calculated as $N(x, y) = Q(x, y)/G(x, y)$.

The absolute light flux $\Phi(t)$ is unknown, but the light intensity $L(t) \propto \Phi(t)$ was continuously monitored with a second PMT. Therefore, it is possible to eliminate the dependence on the intensity of the light and calculate the relative detection efficiency $\mathrm{rDE}(x, y)|_t = N(x, y)/L(t)$.

In the following results, $\mathrm{rDE}_r(x, y)$ is normalised to the mean value of the central region of the photocathode ($r < 30\,\mathrm{mm}$). The results are presented in Figure 7.23. The internal components of the PMT are also visible in the rDE results (see the left side of Figure 7.23) as was the case in the PR results shown in Section 7.2. However, in this case, the detection efficiency remains reasonably constant until ~33 mm, while in the PR measurement a higher sensitivity was found for distances to the PMT centre from 25 mm to 35 mm (see Figure 7.6). This discrepancy agrees with the idea postulated in Section 7.2 that areas with increased PR are caused by SPE released from residual photocathode material coating the internal reflective surface. These photoelectrons are unlikely to reach the first dynode and start a multiplication process, which would be necessary to affect the detection efficiency. Still, they can be measured in the PR measurement, as in this case the dynode system is short-cut.

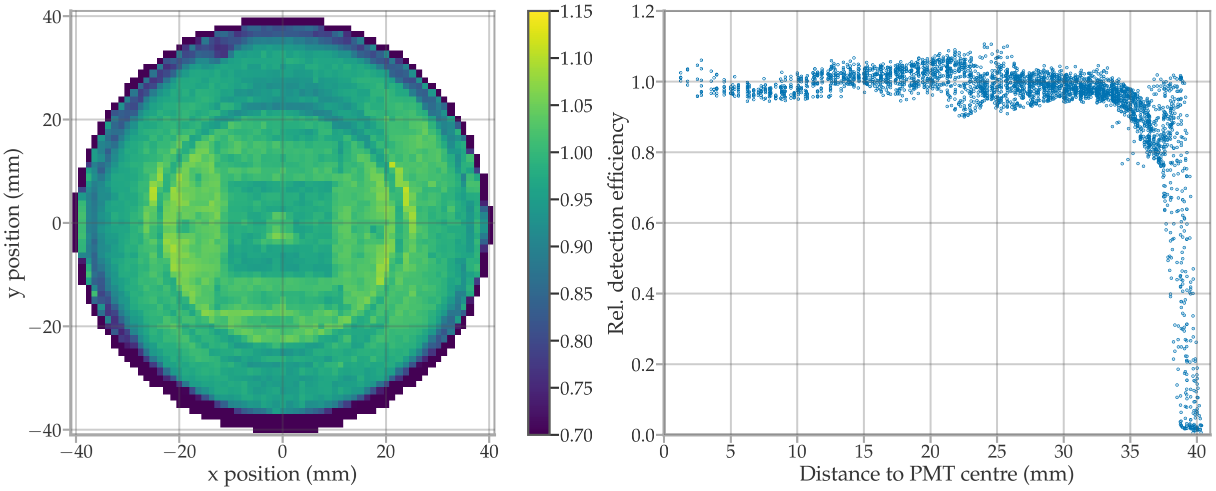

Figure 7.23: *Left:* Relative detection efficiency scan for light peaking at 459 nm. Several internal components are observed in the results due to the internal reflections. *Right:* Relative detection efficiency as a function of the distance to the PMT centre.

The average relative detection efficiency of all measured PMTs is shown against the distance to the PMT centre in Figure 7.24. All PMTs have a similar uniformity with a relatively flat distribution until 33 mm, and the drop in efficiency toward the edges of the photocathode also follows a similar fashion for all PMTs.

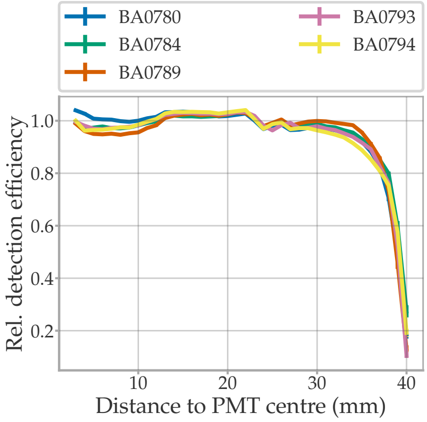

Figure 7.24: Mean relative detection efficiency against distance to PMT centre of all measured PMTs (legend corresponds to the serial number of the PMT).

In principle, once the detection and quantum efficiency of a position on the photocathode is known, it is possible to calculate the collection efficiency following the same scheme as in Section 6.4.2. This is done by calculating $\mathrm{rDE}_{x,y}/\mathrm{PR}_{x,y}$ at each position on the photocathode (x, y). This should result in a *relative* collection efficiency, as the detection efficiency is not known in absolute terms. The results are shown in Figure 7.25. Here, the data were normalised to the mean of the central region of the photocathode ($r < 30$ mm).

Until $r \approx 24$ mm from the PMT centre, $\mathrm{rDE}_{x,y}/\mathrm{PR}_{x,y}$ remains flat, and the patterns caused by the reflections on internal components are fully compensated. For larger distances, $\mathrm{rDE}_{x,y}/\mathrm{PR}_{x,y}$ suddenly drops to about 0.8. This marks the position where the inner reflective coating of the PMT starts (see Figures 7.7 and 7.5). Two effects probably cause this:

- As mentioned in Section 7.2, the PR values may have an extra contribution due to SPEs released by residual photocathode material on the inner reflective coating (see Figure 7.7). This would overestimate the QE at that position on the photocathode. In fact, the highest PR areas (see Figure 7.6 left) also appear in Figure 7.25 as low $\mathrm{rDE}_{x,y}/\mathrm{PR}_{x,y}$ regions.
- Due to the reflections of the beam on internal components, the measured values at the position (x, y) are a sum of several components. In the case of the PR this is given by

$$\mathrm{PR}(x, y) = \mathrm{QE}(x, y) + \sum_{i=1}^{N_r} k_i \cdot \mathrm{QE}(x_i, y_i),$$

where k_i is the fraction of the beam intensity hitting the photocath-

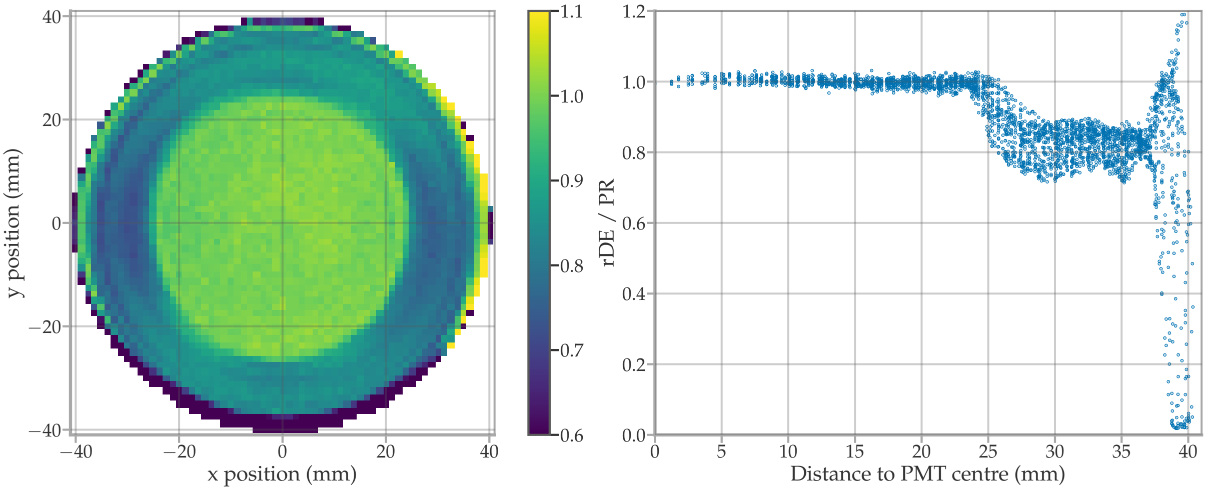

Figure 7.25: The relative detection efficiency data (Figure 7.23) divided by the PR values (Figure 7.6). *Left* as a 2D-map, *right* against the distance to the PMT centre.

ode position (x_i, y_i) and N_r is the number of secondary crossings through the photocathode. This is also true for the measurement of the detection efficiency. Thus, $\mathrm{rDE}_{x,y}/\mathrm{PR}_{x,y}$ will only result in the actual relative collection efficiency if the sum of secondary components is very small, or if the beam runs perpendicular to the surface (in which case the beam is reflected towards the same entry point).

Thus, the data after $r \approx 24$ mm are not reliable to be interpreted as collection efficiency. However, for the central region, most of the internal surfaces are perpendicular to the beam. Electrons released from photocathode residues on the frontal plate will not contribute to the PR measurement, as only the current between the photocathode and the short-cut dynode system is measured. Thus, for this region $\mathrm{rDE}_{x,y}/\mathrm{PR}_{x,y}$ probably approximates the relative collection efficiency well, which is supported by the fact that the reflection patterns were fully compensated in this area. The results of all measured PMTs are shown in Figure 7.26, where the average relative collection efficiency is plotted against the distance to the PMT centre up to $r = 24$ mm. It is apparent that the collection efficiency decreases slightly towards the edges of the photocathode, with an average of 0.986 ± 0.01 at $r = 23$ mm. In Section 6.4.2 it was argued that the centre of the PMTs features a collection efficiency compatible with 100 %. If this is the case, the results in Figure 7.26 can also be interpreted as the absolute collection efficiency as they were normalised to the value of the central area.

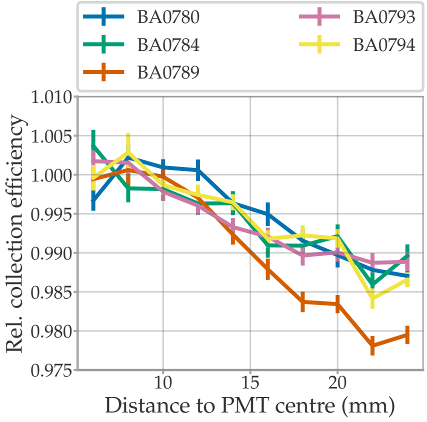

Figure 7.26: Mean relative collection efficiency against distance to the PMT centre of all measured PMTs (serial number of PMT in legend).

7.4 MAGNETIC FIELD DEPENDENCE

As introduced in Section 6.5, several performance parameters of the mDOM PMT show a magnetic field dependency. Therefore, whether this dependence also affects the homogeneity of the sensitive area and the observed patterns is of interest. This is, for example, relevant if the PMT photocathode response is intended to be simulated.

The same setup as introduced in Section 7.1 was used to study this question. The Helmholtz coils were set to 192 fields distributed uniformly across the solid angle with the field strength at the South Pole 54.7 µT.

The photocathode of PMT BA0794 was fully scanned for each direction of the field. In this case, fewer photocathode locations[9] were illuminated than in previous measurements, as otherwise it would take prohibitively long[10]. As observed in the previous sections, the most significant deviations are found at the edges of the PMTs. Hence, this region was measured more densely than the central area of the photocathode. The grid size was set to 1.5 mm for points $r \geq 29$ mm and 2.3 mm for $r < 29$ mm. The measurement was performed only in pulse mode with the dynode multiplication system in operation, as the magnetic field is not expected to affect the photocurrent response (see Section 6.5).

The analysis is the same as that presented in previous sections. The total amount of data is very large and a complete presentation of the results goes beyond the scope of this work. In the following subsections, a reduced subset of the transit time and gain data are shown. These are compared to the results of the measurements on the same PMT at $\vec{B} = (0, 0, 0)$ T from Section 7.3.

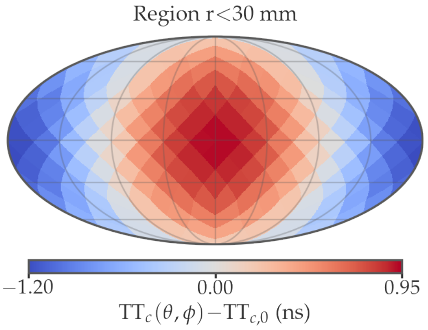

Figure 7.27: Mean transit time of the central region ($r < 30$ mm) for different magnetic field orientations relative to the mean central transit time of the reference measurement at $\vec{B} = (0, 0, 0)$ T.

Online resources available

The best way to appreciate the results of this section is through animated images of the data. In theory, only the figures shown in this section are necessary to understand what is discussed, but it is recommended to look at the animations provided in [148]. The data is publicly available in [149].

7.4.1 RELATIVE TRANSIT TIME

Since the absolute transit time cannot be measured with the setup, a reference value must be chosen to characterise the data qualitatively. In the transit time scans shown until now, this was the average transit time of the central region of the PMT. For the following results, the reference time is the average transit time of the central region of the reference measurement at $\vec{B} = (0, 0, 0)$ T.

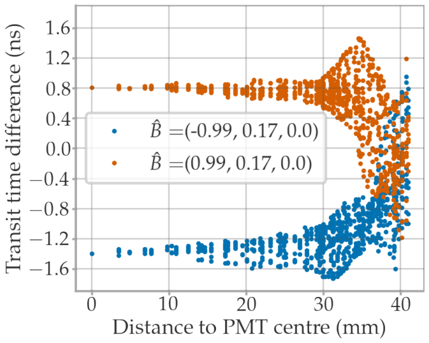

Figure 7.28: Transit time difference against distance to PMT centre for two fields with the maximal absolute value of its x component. Data relative to transit time at $\vec{B} = (0, 0, 0)$ T.

Figure 7.27 shows a Mollweide projection with $\mathrm{TT}_c(\theta, \phi) - \mathrm{TT}_{c,0}$, where $\mathrm{TT}_c(\theta, \phi)$ is the average central transit time ($r < 30$ mm) at field direction (θ, ϕ) and $\mathrm{TT}_{c,0}$ the reference average central transit time at $\vec{B} = (0, 0, 0)$ T. As expected from the results introduced in Section 6.5, a strong dependence on the x component of the magnetic field is observed. However, in this case, the extreme values are (-1.19 ± 0.01) ns and (0.942 ± 0.005) ns, which is a broader range ((2.13 ± 0.01) ns peak-to-peak) than the one observed in the measurement with complete photocathode illumination ((1.77 ± 0.01) ns peak-to-peak, as listed in Table 6.2 for PMT BA0794).[11] Figure 7.28 shows the transit time difference of the scans performed at the fields with the maximum absolute value of the x component, $\hat{B} = \vec{B}/\|B\| = (\pm 0.99, 0.17, 0.0)$, relative to $\vec{B} = (0, 0, 0)$ T. The transit time differences at the edges of the photocathode are relatively small compared

[9] 777 instead of 3304.

[10] Even with this reduced number of grid points, the scans for all magnetic field directions took 41 days for just one PMT.

[11] The uncertainties provided for the peak-to-peak values are the statistical errors. Since the transit time values are means derived from a large data set, the calculated standard errors are typically small. It is worth noting, however, that these uncertainties do not account for potential systematic errors. One example of a systematic error could be introduced by the chosen range for fitting the Gaussian on the transit time histogram.

to those of the central region. This explains the difference in peak-to-peak values: while in Figure 7.27 only the central region was averaged (values at $r < 30$ mm in Figure 7.27), illuminating the photocathode with a plane wave translates into averaging the response across the entire photocathode (this means, from $r = 0$ mm to $r = 40$ mm in Figure 7.28).

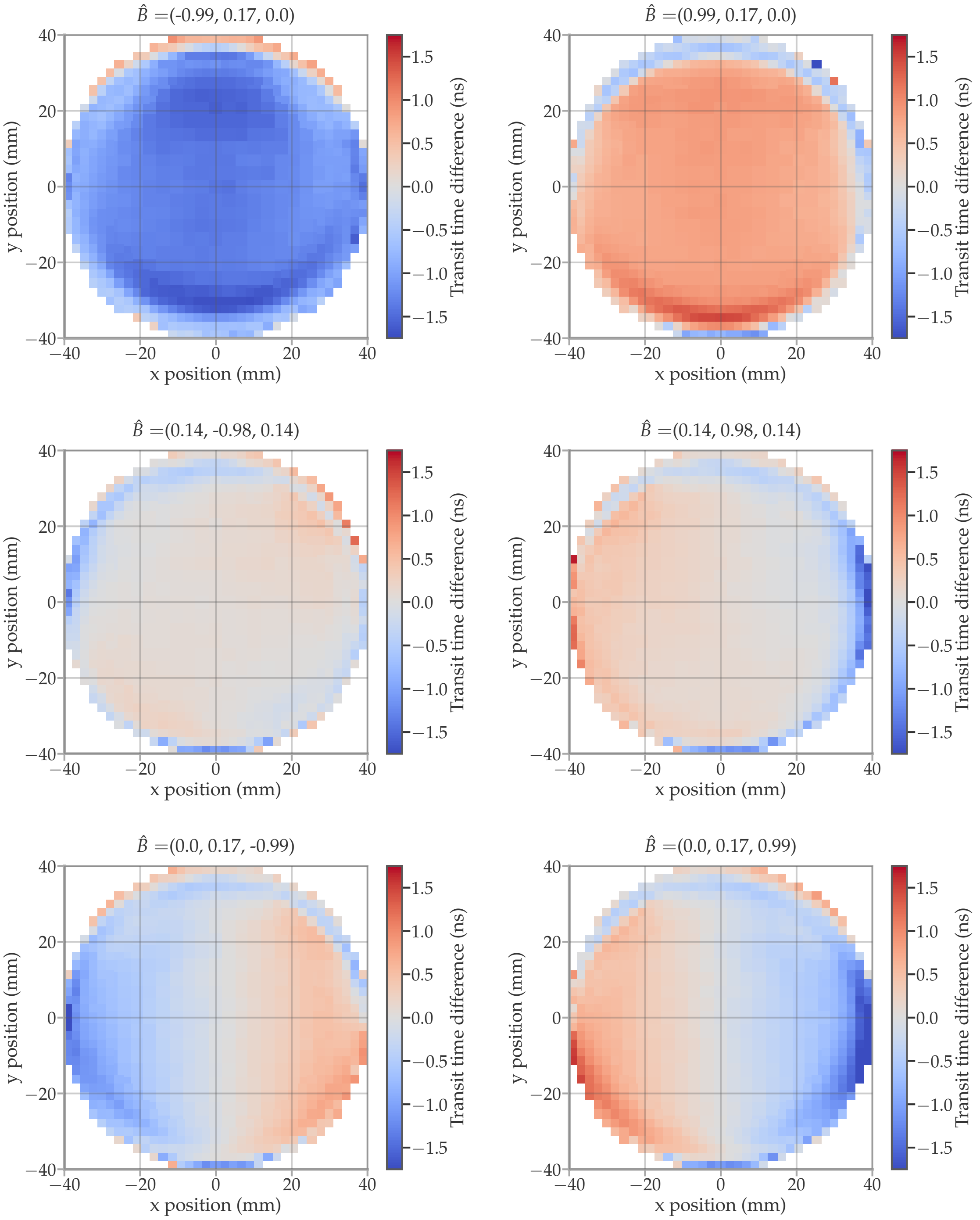

Figure 7.29: Transit time scans relative to the measurement $\vec{B} = (0, 0, 0)$ T for the magnetic field directions with the largest absolute components in the x-axis (top row), y-axis (middle row) and z-axis (bottom row). The left side of each row shows the case for a negative component and the right for a positive component. $\hat{B} = \vec{B}/\|B\|$ is the normalised magnetic field vector.

Figure 7.29 shows the scans at the maximal values of each vector component. On the top row, the same data is shown as in Figure 7.28, where the field is (anti)parallel to the x-axis. The second and third rows show the cases for the maximal y and z components, respectively. As expected from Figure 7.27, the transit time differences for magnetic fields along the y- and z-axes are smaller than for the x-axis. Nevertheless, there are still regions with large deviations at the edge of the photocathode to be observed, especially for the field (anti)parallel to the z-axis. It is apparent that the regions with large deviations appear with a certain symmetry for $\vec{B}$ in the y or z direction. For example, in the last row of Figure 7.29, regions with the largest positive transit time difference are on the opposite side of the regions with the lowest transit time differences. It should also be noticed that the position of these regions flips if the field is in the opposite direction. In Section 6.5, no significant dependence on the y or z component of $\vec{B}$ could be reported. As the largest deviations occur at the edges with an opposite effect across the photocathode, these transit time differences are likely to go unnoticed when the PMT is illuminated with diffuse light, as they partially compensate.

In Section 6.5, it was hypothesised that the transit time deviations reflect the position in which the SPEs hit along the curvature of the first dynode, which bends along the y-axis. In this perspective, the results of Figure 7.29 are relatively easy to interpret with the Lorentz force. In the case of a magnetic field aligned with the x axis, the results are compatible with the previous discussion: A magnetic field aligned with x will deflect most of the SPE trajectories in the y direction, causing them to hit the first dynodes at different distances from the second dynode (see Figure 6.48). This is the case because SPEs are likely to have a large z component in their velocity vector at the end of their path to the multiplication system, and thus affect the response of almost the entire photocathode.

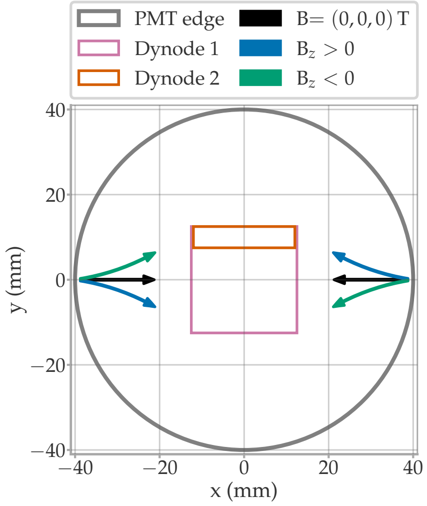

Figure 7.30: Sketch of the front of the PMT illustrating how the trajectories with a large x-component in the velocity vector are deflect by a magnetic field with a significant z component.

Due to the curvature of the photocathode, the SPEs released from the edge of the photocathode should have starting velocities with the largest components in the x and y plane, compared to the SPEs released from the centre, which should follow trajectories mostly near parallel to the z axis. A magnetic field along the z component affects the SPE direction along y if the latter has a large x component in its velocity vector. This can be observed, in fact, in the last row of Figure 7.29, where the SPEs at the edges of the PMT with positive x feature the highest deviations. Figure 7.30 shows a sketch of the front of the PMT with the deviation of the SPEs for a magnetic field along the z axis. As was the case with the magnetic field in the x direction, the transit time is diminished if the SPE is deflected towards the second dynode and increased if diverted in the opposite direction.

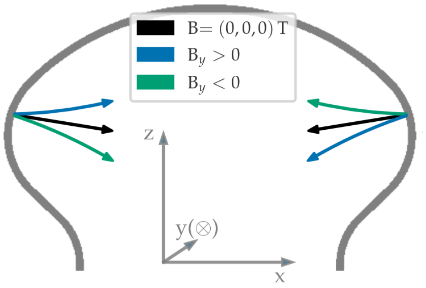

Figure 7.31: Sketch of the side of the PMT illustrating how the trajectories with a large x-component in the velocity vector are deflect by a magnetic field with a significant y component.

A magnetic field aligned with the y-axis cannot deflect the SPEs along that axis, and, therefore, the effects on the transit time are comparatively small. Nevertheless, there are still some small regions with significant transit time differences. As the field does not fully align with the y-axis it could be argued that some of these deviations are caused by the other vector components. However, some regions show a different response when the y component is flipped in sign (compare the left and right maps of the middle row of Figure 7.29), while the other vector components remain constant. These areas are mainly towards the edges of the photocathode and large x. Indeed, SPEs moving in the x direction are deflected along the z-axis, as sketched in Figure 7.31. The results are consistent with SPEs having larger transit times if they are deflected away from the multiplication system and vice versa.

When the magnetic field is not aligned with a coordinate axis, the photocathode response seems to be a combination of the on-axis results. Figure 7.32 shows the results of the transit time scan for a magnetic field $\hat{B} = (-0.56, 0, -0.83)$ and for a field antiparallel to that. As $\vec{B}$ has no y component, the top/bottom map of Figure 7.32 should be compared with the left/right side of the upper and lower rows of Figure 7.29. It can be seen that, although the patterns in Figure 7.32 are more complicated, they appear as a sum of the results in Figure 7.29.

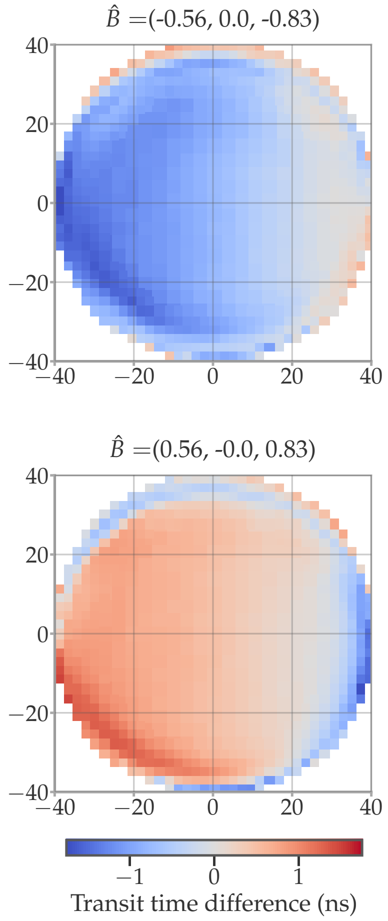

Figure 7.32: Transit time scans relative to the measurement $\vec{B} = (0, 0, 0)$ T for a magnetic field with similar x and z components. *Top*: field vector at $\theta = 146°$, $\phi = -180°$ and *bottom*: field vector at $\theta = 33°$, $\phi = 0°$. The axes labels were omitted but are the same as in Figure 7.29. $\hat{B} = \vec{B}/||B||$ is the normalised magnetic field vector.

7.4.2 GAIN

Figure 7.33 displays the relative difference to the results at $\vec{B} = (0, 0, 0)$ T of the average gain of the central photocathode region $r < 30$ mm. The results are compatible with those shown in Section 6.5, although, as with the transit time, the extreme values cover a broader range. The increase in gain for a magnetic field antiparallel to the y-axis can be clearly noticed, indicating that the excess found in Figure 6.44 is not merely statistical fluctuations.

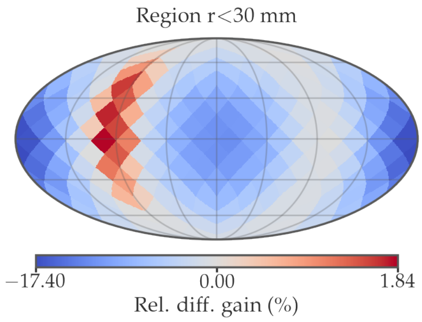

Figure 7.33: Mean gain of the central region of the photocathode ($r < 30$ mm) for different magnetic field orientations relative to the central transit time at $\vec{B} = (0, 0, 0)$ T.

Figure 7.34 shows the gain scans as a relative difference to $\vec{B} = (0, 0, 0)$ T for the magnetic field aligned with each coordinate axis. In the first row, the case for the field (anti)parallel to the x-axis. As expected from Figure 7.33, most of the photocathode responds with a lower gain. In Section 6.5, it was argued that this gain decrease might be mainly caused by a loss of collection efficiency between the dynode stages. As the dynodes are placed perpendicular to the y axis, the velocity vector of the SPEs travelling between the dynodes must have a relatively large y component. A field aligned with the x-axis would cause a deflection in the z direction, which may cause the loss of secondaries. Nevertheless, any effect at the inter-dynode stage should result in a relatively homogeneous response for the whole photocathode. As noticeable in the first row of Figure 7.34, this is not the case, which indicates that there are also effects on the trajectory from the photocathode to the first dynode that change the gain. This is also true for the magnetic field aligned with the y- or z-axis. Especially for the latter, the response of the photocathode is symmetric, with regions of higher gain having a lower gain counterpart on the opposite side of the x-coordinate.

SPEs released from one edge of the photocathode have the x and y components of their velocity vector in the opposite direction compared to SPEs released across the photocathode. Hence, symmetrical patterns indicate deflections in the trajectory from the photocathode to the first dynode. However, pinpointing the underlying mechanism that changes the gain is very difficult. In general, the gain should vary via an increase or decrease in the kinetic energy of the SPE before hitting the first dynode and where it hits, as the collection efficiency to the second dynode may change. Therefore, it could be argued that a deflection towards the multiplication system (negative z) causes an increase in gain because the

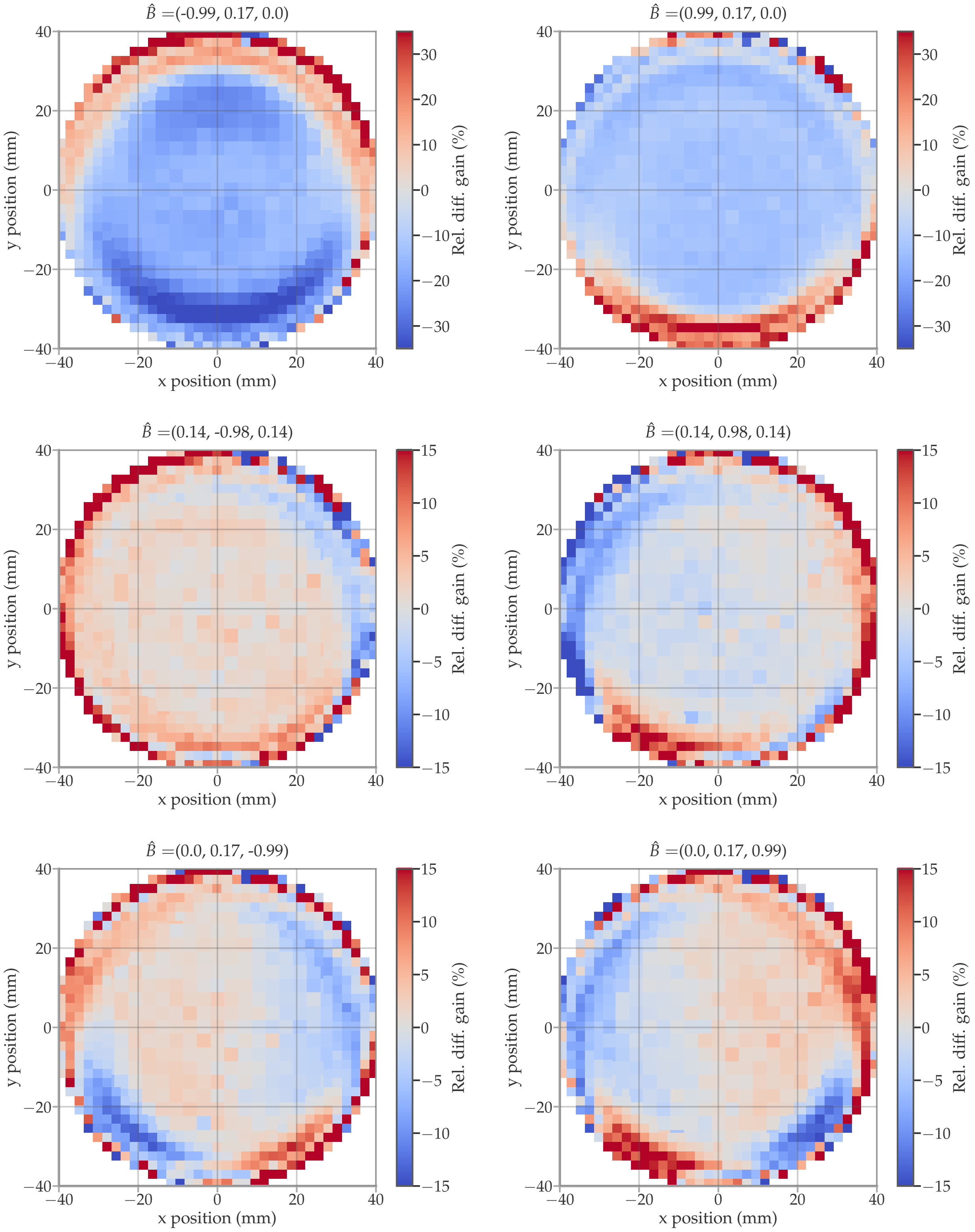

Figure 7.34: Gain scans relative to the measurement $\vec{B} = (0, 0, 0)$ T for the magnetic field directions with the largest absolute components in the x-axis (top row), y-axis (middle row) and z-axis (bottom row). The left side of each row shows the case for a negative component and the right for a positive component. $\hat{B} = \vec{B}/\|B\|$ is the normalised magnetic field vector.

SPE arrives at a higher speed. This idea is indeed supported by the change in gain observed at the upper / lower edges of the photocathode for a magnetic field (anti)parallel to x. For example, for the field antiparallel to x, the SPEs that have a negative velocity component in y are deflected in $-z$, and indeed there is a region with a higher gain at the upper edge of the photocathode. On the lower edge, the opposite is true, with a lower gain due to deflections to $+z$.

A deflection in the $-z$ direction may also explain the regions with lower gain on the right side of the scan with the field antiparallel to y and on the left side of the scan for the field parallel to y. However, the results for the field aligned with the z direction cannot be caused by the same mechanism, as the SPEs cannot be deflected in z but only in the x/y plane. In the scans of the last row of Figure 7.34, the patterns are relatively complicated, with symmetries along the x and y axes. These are probably a result of the first dynode geometry and the shape of the electric field lines. The increase of gain for a field antiparallel to y is challenging to interpret as well. Nevertheless, the almost homogeneous photocathode response shown for this case (left scan of the middle row of Figure 7.34) may indicate that this is an effect occurring at the inter-dynode stages.

Figure 7.35 shows the scans for a field in the x-z plane, which is to be compared with the scans of the top and bottom row of Figure 7.34. As was the case with the transit time, the patterns in the photocathode combine when the field lies between different axes.

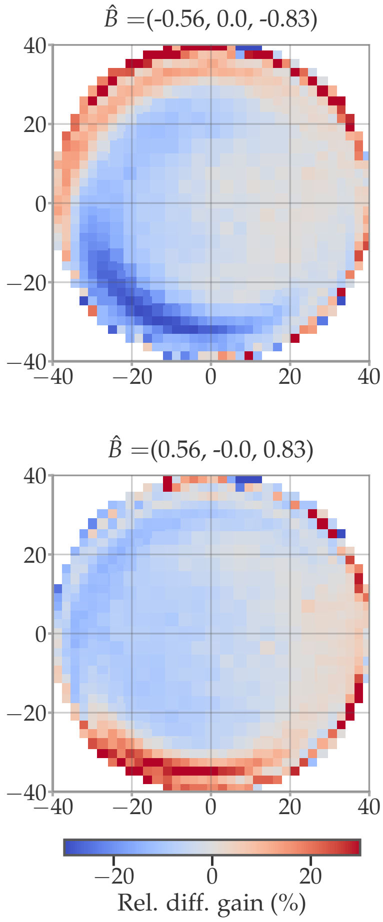

Figure 7.35: Gain scans relative to the measurement $\vec{B} = (0, 0, 0)$ T for a magnetic field with similar x and z components. *Top*: field vector at $\theta = 146^\circ$, $\phi = -180^\circ$ and *bottom*: field vector at $\theta = 33^\circ$, $\phi = 0^\circ$. The axes labels were omitted but are the same as in Figure 7.34. $\hat{B} = \vec{B}/\|B\|$ is the normalised magnetic field vector.

It can be concluded that the homogeneity of the photocathode is complex, and if it were to be included in simulations, the magnetic field must also be considered. In the next section, another dimension is investigated that can potentially increase this complexity: the beam's wavelength.

7.5 Wavelength dependence

All measurements presented in the previous sections were performed with an LED of peak wavelength of 459 nm and a width of 24 nm (FWHM). To investigate the wavelength dependence of the photocathode inhomogeneities, the light source of the setup was replaced by the NKT supercontinuum laser system. The UV extension modules do not yet have a fibre connection, and therefore cannot be attached to the 3D scanner. Hence, the photocathode could be scanned using only the wavelength filter[12] starting from 460 nm.

The laser light output is well collimated, with a laser beam quality of $M^2 < 1.1$ and a beam width of ∼0.14 mm.[13] Thus, the compensation for the photocathode curvature along the z-axis, as explained in Section 7.1.1, is no longer necessary. Apart from that, the setup and measurement methods are the same as before (see Section 7.1).

Ideally, one would repeat the measurements as before, capturing the photocurrent response with short-cut dynodes and determining the pulse performance parameters in a second. However, measuring the photocurrent without cathode saturation with the NKT laser configuration is not possible: as the maximum repetition rate of the laser is 20 kHz,

[12] LLTF VIS HP8 from NKT Photonics.

[13] The beam size is measured in Figure 9.10 of Section 9.2.

each laser pulse has to produce a very large photocurrent to measure a signal above the noise of the PMT. Compared to the light source used before which was configured with a repetition rate of 20 MHz during a PR measurement, this means that with the NKT laser system, the photocathode saturates at an integrated photocurrent 1000 times smaller. Practically, this translates into saturation for integrated currents at the pC level, while the measured background is on the order of 0.1 nA. Therefore, in this section, only the performance in pulse mode is studied.

The PMT of serial number BA0784 was scanned with the wavelengths from 460 nm to 640 nm in 20 nm with a light intensity at SPE level. A set of ND filters was used to control the light intensity (their transmittance was determined in Section 6.4.2). Once the fibre points to a location on the photocathode, all wavelength steps are collected before moving to the next location. During data collection, which took ~6.5 d in total, the measurement had to be stopped due to external reasons, which caused the loss of 27 points in the photocathode for $x = -12.5$ mm and y from -37.5 mm to -21.25 mm. These points were remeasured after the data was analysed, but probably because of a slightly different fibre position, these points seem to be systematically shifted. As this represents less than 1 % of the total number of measured grid points, it was not considered necessary to repeat the measurement.

A second series of measurements were performed at a higher light intensity in the order of 10 PE to 50 PE per waveform to calculate the detection efficiency. With this light level 10,000 waveforms provide enough statistics (compared to 45,000 at SPE level). This allows for a shorter wavelength step of 10 nm, as each wavelength step takes less time.

First, the wavelength dependence of the photocathode homogeneity for the gain is presented in Section 7.5.1, followed by the relative transit time and TTS in Section 7.5.2. Finally, Section 7.5.3 delves into the dependence of the detection efficiency.

7.5.1 GAIN

Figure 7.36 shows the gain map for a light beam of wavelengths 460 nm and 640 nm. As expected from the results of Section 6.2, the gain increases with the wavelength for most regions of the photocathode. After closer

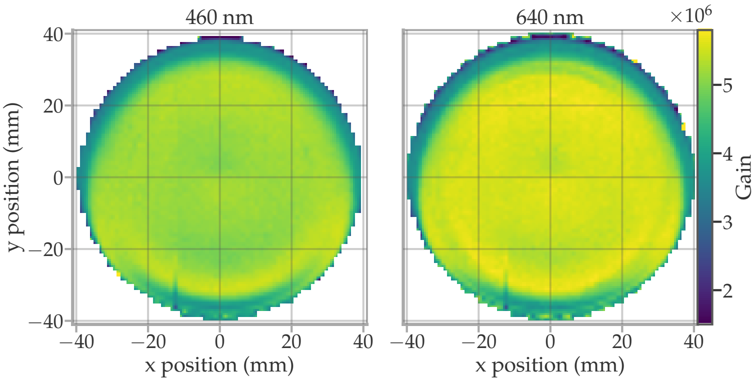

Figure 7.36: Gain map of the PMT BA0784 for monochromatic light at 460 nm (*left*) and 640 nm (*right*).

inspection, it can also be observed that the map at 640 nm shows slightly more inhomogeneities, implying that the gain's wavelength dependence is not constant for the entire photocathode area.

For example, the map at 640 nm shows a lower gain region at $r \approx 30$ mm and x from −20 mm to 20 mm. The wavelength dependence at $(0, 30)$ mm and at the centre of the photocathode is shown in Figure 7.37. The local gain is relatively independent of the wavelength at $(0, 30)$ mm, in contrast to the increase at the centre of the photocathode. The gain versus wavelength curves were fitted with a linear function to study the wavelength dependence of all the measured points on the photocathode. It is clear from Figure 6.18 that a linear relationship between gain and wavelength should not be expected, but it can still be helpful to show trends in the data.

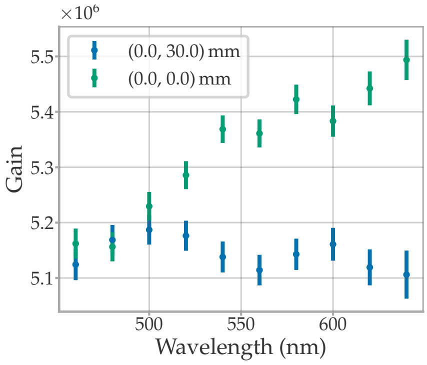

Figure 7.37: Local gain at the photocathode positions $(0, 30)$ mm and $(0, 0)$ mm as a function of the wavelength.

Figure 7.38 shows the fitted slope in dimensions of the relative change of the gain (in percentage) for every 100 nm. There is a general tendency for the local gain to increase with wavelength at an average level of (4.11 ± 0.02) %/100nm until $r \approx 25$ mm, but towards the edges of the photocathode, there are regions of lesser increase. Some points show a negative slope, meaning the gain tends to decrease with the wavelength in these locations. The inhomogeneity differences between the two scans in Figure 7.36 are reflected in the slope map on the left side of Figure 7.38.

In Section 6.2.3 , it was argued that the increase in gain with larger wavelengths could be explained by an improvement in the homogeneity of the SPEs' trajectories. The smaller the wavelength, the higher the initial energy of the SPEs, changing the path to the first dynode. On the one hand, if the undeviated trajectory is optimal, an SPE with initial kinetic energy will likely wander outside this optimal path and be multiplied less. On the other hand, if the undeviated path is sub-optimal, a deviation due to a high initial energy can result in a 'better' trajectory and hence a higher gain. This reasoning could explain both the positive slope region in the centre of the PMT and the negative slope areas toward the edges in Figure 7.38.

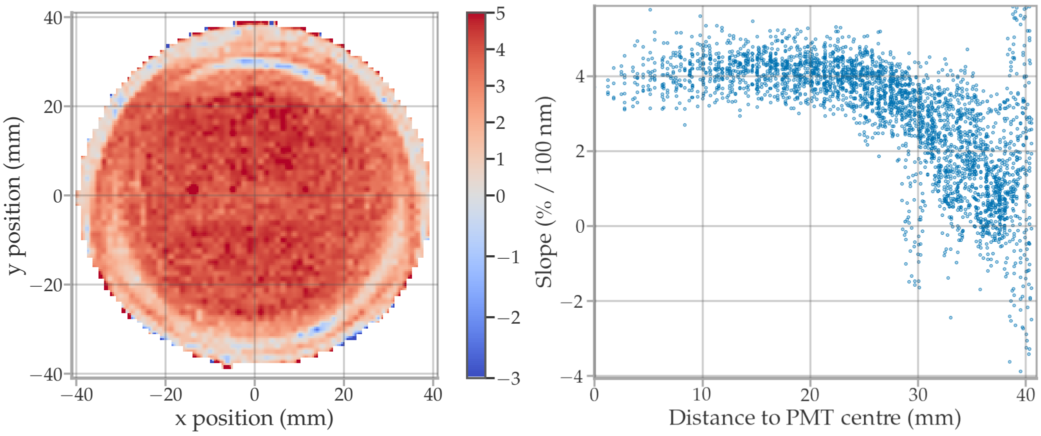

Figure 7.38: On each position on the photocathode, the gain versus wavelength curve (e.g. see Figure 7.37) was fitted with a linear function. The slope of the fit is shown in dimensions of relative change of the gain in percentage every 100 ns in the map representation (*left*) and against the distance to the PMT centre (*right*).

7.5.2 TTS

Following the results from Section 6.3.3 it is expected that the TTS decreases with wavelength for most of the photocathode. However, as with the gain, not all regions of the photocathode showed the same response. Figure 7.39 presents the wavelength dependence of the TTS for the centre of the photocathode and at $(-26.25, 22.5)$ mm. Although the central point follows the expected trend, the more peripheral location shows the opposite behaviour, increasing from (1.20 ± 0.01) ns for 460 nm to (1.95 ± 0.04) ns for 640 nm.

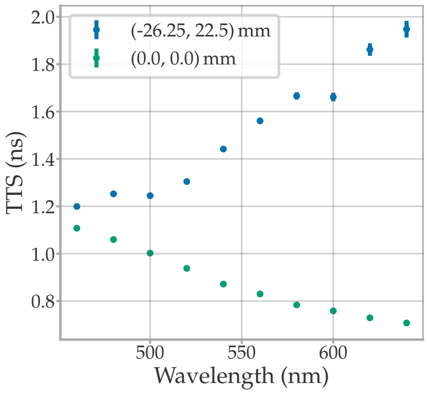

Figure 7.39: Local TTS at the photocathode positions $(-26.25, 22.5)$ mm and $(0, 0)$ mm as a function of wavelength.

The same approach as in the last subsection was taken for the analysis of TTS scans. Figure 7.40 shows the slope of the linear fit of the TTS-wavelength curve at each position on the photocathode. There is a clear tendency of the TTS to decrease with the wavelength until $r \approx 30$ mm with an average slope of (-0.177 ± 0.001) ns/100nm. Most points further towards the edges show a positive gradient, which means a worsening of the TTS with the wavelength, with regions showing up to ~0.4 ns/100nm.

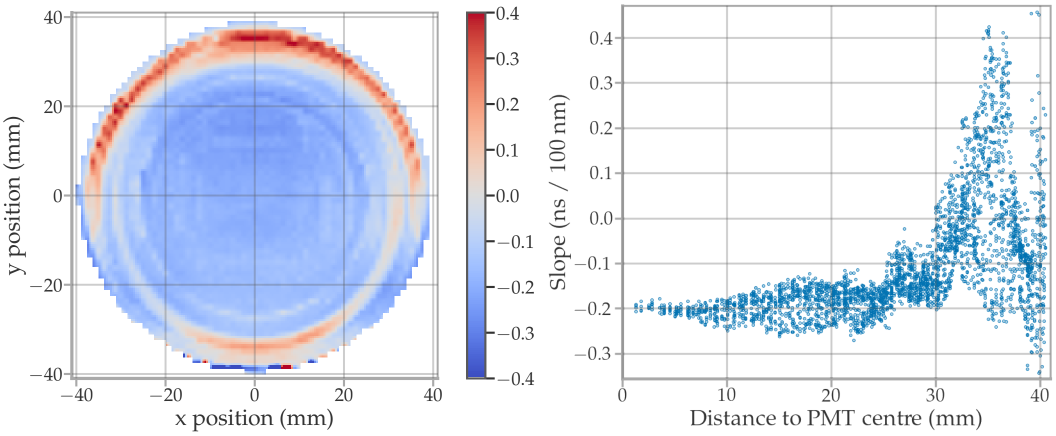

Figure 7.40: On each position on the photocathode, the TTS versus wavelength curve (e.g. see Figure 7.39) was fitted with a linear function. The slope of the fit is shown in ns/100 ns in the map representation (*left*) and against the distance to the PMT centre (*right*).

7.5.3 DETECTION EFFICIENCY

The same approach was used to calculate the detection efficiency as in Section 6.4.2 following Equation 6.19. A second measurement run using bright light pulses (on the order of 10 PE to 50 PE) was performed to obtain a precise average charge $Q_{x,y}$ at each measured point (x, y) on the photocathode. The beam is measured with a second PMT every 50 grid steps to reference the light intensity over time. This reference measurement was calibrated using the photodiode to obtain the absolute light flux.

As measuring with high light intensity requires fewer waveforms to gather enough statistics, the wavelength step was reduced to 10 nm. The local gains in wavelength steps that were not measured during the previous measurement run are interpolated, assuming a linear function between nearest neighbours.

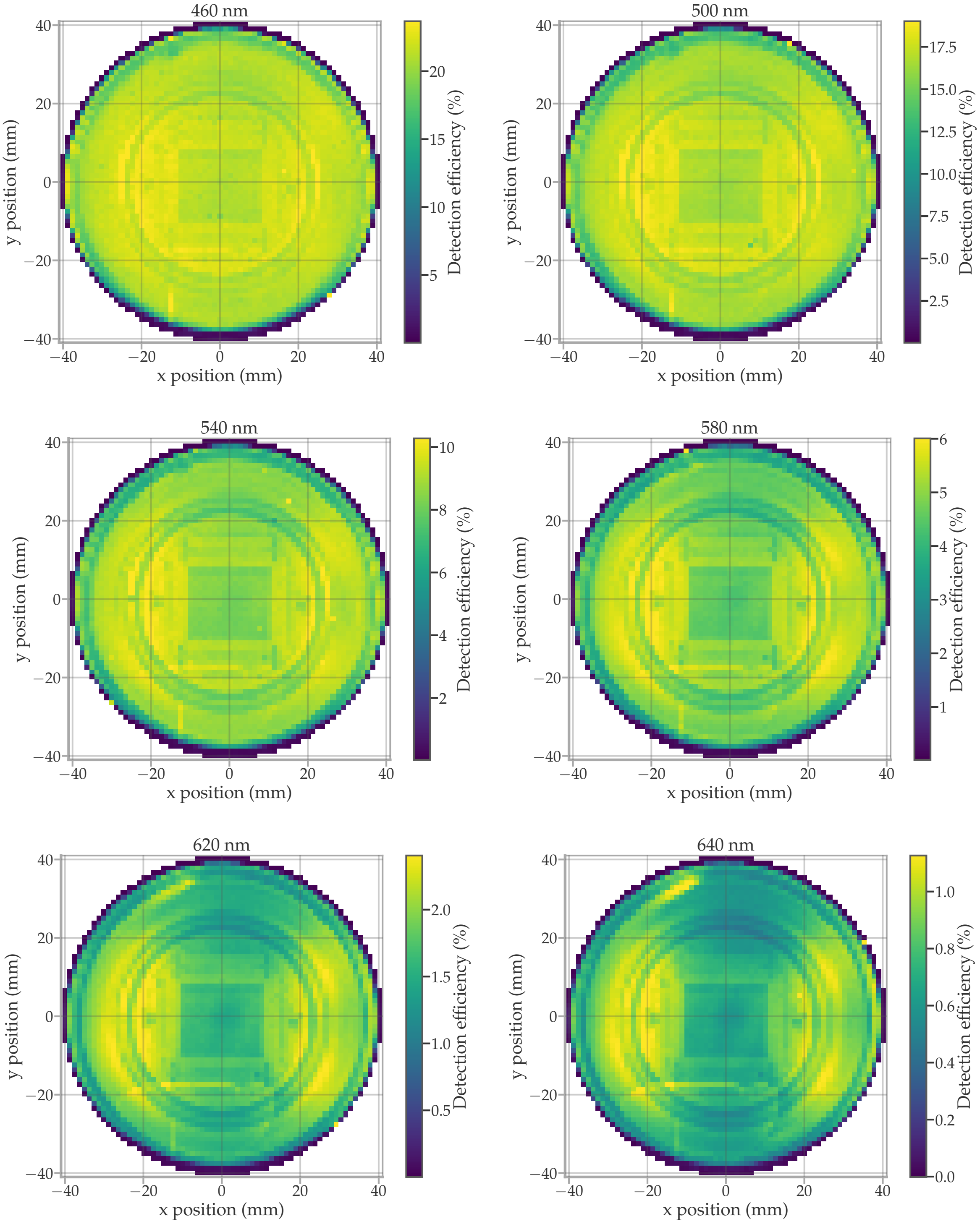

Figure 7.41: Detection efficiency scan measured with a light beam of various wavelengths ranging from 460 nm to 640 nm. The range of the colour-bar of each plot was chosen using the 99 % percentile as maximum and 1 % as minimum.

Figure 7.41 shows the calculated detection efficiency scans for some of the wavelengths from 460 nm to 640 nm. Whereas the performance for shorter wavelengths is compatible with the results of Section 7.3.4, starting from 540 nm (left graph of the middle row of Figure 7.41), new patterns start to appear. These inhomogeneities increase for longer wavelengths and do not appear to be caused by reflections of the beam on the internal surfaces, as was the case for most patterns in the measurement at 459 nm.

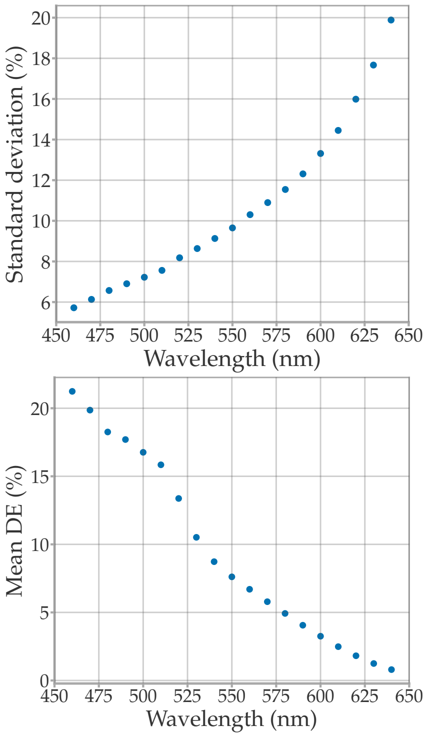

Figure 7.42: *Top:* normalised standard deviation of the scanned detection efficiencies as a function of the wavelength. The values were normalised to the mean efficiency of the respective scan. *Bottom:* Average detection efficiency of each scan.

The top-side Figure 7.42 shows the standard deviation of the points within a scan as a function of the wavelength. The standard deviation was normalised to the mean detection efficiency, which is presented in the lower graph of Figure 7.42. Only points within $r < 38$ mm were considered to exclude the drop in efficiency at the edges. The standard deviation increases monotonically with the wavelength from ~5.7 % at 460 nm to ~20 % at 640 nm. The rate of increase also rises with wavelength, meaning that the uniformity of the response will likely continue to deteriorate in the infrared. However, the detection efficiency also decreases rapidly for these wavelengths. For this reason, the average standard deviation weighted by the mean detection efficiency is only ~8.1 %. If the UV region was taken into account, this number would probably be even lower.

This worsening of the response uniformity has been reported before [115, p. 62] [129, p. 108], although its cause is not discussed in detail. In [115] it is suggested that the sensitivity strongly depends on the surface conditions of the photocathode at the infrared limit of the PMT, hence the increasing fluctuations.

[129]: Flyckt et al. (2002), *Photomultiplier tubes - principicles and applications*

[115]: Hamamatsu Photonics K.K. (2017), *Photomultiplier tubes - Basics and Applications*

In order to better understand these inhomogeneities, the three-step model for photocathodes can be used. Here, the photoemission process can be divided into the following steps [150]:

[150]: Spicer et al. (1993), *Modern theory and applications of photocathodes*

- Photoexcitiation of an electron in the valence to the conduction band. The probability can be described with the absorption length $\beta(\lambda)$ of the photocathode, which depends on the wavelength λ. The fraction of the beam that is absorbed is $1 - \exp(-T/\beta)$, where T is the thickness of the photocathode.
- Transport of the photoelectron to the photocathode surface. As the scattering probability is proportional to the distance travelled, the probability of the electrons reaching the surface with sufficient energy decreases with thickness.
- Escape of the photoelectron to vacuum (electron should have an energy above the vacuum level).

Thus, the optimal layer thickness of the photocathode depends on the absorption coefficient for the photons and the scattering length of the photoelectrons. Assuming that the electron transport is not affected by the thickness variations in the mDOM PMT, inhomogeneities in the response should result from different amounts of absorbed photons.[14] Since the absorption length of the photocathode increases with wavelength [151], achieving the same sensitivity at longer wavelengths as at shorter wavelengths requires a thicker photocathode.

The ratio R of absorbed photons of two photocathode regions with thicknesses T_1 and $T_2 = \alpha \cdot T_1$ respectively, can be calculated as

[151]: Motta et al. (2005), *Optical properties of Bialkali photocathodes*

[14] Note that this assumption is well founded, as otherwise the efficiency inhomogeneities should be already noticeable at lower wavelengths.

$$R = \frac{1-\exp\left(-\frac{\alpha \cdot T_1}{\beta}\right)}{1-\exp\left(-\frac{T_1}{\beta}\right)} \approx \frac{\frac{\alpha \cdot T_1}{\beta} - \frac{\alpha^2 \cdot T_1^2}{2\beta^2} + \ldots}{\frac{T_1}{\beta} - \frac{T_1^2}{\beta^2} + \ldots}, \tag{7.1}$$

where the power series definition $e^x = \sum_{n=0}^{\infty} x^n/n!$ was used. For the case where $T \gg \beta$, most photons are absorbed and $R \sim 1$, while for $\beta \gg T$ the higher-order terms approach zero and $R \rightarrow \alpha$. Thus, the larger the absorption length of the photocathode relative to its thickness, the more noticeable the differences in thickness along the photocathode.

The Münster IceCube group is working on measuring photocathode properties, such as its thickness and absorption length, through ellipsometry. Infrared scans may provide complementary results and verify the ellipsometry measurements by determining the relative change in photocathode thickness (if the conditions for $R \approx \alpha$ are met).

7.6 LOM, D-Egg and Gen1-DOM PMTs

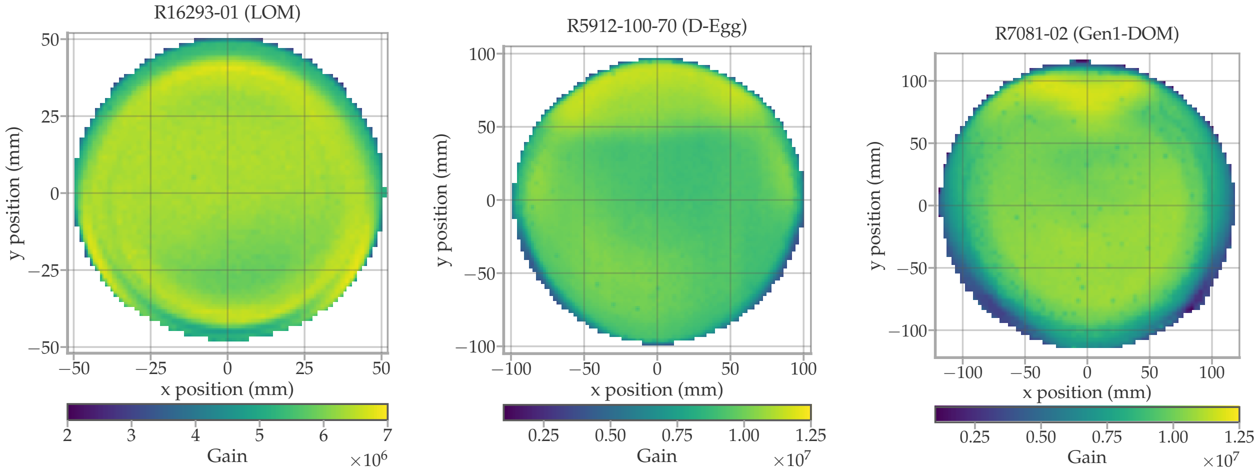

Figure 7.43: Photocathode scan of the gain for the three larger Hamamatsu PMT types, used in the LOM (*left*), D-Egg (*centre*) and Gen1-DOM (*right*).

Two Hamamatsu PMTs of the type candidate to be used in the LOMs, two Hamamatsu PMTs used in D-Eggs and one PMT of the type used in the IceCube Gen1-DOMs, were measured with the setup and method presented in Section 7.1. For these PMTs, only the measurement in pulse mode was performed with the PMTs driven at nominal gain. Custom-built bases would be needed to shorten the dynodes to measure the photocurrent response. In this section, the results for the relative transit time and gain are presented and compared.

Figure 7.43 shows the gain map of the three types of PMTs. As with the mDOM PMT, the photocathode features inhomogeneities in the gain response, and the y-axis appears as the symmetry axis. The patterns of the two larger PMTs, the D-Egg and Gen1-DOM, are similar, with a larger local gain in the northern region of the photocathode. Conversely, the LOM PMT patterns resemble those of the mDOM PMT (cf. Figure 7.11).

The data were binned by the distance to the PMT centre, normalised to the radius of the frontal PMT bulb R_0 to compare all PMTs. The gain in each bin, of width 0.01, was averaged. Figure 7.44 shows the resulting gain curve, which was normalised with the average gain in the photocathode central region ($r < 0.4 \cdot R_0$). The four PMT types feature a relatively constant gain at the centre, but it drops toward the edges of the photocathode. The average gain of D-Egg PMT also shows an increase before the drop due to the larger gain in the northern region (see the mid plot of Figure 7.43). The Gen1-DOM PMT has a gain degradation much earlier than the other PMTs, dropping at $\sim 0.6 \cdot R_0$while the other PMTs knick at $\sim 0.8 \cdot R_0$. The 10" PMT even reaches an average gain of zero at $\sim 0.95 \cdot R_0$, while the other PMTs always show some multiplication level. The R_0 used for normalisation is the radius of the PMT glass given by Hamamatsu data sheets. Nevertheless, the photocathode is not guaranteed to be sensitive over the entire frontal area of the PMTs, and the radius of the photocathode is given as a lower bound. For example, for the Hamamatsu R7081-2 PMT $R_0 = 126.5$ mm, the sensitive radius is given as a minimal 110 mm (which would correspond to $\sim 0.87 \cdot R_0$). All measured PMTs, except the Gen1-DOM PMT, were sensitive over the entire frontal area given by R_0. As only one 10" PMT could be measured, it is unknown whether this is a feature across all PMTs or only the measured PMT.

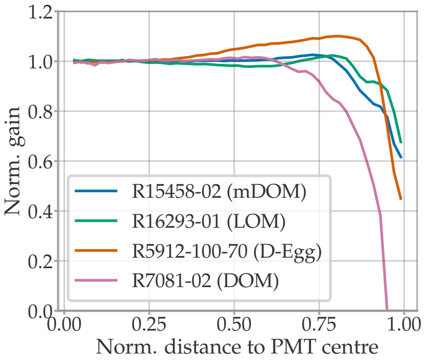

Figure 7.44: Local gains were binned along the radial axis. This figure shows the average gain at each bin. The radial axis was normalised to the maximal radius of the PMT R_0 and the gain to the mean value of the central region ($r < 0.4 \cdot R_0$).

Furthermore, in Figure 7.44, the mDOM and LOM PMTs have a more homogeneous response than the larger PMTs of the D-Egg and Gen1-DOM. The same conclusion is drawn by calculating σ_A, as shown in Figure 7.45. The standard deviation of all local gains 19.3 % and 17.9 % for the R7081-2 and R5912-100-20 PMTs, respectively, while the R1693-01 PMT shows the best performance in this regard, with only 7.9 %.

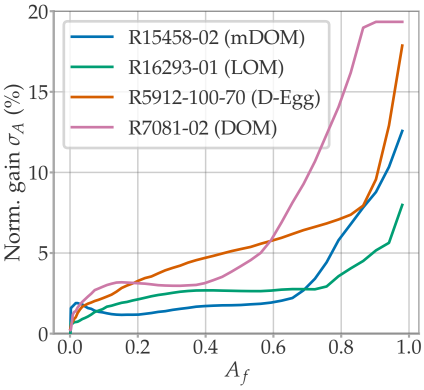

Figure 7.45: Normalised σ_A of the local gains in dependence of the fraction of area A_f to which the points used correspond. Normalised to the average gain of the central region $r < 0.4 \cdot R_0$ (see text).

Figure 7.46 depicts the relative transit time maps of the three PMT types. Similarly to the mDOM PMT, the response for the transit time is homogeneous at the central region of the PMTs but worsens towards the edges. In these cases, there is also an asymmetry with respect to the x-axis due to the orientation of the first and second dynodes. The data are shown again in Figure 7.47 against the distance to the PMT centre. Taking into account the peak-to-peak values, the worst performance is shown by the R16293-01 PMT with 11.5 ns, followed by the mDOM and DOM PMTs with 9.2 ns and 8.3 ns, respectively, while the D-Egg PMT shows the smallest deviation with only 6.2 ns peak-to-peak.

The uniformities look rather universal throughout all PMT types, and any potential systematics caused by them are already present in the current IceCube detector. Nevertheless, the shorter distances between modules in the dense instrumentation of IceCube Upgrade may make these systematics more important, as timing deviations impact the reconstruction accuracy. The impact of these inhomogeneities on low-energy reconstruction should therefore be further investigated.

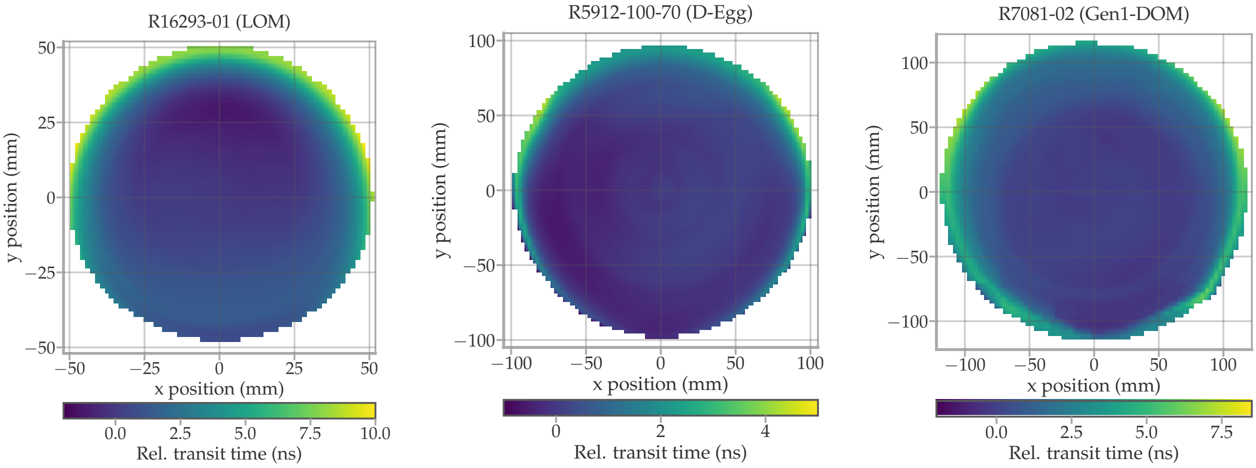

Figure 7.46: Photocathode scan of the transit time, relative to the average transit time of the PMT centre ($r < 0.4 \cdot R_0$), for the three larger Hamamatsu PMT types used in the LOM (*left*), D-Egg (*centre*) and Gen1-DOM (*right*).

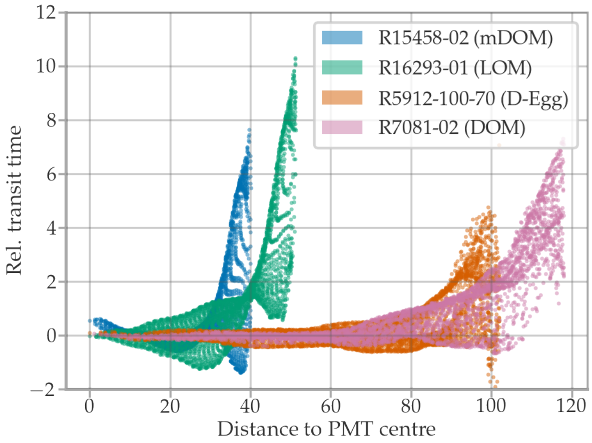

Figure 7.47: Relative transit time data against the distance to the PMT centre for the four measured types of Hamamatsu PMTs.

8

Photomultiplier background

Since the glacial ice at the South Pole has no bioluminescence or radioactivity of significant level, the modules are the main optical background source. A low background is crucial not only for recording 'cleaner' neutrino events, but also to not saturate the bandwidth of the cables that connect the modules to the surface, which is limited to ~0.5 Mbps per module.

Initial studies showed that the PMT background was expected to be negligible compared to the noise introduced by other mDOM components. However, it was later observed that the last ~90 % of produced mDOM PMTs were affected by a very high background. The dark rate of the mDOM PMTs of early and late production is characterised in Section 8.1.

The signal-induced background (see Section 5.4.2) is low in terms of rate, but knowledge of it is important since it can produce a correlated signal within a neutrino event. These correlated pulses are described in Section 8.2.

Other components of the mDOM are also critical sources of background, such as photons produced by radioactive decays in the pressure vessel. These components are introduced later in Chapter 11, dealing with the background of the assembled module.

8.1 Dark rate

In this section, the dark rate of the mDOM PMT is characterised. The measurement method used is introduced in Section 8.1.1, although the specific setup of a study is explained in their corresponding section. In Section 8.1.2 and Section 8.1.3, the intrinsic dark rate and its time and charge distribution are described for PMTs from early and late production, respectively.

8.1.1 Measurement method

The PMTs must be thoroughly shielded from all external light to prevent overestimation of the background. Moreover, the measured rate has to be monitored, discarding the initial portion of the data if the PMT was found to be excited because light exposure during handling or storage of the PMT can temporarily increase the dark rate. This could mean a day of discarded data if the PMT was not handled with care. However, only a few hours are generally necessary if the laboratory is kept at low light.

Furthermore, the measurements must be performed at low temperatures since the dark rate is strongly temperature dependent due to the thermionic emission (see Section 5.4). Therefore, the measurements were performed inside a dark box in a climate chamber [1].

In the following studies, two different measurement methods were used. The quickest and easiest method is to count the triggered waveforms per unit of time. For the oscilloscope *Picoscope 6404C*, this is done by setting the readout in *rapid block mode*. Here, a block of N ($N \geq 2$) triggered waveforms is measured before transferring the data to the PC. The time t required to trigger the whole block is measured by the PC with the *time* Python package, and the rate can be calculated with N/t. This counting method has a dead time on the order of 1 µs, caused by the re-arming of the trigger [152, pp. 71–72].

Moreover, since no data from the PMT pulses are extracted, this method cannot provide information such as the time distribution of the background or its charge. A similar approach can be taken with the *Lecroy Waverunner 8404M-MS* oscilloscope, which provides a *hold-off* trigger function and a time measurement between triggers integrated into the oscilloscope. With the hold-off feature, the oscilloscope does not read a waveform until N trigger conditions are met. Since the oscilloscope directly measures the time and only one waveform is read every N triggers, the dead time is on the order of a few nanoseconds. Nevertheless, in this case, one is also blind to the time or charge distributions of the measured background.

A second method is used in this work in case a more detailed characterisation of the dark rate is needed. Here, the oscilloscope is randomly triggered and a long waveform is measured (from 1 ms to 10 ms). The waveform is processed on the PC with the *scipy.signal.find_peaks* Python package [128] following the MPA method described in Section 6.1.2. In this way, the charge, arrival time, and amplitude of every pulse inside the waveform are saved. The rate is the mean number of pulses inside a waveform over the length of the waveform. This method provides all the extractable background information, and the dead time is as small as the length of a single PMT pulse. Nevertheless, it requires a much longer measurement time for the same statistics compared to the first method.

Regardless of the method, an amplitude trigger level must be defined. As most of the dark rate pulses have a charge in the order of SPE, the amplitude threshold translates to a cut on the charge of the pulse, which can skew the obtained dark rate value if the trigger level is set too high. Since different PMT types produce various pulse shapes and amplitudes, the dark rate values are specified with a trigger level in PE instead of volt. Currently, there is no convention on how the trigger level is translated into PE. In the author's experience, most of the time the calculation is made using the mean amplitude of SPEs $\hat{A}$: If $\hat{A} = 10\,\mathrm{mV}$ and the trigger level is set at 2 mV, this results in a threshold of $2\,\mathrm{mV}/10\,\mathrm{mV} = 0.2\,\mathrm{PE}$. This is a very simple idea, but prone to misunderstandings, as the charge and amplitude distributions are asymmetric and difficult to measure without the influence of the pedestal in the low charge region, which makes the definition of the mean amplitude $\hat{A}$ rather ambiguous.

[1] CTS C-70/350.

[152]: Unland Elorrieta (2017), *Studies on dark rates induced by radioactive decays of the multi-PMT digital optical module for future IceCube extensions*

[128]: Virtanen et al. (2020), *SciPy 1.0: Fundamental Algorithms for Scientific Computing in Python*

For the results shown in this work, the PE threshold was calculated with a calibration which is compatible with the conventional definition mentioned above. The charge and amplitude of several pulses in the SPE region are measured and saved, which are then treated as follows:

- The pulses are sorted by their amplitude.
- The charge is translated into PE by dividing it by the gain (with the gain expressed in Coulomb).
- The mean charge C_A of pulses within the amplitude interval $[A - s/2, A + s/2]$ is calculated, where s is a step defined according to the amount of data and the dynamic range of the oscilloscope. For the calibration shown in this section, $s = 0.3\,\mathrm{mV}$ was used.
- The relationship between C_A and A is fitted with a linear function. The trigger in PE is extrapolated using this fit function.

Figure 8.1 shows an example of such a calibration. This can be performed with an external trigger and illumination, as in a gain calibration, or with the data of the dark rate measurement itself, if the MPA method is used. In both cases, care has to be taken not to include data in the low-charge region, to avoid the baseline noise.

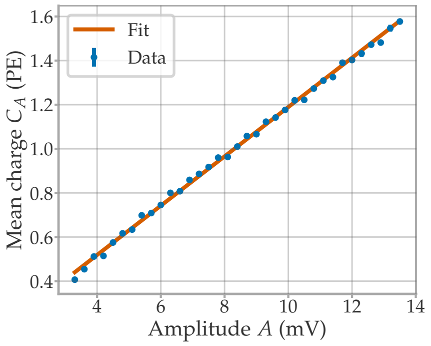

Figure 8.1: Example of a calibration to translate the amplitude of PMT pulses to their charge.

8.1.2 R15458 serial number DM01130 and earlier

To show the general temperature dependence of the dark rate, two PMTs (BA0373 and BA0375) were measured with the rapid method in the temperature range of −45 °C to 20 °C in 5 °C steps. The gain of these two PMTs was calibrated at these temperatures (see Section 6.2.2), so the voltage was adjusted as a function of temperature to keep the PMTs at nominal gain. The climate chamber was kept for 2 h hours at each temperature step and the dark rate was constantly measured. The average dark rate of the last hour[2] of each temperature is shown in Figure 8.2.

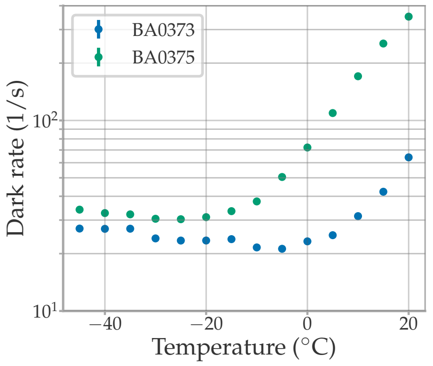

Figure 8.2: Dark rate of two PMTs as a function of temperature. Error bars smaller than markers.

As introduced in Section 5.4, the background is dominated by the thermionic emission at room temperature. Here, the rate is quite different for both PMTs, with $64\,\mathrm{s}^{-1}$ for BA0373 and $351\,\mathrm{s}^{-1}$ for BA0375, respectively. This disparity decreases significantly towards lower temperatures, where the thermionic emission loses dominance. The field emission and photons produced by radioactive decays inside the PMT glass are the most significant sources at cold temperatures. The average rate between −45 °C and −15 °C is $(24.7 \pm 0.7)\,\mathrm{s}^{-1}$ and $(32.0 \pm 0.6)\,\mathrm{s}^{-1}$ for PMT BA0373 and BA0375, respectively. In this temperature region, the dark rate decreases linearly, with the temperature having an average slope of $-0.20\,\mathrm{s}^{-1}/°\mathrm{C}$.

To collect more statistics, another 13 mDOM PMTs were measured in a smaller temperature range of −20 °C to 20 °C in 5 °C steps. In the physical region of IceCube Upgrade, the modules are at temperatures from −26.5 °C to − 18 °C [153] and the characterisation at very low temperatures is thus not necessary. The dark rate was calculated using the method with long waveforms described in Section 8.1.1. The trigger level for pulse extraction was set to 1.25 mV for all temperatures. The PMTs were driven at the nominal voltage measured at room temperature.

[2] It takes around one hour for the PMT to reach the set temperature.

[153]: IceCube Collaboration (2020), *South Pole Ice Temperature*

Since the amplitude, arrival time, and charge of all dark rate pulses were saved, it is possible to characterise the background beyond only the rate. In Figure 8.3, the charge spectrum of the dark rate at room temperature and −20 °C is presented. Most of the pulses are in the SPE region, although a tail at higher charges can be observed. These are probably contributions from afterpulsing and atmospheric muons, which are expected to produce MPE pulses (see Section 5.4).

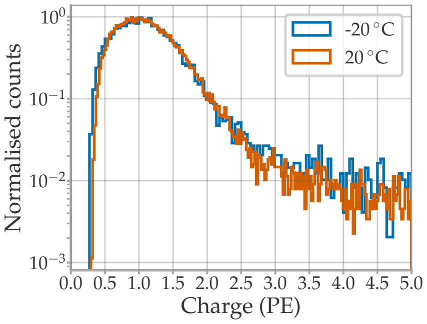

Figure 8.3: Combined dark rate charge spectrum of all measured PMTs at room temperature and −20 °C.

As was shown in Section 6.2.2, the gain increases at lower temperatures. Consequently, the threshold in PE varies at each temperature step since the high voltage applied to the PMT and the trigger level were left constant during the whole measurement. The mean effective threshold level in PE calculated was (0.270 ± 0.012) PE at −20 °C and (0.305 ± 0.010) PE at 20 °C. As expected, the threshold decreases with temperature as the pulses are slightly more prominent due to the gain increase. This can also be noticed at the lower charges in Figure 8.3, with the measurement at −20 °C reaching slightly further to the left.

Figure 8.4 shows the complementary cumulative distribution (CCDF)[3] of the data at −20 °C in the low charge region to quantify how much the trigger difference affects the calculated rates. A trigger at (0.270 ± 0.012) PE is expected to measure only ∼0.06 % higher rates than at (0.305 ± 0.010) PE; thus, these trigger differences are negligible and should not introduce any artificial temperature dependence in the calculated rates.

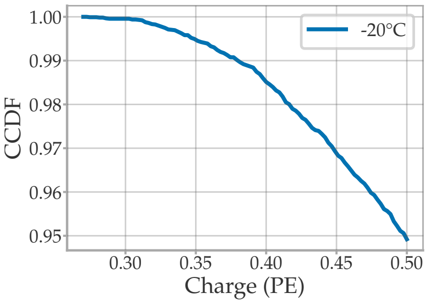

Figure 8.4: Complementary cumulative distribution of the dark rate charge spectrum at −20 °C (see Figure 8.3).

Figure 8.5 shows the mean dark rate of all measured PMTs with respect to temperature. In addition, the 68 % interval calculated from the results of all PMTs is shown as a shaded region. The variance of the dark rate of different PMTs increases with temperature, but at the temperatures relevant for IceCube, the results are very similar between PMTs. At −20 °C the mean is $(35.2 \pm 1.5)\,\mathrm{s}^{-1}$ with the 68 % region in $[29.9\,\mathrm{s}^{-1}, 41.7\,\mathrm{s}^{-1}]$.

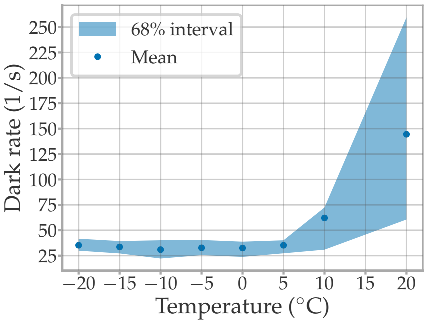

Figure 8.5: Mean dark rate of 15 mDOM PMTs and the 68% interval.

The time difference between subsequent dark rate pulses Δt was calculated and represented as a histogram. The left side of Figure 8.6 shows the case for the data taken at room temperature on a logarithmic scale. In the right part of the distribution from $\Delta t \approx 100\,\mu\mathrm{s}$ to $\Delta t \approx 100\,\mathrm{ms}$, there is a Gaussian-like region. This is produced by background sources that are random in nature, such as the thermionic emission.

A random background of mean rate μ (pulses per second) is a Poissonian process since the probability of a noise event is time independent. Let D be the time interval between consecutive pulses. The probability that D is larger than a given time Δt is

$$P(D > \Delta t) = \frac{(\mu \cdot \Delta t)^0 e^{(-\mu \cdot \Delta t)}}{0!} = \exp(-\mu \cdot \Delta t). \tag{8.1}$$

The cumulative density function (CDF) $F(t)$ of this process is given by

$$F(\Delta t) = P(D \leq \Delta t) = 1 - \exp(-\mu \cdot \Delta t). \tag{8.2}$$

With the CDF the probability density function (pdf) $f(\Delta t)$ can be obtained by its derivative, which in this case is just an exponential decay. As the

[3] This is $1 - F(x)$, where $F(x)$ is the cumulative distribution.

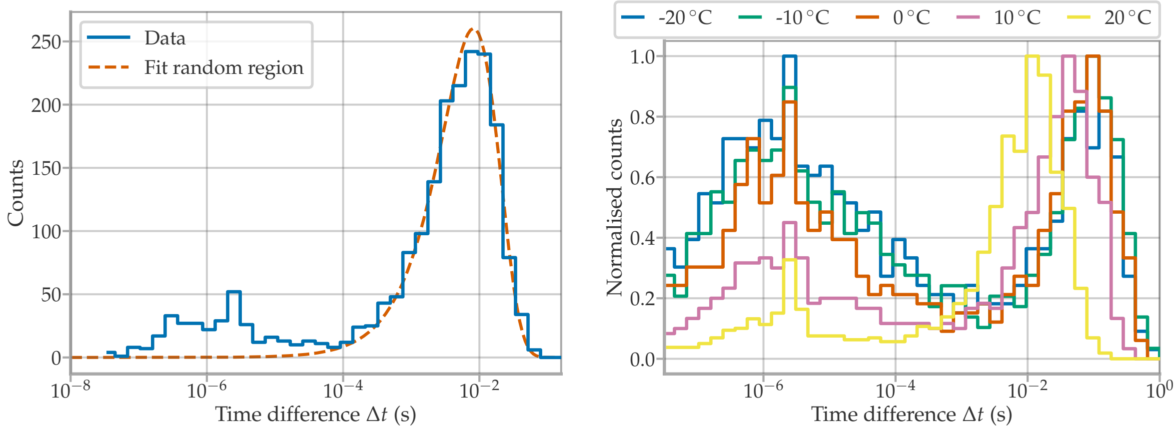

Figure 8.6: Time difference between subsequent background pulses Δt spanning from ~100 ns to ~100 ms. *Left:* for an mDOM PMT at room temperature. The peak produced by random pulses was fitted with Equation 8.3. *Right:* average Δt histogram from 13 PMTs at different temperatures.

results are represented on logarithmic scale, the substitution $\Delta t = 10^x$ is applied, from which follows

$$\begin{aligned} f(x) &= \frac{d}{dx}[1-\exp(-\mu\cdot 10^x)] \\ &= \mu\cdot 10^x\cdot\log(10)\cdot\exp(-\mu\cdot 10^x). \end{aligned} \tag{8.3}$$

The random contribution of the Δt-histograms was fitted with Equation 8.3, from which the random rate μ_R is extracted. The correlated background appears at shorter time differences, and its contribution to the rate μ_C is determined by subtracting the random μ_R from the total rate μ_T. This was carried out with all PMTs at all temperature stages and for the example shown on the left side of Figure 8.6, this resulted in $\mu_R = (122 \pm 3)\,\mathrm{s}^{-1}$ and $\mu_C = (173 \pm 7)\,\mathrm{s}^{-1} - \mu_R = (51 \pm 8)\,\mathrm{s}^{-1}$.

Figure 8.7 shows the mean dark rate between all PMTs separated by their correlated and random components. The random component of the rate increases with temperature due to the thermionic effect. The correlated fraction decreases linearly with rising temperature, as was also observed in Figure 8.2. Below 0 °C, the correlated background dominates, as also reflected in the Δt histograms shown on the right side of Figure 8.6. For lower temperatures, the peak caused by random pulses becomes less prominent and appears further to the right, meaning that random pulses are further apart in time. The correlated distribution, on the other hand, is broader at lower temperatures, with Δt spanning from milliseconds to hundred of nanoseconds, peaking at the order of microseconds. The peak at a Δt of ~2.5 µs appears at all temperatures as is caused by afterpulses type II (see Section 8.2.3).

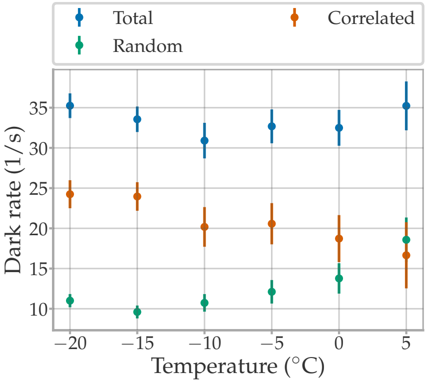

Figure 8.7: Dark rate against temperature separated in its random and correlated contributions. The results are averages calculated from 13 PMTs.

The correlated rate is produced by *bursts* of pulses that arrive close to each other temporally. By this definition, a burst must be at least 2 pulses in size. For the following calculations, all pulses arriving with a Δt < 1 ms after the previous pulse are defined to be temporally correlated inside one burst event. This single burst stops growing in size once a subsequent pulse with Δt > 1 ms is measured. The cutoff at 1 ms was

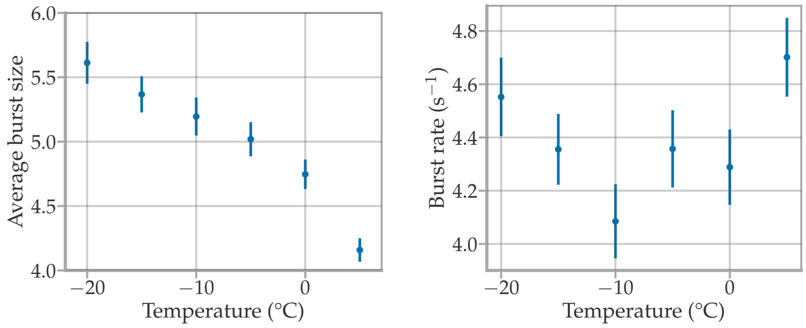

Figure 8.8: *Left:* Mean size of burst of correlated background pulses as a function of temperature. *Right:* Rate of burst events as a function of temperature.

chosen to include as many correlated photons as possible, considering the Δt histograms shown on the right side of Figure 8.6. The random Poissonian peak dominates this region at higher temperatures, so only the data taken at ≤ 5 °C is considered next.

Figure 8.9 presents the burst size distribution of all PMTs at −20 °C and 5 °C. The most probable burst size is 2, but the distribution is broad even with bursts containing more than 20 photons. It can also be noticed that at −20 °C larger burst sizes are more common. This trend is true for the entire measured temperature range, as displayed on the left side of Figure 8.8, where the average burst size is presented against the temperature.

Figure 8.10 shows the time difference between subsequent bursts $\Delta\tau$ for the data at −20 °C. The distribution follows a Poissonian random distribution fitting well with Equation 8.3. From the fit, the rate of burst events per second is obtained, which is shown on the right side of Figure 8.8 for all temperatures. Taking into account the uncertainties, the burst rate does not show any significant temperature dependence, with an average of $(4.39 \pm 0.06)\,s^{-1}$.

Similar results have previously been reported for different types of PMTs in [154], with the same treatment of cluster sizes and rates, and in [2] for the IceCube DOM PMTs. However, the physical mechanism that produces the bursts of correlated pulses is not well discussed in the literature, with [154] pointing towards some trap mechanism in the photocathode.

Notwithstanding, the observed results are consistent with an optical background from radioactive decays. Scintillation and Cherenkov photons are produced after isotopes –from natural decay chains and ^{40}K– decay inside the PMT glass. On the one hand, the scintillation yield (number of photons emitted per deposited energy) of borosilicate glass decreases with temperature [152]. This agrees with the mean burst size behaviour shown on the left side of Figure 8.8. The rate of burst events should be directly proportional to the decay rate of the isotopes, which is temperature independent, which explains the results shown on the right side of Figure 8.8. Scintillation and its temperature dependence are explained in more detail in Section 11.2, which is dedicated to the background generated by radioactive decays in the glass of the mDOM pressure vessel and PMTs.

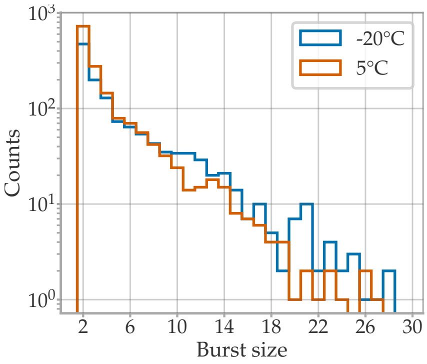

Figure 8.9: Burst size distribution for the data taken at 5 °C and −20 °C.

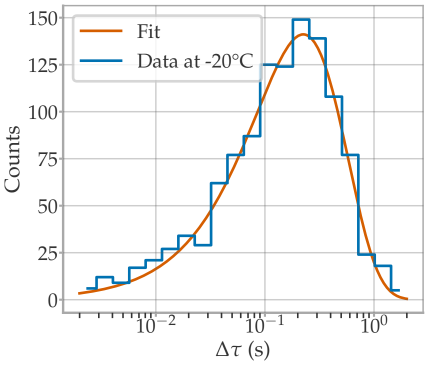

Figure 8.10: Time difference between subsequent bursts for the data taken at −20 °C.

[154]: Meyer (2010), *Spontaneous electron emission from a cold surface*

[2]: Aartsen et al. (2017), *The IceCube Neutrino Observatory: Instrumentation and Online Systems*

[152]: Unland Elorrieta (2017), *Studies on dark rates induced by radioactive decays of the multi-PMT digital optical module for future IceCube extensions*

8.1.3 R15458 serial numbers after DM01130

During the acceptance tests of the mDOM PMTs in Aachen and Dortmund, it was found that the dark rate of PMTs of a serial number higher than DM01130 was noticeably higher than expected and did not meet the requirements set between the collaboration and the manufacturer.

Two PMTs[4] were measured with the setup in Münster. The measurements were performed with the long-waveform method, and the PMTs were driven at the nominal voltage that was determined at room temperature. Therefore, also here, the effective threshold levels vary slightly at each temperature step but are in the same level as in the last section.

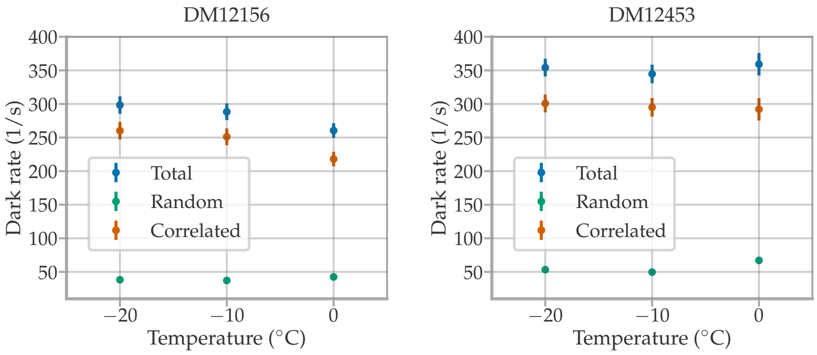

Figure 8.11: The dark rate against temperature separated in the random and correlated components for the PMTs DM12156 and DM12453.

Data analysis was carried out following the same scheme as in Section 8.1.2. Figure 8.11 shows the calculated total rate with its correlated and random contributions of both PMTs. The rate is more than six times that expected in Section 8.1.2 and the majority is caused by correlated pulses. The temperature behaviour of the correlated and random components are qualitatively compatible with the results of the last section.

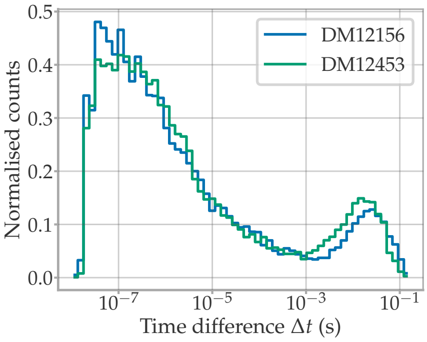

Figure 8.12: Time difference between subsequent background pulses for the data taken at −20 °C.

The significant correlated component can be clearly seen in the Δt distributions presented in Figure 8.12. Although the correlated distribution peaked at $\sim$1 µs for PMTs with an early serial number, in this case, it does at $\sim$100 ns. This has as a consequence that a significant portion of the distribution could be missing at the smaller Δt due to the dead time of the measurement of $\approx$ 20 ns.

The dead time is given by the length of the integration gate of the pulses. Pulses that arrive within this time window are integrated together and populate the MPE region of the charge histogram. Figure 8.13 shows the charge distribution of the two new PMTs compared to the mean distribution of the early PMTs at −20 °C. The three spectra are compatible until around 4 PE; hence, there does not seem to be a larger amount of pulses that coincide inside the dead time with the new PMTs. After 4 PE, the low-rate PMTs show a higher MPE probability relative to the SPE peak. These MPE pulses are probably caused by atmospheric muons crossing the photocathode. The muon rate should be similar between all measurements, and thus their relative contribution to the spectra is larger when the intrinsic PMT background is low.

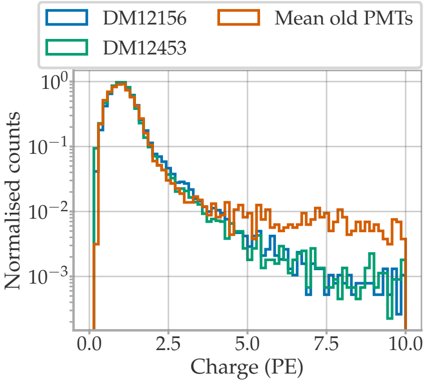

Figure 8.13: Charge spectrum of the background of the PMTs DM12156 and DM12453, and the average distribution of the early production PMTs.

Following the same procedure as in Section 8.1.2, the burst size and rate were calculated from the correlated pulses. As the left-hand side of

[4] Serial numbers DM12156 and DM12453

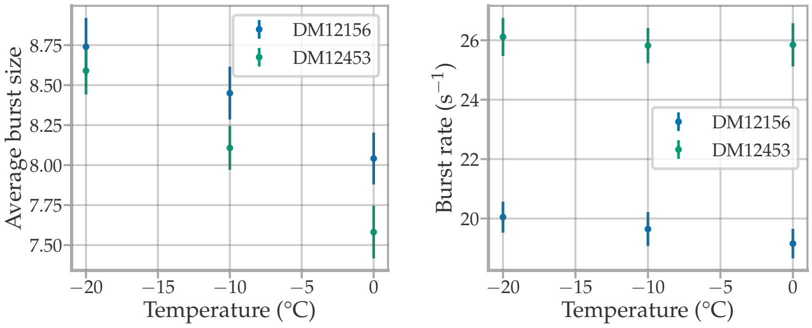

Figure 8.14: *Left:* Mean size of burst of correlated background pulses against the temperature of the PMTs DM12156 and DM12453. *Right:* Rate of burst events as a function of temperature.

Figure 8.14 reveals, the average burst size is approximately 56 % larger with high background PMTs compared to the ones of earlier serial numbers. However, the most significant change is in the burst rate, which with an average of (22.77 ± 0.24) s^{-1} is approximately four times the rate of early PMTs.

Following the hypothesis for the source of correlated background of last section, the most natural conclusion is that the PMTs of serial numbers after DM01130 had increased amounts of isotope contamination in the bulb glass, causing the rise of the burst rate and thus of the correlated noise. After internal communications between IceCube members and the manufacturer, this hypothesis was confirmed. The reason for this increase in contamination and additional details, such as the isotope concentrations in the glass, were provided to the IceCube Collaboration. However, the manufacturer asked that this information be kept confidential and it will not be discussed further in this work.

As most of the rate is caused by real photons produced inside the glass of the PMT, the dark rate should be lower once the PMT is installed inside the mDOM. The fraction of photons that travel inside the glass tube through total reflection greatly diminishes when the outer boundary is optically coupled with gel, which has a refraction index similar to that of glass.

A known method to estimate the drop in rate expected from the optical coupling is to cover the exterior of the PMT with black tape. This was done with both PMTs, taking care to remove any air bubbles between the tape and the PMT glass. Then, the measurement was repeated at the same temperatures and nominal voltage. The calculated dark rates are shown in Figure 8.15. On average, the taped PMT rate is 1.70 ± 0.08 lower than the untaped case. From the PMT acceptance tests in Aachen and Dortmund, the average dark rate at −20 °C of PMTs with serial number after DM01130 is 369 s^{-1} with a standard deviation of 71 s^{-1} [155]. This would imply an average of 217 s^{-1} once the PMTs are installed in the mDOMs, without considering additional background components.

The first estimate of the total dark rate for a deployed mDOM was calculated with Geant4 simulations to be approximately 350 s^{-1} per PMT [152]. In these calculations, the intrinsic background of the PMT was neglected. Thus, the new PMTs with higher contamination are now a significant source of the total dark rate. Chapter 11 goes deeper into the

[152]: Unland Elorrieta (2017), *Studies on dark rates induced by radioactive decays of the multi-PMT digital optical module for future IceCube extensions*

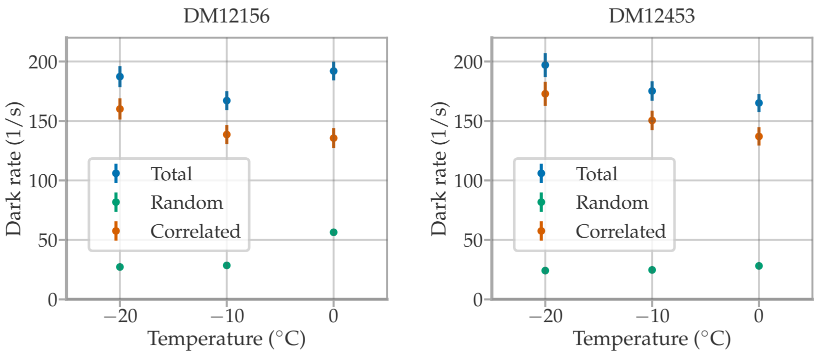

Figure 8.15: The dark rate against temperature separated in the random and correlated components for the PMTs DM12156 and DM12453 with the exterior surface covered with black tape.

mDOM background caused by radioactive decays and the inclusion of the noise of the new PMTs in the simulations.

8.2 SIGNAL-INDUCED BACKGROUND

Table 8.1: Probability of signal-induced background of the Hamamatsu PMT R12199-01 HA MOD and its predecessor R12199-02 measured at the respective gain G at room temperature. The numbers in brackets right to the values indicate the number of tested PMTs. Data from [125, 126, 156].

	R12199-02 ($G = 3 \times 10^6$)		R12199-02 ($G = 5 \times 10^6$)		R12199-01 HA MOD ($G = 5 \times 10^6$)	
Pre-pulses	0.2%	[6960]	0.16%	[20]	0.26%	[102]
Delayed pulses	3.2%	[6960]	3%	[179]	2.46%	[102]
Afterpulses Type I			6.3% †	[38]	1.3%	[2]
Afterpulses Type II	7.1%	[6960]			3.1%	[12]

†: Probability of afterpulses type I and II together.

The different types of signal-induced background were presented in Section 5.4.2. Prepulses of the mDOM PMT are discussed in Section 8.2.1, delayed pulses and afterpulsing type I in Section 8.2.2 and afterpulsing type II in Section 8.2.3. Finally, Section 8.2.4 examines a rare kind of afterpulsing that arrives late and is not well researched in the literature.

IceTray [157] supplies the framework for the simulation and reconstruction of neutrino events of the IceCube detector. This software manages information (in the so-called *I3Frames*) between different modules (the *I3Modules*). One of the modules is in charge of simulating the PMT response and needs various parameters to describe their behaviour. In the following sections, the parameterisation of the signal-induced background for the IceCube software is also included.

Several studies have characterised the afterpulses of the PMT model family R12199 from Hamamatsu. Table 8.1 summarises the results of [126] with the correlated background probability for the R12199-02 and R12199-01 HA MOD PMTs. The performance of both is comparable. In addition, in [126] it was shown that the temperature dependence of the signal-induced background is negligible. The behaviour of the successor model, the R15458 PMT used in the mDOM, is also similar, and measurements are to be published in [141].

[157]: DeYoung (2005), *IceTray: A software framework for IceCube*

[126]: Unland Elorrieta et al. (2019), *Characterisation of the Hamamatsu R12199-01 HA MOD photomultiplier tube for low temperature applications*

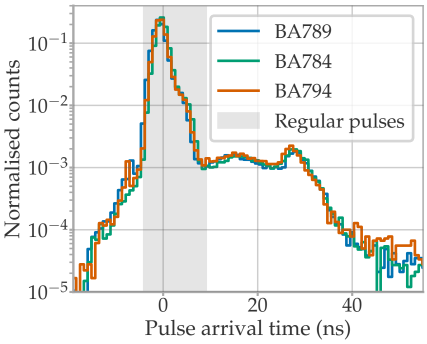

Figure 8.16: Arrival time distribution of pulses measured with a PMT triggered in coincidence with the LED driver. The time is relative to the mean arrival time of the regular pulses.

The general measurement procedure involves simultaneous external triggering with an LED and analysis of the PMT signal using the MPA method (see Section 6.1.2). The information (time, charge, and height) of all pulses that surpass a set threshold (typically corresponding to ~0.3 PE) is saved. As introduced in Section 6.3, the 'regular pulses' produce a Gaussian-like distribution. The mean time is determined by fitting a Gaussian to this distribution, and the detection time of all detected pulses is corrected by the mean. Figure 8.16 illustrates the histogram of arrival times after such a measurement on three mDOM PMTs. Here, it is possible to differentiate between the sources introduced in Chapter 5. For example, on the time scale displayed in Figure 8.16, if the pulse appears after a regular PMT pulse from the LED flash, then it is an afterpulsing type I (caused mainly by inelastic backscattering of the SPE on the first dynode). However, if the pulse appears without another pulse being measured at the expected arrival time, it is probably a delayed pulse (elastic scattering on the first dynode). Pulses arriving before the main peak are an indication of prepulses (photons releasing an electron at the first dynode). For all the distributions, there is also a small contribution from the random background of the dark rate. Afterpulsing type II (ions hitting the photocathode) is measured the same way, but reading longer waveforms of several microseconds.

Conventionally, the probability for a specific correlated background is calculated by integrating the arrival time histograms over a defined time window, obtaining the number of correlated pulses N_c. The latter is divided by the number of regular pulses N_{main} and then expressed as a percentage $N_c \cdot 100\%/N_{\text{main}}$.[5] The requirements for the mDOM PMTs were set such that

- **Prepulses** are defined to arrive between 20 ns and 10 ns before the regular signal, and their probability should be less than 1 % when measured with a 0.2 PE threshold.
- **Delayed pulses** should be less than 5 % in a time window of 15 ns to 80 ns after the mean time of the regular pulses.
- **Type II afterpulses** are measured between 100 ns and 12 µs after regular pulses, and PMTs are required to produce them with a probability of less than 15 %.

These probabilities are measured on all PMTs by Hamamatsu at room temperature before delivery. The PMTs are measured again at IceCube's testing facilities in Aachen and Dortmund at −20 °C, following a scheme similar to that described above.

In the case of afterpulses type II, the probability is also sometimes measured following another definition. In this case, instead of a ratio between the *number* of pulses, the ratio between the *charge* transferred by the afterpulses and the charge of the regular pulses is used [129, p. 4-41]. The parameterisation in IceTray is derived from this latter definition and is described in Section 8.2.3.

[5] If the dark rate is high, also a background correction has to be made to both numbers.

[129]: Flyckt et al. (2002), *Photomultiplier tubes - principicles and applications*

8.2.1 Prepulses

As introduced in Section 5.4.2, prepulses are caused by photons releasing an electron on the first dynode. These are detected earlier than a regular pulse since the transit time between the photocathode and the first dynode is missing. Furthermore, their charge is a factor δ_1 smaller than usual, where δ_1 is the mean gain of the first dynode.

PMTs that aim for single-photon resolution, as used in photon counting experiments, have a δ_1 of at least 12 [129, p. 2-9], which translates into an upper limit on the mean prepulses charge for these PMTs of ~0.08 PE. Therefore, the prepulse probability calculated from a measurement with a charge threshold of 0.2 PE is very small, as most prepulses are either buried in the baseline noise or do not meet the trigger condition.

[129]: Flyckt et al. (2002), *Photomultiplier tubes - principicles and applications*

Nevertheless, a trigger-free prepulse probability is needed to model the PMT behaviour correctly. This is important for very bright events, where the sum of several prepulses can produce a pulse with a charge in the SPE region.

In IceTray, prepulses are parameterised by four variables[6]: their probability, the average arrival time relative to a regular pulse, a scaling factor for the charge, and the high voltage of the measured PMT. The charge is sampled from the charge template of a normal SPE and divided by the scaling factor. Data from a single PMT are used in the simulation. Therefore, the high voltage of the PMT is needed to adjust the arrival time of other PMTs that work at different voltages since a higher voltage will reduce the transit time of the electrons. The measurement of these four variables for the PMT mDOM is introduced in the following.

Mean arrival time of prepulses

To determine the prepulse arrival time, the same measurement technique was employed as with the DOM 10″ PMT. The PMT was illuminated with plane waves from the front with varying intensities. First, the arrival time of standard pulses relative to the trigger was found using a low light intensity. Next, a very high light intensity was used to distinguish the prepulses.

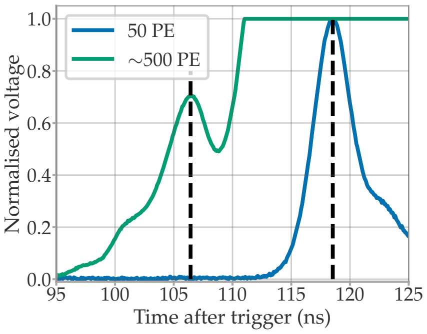

Figure 8.17: Mean PMT waveform for an LED pulse of 50 PE and 500 PE. The former is used to determine the average arrival time of the main pulses and the latter for the position of the prepulses.

This measurement was performed with an mDOM PMT of serial number BA0780 at its nominal voltage of 1118 V. For both light intensities, 10,000 waveforms were saved[7]. The average waveforms are shown in Figure 8.17. For the low-intensity case, a pulse equivalent to ~50 PE was measured, with its maximum at 118.5 ns. In the case of bright LED pulses, the regular pulses had an order of magnitude higher charge. As the DAQ was configured to measure low voltages, the waveform is saturated in the region of regular pulses. A distribution of the sum of several prepulses is observed with its maximum at 106.4 ns. The difference between these two maxima, −12.1 ns, is used as the mean prepulse arrival time. However, it should be noted that the prepulse distribution goes down to 95 ns, which means that prepulses down to −23.5 ns are possible.

[6] As of November 2022.

[7] With the oscilloscope Lecroy Waverunner 8404M-MS 40 GS/s.

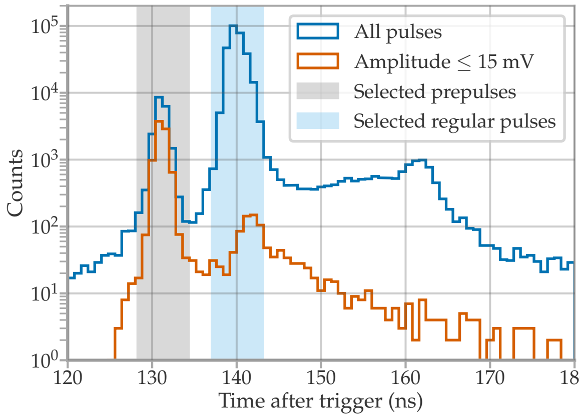

Figure 8.18: Arrival time of pulses in the measurement of the prepulse charge. The blue curve shows the time of all saved pulses, while the orange distribution shows the time of pulses of small amplitude (≤ 15 mV), revealing the prepulse peak. The shaded areas show the intervals for the selected prepulses and regular pulses used for further analysis.

Prepulse mean charge

The prepulse charge is difficult to separate from the pedestal in PMTs operating at nominal gain. However, this changes when a higher gain is used, as the charge output separates from the pedestal.[8] As mentioned above, determining the average prepulse charge involves finding out the gain of the first dynode δ_1, and vice versa. Following Equation 5.2, the gain of a single dynode follows a power law analogous to the total PMT gain. Therefore, a 'prepulse charge calibration' was performed at high voltages to extrapolate the behaviour of the PMT at nominal voltage.

Five PMTs were measured at voltages between 1600 V and 1800 V, where the gain of the PMTs can reach over 100e+6. In this measurement, collimated light was used,[9] pointing directly at the centre of the PMT and at the first dynode, so the probability of prepulses is maximised. The light intensity was set low to resolve the charge spectrum at an SPE level. Individual pulse information was stored in the LED-triggered waveforms,[10] including arrival time and charge.

The prepulses were selected from the data using the arrival time of the pulses. Figure 8.18 shows the arrival time distribution for the mDOM PMT BA0793 at 1795 V, where two prominent peaks can be identified. Since the prepulses arrive earlier, they should produce the peak on the left. This was confirmed by producing the arrival time distribution again, but only with low amplitude pulses ≤15 mV. The charge distributions of the regular pulses and prepulses were built by selecting the pulses of time ±3 ns around the maximum of their respective peak arrival time, represented by the shaded regions in Figure 8.18. An example of a regular pulse and prepulse charge distribution is illustrated in Figure 8.19.

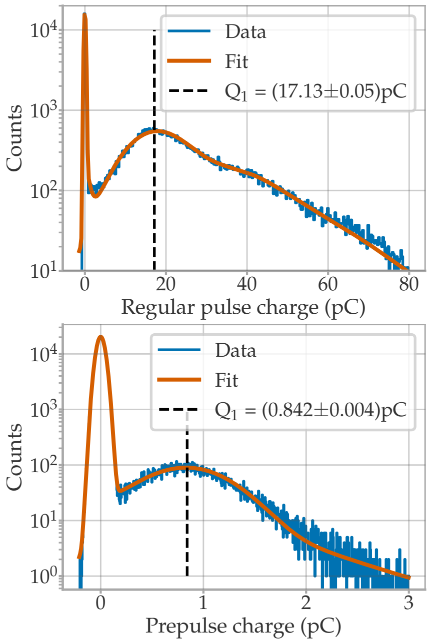

Figure 8.19: Charge spectrum of regular PMT pulses (*top*) and prepulses (*bottom*) for a PMT driven at a large gain ($\sim 10^8$). Data were fitted with Equation 5.6, and vertical lines indicate the best fit for the mean SPE charge.

The charge distributions were fitted with the model described in Equation 5.6. The gain of the first dynode was calculated with the ratio of the fitted positions of the SPE Gaussian peaks Q_1,

$$\delta_1 = \frac{Q_1^{\text{regular}}}{Q_1^{\text{prepulses}}}. \tag{8.4}$$

The ratios δ_1 versus all measured gains with the mDOM PMT BA0793 are shown in Figure 8.20. Since the PMT gain and δ_1 follow a power law

[8] The pedestal depends only on the intrinsic electronic noise of the DAQ baseline.

[9] PicoQuant PDL 800-B with LED head PLS-8-2-719 and 60FC-SMA-0-A7.5-01 lens collimator by Schäfter & Kirchhoff.

[10] Oscilloscope used: Picoscope 6404C.

function with the voltage (see Equation 5.2 and Equation 5.4), δ_1 can be expressed as a function of the gain G itself,

$$\delta_1 = \alpha \cdot G^{\beta}. \qquad (8.5)$$

The points were fitted with Equation 8.5, from which the δ_1 at gains close to the nominal gain (5×10^6) were extrapolated. Figure 8.21 shows the extrapolated δ_1 for gains from 4×10^6 to 6×10^6 for all measured PMTs. The results agree with each other considering the 1σ uncertainty regions, except for PMT BA0784, which may hint at PMT-to-PMT variations.

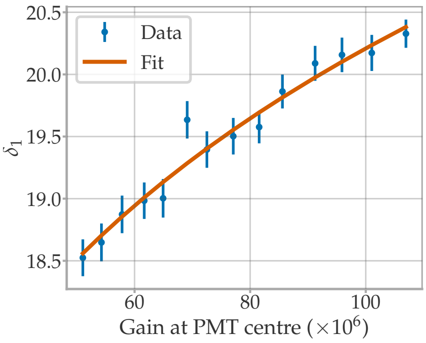

Figure 8.20: Calculated ratios δ_1 with Equation 8.4 as a function of the gain. The line marks the fit with a power law (Equation 8.5).

As in this measurement the ‘reference’ is the gain at the centre of the PMT, it may not be straightforward which gain to use as nominal, since the PMTs are calibrated with full illumination of the photocathode. Nevertheless, the mean curve in Figure 8.21 features a relatively small slope, with $\delta_1 = (13.85 \pm 0.29)$ and (14.15 ± 0.21) at gain 4.5×10^6 and 5.5×10^6, respectively. Following the results of Section 7.3.1, one might expect a gain of $\sim 5.3 \times 10^6$ at the centre in a PMT calibrated with frontal plane waves. For this case, the expected ratio is (14.09 ± 0.23). Since the ratio of the local gain at the centre of the PMT to the ‘global’ gain depends on the calibration method, the in-ice calibration will likely result in a different central gain. However, since this systematic yields only a small difference in δ_1, the nominal value at 5×10^6, $\delta_1 = (14.00 \pm 0.25)$, was taken as the reference for IceTray.

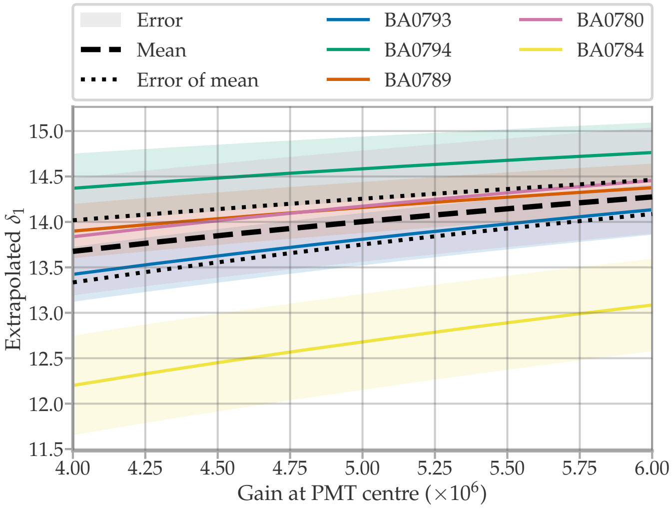

Figure 8.21: δ_1 at gains close to the nominal extrapolated from the fit of the data with Equation 8.5. Each colour represents the results of one PMT, with the shaded region marking the 1σ-interval. The black dashed line represents the mean between all PMTs, and the dotted line represents its 1σ-interval.

Threshold-free prepulse probability

The same measurement setup was used to determine the trigger-free prepulse probability. In this case, one is interested in the probability of producing a prepulse when measuring a certain frontal light flux. Thus, the LED was not collimated and ensured that the light pulse illuminated most of the photocathode area without overpassing its edges. The LED was driven at a repetition rate $f = 100\,\text{kHz}$ and set to a high intensity so that the prepulses formed a distinguishable amplitude in the oscilloscope.

For the calculation of the probability, the absolute light intensity is needed. This was measured with a calibrated photodiode[11] before and after the measurement of each PMT. At least 10k photons per LED flash are needed to obtain a measurable photocurrent (order of 0.1-1 nA). Therefore, during the measurement with the PMTs, an ND filter of known light transmission T was placed in front of the LED. The average number of photons per LED flash illuminating the PMTs was calculated as $N_p = \Phi \cdot T/f$, where Φ is the flux measured by the photodiode (see Equation 6.16.).

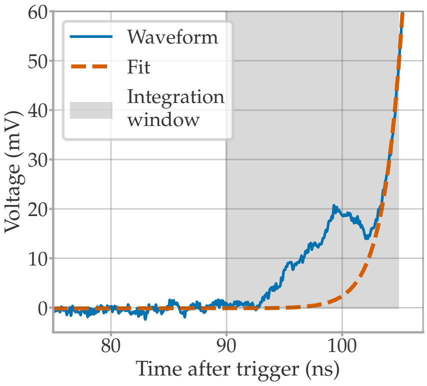

Figure 8.22: The waveform of a single LED flash zoomed in the prepulse region. The DAQ is saturated in the region of regular pulses. A fit is performed to estimate the charge of the background and prepulse peak.

The waveforms of 15,000 LED pulses were measured for three different PMTs. The PMTs were driven at their nominal voltage. Each waveform was analysed separately, where the main pulse and the baseline of the waveform were fitted with an exponential and a constant, respectively. The charge of the prepulse contribution Q_{pre} was calculated by integrating the waveform and subtracting the integral of the fitted portion. The fit of one of the waveforms is presented in Figure 8.22. With the average charge $\overline{Q}_{\mathrm{pre}}$, the mean number of prepulses $\overline{N}_{\mathrm{pre}}$ in a waveform is calculated with

$$\overline{N}_{\mathrm{pre}} = \frac{\overline{Q}_{\mathrm{pre}}}{q_{\mathrm{pre}}} = \frac{\overline{Q}_{\mathrm{pre}}}{5 \times 10^{6} \cdot e/\delta_1}, \tag{8.6}$$

where $q_{\mathrm{pre}} = 5 \times 10^{6} \cdot e/\delta_1$ is the average charge of a single prepulse and e is the elementary charge. The number of regular pulses per LED flash N_r cannot be estimated by integrating the waveform, as it is saturated. This number was estimated as $N_r = N_p \cdot \epsilon$, where ϵ is the QE of the PMT for the LED spectrum (obtained in the measurements of Section 7.2). The probability of prepulse relative to the number of regular pulses is $P = \overline{N}_{\mathrm{pre}}/N_r$. The measured values and calculated P for each PMT are listed in Table 8.2.

The mean threshold-free prepulsing probability is (5.77 ± 0.20) %.[12] The values have a possible systematic error of ~10 % because the QE of the PMTs was used instead of their (unknown) detection efficiency.

Table 8.2: Values obtained from the measurement of three mDOM PMTs for the estimation of the threshold-free prepulse probability P. The QE of the PMTs ϵ is given in percentage and was obtained from the measurements introduced in Section 7.2.

	$\overline{N}_{\mathrm{pre}}$	N_p ($\times 10^3$)	ϵ (%)	P (%)
BA0784	53.3(10)	4.44(25)	23.06(2)	5.2(3)
BA0789	63.1(11)	4.46(25)	22.28(3)	6.3(4)
BA0794	59.2(11)	4.28(24)	24.03(2)	5.76(34)

8.2.2 LATE PULSES AND AFTERPULSING TYPE I

This section investigates and explains in more detail the features observed in an arrival time distribution measurement, such as in Figure 8.16. The PMT was illuminated with a plane wave from an LED[13] with an intensity producing a waveform occupancy of ~9 % (μ~0.09 PE).[14] Two measurements were performed, each with 3×10^{8} PMT waveforms analysed to obtain detailed distributions. In the first measurement, the PMT (BA0789) was operated at its nominal voltage (1158 V). In the

---

[11] Newport 818-UV, see Section 6.4.1.

[12] Measuring the prepulsing with a threshold of 0.2 PE results in a probability of less than 0.3 % for the three PMTs, fulfilling the requirements listed in Section 8.2.

[13] PicoQuant PDL 800-B with LED head PLS-8-2-719. Driven at a frequency of 10 kHz.

[14] Oscilloscope used: Picoscope 6404C.

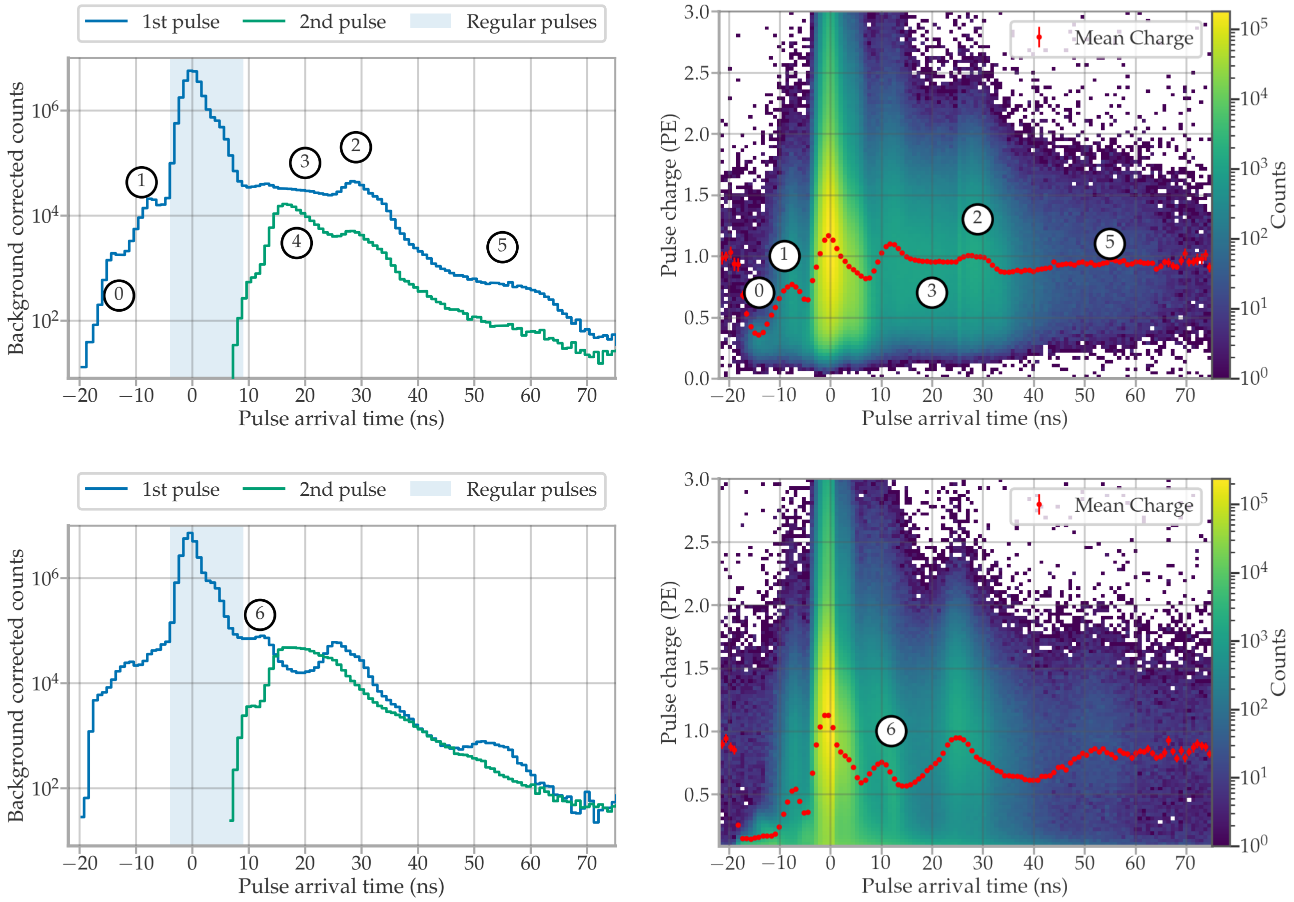

Figure 8.23: *Left:* Arrival time distribution of PMT pulses with contributions of prepulses, delayed pulses, and AP1. The blue curve shows the data of the first measured pulse in each waveform and the green line of the second. The circled numbers mark different features that are discussed in the text. *Right:* Charge-time histogram of the first pulse of each waveform. The red points mark the mean charge of the corresponding time bin. *Top* plots show data of PMT BA0789 at its nominal voltage (1158 V) and *bottom* of the same PMT at (1450 V).

second measurement, the same PMT was operated at 1450 V, resulting in a gain of ~22 × 10^6. As will become apparent in the following, this second measurement was performed to identify the characteristics of the distributions more clearly. Underamplified pulses that cannot exceed the trigger level at a nominal gain may become detectable at higher gains.[15]

The top of Figure 8.23 presents the PMT results at nominal voltage, and the bottom shows the results at the higher gain. The arrival time of the pulses is shown on the left side of Figure 8.23. Pulses with arrival times between −4 ns to 9 ns are marked as 'regular pulses'. The blue curve shows the arrival time of the first pulse measured in the waveforms, and the green curve shows the distribution of the second pulse (if any was measured). The first pulses are produced mainly by regular pulses, prepulses and delayed pulses. The distribution of the second pulses is primarily made up of type I afterpulses (AP1), as they require a previous pulse to have occurred. However, a complete separation between the effects cannot be guaranteed, since the first pulse of an inelastic backscatter may not overpass the trigger, registering only the second pulse.

The right-hand side of Figure 8.23 presents the charge of the first pulses versus their arrival time. The charge along each time bin was averaged and

[15] As the baseline noise remains constant, the trigger level of the oscilloscope does not have to be increased using higher gains.

overlayed over the histogram with red dots. The charge-time-distribution of the regular pulses (arrival times from −4 ns to 9 ns) reflects the same behaviour seen in Figure 7.21 of Chapter 7, as the regions of the photocathode with the largest time deviations produce pulses with the lowest charge.

Following the different effects introduced in Section 5.4.2, the features marked with numbers in Figure 8.23 can be explained as follows:

- Prepulses (marked with ⓪) are observed from −20 ns to − 10 ns, especially on the right side of Figure 8.23 due to their very low charge. The high gain measurement shows a larger range with prepulses as they can exceed the trigger level more easily.[16] At nominal gain, the lowest charge is recorded at ~ -14 ns, which can be assumed to be the average time it takes for an SPE to travel from the cathode to the first dynode $t_{k,d1} \approx 14$ ns for this PMT.
- The peak marked as ① at ~ -6 ns consists of pulses with a larger charge than the prepulses but smaller than regular pulses. These are probably caused by SPEs that skip the first dynode and directly hit the second dynode. The charge of such a pulse should be a factor $\sim \delta_2$ smaller, where δ_2 is the gain of the second dynode. [17]
- The peak marked with a ② is caused by SPEs elastically backscattering at the first dynode, arriving a short distance from the photocathode and then accelerating back toward the first dynode. Here a delay of approximately $2 \cdot t_{k,d1} \approx 28$ ns is expected, which corresponds to the maximum of the peak. As these electrons scatter elastically, they have a charge close to 1 PE. At the higher-gain distribution, this peak appears earlier (at ∼25 ns) since electrons travel faster at higher voltages.
- SPEs that scatter inelastically at the first dynode should arrive earlier than $2 \cdot t_{k,d1}$ because they do not travel all the way back to the photocathode. The energy transferred to the first dynode can release secondaries, in which case an underamplified pulse is measured first. At nominal gain, a plateau in the first-pulse curve is observed in this time region (marked with a ③). However, in the high gain measurement, this plateau does not exist. In addition, the peak of the second pulses is higher in the high voltage measurement than in the nominal voltage (peak ④). This shows that the underamplified pulses have a very low charge and are often buried in the baseline noise without crossing the trigger. An AP1 will be misclassified as a delayed pulse in such a case. This can be confirmed numerically, with the probability that an AP1 measured at nominal voltage being 0.77 % and in the high gain measurement 2.65 %. [18]
  Figure 8.24 shows the charge distribution of the high gain measurement. Here, the distribution of the regular pulses, those measured before a second pulse (an AP1), and also those of the regular pulses without an accompanying AP1 are shown separately. Indeed, pulses measured before an AP1 have a very low charge, peaking at the DAQ lower limit of 0.09 PE. At nominal voltage, the DAQ lower limit is ∼0.3 PE, so many of the underamplified pulses are lost. A higher gain may further increase the separation of AP1 from delayed pulses.

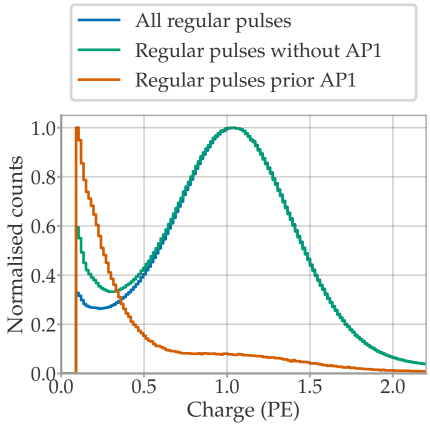

Figure 8.24: Normalised charge distribution of all regular pulses (blue), regular pulses without neighbouring pulses (green) and regular pulses measured before an AP1 (orange).

---

[16] This implies that SPEs released from different regions of the first dynode will produce prepulses arriving at different times. In addition, prepulses arriving earlier have a lower charge and are, therefore, difficult to measure at nominal voltage. In principle, this makes sense since SPEs released in the region close to the second dynode will have a shorter trip and probably also a lower velocity before arriving to the second dynode.

[17] This may be unintuitive, as the first guess may be a factor δ_1 smaller. However, electrons coming from the photocathode have a higher kinetic energy than electrons travelling between dynodes due to the multiplication ratio used in the mDOM PMT (3:1....:1). Therefore, an SPE directly hitting the second dynode should release a similar number of secondaries as the first dynode. Thus, practically a factor δ_2 is missing from the total charge.

[18] Uncertainty of both percentages smaller than given significant digits.

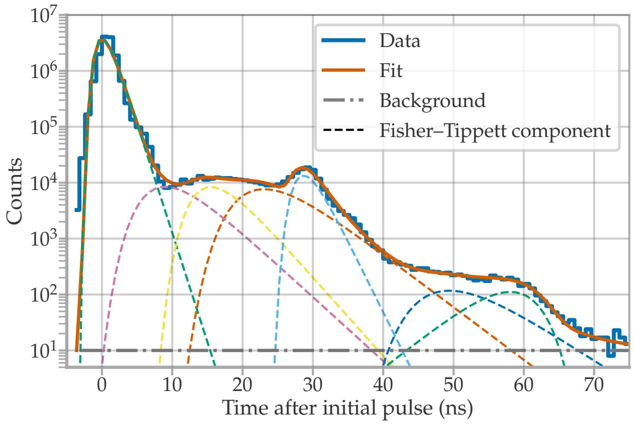

Figure 8.25: Arrival time histogram of PMT pulses fitted with several Fisher-Tippet functions for the parameterisation in IceTray. Data of the mDOM PMT BA0784 at 1135 V. The best-fit parameters are listed in Table C.1 in Appendix C.

- Scattered SPEs can scatter a second time, producing a peak at $4 \cdot t_{k,d1} \approx 56$ ns if the scattering was elastic in both cases. Twice scattered SPEs manifest as a second plateau of low probability after ② (marked with a ⑤). Pulses with an arrival time between $2 \cdot t_{k,d1}$ and $4 \cdot t_{k,d1}$ should have scattered inelastically at least once, and thus an underamplified pulse should have been produced before them. Indeed, the high gain measurement shows a better separation between the delayed and AP1 pulses, with the curve of second pulses covering a larger portion in this region than in the measurement with nominal voltage.
- The measurement with high gain features a small peak at 10 ns (marked with a ⑥), which is also noticeable in the charge distribution. The histogram measured with nominal voltage also features this peak, although smaller and later, at ~13 ns. The cause for this peak could not be found. A light reflection in the setup can be excluded since the time varies changing the PMT voltage. The peak position coincides with $t_{k,d1}$, which may indicate that the first dynode produces photons. However, in such a case, the peak should be measured as a second pulse and not in the first-pulse distribution. In the literature, photon production is often discussed for the last dynodes since they are bombarded with the most electrons. Such photons should produce a peak at ~43 ns, which is not found in the measured PMT.

As introduced in Section 6.3, the arrival time of regular PMT pulses are modelled in IceTray with a Fisher-Tippett function. A sum of these functions is also used to describe the broader distributions produced by delayed pulses. As of the time of writing this thesis, no module exists for the simulation of AP1.

On the one hand, the time of a pulse is randomly sampled from the sum of Fisher-Tippett functions that model the measured time histogram. In the simulation, only the data from one PMT is used, scaling the arrival times by the PMT voltages. On the other hand, the charge is sampled from an SPE template independently of the pulse origin. Therefore, the observed effects on the charge distribution in Figure 8.23 are not considered. In the case of the mDOM PMT, data from PMT BA0784 at its nominal voltage (1135 V) were used. Only the first pulse of the waveforms was used to produce the arrival time histogram to avoid AP1 pulses. The data and the fit are presented in Figure 8.25. The best-fit parameters are listed in Table C.1 in Appendix C.

8.2.3 AFTERPULSES TYPE II

Using the same setup as in the last section but recording longer waveforms, the signal-induced afterpulsing type II (AP2) was also measured. Figure 8.26 displays the time distribution of the correlated pulses on the microsecond scale of the mDOM PMT BA0375. The different peaks are caused by the drift time of different ions, which is proportional to $\sqrt{m/q}$ [158], where m and q are their mass and net charge, respectively. Common ions causing these afterpulses in PMTs are, among others, H^+, He^+, Cs^+ and CH_4^+ [158].

[158]: Ma et al. (2011), *Time and Amplitude of Afterpulse Measured with a Large Size Photomultiplier Tube*

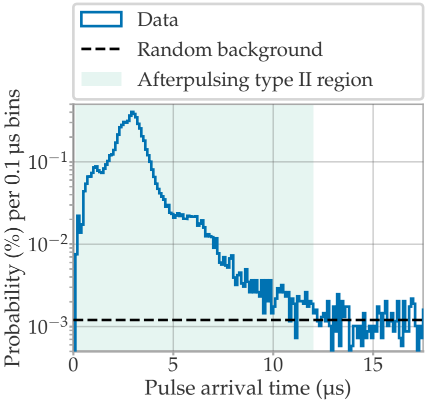

Figure 8.26: Arrival time distribution of PMT pulses measured after a regular pulse. Relative to the mean time of regular pulses produced by the LED flashes.

The different ions are noticeable not only in the arrival time but also in the pulse charge. Figure 8.27 presents a two-dimensional histogram with the charge and time of the AP2 of the same PMT. Although most pulses follow an SPE distribution, specific ions also produce MPE charge of up to ~20 PE,[19] as the peaks at ~1 µs and ~3.2 µs in Figure 8.27.

The parameterisation of the AP2 in Icetray is similar to that of the late pulses. As before, only the time distribution and probability are parameterised, while the charge is assumed to follow the SPE distribution. As observed in Figure 8.27, this is a rough assumption, as the AP2 charge distribution can be as large as a few tens of PEs.

When parameterising the AP2 time distribution, it is not possible to directly use a pulse time histogram such as in Figure 8.26. This is because the different ions produce pulses of varying charge, and using such a histogram would result in an incorrect charge per time calculation. Instead, a waveform from the PMT signal to a very bright LED pulse (where the afterpulses generate a signal in the mV range) is used as the probability distribution. As the amplitude of the waveform is proportional to the charge, it delivers the correct parameterisation of the time pdf. The mDOM PMT BA0780 was illuminated with very bright LED flashes[20] in the order $\mathcal{O}(10^5\,\text{PE})$. The PMT was operated at its nominal voltage of 1118 V. Figure 8.28 shows the mean of 10,000 waveforms,[21] which was

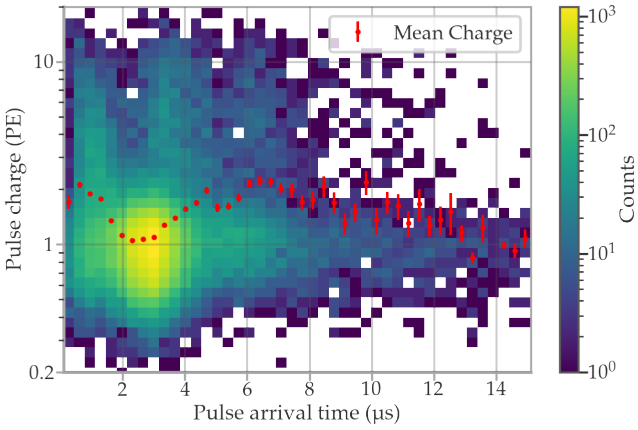

Figure 8.27: Two-dimensional histogram of the charge and arrival time of AP2. The DAQ and pulse extraction limit the measurable charge to a range from ~0.2 PE to ~20 PE.

---

[19] Larger charges can not be excluded, as in the measurement the dynamic range of oscilloscope saturated at 200 mV.

[20] PicoQuant PDL 800-B with LED head PLS-8-2-719. Driven at a frequency of 10 kHz.

[21] Oscilloscope used: Lecroy Waverunner 8404M-MS 40 GS/s.

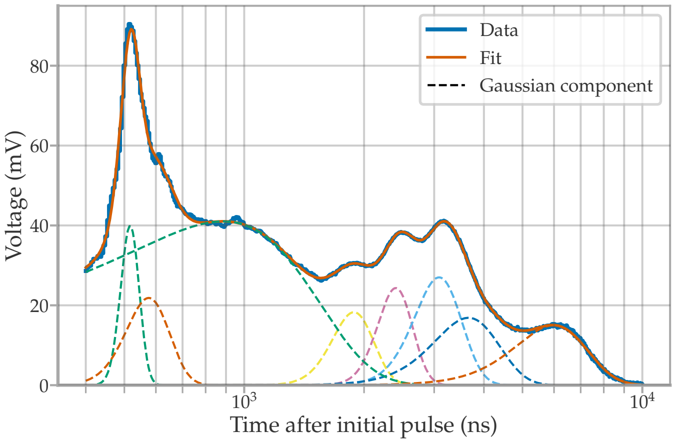

Figure 8.28: Average waveform for a very bright LED pulse, which produces a large number of afterpulses. The waveform was fitted with several Gaussian functions for the IceTray parameterisation. Best-fit parameters are listed in Table C.2 in Appendix C.

calculated directly in the oscilloscope using its averaging function. The waveform was fitted with Gaussians, following the parameterisation used in IceTray (the fit parameters of the Gaussians are listed in Table C.2 in Appendix C). The sum of Gaussians models the data well for most of the waveform, with a slight deviation for the range 0.9 µs to 1 µs. A better fit could be obtained by adding more Gaussians. However, since only one PMT is used for the parameterisation, the most significant MC-data deviations will stem from the intrinsic PMT to PMT variation.

In the mDOM PMT acceptance tests, the probability is calculated as the ratio of *number* of AP2s to the number of regular pulses (as explained in Section 8.2). However, since in Icetray an SPE distribution is assumed for these pulses, the less familiar probability definition has to be employed, using the ratio of *charge* transferred by the AP2s to the charge of regular pulses. In the following, the former is referred to as *pulse ratio* and the latter as *charge ratio*, expressed as a percentage in either case. This means that the simulation will generate the correct extra charge produced by AP2s, but overestimate the number of pulses.

To measure the charge ratio, the PMT was illuminated with a plane wave of varying brightness. The light intensity was increased stepwise, where 20,000 waveforms of 30 µs length were read with an oscilloscope during each step. The waveforms were integrated with the time window defined for afterpulses type II (100 ns to 12 µs after the regular pulses), resulting in the charge Q_S. The charge introduced by the dark rate and the baseline Q_B was estimated by integrating the waveform at later times but using an integration window of the same length (from 15.1 µs to 27 µs). The charge introduced by the afterpulses Q_AP is calculated with $Q_\mathrm{AP} = Q_\mathrm{S} - Q_\mathrm{B}$. For the normalisation, the charge of the main LED peak Q_main was also integrated with the time window of ±15 ns.

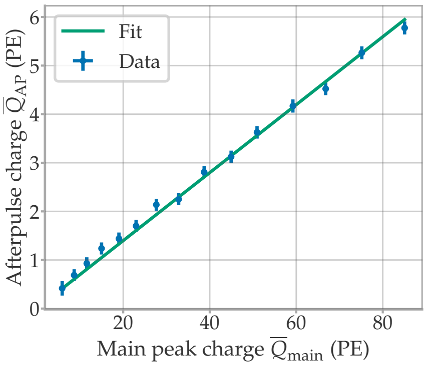

Figure 8.29: Charge added by afterpulses type II against the direct charge measured from LED flashes at increasing intensities. The slope of the linear fit defines the mean afterpulse charge transfer. Data measured with PMT BA0789.

Figure 8.29 shows the mean charge introduced by the AP2s $\overline{Q}_\mathrm{AP}$ against the average charge of the main peak $\overline{Q}_\mathrm{main}$ calculated from all waveforms at each light intensity for the mDOM PMT BA0789. The data points were fitted with a linear function $f(x) = a \cdot x$, of which the slope a represents the charge ratio. In total, six PMTs were measured with this procedure and also with the conventional afterpulse probability following the pulse ratio.

	Charge ratio (%)	Pulse ratio (%)	Factor
BA0375	8.96(8)	6.28(17)	1.43(4)
BA0780	4.76(12)	3.58(33)	1.33(13)
BA0784	7.71(10)	6.27(21)	1.23(4)
BA0789	7.00(7)	5.49(19)	1.27(5)
BA0793	6.56(9)	4.71(21)	1.39(6)
BA0794	7.75(8)	6.1(4)	1.27(9)
Mean			1.321(31)

Table 8.3: The AP2 probability of six PMTs measured following the two definitions. The charge ratio is the fraction between the charge produced by AP2s and the charge of the regular pulses. The pulse ratio specifies the fraction between the number of AP2 and the regular pulses. The last column is the fraction between the charge and pulse ratios.

Table 8.3 lists the resulting AP2 probabilities. As expected, the probability defined with the charge ratio is larger than the one defined with the pulse ratio since the afterpulses can have MPE charges. On average, the charge ratio is a factor (1.321 ± 0.031) greater than the pulse ratio. Therefore, the best value for the probability used in IceTray is the mean pulse ratio calculated during the acceptance testing of the mDOM PMTs ((5.65 ± 0.03) % [155]) multiplied by (1.321 ± 0.031), i.e. (7.46 ± 0.18) %.

8.2.4 Late afterpulsing

Studies on IceCube data have hinted towards late afterpulses (LAPs) of low probability in the ~100 µs region. This kind of afterpulsing has also been measured in other PMT models, with the first publication only being one decade old [159]. To confirm this effect, the IceCube collaboration has made measurements to exclude possible systematic errors. In this context, the mDOM PMT was also tested for this kind of afterpulses.

[159]: Poleshchuk et al. (2012), *An Observation of a new class of afterpulses with delay time in the range of 70-200 microseconds in classical vacuum photomultipliers*

The measurement setup for detecting LAPs is the same as explained in Section 8.2. However, since these pulses are of low probability, many waveforms have to be measured. In addition, the light intensity of the LED was set such that ~400 PE were measured in the main PMT pulse. The bright LED flashes improve the separation of signal (LAP) from the background (dark rate) and reduce the total measurement time. Pulses were extracted with the MPA method from waveforms of 220 µs length.

During this measurement, the oscilloscope's dynamic range was optimised for SPE pulses and saturated for pulse amplitudes larger than 195 mV. Thus, the PMT pulse caused directly by the LED flash saturated the DAQ. However, since the number of PEs measured at the main PMT pulse is needed for calculating the LAP probability and the intensity of the LED flash changes slowly over time, the main pulse was monitored with a separate measurement at the beginning of every set of 10^5 waveforms. Here, the PMT pulse from the flash was integrated 1000 times in waveforms of 200 ns length after increasing the oscilloscope dynamic range to read the complete pulse of height 2 V to 4 V. Figure 8.30 shows the mean charge of the main pulse $\overline{Q}_{\mathrm{main}}$ during the measurement of four mDOM PMTs.

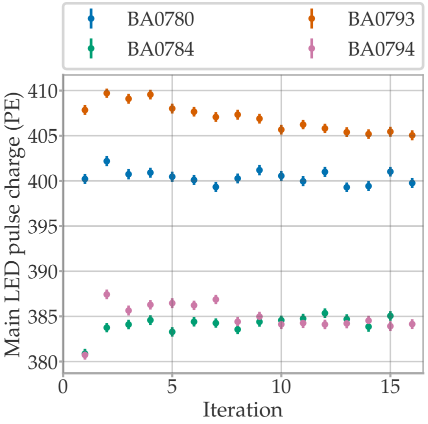

Figure 8.30: Mean charge of the main PMT pulse caused by the LED flash. The pulse charge was measured every 10^5 waveforms as the LED intensity changes slowly with time.

The arrival times of the afterpulses were grouped in a histogram and the counts were normalised by the total number of photoelectrons released by the LED flash. For the latter, it was assumed that all the LED flashes in

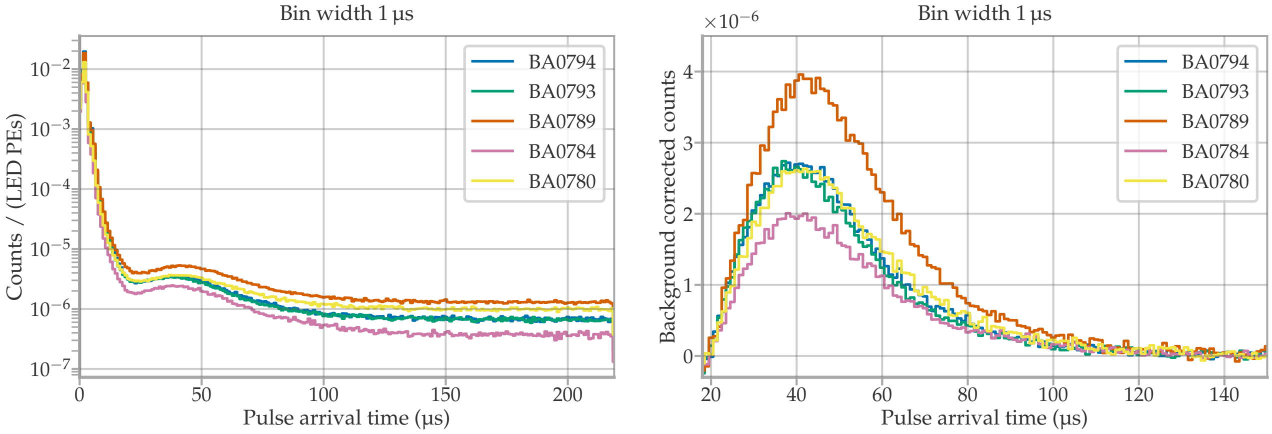

Figure 8.31: *Left:* Arrival time histogram of the measured PMT pulses. The pulse counts were divided by the total number of PEs released by the LED flashes. *Right:* The arrival time histograms were fitted with an exponential and a constant to isolate the LAP distribution. This plot shows the histogram subtracted from the fit.

a set had the same charge as the mean charge measured at the beginning of the set $\overline{Q}_{\text{main}}$.

The left side of Figure 8.31 shows the normalised histograms of five mDOM PMTs. On the very left of the histogram, a prominent peak caused by AP2 is found. Integrating this region until 12 µs results in a ∼ 5 % to 6 % probability, as expected from Section 8.2.3. For times above ∼150 µs a constant is measured from the contribution of the random dark rate. An excess of counts above the background can be observed at ∼40 µs. This excess in counts was isolated by fitting the contribution from the AP2 from 5 µs to 15 µs with an exponential and the background with a constant from 150 µs to 220 µs. The right side of Figure 8.31 presents the same histograms but with the fitted background subtracted. Integrating the background corrected histograms results in an average probability for this kind of afterpulsing of (0.0108 ± 0.0026) %, with PMT BA0789 showing the highest probability (∼0.016 %) and BA0784 the lowest (∼0.008 %). The peak of the background corrected histograms were fitted with a Gaussian, resulting in an average arrival time of (40.2 ± 0.7) µs.

The probability of AP2 is ∼5 %; thus, the probability of measuring a second AP2 produced by an initial AP2 event is ∼0.25 %. The time distribution of a 'second-order' AP2 should be similar to the convolution of the 'first-order' AP2 distribution with itself. Analogously, an AP2 of 'third-order' should follow a time distribution similar to the convolution between the first and second order AP2 and has a probability of ∼0.01 %. The latter is of the same order of magnitude as the observed late afterpulses probability. The convolution of the AP2 distribution from first to fifth order is shown in Figure 8.32 and compared to the measured LAP. Since first-order AP2 pulses arrive mostly between 1 µs and 5 µs, higher-order AP2 cannot explain the LAP distribution.

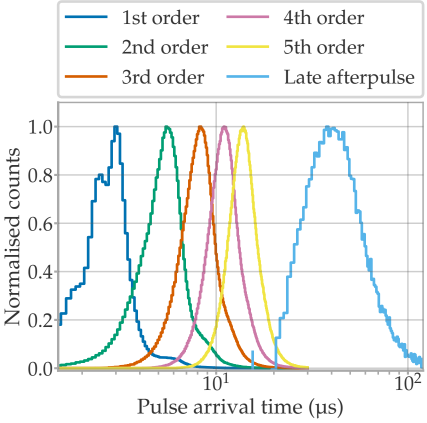

Figure 8.32: The AP2 distribution of the mDOM PMT BA0794 was convoluted up to five times to simulate the time distribution of higher-order AP2 (an AP2 caused by an AP2). The LAP distribution appears much later, excluding the possibility that this is caused by high-order AP2.

Nevertheless, to completely exclude the possibility of higher order AP2, a longer measurement of the mDOM PMT BA0784 was performed with the LED light at SPE level. In this case, pulses that arrived after the first measured AP2 were excluded. Thus, only the first two measured pulses are used in the data analysis at most: the initial pulse from the LED light and the first AP2. The resulting time distribution histogram is shown in Figure 8.33. The peak around 40 µs can still be found for this data set, although with a lower signal-to-background separation. This confirms that the LAP distribution is independent of the normal AP2.

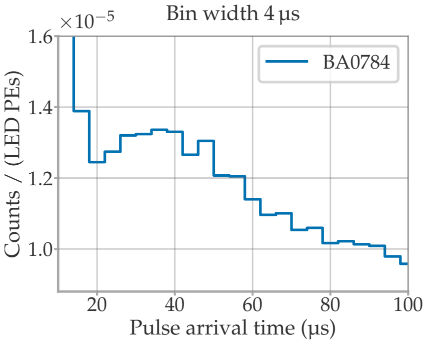

Figure 8.33: Arrival time histogram of only the first afterpulse measured with the LED at SPE level.

The measurement was repeated with a 10″ Hamamatsu PMT R7081-02 (used in the IceCube-Gen1 DOMs) and a 4″ Hamamatsu PMT R16293-01 (candidate PMT type for the LOM). The background corrected histograms are shown in Figure 8.34. The probability for this kind of afterpulsing is in the same order of magnitude as with the mDOM PMTs. Fitting a Gaussian to the histograms results in a peak position of (46.0 ± 0.4) µs and (122.7 ± 1.4) µs for the LOM and DOM PMTs, respectively. The results of the DOM PMT agree with other studies with IceCube data.

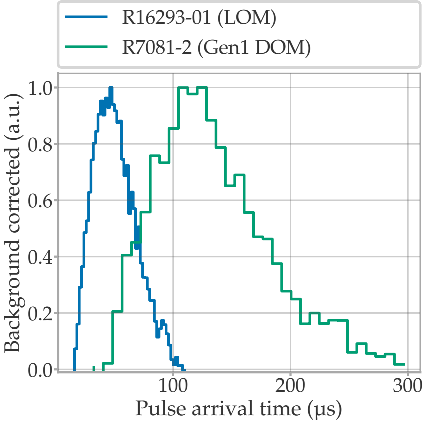

Figure 8.34: Background corrected arrival time distribution of LAPs of a LOM and DOM PMT.

The source of these LAPs is unknown. Since the three PMT types were measured with the same setup but the arrival-time distributions peak at different times, external sources for this effect, such as LED afterglow, can be excluded. The ion-induced afterpulses are measured after a drift time proportional to $\sqrt{m/q}$. The drift time further depends on the applied voltage, the electric field's shape, and the PMT's size. To obtain a reference, the last peak of the AP2 time distribution of each PMT type was fitted with a Gaussian, as presented in Figure 8.35. This peak is believed to be caused by Cs^+ in both the mDOM and DOM PMTs [125, 160]. Due to the similarity between the LOM and mDOM PMT AP2 distributions, it can be assumed that the same ion causes the last peak for both PMT types. A rough estimate for the mass m_{LAP} needed by a cation to produce the LAPs can be made following the proportionality

$$m_{\mathrm{LAP}} = \left(\frac{t_{\mathrm{LAP}}}{t_{\mathrm{Cs}^+}} \cdot \sqrt{m_{\mathrm{Cs}}}\right)^2, \tag{8.7}$$

with t_{LAP}, t_{Cs^+} the mean arrival time of the LAP and the Cs^+ peak, respectively, and $m_{\mathrm{Cs}} = 132.9\,\mathrm{u}$, the mass of caesium. Table 8.4 lists the fitted mean of the Gaussians of the Cs^+ and LAP peaks. In the last column are the results of a back-of-the-envelope calculation for the mass following Equation 8.7. For the three PMT types, a mass in the same order of magnitude is estimated (average $(2.5 \pm 0.3) \cdot 10^4\,\mathrm{u}$). Such large masses could hint, for example, to a heavy polymer [161] or protein [162].

[125]: Aiello et al. (2018), *Characterisation of the Hamamatsu photomultipliers for the KM3NeT Neutrino Telescope*

[160]: Haser et al. (2013), *Afterpulse measurements of R7081 photomultipliers for the Double Chooz experiment*

[161]: Gies (2021), *Chapter 9 - Mass spectrometry of polymers*

[162]: Karas et al. (1988), *Laser desorption ionization of proteins with molecular masses exceeding 10,000 daltons*

The LAPs were observed in neutron echo studies on IceCube data [163]. Here it is intended to separate hadronic from electromagnetic showers by the indirect detection of neutron capture in the ice. A portion of the neutrons released during a particle shower is captured in a hydrogen nucleus of the ice. The time distribution of this neutron capture follows an exponential function with decay time $\tau = 222.2\,\mu\mathrm{s}$ [163, p. 39]. The hydrogen atom with the captured neutron forms an excited deuterium state, which releases a gamma of 2.223 MeV after deexcitation. The gamma can then interact with the ice and produce charged particles and Cherenkov photons. This delayed Cherenkov signal is expected to make up 0.1 % of the detected photons in a high-energy hadronic shower, while in an electromagnetic cascade, only 0.007 % [163, p. 40]. These percentages are similar to the measured LAP pulses, which makes them a critical background in such a study.

[163]: Steuer (2018), *Cascade type identification in IceCube and an application in a search for new physics*

The usage of smaller PMTs in the mDOM and LOM may reduce the impact of this LAP background, as the LAP arrival time (~40 µs compared to ~120 µs of the DOM PMTs) will affect only the beginning of the exponential decay of the neutron capture.

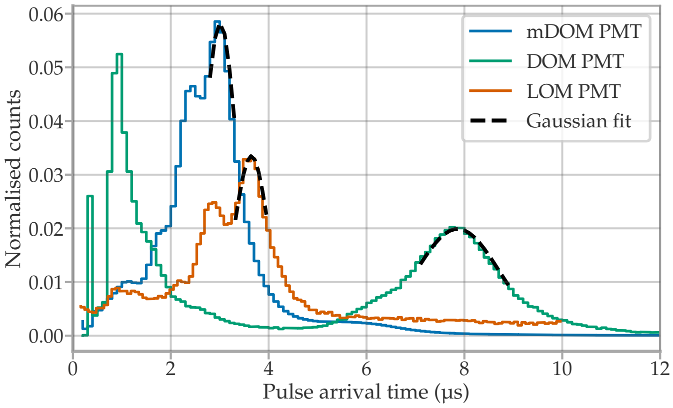

Figure 8.35: AP2 distribution of an mDOM, LOM and DOM PMT. The last peak, believed to be caused by Cs^+, was fitted with a Gaussian to determine its mean arrival time.

Table 8.4: Mean arrival time of the Cs^+ AP2 peak and the LAP peak determined from a fit with a Gaussian for an mDOM, LOM and DOM PMT. The last column shows the estimated mass an ion would need to feature a drift time equal to the LAP peak time using Equation 8.7.

PMT	Cs^+ time (µs)	Late afterpulses time (µs)	Estimated mass ($\cdot 10^4$ u)
mDOM (BA0794)	3.01 ± 0.01	39.7 ± 0.2	2.31 ± 0.03
LOM	3.65 ± 0.01	46.0 ± 0.4	2.11 ± 0.04
DOM	7.86 ± 0.01	122.7 ± 1.4	3.24 ± 0.07

9

PMT response simulation in Geant4

Over the years, the IceCube Münster group has developed a detailed Geant4 simulation of optical modules, which is a powerful tool that allows, among others, for optimising the geometry of modules, estimating their response in non-accessible environments (ice and water) and other physics studies. Geant4 is based on C++ and was developed at CERN and KEK to simulate particles passing through matter using Monte-Carlo methods [164]. Section 9.1 briefly introduces the Geant4 framework with a focus on the geometry definition of the PMT.

[164]: Allison et al. (2016), *Recent developments in Geant4*

The initial PMT model in the Geant4 framework was relatively simple. This model was updated to include the measurement results of the photocathode homogeneity of Chapter 7. For this, it was important to include the simulation of internal components of the PMT. Reflections on these internal components give photons a second opportunity to cross the photocathode. As seen in Section 7.2, this artificially increases the measured efficiency. Furthermore, the PMT response, even for a thin collimated beam, will depend on the incoming angle since the reflected photons may cross a different point on the photocathode. The characterisation of the internal reflections is introduced in Section 9.2.

The geometry and optical properties of the new PMT model of the Geant4 framework are introduced in Section 9.3. The last section (Section 9.3.5) also shows the effects of these changes on the estimated effective area of the mDOM.

9.1 Geant4 framework

Geant4 gives the user a wide range of tools for constructing a particle physics simulation, its analysis, and the visualisation of physic events. On the one hand, it is possible to define the geometry of the detector setup and its environment with realistic properties of the materials, which can be determined by the user or selected from the Geant4 database. On the other hand, the particles of interest can be selected with preprogrammed distributions for their starting parameters (energy, position, and momentum). Geant4 includes an extensive collection of physical models for the interaction of the particles in a wide range of energy ranges, which have been validated with different experiments [165].

[165]: Agostinelli et al. (2003), *GEANT4–a simulation toolkit*

The Geant4 framework used in this thesis is an extension of the simulation initially written in the scope of two PhD thesis [108, 166], which was generalised for the simulation of any optical module.

[108]: Classen (2017), *The mDOM - a multi-PMT digital optical module for the IceCube-Gen2 neutrino telescope*

[166]: Herold (2017), *Simulation and Measurement of Optical Background in the Deep Sea Using a Multi-PMT Optical Module*

9.1.1 GEOMETRY DEFINITION

The simplest geometry definition in Geant4 is based on building with primitive building volumes (spheres, cylinders, ellipsoids, cubes, etc.). The shape of these solids can be further adjusted by means of Boolean operations, such as the subtraction, union, and intersection of at least two volumes. Geant4 also allows for the import of CAD files with objects that can be defined as solids. This is advantageous for geometries that are too complex using primitive building blocks, but comes with the price of a longer startup time of the simulation.

Each of these solids is assigned a material, which also has a table of *physical properties* constraining the possible interactions with particles. If an object is not configured with physical properties, particles are not affected by its boundaries or volume. A solid can also have a table of *material properties*. Within the scope of the OM simulation, the most important material properties are the refractive index and absorption length. In this regard, the properties of glass and gel of different brands can be chosen, which were provided by the manufacturer or measured in [108]. Moreover, optical properties can be defined at the boundary between two volumes, with which, for example, the reflectivity of an object can be defined.

[108]: Classen (2017), *The mDOM - a multi-PMT digital optical module for the IceCube-Gen2 neutrino telescope*

The construction of the first and simpler PMT model is introduced in Section 9.1.3.

9.1.2 PARTICLE TRACKING AND PHYSIC INTERACTION

The simulation usually starts with a single primary particle. This particle has starting properties (energy, location, direction, etc.) that are randomly sampled from distributions defined by the user. This particle then interacts with the simulated geometry and, if applicable, also produces secondary particles, depending on the implemented processes.

Following object-orientated programming, the generation and tracking of particles are hierarchically segmented into different classes. These receive a certain nomenclature, which is introduced in the following. The simulation of a single primary particle is called an **event**. A simulation **run** consists of a set of events that share the same detector implementation, primary generation, and physics conditions. The propagation of the particles through geometry, the so-called *tracking*, is performed stepwise, in steps with a tolerance optimised for performance but preserving the required precision. All physical processes and interactions are a **step**. This object holds information about the physical process, such as the deposited energy and the step length. A **track** contains the most recent step and also has the information required to make the next step, such as the particle position, time since the last step, and a pointer to the geometric volume containing the particle. A step is accompanied by **steppoints**, which keep information about the beginning or end points of the step, such as the physical process that occurred at the step point, geometrical position and global time [165, 167].

[165]: Agostinelli et al. (2003), *GEANT4–a simulation toolkit*
[167]: Geant4 Collaboration (2021), *Geant4 User Guide for Toolkit Developers — Release 11.0*

Table 9.1: Particles and physics processes needed in the physics list for a Geant4 simulation with optical photons.

Particle	Process	Geant4 Class
Optical photon	Absorption	G4OpAbsorption
	Optical processes at interfaces between volumes	G4OpBoundaryProcess
	Mie scattering	G4OpMieHG

As mentioned above, Geant4 provides a library of physics models. The user has to specify the particles and processes that should be taken into account in a **physics list**. As an example, the processes and particles needed for a simple study with photons are listed in Table 9.1. For these processes to work, it is important that the volumes have the respective material properties defined (refraction index, absorption/scattering length, reflectance, etc.).

9.1.3 Simplified PMT model

The simpler PMT model is based on the scheme introduced in [108] and consists of a glass bulb containing a volume representing the photocathode. During particle tracking, if a photon enters this volume, it is *stopped and killed* and saved as a hit. If necessary, the QE can be considered directly after this step, either dropping or weighing the photon depending on the detection efficiency.

[108]: Classen (2017), *The mDOM - a multi-PMT digital optical module for the IceCube-Gen2 neutrino telescope*

The technical drawings provided by the manufacturer of the different PMTs helped define the most accurate geometry of the entrance window as possible. For example, Figure 9.1 shows the technical schematic of the mDOM PMT with the relevant values. The line was extracted as x-y data using [168]. These data points are presented on the left side of Figure 9.2.

[168]: Rohatgi (2021), *Webplotdigitizer: Version 4.5*

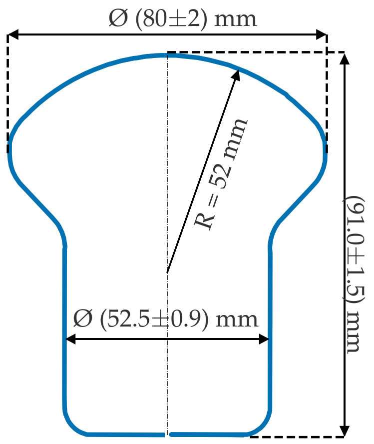

Figure 9.1: Technical drawing of the mDOM PMT provided by Hamamatsu.

To reproduce the shape of the entrance window, the line was fitted with a circle and an ellipse, which are the cross sections of an ellipsoid and a sphere, both primitive volumes available in Geant4. Other PMT models were fitted with two ellipses. If the circle and ellipse are centred with the symmetry axis of the PMT, they are described by only two and three free parameters, respectively. However, since the curvature of the central region of the PMT is given by the radius of 52 mm, the fit of the circle only has one free parameter, its position on the z-axis. On the other hand, the semi-major axis of the ellipse is also constrained by the technical drawing to 40 mm. Thus, the ellipse fit only varied the minor axis and its position on the z-axis.

One of the intersection points between the ellipse and the circle has to be chosen as the transition point between the two curves to ensure a smooth transition. This was done using the residuals of the two models, presented on the right side of Figure 9.2. The ellipse fits the technical drawing better than the circle at the second intersection point $|x| > 37.25$ mm. Therefore, the spherical sector was constructed in the simulation with a half-cone angle that matched this intersection point. At the very edge at $|x| > 39.8$ mm, the ellipse also results in large residuals, since the PMT ends with a rather sharp slope.

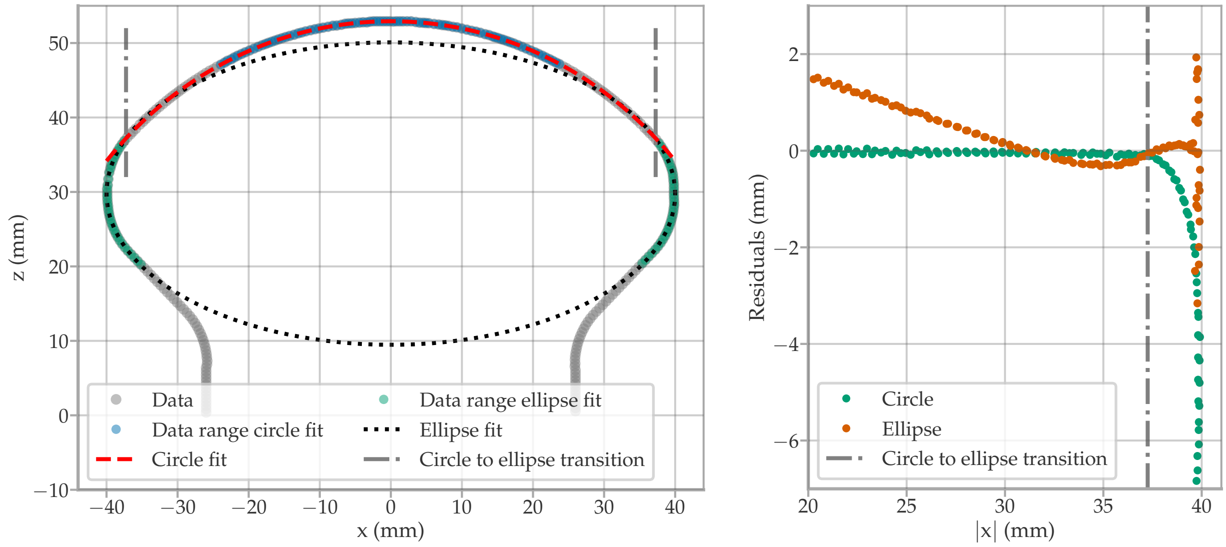

Figure 9.2: *Left:* The data of the technical drawing of the mDOM PMT were fitted with an ellipse and a circle to match the shape of the frontal window. The different colours mark the data region used for the respective shape fit. *Right:* Residuals of the circle and ellipse fits. The dashed point lines in both graphs mark the intersection point between the two shapes, which delimits the spherical sector built in Geant4.

A tube was added to the union volume between the ellipsoid and spherical sector, resulting in the glass bulb model. A second, smaller volume of the same shape was built, which represents the vacuum inside the PMT. Here, a constant wall thickness of 1.95 mm was assumed, the mean value measured with a calliper on an open PMT. The photocathode was constructed also with the union of an ellipsoid and a spherical sector. The bottom part of the ellipsoid along its major axis was removed. Here, a disk of width 0.1 mm was added that acts as an optical absorber to avoid measuring photons from the back of the PMT. The cross section of the Geant4 model is shown in Figure 9.3, together with the technical drawing. Two regions of the PMT are not well modelled by the simulation: where the ellipsoid meets the tube and at the end of the tube, where the technical drawing ends with a curve. Considering the detection principle assumed in this simple scheme, these two deviations do not matter, especially with the mDOM, as these regions are not exposed directly to photons.

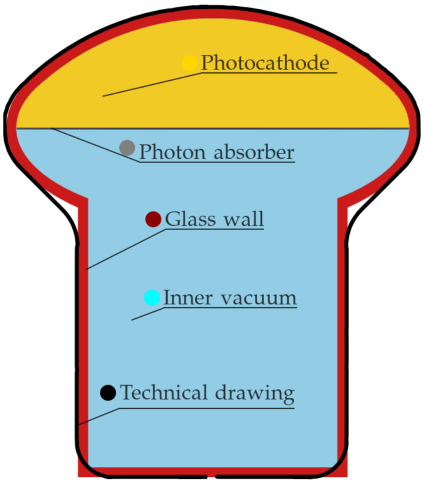

Figure 9.3: Cross section of the PMT model as seen by the Geant4 visualiser. The black line is the technical drawing overlaid on the simulated model.

The refractive index of the photomultiplier glass is specified in Figure 9.4. The absorption length is not defined for this glass as the hits are weighted by the measured QE curve in simulation studies that require PMT sensitivity. The measured QE accounts for the effects of glass transmission, rendering the simulation of this parameter unnecessary.

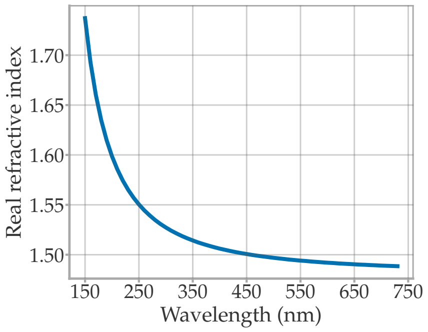

Figure 9.4: Real component of refractive index defined for the PMT glass in Geant4. Data from [108].

Since any photon that enters the photocathode volume is removed from further simulation, the photocathode does not have any optical properties defined, other than a wavelength-independent refraction index of 2.

Although this PMT model is enough for most studies, if systemics from photocathode inhomogeneities are to be simulated, the approach assuming the photocathode as a volume is too rough. The inclusion of internal reflections needs a change in the geometry of the model and also in the detection mechanism because the photocathode has to have some level of transparency. In addition, several materials properties must be defined, for example, the reflectivity of the internal components, which is presented in the next section.

9.2 REFLECTIONS AT INTERNAL COMPONENTS

The most critical components to consider are the surfaces facing the PMT window, which are depicted in Figure 7.7. In the following, the optical properties of the first dynode (marked "D" in Figure 7.7), the frontal plate of the multiplier system (C) and the reflective coating on the glass bulb (A) are investigated and modelled in Geant4. Smaller elements, such as the rectangular flaps (E) were not studied as they are too small for the measurement setups. Each material had to be isolated to measure its optical properties. This was done by opening a PMT and removing a sample of each component.

The characterisation of the internal reflections is separated into two parts. First, the reflectivity spectrum is measured and presented in Section 9.2.1. Then, the angular distribution of the reflected light is studied in Section 9.2.2.

9.2.1 REFLECTIVITY SPECTRUM

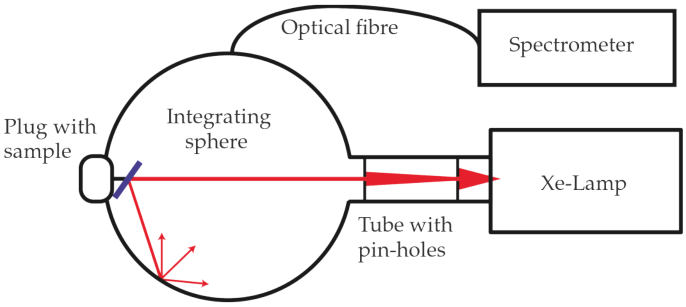

Figure 9.5: Schematic of the setup for the measurement of the reflectance spectrum of the samples. The xenon lamp provides white light, and the red beam in the diagram is only for clarity.

The setup to measure the wavelength dependence of the reflectance is shown in Figure 9.5. The calculation of the reflectivity requires three measurement steps. First, the sample is placed inside an integrating sphere[1] opposite the entrance of the light from a xenon lamp[2]. The light of the lamp is guided through a series of pinholes inside a tube to achieve collimation such that only the sample is illuminated. An optical fibre is placed on one entrance orthogonal to the light beam. The other end of the fibre is fed to a spectrometer[3]. The sample is orientated at such an angle that the beam is reflected away from the fibre, avoiding measuring direct reflections. The relative light intensity is recorded by the spectrometer $S(\lambda)$ as a function of the wavelength from $\lambda = 250\,\text{nm}$ to $\lambda = 800\,\text{nm}$. This is done in two independent measurements because the spectrometer has to change its grating to cover the desired wavelength range (once from 250 nm to 570 nm and the second from 480 nm to 800 nm).

A second configuration is measured, replacing the sample port with a light trap. Light scattered in the collimation tube and released with random angles into the integrating sphere produce a constant background

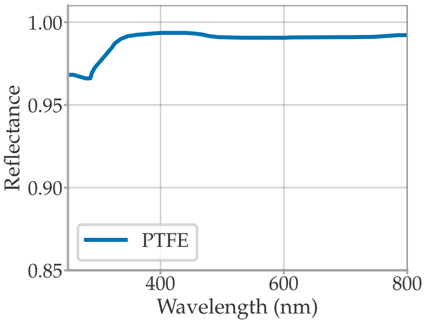

Figure 9.6: Reflectance of the PTFE surface of the plugs and internal coating of the integrating sphere. Data extracted from [169].

[1] Newport 819C-IS-5.3.

[2] LOT LSE140 / 160.25.C.

[3] Andor Solis Kymera 193i-B1 with CCD camera Andor Solis Newton CCD DU920P-OE.

that has to be corrected. The trap absorbs the direct beam of the output of the collimated xenon lamp, but the scattered light is still measured. In the following, the curve measured in this step is represented as $B(\lambda)$.

Finally, a third configuration of the setup is measured. A plug with the internal reflective coating of the sphere is placed in the sample port. In this case, the direct beam is reflected in the integrating sphere with the reflectance of the plug $R_S(\lambda)$. The curve obtained with the spectrometer $N(\lambda)$ serves as the normalisation of the light source. Figure 9.6 shows the typical reflectance curve provided by the manufacturer of the PTFE plug used in the setup.

Three samples of each component (first dynode, frontal plate, and mirrored surface) were measured. Figure 9.7 shows $S(\lambda)$, $N(\lambda)$ and $B(\lambda)$ of one of the samples. The step at 480 nm is produced by a difference in the efficiency of the two gratings used in the spectrometer. Although $B(\lambda)$ and $N(\lambda)$ are independent of the measured sample, they are time-dependent, as the output of the xenon lamp drifts slowly with time. Thus, these curves were measured once for each sample.

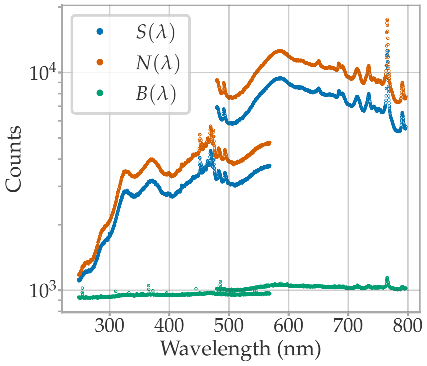

Figure 9.7: Spectrometer output for the three setup configurations (see text). The data correspond to the first sample of the mirrored surface. The spectrometer performs two independent measurements using two gratings to cover the entire spectral range, once from 250 nm to 570 nm and the second from 480 nm to 800 nm. This causes a step on the curves.

The reflectivity of a sample $R(\lambda)$ is calculated as

$$R(\lambda) = R_S(\lambda)\frac{S(\lambda) - B(\lambda)}{N(\lambda) - B(\lambda)}. \tag{9.1}$$

This calculation was performed for each grating curve, and then the data points were averaged in steps of 10 nm. Since the spread between the three samples of each component is not large, these were averaged. The mean reflectance of each component is shown in Figure 9.8. The first dynode and the frontal plate show very similar behaviour. After confirmation with Hamamatsu, these components are based on the same metal mixture, making their similarity in reflectance plausible.

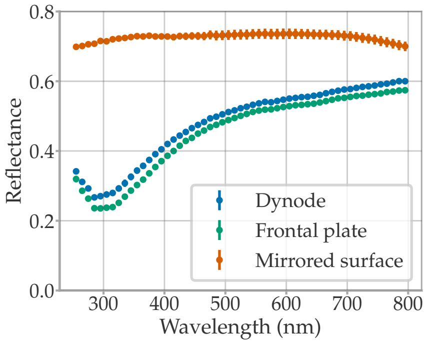

Figure 9.8: Mean reflectance spectrum of each component. The uncertainty is the standard error calculated between different samples and, thus, may be larger than expected from statistics alone.

As the integrating sphere integrates all kinds of reflections from the sample (diffuse and specular reflections), the calculated curves are the total reflectance of the samples. The characterisation of the angular distribution of the reflected beam is performed in the next section.

9.2.2 ANGULAR DISTRIBUTION OF REFLECTED LIGHT

In this section, the angular distribution of light reflected on the internal components is measured and modelled with the tools available in Geant4.

The optical treatment of a surface in Geant4 is based on [170]. It assumes that a surface is a collection of micro-facets with different angles to the normal of the surface. In the *unified* model, the angle distribution follows a Gaussian with a standard deviation σ_α set by the user. The extreme cases of fully specular and diffuse surfaces are covered by the models *glisur polished* and *glisur ground*, respectively. An in-depth description of these models can be found in [171].

A sketch of the measurement setup is presented in Figure 9.9. It consists of a collimated beam[4] pointing at a sample and a CCD camera[5] measuring

[170]: Levin et al. (1996), *A more physical approach to model the surface treatment of scintillation counters and its implementation into DETECT*

[171]: Geant4 Collaboration (2021), *Book For Application Developers — Release 11.0*

[4] 4: NKT Photonics SuperK COMPACT with wavelength filter LLTF VIS HP8. Wavelength used: 500 nm.

[5] 5: Andor Solis Newton CCD DU920P-OE.

the reflected beam. The distances between the fibre and the sample, as well as between the sample and CCD sensor, were logged to accurately reproduce the measurement in Geant4.

However, it is important to first know if the collimation is good at the distances relevant for the measurement. The width of the beam was measured with the laser directly pointing to the CCD camera. Figure 9.10 depicts the image for the fibre 3 cm in front of the sensor. A fit with a 2D Gaussian distribution reveals a thin beam of only $\bar{\sigma}_{x,y} = (143 \pm 5)\,\mu\mathrm{m}$, where $\bar{\sigma}_{x,y}$ is the average of the standard deviations along the axis x and y, $\bar{\sigma}_{x,y} = 0.5 \cdot (\sigma_x + \sigma_y)$. A picture was also taken at a distance of 10 cm and 45 cm. Fitting these distributions concluded that the divergence of the beam causes a linear increase of $\bar{\sigma}_{x,y}$ of only $(1.35 \pm 0.14)\,\frac{\mu\mathrm{m}}{\mathrm{cm}}$.

The distance between the sample and the laser was the same for all samples. Still, the distance between the sample and the CCD sensor varied depending on how wide the reflected distribution was. The top row of Figure 9.11 shows the pictures taken from the reflected beams of the three samples. All display a wider pattern than the laser directly pointing to the camera. This excludes a pure specular reflection of any of the measured surfaces.

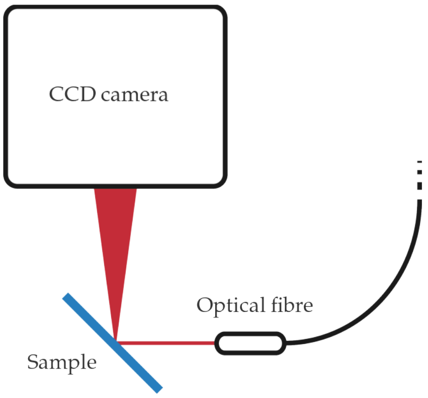

Figure 9.9: Setup of the measurement of the angular distribution of the reflected light on samples of the internal components of the PMT.

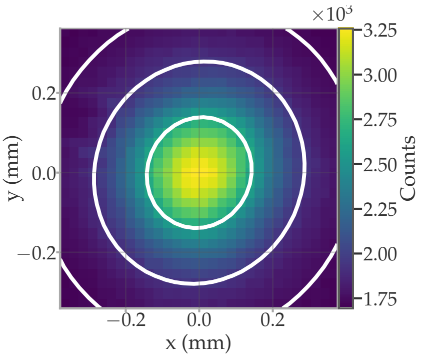

Figure 9.10: Image taken by the CCD sensor of the beam with the fibre at 3 cm distance to the sensor. The contours mark the σ, 2σ and 3σ levels of the fit of a 2D Gaussian.

Since the model in Geant4 assumes a Gaussian distribution, the reflected beams are fitted with a 2D Gaussian of equal widths $\sigma = \sigma_x = \sigma_y$. Furthermore, due to the granularity and surface texture reflected on the pictures, the images were smeared with a Gaussian filter[6] of standard deviation σ_s before fitting. Care was taken to keep the σ_s one order of magnitude smaller than the fitted σ to avoid dominating the fit results by the filter. The fitted width of the distribution was corrected $\hat{\sigma} = \sqrt{\sigma^2 - \sigma_s^2}$ for the calculations hereafter. The second row of Figure 9.11 shows the smeared data with a contour at the levels of σ, 2σ and 3σ of the fit.

A simplified setup was modelled in Geant4. The initial positions of the simulated photons were sampled from a 2D Gaussian following the fitted values of the beam in Figure 9.10. The photons were directed to a flat square defined with an optical boundary of the *unified* model, simulating the sample. The CCD camera was represented as a thin surface with the dimensions of the CCD sensor and 100% detection efficiency. The sensor was placed at the same distance to the sample as in the measurement. When a reflected photon hit the simulated sensor, the position on the rectangle was saved, and the simulation of that photon was stopped.

The simulation results were represented in a 2D-histogram and fitted with a 2D-Gaussian. Such a calculation is performed for different σ_α of the Gaussian describing the angle of the micro-facets in Geant4. As an example, the results of the sample of the mirrored surface are presented in Figure 9.12. The best estimates for the σ_α modelling the measurements were calculated by interpolating the data points of the simulation results and are listed in Table 9.2 in degrees.

As expected from Figure 9.11, the dynode shows the largest surface roughness with $\sigma_\alpha = 1.18°$, one order of magnitude larger than the frontal plate and the mirrored surface, which feature similar values.

[6] For this the method *gaussian_filter* from the *scipy.ndimage* module in Python was used.

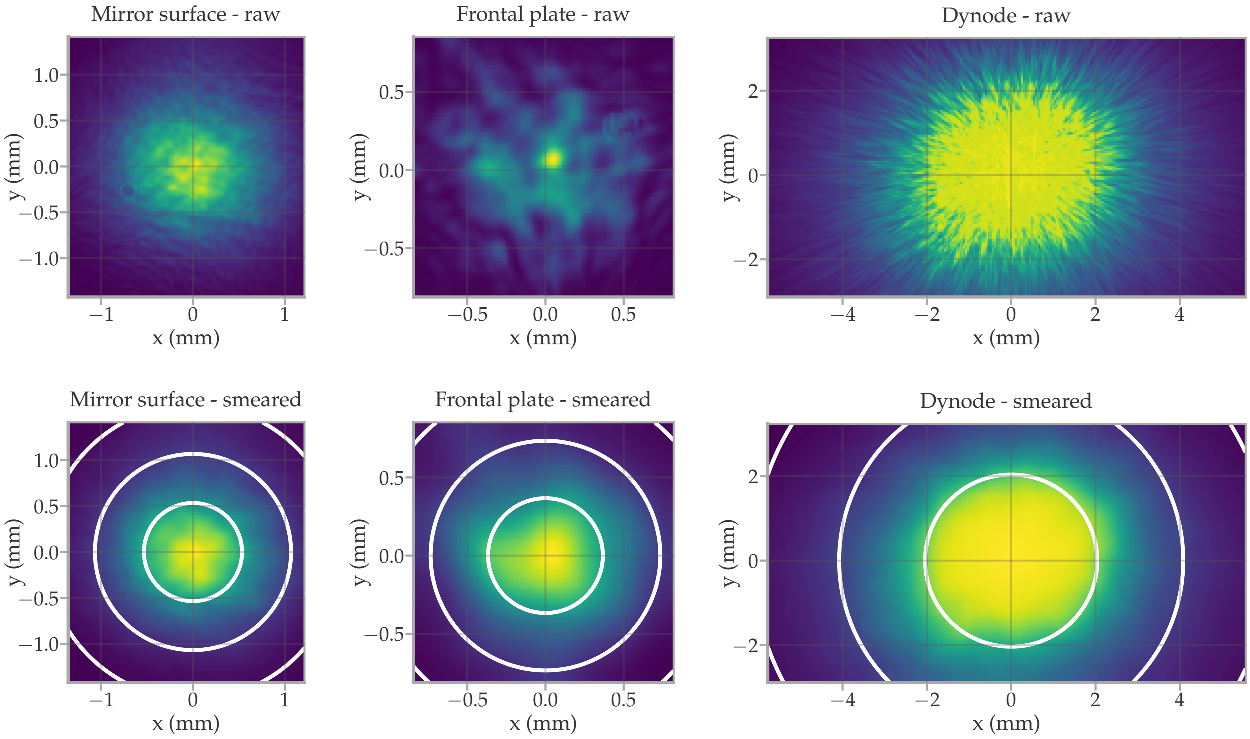

Figure 9.11: *Top:* Raw image taken by the CCD sensor of the reflected beam from the samples of the mirror surface (left), frontal plate (centre) and dynode (right). The colour map is linear but colour bars were omitted for clarity. *Bottom:* The images smeared with a Gaussian filter. Contours show the σ, 2σ and 3σ levels of the 2D Gaussian fit.

For comparison purposes, the measurement was repeated with a piece of an mDOM reflector, which in Geant4 was always simulated as 100 % specular. The resulting σ_α is also listed in Table 9.2. The specularity assumption taken in [108] is well justified, with an average deviation to the specular case of only 0.037°. Nevertheless, this material was also updated with the measured σ_α.

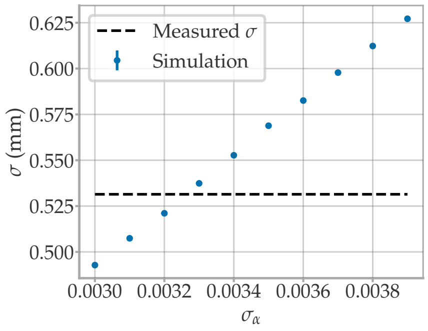

Figure 9.12: Fitted σ from a symmetric 2D Gaussian on the simulated setup modelling the sample with different σ_α. The dashed line marks the measured σ. Calculation for the mirrored surface sample.

9.3 PMT MODEL WITH INTERNAL REFLECTIONS

To model the PMT response following the measurement of the response homogeneity of Chapter 7, the Geant4 PMT geometry was redeveloped. Instead of stopping the photons when they hit the photocathode volume, this new model allows for the transmission of a portion of the light into the PMT after the photocathode absorbs a fraction of the photons proportional to the QE of the PMT. The transmitted light can reflect on the internal structures of the PMT and cross the photocathode again.

Several steps had to be taken to renovate the Geant4 model successfully. As already presented in Section 9.2, it was necessary to measure the reflectivity and surface quality of the internal components to define realistic properties in the simulation. The next step involved updating the geometry of the PMT glass tube, and the frontal components of the dynode structures were modelled. Moreover, a new geometry of the photocathode layer with realistic optical properties was defined. The latter two steps are explained in detail in the next subsections.

Table 9.2: The σ_α value set in Geant4 to reproduce the measured angular distribution of the reflected light. Given in degrees, in Geant4 it has to be listed in radians.

	σ_α (°)
Mirrored surface	0.199
Frontal plate	0.127
Dynode	1.18
mDOM reflector	0.037

9.3.1 GEOMETRY

The photocathode geometry was changed to a thin layer with constant thickness following the same shape as the frontal window of the PMT. For this, a second smaller union of an ellipsoid with a spherical sector is created, which is subtracted from the original photocathode volume introduced in Section 9.1.3, leaving only the thin layer. The thickness of the layer was set to 20 nm, which is the best fit for a bialkali PMT measured in [151].

[151]: Motta et al. (2005), *Optical properties of Bialkali photocathodes*

The region where the ellipsoid meets the tube did not agree with the technical drawing in the simple PMT model (see Figure 9.3). This had to be improved, as the mirrored surface of this region will be simulated in the new PMT model. This was achieved by fitting the technical schematic, similar to the front window in Section 9.1.3, thus, the following explanation is brief. In this case, a line and a circle were fitted, which are the cross sections of a cone and a torus, primitive volumes available in Geant4. The fit of these two shapes is shown in Figure 9.13. The line is used for the parameterisation of the inner side of a hollow cone. In this case, the torus and cone are used to subtract a large tube, leaving a volume with a cross section that matches the fitted curve. The PMT model, as seen in the Geant4 visualiser, is presented on the left side of Figure 9.14. The simulated PMT glass bulb is almost a perfect match to the technical drawing, except for the end of the tube. As explained before, this region is not relevant for optical simulation.

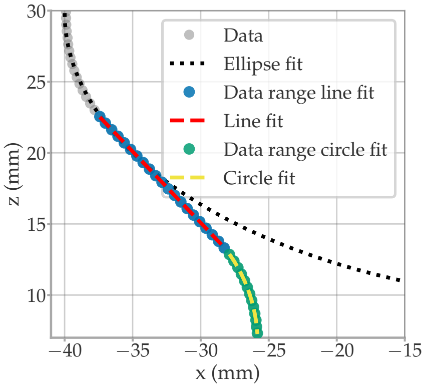

Figure 9.13: The data of the technical drawing of the mDOM PMT are fitted with a line and a circle to match the shape of the back side of the glass tube (cf. Figure 9.2). The different colours mark the data region used for the respective shape fit.

The photocathode layer was subtracted using a second ellipsoid with the same major axis as the one used for its construction, but with a minor axis that was 220 nm smaller. This prevented an abrupt cutoff at the edges. Figure 9.15 shows the thickness of the photocathode against the coordinate x. This subtraction is necessary as otherwise, internal reflections at these sharp corners artificially increase the simulated sensitivity of the PMT in this region (see Section 9.3.3).

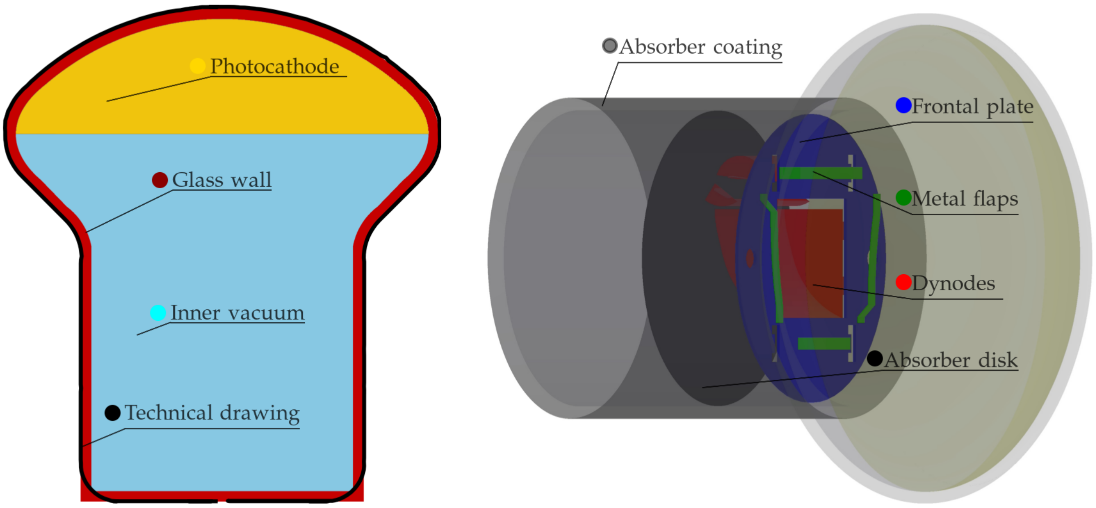

Figure 9.14: The PMT model as seen from the Geant4 visualiser. *Left:* Cross section of the geometry only with the glass, vacuum, and photocathode volumes. The black line is the technical drawing overlaid on the simulated model. *Right:* Side view of the PMT model.

Internal components on which frontal light can reflect were included using a CAD import tool [172]. The CAD model of the PMT was built within the scope of a PhD thesis [173, Ch. 4]. The right side of Figure 9.14 shows the imported frontal part of the multiplication system, as seen in the Geant4 visualiser. The optical properties of the frontal plate and the dynodes measured in Section 9.2 were applied to the respective volumes. For the thin metal flaps, the reflectance of the frontal plate was assumed with a complete diffuse surface finish. The mirror on the glass tube was defined as a boundary property between the inner vacuum (light blue on the left side of Figure 9.14) and the glass wall (red on the left side of Figure 9.14), so no solid for this layer was defined. Any photon that transitions from the glass wall to the inner vacuum or vice versa is absorbed or reflected with the properties measured in Section 9.2. This assumes a larger mirrored surface than in the actual PMTs (cf. Figure 9.16). Thus, a tube of 0.5 mm wall thickness was added that models the HA coating to avoid reflections on the outside of the PMT. Here, it was assumed that the HA coating is completely opaque. In addition, a photon absorber disk was added behind the multiplication system to avoid photons being reflected back to the photocathode. In reality, there is a small probability for photons that travel to the back of the PMT to be reflected on the glass and be detected. This was considered negligible, as the glass on the back of the PMT has a matt finish, and there are many components on the way which are not included in the Geant4 model.

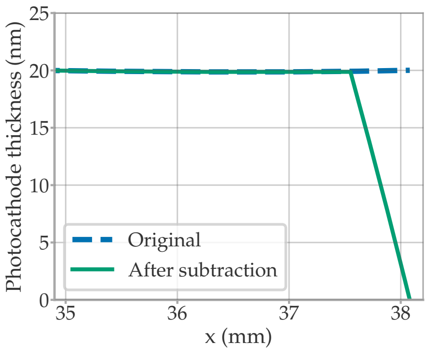

Figure 9.15: Photocathode thickness at the edges of the PMT in Geant4. The sharp cut-off at the end of the volume was softened by subtracting a second ellipsoid.

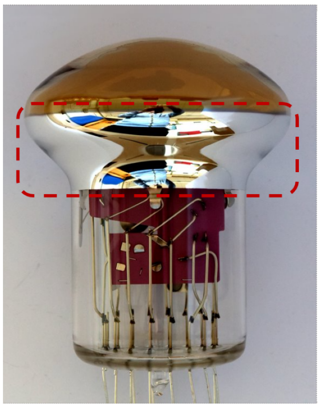

Figure 9.16: Photograph of an mDOM PMT without HA coating highlighting the mirrored surface.

[172]: Poole et al. (2012), *A CAD Interface for GEANT4*

[173]: Schmiemann (2019), *Squark Annihilation Contributions to Neutralino Dark Matter in NLO SUSY-QCD*

9.3.2 Optical properties of photocathode and PMT glass

In the simple PMT model introduced in Section 9.1.3 only the refraction index of the PMT glass was necessary. As the new scheme relies on the absorption of photons in the photocathode layer, it is necessary to define realistic optical properties, the refraction index and absorption length, for both the photocathode and the PMT glass. These were defined as follows:

PMT glass: The refraction index $\hat{n}$ provided in [174] was used, which is given in its real n and imaginary κ components, $\hat{n} = n - i \cdot \kappa$. From the imaginary component the absorption length $\alpha(\lambda)$ was calculated in dependence of the wavelength λ [175, p. 128]:

$$\alpha(\lambda) = \frac{\lambda}{4\pi\kappa(\lambda)}. \tag{9.2}$$

Figure 9.17 shows the extracted absorption length in metres. For wavelengths larger than 300 nm the PMT glass features practically no absorption, since the bulb wall thickness is 1.95 mm and the absorption length in this wavelength range is always greater than 10 mm. However, the decrease in absorption length towards shorter wavelengths will produce the expected cut-off in sensitivity at approximately 280 nm, where $\alpha \approx 1$ mm. Because the data used are from another glass brand than the one used in the PMTs, the absorption length will probably differ from reality. However, as in the following the absorption length of the photocathode layer is calculated to match measurements, any discrepancies in the glass

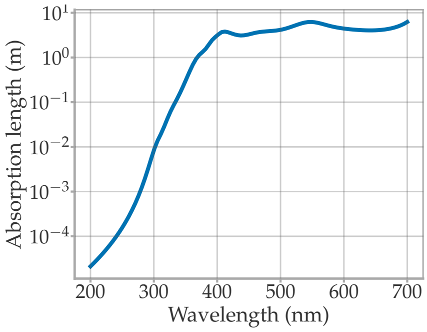

Figure 9.17: Absorption length calculated from the complex refractive index following Equation 9.2, used for the PMT glass the Geant4 simulation. Data from [174] of a borosilicate glass sample of type N-BK7.

[175]: Hecht (2002), *Optics*

transmittivity will be accounted for by the properties of the photocathode layer.

The real component of the refractive index is the same as in the simple PMT model presented in Figure 9.4.

Photocathode layer: It is difficult to find the refractive index of photocathodes within the literature, [151] being the only publication that provides the real and imaginary part for a relatively large wavelength range. The real component of the refraction index defined of an RbCsSb photocathode is displayed in Figure 9.18. The data shown are used for the photocathode layer in the simulation, but it has to be noted that there are no data points for wavelengths shorter than 380 nm. In the case of extrapolation for $\lambda < 380$ nm Geant4 uses the nearest defined value. Elipsometry measurements on the photocathode of the mDOM PMT are planned in the Münster IceCube group, which will cover the whole spectral range and hopefully provide a direct measurement of the real and complex refractive index of the photocathodes used in the mDOMs.

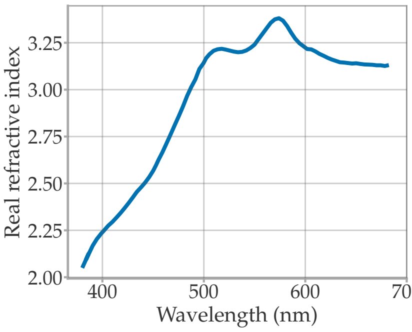

Figure 9.18: Real component of the refractive index of a RbCsSb photocathode used in the Geant4 simulation. Data from [151].

[151]: Motta et al. (2005), *Optical properties of Bialkali photocathodes*

The imaginary refractive index is also provided in [151] for the RbCsSb photocathode and thus the absorption length could be calculated following Equation 9.2. Nevertheless, as in the simulation the absorption of a photon in the photocathode layer directly implies the detection of the photon, the absorption length was calculated to match the average QE curve from the right side of Figure 6.35. For this calculation, the QE measurement was replicated in Geant4, with a beam of 1 cm diameter illuminating the centre of the PMT. The absorption length was set wavelength independent and varied in the range from 1 nm to 10 µm. The wavelength of the beam was varied from 250 nm to 700 nm in 5 nm steps. Absorbed photons in the photocathode layer were counted as detected. From here, a curve of the fraction of detected photons against absorption length is obtained for each wavelength. The results for 270 nm and 400 nm are shown in Figure 9.19. As expected from the PMT glass transmission, a larger portion of photons are detected at 400 nm than 270 nm at any given absorption length. The data points were fitted with the function

$$f(\alpha) = a \cdot (1 - \exp(-b/\alpha)), \tag{9.3}$$

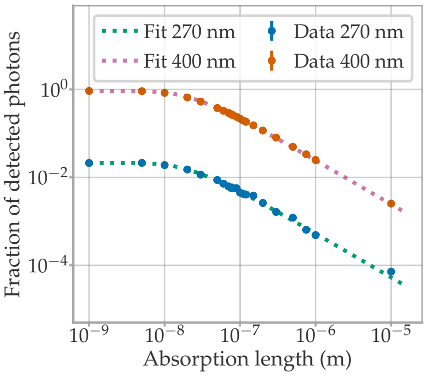

Figure 9.19: Simulation results of the fraction of absorbed photons in the photocathode layer versus the absorption length defined for this layer. The results for a beam of 270 nm and 400 nm are shown. The points were fitted with Equation 9.3.

where a and b are free parameters. The variable a scales proportional to the transmission of the PMT glass and b proportional to the effective thickness of the photocathode layer. The fit model is very simple as it features only a single parameter for the distance travelled by the light. Fractions of the beam can be reflected multiple times in the photocathode layer increasing the path travelled. However, it is correct in the first order and should be sufficient to reproduce the measured QE, considering the large variation from PMT to PMT of the QE curves (see Figure 6.35).

After fitting, the absorption length α was calculated by equalising Equation 9.3 to the measured mean QE for each simulated wavelength. The resulting absorption length used in Geant4 for the photocathode layer is shown in Figure 9.20.

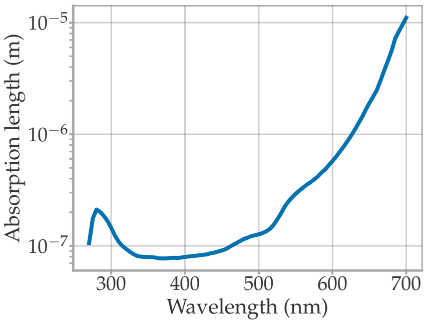

Figure 9.20: Absorption length of the photocathode layer in Geant4 that matches the fraction of absorbed photons to the measured mean QE (from right side of Figure 6.35).

As final test, the simulation was run with the newly defined α counting the photons absorbed in the photocathode layer and calculating the fraction

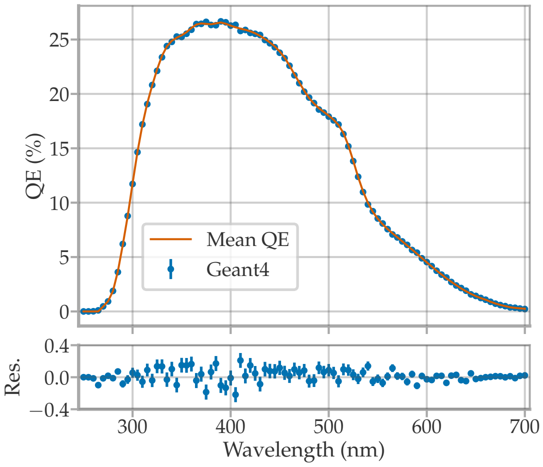

Figure 9.21: Measured and simulated QE. The measurement is the average QE of the mDOM PMTs measured by IceCube collaborators [141]. The simulated QE is the fraction of photons absorbed in the photocathode layer. The lower graph shows the difference between the measurement and simulation.

of photons detected at each wavelength. Figure 9.21 shows the fraction of detected photons in the simulation compared to the measured QE. At the bottom of the graph is also the difference between measurement and simulation, which shows deviations of less than 0.4 % (χ^2/ndof= 1.49).

9.3.3 "Collection efficiency" weighing

The next step is to match the simulation with the efficiency measurement results. The setup used to measure the uniformity of the photocathode in Chapter 7 was reproduced by simulating a Gaussian beam with FWHM and divergence as in Figure 7.2. Here, the distance between the beam origin and the PMT glass was modelled as in the real measurement (Figure 7.3). The beam of a wavelength of 459 nm was then simulated at different positions in a grid of 1 mm × 1 mm.

As mentioned in Section 9.3.1, the edges of the photocathode layer were smoothed to avoid an abrupt cutoff in layer thickness. Figure 9.22 shows the mean fraction of detected photons relative to the distance to the PMT centre[7] for a photocathode layer without this subtraction and with a softer cutoff (see Figure 9.15). Also depicted are the data for the mean photocurrent response from Figure 7.9 are also shown for comparison.

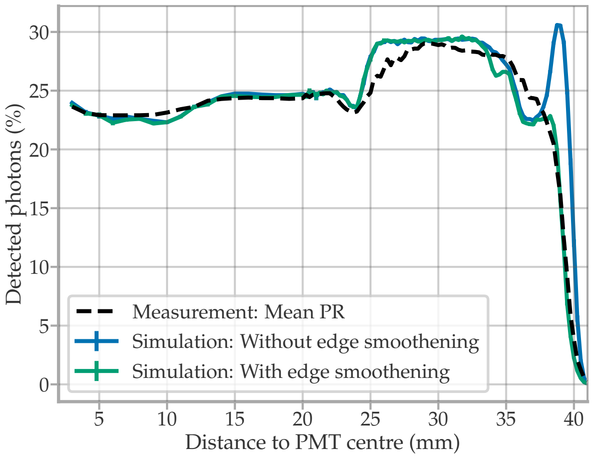

Figure 9.22: The percentage of detected photons against the distance to the PMT centre for a simulated photocathode layer of constant thickness and a layer subtracted at the edges reducing its thickness (see Figure 9.15). In black is the average measured photocurrent response (PR) from Figure 7.9.

---

[7] Following the coordinate system of Figure 7.5.

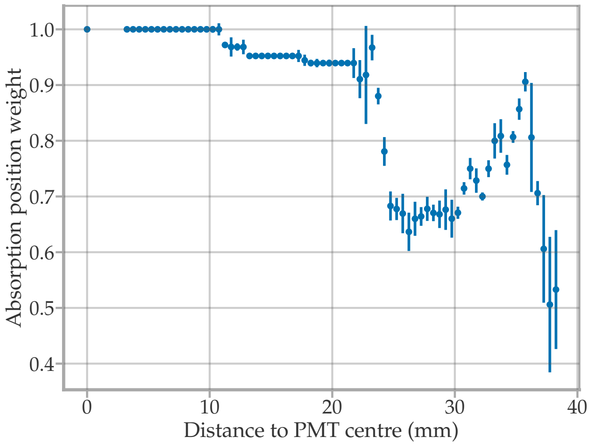

Figure 9.23: Weights calculated with the best-fit parameters against the distance to the PMT centre. The photons absorbed in the photocathode layer are weighted, interpolating the shown curve depending on the location of their detection. The weights model the collection efficiency of the PMT.

The photocathode with abrupt cutoff features a peak of efficiency at the edges, which is not present in the measurement. The subtracted photocathode shows better agreement right at the edge, but the shapes of the curves differ in the range from 24 mm to 37 mm. This region is mainly influenced by back-reflections from the mirrored surface of the PMT. Thus, this disagreement indicates that the simulated geometry is not entirely correct. This is, in part, to be expected. The wall thickness of the PMT varies depending on the location (for example, the glass in front of the photocathode in the central area is thinner than at the edges), while the simulations assume a constant wall thickness following the shape of the technical drawing.

However, the goal of the simulation is to model the PMT under normal operating conditions. Hence, the simulated efficiency should reflect the measurement of the detection efficiency (refer to Section 7.3.4) rather than the photocurrent response, where the collection efficiency is not relevant. Thus, in Geant4, the detected photons need to be weighted based on their location of absorption on the photocathode. These weights should represent the probability of the absorbed photon being detected and simulate the PMT collection efficiency.

For the calculation of these weights, it was assumed that the collection efficiency is the same within a PMT radius. The weights were calculated by adjusting the simulation response to match the mean relative detection efficiency against the distance to the PMT centre from Section 7.3.4.[8] The technicalities of the fit procedure can be found in Appendix D.

The calculated weights are shown in Figure 9.23. If the QE model of the simulation were perfect, the weights would be equal to the real collection efficiency of the PMT. In fact, the results show similarity to the data on the right side of Figure 7.25, which is remarkable considering that they are almost completely independent. Nevertheless, due to the reasons mentioned above, they also absorb systematics, such as inaccuracies in the geometry simulation. The fit achieved with these parameters is good, as shown in Figure 9.24. The resulting detection efficiency scan of the simulation running with the calculated weights is presented in Figure 9.25.

Although the results agree very well with the measurement, the fact

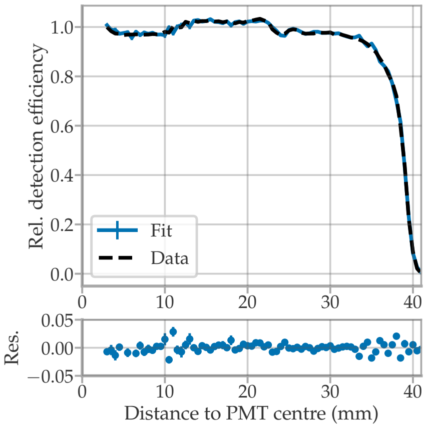

Figure 9.24: Fit to the mean relative detection efficiency used to calculate the weights that model the collection efficiency.

[8] The mean of all curves in Figure 7.24.

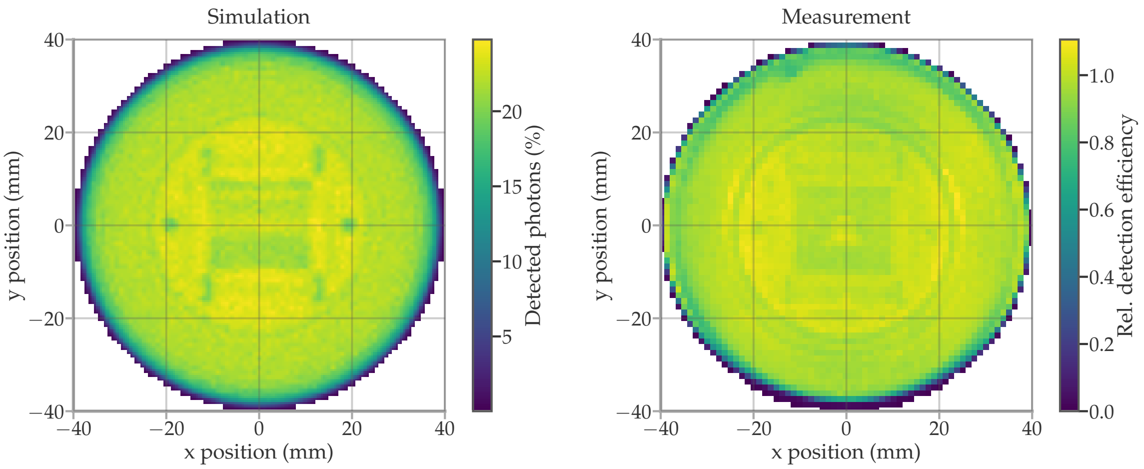

Figure 9.25: *Left:* Geant4 simulation result reproducing the detection efficiency scans of the mDOM PMT using the "collection efficiency weights" of Figure 9.23. *Right:* Real measurement of a relative detection efficiency scan of one particular PMT for comparison.

that the calculated weights compensate for possible deviations in the simulated geometry means that this level of data-simulation agreement will only be true for light parallel to the tube axis. To ensure a correct simulation for photons of all incoming angles, it is important to model the curvature of the mirrored surface of the tube glass and the thickness of the photocathode layer as well as possible. The IceCube group in Münster is working on these rubrics to improve the framework introduced in this chapter.

9.3.4 SIMULATING TRANSIT TIME AND GAIN INHOMOGENEITIES

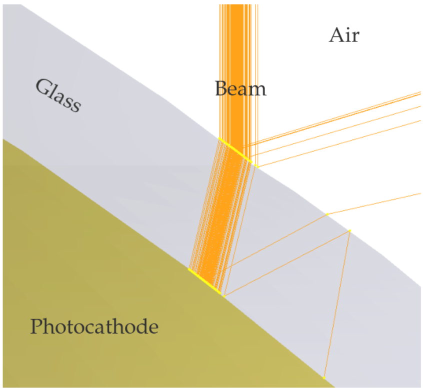

Figure 9.26: Beam refraction and reflection on the PMT glass window toward the centre of the photocathode. Picture from the Geant4 visualiser.

The PMT response in the Geant4 simulation was improved by adding a module that returns the transit time and charge of each detected photon. In this module, the scan data from Section 7.5 in the form of 2D histograms that are interpolated.[9]

However, the scan data must be corrected before use, as the x and y coordinates of the beam do not necessarily correspond to the primary spot on the photocathode that is illuminated. The air-glass boundary refracts the beam, as shown in Figure 9.26. A scan with a thin beam was simulated with a photocathode that is 100 % efficient to avoid internal reflections. The absorption positions of the photons were saved, and the x and y values were transformed into polar coordinates (R_A, ϕ_A). Figure 9.27 shows the absorption position R_A divided by the the beam position R_B. Due to the curvature of the PMT window, the beam is always deflected towards the tube axis except for the centre of the PMT. The points in Figure 9.27 were fitted by a polynomial of 15th degree $p(r)$. The measured scan data that are intended to be used in Geant4 were corrected by scaling their coordinates x and y by $p(R)$ with $R = \sqrt{x^2 + y^2}$.

In the simulation, all the wavelength-dependent scans of the gain, SPE resolution, transit time and TTS from Section 7.5 are loaded into memory. In the following $T_\lambda(x, y)$ refers to the interpolation using a scan measured with the wavelength λ.

---

[9] The measurements are used as input in *TGraph2d* objects, which is a class from the ROOT library [176]. TGraph2d interpolates in two dimensions using the Delaunay triangulation.

The PMT response module in Geant4 receives the wavelength λ_0 and (x_0,y_0) position on the coordinates of the photocathode of all detected photons. If λ_0 corresponds to one of the measured scans, the interpolations $T_{\lambda_0}(x_0, y_0)$ are used directly. For the pulse time, the relative transit time and TTS scan are interpolated, and for the charge, the gain (in PE units) and SPE resolution maps are used. The pulse time is generated by randomly sampling from a Gaussian distribution with a mean equal to the interpolated transit time and a standard deviation equal to the interpolated TTS. The charge is generated similarly by sampling from a Gaussian with a mean equal to the interpolated gain and a standard deviation equal to the product of the interpolated SPE resolution and the interpolated gain. If λ_0 lies between two measured wavelengths λ_{-1} and λ_1, both $T_{\lambda_{-1}}(x_0, y_0)$ and $T_{\lambda_1}(x_0, y_0)$ are computed, and the outputs are linearly interpolated before their use in the Gaussian sampling. If λ_0 is outside the measured interval, the scans of the nearest wavelength are used.

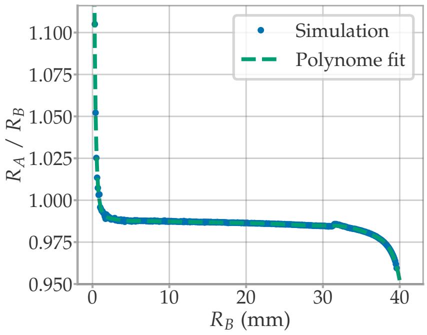

Figure 9.27: Photon absorption position R_A normalised with the position of the beam R_B as a function of R_B. The dashed line shows the fit of a polynomial of 15th degree on the simulation results. Due to the curvature of the PMT window, the beam deflects towards the PMT centre.

To test the simulation, the scan measurement was replicated for a beam of 460 nm. For each beam position, the average pulse time and charge weighted with the efficiency weights from Section 9.3.3 were calculated. Figure 9.28 shows the results of the simulation in conjunction with the measured scans.

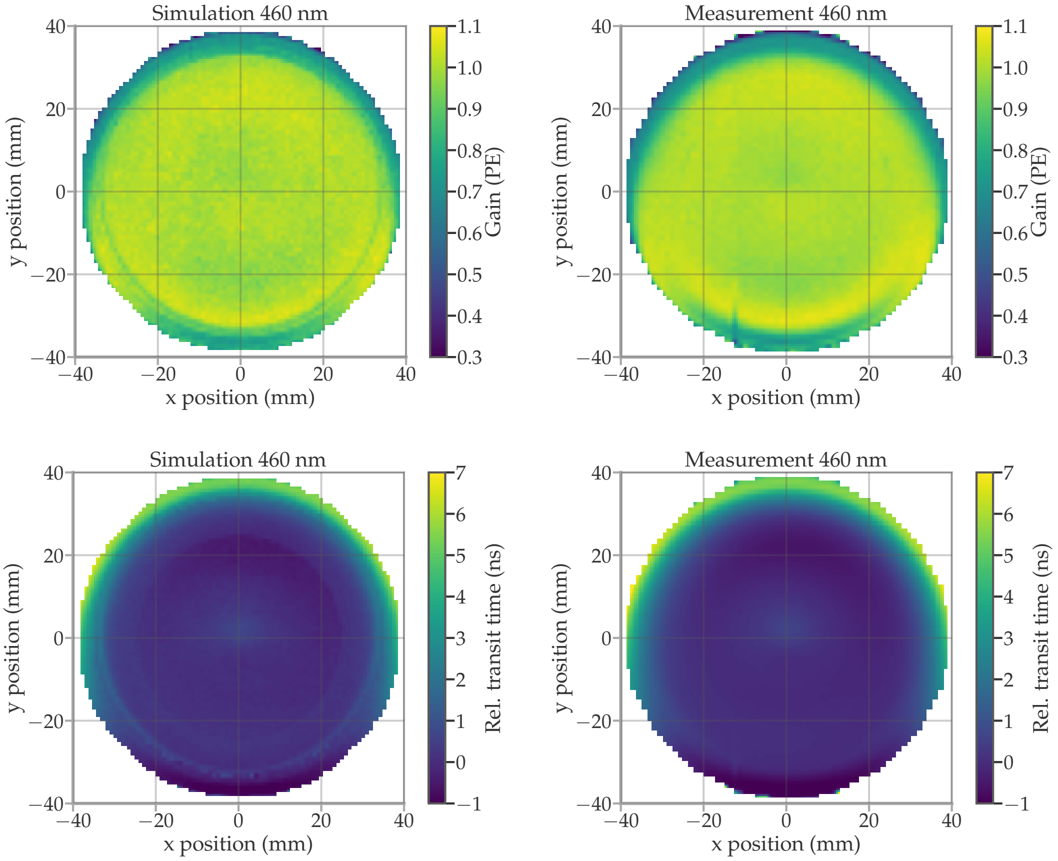

Figure 9.28: Comparison between the scans produced by the simulation (left column) and the measurements (right column). The top row shows the scans of the gain normalised to units of PE, and at the bottom, the relative transit time.

The simulation results show patterns that are not present in the measurement. This is to be expected since the measurement does not provide the parameters for a location on the photocathode but rather the average response from different spots that are illuminated due to the reflections on internal components. However, the scans are implemented in Geant4 as if they *were* the actual response of a particular photocathode location. Extracting the response parameter with less influence from reflection would require scanning the photocathode with a beam from at least two different angles. This way, two spectra would be available for each position, each with different contributions from reflections, and thus, in principle, a non-degenerate data set. With the current setup, this is not possible.

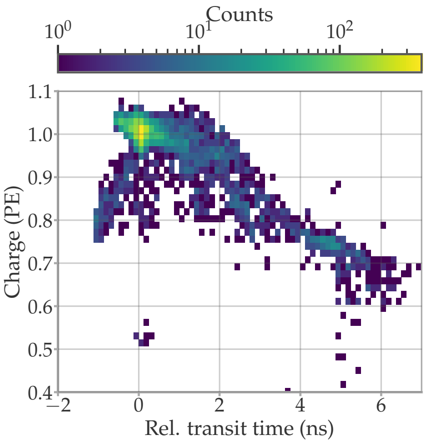

Figure 9.29: Mean charge against the mean transit time calculated from a simulated scan. To be compared with the left side of Figure 7.21.

However, the simulation scans generally reproduce the measurement well. Furthermore, the correlation between charge and transit time is simulated correctly, as shown in Figure 9.29 (cf. right side of Figure 7.21). Moreover, the arrival time distributions for the PMT being illuminated with plane waves are also well reproduced by the simulation. Figure 9.30 shows the time distribution produced by a tilted and frontal plane wave, as well as for a collimated beam illuminating the centre of the PMT. The results are consistent with the measurements.

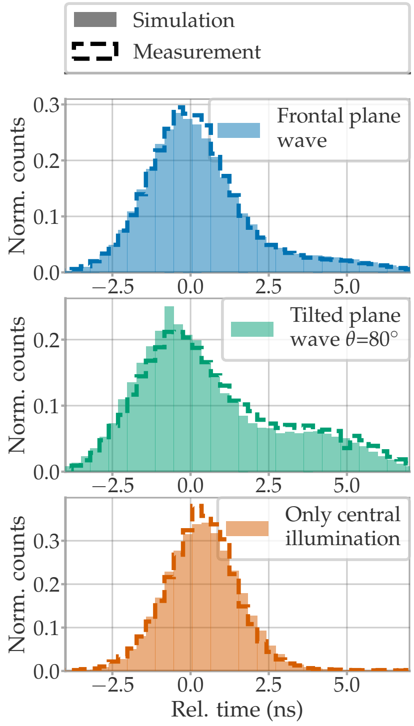

Figure 9.30: Transit time distribution for a simulated plane wave (frontal and with an 80° angle with respect to the tube axis) covering the entire PMT and a collimated beam of 1 mm radius illuminating the centre of the PMT. To be compared with the measurement results presented in Figure 6.25 and Figure 7.20.

9.3.5 Effects on mDOM effective area

During the mDOM development, its sensitivity was optimised by simulating the optical properties of various materials and by altering the geometry and positioning of the mechanical components, such as the reflectors (see [108, Sec. 10.4.2]). The metric to optimise the module's sensitivity was the effective area $A_{\mathrm{eff}}(\theta,\phi)$. This represents the area that is detected from a plane wave of incidence angle of θ (zenith) and ϕ (azimuth) with respect to the module. This parameter is calculated with Geant4 by simulating a disk emitting mono-energetic photons perpendicular to its surface with a uniform density profile (see Figure 9.31). After simulating N photons from a plane of area A_{rad} (which has to be larger than the projected area of the mDOM), the effective area is calculated as

$$A_{\mathrm{eff}}(\theta,\phi) = \frac{N_{\mathrm{det}}(\theta,\phi)}{N} \cdot A_{\mathrm{rad}}, \tag{9.4}$$

where N_{det} is the number of photons detected by the module. To optimise the sensitivity over multiple directions, $A_{\mathrm{eff}}(\theta,\phi)$ is calculated for various angle pairs, and the mean effective area, $\overline{A}_{\mathrm{eff}}$, is determined. The n angle pairs are chosen using *Healpy*, which separates a sphere into n pixels of equal area. Thus,

$$\overline{A}_{\mathrm{eff}} = \frac{1}{n}\sum_{i=1}^{n} A_{\mathrm{eff}}(\theta_i,\phi_i). \tag{9.5}$$

Since the effective area is wavelength dependent, the calculation must be repeated for different wavelengths, typically from 300 nm to 700 nm. Shorter wavelengths are absorbed by the pressure vessel, whereas the QE of the PMT approaches zero at longer wavelengths.

[108]: Classen (2017), *The mDOM - a multi-PMT digital optical module for the IceCube-Gen2 neutrino telescope*

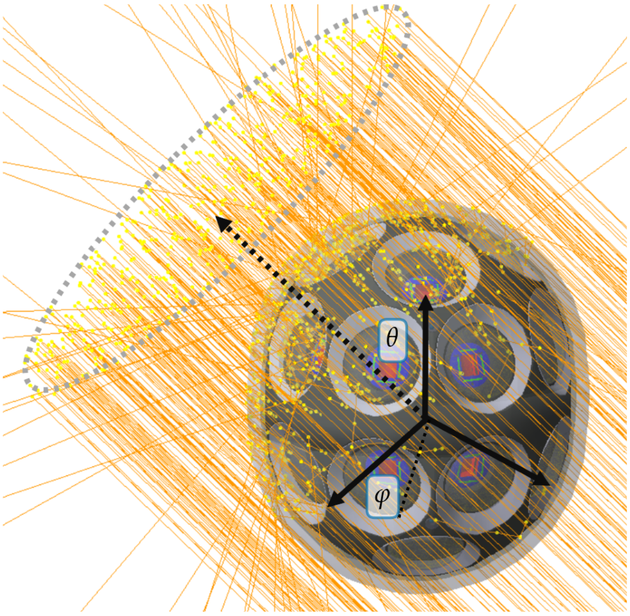

Figure 9.31: Screenshot of an mDOM illuminated by a disk emitter simulating the incidence of a plane wave from the direction θ (zenith) and ϕ (azimuth) using the Geant4 visualiser. The photon trajectories are represented by orange lines, and yellow dots mark the locations of physical interactions.

This simulation was carried out with an mDOM in an ice environment, once using the simplified PMT geometry and once with the model using internal reflections. The mDOM average effective area $\overline{A}_{\text{eff}}$ for different simulated wavelengths is shown in Figure 9.32. The 'new' model includes internal reflections, and the 'old' model is the simplified PMT model discussed in Section 9.1.3. The use of the new geometry leads to a sensitivity improvement of approximately 22%. The increase is expected, as the sensitivity studies in [108, Sec.10.4.2] were intentionally conservative. In Section 6.4.1, it was noted that the QE is measured by illuminating the centre of the PMT in order to minimise the impact of internal reflections and obtain the closest value to the 'true' QE of the photocathode. The simplified model weighs hits using a QE curve measured in this way (the curve shown in Figure 9.21), so the boost in sensitivity from internal reflections is not taken into account. As a result, the new PMT model provides a more accurate calculation of the real effective area of the mDOM.

It is also important to consider the simulation time when using the new model. Due to the requirement for simulating photons in a more complex geometry, simulations take approximately ~29 % longer when using the new model compared to the older one. Additionally, if the class with random sampling and interpolations of the transit time and charge is used (as introduced in Section 9.3.4), the simulation time increases by another ~3 %. Therefore, in studies where the simulation of the transit time, charge, and highest efficiency accuracy are not crucial, using the older model may still be beneficial if simulation time is of concern.

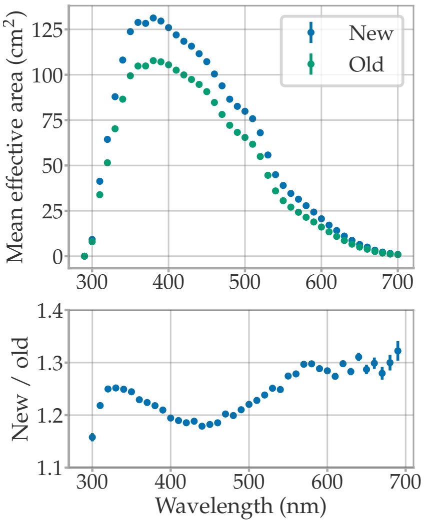

Figure 9.32: Mean effective area at different wavelengths for an mDOM in ice using PMTs of simplified geometry (old) and the model including internal reflections (new). The bottom plot presents the ratio between the areas of the two models.

[108]: Classen (2017), *The mDOM - a multi-PMT digital optical module for the IceCube-Gen2 neutrino telescope*

mDOM module Characterisation and Simulation

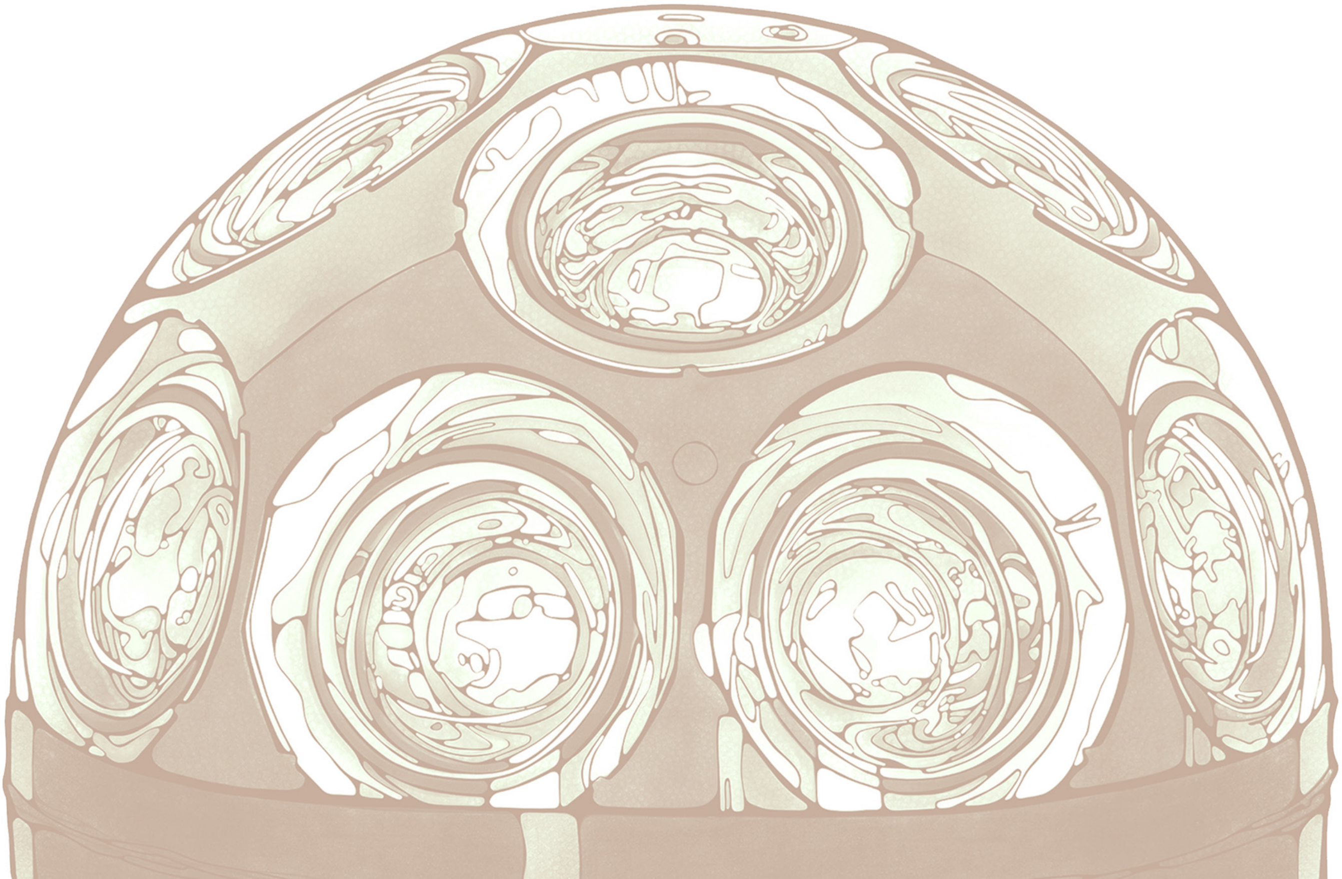

10

Testing the mechanical design of the mDOM

The design of the pressure vessel and the internal 3D printed support structure were introduced in Section 4.1. As explained then, the main role of the pressure vessel is to protect the inner components from the environment while allowing for the transmission of photons to the PMTs. It is also required to withstand pressures up to 700 bar. The pressure tests performed to verify the design are presented and discussed in Section 10.1.

The support structure fixes the PMT and calibration devices in their position and provides a mounting surface for the mainboard. It is also the boundary limiting the liquid gel entering the module during the module's production. The thermal expansion coefficient of the print material, polyamide (PA12), is approximately one order of magnitude larger than that of glass. The thermal stress created after the module is cooled has to be sustained by the gel layer connecting the support structure and the pressure vessel. This caused ruptures and delaminations on the first prototypes built. Therefore, the design of the support structure and the assembly method of the mDOM had to be optimised several times to ensure that the gel layer was not damaged after freezing. The thermal stress studies are presented in Section 10.2.

10.1 Pressure tests

The pressure vessel must withstand enormous pressures from the environment. On the one hand, there is the hydrostatic pressure of ~200 bar due to the weight of the water at the deployment depth. On the other hand, there are also peak pressures of up to ~690 bar when the boreholes refreeze [2]. This is due to the positive gradient of temperature with depth, causing the water to begin to freeze from the surface down the length of the hole, building up pressure.

Although during the design process of the pressure vessel, care was taken to calculate and simulate the stability of the pressure vessel with a reasonable margin of safety (see [108, Ch. 8]), a pressure test of the vessels is mandatory. Several tests were carried out with the hyperbaric test chamber at Nautilus GmbH. In the first circumstance, only the glass container was tested and is described in Section 10.1.1. The vessel was empty of any other components of the mDOM and, as such, did not verify the entire design, but this was important to measure the elasticity of the module and confirm the simulation studies carried out in [108].

[2]: Aartsen et al. (2017), *The IceCube Neutrino Observatory: Instrumentation and Online Systems*

[108]: Classen (2017), *The mDOM - a multi-PMT digital optical module for the IceCube-Gen2 neutrino telescope*

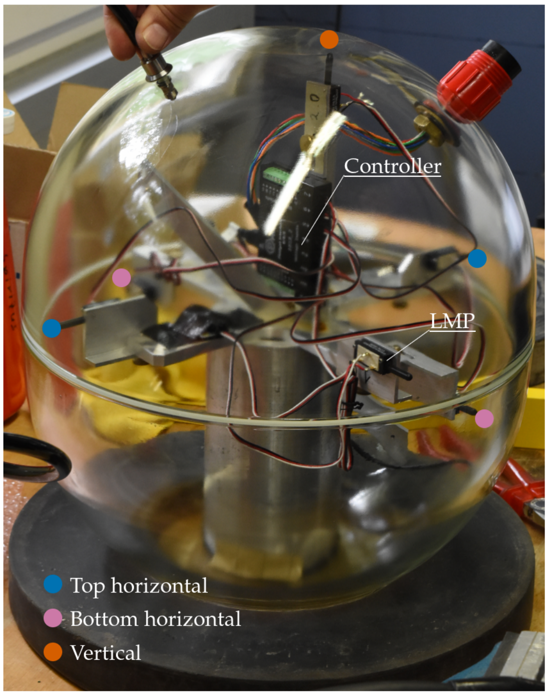

Figure 10.1: Photo of an mDOM pressure vessel with the deformation logger inside. The circles mark the approximate positions where the LMPs touch the pressure vessel.

As introduced in Section 4.2, the Design Verification Test (DVT) of the mDOMs also envisages a pressure test of several modules. The pressure test of one of the DVT modules is described in Section 10.1.2.

10.1.1 Pressure vessel with deformation logger

The first tests were carried out in 2018, in which three consecutive increases and decreases in pressure were performed with a single vessel. Also of interest was the measurement of the behaviour of the glass under these extreme conditions. In the scope of [108] a deformation measurement device was designed and constructed in cooperation with the IceCube group of DESY-Zeuthen. In the framework of this thesis, the deformation logger was calibrated, and the data acquisition during the pressure test and its analysis was carried out. The following section presents a brief description of the device and its calibration.

[108]: Classen (2017), *The mDOM - a multi-PMT digital optical module for the IceCube-Gen2 neutrino telescope*

Pressure vessel deformation logger

The deformation logger consists of several Linear Motion Potentiometers (LMPs) attached to a metal frame. A picture of this device inside the pressure vessel is shown in Figure 10.1.

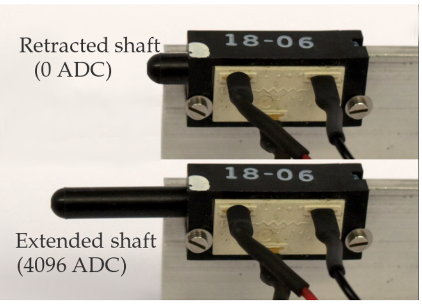

Figure 10.2: Picture of a fully retracted and fully extended LMP.

An LMP is a potentiometer with an electrical resistance that is proportional to the indentation of the retractable LMP shaft. The LMPs were attached to a controller[1], which provides a 5 V output voltage to the LMPs and digitises the voltage drop. The ADC output of the controller ranges from 4096, for a fully extended shaft to 0, for a fully retracted shaft (see Figure 10.2). With an LMP shaft length of 12.5 mm, the dynamic range of the board achieves a digital resolution of ~3 µm. The controller is

[1] PhidgetInterfaceKit 8/8/8

connected to a modified DOM-PCA, which provides a USB cable to the inside of the module, and on the outside it is ultimately routed to a computer after several adapters.

To calibrate the LMPs and test their linearity, the 3D scanner introduced in Section 7.1 was used. The LMPs were attached to the scanner, and the shaft was pressed against a flat surface perpendicular to it. The board output was recorded with increasing indentation, resulting in the data shown in the upper plot of Figure 10.3. The results of each LMP were fitted with a linear function. The relative difference between the fit and the data is displayed in the lower graph of Figure 10.3. It can be seen that the best linearity is achieved at mid-indentations and that, especially in the vicinity of a fully extended shaft, the linearity is worst, reaching deviations of more than 15 %. This is probably caused by the wiggle room available for the shaft to move at different angles from the normal vector to the wall and is not a problem of the resistor itself. Therefore, caution must be taken during the use of these devices to measure around the intermediate shaft indentation, where the deviation from the linear behaviour is always less than 0.75 %. In this region, all sensors have a similar response, with an average slope of $-3.08\,\mu\text{m/count}$ and a standard deviation of $0.03\,\mu\text{m/count}$ between all measured LMPs.

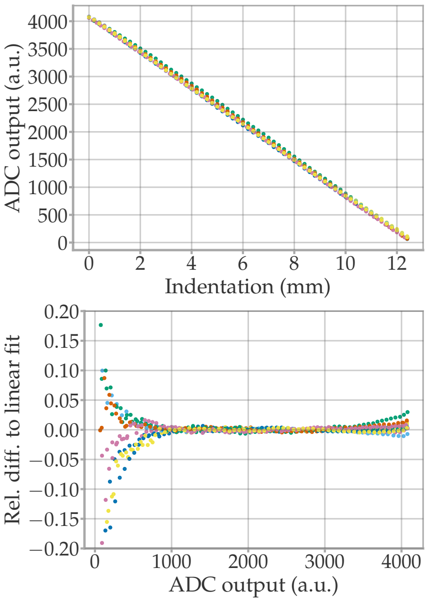

Figure 10.3: Calibration of the LMPs used. *Top:* ADC output from the LMPs controller against the indentation of the LMP shaft. *Bottom:* Relative difference between the data and the linear fit.

Pressure tests

At the cylindrical part of each half-sphere, two sensors were placed at the same height but radially opposed. Therefore, the sum of the horizontal LMP pairs is a reasonable estimate of the total reduction in diameter of the equatorial region. Furthermore, one sensor pointed in the zenith direction. Since the pressure logger was fixed on the bottom half of the pressure vessel, the output of the zenith sensor is already a sum of the deformation of both half-spheres and, as such, an estimation of the total diameter reduction along the zenith axis.

The hyperbaric chamber can be programmed with pressure profiles that set the desired pressure over time. Three pressure tests with different profiles were performed. In each case, the pressure is increased at different rates until a maximal pressure is reached, whereafter, the pressure is decreased, mirroring the curve used during the rump-up. The first test profile, in the following called *Profile 300*, started with an increase of 20 $\frac{\text{bar}}{\text{min}}$ until it reached an end pressure of 300 bar. The second, *Profile 700*, started with a steeper slope of 30 $\frac{\text{bar}}{\text{min}}$ for 10 min, then the rate was reduced to 20 $\frac{\text{bar}}{\text{min}}$, until reaching a maximum pressure of 700 bar. The last profile was for a long-term test of a total of 4.7 d, with comparatively shallow pressure slopes. The pressure was increased by 3.5 $\frac{\text{bar}}{\text{min}}$ until 300 bar, where the pressure was maintained for 23 h. Subsequently, the pressure increased at 15.75 $\frac{\text{bar}}{\text{h}}$ until it reached 700 bar. The actual applied pressure, measured by the hyperbaric chamber, is shown in Figure 10.4 for the three profiles.

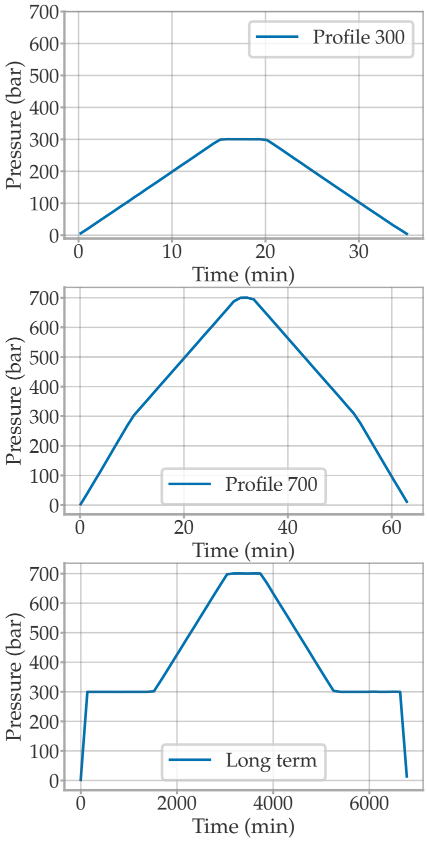

Figure 10.4: The actual pressure profile of the tests performed as measured by the hyperbaric chamber.

The output of all sensors during the three tests is shown in Figure 10.5. Here, the pressure profiles are reflected in the data, from which a shrinkage of the pressure vessel proportional to the applied pressure can be deduced.

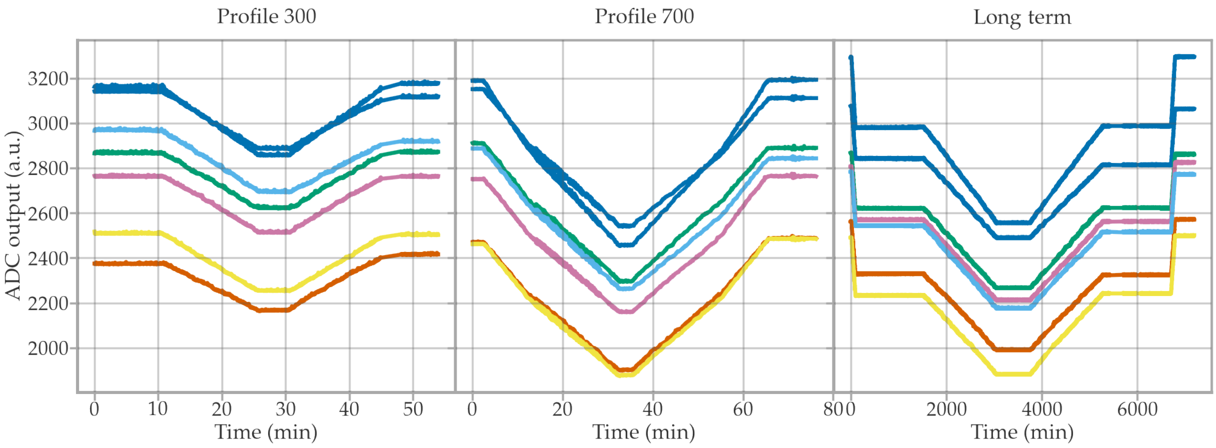

Figure 10.5: ADC output of the LMPs during the three pressure tests. Each colour shows the output of a different LMP. The pressure profiles in Figure 10.4 are reflected in the data due to the elastic shrinkage of the pressure vessel.

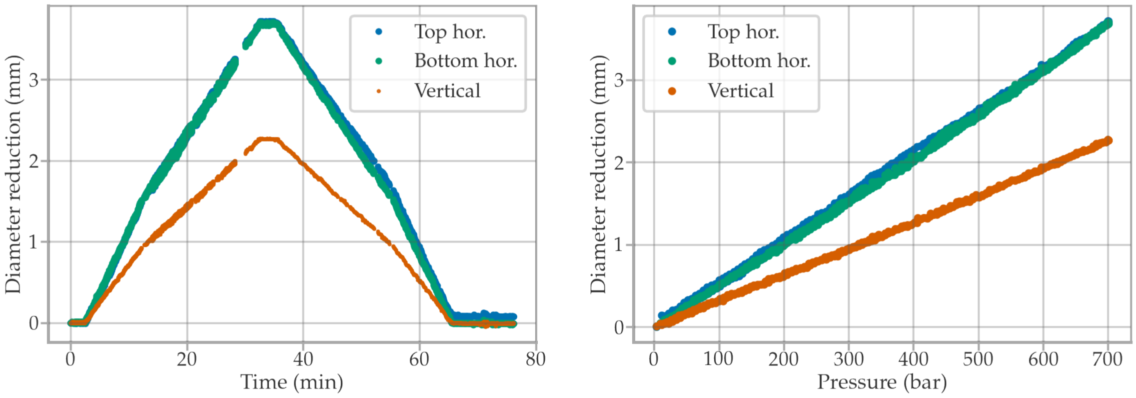

Figure 10.6: Diameter reduction of the pressure vessel in the equatorial region for the top and bottom half-spheres and along the zenith of the vessel for the pressure test following Profile 700. *Left:* deformation against time. *Right:* deformation against pressure.

The ADC values were always between 1900 and 3300, which are in the linear region of the resistors (see the bottom plot of Figure 10.3).

The raw LMP data were translated into total indentation using the calibration shown in Figure 10.3. The results of the sensor pairs along the horizontal were summed to obtain the total diameter reduction. The left side of Figure 10.6 presents the results for Profile 700. Both half-spheres show a very similar behaviour along the equatorial, with a maximal deformation of (3.692 ± 0.003) mm at the 700 bar plateau. The diameter reduction along the poles of the pressure vessel is much lower during the entire test, with a maximum diameter reduction of (2.264 ± 0.002) mm. The right side of Figure 10.6 shows the same data on diameter reduction, but versus the pressure inside the chamber, rather than time. A near-perfect linear behaviour can be observed for the three lines, implying that the deformation was always elastic during the increase and decrease of the pressure. The data from Profile 300 and the long-term measurement show the same behaviour.

The reduction in diameter as a function of pressure of the three tests was fitted with a linear function, and the resulting slopes are listed in Table 10.1. Most of the values do not agree within their uncertainties.

	Hor. bottom ($\frac{\mu\text{m}}{\text{bar}}$)	Hor. top ($\frac{\mu\text{m}}{\text{bar}}$)	Vertical ($\frac{\mu\text{m}}{\text{bar}}$)
Profile 300	5.162 ± 0.009	5.124 ± 0.011	3.119 ± 0.009
Profile 700	5.221 ± 0.005	5.237 ± 0.007	3.219 ± 0.004
Long term	5.237 ± 0.009	5.034 ± 0.016	3.219 ± 0.005

Table 10.1: Slope of the linear reduction in diameter in the equatorial region of the bottom and top half sphere (*"Hor. bottom"* and *"Hor. top"*), and along the zenith of the module (*"Vertical"*), calculated from the three pressure tests. Uncertainties are the fit errors.

These systematic variations are probably caused by the LMPs not being completely normal to the vessel wall. Due to the wiggle room of the shaft, the angle to the wall may change after moving the module. The average shrinkage rate for the cylindrical region of the pressure vessel is (5.152 ± 0.004) µm/bar and for the spherical region, measured by the vertical sensor, (3.185 ± 0.004) µm/bar. The standard deviation of the horizontal deformations is 0.09 µm/bar and vertical 0.05 µm/bar, which can be understood as a systematic error caused by the wiggle room of the shaft position against the pressure vessel.

These results agree qualitatively well with the calculations performed in [108], although the model overestimated the horizontal deformation: the expected diameter reduction at 700 bar was calculated with Lamé equations to 4.6 mm in the cylindrical region of the pressure vessel and 2 mm in the spherical section.

[108]: Classen (2017), *The mDOM - a multi-PMT digital optical module for the IceCube-Gen2 neutrino telescope*

10.1.2 Pressure testing DVT 04 - Rapunzel

Although the last section showed that the pressure vessel is capable of resisting high pressures, whole mDOMs also have to be tested. Here, it is important to check whether the shrinkage of the module causes problems with the internal components of the module. Thus, for example, a visual inspection is performed before and after the pressure test to observe if any ruptures or delaminations in the gel layer occur or if any of the reflectors jump out of their position. Furthermore, so-called functional check-outs (FC) are performed before, during, and after the test to verify the correct functioning of all electronics and sensors.

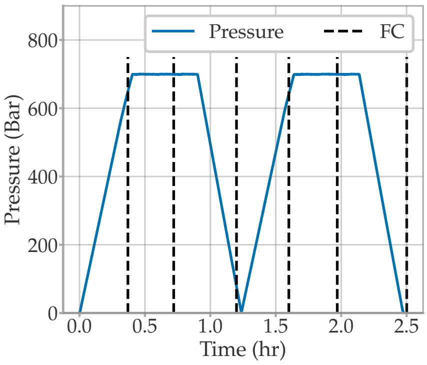

Figure 10.7: Pressure profile as measured by the hyperbaric chamber during the DVT-04 pressure test. The dashed lines mark the start of an FC, each taking ~10 min.

The first DVT tested was DVT-04, also known as *Rapunzel*[2], on December 2021. The pressure profile measured by the hyperbaric chamber is shown in Figure 10.7. During the test, six FCs were performed at times marked in the figure. Each FC involved the following tests:

- Mainboard's DDR3 memory test (read/write).
- Readout of all mainboard sensors (light sensor, temperature, pressure, and magnetometer).
- Calibration of all ADCs.
- Upload of a dummy FPGA firmware file, read back, and erase the file again.
- Discriminator threshold scan of each PMT's AFE.
- Testing of the AFE Pulser saving triggered waveforms.
- Test of the flasher chains. This involves calibrating the LED chain voltage and measuring the PMT pulses produced by the LED light.
- PMT performance is tested by measuring the SPE charge distributions of all PMTs with the flashers.

[2] At the date of testing, the mainboard FPGA firmware was 0x1F, the ICM firmware 1535, and Iceboot version x36. The mainboard was version Rev2.

- Taking a picture with each camera with the illumination LEDs of the camera board turned on.

The original FC test suit also contained an upload and flash of the µBase firmware of every PMT. However, this test was skipped, as flashing was prone to fail with the FPGA firmware used at the time, producing long delays in the FCs. A single FC took around 10 min. During the rest of the time, the dark rate of each PMT was measured, as well as the mainboard temperature and pressure sensors.

The internal pressure and temperature given by the mainboard are shown in Figure 10.8. The temperature increases as a result of the heat produced by the electronics, forming a plateau at ~29.5 °C that almost reached thermal equilibrium. The internal pressure mirrors the outside pressure due to the shrinkage of the module, as expected from the ideal-gas law. It also features a slope toward higher pressures with time, as a result of the increase of the internal temperature, also expected from the ideal-gas law.

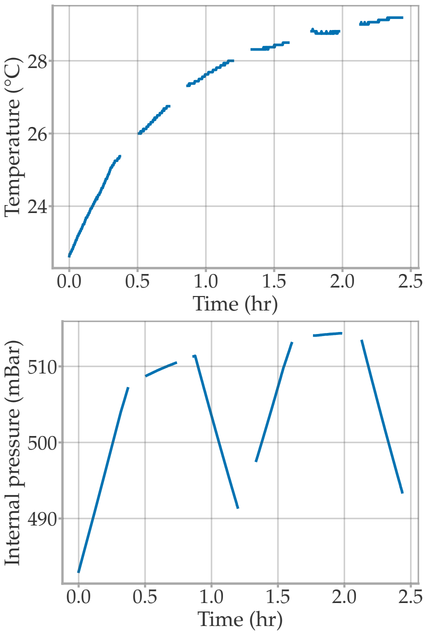

Figure 10.8: Internal temperature (*top*) and pressure (*bottom*) measured by the mainboard during the pressure test. During the FCs, the data were not taken, leaving blank spaces.

The dark rate of the 24 PMTs is shown on the left side of Figure 10.9. As a result of exposure to light from the environment, the PMTs initially featured a very high dark rate, which decreased exponentially with time. After the fifth and sixth FC, the hyperbaric chamber camera and its auxiliary light were turned on to visually inspect the module. This excited some of the PMT channels that started again at a higher dark rate level, as can be seen in Figure 10.9 at time ~1.7 h and ~2.1 h.

All FCs produced similar results, without any unexpected behaviour. As an example, the combined SPE distribution of all PMT channels measured in each FC is shown on the right side of Figure 10.9, where no significant differences can be observed.

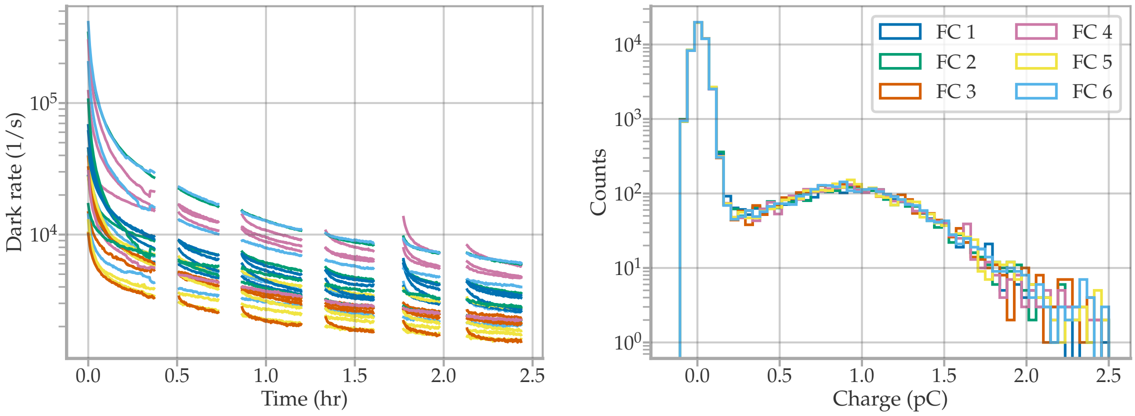

Figure 10.9: *Left:* Dark rate of all PMT during the pressure test. While a FC is run, the rate was not measured, leaving blank spaces. *Right:* Combined SPE spectra of all PMTs measured in each FC.

Figures 10.8 and 10.9 show that both the PMT and the mainboard functioned throughout the pressure test. Furthermore, since no abnormalities were found in the data or after visual inspections of the module, the test was considered successful. In April 2022, a second module was successfully tested, DVT 08 *Schneewittchen* [177], further increasing the certainty that the mDOMs will be able to withstand high pressures after deployment.

[177]: Kappes (2022), *mDOM Pressure Test (presentation)*

10.2 INTERNAL THERMAL STRESS

The gel is the main component that holds the entire inside of the module in place. It must compensate for vibrations during transport, shrinkage of the pressure vessel after deployment, and any thermal expansion or contraction of the support structure.

Early tests with mechanical prototypes of the mDOM performed in the scope of this thesis showed that the thermal stress was too large for the soft gel. The gel layer of these modules tore at temperatures around 0 °C, too high compared to the chilling temperatures found at the South Pole (see Figure 10.10). This initiated a campaign to improve and redesign the support structure and change the optical gel type.

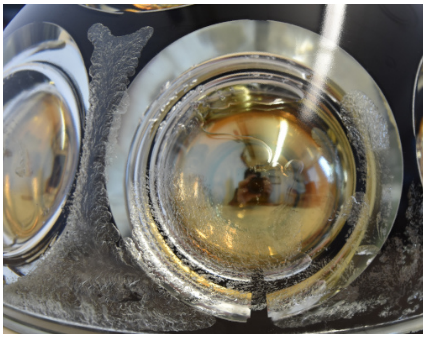

Figure 10.10: Aftermath of cooling one of the first mechanical prototype. The gel breaks and delaminates as a result of thermal stress.

The change in gel type was very important to solve the thermal stress problem. Measurements of gel properties are described in Section 10.2.2.

All modifications were tested with prototype half-modules, *demonstrators*, which contain all mechanical components of an mDOM that are in contact with the gel layer. The demonstrators were placed in a fridge at −60 °C[3] and monitored with cameras for weeks. A summary of the observations from the demonstrator studies is given in Section 10.2.3.

To better understand the changes in the support structure, the next subsection briefly describes the original design.

[3] At depths where the mDOM is going to be deployed, the lowest temperature is ∼−40 °C. However, the test temperature was set lower for a higher safety factor

Early support structure design

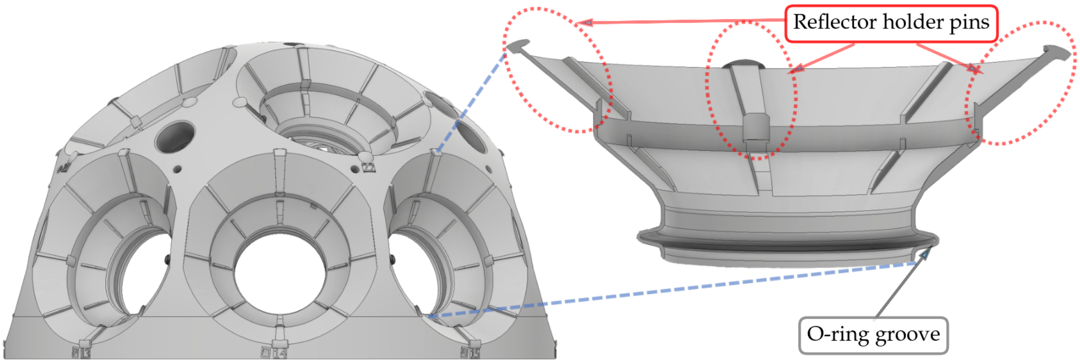

Figure 10.11: CAD rendering of the support structure design used for the first demonstrators. On the right side, a zoom-in over the cross section of a PMT cup. The reflectors were attached to the pins of the support structure.

Figure 10.11 shows the CAD rendering of the support structure used for the first demonstrators, which was based on the KM3NeT design. The model was 3D printed with an SLS printer using PA12 as the source material.

The reflectors were mechanically fixed in place by pins in the support structure. In this early model, there were four pins for each reflector, although this number was increased in subsequent designs. Ultimately, these pins were removed and the reflectors are glued to the support structure.

This structure was very rigid, with a wall thickness of 2 mm and other design characteristics that were deliberately added to increase structural stability. For example, in the equatorial region, the cylinder terminated on a ring, greatly reducing the flexibility of the support structure to move radially. Furthermore, the cones of the equatorial PMTs were firmly united with rectangular flaps, which were intended to hold cables from the different devices. These two components can be seen in Figure 10.12.

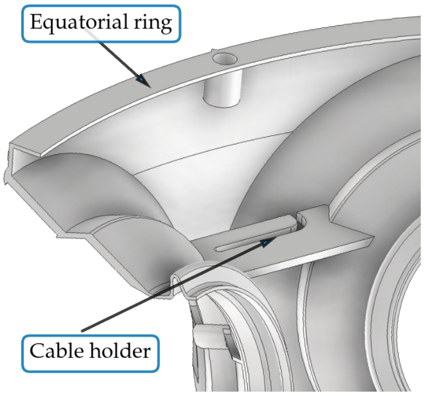

Figure 10.12: Partial view of the internal region of the early design of the support structure. The edge of the equatorial region terminated with a ring and a cable holder united the equatorial PMTs.

This early design had to be improved to reduce the thermal stress. Several of the changes in the support structure were based on finite element analysis studies performed within the scope of this thesis, which are introduced in the next section.

10.2.1 Finite element analysis

To study which design changes would be most appropriate, a finite element analysis (FEA) was performed with a simplified version of the module. The final element method is a numerical approach to solving partial differential equations (PDEs) constrained by boundary conditions. This is a 'divide-and-conquer' approach, where a large system, such as a complicated geometry, is separated into smaller finite elements by constructing a mesh of the object. This discretisation approximates the PDEs with a set of numerical equations, the solution of which is, in turn, an approximation of the real solution of the PDEs. This method is used in different software for a wide range of applications. For this work SimScale [178] was used, which is capable of simulating thermomechanical boundary conditions.

[178]: SimScale GmbH (2020), *SimScale: Simulation Software Engineering in the Cloud*

The first simulated geometry was a half-module with the correct dimensions of the pressure vessel but a simplified support structure consisting of a plastic shell following the shape of the vessel. Between this shell and the vessel, a gel layer of 3 mm was placed. The cross section of the geometry is shown in the picture on the left of Figure 10.13. The properties of the material applied to the three volumes are listed in Table 10.2.

Table 10.2: Material properties defined in the FEA studies. Values obtained from the manufacturers. κ is the thermal expansion coefficient, E Young's modulus, and ν the Poisson's ratio.

	κ (K^{-1})	E (MPa)	ν
Glass	3×10^{-6}	6.3×10^{4}	0.2
Gel	3×10^{-4}	0.4	0.49
PA12	10−4	1800	0.4

In the FEA study, the steady state solution was simulated after changing the temperature with a $\Delta T = -80\,°\mathrm{C}$. The software provides several output parameters, such as the stress and strain tensors at the mesh nodes of the simulated volumes.

Standard yield criteria for ductile materials, such as the von Mises yield criterion, are based on the stress tensor. Since the tensor components depend on the coordinate orientation, the matrix is diagonalised, which is always possible because of its symmetry [179]. The components on the diagonal, σ_i, are called the principal stresses and are independent of the orientation of the system. Yield criteria are based on σ_i, such as in the case of the von Mises yield criterion, which is defined as

[179]: Yang (1980), *A Generalized von Mises Criterion for Yield and Fracture*

$$k^2 = \frac{1}{2}((\sigma_1 - \sigma_2)^2 + (\sigma_2 - \sigma_3)^2 + (\sigma_1 - \sigma_3)^2).$$

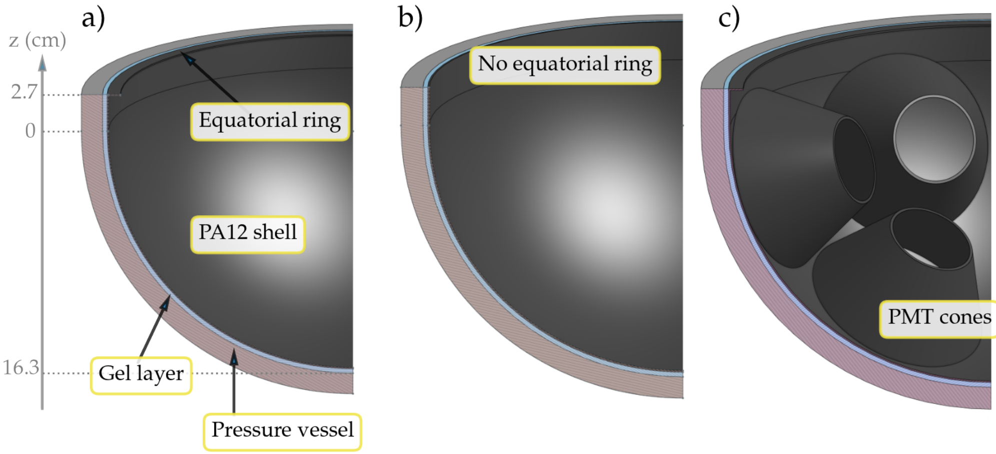

Figure 10.13: Rendering of one quarter of the simulated half-module for the FEA studies. **a)** the default basic geometry with only three layers representing the pressure vessel, the gel layer and the PA12 shell, including the equatorial ring for the structural integrity of the initial support structure design (see Figure 10.12). **b)** same configuration as a), but without the equatorial ring. **c)** same configuration as a), but with cones resembling the PMT cups (see Figure 10.11).

The calculated von Mises yield of an FEA analysis can be compared to the critical value k at which a certain material yields to verify whether the system is sufficiently resilient.

Elastomers are usually better described in the strain space [180]. In this case, the same approach is taken, but with the strain tensor. Thus, after diagonalisation one obtains *principal strains* ε_i. Different criteria using ε_i can be found in the literature; most of them are directly analogous to the criteria in the stress space [180, p. 111]. Which criterion is best suited depends on the material studied. In this context, no material found in the literature matches the properties of the gel entirely, and several criteria were tested with the simulation results. These deviate numerically, but qualitatively point in the same direction. Furthermore, since there is no reference critical value for the gel to compare the results with, which criterion is taken is not important for the current study[4]. Therefore, the simulation results are presented below with the criterion

[180]: Rosendahl (2020), *From bulk to structural failure: fracture of hyperelastic materials*

$$\overline{\varepsilon} = \sqrt{\epsilon_1^2 + \epsilon_2^2 + \epsilon_3^2}, \tag{10.1}$$

which is referred to as the average true strain criterion [180, p. 111]. Equation 10.1 is calculated for the simulation output at each node in the gel volume mesh. Since the geometry is radially symmetric, the strains are averaged along the z-axis in 1 mm steps. The coordinates are shown in Figure 10.13, where $z = 0$ mm is the boundary between the spherical ($z < 0$) and conical ($z > 0$) regions of the pressure vessel.

With the true strain criterion as a metric, it is possible to simulate different geometries of the simulation volume and test which changes can decrease the thermal stress inside the mDOM.

The first parameter studied was the thickness of the PA12 shell. Figure 10.14 shows the average true strain criterion for a support structure of wall thickness 0.5 mm, 0.75 mm, 1 mm and 2 mm. The largest strain is found in

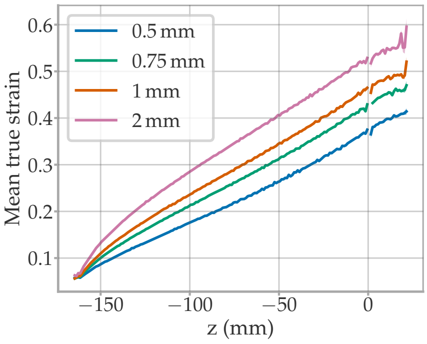

Figure 10.14: Mean true strain $\overline{\varepsilon}$ against height z for a PA12 shell of different wall thicknesses.

[4] Furthermore, the conclusions made in this section are also obtained when working with the stress tensor.

the equatorial region, which is expected, because in the equatorial plane the contraction of the shell pulls the gel to the centre. The shrinkage in the z direction can be partially compensated for, as the support structure can move in this direction with the gel. This also agrees with the tests of half modules in the cold, where the largest delaminations are found in the equatorial region (see Figure 10.10). In Figure 10.14 it is also clear that the thinner the support structure is, the smaller the expected strain.

A thinner support structure means greater flexibility. Therefore, the equatorial ring, which was initially designed to increase the structural integrity of the support structure, may be a contributor to thermal stress. This was tested by simulating the shell without the ring (Figure 10.13b). In this case, a finer mesh was used, since the results on the vertical edge varied greatly with the coarse mesh. The resulting strain curve is presented in Figure 10.15. For low z the results are similar until $z \sim 24$ mm, where the structure with the equatorial ring has up to ~ 50% larger strain.

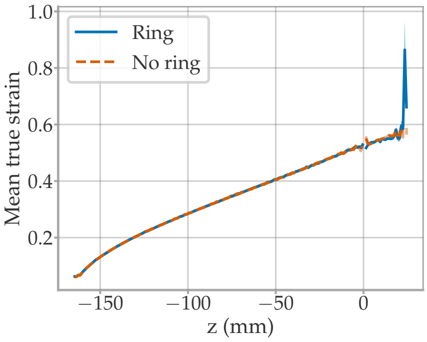

Figure 10.15: Mean true strain $\overline{\varepsilon}$ against height z for the PA12 shell with and without an equatorial ring (cf. Figure 10.13 a) and b))

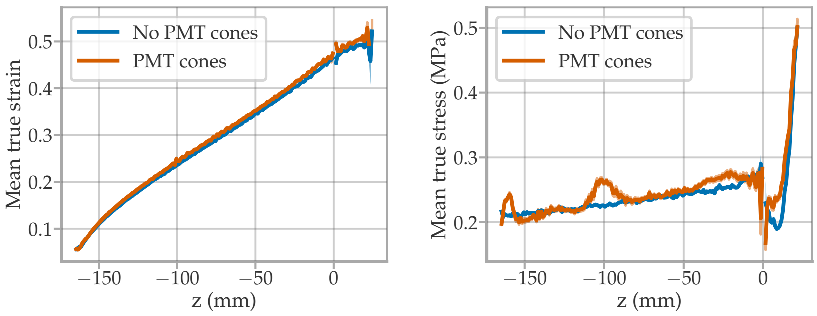

Figure 10.16: Comparison of a PA12 shell with and without PMT cones (cf. Figure 10.13 a) and c)). Mean true strain $\overline{\varepsilon}$ (*left*) and the mean true stress (*right*) against height z.

The geometry used until now is relatively simple. To test whether the cups that hold the PMTs in the support structure also increase stability and thermal stress, they were modelled as basic cones, with the same opening angle and length. The cross section of the geometry can be seen in Figure 10.13 c). The resulting true strain curve is shown on the left side of Figure 10.16. Here, only a slight increase is found compared to the simpler design. However, the effects of the PMT cones are more noticeable when using the mean true stress $\sqrt{\sigma_1^2 + \sigma_2^2 + \sigma_3^2}$ instead of the strain, as seen on the right side of Figure 10.16. Nevertheless, in the equatorial region, where the largest stress is found, no significant differences are observed between the two geometries. This shows that components of the support structure that do not cover large areas probably do not affect the strain as much as, for example, the equatorial ring.

The thickness of the gel layer can be varied indirectly by reducing the diameter of the support structure. The strain curve for a gel layer of 3 mm, the baseline value for the shortest layer thickness in the initial mDOM design, to 10 mm is shown in Figure 10.17. It is clear that a larger gel layer reduces the average true strain. This result is not difficult to understand: The strain is the relative change in length, and since the thermal shrinkage of the plastic shell is constant, increasing the layer thickness directly reduces the strain. The largest $\overline{\varepsilon}$ reduction is therefore in the first step

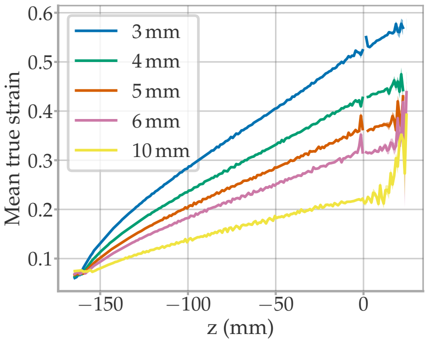

Figure 10.17: Mean true strain $\overline{\varepsilon}$ against height z for different gel layer thicknesses.

from 3 mm to 4 mm, and further increasing the layer thickness reduces the strain in smaller proportions.

However, this is not true for the region $z >\sim 15$ mm, where increasing the layer thickness further than 5 mm does not show large improvements. This can be partially explained by the coarse mesh of the simulated volume. However, it should be noted that the gel suffers a diagonal strain in this region as a result of the vertical movement of the structure toward the bottom of the vessel. This vertical component of the strain is not reduced by increasing the thickness of the layer, as this increase is on the perpendicular axis. The top of Figure 10.18 shows the average displacement in the z direction of the support structure. As expected, the largest deviation is at the very top of the shell and becomes smaller toward the bottom of the support structure, where the displacement is mostly given by the thermal contraction of the gel layer. This displacement has to be compensated for by the gel because the glass-gel and gel-shell boundaries are fixed in the simulation (and in reality if no delamination occurs). This is appreciable at the bottom of Figure 10.18, where the displacement is shown in scale with the simulated volume.

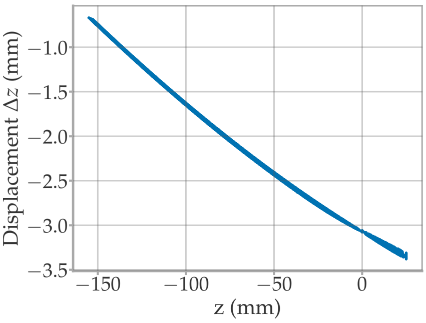

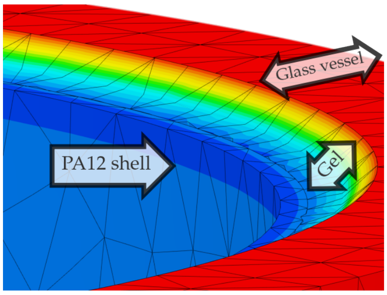

Figure 10.18: *Top:* vertical displacement Δz from the simulated plastic shell at different heights. *Bottom:* Rendering of the displacement effects on the gel layer at true scale. Since the contact boundaries of the gel are fixed, there is a diagonal strain. The colours indicate the displacement Δz, from $\Delta z = 0$ mm in red to $\Delta z = -2.5$ mm in blue.

The last test was related to the material of the support structure. At the time of the studies, there were several printing materials available. In addition to PA12, glass-enforced PA12 (PA12-GF) and polypropylene (PP) were also of interest. The former has a 30 % lower thermal expansion coefficient than PA12, but a larger Young modulus, while PP features a 10 % lower expansion coefficient and is very flexible. The properties used in the simulation are listed in Table 10.3. The true strain curve using the geometry of Figure 10.13c) with the different materials is shown in Figure 10.19. Both PA12-GF and PP show a smaller strain compared to PA12. The small Young's modulus of PP provides a larger improvement than the lower thermal expansion coefficient of PA12-GF. However, this is not the case between PA12 and PA12-GF, where, although Young's modulus is doubled, the strain is still strongly reduced due to its 30 % lower thermal expansion coefficient.

Table 10.3: Thermal expansion coefficient κ and Young's modulus E of the SLS printing materials studied. Values from the manufacturer.

	κ (K^{-1})	E (MPa)
PA12	10^{-4}	1800
PA12-GF	$7 \cdot 10^{-5}$	3600
PP	$9 \cdot 10^{-5}$	750

Summarising the observations, it can be concluded that the thermal stress can be reduced by

- increasing the flexibility of the support structure. This can be accomplished by reducing the wall thickness or eliminating structures that increase its stability.
- increasing the thickness of the gel layer.
- using an alternative printing material, with a lower Young's modulus and a lower thermal expansion coefficient.

Section 10.2.3 discusses how these conclusions were implemented in the mDOM design.

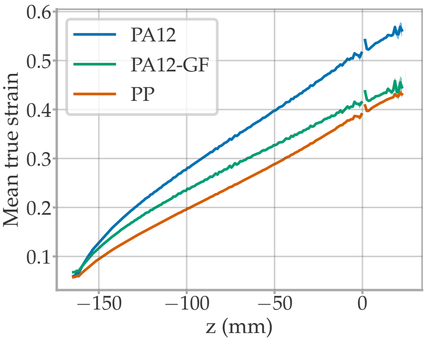

Figure 10.19: Mean true strain $\overline{\varepsilon}$ against height z for a plastic shell of different materials.

10.2.2 TESTING THE MECHANICAL PROPERTIES OF THE GEL

The first demonstrator, which failed at 0 °C (Figure 10.10), was built with the gel type used in the IceCube DOMs[5]. A second gel candidate was the one used in the KM3NeT modules, which, however, was shown to

[5] QSI QGel 900.

crystallise at around −35 °C and remain in a hard and opaque condition. Several gel brands commercially available in Germany were tested, but none had the desired mechanical and optical properties. The finally successful candidate was gel from Shin-Etsu, a Japanese company. This gel is used in D-Eggs and, as such, was well tested by IceCube colleagues.

The first test that has to be performed with any new gel candidate is its compatibility with the other mDOM components with which they come in contact. This is done by submerging samples of the mDOM components in freshly mixed liquid gel. Clear indications of incompatibility are uncured gel around the sample or yellowing of the gel over time. The Shin-Etsu gel was compatible with all mDOM components.

Table 10.4: Mechanical properties of three gel types from Shin-Etsu. Values provided by the manufacturer. E is the Young's modulus, ν the Poisson ratio, TS the tensile strength, and EB the elongation at break.

	A	B	C
E (MPa)	0.4	0.17	0.08
ν	0.49	0.49	0.49
TS (MPa)	0.2	0.2	0.2
EB (%)	—	520	840

There were different types of gel available from the same provider. They differed in their Young's modulus and elongation at break, but all other mechanical properties remained constant, as listed in Table 10.4. Young's modulus E measures the stiffness of a material when a load is applied along one axis. In a stress-strain curve, Young's modulus of the material determines the slope of the linear region

$$E = \frac{\sigma}{\epsilon},$$

where σ is the stress and ϵ is the strain. The strain describes the relative change in length along the studied axis and is therefore dimensionless. The stress is the applied force divided by the cross-sectional area of the sample (in this case, perpendicular to the load).

The Poisson's ratio ν describes the deformation of a material on the perpendicular axis relative to the direction of the applied force

$$\nu = -\frac{d\epsilon_{\text{transverse}}}{d\epsilon_{\text{axial}}},$$

where transverse and axial are the strains in the transverse and axial directions, respectively. As shown in Table 10.4, the Poisson's ratios of the studied silicon gels are all 0.49, which means that they are near incompressible[6].

The mechanical properties of the different types of Shin-Etsu gel were measured using the setup shown in Figure 10.20. PA12 samples were glued from one side to a screw and suspended in liquid gel to cure. The screw was attached to a load cell[7] while the gel recipient was fixed in position. The screw was pulled with a step motor while measuring the distance travelled by the screw with an LMP. The samples were pulled until they detached from the gel. Because a load-distance curve depends on the sample size and the amount of gel, the results were translated into a stress-strain dependence. The stress is calculated by dividing the load by the area of the sample, and the strain is calculated by dividing the distance by the thickness of the gel layer.

A typical stress-strain curve is measured by stretching a piece of material along one axis. Since the setup used in this section is different, and more factors are in play, one should not interpret the results as reflecting normed gel properties. On the one hand, the force is applied through a sample of PA12, which was cured in the gel. Thus, if the adhesion force

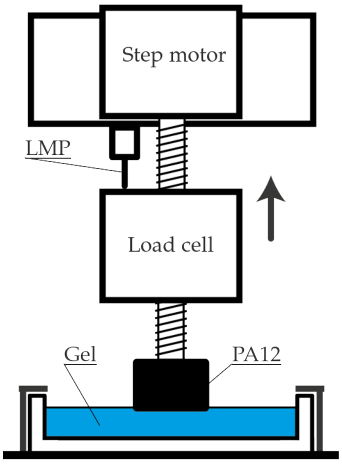

Figure 10.20: Sketch of the setup used to measure stress-strain curves.

[6] With $\nu = 0.5$, the volume of the material cannot be changed, and a shift in length along one axis has to be completely compensated by the perpendicular axis.

between the sample and the gel is less than the stress, the sample can partially or fully delaminate, and the stress-strain curve will not provide a true breaking point for the gel. On the other hand, only a portion of the gel is being stretched, not the whole volume, and therefore, there is a horizontal component to the stress, which is not the case in a standard stress-curve measurement.

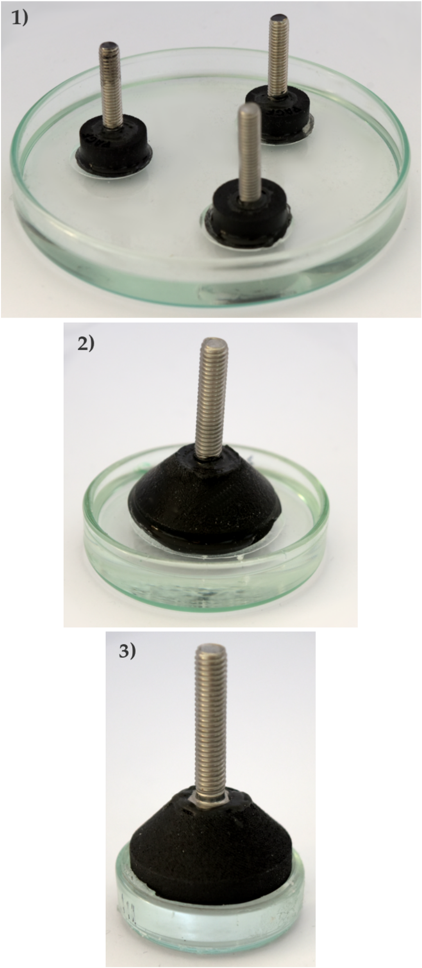

Figure 10.21: Photograph of the PA12 samples and Petri dishes used for measuring the stress-strain curves.

The first measurements were made with two different sample geometries. In one case, 11 cm Petri dishes filled with gel were used, each containing three PA12 samples of radius 10 mm (see picture **1)** in Figure 10.21). One such dish was assembled per gel type. In the second case, 5 cm Petri dishes containing a single PA12 sample of radius 15.5 mm were employed (see picture **2)** in Figure 10.21). In this case, two samples per gel type were measured.

The results are shown in Figure 10.22. The different gel types produce different slopes in the proportional region at the beginning of the stress-strain curve. The mean slopes are (2.4 ± 0.1) MPa, (0.88 ± 0.01) MPa and (0.34 ± 0.01) MPa for gel A, B and C, respectively. This is expected from the Young's moduli of the gel types (see Table 10.4).

In the case of gel A, the detachment was through delamination of the sample (see sample on the right of Figure 10.23). The delamination causes a steep reduction in stress at a strain of ∼0.1, while the plateau between 0.2 to 0.8 is caused by the resistance of the gel on the sides of the sample. From this, one can conclude that the adhesion of PA12 to the gel is ∼0.25 MPa. The samples in gel types B and C detached mainly by internal rupture of the gel layer (see sample on the left of Figure 10.23). This prolongs the plastic region of the curves and delays the complete detachment point. The gel C can be stretched further than B, reaching strains of ∼0.9 before complete detachment due to its improved elongation at break.

In the case of a simplified geometry, where the holding structure and the pressure vessel are spheres with a gel layer of constant thickness L between them, after a reduction of temperature of ΔT the gel would have to endure a strain of

$$\frac{\Delta L}{L} = \frac{\Delta T \cdot \kappa \cdot R}{L}, \tag{10.2}$$

where R and κ are the radius and thermal expansion coefficient of the support structure, respectively. For an mDOM-like case of $R = 160\,\mathrm{mm}$, $\Delta T = 60\,^{\circ}\mathrm{C}$, $\kappa = 1 \times 10^{-4}\,\mathrm{K}^{-1}$ and $L = 4\,\mathrm{mm}$ this results in a strain of 0.24. Interpreting the results naively would mean that gel C should easily meet the requirements. However, only a small area of the gel was stretched in the measurements, which resulted in partial compensation of the stress by the surrounding gel.

To simulate the more extreme case, where no gel can be moved to compensate for the stress, a sample was produced with an area slightly smaller than that of the gel reservoir (see picture **3)** in Figure 10.21). Because the gel cannot deform in the direction perpendicular to the load (since the mechanical bond between glass and gel is very strong), the results reflect the bulk modulus and not the young modulus. The bulk modulus K describes the resistance of a material to compression

7: Model DBBP-02.

following

$$K = -V\frac{dP}{dV},$$

where P is the applied pressure and V is the volume. Since the volume of the gel layer is directly proportional to its thickness and the stress is equal to the pressure, the initial slope in the curve should be directly proportional to the bulk modulus. The measured curves are presented in Figure 10.24. In this case, the stress increases faster to higher values, and all gel types show a similar slope. This is expected from the Poisson ratio of the gel, making it almost incompressible. Furthermore, as $\nu = (3K - E)/6K$ and all gel types have $\nu \sim 0.5$, they are expected to have similar K with $K \gg E$.

With this arrangement, all of the samples in gel types A and B detached from the gel by internal rupture of the gel, whereas with gel C they were delaminated. In addition, in this case, the maximal stress before delaminating is around 0.25 MPa. This means that without improving the adhesion between PA12 and the gel, increasing the elongation at break without reducing the Poisson ratio of the gel will not further improve the situation.

This may also imply that gel C has reduced gel adhesion to PA12 compared to gel A and B since all samples detached at around the same maximal stress. However, better cohesion should be prioritised over adhesion to PA12, as gel ruptures can reduce the sensitivity of the modules if they occur in front of the PMTs. Delaminations of the holding structure, on the other hand, have a low optical impact. As long as the adhesion to the glass is strong, even total delamination of the holding structure would not endanger the structural integrity of the module since the PMTs would hold all components in place.

The stress vector inside the gel is very different from the one tested here. As discussed in Section 10.2.1, the final forces are not just perpendicular to the support structure surface because of the thermal contraction of the gel. Nevertheless, a higher elongation at break combined with a low young modulus helps to avoid delaminations (since less force is applied to the adhesion boundary between the gel and the support structure) and internal gel ruptures.

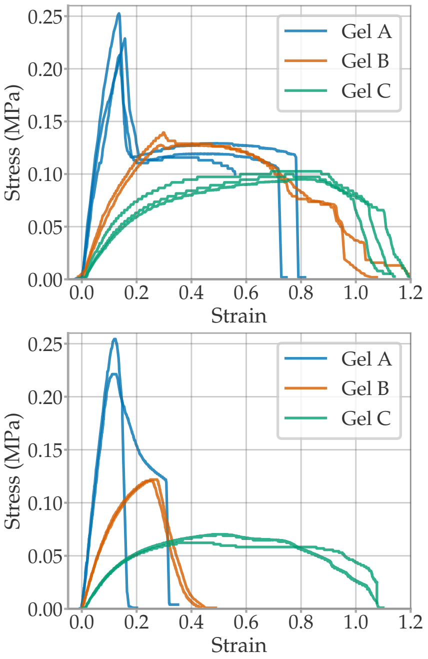

Figure 10.22: Stress–strain curve measured pulling PA12 samples cured in three different gel types. *Top:* PA12 sample of 10 mm radius (case **1)** in Figure 10.21), and *bottom:* samples of 15.5 mm radius (case **2)** in Figure 10.21).

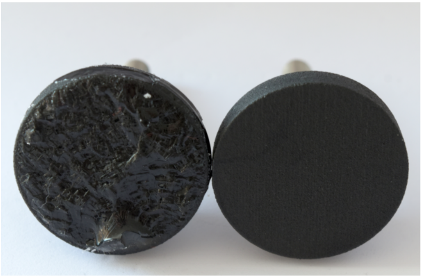

Figure 10.23: Photograph of two samples after measurement. The sample on the left came off by breaking the gel, while the sample on the right delaminated cleanly from the gel layer.

10.2.3 Freezing tests of demonstrators

The most important test to solve the thermal stress problem was the iterative redesign of the support structure and the building of demonstrators, which were later observed inside a refrigerator at −60 °C. This corresponds to $\Delta T = -80\,°\mathrm{C}$ since the construction was carried out at room temperature. The optical module is required to withstand temperatures down to −45 °C, but the temperatures at the deployment depths range between −26.5 °C to − 18 °C [153], which implies a temperature difference of $\Delta T \sim -40\,°\mathrm{C}$. The demonstrator testing shown in this section was deliberately more demanding to trigger delaminations and gel breakages faster and also to have a larger safety factor once a working design was found.

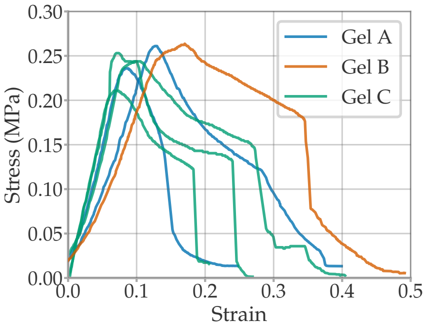

Figure 10.24: Stress-strain curves measured pulling the samples of geometry shown in case **3)** of Figure 10.21.

In total, 17 half-modules were built. The first four were constructed with the help of KM3NeT colleagues in Erlangen using the soft QSI QGel 900[8], which failed at warm temperatures around 0 °C due to its low tensile strength. The following ten demonstrators were constructed in Münster with the Shin-Etsu gel type B using different support structure designs and following various gel pouring methods. In a more mature stage of the support structure design, two further half-modules were constructed with the Shin-Etsu gel type B, but this time at DESY Zeuthen with a professional gel dispenser. The last two demonstrators were constructed in Münster with Shin-Etsu gel type C, which was made available the last.

[153]: IceCube Collaboration (2020), *South Pole Ice Temperature*

[8] Used in the current IceCube DOM.

A lot of trial and error was involved in developing a gel pouring method. In general terms, three approaches were tested. The first and more straightforward method was adapted from the procedure followed in Erlangen for the KM3NeT modules. It involves mixing the two gel components in a recipient and evacuating this recipient to low pressures to extract the air bubbles introduced during the mixing. Afterwards, the recipient is placed on top of the half-module and connected via a plastic tube to an entry hole of the support structure, with the gel flowing via gravity.

Many of the failures found in the demonstrators were caused by expanding air bubbles from behind the PMTs or reflectors stretching under the strain of the gel. Therefore, effort was made to avoid the introduction of air into the gel. Many bubbles were formed during the pouring itself, which meant that the half-module also had to be evacuated after the gel was introduced to extract the newly formed bubbles. This step is not necessary for the KM3NeT modules since their working temperature is around 13 °C [181, p. 121] (less thermal stress as $\Delta T \sim 7\,^{\circ}\mathrm{C}$).

[181]: Bagley et al. (2009), *KM3NeT: Technical Design Report for a Deep-Sea Research Infrastructure in the Mediterranean Sea Incorporating a Very Large Volume Neutrino Telescope*

This led to the idea of sealing the pouring mechanism and setting the half-module at low pressure during pouring. In this setup, the pressure inside the gel container and the half-module could be set separately. This allowed the control of the gel flow by changing the pressure difference between the recipient and the half-module. An important observation here is that the gel produced many bubbles when set under motion at very low pressures. This effect was confirmed with different measurements, but its physical origin is not well understood. To avoid this foam production, the half-module was always at a pressure above ~500 mBar during pouring[9].

[9] Recent measurements in DESY have shown that the pressure boundary at which this effect starts to be noticeable is ~200 mBar.

The third method used a commercial two-component mixer. This mixes the gel with a static mixer without introducing air into the mixture. Since air can be trapped in cavities of the support structure, it is still necessary to evacuate the half-module after pouring.

For the evacuation of the module itself, it was found that the best approach was to

- first pour only ~70 % of the gel level. During the low-pressure air extraction, a lot of foam is produced in the gel, which can get inside the module if it is not well controlled. Having a lower filling level makes the evacuation process easier.

- evacuate the half-module until just before the foam reaches the equatorial region. Once this level is reached, the module is vented to normal pressure to pop the bubbles formed. Then it is evacuated again, approaching lower pressures before the foam arrives in the equatorial region. This is done in several cycles until an end pressure of ~5 mBar.
- pour gel to the final fill level.
- evacuate as low as possible without overflowing the gel into the module. Here, a pressure of ~200 mBar can be reached without the risk of a spill.

Regarding the support structure, the following design changes were found to be essential to solve the thermal stress problem:

- For more efficient and successful air extraction, any location that is prone to produce air pockets during pouring was connected to *air channels* routed inside the support structure (see Figure 10.25).
- Following the FEA studies of Section 10.2.1, Figure 10.14, the wall thickness of the support structure was reduced from 2 mm to the minimum allowed by the manufacturer 0.8 mm. Furthermore, because it is difficult to control this parameter, the support structures are weighed before the assembly of the modules. An increase in weight would indicate an increase in wall thickness.
- The minimum gel layer thickness was increased from 3 mm to 4 mm, as it is expected to reduce the strain (see Figure 10.17). This meant a reduction of the diameter of the support structure.
- Components that make the support structure rigid, such as the equatorial ring or the flaps that connect the equatorial PMTs (see Figure 10.12), were removed from the design.
- *Expansion joints* were added (see Figure 10.26) to allow greater flexibility. Furthermore, the diameter in the equatorial region was set a few millimetres larger. The support structure is contracted to the correct diameter during production by an external support mechanism until the gel cures. This results in a radial *spring force*, (partially) compensating for the thermal contraction.

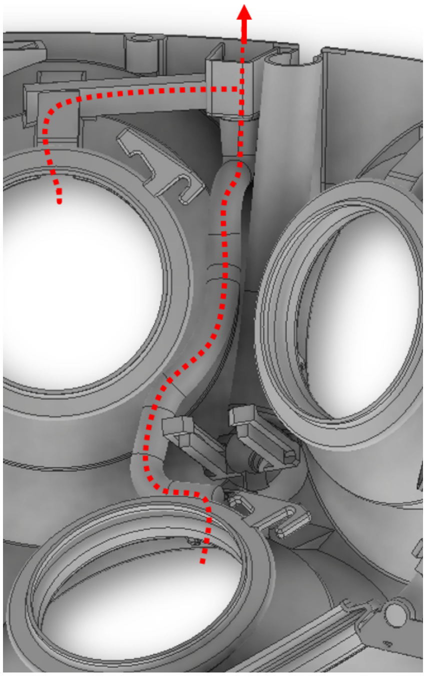

Figure 10.25: Zoom into the internal region of the support structure and air channels. The red arrow shows the direction in which the otherwise trapped air is released.

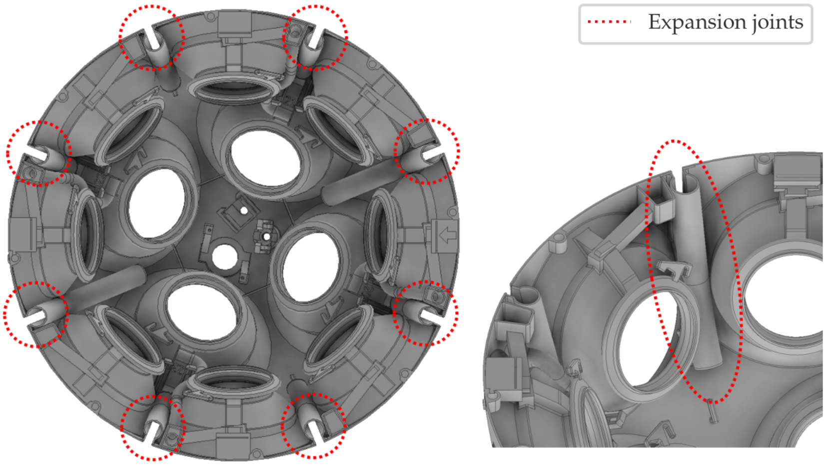

Figure 10.26: Top view of the internal region of the support structure. The red dashed circles mark the position of the expansion joints, which were added to form a radially outward pushing force after module assembly.

The last four built half-modules had practically the same support structure design but, as mentioned above, two of them were filled with gel type B and two with type C. Both gel type B modules were constructed using the commercial gel dispenser at DESY. After the demonstrators were set to low temperatures in the freezer, they performed very well without any significant damage to the gel that could affect the sensitivity of the module. However, cracks appeared inside the expansion joints (see Figure 10.27).

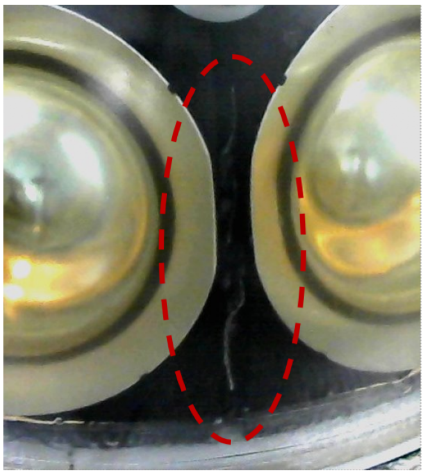

Figure 10.27: Photograph of one of the last demonstrators with Shin-Etsu gel type B. Although no gel damage occurred that could affect the module's sensitivity, the gel inside the expansion joints cracked under the thermal stress.

The two type C demonstrators were poured in Münster with the gravity feed method and thus had to be evacuated longer to extract the bubbles. However, these modules did not develop gel failures, not even within the expansion joints after a total of 146 days inside the freezer. This confirmed the benefits of the larger strain capabilities of the new gel, as studied in Section 10.2.2. The success of these half-modules led to the change of the mDOM baseline gel to the Shin-Etsu type C.

The thermal expansion issues were solved entirely with the aforementioned design changes and the pouring method, which allowed the construction of the first batch of mDOM DVTs. Nevertheless, new problems emerged once the first modules were built as a result of the expansion of (initially invisible) air bubbles inside the gel a few days after two half-modules were sealed. These bubbles are unrelated to thermal stress since they appeared at room temperature. The source of this effect and its solution are explained briefly in Appendix E.

11

Intrinsic mDOM Background

Chapter 8 introduced the first concepts of why a low noise is important for IceCube and presented the intrinsic background of the mDOM PMTs. Unfortunately, the dark rate of the PMTs increases after their assembly into an optical module. For the case of the mDOM, mainly two sources were of concern.

On the one hand, as introduced in Section 5.4, PMTs may exhibit a higher dark rate if placed near conductive components. As the assembled PMTs in the mDOM are surrounded by metal reflectors, it was important to understand this PMT behaviour. This is reviewed in Section 11.1, where the mDOM PMT is measured under the influence of external electric fields and also near the mDOM reflectors.

On the other hand, radioactive decays in the mDOM pressure vessel are a major source of photons. The pressure vessel has a trace amount of isotopes stemming from the glass's raw material and also introduced by the furnace during the melting of the glass. These decays can produce secondary particles as α, β and γ particles. These particles deposit energy in the glass, which can then scintillate. Cherenkov photons can be produced as well, if a charged secondary has enough energy. Section 11.2.4 introduces the characterisation of the scintillation properties of the mDOM pressure vessel and Geant4 simulation results regarding this background.

Finally, the Geant4 studies results are validated with the measurement of the background of DVT 04 in Section 11.3.

11.1 Influence of external conductive components

PMTs operated at negative high voltage may exhibit an increased dark rate due to the influence of external electric fields. Therefore, it is necessary to avoid placing conductive objects near the photocathode or an unprotected tube. In the mDOM, the reflectors enhance the sensitive area and are positioned very close to the photocathode. Several studies were performed in [108], leading to design decisions of having the insulating HA coating provided by the manufacturer and also connecting the reflectors to the photocathode potential. The effects observed in [108] are revisited in this section and further investigated, studying the effectiveness of the HA coating and the influence of the reflector potential on the dark rate.

The following studies will be discussed and interpreted together with the results of [173, Ch. 4] (also published in [126]), where the influence of electric potentials near the mDOM PMT was investigated with a

[108]: Classen (2017), *The mDOM - a multi-PMT digital optical module for the IceCube-Gen2 neutrino telescope*

[173]: Schmiemann (2019), *Squark Annihilation Contributions to Neutralino Dark Matter in NLO SUSY-QCD*

[126]: Unland Elorrieta et al. (2019), *Characterisation of the Hamamatsu R12199-01 HA MOD photomultiplier tube for low temperature applications*

finite element simulation using COMSOL Multiphysics®.[1] The PMT components were modelled using their actual dimensions. The voltages were assigned to the different parts of the multiplier system and the photocathode corresponding to a cathode-anode voltage of −1300 V. The bottom left of Figure 11.1 shows a cross section of the simulated geometry.

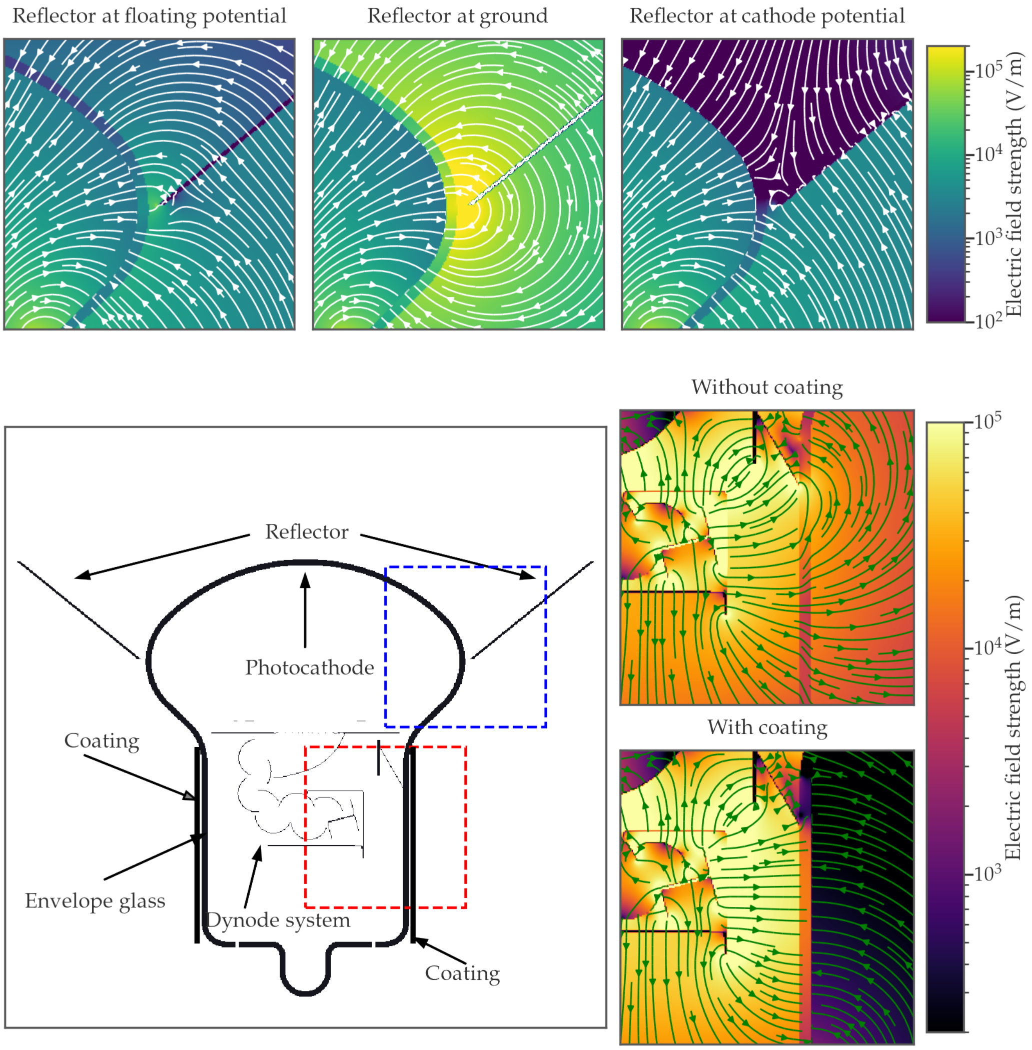

Figure 11.1: Results of a finite-element simulation of the Hamamatsu PMT at an operating voltage of −1300 V, from [173, Ch. 4] and modified. *Top row*: Electric field around the PMT entrance window with the reflector on floating potential (left), ground (middle) and photocathode potential (right). *Lower left:* Cross-section of the simulated geometry. The real coating thickness of about 0.3 mm was increased in this visualisation for the sake of clarity. The blue dashed box indicates the region of the images in the top row and the red box those of the two plots on the lower right. *Lower right:* Electric field next to the dynode system with the envelope glass with and without HA coating at photocathode potential. The colour scales indicate the electric field strength in V/m, and the arrows indicate the direction of the field in the plane.

11.1.1 Influence of external field around a PMT tube

The two images on the bottom right of Figure 11.1 show the electric field near the dynode system resulting from a PMT with and without HA coating. From the figure, it is apparent that the coating increases the electric field strength between the dynode system and the glass by 80 %,

---

[1] COMSOL Multiphysics v.5.2. www.comsol.com. COMSOL AB, Stockholm, Sweden.

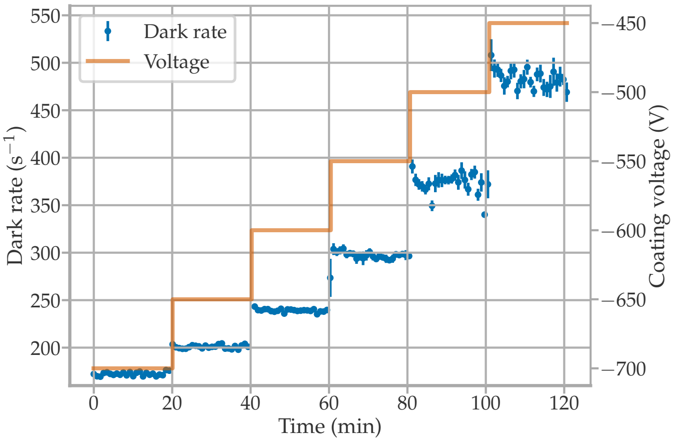

Figure 11.2: A conductive tape wrapped around a PMT tube was set at different voltages. The figure shows the dark rate of the PMT against time and voltage of the coating. An instant increase in the dark rate with the coating voltage is observed. Data published in [126] and measured by the author.

resulting in an increased electron repulsion from the coating towards the dynode system. In addition, the coating isolates the dynode structure from objects outside the PMT if these are at floating or ground potential. They can attract photoelectrons and secondary electrons, causing collisions of these particles with the glass envelope and thereby producing background pulses via scintillation.

To investigate the effects of objects at different potentials around the tube and of the HA coating on the dark rate, an aluminium adhesive tape was attached to the tube of an uncoated Hamamatsu PMT. This tape covered the same region that the HA coating would wrap around. This conductive layer was connected with a cable to a different channel of the same voltage supply as the PMT, with both voltage channels having a common ground.

The dark rate was measured using the trigger-counting method (see Section 8.1.1) while increasing the voltage applied to the tape in a step-wise manner in 20 min intervals. The results are shown in Figure 11.2. The dark rate increases following the voltage in a step-wise manner. The measurement was carried out inside a climate chamber and repeated at lower temperatures. Figure 11.3 shows the average dark rate as a function of the voltage applied to the coating for the PMT at room temperature and at −30 °C. In both cases, the rate does not appear to be affected at voltages close to the photocathode potential. However, it increases rapidly for higher voltages, reaching a maximum with the aluminium band at ground potential. Nevertheless, the voltage at which the rate starts increasing is lower at room temperature. Also, the overall rate is consistently one order of magnitude higher at room temperature than at −30 °C. The temperature dependence for the coating at cathode potential and −300 V is shown in Figure 11.4. Although the rate is higher for all temperatures with the coating closer to ground potential, it is clear that this effect has a strong temperature dependence being the largest at room temperature, while at −40 °C the rate increases only by ~25 %. The curve for the tape at cathode potential follows the expected curve from an HA-coated PMT.

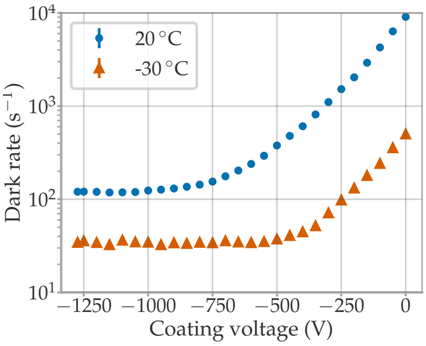

Figure 11.3: Mean dark rate of the PMT in dependence of the coating voltage at 20 °C and −30 °C. Uncertainties are smaller than data point markers. Data published in [126] and measured by the author.

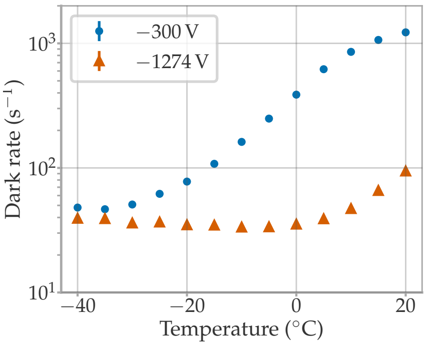

Figure 11.4: Dark rate of the PMT at different temperatures for a coating voltage at −300 V and −1274 V (the nominal voltage of the PMT). Error bars smaller than points.

This noise increase was also observed in studies cited in [116]. They were explained either through the release of electrons from residual alkali

[116]: Wright (2017), *The Photomultiplier Handbook*

metals sitting on the bulb walls or through luminescence of the envelope glass. Both hypotheses are compatible with the voltage dependence measurement results: at higher potential differences, more electrons are deflected into the glass envelope, increasing the overall rate. The rate increase is constant in time, which is expected since the same fraction of electrons is deflected at all times. Nevertheless, the measured temperature dependence disfavours the luminescence hypothesis since the luminescence yield should decrease with temperature (see Section 11.2).

Two additional PMTs were measured to verify that the HA coating effectively shields the PMT from electric potentials outside the PMT. One of the PMTs had the HA coating provided by the manufacturer, and the other was coated only with a layer of insulating tape. Around the tube of each PMT, a metallic ring was placed, which was connected with a cable to the high-voltage supply. The dark rate was measured with the trigger-counting method while the voltage of the ring was decreased step-wise to the photocathode potential. The average dark rate at each voltage step is shown in Figure 11.5. As expected, the PMT without HA coating measured a very high dark rate for voltages between ground and ∼−400 V, while the coated PMT showed no increase in dark rate at these potentials. Somewhat unexpectedly, though, the dark rate of the coated PMT increases with the ring reaching cathode potential. This is probably caused by corona discharges since the ring itself was not coated with insulating tape, and the support structure of the setup, which has metallic parts, was left at floating potential.

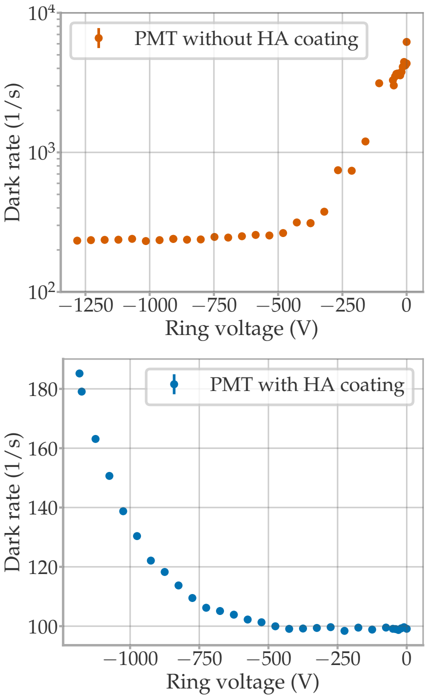

Figure 11.5: Dark rate of a PMT with (*top*) and without (*bottom*) a HA coating, surrounded by a metal ring which is set to various potentials.

Overall, the HA coating seems to solve some of the negative aspects of utilising negative high voltage. Should a coating fail, it was shown that this dark rate source diminishes at low temperatures (see Figure 11.4), increasing the confidence that operating polarity is not an issue for the mDOM.

11.1.2 Influence of reflector on single PMT

For the following studies, a 3D printed support structure similar to the one used in the mDOM was used, but for a single PMT with a reflector. Here the reflector, instead of being connected to the cathode pin, was connected to a second channel of the voltage source used for the PMT, ensuring a common ground.

The dark rates were measured with the trigger counting method. The first measurement was performed with the reflector successively at floating potential, ground and cathode potential, resulting in the curve

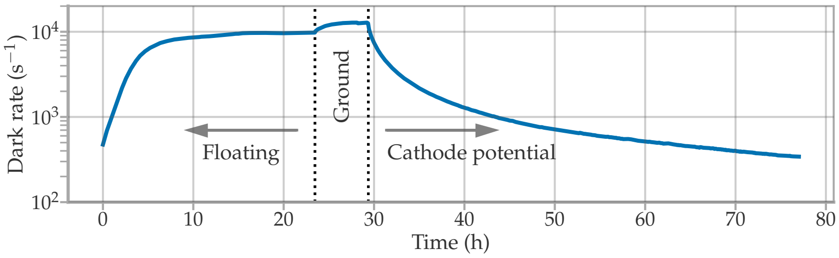

Figure 11.6: Dark rate against time of a PMT with a reflector positioned in front of its photocathode (see Figure 11.1). The reflector was set at floating, ground and photocathode potential sequentially. The rate uncertainty is smaller than the line width. Data published in [126] and measured by the author.

shown in Figure 11.6. In the first phase of the measurement, the reflector was held at floating potential[2] resulting in a slow increase of the dark rate until it reached a plateau of ~9600 s^{-1}. Next, the reflector was connected to ground, which slowly increased the rate until a second plateau was reached at ~12 800 s^{-1}. Finally, the reflector was connected to the photocathode potential, leading to a slow rate reduction. After ~45 h, the dark rate reaches a value comparable to that of the PMT without the reflector. Remarkably, the rate increase and decrease took much longer than the rate variation in the last section, which was almost instantaneous upon changing the coating potential (see Figure 11.2).

The top row of Figure 11.1 shows the electric field strength near the photocathode and reflector for the three measured scenarios. The left plot shows the reflector at floating potential. In this configuration, high field strengths are found in the vicinity of the photocathode. The maximum is 4.6 kV/m in the region of the smallest distance between the reflector and the PMT (1 mm distance). The centre figure shows the situation if the reflector is at ground potential. Here the field strength reaches 0.14 MV/m in the region of the shortest distance to the PMT. In the two figures, it can be observed that the areas farther away from the reflector also show relatively high values. At the surface of the glass, near the centre of the photocathode, the field strength rises to 0.4 kV/m and 12 kV/m, in the case of floating and ground potential, respectively. In contrast, when the reflector is connected to the photocathode potential, as shown on the right side of Figure 11.1, the field strength along the photocathode layer varies only between ~ 5 V/m and 25 V/m.

In a second measurement, the reflector was set at various voltages ΔV_{refl} relative to the photocathode potential. This means, for example, $\Delta V_{\mathrm{refl}} = 0$ V if it is at the photocathode potential (−1180 V) and $\Delta V_{\mathrm{refl}} = 400$ V if it is connected to −780 V. The dark rate was measured for 3 h at every potential step with ΔV_{refl} from 0 V to 400 V. Since the rate increases slowly with the reflector voltage, the plateau observed in Figure 11.6 is not reached during this time interval. Figure 11.7 shows the average rate over the last hour of each voltage stage. This procedure was performed once at room temperature (20 °C) and again at 30 °C. At 20 °C, the rate increases with ΔV_{refl}, as expected. However, unlike the results in Figure 11.6, the rate remains constant throughout the measurement at −30 °C.

To further explore this behaviour, the dark rate was measured at different temperatures between −30 °C and 20 °C with the reflector at a constant voltage of $\Delta V_{\mathrm{refl}} = 400$ V. The data are presented in Figure 11.8. There is almost no noticeable change in the dark rate at low temperatures. With increasing temperature, the dark rate increases abruptly due to the thermal emission of electrons from the photocathode. At 0 °C, 10 °C and 20 °C the rate increases further after the temperature stabilises due to the influence of the reflector potential. The dark rate was fitted with a linear function using the data taken 30 min after the temperature change. The slope obtained at each temperature is shown in Figure 11.9. The slope increases with temperature and even at −30 °C a non-zero slope is measured. Nevertheless, it should be emphasised that the slopes for temperatures between −30 °C and −10 °C are compatible with a constant

[2] The cable was not attached to the high voltage supply.

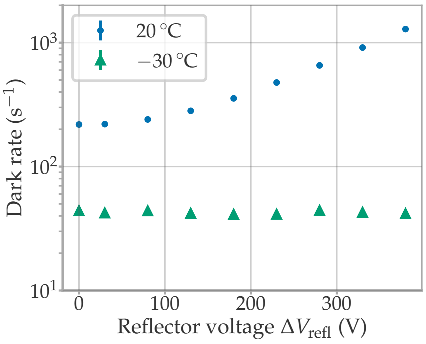

Figure 11.7: Average dark rate against the reflector voltage for a measurement at 20 °C and −30 °C. Rate errors smaller than marker size. Data published in [126] and measured by the author.

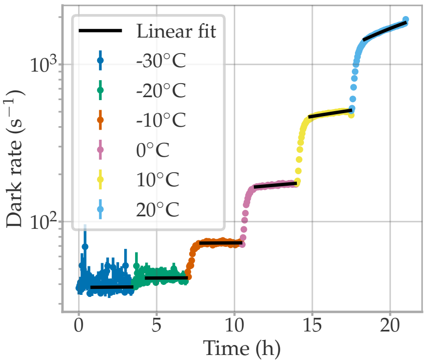

Figure 11.8: Dark rate against time with varying temperature and a reflector at 400 V relative to the photocathode potential. Lines show linear fit of the last 30 min of the data at each temperature step. Data published in [126] and measured by the author.

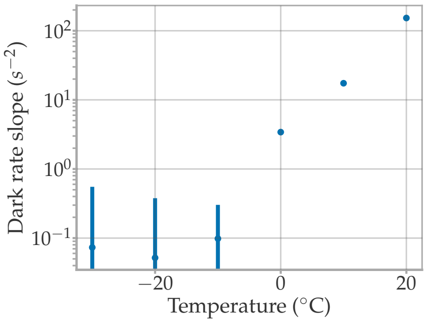

Figure 11.9: Slope of linear fits in Figure 11.8. Data published in [126] and measured by the author.

rate taking into account the uncertainties. The small slope at −30 °C would explain the constant rate in Figure 11.7, since in each step the dark rate was measured only for 3 h.

The measurement was repeated with the reflector at photocathode potential. Figure 11.10 shows the average dark rate of the last five minutes of each temperature step for the measurement with the reflector at $\Delta V_{\mathrm{refl}} = 400\,\mathrm{V}$ and at cathode potential. The dark rate is always greater with the reflector at $\Delta V_{\mathrm{refl}} = 400\,\mathrm{V}$ than at cathode potential. For temperatures lower than 0 °C this difference can not be fully explained by the dark rate increase shown in Figure 11.8, since the slopes are very small. This means that having the reflector at a different potential than the photocathode has an immediate effect on the dark rate, as is the case with the measurements in the HA coating investigations (see Figure 11.2).

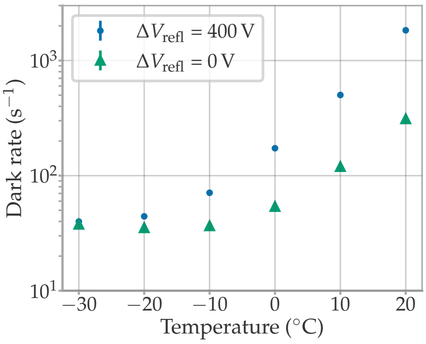

Figure 11.10: Dark rate of the PMT against temperature with a reflector at photocathode potential ($\Delta V_{\mathrm{refl}} = 0\,\mathrm{V}$) and $\Delta V_{\mathrm{refl}} = 400\,\mathrm{V}$.

The slow increase and decrease of the rate indicate that this effect is different from the one presented in the section on the HA coating. Furthermore, the temperature behaviour cannot be explained by the luminescence hypothesis nor by possible electrical discharges between the reflector and the PMT.

In studies such as [182], it has been reported that the PMT photocathode is very sensitive to electric field gradients, reducing the sensitivity of the PMT with time. This has been explained as a damage to the photocathode through poisoning by the migration of sodium ions from the enveloping glass to the bialkaline layer. This could also explain the results since the ions transported to the photocathode may deposit enough energy to release photoelectrons and produce the observed change in the dark rate. According to [183], ion transport is directly proportional to temperature. Therefore, as observed in the measurements, one would expect a slower increase in the dark rate at lower temperatures. However, why this process stabilises, and the dark rate reaches a plateau, is not clear. Further studies involving ion transport simulations with COMSOL are planned in the Münster IceCube group.

[182]: Lavoie (1967), *Photomultiplier Cathode Poisoning*

[183]: Mehrer et al. (2008), *Diffusion and ionic conduction in oxide glasses*

It can be concluded that, even at low temperatures, connecting the reflectors to the photocathode potential is mandatory if a stable dark rate behaviour is desired. The following Section 11.1.3 explores a possible drawback of this solution: corona discharges between neighbouring reflectors.

11.1.3 Corona discharge between reflectors

As discussed in Section 11.1, in the mDOM the reflectors are connected to the photocathode potential of the nearest PMT. Since the nominal voltage of each PMT varies, neighbouring reflectors will most likely be at different potentials. The leakage current between them is expected to be low, since the gel has a volume resistivity of ~0.7 PΩ cm and the holding structure of >1 TΩ.[3] Nevertheless, since reflectors are thin and have sharp edges, the possibility of corona discharges between neighbouring reflectors had to be verified.

[3] The volume resistivity of gel was provided by the manufacturer. The resistivity of the holding structure was measured with an insulation tester (METRISO 5000A).

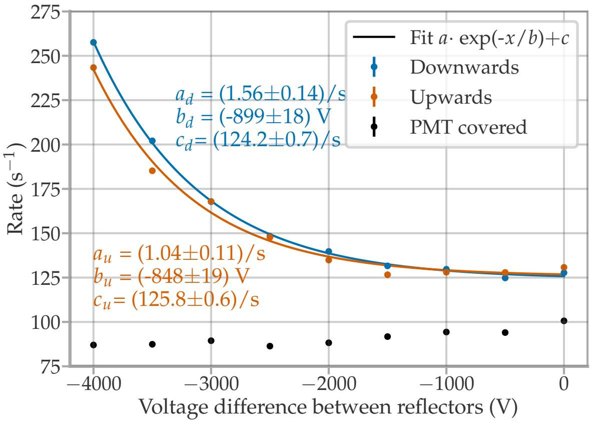

Figure 11.11: Pulse rate measured by the PMT in front of two reflector pieces set at different voltages. The data were fitted with an exponential function. A verification measurement with covered PMT is shown in black points. The uncertainties are smaller than the data point markers.

Two pieces of reflectors were placed at a distance of 7 mm (the shortest gap between two reflectors in the mDOM) in a recipient, which was filled with gel and left to cure. Each reflector piece was connected with a cable to a channel of a high-voltage supply, so the voltage of each piece could be set independently. Both high-voltage channels had a common ground. A PMT was placed ~8 cm in front of the recipient. The PMT was driven with positive high voltage to avoid an artificial increase of the dark rate. One of the reflector pieces was always left at 0 V and the other at negative voltages, in order to not perturb the measuring PMT. The rate of the PMT was measured with the trigger-counting method, while varying the potential difference between the two reflectors.

Figure 11.11 shows the average rate at each voltage step. First, the voltage of one of the pieces was decreased step-wise[4]. Subsequently, the measurement was repeated, but the voltage was instead set to the minimal value at the beginning and then increased step-wise[5].

The rate remains fairly constant at the voltages from 0 V down to −1000 V. Nevertheless, for lower voltages, the PMT rate starts to increase exponentially. Fitting an exponential function to both curves results in similar fit parameters, with an exponential constant of (−899 ± 18) V and (−848 ± 19) V for the downward and upward measurements, respectively. Figure 11.12 shows the raw data for the voltages between −2000 V and −4000 V of the *downward* measurement. The rate increase is immediate and constant for a set voltage, which supports the idea of this increase coming from real photons.

A third measurement was done to ensure that the measured rate increase stems from light production between the reflectors and not from the strong electromagnetic fields. Here, the PMT was covered with a thin black plastic cup, covering the whole photocathode, while the voltage of the reflector piece was decreased as in the last measurement. The results are also presented in Figure 11.11. The exponential increase of the rate is absent, but there is a slight decrease in the rate with the reflector voltage. This is because the PMT was still in the exponential decay region after being excited by external light while the setup was changed. The rate of the covered PMT is ~40 s^{-1} lower than that of the uncovered PMT with both reflectors at ground, probably because the dark box was not completely light-tight.

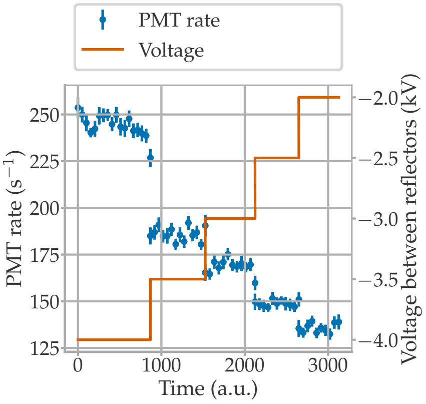

Figure 11.12: Raw data of the PMT rate during the *downward* measurement. The rate increase is immediate with the voltage between the reflectors.

[4] *Downwards*-label in the Figure 11.11

[5] *Upwards*-label in the Figure 11.11

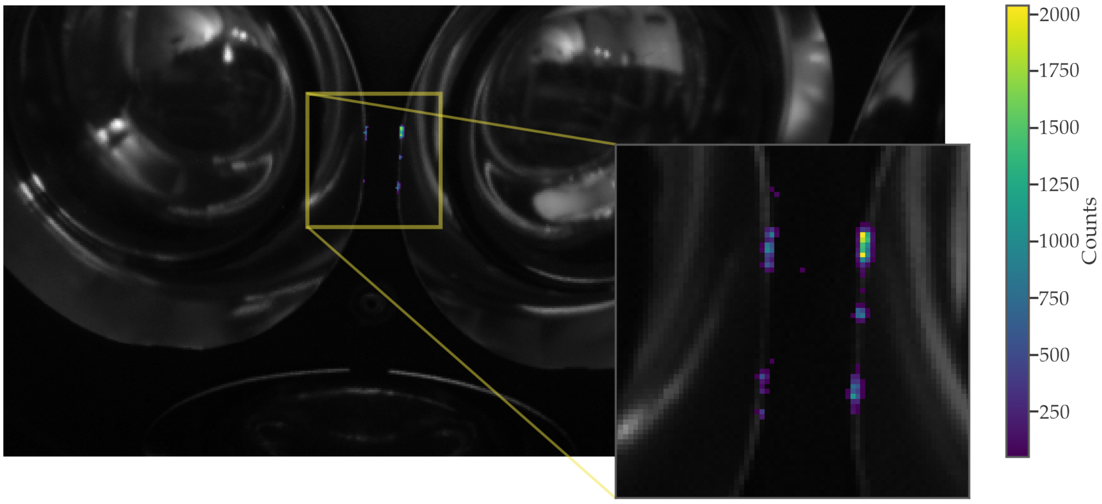

Figure 11.13: Composite image of corona discharges between reflectors at 8 kV potential difference. The right plot shows a zoom of the region marked by the yellow box on the left. The image in grey scale was taken with external light illuminating the module. The signal, in colours, was taken with the dark box closed.

From the results presented, the indications for some kind of continuous corona discharge between reflectors are strong. To confirm this hypothesis, an mDOM half-module was produced with several of the reflectors connected to cables, which were connected to the high-voltage module. The reflectors had no connection to the cathode pin, in order to protect the PMT. This half-module had all the mechanical components of the mDOM, including the 3D-printed holding structure and the optical gel. A CCD camera[6] with a lens[7] attached was placed ~35 cm in front of the half-module. Two neighbouring equatorial PMTs were connected to −4000 V and 4000 V, respectively. This was the maximal voltage which the high voltage module[8] could supply. The CCD camera measured 20 *accumulations* of one hour each. During an accumulation, each pixel's signal is collected and the charge is read out at the end. After a read-out, noise is introduced; thus it is better to have long accumulation times. Nevertheless, the longer the accumulation, the more cosmic rays pass through the sensor, producing saturated pixels. The software can filter out these pixels by measuring at least three accumulations, producing a clean image.

After the 20 h measurement, a second shot of the same duration was taken with the reflectors disconnected from the high-voltage supply. This frame represented the background of the first measurement and was used as a correction, subtracting it from the first picture.

Lastly, a third picture of only 0.7 s exposure time is taken, with the dark box open and an external light illuminating the module. The composite image from this picture, together with the background-corrected frame, is shown in Figure 11.13. Here, a cut was applied to the background-corrected frame, removing all counts lower than 50. This is necessary to produce a clear image since the background pixels have counts that form a Gaussian distribution due to statistical variations, as seen in Figure 11.14.

From the composite image, it is clear that there is photon production along

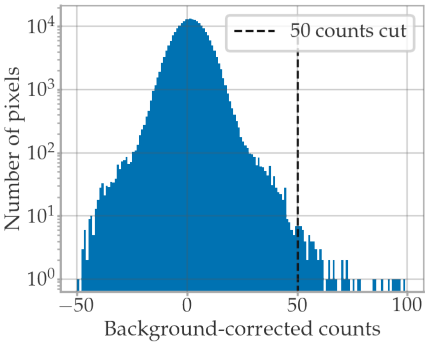

Figure 11.14: Pixel counts of the background-corrected image. Most of the pixels contain only background noise. The dashed line shows the count cut used to generate the signal frame of Figure 11.13.

[6] Andor Solis Newton CCD DU920P-OE.

[7] Nikon AF-S NIKKOR 18-55 mm.

[8] CAEN DT1470ET.

the nearest edges of the neighbouring reflectors. The total excess detected in counts (after the aforementioned cut) is 44081, which translates into a photon rate detected by the sensor of $\sim 0.6\,\mathrm{s}^{-1}$.

It was agreed with the manufacturer that the nominal voltage should be between 900 V and 1500 V. Therefore, the maximal difference in voltages between two reflectors is 600 V. Following the results of Figure 11.11, this maximal potential difference is too small to produce any measurable amount of photons. Nevertheless, for safety, the PMTS are matched according to their nominal voltage for the mDOM production. In this way, neighbouring reflectors will be connected to similar potentials, excluding any significant increase in the background due to the effects measured in this section.

11.2 BACKGROUND CAUSED BY RADIOACTIVE DECAYS

Particles from radioactive decays in the pressure vessel deposit energy in the glass, which can lead to scintillation. A brief introduction to the scintillation process is provided in Section 11.2.1. The background caused by radioactive decay in the pressure vessel and gel of the mDOM was characterised in detail by the author in the Master thesis [152]. The main objective of [152] was to simulate the decays in Geant4 to estimate the dark rate of a deployed mDOM. Since scintillation is a specific property of the material in question, these properties had to be measured in the laboratory with samples. The scintillation properties of the pressure vessel were remeasured with extended methods in the context of the thesis [184] co-supervised by the author. As the parameters obtained from these studies are used and improved in subsequent sections, a summary of the results from [152, 184] is provided in Section 11.2.2. In the scope of this thesis, the measurement of the scintillation time distribution was enhanced, as discussed in Section 11.2.3, to achieve a more accurate model of the scintillation process.

[152]: Unland Elorrieta (2017), *Studies on dark rates induced by radioactive decays of the multi-PMT digital optical module for future IceCube extensions*

[184]: Dittmer (2020), *Characterisation of scintillation light induced by radioactive excitation in the mDOM glass pressure vessel*

Section 11.2.4 presents Geant4 estimations for the mDOM background in ice. Because most mDOM PMTs were affected by a higher amount of radioactive isotopes in their glass, the scintillation properties of the PMT glass must also be determined. However, measurements of the scintillation properties are time-consuming and are currently being planned by the IceCube group in Münster. In Section 11.2.5, the scintillation parameters are estimated from the dark rate measurements presented in Section 8.1.3 to make some initial estimates of the impact of the new PMTs on the dark rate of the assembled modules.

11.2.1 SCINTILLATION PROCESS IN INORGANICS

In the following, the main concepts of scintillation are briefly introduced. A more in-depth but brief description can be found in [152, Ch. 4], while for avid readers, books [185–187] are recommended.

[152]: Unland Elorrieta (2017), *Studies on dark rates induced by radioactive decays of the multi-PMT digital optical module for future IceCube extensions*

[185]: Lecoq (2020), *Scintillation Detectors for Charged Particles and Photons*

[186]: Lecoq et al. (2006), *Inorganic Scintillators for Detector Systems*

[187]: Ronda (2007), *Luminescence: From Theory to Applications*

Scintillation is a luminescence process following electronic excitation by a high-energy particle. This can occur in various materials, including gases and organic or inorganic solids.

In a crystal lattice, the electronic energy levels are condensed into a band structure. The outermost filled orbital of the atoms forms the valence band (VB), while the lowest unoccupied energy band is the conduction band (CB). In a semiconductor or insulator, such as borosilicate glass, these two bands are separated by a gap of width E_g, which should be empty of electron states in a pure homogeneous crystal.

In a lattice, the electron deexcitation occurs via *radiative transitions* emitting a photon or via *non-radiative transitions*. The most important of the non-radiative transitions is phonon excitation. Normally, only a tiny fraction of the deposited energy is released radiatively.

A radiative transition can be divided into *intrinsic* and *extrinsic*, also known as activated or characteristic emission [188, p. 22]. These are illustrated in Figure 11.15. The intrinsic emission is the deexcitation of an electron from the conduction band to the valence band (case *(a)* in Figure 11.15). If the light has an energy $\geq E_g$ it can be reabsorbed by an electron in the valence band, making the material opaque to these photons. The released photon can also have an energy $< E_g$ in the case of a partial energy transfer to phonons.

[188]: Yacobi et al. (1990), *Cathodoluminescence Microscopy of Inorganic Solids*

Impurity atoms can introduce energy levels within the band gap. The emission triggered by impurities in the crystal is extrinsic and is illustrated in the case *(b)* of Figure 11.15. Such additional energy levels are also produced by lattice defects, such as dislocations, which can produce both shallow and deep energy levels. By definition, in this case, the emitted photons will have an energy $< E_g$, and the material is transparent to this emission. Dedicated scintillators used in detectors have impurities introduced on purpose to increase their efficiency, and most of the detected light is extrinsic in nature.

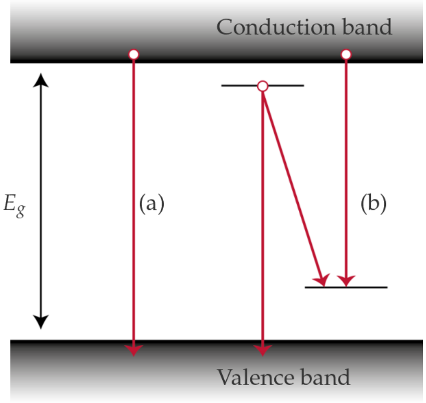

Figure 11.15: Schematic diagram showing transitions between the conduction band, the valence band and impurity energy levels. Based on [188, p. 25].

Scintillator materials are typically modelled empirically by three parameters:

- The scintillation **yield** is the mean number of photons emitted by the material per unit of absorbed energy (MeV^{-1}).
- The scintillation **lifetime(s)** describes the time distribution of the photon emission. A single exponential decay is usually sufficient in a homogeneous sample in which a single electronic transition predominates. In the case of borosilicate glass, the time distribution is a sum of many different transitions, and a multi-exponential function $f(t)$ has to be used:

$$f(t) = \sum_{i=1}^{N} \frac{\alpha_i}{\tau_i} \cdot \exp -(\frac{t}{\tau_i}), \tag{11.1}$$

  where τ_i are the lifetimes of the transitions and α_i their fractional contributions where $\sum_{i=1}^{N} \alpha_i = 1$.
- The scintillation **spectrum**, which describes the energy distribution of the emitted photons.

These parameters are expected to change with temperature. The non-radiative decay rate usually increases with temperature because of thermal quenching, effectively decreasing the scintillation yield. In such a case, the observed lifetime of the photon emission τ should also decrease with temperature, because $\tau^{-1} = r_\mathrm{r} + r_\mathrm{nr}$, where r_r and r_nr are the radiative and non-radiative decay rates, respectively [187, p. 31].

[187]: Ronda (2007), *Luminescence: From Theory to Applications*

The scintillation parameters also depend on the type of high-energy particle impinging on the material. Therefore, these have to be determined using particle sources of interest [189, p. 255].

[189]: Knoll (2010), *Radiation detection and measurement*

The next section summarises the initial measurements of the scintillation properties of the mDOM pressure vessel. The method for measuring the scintillation lifetime was improved in the scope of this work. This method and the measurement results are presented in Section 11.2.3.

11.2.2 Scintillation properties of mDOM Pressure vessel

This section summarises the results of two Master theses [152, 184]. In [152], the amount of radioactivity of the mDOM glass (VITROVEX® [9]) was measured by gamma spectroscopy. Several gamma emitters were found, coming from the natural decay chains ^{238}U, ^{235}U and ^{232}Th, as well as from the isotope ^{40}K. Table 11.1 lists the average activities of the glass samples, where it was assumed that the chains were in secular equilibrium.

[152]: Unland Elorrieta (2017), *Studies on dark rates induced by radioactive decays of the multi-PMT digital optical module for future IceCube extensions*

[184]: Dittmer (2020), *Characterisation of scintillation light induced by radioactive excitation in the mDOM glass pressure vessel*

[9] NAUTILUS Marine Service GmbH, `www.vitrovex.com`.

Table 11.1: Mean specific activity of all the measured mDOM pressure vessels. Two half-spheres weight 13 kg. Data from [152] measured by the author.

	Specific activity (Bq/kg)
^{40}K	60.98 ± 0.86
^{238}U chain	4.61 ± 0.07
^{235}U chain	0.59 ± 0.05
^{232}Th chain	1.28 ± 0.05

The scintillation parameters for alpha particles of the VITROVEX glass were measured in [152]. In general, the experiments consist of irradiating a sample with a ^{241}Am α-source and measuring the emission with a PMT. In the case of yield and lifetime, these measurements were temperature dependent using a climate chamber. Due to the size and low activity of the radioactive source, the spectrum measurement was only been performed at room temperature.

The yield was calculated by measuring the number of photons produced by the glass with a PMT placed facing the sample. For the yield calculation, the activity of the radioactive source was needed, which was measured with an alpha spectrometer. The experiment is then simulated in Geant4 and the yield necessary to obtain the measured rate was estimated. Figure 11.16 shows the yield for alpha particles obtained as a function of temperature. In [184], the yield was measured for electrons in an analogue way. This was a factor ∼1.7 higher than the yield for alpha particles and had a similar temperature dependence.

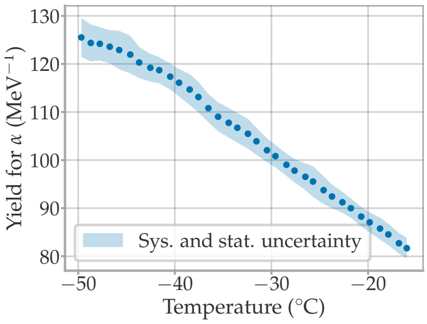

Figure 11.16: Scintillation yield for alpha particles of the VITROVEX sample. Data measured by the author in [152].

The scintillation spectrum was measured by placing the irradiated sample at the input of a monochromator. The light wavelength was selected stepwise and is measured by a PMT at the device's output. In [152], the spectrum was contaminated by air scintillation, so the measurement was repeated in [184] using a vacuum chamber. Figure 11.17 shows the resulting spectrum.

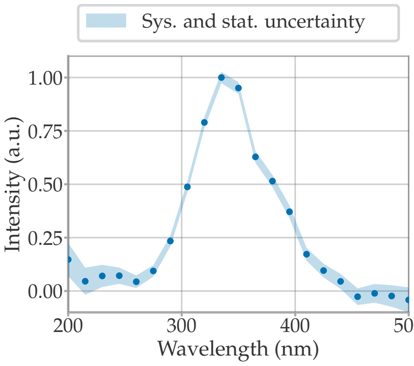

Figure 11.17: Scintillation spectrum for alpha particles of a VITROVEX sample. Data from [184].

Finally, the lifetime was measured with a masked source so that only a few particles reached the sample every second. PMT waveforms of 100 µs were read from the PMT, saving the information of all pulses with the MPA method. Figure 11.18 shows the histogram of the pulse times obtained. This distribution was fitted with a sum of three exponential decays. This measurement requires complex corrections because the pulse times used for the histogram are relative to the first pulse measured at the wave source. However, to calculate the distribution correctly, the time should be relative to the decay time. This problem was solved with a new method developed in the course of this thesis, which will be introduced in the next section.

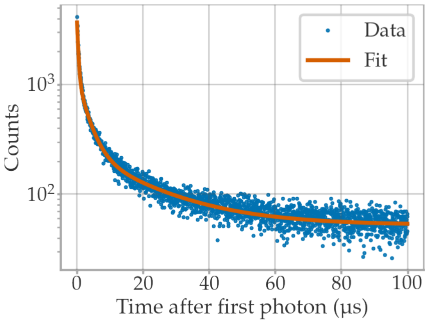

Figure 11.18: Scintillation time distribution relative to the first photon measured. Measured with alpha particles irradiating a VITROVEX sample. Data measured by the author in [152].

11.2.3 IMPROVED LIFETIME MEASUREMENT METHOD

As explained above, constructing the time histograms using the first photon of the wave functions as $t = 0$ produced systematics that were difficult to correct. A second measure of the scintillation lifetime was designed using the gamma particles emitted by the source. ^{241}Am decays to an excited state of ^{237}Np while emitting an alpha particle. The main decay channel (84.8 %) is to the 59.54 keV excited state of ^{237}Np via the emission of a 5.486 MeV alpha particle. The excited state decays with a lifetime of 68.1 ns to the ground state, 36 % of the time radiatively emitting a gamma particle [190].

[190]: Basunia (2006), *Nuclear Data Sheets for A = 237*

Figure 11.19 illustrates the measurement setup. A VITROVEX glass sample was irradiated with an ^{241}Am source. The distance between the source and the sample was kept as short as possible to mitigate air scintillation. The light emitted was measured with an mDOM PMT[10] facing the sample. At the back of the source was a scintillator module. This consists of a scintillator coupled to a PMT and a pre-amplifier. The pre-amplifier signal was routed to an amplifier.[11] The unipolar output of the amplifier and the signal of the mDOM PMT were connected to an oscilloscope.[12] A high-voltage module supplied 1200 V to the scintillator module and the nominal voltage to the mDOM PMT. The latter was adjusted to change with temperature using the results of Figure 6.11.

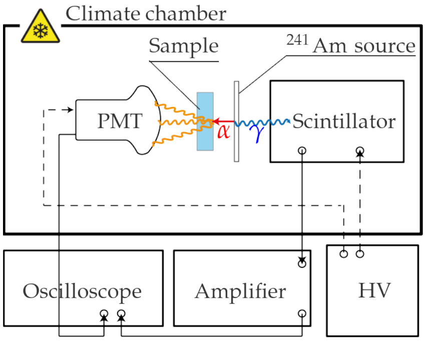

Figure 11.19: Simplified schematics of the experimental setup used for the scintillation lifetime measurement.

A coincident trigger was configured in the oscilloscope, where a trigger level was set on the scintillator channel (trigger A) and on the PMT channel (trigger B). Due to the different cable lengths and PMT transit times, the PMT signal arrived before the scintillator signal. Thus, the conditional coincident triggers were set such, that a waveform was measured if the trigger B was activated within 500 ns before trigger A. In this way, the arrival time of the pulses is relative to the ^{237}Np gamma detected by the scintillator. The oscilloscope was configured to measure the time window −20 µs to 980 µs relative to trigger A. Furthermore, only waveforms with at least five pulses in the first 100 µs were considered, to avoid coincident background events.

The rate of alpha particles hitting the glass had to be reduced, so the probability of measuring more than one decay per waveform was low. This was achieved by masking the source leaving only a pinhole of area ~1 mm^2. The setup was placed inside the climate chamber. The measurement was performed from −50 °C to 0 °C in steps of 10 °C. The temperature was changed once $2 \cdot 10^5$ pulses had been measured, which required ~ 8000 waveforms. Before starting the measurement at each temperature, all components were allowed to settle to the final temperature. Due to the

[10] SN BA0373.

[11] ORTEC Spectroscopy amplifier 451.

[12] Lecroy WaveRunner 640Zi.

strict conditional triggering, a waveform was triggered and analysed every ~2 s, making this measurement relatively time-consuming.

As the lifetime of ^{237}Np and the time resolution of the scintillator are not negligible, the time of trigger A will also not correspond to the decay time. The measurement was simulated with a simple model to check how this time deviation may affect the results.

Toy model simulation of measurement

The measurement was simulated in Python with random sampling. The following steps were taken to simulate a single waveform:

- a) The emission time of the gamma particle t_γ is sampled from an exponential function with lifetime τ_γ. An offset t_1 is added to t_γ, simulating the signal's transit time.
- b) The pulse times t_p are sampled N-fold from an exponential of lifetime τ_p, where N is the number of pulses in a single waveform. Here, an offset t_2 is also added to the sampled values.
- c) The pulse times are shifted relative to the gamma particle, $t'_p = t_p - t_\gamma$. In the measurement, the measured pulse times are always relative to the first trigger, the pulse from the scintillator.

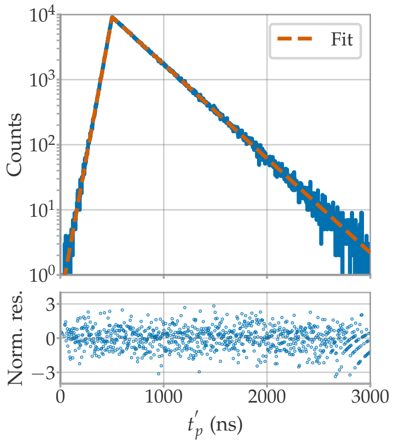

Figure 11.20: Histogram of the sampled pulse times using a single exponential decay simulating the scintillation. The fit was performed with Equation 11.2. The lower plot shows the normalised residuals (residuals divided by the uncertainty of the corresponding bin).

Figure 11.20 shows the histogram of t'_p of 10^5 simulated waveforms with $\tau_\gamma = 50\,\text{ns}$, $\tau_p = 300\,\text{ns}$, $t_1 = 1\,\mu\text{s}$, $t_2 = 1.5\,\mu\text{s}$ and N sampled from a Poisson distribution of $\mu = 10$. The time distribution follows an asymmetric Laplace distribution, which can be written in the form

$$L(t, t_0, \tau_1, \tau_2) = \frac{1}{\tau_1 + \tau_2} \exp\left[-(t - t_0)\left(\sqrt{\frac{\tau_1}{\tau_2}}\right)^{s} \frac{s}{\sqrt{\tau_1 \tau_2}}\right], \qquad (11.2)$$

where $s = \operatorname{sgn}(t - t_0)$ is the sign function.[13] It consists of two exponential distributions of lifetimes τ_1 and τ_2 back-to-back around $t = t_0$. Fitting the histogram of Figure 11.20 with Equation 11.2 results in $\tau_1 = (50.04 \pm 0.14)$ ns and $\tau_2 = (299.88 \pm 0.33)$ ns, which means that the lifetimes used for sampling are obtained back without distortions. The fitted offset $x_0 = (499.86 \pm 0.18)$ ns corresponds to the difference between the offsets added to the sampled times $t_0 = t_2 - t_1$.

The sampling was repeated to test the case of a multi-exponential scintillation time distribution. In step b), half of the photons were sampled from an exponential function of lifetime τ_{p1} and the other half from an exponential of lifetime τ_{p2}. Using the same values for τ_γ, t_1, t_2 and N, and with $\tau_{p1} = 300\,\text{ns}$ and $\tau_{p2} = 5\,\mu\text{s}$, the histogram shown in Figure 11.21 is obtained. Again, a mirrored exponential with a lifetime of τ_γ is seen for $t'_p < t_2 - t_1$. The sum of exponentials with the photon lifetimes τ_{p1} and τ_{p2} is observed at $t'_p > t_2 - t_1$.

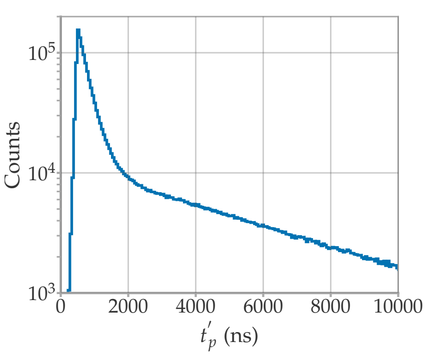

Figure 11.21: Histogram of the sampled pulse time using two exponential decays simulating the scintillation emission.

Thus, the analysis approach for the measurement data should be to find the offset time $t_0 = t_2 - t_1$, discard all data at times $t'_p < t_0$ and fit the histogram of $t'_p - t_0$. Since the lifetimes can span several orders of magnitude, the fit must be performed with the decadic logarithm of the

[13] Conventionally, the asymmetric Laplace distribution is expressed with a scale parameter λ and asymmetry parameter κ. With the substitutions $\kappa = \sqrt{\tau_1/\tau_2}$ and $\lambda = 1/\sqrt{\tau_1\tau_2}$ the form of Equation 11.2 is obtained.

measured times. These steps were applied to the data in Figure 11.21, resulting in the distribution shown in Figure 11.22.

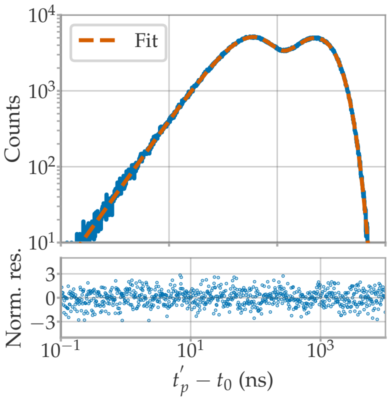

Figure 11.22: Histogram of the pulses from Figure 11.21 with time $t'_p > t_0$ on a decadic logarithmic scale. The fit was performed with Equation 11.4. The lower part shows the residuals divided by the uncertainty of the corresponding bin.

As derived in Section 8.1.2, an exponential distribution of lifetime τ has the following form in the decadic logarithmic scale:

$$S(t,\tau) = \frac{1}{\tau} 10^t \log(10) \exp\left(-\frac{10^t}{\tau}\right). \tag{11.3}$$

Following Equation 11.1, the distribution in Figure 11.22 was fitted with

$$f(t) = H \cdot \left[\alpha_1 \cdot S\left(t, \tau_{p1}\right) + (1-\alpha_1) \cdot S\left(t, \tau_{p2}\right)\right], \tag{11.4}$$

where H is a scaling parameter and α_1 is the fractional contribution of $S\left(t, \tau_{p1}\right)$.[14] For the latter, the fit resulted in $\alpha_1 = 0.463 \pm 0.003$. Recall that the same number of pulses were sampled from the two exponentials; thus, $\alpha_1 = 0.5$ is expected. The reason for this deviation is that a larger portion of the discarded pulses in the region $t'_p < t_0$ originate from the exponential with shorter lifetime (in this case τ_{p1}).

The fraction of the exponential decay used for fitting $\xi(\tau_p, \tau_\gamma)$ is calculated by integrating Equation 11.2

$$\xi(\tau_p, \tau_\gamma) = \int_{t_0}^{\infty} L(t, t_0, \tau_\gamma, \tau_p) = \frac{\tau_p}{\tau_p + \tau_\gamma}. \tag{11.5}$$

Thus, the original fractional contributions α_i are a fraction $\xi(\tau_i, \tau_\gamma)$ smaller after discarding the data in $t'_p < t_0$. Renormalising, the observed α'_1 should amount to

$$\alpha'_1 = \frac{\alpha_1 \xi(\tau_{p1}, \tau_\gamma)}{\alpha_1 \xi(\tau_{p1}, \tau_\gamma) + (1-\alpha_1)\xi(\tau_{p2}, \tau_\gamma)}, \tag{11.6}$$

which results in $\alpha'_1 = 0.464$ using the values used in this example, which is well in agreement with the fit result.

Generalising Equation 11.6 for a sum of M exponentials, the observed fractional contributions are $\alpha'_i = \alpha_i \xi_i / N$, where $\xi_i = \xi(\tau_{pi}, \tau_\gamma)$ and $N = \sum_{j=1}^{M} \alpha_j \xi_j$. Thus, after fitting a distribution obtained with data handled as explained, the corrected fractional distributions are calculated with

$$\alpha_i = \frac{\alpha'_i \xi_i^{-1}}{\sum_{k=1}^{M} \alpha'_k \xi_k^{-1}}. \tag{11.7}$$

Therefore, the envisioned measurement with gamma detection as trigger signal should produce data for accurate fits of the lifetimes τ_i. Nevertheless, the fitted fractional contributions will need minor analytical corrections. The method was also validated with toy simulations with up to five exponential distributions using different combinations of input values.

---

[14] Since this example uses only two exponentials, $\alpha_2 = (1 - \alpha_1)$.

Analysis of real data

The first step of data analysis is to determine the time t_0 of the asymmetric Laplace distribution. The pulse times at the beginning of the waveforms were grouped into a histogram to locate the approximate position of t_0. The upper part of Figure 11.23 shows the histogram of the data measured at −50 °C. A peak is clearly seen close to 0 ns. The peak is zoomed in to fit the asymmetric Laplace distribution, as presented at the bottom of Figure 11.23. In this example, the fitted position is $t_0 = (-234.3 \pm 2.4)$ ns. The fitted t_0 agree within their uncertainties between the data at different temperatures. In the following, only the pulses detected after t_0 are used and their detection time is corrected by this value.

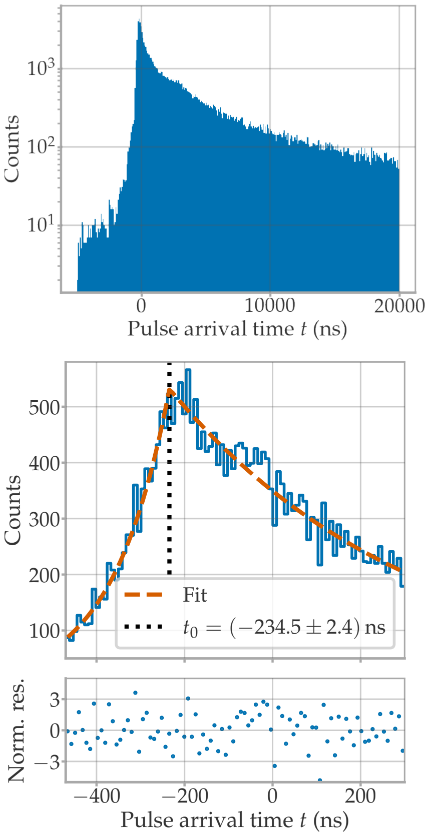

Figure 11.23: Histogram of the pulse times at the beginning of the waveforms measured at −50 °C. *Top:* the pulses in the time range −5 µs to 20 µs. *Centre:* Zoom of the peak of the histogram. The fit was performed with Equation 11.2. The lower plot shows the residuals divided by the uncertainty of corresponding bin.

As explained above, the source was masked such that only a few alphas hit the glass sample every second. However, there is always the probability that more than one decay is recorded within a waveform. An easy way to differentiate single-decay waveforms from multi-decay waveforms is to plot the time difference between a photon and its predecessor on a logarithmic scale against the arrival time of the photon. An example of a multidecay waveform is shown at the top of Figure 11.24. Since the time distribution follows a sum of exponential decays, the shortest Δt are at the beginning of the decay, increasing rapidly to larger Δt. A second peak with a similar shape appears at ~5 ms, indicating a second decay. In comparison, at the bottom of Figure 11.24, a waveform with likely a single decay is shown.

Since the decays are randomly distributed, the second decay can be found at any time within the multiple decay waveforms. This can be observed on the left side of Figure 11.25, where the Δt of all the pulses measured at −50 °C are presented as a 2d histogram. Only the single decay waveforms are useful to fit the time distribution of the scintillation. Therefore, a data selection had to be performed.

The selection of single-decay waveforms is performed by calculating a score for each waveform of the form

$$\chi_r^2 = \frac{\sum_{i=1}^{N} (\Delta t_i - \mu_i)^2}{N}, \tag{11.8}$$

where $\Delta t_i = t_i - t_{i-1}$ is the time difference from a pulse to its predecessor, N is the number of pulses inside the waveform and $\mu_i = \min(\Delta t_B, t_i)$.[15] Here, Δt_B is the expected time difference between background pulses, which is calculated as

$$\Delta t_B = 1\,\mathrm{ms}\frac{N_w}{N_p}, \tag{11.9}$$

where N_p is the number of pulses in the last millisecond of all waveforms and N_w is the number of waveforms. If $\Delta t_B \to \infty$ (i.e. there are no background pulses), then χ_r^2 is minimal for $\Delta t = t$. It has to be pointed out that $\Delta t = t$ is strictly only valid in the case of waveforms with two pulses and the first pulse being at $t = 0$ s. Nevertheless, for the pulses of the first decay in the waveforms, the time of the predecessor photon t_{i-1} is very small compared to its successor t_i, since the photons are distributed

[15] 15: The score in Equation 11.8 is based on reduced chi-square statistics with variance $\sigma^2 = 0$ and N degree of freedom (as there are no fitted parameters).

over several orders of magnitude in time and thus $\Delta t_i = t_i - t_{i-1} \approx t_i$. This approximation is no longer valid if there is a second decay later in the waveform, as in the case shown at the top of Figure 11.24.

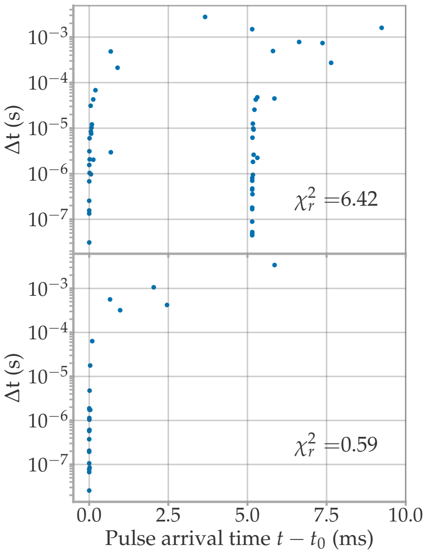

Figure 11.24: Time difference between pulses Δt of two exemplary waveforms against the arrival time of pulses. *Top:* The data shows two nearly vertical lines, produced by two different decays. *Bottom:* The data features a single line, thus it can be assumed that it is caused mainly by a single decay.

Since AP2 pulses are expected to appear at $\Delta t \sim 10^{-5.5}$ (see Section 8.2.3), pulses with Δt in the interval 1 µs to 8 µs are excluded from the χ_r^2 calculation. In the case of the waveforms of Figure 11.25, the two decay waveform scores $\chi_r^2 = 6.42$ and the single decay waveform $\chi_r^2 = 0.59$. The next step is to determine a boundary χ_r^2 for selecting the waveforms.

The χ_r^2 distribution of all the waveforms measured at −50 °C is depicted in Figure 11.26. The initial peak at low values is produced by waveforms that match the model the best, and higher values are primarily produced by multi-decay waveforms. To establish a selection boundary, the left χ_r^2 peak is fitted with a Gaussian distribution with mean μ and standard deviation σ. The best waveform selection was found to be using $\chi_r^2 < (\mu + 1.5 \cdot \sigma)$ as the selection limit, after visual inspection of a random subset of waveforms at all measured temperatures. The 2d-histogram of the selected waveforms at −50 °C ($\chi_r^2 < 1.08$) is displayed on the right side of Figure 11.25. On average, ~25 % of the waveforms are discarded at each temperature stage due to this selection. As these waveforms contain many photons, only ~57 % of the measured pulses remain for the analysis.

It has to be noted that the time distribution of the remaining pulses is relatively insensitive to the selected score boundary as long as the largest χ_r^2 are excluded. This can be seen in Figure 11.27, where the time histogram of the selected pulses is presented for different χ_r^2 cuts for the data measured at −50 °C. The histogram remains constant for selection scores between 1 to 1.5.

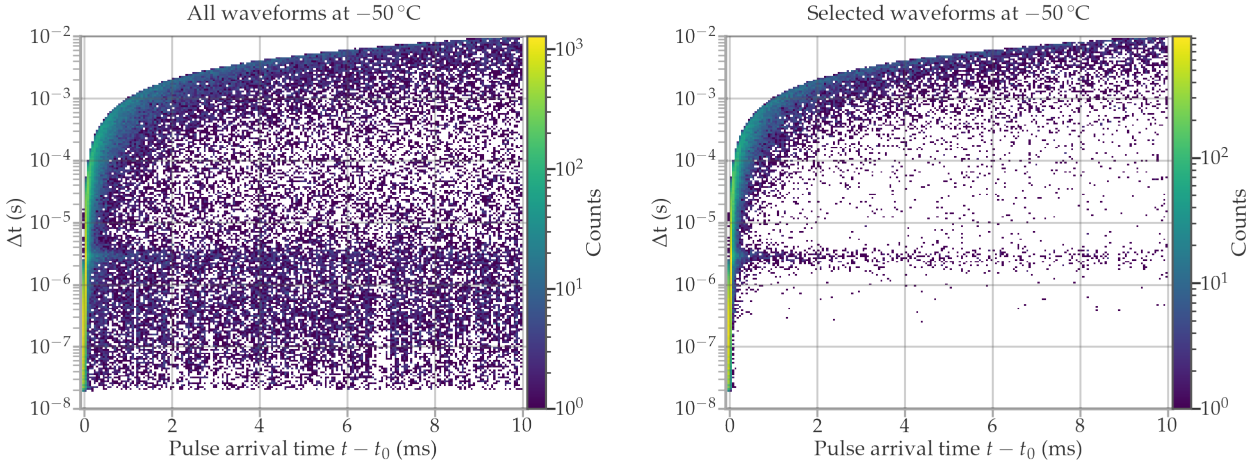

Figure 11.25: Two dimensional histogram of the time difference between pulses Δt of waveforms measured at −50 °C against the arrival time of pulses. *Left:* shows all the measured data and *right* only of the selected waveforms. The line observed at $\Delta t \sim 10^{-5.5}$ are caused by AP2.

The next step is to fit the time distribution of the selected pulses. As the fits are performed in a decadic logarithm scale, the time pulses are transformed with $x = \log_{10}(t - t_0)$. All numerical calculations are performed with x, but most of the following figures will be plotted with $t - t_0$ and logarithmic x-scale, which results in the same shape.

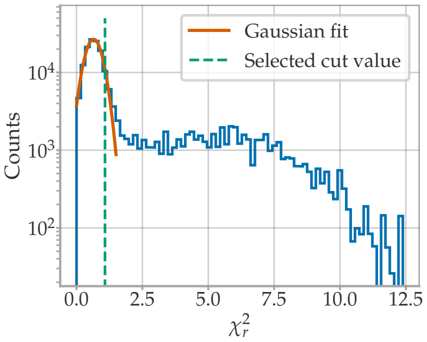

Figure 11.26: Distribution of the χ_r^2 of all waveforms for the measurement at −50 °C. Large χ_r^2 are produced by waveforms with multiple decays. The peak at low values is fitted with a Gaussian in order to set a limit for the single-decay-waveform selection.

The measured histograms are contaminated with two background sources: correlated AP2 $C(x)$ and uncorrelated dark rate $U(x)$. The PMT dark rate R_{dr} can be regarded as constant for a given temperature. Thus, it appears as $U(x; R_{dr}) = R_{dr} \cdot 10^x$ in the decadic logarithmic representation. This uncorrelated background sets the limit to the longest measurable lifetime of the measurement.

The AP2 background is correlated to a signal and depends on the intrinsic SPE time response of the PMT. Therefore it is difficult to model with an analytical function, and an extra measurement has to be performed first. Theoretically, $C(x) = F(x) * A(x)$, where $F(x)$ is any generic function describing the signal, $*$ is the convolution operator, and $A(x)$ is the AP2 time distribution, which has to be measured.

The complete fit model $f(x)$ is

$$\begin{aligned} f(x) &= \sum_{i=1}^{N} \alpha_i \cdot S_i(x; \tau_i) + U\left(x; R_{dr}\right) + C(x) \\ &= \left(\sum_{i=1}^{N} \alpha_i \cdot S_i\left(x; \tau_i\right) + U\left(x; R_{dr}\right) \right) * \left(\delta + h \cdot A\left(x\right)\right) \\ &= \left(\sum_{i=1}^{N} \frac{\alpha_i}{\tau_i} 10^x \log\left(10\right) \exp\left(-\frac{10^x}{\tau_i} \right) + R_{dr} \cdot 10^x \right) * \left(\delta + A\left(x\right)\right), \end{aligned} \tag{11.10}$$

where N is the number of exponential decays modelling the scintillation time distribution, and δ is the Dirac delta function. In total, there are $2N + 1$ free parameters.

The AP2 time distribution of the PMT was determined using an LED employing the same setup as explained in Section 8.2. Figure 11.28 shows the resulting $A(x)$ distribution in a logarithmic scale. As expected, the PMT

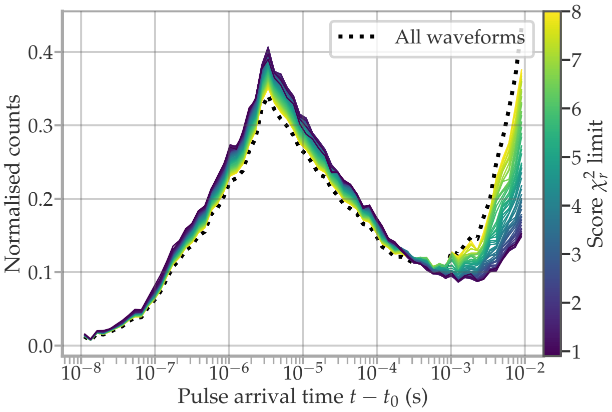

Figure 11.27: Time distribution of measured pulses in dependence of the score limit for the waveform selection.

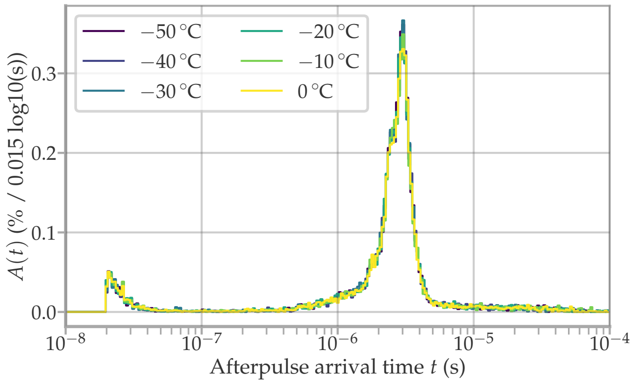

Figure 11.28: AP2 probability against its arrival time. Measured with mDOM PMT BA0373 at different temperatures.

AP2 response is most likely in the microsecond region, and the probability and time distribution do not change much with the temperature.

Since the AP2 and scintillation data are represented as histograms, the fit model with its convolution is constructed according to the following steps:

- The number of counts n_k expected in bin k from the scintillation function $\sum_{i=1}^{N} \alpha_i \cdot S_i(x; \tau_i)$ and the uncorrelated background $U(x; R_{dr})$ are calculated with

$$n_k = \int_{x_k}^{x_{k+1}} \left[\sum_{i=1}^{N} \alpha_i \cdot S_i(x; \tau_i) + U(x; R_{dr}) \right] dx, \tag{11.11}$$

  where x_k and x_{k+1} are the edges of bin k. In the following, the histogram built from all bins is referred to as M.
- The AP2 time distribution is in the form of two lists with the same number of elements. Let us call $\{T_i\}$ the list of the times in $\log_{10}(t)$ and $\{P_i\}$ the list of probabilities (x and y-axis of Figure 11.28).
  The convolution of Equation 11.10 is calculated by building a weighted histogram W_k for each bin k of M. The number of bins and range used for these histograms is the same as the one used for M. The number of counts w_l in bin l of W_k is

$$w_l = n_k \cdot \sum \{P_i | \, x_l < \log_{10}(10^{T_i} + 10^{x_{k/2}}) < x_{l+1}\}, \tag{11.12}$$

  where $x_{k/2} = (x_k + x_{k+1})/2$ is the mid value of bin k, and x_l and x_{l+1} are the edges of the bin l. The last term of Equation 11.12 stands for a conditional sum, where only the elements that comply with the condition $x_l < T_i + x_{k/2} < x_{l+1}$ are considered.
  As the times are in a decadic logarithm scale, the convolution is different for each bin. Figure 11.29 shows the histogram W_k for $x_{k/2} = -8$ (10 ns), $x_{k/2} = -5$ (10 µs) and for $x_{k/2} = -3$ (1 ms), in all cases for $n_k = 1000$. As the AP2 probability of the used PMT is ~6 %, each histogram has approximately 60 counts. In the case of $x_{k/2} = -8$, the calculated AP2 appear in a similar fashion as the measured distribution of Figure 11.28. On the other extreme, for $x_{k/2} = -3$, all AP2 pulses are grouped on the same bin, as the bin width after −3 is > 100 µs.
- The sums of all counts of the histograms W_k form the convoluted

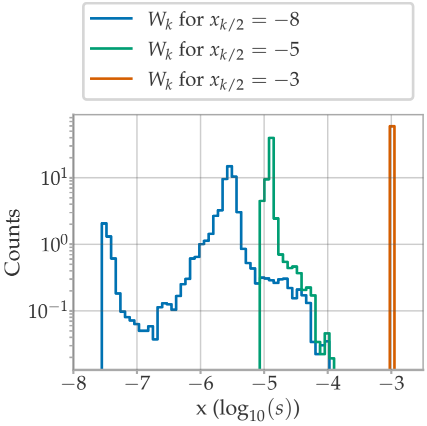

Figure 11.29: Expected AP2 time distributions for pulses located at $x_{k/2} = -8$ (10 ns), $x_{k/2} = -5$ (10 µs) and $x_{k/2} = -3$ (1 ms).

background $C(x)$. This is added to the histogram M, finishing the histogram of the fit model.

All bins of the data had over 20 counts, and thus Gaussian statistics were assumed instead of Poisson. The fit is performed using the chi-squared distribution as minimisation function

$$\chi^2 = \sum_k \frac{(y_k - m_k)^2}{y_k}, \tag{11.13}$$

where y_k and m_k are the bin counts of the bin k of the data and model, respectively. The minimisation was performed with Minuit [191, 192].

The number of exponential decays N was increased stepwise, making a new fit each time and calculating the goodness of fit χ^2/ndof. Figure 11.30 shows the mean χ^2/ndof for $N = 5$ to $N = 8$. The fit improvement from $N = 7$ to $N = 8$ is marginal, and thus N was not further increased. The fit of the measurement at −20 °C is presented in Figure 11.31 for $N = 5, 7$ and 8. Also here the improvement is noticeable from $N = 5$ to $N = 7$, but it is hard to see any difference between $N = 7$ and $N = 8$.

For the purposes of this work, the number of exponential decays and their correct differentiation is not important, since only an effective time distribution is sought for the scintillation simulation in Geant4. Therefore, the model with the best goodness of fit $N = 8$ was used. The draw-back of this, is that the fit parameters are highly correlated and have large uncertainties. The parameters of the various exponential decays should not be directly connected to physics (e.g. the lifetime of a certain electron transition), since even at $N = 2$ the parameters α_i and τ_i are correlated and their precise resolution is difficult [193, p. 103].

The fitted fractional contribution of each exponential decay α_i was corrected with Equation 11.7. The left-hand side of Figure 11.32 shows the effect of this correction on the spectrum measured at −20 °C. As expected, the correction increases the contribution of the shortest lifetime (in this case, the one for $\tau_1 = (320 \pm 13)$ ns) and reduces the relative intensity of the other components.

The right-hand side of Figure 11.32 shows the scintillation time distribution obtained at different temperatures. As introduced in Section 11.2.1, the observed lifetimes are expected to decrease with increasing temperature because the rate of non-radiative transitions increases. The results are in line with expectations. Furthermore, it can be observed that slower transitions are affected more than faster ones. The very late photons are probably produced by trapped electrons, which, due to their larger lifetimes, can more easily be released via non-radiative transitions at higher temperatures. Table C.3 in Appendix C lists the final results for all measured temperatures.

The measurement and analysis method presented provides a significant improvement over the first lifetime measurements in [152]. Figure 11.33 shows the scintillation time distribution of the VITROVEX sample at −50 °C of this work compared to [152]. The two fastest lifetimes were fitted in both works at a similar position. However, it is clear that the use of 100 µs waveforms in [152] was insufficient to capture all the emissions.

[191]: Dembinski et al. (2020), *scikit-hep/iminuit*

[192]: James et al. (1975), *Minuit: A System for Function Minimization and Analysis of the Parameter Errors and Correlations*

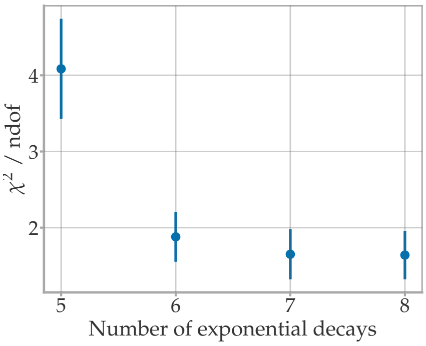

Figure 11.30: Mean goodness of fit χ^2/ndof against the number of exponential decays used in the fit function. The mean and standard deviation are calculated from the fits at the different temperatures.

[193]: Lakowicz (2006), *Principles of Fluorescence Spectroscopy*

[152]: Unland Elorrieta (2017), *Studies on dark rates induced by radioactive decays of the multi-PMT digital optical module for future IceCube extensions*

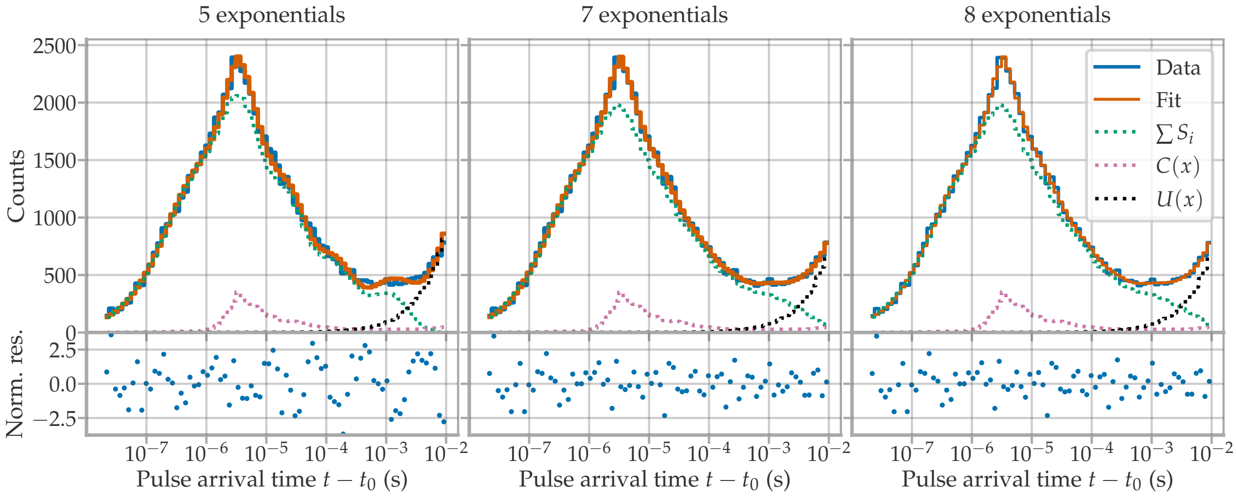

Figure 11.31: Best fit of the data measured at −20 °C using $N = 5$ exponential decays (*left*), $N = 7$ (*centre*) and $N = 8$ (*right*). The different components of the fit functions are also plotted separately with dotted lines. Here, $\sum_i S_i$ is the sum of exponential decays from the scintillation, $U(x)$ is the uncorrelated dark rate, and $C(x)$ the correlated background. The lower figures show the residuals divided by the uncertainty of corresponding bin.

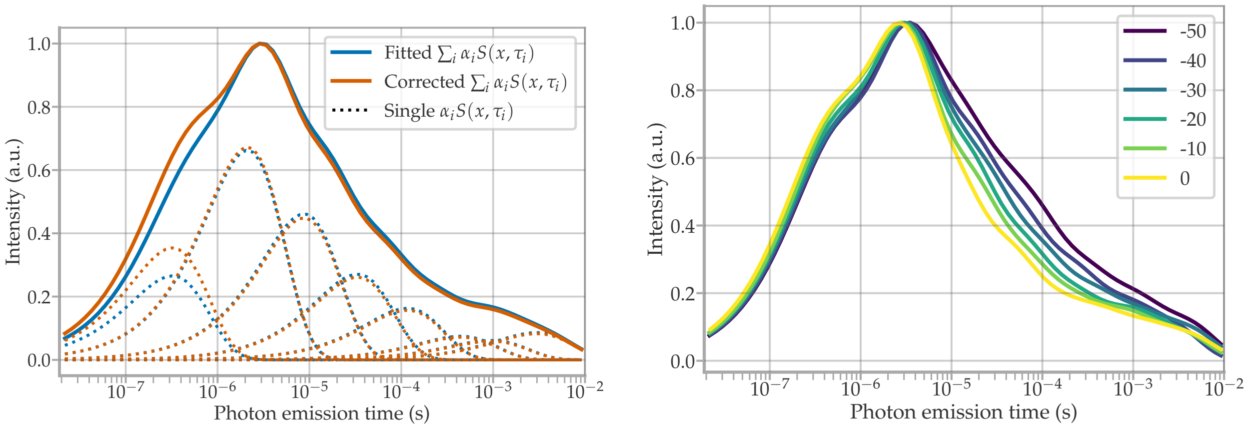

Figure 11.32: *Left:* Scintillation time distribution with the original fit parameters (blue) and after correction with Equation 11.7. The single exponential decays $\alpha_i \cdot S(x; \tau_i)$ are shown with dotted lines. *Right:* Scintillation time distribution determined at the different temperature steps. A faster emission is observed at higher temperatures.

Furthermore, performing the fits on a linear scale produces a strong correlation between the constant background parameter and the longest lifetime (see Figure 11.18). Although in logarithmic scale the random background also limits the longest resolvable lifetime, it can be fitted more easily due to its growth $\propto 10^x$.

Nevertheless, the measurement presented in this work has room for improvement. The fact that the scintillation peak coincides with the AP2 peak is suspicious. To test whether this peak is caused exclusively by AP2, the fit was repeated with an additional free parameter h scaling $A(x)$. These fits resulted in values close to $h \approx 1$ without producing significant differences in the final scintillation time distributions. The measurement could be repeated with a smaller PMT (such as the Hamamatsu R7600), so the position of the AP2 peak appears at shorter times.

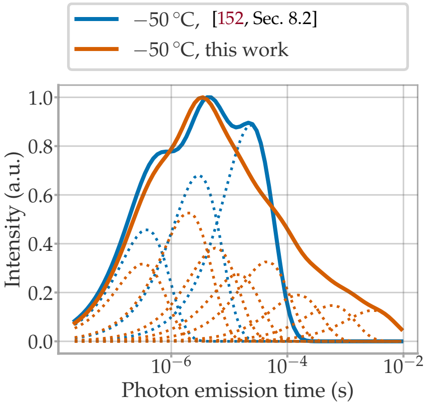

Figure 11.33: Scintillation time distribution of a VITROVEX glass sample at −50 °C as measured previously by the author in [152] and in this work.

11.2.4 SIMULATION OF RADIOACTIVE DECAYS IN THE MDOM

The Geant4 framework used in this work was introduced in Section 9.1. The simulation of radioactive decays in the mDOM pressure vessel uses the measured scintillation parameters and the specific activity of the isotopes. The code is designed to simulate the 'live time' of the mDOM in air or ice, decaying isotopes in a time window t_w. The most basic output is a list with the time of the detected photons. From this, one can, for example, calculate the expected dark rate of the module with n/t_w, where n is the number of detected photons.

The simulation takes the following steps:

- First, the number of decays to be simulated in the time window t_w is calculated using the data listed in Table 11.1, considering that one mDOM pressure vessel weighs 13 kg. Then, four runs are started, one for each decay chain. A run consists of N events, where N is the number of decays calculated for the respective chain.
- Each event starts with a single isotope randomly positioned within the volume of the pressure vessel. If this isotope is part of a chain, the run will continue with each decay until a stable isotope is reached.
- The isotope decays at t_0, which is randomly sampled from a flat distribution with limits $[0, t_w]$. Secondary particles produced by the decay move through the module and can produce Cherenkov or scintillation photons.
- It is not possible to resolve time correlations longer than the average period between dark rate pulses. Therefore, if the daughter nucleus is unstable and has a lifetime longer than 1 s, its decay time is randomised again by sampling from a flat distribution with limits $[0, t_w]$. This assumes that the chain is in secular equilibrium.
- Photons detected by the PMTs (QE is considered) are saved for further analysis.

For the simulation to work, some physical processes need to be active. These are listed in Table 11.2. The original scintillation class provided by Geant4 only allows the simulation of single or double exponential decays. This was extended in *OMSimScintillationProcess* to accept any number of exponential decays and the user only has to provide a list of lifetimes and fractional contributions. In addition, in this extended class, the scintillation yield can be selected for each particle separately.

The Geant4 class for radioactive decays was also replaced with *OMSimRadioactiveDecayProcess* to change the decay times, as explained above. By default, Geant4 decays isotope daughters randomly sampling from an exponential with the actual isotope lifetime. For long-lived isotopes, this produces photon detection times in the order of 1×10^{13} s, which is too large of a number to calculate correlations between pulses on the subsecond scale efficiently.

In the following, two different studies using this simulation are presented. First, the expected dark rate per PMT is estimated. This was important at the beginning of the mDOM development to estimate the baseline

Table 11.2: Particles and physics processes included in the simulation with their corresponding classes. The OMSimScintillationProcess and OMSimRadioactiveDecayProcess classes are a modified version of *G4Scintillation* and *G4RadioactiveDecayBase* (see text).

Particle	Process	Class
Optical photon	Absorption	G4OpAbsorption
	Optical processes at medium interfaces	G4OpBoundaryProcess
	Mie scattering	G4OpMieHG
Ions	Scattering	G4hMultipleScattering
	Ionisation	G4ionIonisation
	Radioactive decay	OMSimRadioactiveDecayProcess
Alpha	Scattering	G4hMultipleScattering
	Ionisation	G4ionIonisation
Electron / Positron	Scattering	G4eMultipleScattering
	Ionisation	G4LivermoreIonisationModel
	Brehmsstrahlung	G4eBremsstrahlung
	Cherenkov radiation	G4Cerenkov
	Positron annihilation	G4eplusAnnihilation
Gamma	Pair production	G4LivermoreGammaConversionModel
	Compton effect	G4LivermoreComptonModel
	Photoelectric effect	G4LivermorePhotoElectricModel
All particles above except photons	Material scintillation	OMSimScintillationProcess

data bandwidth needed by the modules. Subsequently, the multiplicity is investigated, i.e., the rate of coincidences between PMTs.

Dark rate caused by radioactive decays in pressure vessel

A single mDOM is simulated in an environment of ice. The module response at different temperatures is simulated by using the corresponding scintillation yield and lifetime measurements. A live time of $t_w = 1\,\mathrm{min}$ was simulated at each temperature, saving the time of the detected photons and PMT number where they were detected.[16]

The left side of Figure 11.34 shows the average Δt distribution of consecutive photons detected in a PMT at different temperatures. When only one photon from a decay is measured, it has no temporal correlation with another pulse and contributes to the Poisson distribution in the right part of the Δt curve. If more than one photon is measured after a decay, they will be timely correlated. If these are scintillation photons, they follow the time distribution of Figure 11.32. The time difference of these scintillation photons contributes to the peak at $\Delta t \sim 10^{-6}\,\mathrm{s}$. On the other hand, Cherenkov emission occurs rapidly, producing the peak at $\Delta t < 10^{-9}\,\mathrm{s}$. The relative height of the Poissonian peak increases with temperature since the lower the yield, the less likely it is to measure multiple photons from a decay. Similarly, with the Cherenkov peak: while the number of scintillation photons decreases with temperature, the average number of Cherenkov photons emitted is constant, increasing the relative intensity of the Cherenkov peak.

[16] The timing of the PMTs was not simulated.

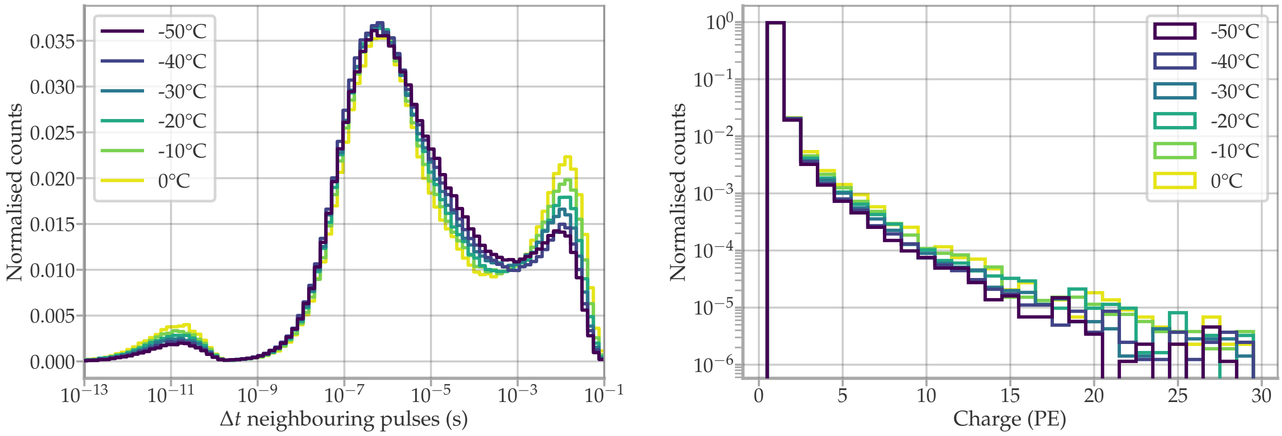

Figure 11.34: *Left:* Time difference between subsequent pulses Δt simulated at each temperature step. *Right:* The charge spectrum of the simulated background pulses. The pulse charge was estimated grouping photons that have a $\Delta t < 10^{-8}$ s.

Since the PMT has a limited time resolution, not all detected photons will produce an independent pulse but rather form MPE pulses. To estimate the amount of MPE pulses, a list was created with the charge of each photon, which initially is 1 PE for all hits. If a photon has a $\Delta t < 10$ ns with respect to the previous pulse, these two pulses were merged by adding their charges. The right-hand side of Figure 11.34 shows the generated charge spectrum. Most simulated pulses are SPE, but the MPE fraction increases with temperature from ~2.6 % at −50 °C to ~3.3 % at 0 °C. Mainly Cherenkov photons cause the MPE contribution, and since the scintillation yield diminishes with increasing temperature, the MPE fraction becomes larger.

Finally, the average background rate of each PMT was calculated. The background rate only provides the number of pulses per second. Therefore, for this calculation, any photon detected within a window of 10 ns after a previous photon was discarded. Figure 11.35 shows the average rate for each PMT in the mDOM caused by radioactive decays in the pressure vessel. The rate decreases with temperature following the temperature dependence of the yield (see Figure 11.16).

Thus, at −20 °C, temperature near the expected in IceCube Upgrade, each PMT should measure (406 ± 10) 1/s photons from radioactive decays in the glass of the pressure vessel. The given uncertainty only considers the systematics from the scintillation yield shown in Figure 11.16. However, [184] showed that the scintillation parameters change between different production batches of the glass. Also the amount of radioactivity in the glass can vary between batches, as was measured in [152]. Thus, the given rate here should be taken with caution. Nevertheless, the first dark rate measurements with DVT modules showed an acceptable agreement with the simulation, as will be presented in Section 11.3.

The pressure vessels used in the mDOM production stem from two batches. The scintillation parameters and radioactivity of a few of these pressure vessels are planned to be measured before their assembly. This measurements should provide the best parameters for future simulation studies.

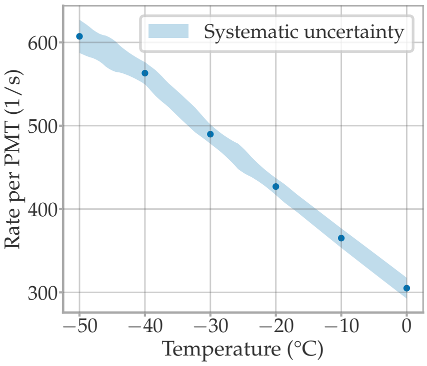

Figure 11.35: Mean dark rate per PMT produced by radioactive decays inside the pressure vessel. The shaded region shows the systematic uncertainty, which stems from the uncertainty of the scintillation yield (see Figure 11.16).

[184]: Dittmer (2020), *Characterisation of scintillation light induced by radioactive excitation in the mDOM glass pressure vessel*

[152]: Unland Elorrieta (2017), *Studies on dark rates induced by radioactive decays of the multi-PMT digital optical module for future IceCube extensions*

Background multiplicity rate

One of the advantages of a multi-PMT design is the ability to measure photons from an event simultaneously in several PMTs within the same module (local coincidence). The first study to utilise local coincidence in the mDOM investigated the potential to detect neutrinos from core-collapse supernovae (SN) [109]. These neutrinos have an energy of a few MeV, which is too low to cause detectable signatures across multiple modules in the vast majority of cases. However, light produced by interactions close to the strings can be detected by several PMTs within a single module. Figure 11.36 shows the multiplicity[17] histogram estimated for a SN of 27 $M_\odot$ progenitor mass at 10 kpc for a detector built with 10,000 mDOMs [109]. In contrast, a flux of SN neutrinos in the current IceCube detector may only be recognised as a collective rate enhancement in all photomultipliers [194].

[109]: Lozano Mariscal et al. (2021), *Sensitivity of multi-PMT optical modules in Antarctic ice to supernova neutrinos of MeV energy*

[17] Multiplicity is the number of PMTs that detected photons 'simultaneously' inside a pre-defined time window.

[194]: Köpke (2018), *Improved Detection of Supernovae with the IceCube Observatory*

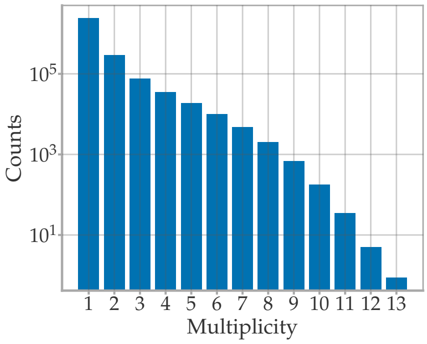

Figure 11.36: Multiplicity events for a detector with 10,000 mDOMs for a SN with 27 $M_\odot$ progenitor mass at 10 kpc. The multiplicity was calculated for a time window of 20 ns. Data from [109].

It was shown that the sensitivity to MeV neutrinos can be significantly increased using conditional triggers based on local coincidences with the mDOM [109]. For this local coincidence study, it was essential to determine the baseline multiplicity rate of the modules. The multiplicity caused by the radioactive decay inside the pressure vessel was the most significant contributor to the background. This section summarises how this background multiplicity rate was determined by the author using the Geant4 simulation and explains the source of the largest multiplicities.

The Geant4 simulation was configured and run as introduced at the beginning of this section. However, as only a few supernovas are expected during the detector lifetime, the trigger has to exclude background events with high confidence. This means that a very long live time t_w must be simulated to simulate the rarest events. Consequently, the simulated data cannot be saved in the form of lists of photons, as the storage required would be too large. Instead, the simulation was run in a loop using $t_w = 20\,\text{min}$. The detected photons were analysed at the end of each loop, and a multiplicity histogram was filled and saved. The multiplicity was calculated as follows:

- The detection time of all photons was sorted ascendingly.
- A time window of 20 ns is open, starting with the first detected photon. If $m-1$ other PMTs measured a photon in this time window, there was a multiplicity m event. Multiple photons detected in a single PMT do not contribute to the multiplicity.
- The next time window is opened, with the first photon outside the previous time window.

The results are represented as a rate, i.e. the number of multiplicity events expected per second. The lowest resolvable rate for a multiplicity is $1/T_w$, where $T_w = N \cdot t_w$ is the total simulated live time and N the number of simulation runs. The first simulations were run isolating the scintillation and Cherenkov process to check whether there was a dominant source. Figure 11.37 shows the multiplicity rate for a single mDOM with the Geant4 configured in three ways: only using Cherenkov photons, only considering scintillation, and both processes activated. The multiplicity 1 corresponds to the total dark rate of the module and is entirely dominated

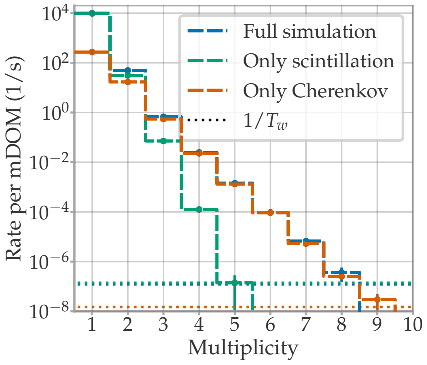

Figure 11.37: Multiplicity rate distribution for a single mDOM in ice. The simulation was performed once with both scintillation and Cherenkov active, and also with each process alone. The horizontal dotted line indicates the smallest resolvable rate in the simulated live time T_w.

by scintillation, which agrees with the results shown in the previous section. However, Cherenkov starts to overshadow the scintillation's influence at increasing multiplicities. Scintillation photons produce only $\sim 11\,\%$ of the rate at multiplicity 3, decreasing to $\sim 0.01\,\%$ for multiplicity 5. If one is interested in characterising the higher multiplicity region, one can take advantage of the Cherenkov dominance, as deactivating scintillation boosts the simulation time dramatically. From now on, all rates were simulated and calculated using Cherenkov only.

Geant4 is capable of saving events for their later visualisation. Using this tool, it was determined that the high multiplicity events were produced almost entirely by gamma particles interacting in the ice. Indeed, further data analysis showed that most of these events are caused by ^{208}Tl from the ^{232}Th natural chain. To confirm this, each component listed in Table 11.1 was simulated separately. In case of the ^{232}Th chain, it was truncated right before the ^{208}Tl decay (which is the isotope previous to the last isotope of the chain). Additionally, a simulation was run decaying ^{208}Tl exclusively. Figure 11.38 shows the fractional contribution of each component to the total rate. The ^{208}Tl decays produce the majority of the rate from multiplicity 5 onward.

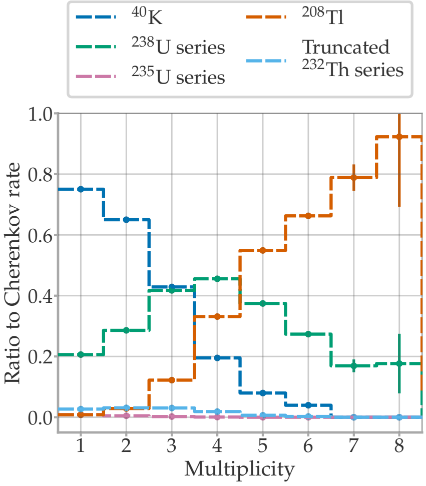

Figure 11.38: Fractional contribution of each decay chain to the multiplicity rate (only considering Cherenkov radiation). The ^{232}Th was truncated right before a ^{208}Tl decay to separate both components.

^{208}Tl decays via β^- into an excited state of ^{208}Pb (stable, last isotope in the series), which de-excites emitting a gamma of $E_\gamma = 2.614\,\mathrm{MeV}$ [195]. This is the highest energy gamma emitted from all the isotopes present in the pressure vessel. Gamma particles can interact with the ice mainly via the photoelectric effect (emitting an electron of energy $E_\gamma - B$, with B the binding energy of the electron), Compton scattering (with a maximal energy transfer to the electron of $2E_\gamma^2/(m_e c^2 + 2E_\gamma)$, that is 2.381 MeV for $E_\gamma = 2.614\,\mathrm{MeV}$) and pair production [189]. In all cases, an electron is emitted, nevertheless, they have to surpass the Cherenkov energy threshold E_{th} to produce photons, with

[195]: Martin (2007), *Nuclear Data Sheets for A = 208*

[189]: Knoll (2010), *Radiation detection and measurement*

$$E_{\mathrm{th}} = m_e c^2 \left(\sqrt{\frac{n^2}{n^2 - 1}} - 1 \right) \approx 280\,\mathrm{keV}, \tag{11.14}$$

where $m_e c^2 = 511\,\mathrm{keV}$ and $n = 1.31$ is the refractive index of ice. Figure 11.39 shows the gamma cross section in water for the photoelectric effect (σ_{ph}), Compton scattering (σ_C) and pair production (σ_{pp}). It is clear that virtually all photons measured from gamma particle interactions emitted in radioactive decays will originate from Compton-scattered electrons.

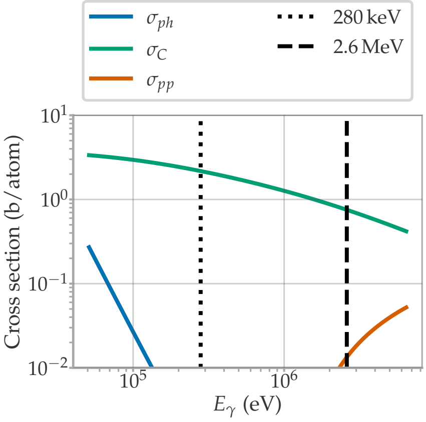

Figure 11.39: Energy dependence of the interaction cross section of gamma particles in water. σ_{ph}, σ_C and σ_{pp} stand for the cross section of the photoelectric effect, Compton scattering and pair production, respectively. Cross sections were calculated using the equations of [196]. The dashed vertical line shows the energy of the gamma particle emitted during the ^{208}Tl, and the dotted line shows the threshold energy of electrons for Cherenkov emission.

Figure 11.40 displays a screenshot of a gamma emission after a ^{208}Tl decay, as seen in the Geant4 user interface. In this example, the gamma particle scatters multiple times, with three of the scattered electrons overpassing the E_{th} threshold and producing Cherenkov cones. It is not difficult to visualise how such events can produce large multiplicities depending on the path taken by the gamma particle.

However, although the ^{208}Tl decay releases the highest energy gamma, this E_γ is not an extreme outlier. Figure 11.41 shows the gamma emission rate for an mDOM pressure vessel for gammas with $E_\gamma > 1\,\mathrm{MeV}$. ^{214}Bi, from the ^{238}U decay chain, produces a rate of multiple high energy gamma

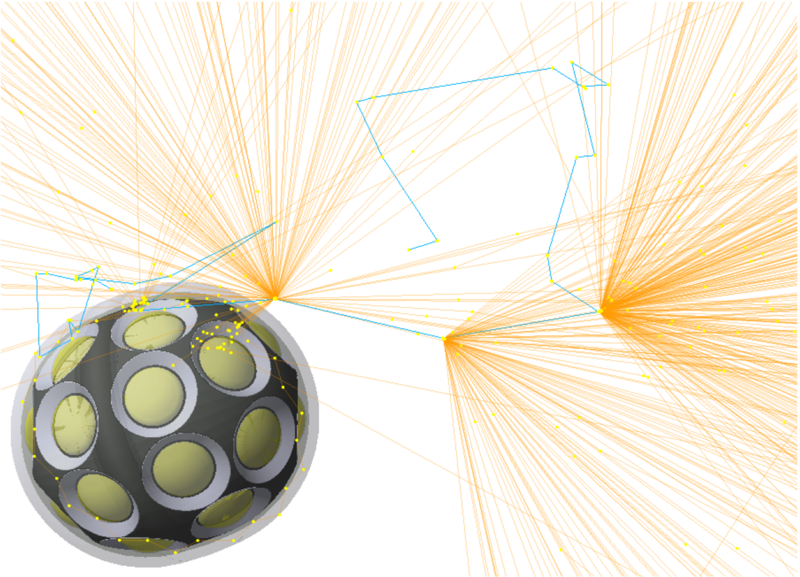

Figure 11.40: Example of a ^{208}Tl decay inside the mDOM pressure vessel as seen in the Geant4 visualiser. The cyan lines show the trajectory of the released gamma particle, while the orange lines show the path of photons. The yellow dots show interaction points. The gamma scatters multiple times, and in three cases, the scattered electron has an energy above the Cherenkov threshold, producing photons.

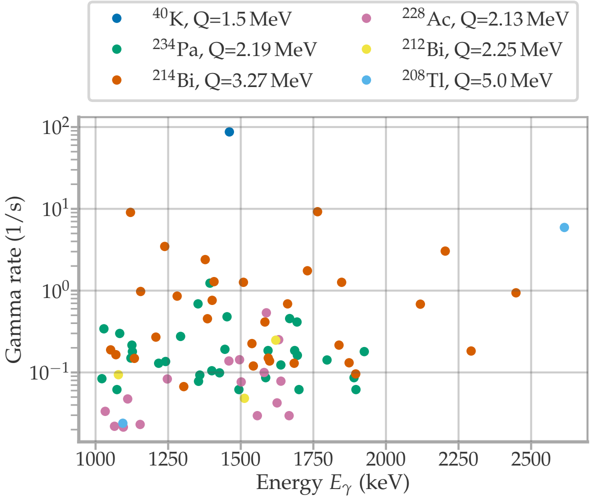

Figure 11.41: Gamma emission rate per mDOM pressure vessel against the energy of the gamma particle. Only gamma particles with $E_\gamma > 1$ MeV were considered. The legend of the figure shows the mother isotope, after whose decay the gamma is emitted. Also the Q-value of the decay is given in the labels. Data was collected using the Python package *PyNe* [197].

of up to $E_\gamma = 2.448$ MeV. For example, a rate of $\sim 3\,\mathrm{s}^{-1}$ of a $E_\gamma = 2.204$ MeV gamma particle is expected from ^{214}Bi, which is in the same order as the ^{208}Tl decay with a gamma emission rate of $\sim 6\,\mathrm{s}^{-1}$. However, the main difference between the ^{208}Tl and ^{214}Bi is their Q-value. With a Q-value of $Q = 5.0$ MeV, ^{208}Tl is the decay with the largest amount of energy released from all the isotopes displayed in Figure 11.41. Thus, the highest multiplicities are produced by the (potentially) high-energy electron released after the β^- ^{208}Tl decay in the pressure vessel and the Compton scattered electrons in the ice. On the other hand, ^{40}K can either decay via electron capture to ^{40}Ar or β^- to ^{40}Ca. There are no gamma transitions for the latter; thus, solely the decay to ^{40}Ar produces the (largest) gamma emission rate shown in Figure 11.41. Thus, a coincident detection of a gamma and β^- particle is not possible in the case of ^{40}K. Nevertheless, due to its high specific activity (see Table 11.1), this isotope is the main culprit of the low multiplicity rate caused by Cherenkov photons, as observed in Figure 11.38.

With a Q =3.16 MeV, ^{214}Bi has the second largest Q-value of the gamma emitters presented in Figure 11.41. However, the released β^{-1} has a smaller maximal energy compared to ^{208}Tl, especially in the cases of the highest gamma energy emissions. Nevertheless, ^{214}Bi is the most important isotope for the high-multiplicity rate in the ^{238}U, as observed in Figure 11.42, where the fraction of the ^{238}U multiplicity rate caused by ^{214}Bi is presented. With Figure 11.38 and Figure 11.42, it can be concluded that multiplicities larger than 4 are almost exclusively produced by ^{208}Tl and ^{214}Bi, with a minor contribution of ^{40}K.

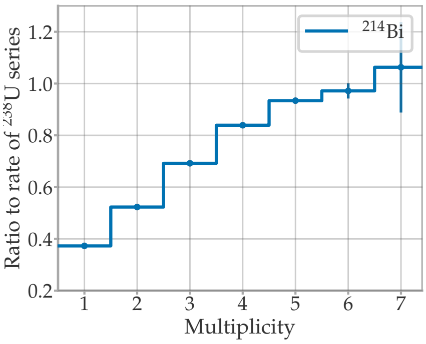

Figure 11.42: Fractional contribution of ^{214}Bi to the total multiplicity rate produced by Cherenkov photons from the ^{238}U decay series (only considering Cherenkov radiation).

Figure 11.43 shows the sum of all fractional contributions from Figure 11.38. For all multiplicities, the sum is compatible with 1, considering the uncertainty. Recall that for Figure 11.38 each contribution was simulated separately, but normalised with the rate from the simulation which mixed all isotopes. This means that the probability of two isotopes decaying simultaneously and producing a high multiplicity event is negligible in the simulated time scales. If this were not the case, the sum would be < 1, since the rate from these coincidences would be missing. From this, one may also conclude that coincident decays from neighbouring modules are also very unlikely to produce a high multiplicity event.

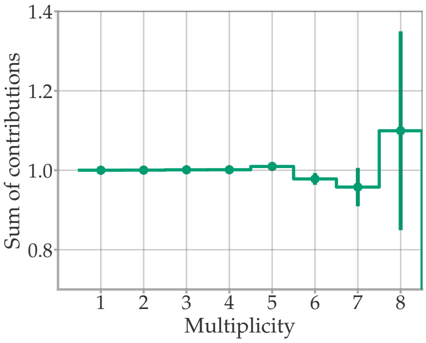

Figure 11.43: Sum of the fractional contributions shown in Figure 11.38. As the rate sums to 1, the probability of mixing different decays in a single time window is negligible.

The calculated multiplicity rates presented in this section suffer from large systematic uncertainties. On the one hand, they scale with the specific activity provided in Table 11.1 and thus, any systematic from this measurement will propagate directly to the calculated rate. On the other hand, small changes in the simulated geometry of the mDOM produce relatively large changes in the multiplicity. At one point during the development of the Geant4 framework, the geometry of the pressure vessel was changed to include the 2.8 ° wall inclination of its equatorial region (see Figure 4.2), which until that point was approximated as a cylinder with the 0 ° wall inclination. The ratio of the multiplicity rate of these two geometries is presented in Figure 11.44. With the improved geometry, the rate for multiplicities ≥ 2 increased to approximately double the previous rate, demonstrating the sensitivity of multiplicities to the shape of the pressure vessel. All the rates shown in this section were calculated with the up-to-date mDOM geometry. However, there is still room for future improvements in the Geant4 model, such as refining the holding structure geometry, which may change the expected multiplicity rate again.

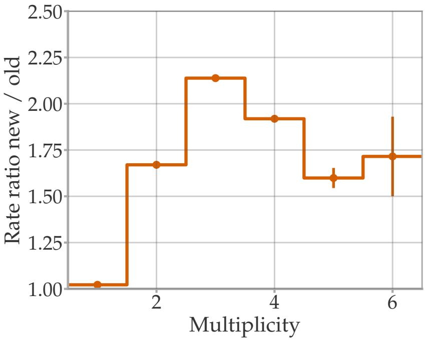

Figure 11.44: The fraction between the multiplicity rate simulated with the updated pressure vessel geometry and the simpler model.

Furthermore, the internal components of the mDOM, such as the mainboard, cables, and PMT dynodes, are not simulated in Geant4. Many of these components are dense materials. The cross section of gamma particles scales with the atomic number of the target material. Thus, these components may act as gamma particle absorbers and the calculated multiplicity rates would be potentially overestimated. For a quick estimation, a simulation was run with the photocathode of the PMTs as a 100 % gamma particle absorber. Thus, a large fraction of the gamma particles passing through the mDOM were deleted from the simulation. In this case, the rate for multiplicities > 4 was reduced by ~15 %. This is a rather small deviation compared to the geometry effects shown in Figure 11.44. However, an update of the Geant4 geometry with the internal components should be considered once larger uncertainty sources are solved or excluded.

Finally, the multiplicity rates discussed in this section are caused only by radiation from the pressure vessel. The amount of data on the specific activity of the PMT glass is relatively small, but traces of all natural decay chains can also be found in the tube glass. Section 11.2.5 deals with the simulation of radioactive decays inside the PMT glass and presents the first estimations of the multiplicity rate from this radiation.

11.2.5 Simulation of mDOM PMTs with increased radioactivity

As introduced in Section 8.1, ~90 % of the mDOM PMT glass tubes were produced with a higher radioactive contamination. Due its large number of PMTs, ~2 kg of the mDOM weight stem from PMT glass. The isotope concentrations of the glass were kindly provided by Hamamatsu in the form of specific activity for ^{40}K and the natural decay chains. These activities are the backbone for a Geant4 simulation of these decays, but remain confidential.

Radioactive decays in PMTs were simulated using the same Geant4 framework as in Section 11.2.4. Here, instead of generating the isotopes inside the pressure vessel, they were randomly positioned inside the PMT glass.

Measurements of the scintillation parameters of the PMT glass are currently planned inside the Münster IceCube group. To make an initial calculation of the impact of the new PMT dark rate for the module as a whole, the scintillation parameters were estimated using the dark rate measurements made in Münster and the mass testing of the IceCube collaborators in Aachen and Dortmund. These estimations only involved the time distribution of the scintillation and the yield. The scintillation spectrum cannot be assessed with the currently available data and needs its own dedicated measurement. Thus, in the following discussion, it was assumed that the spectrum of the PMT glass was the same as the one from VITROVEX glass (see Figure 11.17).

The first simulations were performed modelling the dark rate experiments with a single PMT. The environment surrounding the PMT was air, to match the real measurement conditions.

In a first iteration, the PMT glass was defined with the scintillation lifetimes of the VITROVEX glass. Subsequently, the time difference between simulated detected photons Δt was calculated and represented in a $\log10(\Delta t)$ histogram. The latter was compared to the measured distribution at −20 °C of Section 8.1.3 (see Figure 8.12). The lifetime constants were iteratively adjusted until a reasonable agreement between the simulation and measurements was found. Here, the adjustment was performed 'by hand' since a fit would have taken prohibitively long due to the large number of fit parameters and long simulation time. Moreover, a perfect reproduction between simulation and measurement was not sought, but only a reasonable agreement, as the undergoing measurements of the scintillation parameters will provide the best results. The resulting comparison of the MC data is shown in Figure 11.45.

After the time constants were evaluated, the expected dark rate was simulated for various scintillation yields. An artificial dead time of 100 ns was set to match the measurement configuration of the PMT mass testing facilities of Aachen and Dortmund. Figure 11.46 shows the calculated rate against the configured scintillation yield in the simulation. As reported in Section 8.1, the average dark rate measured at the Aachen and Dortmund facilities was 369 s^{-1} at −20 °C. In the testing facilities, the mean probability of AP2 was measured to 5.65 % (see Section 8.1.3), which has to be subtracted from the rate, resulting in a target rate of 348 s^{-1}. Fitting the data shown in Figure 11.46 with a linear function results in a yield of $(120.8 \pm 0.9)\,\mathrm{MeV}^{-1}$ to match the corrected mean dark rate. As was introduced in Section 5.4, there are several sources for the PMT intrinsic background. In this Section, however, it was assumed that the dark rate of the new mDOM PMTs is only produced by radioactive decays in the glass. Notwithstanding, this approximation is not far from reality, as the original mean dark rate of this PMT type was $(35.2 \pm 1.5)\,\mathrm{s}^{-1}$ (see Section 8.1.2).

To test the estimated parameter values and the simulation, the dark rate and its Δt-distribution for PMT in a gel environment were calculated. This was compared with the measurement results shown in Section 8.1.3 of a PMT with its surface covered with black tape. Recall that this measurement was done to estimate the dark rate of the PMTs coupled to the gel, where a lower dark rate is expected than in air, because the near-matching refraction indices reduce the total internal reflection inside the bulb's glass.

Figure 11.47 presents the Δt-histogram of the simulation and measurement showing a good MC-data agreement. Furthermore, this simulation resulted in an expected dark rate of $(203.5 \pm 2.5)\,\mathrm{s}^{-1}$. This means a rate fraction between the PMT simulated in air and gel of (1.725 ± 0.021). The measurements of Section 8.1.3 comparing the PMT dark rate in air and with a taped surface resulted in a compatible fraction of (1.70 ± 0.08). This means that although the estimation of the scintillation parameters was made in an air environment, the simulation is still capable of predicting the PMT background under different conditions.

The dark rate simulation of Section 11.2.4 was repeated simulating the radioactive decays in the pressure vessel and each PMT glass. Assuming a PMT dead time of 10 ns, a rate of (715.2 ± 0.7) 1/s is expected for each PMT for an mDOM with 24 high-radioactivity PMTs in ice at −20 °C. Using the background data generated with this Geant4 simulation it was determined by the IceCube Collaboration that the PMTs would still satisfy the requirements in terms of neutrino reconstruction quality and required cable bandwidth.

Also, the multiplicity rate for an mDOM equipped with 24 high-radioactivity PMT was simulated. As was done in the last section, the scintillation process was deactivated during the simulation, and thus the rather crude estimations of the scintillation parameters do not influence the results. Figure 11.48 shows the ratio between the simulated rate that includes

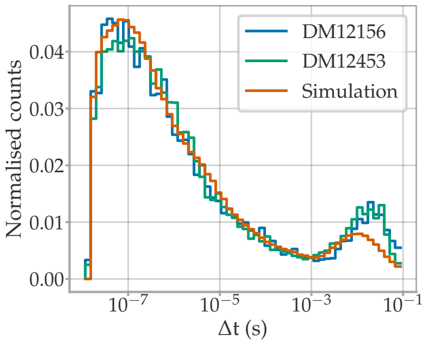

Figure 11.45: Distribution of the time difference between subsequent dark rate pulses Δt. Measurement results from Section 8.1.3. The scintillation lifetimes were adjusted such that the distribution matches the one of the measurements.

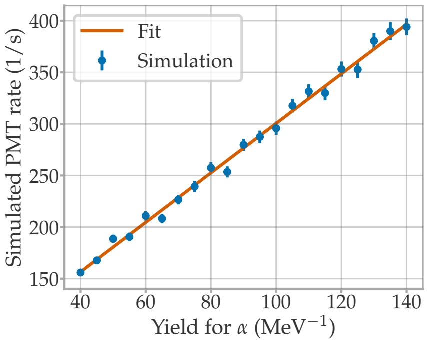

Figure 11.46: Simulated PMT dark rate against the yield for alpha particles configured in Geant4. The data were adjusted with a linear function.

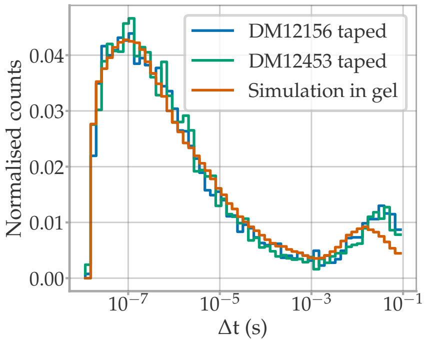

Figure 11.47: Distribution of the time difference between subsequent dark rate pulses Δt. Measurement results are with taped PMTs (see Section 8.1.3). The simulation results are for a PMT in gel.

PMT radioactivity and the simulation that exclusively considers decays in the pressure vessel. The multiplicity rate should increase between ~10 % and ~20 %.

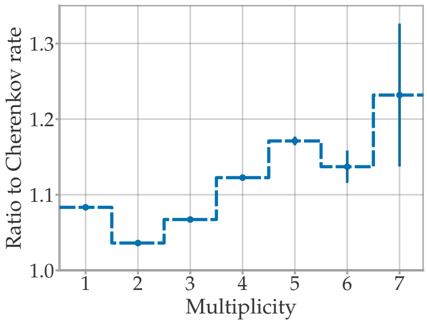

Figure 11.48: Ratio of the multiplicity rate produced by Cherenkov photons in an mDOM with high-background PMTs and an mDOM with early-production PMTs.

11.3 FIRST BACKGROUND MEASUREMENTS WITH DVT 04

After integration of the first DVT modules, there was the opportunity to measure the dark rate of the mDOM and compare it to the simulations. All modules were assembled with PMTs of low intrinsic dark rate (serial numbers <DM01130).

The DVT 04 module, *Rapunzel*, was measured inside a climatic chamber at temperatures of −40 °C, −30 °C, −20 °C, and −10 °C. The measurements presented in this section were controlled with the 'T-mDOM' software developed by the IceCube Collaboration. Before performing the dark rate measurement, the module had to be calibrated.

First, a gain calibration was performed for each PMT in all temperature steps following the procedure described in Section 6.2. The module's internal LEDs were used at a low intensity as the light source for this calibration. The readout of waveforms is triggered by the mainboard together with the LEDs. The resulting charge spectra were adjusted with Equation 5.6. The calculated nominal voltages are presented on the left side of Figure 11.49. Here, the nominal voltages are given as the absolute voltage of the last dynode v_{10}. This is the parameterisation used by the µBase firmware. As expected from Section 6.2.2, the nominal voltages of all PMTs decrease with temperature.

During the dark rate measurement, the waveforms are triggered by the AFE discriminators, which are set to a certain ADC level. Therefore, the ADC trigger of the discriminators had to be configured so that they correspond to a 0.2 PE threshold.

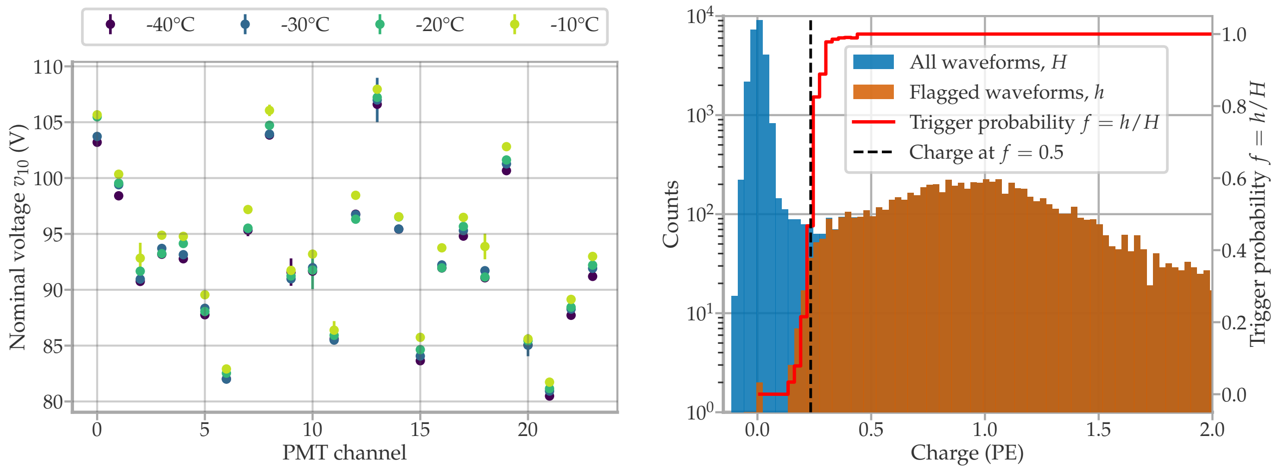

Figure 11.49: *Left:* Calculated nominal voltages of all PMT channels of DVT 04 at −40 °C, −30 °C, −20 °C, and −10 °C. The nominal voltage is given as the absolute value of the voltage of the last dynode v_{10}. *Right:* Charge spectrum of all waveforms (blue) and of those in which the discriminator was activated (orange). The ratio between these two histograms f estimates the probability that a pulse with a certain charge triggers the discriminator. The translation from the discriminator level to PE was defined as the charge at which the ratio is 0.5 (i.e., a 50 % of the pulses with that charge are measured).

For the calibration of the discriminators, again, charge spectra were measured using the internal LEDs. The waveforms have a flag indicating if the discriminators of the respective channel were activated at any given time. Thus, a charge spectrum is built using all waveforms and another using only the waveforms that had the discriminators activated. An example is illustrated on the right side of Figure 11.49.

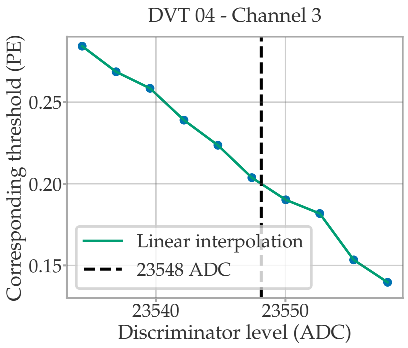

Figure 11.50: The calculated corresponding threshold in PE against the set discriminator level (in ADC counts). The data points were linearly interpolated to find the discriminator level that corresponds 0.2 PE.

The probability for a pulse of certain charge to trigger the discriminator is calculated using the ratio between the counts of the two histograms. The charge where the trigger probability is 50 % defines the discriminator threshold in PE (i.e., a 50 % of pulses with this charge are detected). This process is repeated at multiple discriminator levels and the results are interpolated to find the level that corresponds to 0.2 PE, as exemplified in Figure 11.50. This translation should be independent of the temperature since the nominal voltage is adjusted at each temperature step. Therefore, the discriminator threshold calibration was only performed at −20 °C.

The trigger probability was measured again using the interpolated values for 0.2 PE to validate the calibration. Figure 11.51 shows the results of all PMTs. Although there are undoubtedly deviations between channels, the calibrated thresholds behave similarly, with the average charge at $f = 0.5$ being (0.196 ± 0.040) PE and a standard deviation of 0.02 PE between channels.

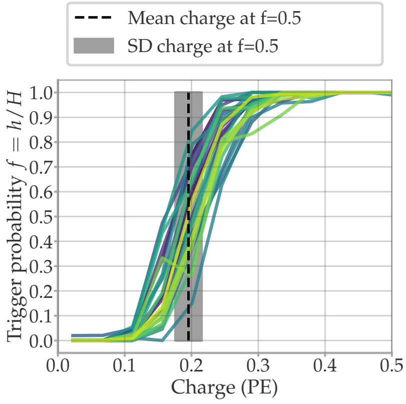

Figure 11.51: The probability that the discriminator is activated in dependence on the charge of the pulse. The discriminators were set at the calibrated threshold levels corresponding to 0.2 PE. Each colour represents one of the 24 PMT channels. SD stands for standard deviation.

After the PMTs and discriminators were calibrated, the dark rate measurement was started. The module's surface was covered with black tape to simulate the optical coupling between the pressure vessel and the ice, ensuring no air bubbles remained between the tape and the glass surface.

Scalers are implemented in the FPGA for each channel to count the threshold crossings of the discriminator. The user can configure the integration period T of the scaler and dead time. For the following measurement, an integration period of 100 ms and a dead time of 80 ns were configured. Thus, the dark rate R of a PMT channel can be calculated with $R = N/T$, where N is the counts integrated by the scaler.

After setting a temperature in the climate chamber, DVT 04 was left inside for at least 12 h. During this time, the mainboard temperature sensor was read to verify that thermal equilibrium was reached before the dark rate measurement (once the internal temperature was constant). The dark rate of all channels was then continuously measured using the scalers for 22 h. In Section 11.1.1 it was discussed that external fields produce a steady increase of the dark rate (Figure 11.6). The dark rate of the module was observed to be constant at all temperatures for all channels. Thus, an influence from fields inside the module or reflectors can be excluded at least in the measured time scale. The raw data are displayed in Figure F.1 and Figure F.2 in Appendix F.

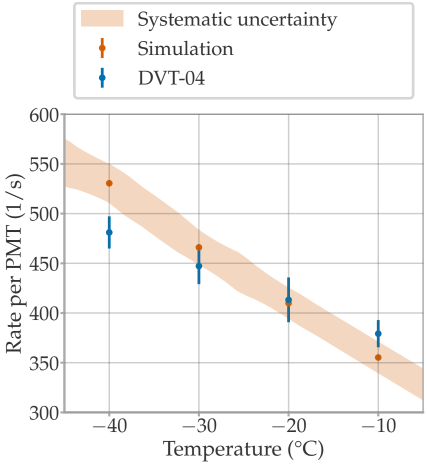

Figure 11.52: Mean PMT dark rate measured in DVT 04 with a taped surface compared to the results of the Geant4 simulation.

Figure 11.52 shows the mean dark rate between all channels at the measured temperatures. A decrease in the rate with temperature is observed, as expected from the results of Section 11.2.4. The simulation results were compared to the measurements by calculating the expected dark rate in Geant4 with an artificial dead time of 80 ns. The hereby obtained rates were scaled by 1.0565 to account for the increase in the rate due to AP2. Also, the intrinsic dark rate of the PMTs had to be considered. For this, the mean dark rate of the low radioactivity PMTs measured in Section 8.1.2 ($(35.2 \pm 1.5)\,\mathrm{s}^{-1}$) was divided by 1.7 [18] and added to the simulated rate. The results are also presented in Figure 11.52, where the systematic uncertainty considers the systematics of the scintillation yield and the standard deviation of the AP2 probability between PMTs.

The agreement between the simulation results and the module is very good, especially considering that the simulation is based on a first-principle approach. Nevertheless, the slopes of the curves differ. This might be explained by a change in the scintillation properties between different batches of pressure vessel production. As mentioned in Section 11.2.4, measurements of the scintillation parameters of mDOM pressure vessels are planned.

At the time of writing this thesis, no module with high dark rate PMTs has yet been assembled to test the estimations of Section 11.2.5.

[18] The measurements of Section 8.1.2 were performed in air, but after optical coupling with optical gel the rate is reduced by the factor 1.7 (see Section 8.1.3 and Section 11.2.5).

12

In situ relative transit time calibration

In the current IceCube detector, the timing is required to be calibrated to a maximum of 4 ns RMS for the individual DOMs and 7 ns RMS for the entire DAQ system. The master-clocks of the DOM motherboards are synchronised using *Reciprocal Active Pulsing Calibration* (RAPCal) [86]. During a RAPCal, the data transmission of the detector is stopped, and a bipolar pulse is sent to each module. Upon reception, the DOM sends back a bipolar pulse to the surface. The emission and reception of each pulse are timestamped with the local clock, thus determining the cable delay. This method allows the clocks to be synchronised with an uncertainty within 1 ns [2]. The synchronisation with the time of PMT pulses is verified using the LED flashers of the DOMs (DOMs measure photons from the LEDs of the DOM below them) and with muon tracks.

[86]: Abbasi et al. (2009), *The IceCube Data Acquisition System: Signal Capture, Digitization, and Timestamping*

[2]: Aartsen et al. (2017), *The IceCube Neutrino Observatory: Instrumentation and Online Systems*

This inter-module time calibration will remain valid for the mDOMs in IceCube Upgrade. However, as it is a multi-PMT module, the relative time between the PMTs of a single module also has to be calibrated. The absolute transit time of each PMT is measured with a sub-nanosecond precision during the final acceptance tests (FAT) of the mDOMs. Nevertheless, as was observed in Section 6.5 and Section 7.4, the transit time of the PMTs depends on the orientation and strength of the magnetic field, with deviations of up to ~2 ns. Therefore, the absolute transit time determined during FAT may require corrections by in situ measurements. This chapter introduces a potential calibration method using the radioactive decays inside the pressure vessel and presents the first tests with DVT 09, *Hänsel*.

12.1 Introduction to the calibration method

The KM3NeT multi-PMT modules are calibrated in situ using the simultaneous detection of Cherenkov light produced in potassium decays in seawater by several PMTs of a module [198, Ch. 11]. Inspired by this method, Geant4 studies in the scope of a Master thesis showed that decays in the mDOM pressure vessel can also be used for relative transit time calibrations [199]. In this section, the explored relative transit time calibration method is introduced and revisited using the new PMT Geant4 model presented in Chapter 9.

[198]: Reubelt (2019), *Hardware studies, in-situ prototype calibration and data analysis of the novel multi-PMT digital optical module for the KM3NeT neutrino telescope*

[199]: T. M. Eder (2019), *Studies on an in-situ calibration method for the IceCube multi-PMT optical module using radioactive decays*

In the following, PMTs and LEDs are referenced using numbers following the order illustrated in Figure 12.1. This numbering corresponds to the numbers physically printed on the 3D support structure next to each PMT of the mDOMs and also to the numbering used in the Geant4 code and output. Additionally, the PMTs are classified on the basis of their

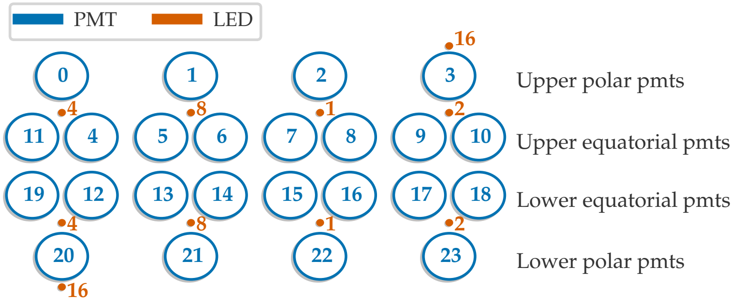

Figure 12.1: Projection of the PMT and LED positions of an mDOM with their corresponding numbers.

zenith angle into four categories: upper polar, upper equatorial, lower equatorial, and lower polar.

As shown in the left panel of Figure 11.34, Cherenkov photons resulting from radioactive decays in the pressure vessel are detected by the mDOM PMTs within a time interval several orders of magnitude smaller than the PMTs' TTS. Therefore, it is reasonable to assume that the Cherenkov emission is instantaneous. If a decay occurs between two neighbouring PMTs, denoted i and j, and results in a coincident detection of Cherenkov photons, the time difference Δt_{ij} between these detections will depend on the flight time of the photons and the transit time difference of the PMTs. Assuming that the decays are uniformly distributed throughout the pressure vessel volume, the differences in photon flight time should average to zero over many decays. This was verified using the Geant4 simulation described in Section 11.2.4. The simulation did not include the scintillation of the pressure vessel because (as will be shown later) it does not contribute to the time interval of interest and only increases the simulation time. An mDOM in an air environment with a live time of $t_w = 10\,\text{min}$ was simulated. The flight time of the detected photons was saved, as well as the total transit time including the simulation of the PMT response introduced in Section 9.3.4.

The top row of Figure 12.2 depicts the Δt_{ij} of neighbouring PMTs considering only the flight time of the photons. Due to the symmetry of the mDOM, four cases are considered in the figure:

- Δt_{pe} considers the time difference between a polar PMT and its immediate equatorial neighbour, such as PMTs 0 and 11, or PMTs 20 and 12 (see Figure 12.1).
- Δt_{ee} groups the time differences between neighbouring equatorial PMTs of the same half-module, such as PMTs 11 and 4 or PMTs 4 and 5.
- Δt_{e1e2} considers the time differences between neighbouring equatorial PMTs of different hemispheres, such as PMTs 11 and 19.
- Δt_{pp} between neighbouring polar PMTs, such as PMTs 0 and 1 or 20 and 23.

The different possible paths that the photons can take result in peaks in the Δt_{ij} histograms. Nevertheless, the distributions are symmetric and centred around zero. These features are on a subnanosecond time scale and cannot be resolved by the PMTs. Therefore, once the PMT time response is considered,[1] a Gaussian-like distribution is obtained for all

[1] Using the sampling method introduced in Section 9.3.4.

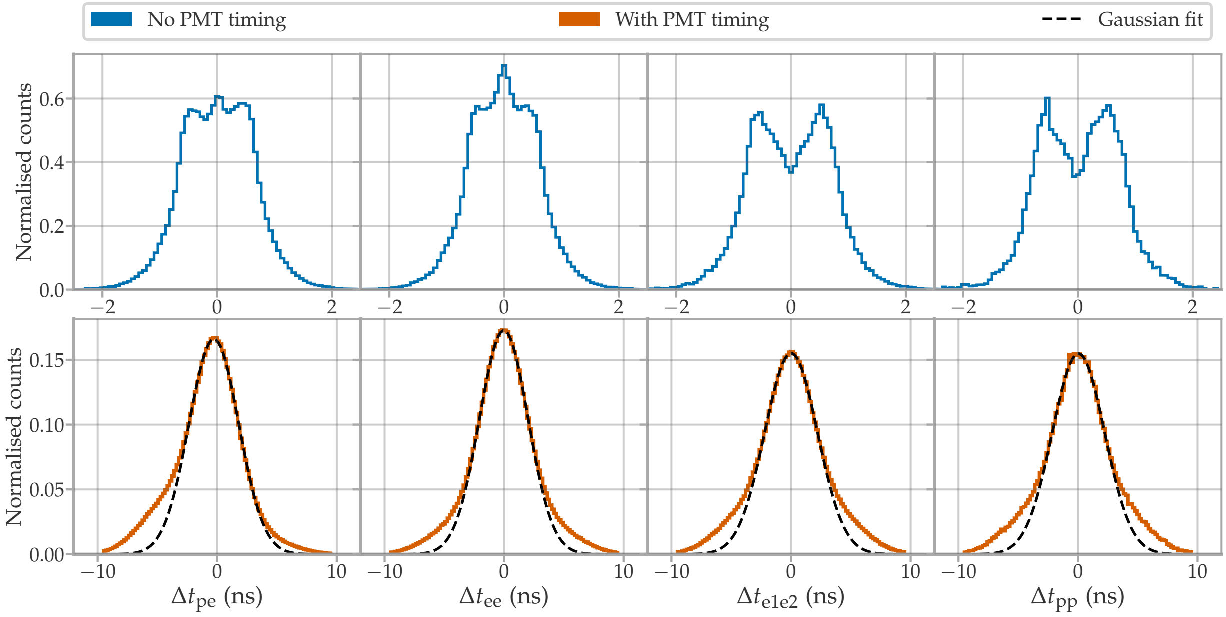

Figure 12.2: Time difference Δt between detected Cherenkov photons produced in radioactive decays for four different PMT combination types (see text for the nomenclature). The top row shows the Δt distribution without considering the PMT time response, while the bottom row shows the same data with the PMT timing included. It is worth noting that the time scale in the figures of the upper row is smaller than that in the lower row. A Gaussian fit was performed on the bottom distributions to estimate the possible systematics of the calibration method.

Δt_{ij} configurations, as presented in the bottom row of Figure 12.2. Note that the x-scales of the upper and lower rows of the figure are different.

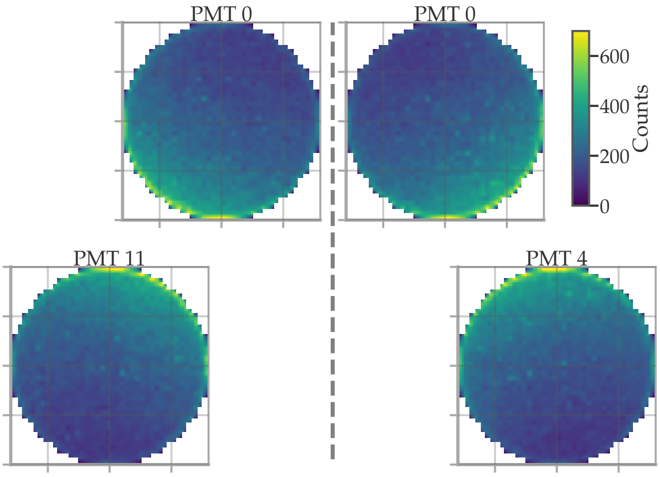

Figure 12.3: Two dimensional histogram of the detection locations on the photocathode of the photons that contribute to the coincidences in the Δt_{ij} distribution of the PMT pair 0 and 11 (left) and 0 and 4 (right). The PMT coordinate system used in this work is reversed when the PMTs are positioned in the mDOM (y axis positive towards the mDOM equator).

Decays between neighbouring PMTs contribute the most to the Δt_{ij} distributions [199]. Figure 12.3 shows the location of the hits that contribute to the Δt_{ij} distribution of the neighbouring PMTs 0 and 11, as well as of 0 and 4. It is clear that these photons are not distributed isotropically on the photocathode and are concentrated in regions directly facing each other near the decay locations. In the case of the pairing of polar-equatorial PMTs, the illuminated edges are at $y \approx 40$ mm (polar PMT) and $y \approx -40$ mm (equatorial PMT), considering the PMT coordinate system used in Chapter 7.[2] This results in asymmetric Δt_{pe} histograms, as these opposite edges show the largest deviations of the PMT transit

[2] The PMTs are positioned in the holding structure with the second dynode entrance towards the equatorial plane of the mDOM. Thus, following the PMT coordinate system used in Chapter 7, the PMT y-axis lies on a single azimuth angle of the mDOM, and the x-axis on a single zenith angle.

time response (see Section 7.3.2). The Δt_{ij} distributions of the other PMT pairs are symmetric, as they illuminate areas of similar homogeneity.

The distributions of Δt_{ij} were fitted with a Gaussian function, considering only the points above 50 % of the peak maximum. The fitted curves are shown in the bottom row of Figure 12.2, and the means of the Gaussian fits μ_{dT} are presented in Table 12.1. Ideally, the Gaussian fit should be centred at zero, indicating an unbiased model for the calibration. However, this was only observed for pairs of equatorial PMTs of different hemispheres (e1e2). The fits for the 'pp' and 'ee' pairs showed a small systematic deviation of a few dozen picoseconds. The largest deviation was observed for polar-equatorial pairs, which showed a mean deviation of (-0.28 ± 0.01) ns. Although an asymmetric function may provide a parametrisation centred around zero, it would increase the complexity of the model and depend on the PMT photocathode homogeneity used in the simulations. Therefore, in the measurements of Section 12.2, a Gaussian model will be used, and the Δt_{pe}-distributions will be corrected by (-0.28 ± 0.01) ns.

Table 12.1: Gaussian mean of the fits shown in Figure 12.2.

Pair	μ_{dT}
pe	(-0.28 ± 0.01) ns
ee	(-28 ± 5) ps
e1e2	(5 ± 7) ps
pp	(41 ± 14) ps

As mentioned above, the scintillation of the pressure vessel does not contribute to the peak of interest of the Δt_{ij}-distribution. To demonstrate this, a simulation of live time $t_w = 1$ min was performed with activated scintillation. Figure 12.4 shows the Δt_{pp} distribution obtained from this simulation without considering the PMT time response compared to the simulation using only Cherenkov photons. As the scintillation lifetime is large, it results in a nearly flat background around the peak of interest. Although the scintillation does not contribute to the sought signal, it has practical implications for measurement requirements. Since most of the PMT background is due to the scintillation, a measurement method that efficiently avoids triggering unwanted scintillation pulses must be used.

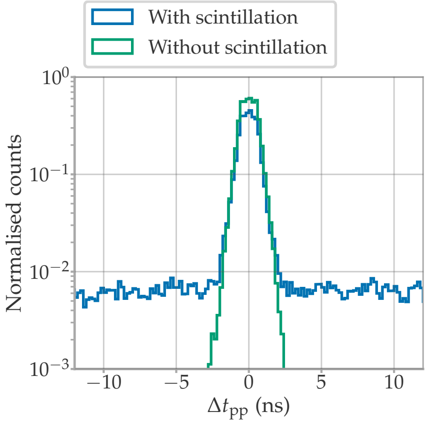

Figure 12.4: Δt_{ij}-distribution without PMT response for polar-polar PMT neighbours with and without simulation of pressure vessel scintillation.

Finally, the simulation results shown in the figures were produced using air as the environment, since the measurements with the DVTs will be performed in the laboratory. The simulations were repeated with the mDOM in ice. The better match between the refraction indices of the pressure vessel and environment results in a reduction of the total background measured by the PMTs, since photons are less likely to reflect back to the PMTs at the vessel-ice boundary. This can be observed in Figure 12.5, where the case of a simulation with activated scintillation in an ice environment is compared with the results in the air. Although the total dark rate is ~51 % lower in ice than in air, the coincident event rate is reduced by a factor ~2.9. This indicates that an important fraction of photons that contribute to the coincidence Δt_{ij}-peak are reflected on the pressure vessel glass before being detected. This means that the in situ measurements will take significantly longer to achieve the same statistics as in the laboratory. Nevertheless, as the mDOM positions are fixed in the ice, the data from several periodic measurements can be added until the required precision is obtained.

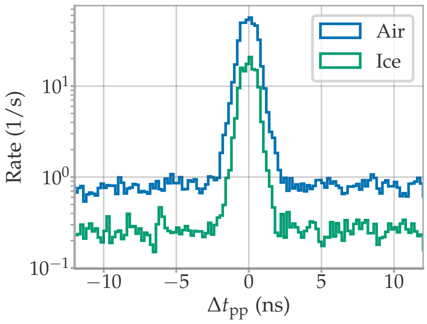

Figure 12.5: Δt_{ij}-distribution without PMT response for polar-polar PMT neighbours with an mDOM in the air and ice environment. The simulation included Cherenkov and scintillation photons.

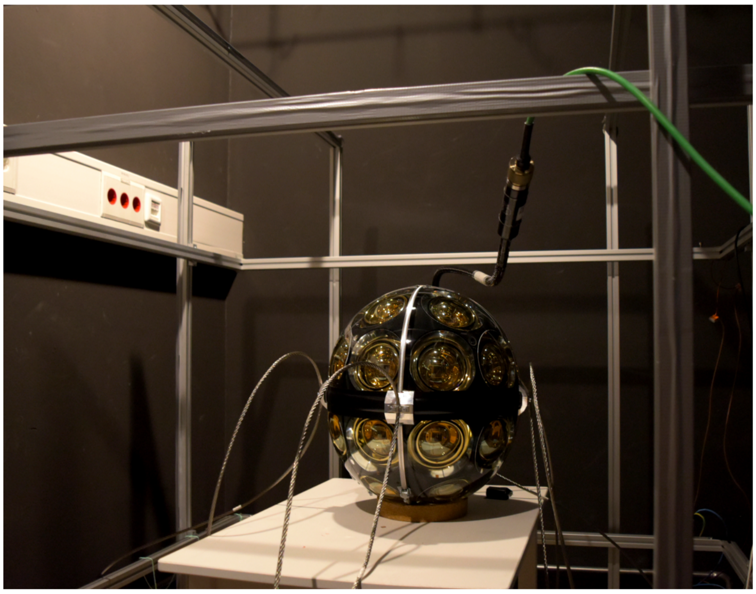

Figure 12.6: Photography of DVT 09 inside the Helmholtz coils in a dark room.

12.2 PROOF OF CONCEPT WITH DVT 09 - HÄNSEL

To take the first steps towards testing the effectiveness of this method, DVT 09 [3] was measured under the influence of different magnetic fields within the Helmholtz coil in a dark room at 18 °C. The PMTs were driven at their nominal voltage. A photograph of the setup is shown in Figure 12.6.

As mentioned in the previous section, only a small fraction of the background contributes to the desired calibration signal. Therefore, an efficient measurement method is required. The mDOM mainboard firmware includes a trigger mode based on local coincidences, which requires that N PMT discriminators have been activated during a time window t_{LC} in order to trigger the read-out. Once this trigger is activated, the waveforms of the desired AFE channels are read in a time range configured by the user. Thus, for this calibration, a twofold coincidence was required ($N = 2$) in a time window of $t_{\mathrm{LC}} = 50\,\mathrm{ns}$, after which 100 ns before and after the trigger was readout on all channels. These numbers were chosen based on the results of the last section, while keeping the windows relatively wide. However, an optimisation in the future may be necessary to achieve faster calibrations. It is important to note that the AFE channels used for communication with the mDOM are assigned different numbers than the PMT channels. However, for consistency, all the numbers shown in this chapter refer to the PMT number following the nomenclature of Figure 12.1. A translation between the two number systems can be found in Appendix G.

The first measurements were performed with the Helmholtz coils compensating for the Earth's magnetic field. All pulses measured in the waveforms were used to build the Δt_{ij} histograms, using the discriminator activation for the determination of pulse time. A total of 10^6 trigger events were measured. Figure 12.7 shows the Δt_{ij} distributions of four PMT pairs of the different types introduced in the previous section. The histograms obtained are similar to the simulated ones, albeit with

[3] The mainboard FPGA firmware used was x24, ICM firmware 1535, and Iceboot version 3a ebbec80. The mainboard version was Rev2a.

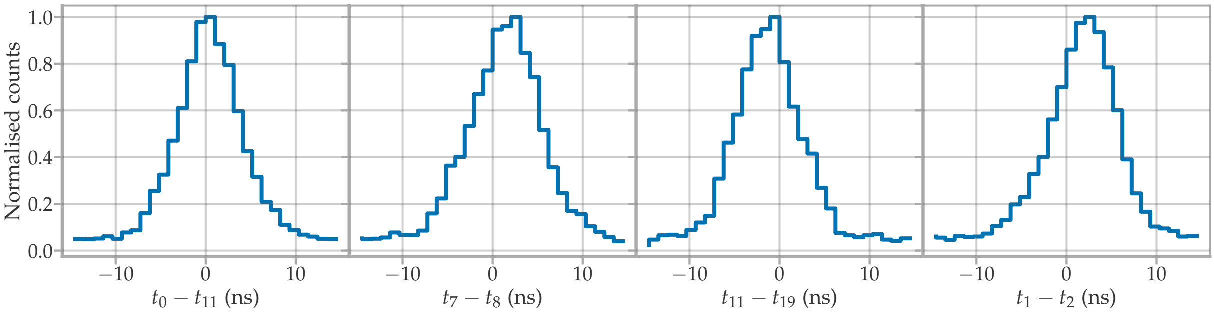

Figure 12.7: Four of the Δt_{ij} distributions measured with the Helmholtz coils compensating for the Earth's magnetic field.

a coarser binning set by the sampling frequency of the discriminator (960 MHz). In Figure 12.2, the polar-polar PMT pairs exhibited symmetric distributions, but in Figure 12.7, the Δt_{12} distribution is asymmetric. This may indicate that the simulated geometry is not accurate, but it is more likely caused by a difference in efficiencies between the PMTs. In the Geant4 simulation, all PMTs had the same detection efficiency (following the scheme presented in Section 9.3.3).

A total of 48 Δt_{ij} distributions were built from the measurement,[4] which have to be fitted simultaneously with a 'global' fit. For this, each PMT was assigned a transit time parameter T_i and the mean of the Gaussian of the distribution Δt_{ij} was set to $(T_i - T_j)$. As the calibration can only determine the transit time differences, the set of parameters $\{T_i\}$ is degenerated. Therefore, the fit parameter T_0 was kept fixed at zero, making the results relative to PMT 0. To reduce the number of free parameters, each distribution was first fitted independently with a Gaussian. The hereby obtained values for the height and standard deviation of the Gaussian of each distribution were kept fixed during the global fit, only varying the T_i parameters. The minimisation was performed using Poisson log-likelihood statistics,

$$\begin{aligned}\mathscr{L}_{\text{Total}} &= \sum_{k=1}^{48} \mathscr{L}_k\left(\{T_i\} \,|\, T_0, \sigma_k, H_k, x_k, y_k\right) \\ &= \sum_{k=1}^{48} \sum_j \left[-\mu_{kj}(T_l, T_m) + y_j \cdot \log\left(\mu_{kj}\left(T_l, T_m\right)\right) - \log(y_j!)\right],\end{aligned} \tag{12.1}$$

where $\mu_{kj}(T_l, T_m) = H_k \cdot \exp\left(-\left(x_j - (T_l - T_m)\right)^2 / (2\sigma_k)\right)$, σ_k and H_k are the fixed standard deviation and amplitude of the Gaussian of the histogram k with bin locations x_k and counts y_k. The indexes l and m correspond to the PMT pair that built the histogram k. The minimisation of $-\mathscr{L}_{\text{Total}}$ was performed with Minuit [191, 192].

Figure 12.8 displays the fit results. To help assess the validity of the results, the relative transit times are plotted against the voltage applied to the PMT during the measurement (in terms of the voltage at the last dynode stage v_{10}). The fitted relative transit time of the PMTs decreases with the applied voltage, which is expected as the electrons are accelerated faster.

Two additional calibrations were conducted using an external magnetic

[4] 4: 8 'pp'-, 16 'pe', 16 'ee'-, and 8 'e1e2'-combinations.

[191]: Dembinski et al. (2020), *scikit-hep/iminuit*
[192]: James et al. (1975), *Minuit: A System for Function Minimization and Analysis of the Parameter Errors and Correlations*

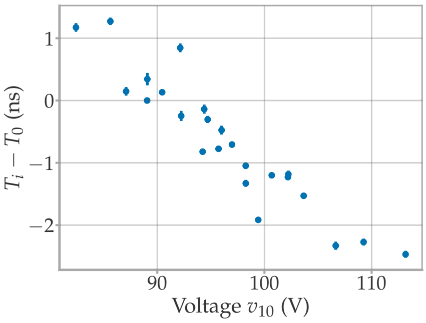

Figure 12.8: Relative transit time fitted from the measurement with the Helmholtz coils compensating the Earth's magnetic field. The results are given in dependence of the voltage applied to the corresponding PMT in terms of the last dynode stage voltage v_{10}.

field of $(\pm 54.7\,\mu\mathrm{T}, 0, 0)$. While this scenario is somewhat unrealistic, as it simulates an Earth magnetic field at the South Pole parallel to the equator-plane of the mDOM, it serves to maximise the effects of the magnetic field on the transit time differences on most of the PMTs. This is because the magnetic field component along the x-axis of the PMT caused the largest deviations, as discussed in Section 6.5. Additionally, since each PMT faces a distinct direction, the magnetic field will affect each PMT with varying intensities.

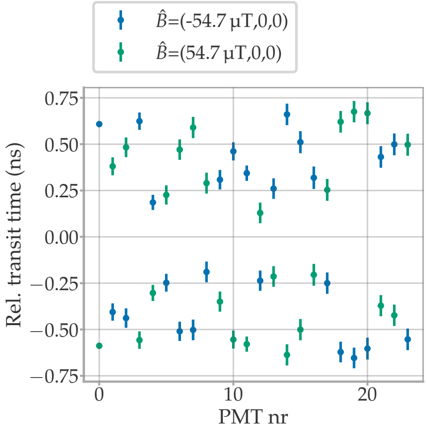

Figure 12.9: Relative transit time fitted from the measurement with Helmholtz coils at $(\pm 54.7\,\mu\mathrm{T}, 0, 0)$. The fit results are relative to the results of the measurement at $(0, 0, 0)$ T.

To facilitate comparison between different measurements, the mean of the fitted $\{T_i\}$ is subtracted from each individual T_i value. Figure 12.9 presents the fitted transit time relative to the measurement at $B = (0, 0, 0)$ T of all PMTs for the measurements at $(\pm 54.7\,\mu\mathrm{T}, 0, 0)$. As expected, the results for the two magnetic field directions are symmetric, as the directions are antiparallel.

To compare the fit results obtained with the measurements of Section 6.5, the data were plotted in Figure 12.10 against the normalised x-component of the magnetic field in the coordinate system of the corresponding PMT $\hat{B}_x^{PMT}$. The data from plane wave measurements of Figure 6.42 are illustrated as grey points for comparison. As expected from Figure 12.9, the results of both field directions follow the same dependency of $\hat{B}_x^{PMT}$. Nevertheless, the slope shown by the results (~0.68 ns) is smaller than for the data of Section 6.5 (~0.89 ns).

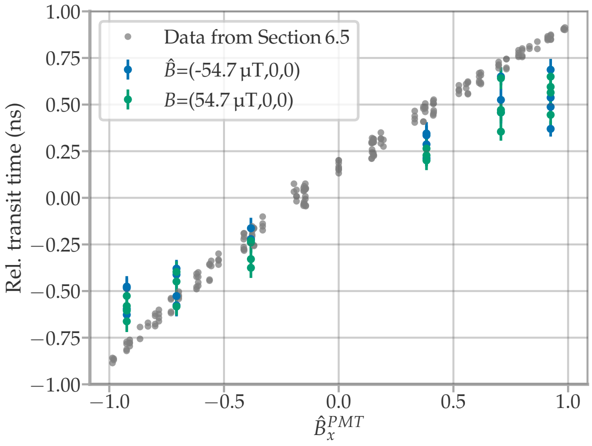

Figure 12.10: The same data as Figure 12.9, this time plotted against the x-component of the magnetic field vector in the coordinate system of each PMT. The data of the measurement on a single PMT using external illumination of Figure 6.42 is presented in grey markers for comparison.

In both measurement setups, the magnetic field strength was set to 54.7 µT, so one would expect the results to show the same slope. This may hint at mDOM components providing a level of magnetic shielding for the PMTs. To test this, the magnetometer on the mDOM mainboard was read with varying magnetic field strength, which was always set along the x axis of the coils. Figure 12.11 shows the measured magnetic field strength against the set strength. First, it should be noticed that the magnetic field strength measured when the coils compensate for the Earth's magnetic field is not zero but (36.94 ± 0.11) µT. This is not surprising, since the electronics inside the mDOM produce their own fields. A minimum is reached at ~22 µT when the external magnetic field partially compensates the intrinsic magnetic field of the mDOM along one axis. The data before the minimum were fitted with a linear function, resulting in a slope of (0.83 ± 0.01). This means that only 83 % of the external magnetic field

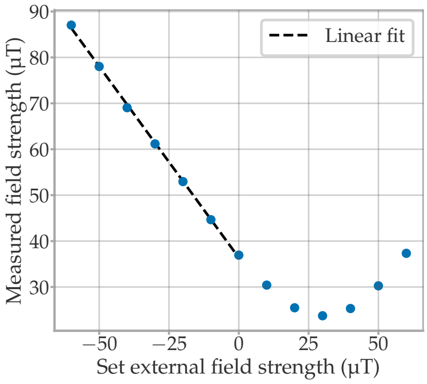

Figure 12.11: Magnetic field strength read by the mDOM mainboard magnetometer against the external magnetic field strength set by the Helmholtz coils. The error bars are smaller than the data markers.

strength reaches the mDOM mainboard. The fraction between the slopes in the results of Figure 12.10 is smaller (0.77 ± 0.02), but a magnetic field shielding may largely explain the deviations. It is important to acknowledge that there are other possible sources of systematics. For instance, the quality of calibration for the mainboard magnetometer remains unknown, and the observed behaviour in Figure 12.11 may well be due to a miscalibration of the sensor. Additionally, even if the readings are accurate, it does not guarantee that the magnetic shielding is consistent at the position of the PMTs. Consequently, it is important to conduct further research to address these potential inconsistencies.

The measurement results provide evidence for the validity of this calibration method. To achieve a complete validation, a comparison of the calibration results obtained from this method with the results of illuminating each PMT with an external light source should be conducted, similar to the relative transit time measurements of Chapter 6 and Chapter 7. Unfortunately, at the time of writing this thesis, such a measurement cannot be performed with the available hardware. However, this validation will be feasible once the mDOM FAT testing at DESY Zeuthen begins.

Lastly, it is important to note that the flashers offer an alternative calibration method. Both simulations and measurements were conducted to assess the performance of the mDOM flashers. As depicted in Figure 12.12, the flashers were integrated into the Geant4 simulation framework as part of a Bachelor's thesis [200] co-supervised by the author. However, the first measurements did not align with either the simulation or the results presented in this section. The disagreement with the simulation may be attributed to the fact that only a small portion of the photons emitted by the flasher are reflected back to the PMTs, and surface imperfections of the glass may significantly increase back-reflected photons during the measurement in air, while in the simulation the surface is modelled completely smooth. Moreover, since most of the photons are released into the environment, reflections on the setup, such as the table on which the mDOM is placed (as shown in Figure 12.6), may dominate the detected photons in the measurement. Therefore, ideally, this calibration method should be performed in a large water tank where the reflections on environmental objects are minimal, and the optical coupling between the pressure vessel and the environment better replicates the conditions on ice.

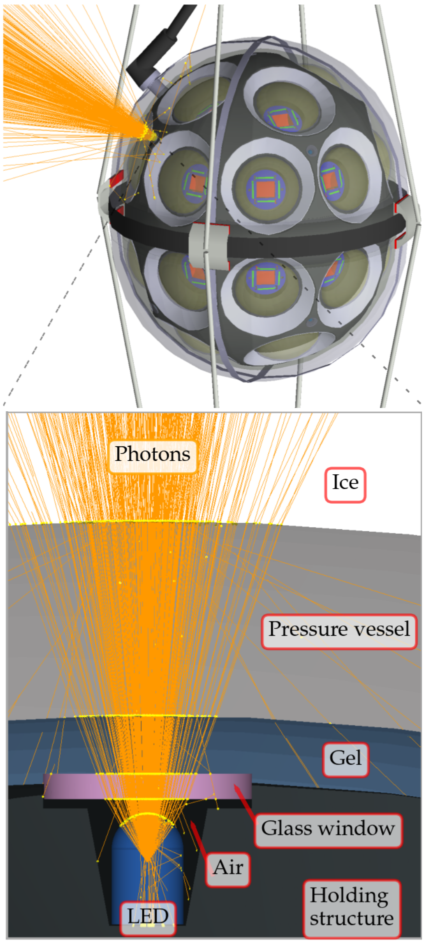

Figure 12.12: Screenshot of the mDOM geometry in the Geant4 visualiser including its flashers.

[200]: A. Tenbruck (2022), *Implementation von LEDs in eine Geant4-Simulation des mDOM-Sensors für das IceCube Upgrade und Simulationsstudien zu deren Emissionsprofil*

13

Summary & Outlook

The mDOM is poised to become one of the primary devices in the IceCube Upgrade, offering a large sensitivity and new tools due to its fine segmentation. To ensure seamless integration with the IceCube detection and reconstruction system, it is essential to have a thorough understanding of the novel technology to be deployed.

In the framework of this thesis, the module was characterised in detail, giving a special focus on the main sensitive device, the photomultiplier. Chapters 6 and 7 delved into the PMT's performance via various measurement techniques, covering a wide range of wavelengths and temperatures and also investigating the influence of magnetic fields. This led to an in-depth understanding of the PMT response across the photocathode area, which was then incorporated in Chapter 9 into a Geant4 simulation toolkit, which provides the most accurate mDOM modelling to date. Although Geant4 simulations are normally too slow for their use in event reconstruction, an accurate mDOM simulation is crucial for the validation of more simple module response models used in reconstruction algorithms. Furthermore, the Geant4 simulation is a powerful tool to make predictions of the mDOM response to different kinds of signal, which can facilitate the optimisation of new calibration strategies and the development of more advanced signal processing techniques.

The deep ice at the South Pole has minimal optical activity, resulting in the modules' own components being the primary source of background noise. In this context, the background of PMTs was studied in Chapter 8 and the complete module in Chapter 11. These investigations revealed that radioactive decays that occur inside the pressure vessel and PMT glass are the most significant background source. The charged particles released in these decays can produce Cherenkov and scintillation photons. The scintillation parameters of the borosilicate glass of the pressure vessel were measured as part of two Master theses [152, 184]. The measurement technique of the scintillation lifetime was improved in this work providing a modelling of the emission time from the nanosecond to the millisecond range. The scintillation parameterisation allows for the simulation of the mDOM background in Geant4. With this, the dark rate of the module in ice was estimated, and rare high-multiplicity events that produce a signal similar to that of low-energy neutrinos were studied. The performance of the simulation was validated using measurements of the dark rate on one of the first built mDOMs. The background simulation is an indispensable tool for estimating in-ice noise of the modules before deployment, and IceCube collaborators are currently using these simulation results to optimise event selection algorithms and calculate the sensitivity of IceCube Upgrade to low energy neutrinos.

The PMT characterisation revealed that the transit time may vary up to

[152]: Unland Elorrieta (2017), *Studies on dark rates induced by radioactive decays of the multi-PMT digital optical module for future IceCube extensions*

[184]: Dittmer (2020), *Characterisation of scintillation light induced by radioactive excitation in the mDOM glass pressure vessel*

~2 ns with a change in magnetic field. As the final rotation and position of the mDOMs are not known before deployment, the magnetic field on the PMTs will likely be different than during the final acceptance test of the modules. Accurate calibration of the transit time is important, as the pulse times serve as the primary estimators for the distance between the particle path and the modules during reconstruction. Therefore, the relative transit time between PMTs of a module will probably need to be calibrated in situ. Chapter 12 provided the proof of concept of a calibration method using Cherenkov photons from radioactive decays in the pressure vessel. For this, Geant4 simulations as well as measurements on a real mDOM were performed. As such, this last chapter integrated all the studies of this work.

At the time of writing of this thesis, the production of the mDOMs is underway. Before production, the capabilities of the mDOM were rigorously tested using verification modules called DVTs. These tests included pressure tests, which were discussed in Chapter 10. The construction of the DVTs was only possible after several mechanical demonstrators were constructed, with which different types of gel were tested and the design of the 3D printed holding structure was optimised. This comprehensive testing process ensures that the mDOM performs reliably for an extended period of time in the low temperatures of the South Pole.

As our understanding of the mDOM performance improves, IceCube Upgrade moves one step closer to achieving its goals. We are now embarking on a new phase of characterising the mDOM at larger scales. This involves two main areas of focus. First, in terms of statistics, all mDOM PMTs have been characterised by the IceCube groups of Aachen and Dortmund, and during the final acceptance test, all modules will be tested, providing a vast amount of data on mDOM performance. Second, novel setups are being constructed to provide validation cross-checks for the Geant4 simulation toolkit and a deeper understanding of mDOM behaviour. A noteworthy setup currently under construction is the water tank setup in Münster (as shown in Figure 13.1), which enables optical modules to be illuminated with different wavelengths in different directions. Since the refractive index of liquid water is similar to that of ice, this setup provides the closest controlled environment for mDOM testing. Moreover, this is an ideal setup to validate the transit time calibration method using radioactive decays of the pressure vessel and also to test a possible calibration method using the mDOM flashers.

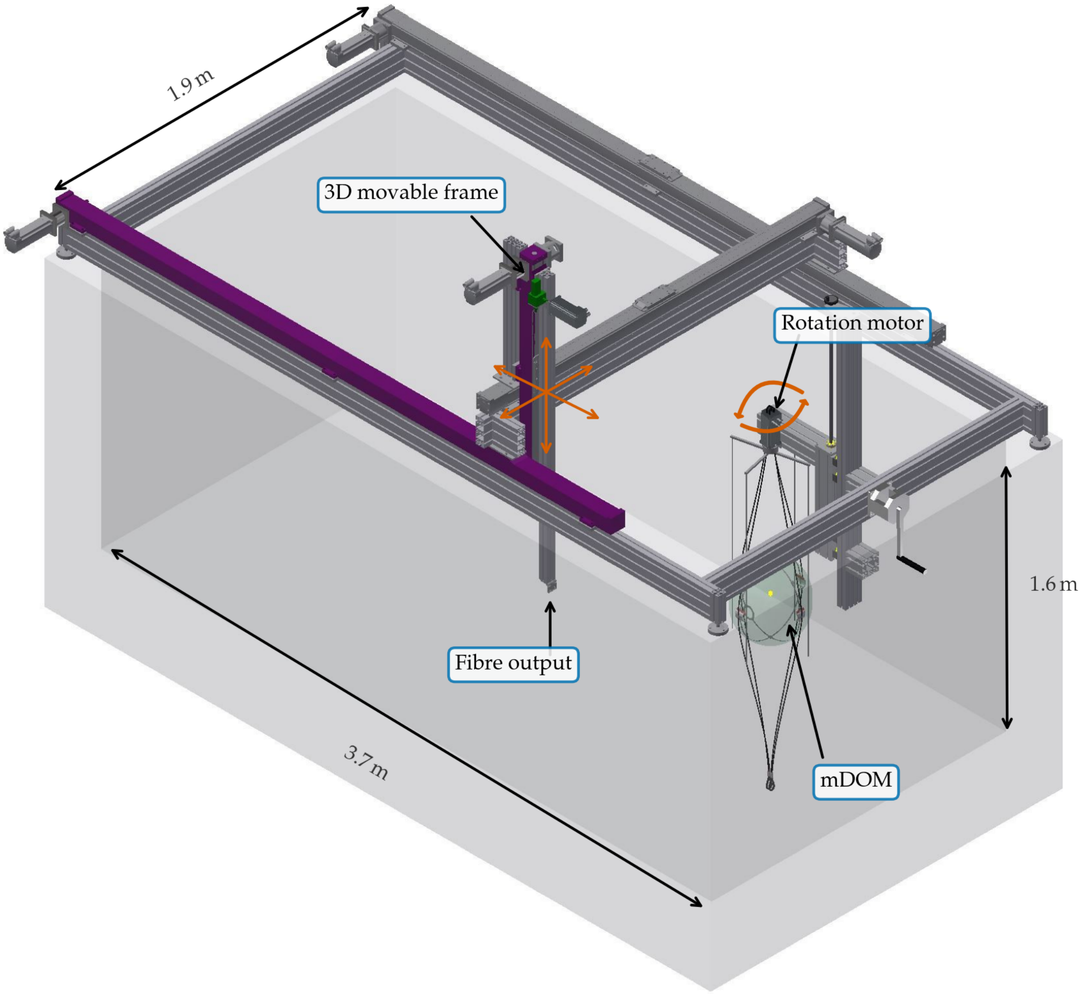

Figure 13.1: Water tank setup currently being constructed at Münster for the characterisation of optical modules. The tank is surrounded by roller shutters that shield it from environmental light (not depicted in the figure).

Bibliography

[1] Maurizio Spurio. *Probes of Multimessenger Astrophysics*. Springer International Publishing, 2018. DOI: `10.1007/978-3-319-96854-4` (cited on pages 1, 6, 8–13).

[2] M. G. Aartsen et al. 'The IceCube Neutrino Observatory: Instrumentation and Online Systems'. In: *JINST* 12.03 (2017), P03012. DOI: `10.1088/1748-0221/12/03/P03012`. arXiv: `1612.05093 [astro-ph.IM]` (cited on pages 1, 22, 31, 39, 110, 146, 195).

[3] M. G. Aartsen et al. 'First observation of PeV-energy neutrinos with IceCube'. In: *Phys. Rev. Lett.* 111 (2013), p. 021103. DOI: `10.1103/PhysRevLett.111.021103`. arXiv: `1304.5356 [astro-ph.HE]` (cited on pages 1, 24).

[4] R. Abbasi et al. 'Evidence for neutrino emission from the nearby active galaxy NGC 1068'. In: *Science* 378.6619 (2022), pp. 538–543. DOI: `10.1126/science.abg3395`. arXiv: `2211.09972` (cited on pages 1, 25, 26).

[5] Aya Ishihara et al. 'The IceCube Upgrade - Design and Science Goals'. In: Sissa Medialab, July 2019. DOI: `10.22323/1.358.1031` (cited on pages 1, 24, 26–28).

[6] M. G. Aartsen et al. 'IceCube-Gen2: the window to the extreme Universe'. In: *J. Phys. G* 48.6 (2021), p. 060501. DOI: `10.1088/1361-6471/abbd48`. arXiv: `2008.04323 [astro-ph.HE]` (cited on pages 1, 28, 29).

[7] M. G. Aartsen et al. 'Evidence for High-Energy Extraterrestrial Neutrinos at the IceCube Detector'. In: *Science* 342.6161 (Nov. 2013), pp. 1242856–1242856. ISSN: 1095-9203. DOI: `10.1126/science.1242856`. arXiv: `1311.5238` (cited on page 4).

[8] B. P. Abbott et al. 'Observation of Gravitational Waves from a Binary Black Hole Merger'. In: *Physical Review Letters* 116.6 (Feb. 2016). ISSN: 1079-7114. DOI: `10.1103/physrevlett.116.061102`. arXiv: `1602.03837` (cited on page 4).

[9] Mark Thomson. *Modern Particle Physics*. Cambridge University Press, 2013. DOI: `10.1017/CBO9781139525367` (cited on pages 4–7).

[10] Y. Fukuda et al. 'Evidence for oscillation of atmospheric neutrinos'. In: *Phys. Rev. Lett.* 81 (1998), pp. 1562–1567. DOI: `10.1103/PhysRevLett.81.1562`. arXiv: `hep-ex/9807003` (cited on page 5).

[11] A. Bellerive et al. 'The Sudbury Neutrino Observatory'. In: *Nucl. Phys. B* 908 (2016), pp. 30–51. DOI: `10.1016/j.nuclphysb.2016.04.035`. arXiv: `1602.02469 [nucl-ex]` (cited on page 5).

[12] S. Abe et al. 'Precision Measurement of Neutrino Oscillation Parameters with KamLAND'. In: *Phys. Rev. Lett.* 100 (2008), p. 221803. DOI: `10.1103/PhysRevLett.100.221803`. arXiv: `0801.4589 [hep-ex]` (cited on page 5).

[13] *The nobel prize in physics 2015*. URL: `https://www.nobelprize.org/prizes/physics/2015/summary/` (cited on page 5).

[14] S. Bilenky. 'Neutrino oscillations: From a historical perspective to the present status'. In: *Nuclear Physics B* 908 (2016). Neutrino Oscillations: Celebrating the Nobel Prize in Physics 2015, pp. 2–13. ISSN: 0550-3213. DOI: `10.1016/j.nuclphysb.2016.01.025`. arXiv: `1602.00170` (cited on page 5).

[15] Particle Data Group et al. 'Review of Particle Physics'. In: *Progress of Theoretical and Experimental Physics* 2022.8 (Aug. 2022). 083C01. ISSN: 2050-3911. DOI: `10.1093/ptep/ptac097` (cited on pages 6, 8, 9).

[16] Stefan Coenders. 'High-energy cosmic ray accelerators: searches with IceCube neutrinos'. PhD thesis. Munich, Tech. U., 2016. URL: https://mediatum.ub.tum.de/doc/1327578/1327578.pdf (cited on page 6).

[17] Ivan Esteban et al. 'The fate of hints: updated global analysis of three-flavor neutrino oscillations'. In: *JHEP* 09 (2020), p. 178. DOI: 10.1007/JHEP09(2020)178. arXiv: 2007.14792 [hep-ph] (cited on pages 6, 7).

[18] Carlo Giunti and Chung W. Kim. *Fundamentals of Neutrino Physics and Astrophysics*. Oxford University Press, Mar. 2007. ISBN: 9780198508717. DOI: 10.1093/acprof:oso/9780198508717.001.0001 (cited on page 6).

[19] X. Qian and P. Vogel. 'Neutrino mass hierarchy'. In: *Progress in Particle and Nuclear Physics* 83 (2015), pp. 1–30. ISSN: 0146-6410. DOI: https://doi.org/10.1016/j.ppnp.2015.05.002 (cited on page 6).

[20] M. Aker et al. 'The design, construction, and commissioning of the KATRIN experiment'. In: *JINST* 16.08 (2021), T08015. DOI: 10.1088/1748-0221/16/08/T08015. arXiv: 2103.04755 [physics.ins-det] (cited on page 7).

[21] M. Aker et al. 'Direct neutrino-mass measurement with sub-electronvolt sensitivity'. In: *Nature Phys.* 18.2 (2022), pp. 160–166. DOI: 10.1038/s41567-021-01463-1. arXiv: 2105.08533 [hep-ex] (cited on page 7).

[22] J. A. Formaggio and G. P. Zeller. 'From eV to EeV: Neutrino cross sections across energy scales'. In: *Rev. Mod. Phys.* 84 (3 Sept. 2012), pp. 1307–1341. DOI: 10.1103/RevModPhys.84.1307. arXiv: 1305.7513 (cited on page 7).

[23] Sheldon L. Glashow. 'Resonant Scattering of Antineutrinos'. In: *Phys. Rev.* 118 (1 Apr. 1960), pp. 316–317. DOI: 10.1103/PhysRev.118.316 (cited on page 7).

[24] M. G. Aartsen et al. 'Detection of a particle shower at the Glashow resonance with IceCube'. In: *Nature* 591.7849 (Mar. 2021), pp. 220–224. DOI: 10.1038/s41586-021-03256-1 (cited on page 7).

[25] J. M. Carceller et al. 'Origin of the High-energy Neutrino Flux at IceCube'. In: *The Astrophysical Journal* 852.1 (2018), p. 59. DOI: 10.3847/1538-4357/aa9d94. arXiv: 1703.10786 [astro-ph.HE] (cited on page 8).

[26] Thomas K. Gaisser, Ralph Engel, and Elisa Resconi. *Cosmic Rays and Particle Physics*. Cambridge University Press, June 2016. DOI: 10.1017/cbo9781139192194 (cited on pages 8, 9).

[27] T. Abu-Zayyad et al. 'The Knee and the Second Knee of the Cosmic-Ray Energy Spectrum'. In: (Mar. 2018). arXiv: 1803.07052 [astro-ph.HE] (cited on page 9).

[28] Siming Liu et al. 'The origin of galactic cosmic rays'. In: *Rev. Mod. Plasma Phys.* 6.1 (2022), p. 19. DOI: 10.1007/s41614-022-00080-6 (cited on page 9).

[29] Chandra X-ray Center. *Tycho's Supernova Remnant*. Accessed: 2023-Jan-25. Harvard-Smithsonian Center for Astrophysics. URL: https://chandra.harvard.edu/photo/2019/tycho/ (cited on page 9).

[30] M. G. Aartsen et al. 'Astrophysical neutrinos and cosmic rays observed by IceCube'. In: *Adv. Space Res.* 62 (2018), pp. 2902–2930. DOI: 10.1016/j.asr.2017.05.030. arXiv: 1701.03731 [astro-ph.HE] (cited on page 10).

[31] Jorge Ernesto Horvath. 'Active Galactic Nuclei (AGNs)'. In: *High-Energy Astrophysics: A Primer*. Cham: Springer International Publishing, 2022, pp. 177–186. ISBN: 978-3-030-92159-0. DOI: 10.1007/978-3-030-92159-0_8 (cited on page 11).

[32] U.F. Katz and Ch. Spiering. 'High-energy neutrino astrophysics: Status and perspectives'. In: *Progress in Particle and Nuclear Physics* 67.3 (2012), pp. 651–704. ISSN: 0146-6410. DOI: https://doi.org/10.1016/j.ppnp.2011.12.001 (cited on pages 11, 12).

[33] Ofelia Pisanti. 'Astrophysical neutrinos: theory'. In: *Journal of Physics: Conference Series* 1263 (June 2019), p. 012004. ISSN: 1742-6596. DOI: `10.1088/1742-6596/1263/1/012004`. arXiv: `1906.12258` (cited on page 12).

[34] Robert Marcus Wagner. 'Measurement of very high energy gamma–ray emission from four blazars using the MAGIC telescope and a comparative blazar study'. PhD Thesis. Technischen Universität München, 2006. URL: `https://mediatum.ub.tum.de/doc/604099/` (cited on page 12).

[35] Jakob van Santen. 'Probing Extraterrestrial Neutrino Fluxes and Atmospheric Charm with Contained Neutrino Events above 1 TeV in IceCube'. In: *Physics Procedia* 61 (2015). 13th International Conference on Topics in Astroparticle and Underground Physics, TAUP 2013, pp. 633–640. ISSN: 1875-3892. DOI: `https://doi.org/10.1016/j.phpro.2014.12.063` (cited on page 13).

[36] Morihiro Honda et al. 'Calculation of atmospheric neutrino flux using the interaction model calibrated with atmospheric muon data'. In: *Phys. Rev. D* 75 (2007), p. 043006. DOI: `10.1103/PhysRevD.75.043006`. arXiv: `astro-ph/0611418` (cited on page 13).

[37] Rikard Enberg, Mary Hall Reno, and Ina Sarcevic. 'Prompt neutrino fluxes from atmospheric charm'. In: *Phys. Rev. D* 78 (2008), p. 043005. DOI: `10.1103/PhysRevD.78.043005`. arXiv: `0806.0418 [hep-ph]` (cited on page 13).

[38] Roberto Aloisio et al. 'Selected Topics in Cosmic Ray Physics'. In: *Multiple Messengers and Challenges in Astroparticle Physics*. Ed. by Roberto Aloiso, Eugenio Coccia, and Francesco Vissani. 2018, pp. 1–95. DOI: `10.1007/978-3-319-65425-6_1`. arXiv: `1707.06147 [astro-ph.HE]` (cited on page 13).

[39] Todor Stanev. 'Cosmogenic neutrinos and gamma rays'. In: *Comptes Rendus Physique* 15.4 (2014). Ultra-high-energy cosmic rays: From the ankle to the tip of the spectrum, pp. 349–356. ISSN: 1631-0705. DOI: `https://doi.org/10.1016/j.crhy.2014.02.013` (cited on page 13).

[40] Markus Ahlers and Jordi Salvado. 'Cosmogenic gamma-rays and the composition of cosmic rays'. In: *Phys. Rev. D* 84 (2011), p. 085019. DOI: `10.1103/PhysRevD.84.085019`. arXiv: `1105.5113 [astro-ph.HE]` (cited on page 13).

[41] De Angelis et al. 'Transparency of the Universe to gamma rays'. In: *Mon. Not. Roy. Astron. Soc.* 432 (2013), pp. 3245–3249. DOI: `10.1093/mnras/stt684`. arXiv: `1302.6460 [astro-ph.HE]` (cited on page 14).

[42] Francis Halzen. 'The observation of high-energy neutrinos from the cosmos: Lessons learned for multimessenger astronomy'. In: *Int. J. Mod. Phys. D* 31.03 (2022), p. 2230003. DOI: `10.1142/S0218271822300038`. arXiv: `2110.01687 [astro-ph.HE]` (cited on page 14).

[43] H. Ikeda et al. 'The Kamioka Proton Decay Experiment'. In: *Third Workshop on Grand Unification*. Birkhäuser Boston, 1982, pp. 56–71. DOI: `10.1007/978-1-4612-5800-1_6` (cited on page 15).

[44] K. S. Hirata et al. 'Observation of ^{8}B solar neutrinos in the Kamiokande-II detector'. In: *Phys. Rev. Lett.* 63 (1 July 1989), pp. 16–19. DOI: `10.1103/PhysRevLett.63.16` (cited on page 15).

[45] K. Hirata et al. 'Observation of a neutrino burst from the supernova SN1987A'. In: *Phys. Rev. Lett.* 58 (14 Apr. 1987), pp. 1490–1493. DOI: `10.1103/PhysRevLett.58.1490` (cited on page 15).

[46] Gisela Anton. 'Neutrino Telescopes'. In: *Probing Particle Physics with Neutrino Telescopes*. WORLD SCIENTIFIC, Jan. 2020, pp. 11–32. DOI: `10.1142/9789813275027_0002`. arXiv: `2010.06012 [astro-ph.IM]` (cited on pages 15, 17, 23).

[47] Arthur Roberts. 'Weak-interaction studies with the DUMAND detector'. In: *AIP Conf. Proc.* 49 (1979). Ed. by Thomas K. Gaisser, pp. 391–408. DOI: `10.1063/1.31633` (cited on page 15).

[48] Christian Spiering. 'Towards high-energy neutrino astronomy'. In: *The European Physical Journal H* 37.3 (July 2012), pp. 515–565. DOI: `10.1140/epjh/e2012-30014-2`. arXiv: `1207.4952 [astro-ph.IM]` (cited on pages 15, 22).

[49] Elisa Resconi. 'The Pacific Ocean Neutrino Experiment'. In: *Proceedings of 37th International Cosmic Ray Conference — PoS(ICRC2021)*. Sissa Medialab, Nov. 2021. DOI: `10.22323/1.395.0024` (cited on page 15).

[50] Z. P. Ye et al. *Proposal for a neutrino telescope in South China Sea*. 2022. DOI: `10.48550/ARXIV.2207.04519` (cited on page 15).

[51] R. E. Jennings. 'Čerenkov Radiation'. In: *Science Progress (1933-)* 50.199 (1962), pp. 364–375. ISSN: 00368504, 20477163. URL: `http://www.jstor.org/stable/43425324` (visited on 04/12/2022) (cited on page 16).

[52] I. Frank and Ig. Tamm. 'Coherent Visible Radiation of Fast Electrons Passing Through Matter'. In: *Selected Papers*. Springer Berlin Heidelberg, 1991, pp. 29–35. DOI: `10.1007/978-3-642-74626-0_2` (cited on page 16).

[53] Teppei Katori et al. 'Neutrino interaction physics in neutrino telescopes'. In: *The European Physical Journal Special Topics* 230.24 (Dec. 2021), pp. 4293–4308. DOI: `10.1140/epjs/s11734-021-00292-w` (cited on page 17).

[54] Dmitry Chirkin and Wolfgang Rhode. *Propagating leptons through matter with Muon Monte Carlo (MMC)*. 2004. DOI: `10.48550/ARXIV.HEP-PH/0407075` (cited on page 17).

[55] R. Abbasi et al. 'An improved method for measuring muon energy using the truncated mean of dE/dx'. In: *Nucl. Instrum. Meth. A* 703 (2013), pp. 190–198. DOI: `10.1016/j.nima.2012.11.081`. arXiv: `1208.3430 [physics.data-an]` (cited on page 17).

[56] M. G. Aartsen et al. 'Search for Astrophysical Tau Neutrinos in Three Years of IceCube Data'. In: *Phys. Rev. D* 93.2 (2016), p. 022001. DOI: `10.1103/PhysRevD.93.022001`. arXiv: `1509.06212 [astro-ph.HE]` (cited on page 17).

[57] P.W. Gorham et al. 'The Antarctic Impulsive Transient Antenna ultra-high energy neutrino detector: Design, performance, and sensitivity for the 2006–2007 balloon flight'. In: *Astroparticle Physics* 32.1 (2009), pp. 10–41. ISSN: 0927-6505. DOI: `https://doi.org/10.1016/j.astropartphys.2009.05.003` (cited on page 18).

[58] Ilya Kravchenko et al. 'Updated Results from the RICE Experiment and Future Prospects for Ultra-High Energy Neutrino Detection at the South Pole'. In: *Phys. Rev. D* 85 (2012), p. 062004. DOI: `10.1103/PhysRevD.85.062004`. arXiv: `1106.1164 [astro-ph.HE]` (cited on page 18).

[59] P. Allison et al. 'Performance of two Askaryan Radio Array stations and first results in the search for ultrahigh energy neutrinos'. In: *Phys. Rev. D* 93.8 (2016), p. 082003. DOI: `10.1103/PhysRevD.93.082003`. arXiv: `1507.08991 [astro-ph.HE]` (cited on page 18).

[60] S.W. Barwick et al. 'A first search for cosmogenic neutrinos with the ARIANNA Hexagonal Radio Array'. In: *Astroparticle Physics* 70 (2015), pp. 12–26. ISSN: 0927-6505. DOI: `https://doi.org/10.1016/j.astropartphys.2015.04.002` (cited on page 18).

[61] M. G. Aartsen et al. 'IceCube-Gen2: A Vision for the Future of Neutrino Astronomy in Antarctica'. In: (Dec. 2014). arXiv: `1412.5106 [astro-ph.HE]` (cited on pages 18, 28).

[62] G. A. Askaryan. 'Excess Negative Charge of an Electron-Photon Shower and Its Coherent Radio Emission'. In: *J. Exptl. Theoret. Phys. (U.S.S.R.)* 41 (Aug. 1961), pp. 616–618 (cited on page 18).

[63] David Saltzberg et al. 'Observation of the Askaryan Effect: Coherent Microwave Cherenkov Emission from Charge Asymmetry in High-Energy Particle Cascades'. In: *Phys. Rev. Lett.* 86 (13 Mar. 2001), pp. 2802–2805. DOI: `10.1103/PhysRevLett.86.2802` (cited on page 18).

[64] P. W. Gorham et al. 'Observations of the Askaryan effect in ice'. In: *Phys. Rev. Lett.* 99 (2007), p. 171101. DOI: `10.1103/PhysRevLett.99.171101`. arXiv: `hep-ex/0611008` (cited on page 18).

[65] J. A. Aguilar et al. 'Design and Sensitivity of the Radio Neutrino Observatory in Greenland (RNO-G)'. In: *JINST* 16.03 (2021), P03025. DOI: `10.1088/1748-0221/16/03/P03025`. arXiv: `2010.12279 [astro-ph.IM]` (cited on page 18).

[66] Christian Glaser. 'Neutrino direction and energy resolution of Askaryan detectors'. In: *PoS* ICRC2019 (2019), p. 899. DOI: `10.22323/1.358.0899` (cited on page 18).

[67] V. Aynutdinov et al. 'The BAIKAL neutrino experiment: From NT200 to NT200+'. In: *Nuclear Instruments and Methods in Physics Research Section A: Accelerators, Spectrometers, Detectors and Associated Equipment* 567.2 (2006). VLVnT2, pp. 433–437. ISSN: 0168-9002. DOI: `https://doi.org/10.1016/j.nima.2006.05.259` (cited on page 19).

[68] Igor Belolaptikov et al. 'Neutrino Telescope in Lake Baikal: Present and Nearest Future'. In: *Proceedings of 37th International Cosmic Ray Conference — PoS(ICRC2021)*. Sissa Medialab, Sept. 2021. DOI: `10.22323/1.395.0002` (cited on page 19).

[69] R. I. Bagduev et al. 'The Optical module of the Baikal deep underwater neutrino telescope'. In: *Nucl. Instrum. Meth. A* 420 (1999), pp. 138–154. DOI: `10.1016/S0168-9002(98)01156-5`. arXiv: `astro-ph/9903347` (cited on page 19).

[70] V.A. Balkanov et al. 'The Baikal deep Underwater Neutrino Experiment: Results, status, future'. In: *Progress in Particle and Nuclear Physics* 40 (Jan. 1998), pp. 391–401. ISSN: 0146-6410. DOI: `10.1016/s0146-6410(98)00047-7`. arXiv: `astro-ph/9801044` (cited on page 19).

[71] A.D. Avrorin et al. 'The optical module of Baikal-GVD'. In: *EPJ Web of Conferences* 116 (2016). Ed. by A. Capone et al., p. 01003. DOI: `10.1051/epjconf/201611601003` (cited on page 19).

[72] Dmitry Zaborov et al. 'Observations of track-like neutrino events with Baikal-GVD'. In: *Proceedings of 37th International Cosmic Ray Conference — PoS(ICRC2021)*. Sissa Medialab, July 2021. DOI: `10.22323/1.395.1177` (cited on page 20).

[73] Zhan-Arys Magysovich Dzhilkibaev et al. 'The Baikal-GVD neutrino telescope: search for high-energy cascades'. In: *Proceedings of 37th International Cosmic Ray Conference — PoS(ICRC2021)*. Sissa Medialab, July 2021. DOI: `10.22323/1.395.1144` (cited on page 20).

[74] M. Ageron et al. 'ANTARES: The first undersea neutrino telescope'. In: *Nuclear Instruments and Methods in Physics Research Section A: Accelerators, Spectrometers, Detectors and Associated Equipment* 656.1 (2011), pp. 11–38. ISSN: 0168-9002. DOI: `https://doi.org/10.1016/j.nima.2011.06.103` (cited on page 20).

[75] A. Albert et al. 'Long-term monitoring of the ANTARES optical module efficiencies using ^{40}K decays in sea water'. In: *Eur. Phys. J. C* 78.8 (2018), p. 669. DOI: `10.1140/epjc/s10052-018-6132-2`. arXiv: `1805.08675 [astro-ph.IM]` (cited on page 20).

[76] A. Albert et al. 'New constraints on all flavor Galactic diffuse neutrino emission with the ANTARES telescope'. In: *Phys. Rev. D* 96.6 (2017), p. 062001. DOI: `10.1103/PhysRevD.96.062001`. arXiv: `1705.00497 [astro-ph.HE]` (cited on page 20).

[77] A. Albert et al. 'All-flavor Search for a Diffuse Flux of Cosmic Neutrinos with Nine Years of ANTARES Data'. In: *Astrophys. J. Lett.* 853.1 (2018), p. L7. DOI: `10.3847/2041-8213/aaa4f6`. arXiv: `1711.07212 [astro-ph.HE]` (cited on page 20).

[78] A. Albert et al. 'Measuring the atmospheric neutrino oscillation parameters and constraining the 3+1 neutrino model with ten years of ANTARES data'. In: *JHEP* 06 (2019), p. 113. DOI: `10.1007/JHEP06(2019)113`. arXiv: `1812.08650 [hep-ex]` (cited on page 20).

[79] S. Adrian-Martinez et al. 'Letter of intent for KM3NeT 2.0'. In: *J. Phys. G* 43.8 (2016), p. 084001. DOI: `10.1088/0954-3899/43/8/084001`. arXiv: `1601.07459 [astro-ph.IM]` (cited on pages 21, 88).

[80] Ronald Bruijn. 'The KM3NeT Digital Optical Module and Detection Unit'. In: *EPJ Web Conf.* 207 (2019), p. 06002. DOI: `10.1051/epjconf/201920706002` (cited on page 21).

[81] S. Aiello et al. 'The KM3NeT multi-PMT optical module'. In: *JINST* 17.07 (2022), P07038. DOI: `10.1088/1748-0221/17/07/P07038`. arXiv: `2203.10048 [astro-ph.IM]` (cited on page 21).

[82] Marek Kowalski et al. 'Physics results from the AMANDA neutrino detector'. In: *Proceedings of International Europhysics Conference on High Energy Physics — PoS(hep2001)*. Sissa Medialab, Dec. 2001. DOI: `10.22323/1.007.0207` (cited on page 22).

[83] R. Abbasi et al. 'Search for point sources of high energy neutrinos with final data from AMANDA-II'. In: *Physical Review D* 79.6 (Mar. 2009). DOI: `10.1103/physrevd.79.062001` (cited on page 22).

[84] Elisa Bernardini. 'AMANDA: Selected physics results'. In: *Nuclear Instruments and Methods in Physics Research Section A: Accelerators, Spectrometers, Detectors and Associated Equipment* 567.2 (2006). VLVnT2, pp. 418–422. ISSN: 0168-9002. DOI: `https://doi.org/10.1016/j.nima.2006.05.271` (cited on page 22).

[85] R. Abbasi et al. 'Determination of the atmospheric neutrino flux and searches for new physics with AMANDA-II'. In: *Physical Review D* 79.10 (May 2009). DOI: `10.1103/physrevd.79.102005` (cited on page 22).

[86] R. Abbasi et al. 'The IceCube Data Acquisition System: Signal Capture, Digitization, and Timestamping'. In: *Nucl. Instrum. Meth. A* 601 (2009), pp. 294–316. DOI: `10.1016/j.nima.2009.01.001`. arXiv: `0810.4930 [physics.ins-det]` (cited on pages 23, 195).

[87] R. Abbasi et al. 'IceTop: The surface component of IceCube'. In: *Nucl. Instrum. Meth. A* 700 (2013), pp. 188–220. DOI: `10.1016/j.nima.2012.10.067`. arXiv: `1207.6326 [astro-ph.IM]` (cited on page 23).

[88] M. Ackermann et al. 'Optical properties of deep glacial ice at the South Pole'. In: *J. Geophys. Res.* 111.D13 (2006), p. D13203. DOI: `10.1029/2005JD006687` (cited on page 24).

[89] M. G. Aartsen et al. 'Measurement of South Pole ice transparency with the IceCube LED calibration system'. In: *Nucl. Instrum. Meth. A* 711 (2013), pp. 73–89. DOI: `10.1016/j.nima.2013.01.054`. arXiv: `1301.5361 [astro-ph.IM]` (cited on page 24).

[90] Martin Rongen. 'Calibration of the IceCube neutrino observatory'. PhD thesis. RWTH Aachen University, 2019. DOI: `10.18154/RWTH-2019-09941` (cited on page 24).

[91] Martin Rongen et al. 'A novel microstructure based model to explain the IceCube ice anisotropy'. In: *PoS* ICRC2021 (2021), p. 1119. DOI: `10.22323/1.395.1119`. arXiv: `2107.08692 [astro-ph.HE]` (cited on page 24).

[92] R. Abbasi et al. 'Improved Characterization of the Astrophysical Muon–neutrino Flux with 9.5 Years of IceCube Data'. In: *Astrophys. J.* 928.1 (2022), p. 50. DOI: `10.3847/1538-4357/ac4d29`. arXiv: `2111.10299 [astro-ph.HE]` (cited on page 24).

[93] M. G. Aartsen et al. 'Characteristics of the diffuse astrophysical electron and tau neutrino flux with six years of IceCube high energy cascade data'. In: *Phys. Rev. Lett.* 125.12 (2020), p. 121104. DOI: `10.1103/PhysRevLett.125.121104`. arXiv: `2001.09520 [astro-ph.HE]` (cited on page 24).

[94] P. Adamson et al. 'Precision Constraints for Three-Flavor Neutrino Oscillations from the Full MINOS+ and MINOS Dataset'. In: *Phys. Rev. Lett.* 125.13 (2020), p. 131802. DOI: `10.1103/PhysRevLett.125.131802`. arXiv: `2006.15208 [hep-ex]` (cited on page 25).

[95] M. A. Acero et al. 'Improved measurement of neutrino oscillation parameters by the NOνA experiment'. In: *Phys. Rev. D* 106.3 (2022), p. 032004. DOI: `10.1103/PhysRevD.106.032004`. arXiv: `2108.08219 [hep-ex]` (cited on page 25).

[96] K. Abe et al. 'Improved constraints on neutrino mixing from the T2K experiment with $\mathbf{3.13 \times 10^{21}}$ protons on target'. In: *Phys. Rev. D* 103.11 (2021), p. 112008. DOI: `10.1103/PhysRevD.103.112008`. arXiv: `2101.03779 [hep-ex]` (cited on page 25).

[97] James Mead. *IceCube Upgrade: ν-oscillations' high-statistics era*. July 2022. DOI: `10.5281/zenodo.6805121` (cited on pages 25, 28).

[98] M. G. Aartsen et al. 'Measurement of Atmospheric Neutrino Oscillations at 6–56 GeV with IceCube DeepCore'. In: *Phys. Rev. Lett.* 120.7 (2018), p. 071801. doi: `10.1103/PhysRevLett.120.071801`. arXiv: `1707.07081 [hep-ex]` (cited on page 25).

[99] Kayla Leonard DeHolton. 'Atmospheric Neutrino Oscillations with 8 years of data from IceCube DeepCore'. In: *PoS* NuFact2021 (2022), p. 062. doi: `10.22323/1.402.0062` (cited on page 25).

[100] R. Abbasi et al. 'Detection of astrophysical tau neutrino candidates in IceCube'. In: *Eur. Phys. J. C* 82.11 (2022), p. 1031. doi: `10.1140/epjc/s10052-022-10795-y`. arXiv: `2011.03561 [hep-ex]` (cited on page 25).

[101] Mark Aartsen et al. 'Multimessenger observations of a flaring blazar coincident with high-energy neutrino IceCube-170922A'. In: *Science* 361.6398 (2018), eaat1378. doi: `10.1126/science.aat1378`. arXiv: `1807.08816` (cited on page 25).

[102] Mark Aartsen et al. 'Neutrino emission from the direction of the blazar TXS 0506+056 prior to the IceCube-170922A alert'. In: *Science* 361.6398 (2018), pp. 147–151. doi: `10.1126/science.aat2890`. arXiv: `1807.08794` (cited on page 25).

[103] Colton Hill et al. 'Performance of the D-Egg optical sensor for the IceCube-Upgrade'. In: *PoS* ICRC2021 (2021), p. 1042. doi: `10.22323/1.395.1042`. arXiv: `2108.05353 [physics.ins-det]` (cited on pages 27, 39).

[104] Nikhita Khera and Felix Henningsen and. 'POCAM in the IceCube Upgrade'. In: *Proceedings of 37th International Cosmic Ray Conference*. Sissa Medialab, July 2021. doi: `10.22323/1.395.1049` (cited on page 27).

[105] John Rack-Helleis et al. 'The Wavelength-shifting Optical Module (WOM) for the IceCube Upgrade'. In: *Proceedings of 37th International Cosmic Ray Conference — PoS(ICRC2021)*. Sissa Medialab, July 2021. doi: `10.22323/1.395.1038` (cited on page 27).

[106] Vedant Basu et al. 'A next-generation optical sensor for IceCube-Gen2'. In: *Proceedings of 37th International Cosmic Ray Conference — PoS(ICRC2021)*. Sissa Medialab, July 2021. doi: `10.22323/1.395.1062` (cited on page 27).

[107] Martin Rongen and Dmitry Chirkin. 'Advances in IceCube ice modelling & what to expect from the Upgrade'. In: *JINST* 16.09 (2021), p. C09014. doi: `10.1088/1748-0221/16/09/C09014`. arXiv: `2108.03291 [astro-ph.IM]` (cited on page 28).

[108] Lew Classen. 'The mDOM - a multi-PMT digital optical module for the IceCube-Gen2 neutrino telescope'. PhD Thesis. Friedrich-Alexander-Universität Erlangen-Nürnberg (FAU), 2017. url: `https://nbn-resolving.org/urn:nbn:de:bvb:29-opus4-86782` (cited on pages 31–33, 44, 49, 128–131, 135, 143, 144, 146, 147, 150, 163).

[109] C. J. Lozano Mariscal et al. 'Sensitivity of multi-PMT optical modules in Antarctic ice to supernova neutrinos of MeV energy'. In: *Eur. Phys. J. C* 81.12 (2021), p. 1058. doi: `10.1140/epjc/s10052-021-09809-y`. arXiv: `2106.14199 [astro-ph.HE]` (cited on pages 31, 186).

[110] M. A. Unland Elorrieta et al. 'Homogeneity of the photocathode in the Hamamatsu R15458-02 Photomultiplier Tube'. In: *Journal of Instrumentation* 16.11 (Nov. 2021), P11038. doi: `10.1088/1748-0221/16/11/p11038`. arXiv: `2109.13868v2` (cited on pages 33, 45, 63, 65, 83, 84, 86, 87).

[111] M Crisler et al. 'The Chicagoland Observatory Underground for Particle Physics cosmic ray veto system'. In: *IEEE Nuclear Science Symposuim & Medical Imaging Conference*. IEEE, Oct. 2010. doi: `10.1109/nssmic.2010.5873871` (cited on page 33).

[112] Lew Classen et al. 'Design and performance of the multi-PMT optical module for IceCube Upgrade'. In: *Proceedings of 37th International Cosmic Ray Conference — PoS(ICRC2021)*. Sissa Medialab, July 2021. doi: `10.22323/1.395.1070` (cited on pages 33–35).

[113] Woosik Kang et al. 'Camera Calibration for the IceCube Upgrade and Gen2'. In: *Proceedings of 37th International Cosmic Ray Conference — PoS(ICRC2021)*. Sissa Medialab, July 2021. DOI: `10.22323/1.395.1064` (cited on page 35).

[114] Roithner LaserTechnik GmbH. *XRL-400-5O Technical Data Sheet*. 2012. URL: `http://www.roithner-laser.com/datasheets/led_div/xrl-400-5o.pdf` (cited on page 35).

[115] Hamamatsu Photonics K.K. *Photomultiplier tubes - Basics and Applications*. 4th ed. Hamamatsu Photonics K.K. - Electron Tube Division, 2017. URL: `https://www.hamamatsu.com/resources/pdf/etd/PMT_handbook_v4E.pdf` (cited on pages 37–39, 41–44, 66, 101).

[116] A. G. Wright. *The Photomultiplier Handbook*. Oxford University Press, 2017. DOI: `10.1093/oso/9780199565092.001.0001` (cited on pages 37, 39–44, 53, 55, 58, 61, 165).

[117] Kimitsugu Nakamura et al. 'Latest bialkali photocathode with ultra high sensitivity'. In: *Nucl. Instrum. Meth. A* 623 (2010). Ed. by Hiroyuki Iwasaki, Takeshi K. Komatsubara, and Yasuhiro Sugimoto, pp. 276–278. DOI: `10.1016/j.nima.2010.02.220` (cited on page 39).

[118] Saul Dushman. 'Electron Emission from Metals as a Function of Temperature'. In: *Phys. Rev.* 21 (6 June 1923), pp. 623–636. DOI: `10.1103/PhysRev.21.623` (cited on page 42).

[119] K. Jensen. 'Fowler-Nordheim equation'. In: *Introduction to the Physics of Electron Emission*. John Wiley & Sons, Ltd, Oct. 2017, pp. 139–148. DOI: `10.1002/9781119051794.ch13` (cited on page 42).

[120] Hamamatsu Photonics K.K. *Photomultiplier tubes and assemblies for scintillation counting & high energy physics*. 2017. URL: `https://www.hamamatsu.com/content/dam/hamamatsu-photonics/sites/documents/99_SALES_LIBRARY/etd/High_energy_PMT_TPMZ0003E.pdf` (cited on page 43).

[121] E.H. Bellamy et al. 'Absolute calibration and monitoring of a spectrometric channel using a photomultiplier'. In: *Nucl. Inst. Meth.* A339.3 (1994), pp. 468–476. DOI: `10.1016/0168-9002(94)90183-x` (cited on pages 45, 220).

[122] M. A. Unland Elorrieta. *Python-Based Fitter for PMT SPE Spectra*. Feb. 2023. DOI: `10.5281/zenodo.7654801` (cited on pages 45, 221).

[123] J. Rademacker. 'An exact formula to describe the amplification process in a photomultiplier tube'. In: *Nucl. Instrum. Meth. A* 484 (2002), pp. 432–443. DOI: `10.1016/S0168-9002(01)02055-1`. arXiv: `physics/0406036` (cited on pages 45, 53–55).

[124] Christian Spiering. 'Neutrino Detectors Under Water and Ice'. In: *Particle Physics Reference Library: Volume 2: Detectors for Particles and Radiation*. Ed. by Christian Wolfgang Fabjan and Herwig Schopper. 2020, pp. 785–822. DOI: `10.1007/978-3-030-35318-6_17` (cited on page 48).

[125] S. Aiello et al. 'Characterisation of the Hamamatsu photomultipliers for the KM3NeT Neutrino Telescope'. In: *Journal of Instrumentation* 13.05 (2018), P05035–P05035. DOI: `10.1088/1748-0221/13/05/p05035` (cited on pages 48, 113, 126).

[126] M. A. Unland Elorrieta et al. 'Characterisation of the Hamamatsu R12199-01 HA MOD photomultiplier tube for low temperature applications'. In: *JINST* 14.03 (2019), P03015. DOI: `10.1088/1748-0221/14/03/P03015`. arXiv: `1902.01714 [physics.ins-det]` (cited on pages 48, 65, 74, 113, 163, 165–167).

[127] Martin Rongen and Merlin Schaufel. 'Design and evaluation of a versatile picosecond light pulser'. In: *JINST* 13.06 (2018), P06002. DOI: `10.1088/1748-0221/13/06/P06002`. arXiv: `1805.00822 [physics.ins-det]` (cited on page 49).

[128] Pauli Virtanen et al. 'SciPy 1.0: Fundamental Algorithms for Scientific Computing in Python'. In: *Nature Methods* 17 (2020), pp. 261–272. DOI: `10.1038/s41592-019-0686-2` (cited on pages 50, 106).

[129] S-O Flyckt and Carole Marmonier. *Photomultiplier tubes - principicles and applications*. Photonis, 2002. URL: `https://www2.pv.infn.it/~debari/doc/Flyckt_Marmonier.pdf` (cited on pages 53, 71, 72, 101, 114, 115).

[130] A.J. Dekker. 'Secondary Electron Emission'. In: *Advances in Research and Applications*. Ed. by Frederick Seitz and David Turnbull. Vol. 6. Solid State Physics. Academic Press, 1958, pp. 251–311. DOI: `https://doi.org/10.1016/S0081-1947(08)60728-6` (cited on page 55).

[131] P. Barrow et al. 'Qualification Tests of the R11410-21 Photomultiplier Tubes for the XENON1T Detector'. In: *JINST* 12.01 (2017), P01024. DOI: `10.1088/1748-0221/12/01/P01024`. arXiv: `1609.01654 [astro-ph.IM]` (cited on pages 55, 56).

[132] M. Furman and M. Pivi. 'Probabilistic model for the simulation of secondary electron emission'. In: *Physical Review Special Topics - Accelerators and Beams* 5.12 (Dec. 2002). DOI: `10.1103/physrevstab.5.124404` (cited on pages 57, 60, 76).

[133] F. Peters. 'Studien zur Wellenlängenabhängigkeit von Performance-Parametern von Photomultipliern des Typs Hamamatsu R12199-01 HA'. Bachelor Thesis. University of Münster, 2020. URL: `https://www.uni-muenster.de/imperia/md/content/physik_kp/agkappes/abschlussarbeiten/bachelorarbeiten/ba_fpeters.pdf` (cited on pages 58, 66).

[134] Karl-Heinz Sulanke. *mDOM Mainboard Final Design Review (presentation)*. mDOM-FDR (only accessible for IceCube members). Apr. 12, 2022 (cited on page 60).

[135] B. Sipp, J.A. Miehe, and R. Lopez-Delgado. 'Wavelength dependence of the time resolution of high-speed photomultipliers used in single-photon timing experiments'. In: *Optics Communications* 16.1 (1976), pp. 202–204. ISSN: 0030-4018. DOI: `https://doi.org/10.1016/0030-4018(76)90085-7` (cited on page 67).

[136] M. Moszyński and J. Vacher. 'Influence of incident light wavelength on time jitter of fast photomultipliers'. In: *Nuclear Instruments and Methods* 141.2 (1977), pp. 319–323. ISSN: 0029-554X. DOI: `https://doi.org/10.1016/0029-554X(77)90782-0` (cited on page 67).

[137] Dick Bebelaar. 'Time response of various types of photomultipliers and its wavelength dependence in time-correlated single-photon counting with an ultimate resolution of 47 ps FWHM'. In: *Review of Scientific Instruments* 57.6 (1986), pp. 1116–1125. DOI: `10.1063/1.1138666`. eprint: `https://doi.org/10.1063/1.1138666` (cited on page 67).

[138] J. Averbeck. 'Nachbau eines Photomultipliers in COMSOL Multiphysics und Untersuchung der Elektronentrajektorien zwischen Photokathode und erster Dynode'. Bachelor Thesis. University of Münster, 2022. URL: `https://www.uni-muenster.de/imperia/md/content/physik_kp/agkappes/abschlussarbeiten/bachelorarbeiten/bachelor_janis.pdf` (cited on page 67).

[139] R. S. Busse. 'Setup and commissioning of a test stand for detailed investigations of quantum efficiency characteristics of photomultiplier tubes, and initial studies for IceCube-Gen2'. Master Thesis. University of Münster, 2017. URL: `https://www.uni-muenster.de/imperia/md/content/physik_kp/agkappes/abschlussarbeiten/masterarbeiten/1703-ma_rbusse.pdf` (cited on pages 68, 77).

[140] Newport Corporation. *818 Series Calibrated Photodiode Sensors*. Accessed: 2022-Aug-25. URL: `https://www.newport.com/medias/sys_master/images/images/hbd/h46/9599504875550/DS-051502-818-Series-Photodiode-Datasheet.pdf` (cited on page 68).

[141] Judith Schneider. Private communication, to be published in PhD thesis with preliminary title "Characterization of the mDOM light detection and signal processing system for the IceCube Upgrade". 2023 (cited on pages 69, 70, 113, 139).

[142] A. G. Wright. 'Method for the determination of photomultiplier collection efficiency, F'. In: *Appl. Opt.* 49.11 (Apr. 2010), pp. 2059–2065. DOI: `10.1364/AO.49.002059` (cited on pages 71, 72).

[143] V. Giordano et al. 'The effects of Earth's magnetic field on 3-inch diameter photomultipliers used in KM3NeT neutrino telescope'. In: *EPJ Web of Conferences* 116 (2016). Ed. by A. Capone et al., p. 01005. DOI: `10.1051/epjconf/201611601005` (cited on page 72).

[144] K. Ueberholz. 'Setup and commission of a magnetic field test stand and studies on the influence of magnetic fields on the performance of the Hamamatsu R12199-02'. Master Thesis. University of Münster, 2020. URL: `https://www.uni-muenster.de/imperia/md/content/physik_kp/agkappes/abschlussarbeiten/masterarbeiten/ueberholz_master.pdf` (cited on pages 72, 75, 77).

[145] K. M. Gorski et al. 'HEALPix: A Framework for High-Resolution Discretization and Fast Analysis of Data Distributed on the Sphere'. In: *The Astrophysical Journal* 622.2 (2005), pp. 759–771. DOI: `10.1086/427976` (cited on page 72).

[146] Abraham. Savitzky and M. J. E. Golay. 'Smoothing and Differentiation of Data by Simplified Least Squares Procedures.' In: *Analytical Chemistry* 36.8 (1964), pp. 1627–1639. DOI: `10.1021/ac60214a047` (cited on page 75).

[147] Daisuke Miyazaki. 'Fresnel Equations'. In: *Computer Vision: A Reference Guide*. Ed. by Katsushi Ikeuchi. Boston, MA: Springer US, 2014, pp. 305–307. ISBN: 978-0-387-31439-6. DOI: `10.1007/978-0-387-31439-6_569` (cited on page 83).

[148] M. A. Unland Elorrieta. *Animated pictures of the Hamamatsu R15458-02 PMT performance under different magnetic field orientations*. Feb. 2023. DOI: `10.5281/zenodo.7650944` (cited on page 91).

[149] M. A. Unland Elorrieta. *Data of homogeneity of the photocathode in the Hamamatsu R15458-02 PMT under different magnetic field orientations*. Zenodo, Feb. 2023. DOI: `10.5281/zenodo.7650918` (cited on page 91).

[150] William E. Spicer and Alberto Herrera-Gomez. 'Modern theory and applications of photocathodes'. In: *SPIE Proceedings*. Ed. by Kenneth J. Kaufmann. SPIE, Oct. 1993. DOI: `10.1117/12.158575` (cited on page 101).

[151] Dario Motta and Stefan Schonert. 'Optical properties of Bialkali photocathodes'. In: *Nucl. Instrum. Meth. A* 539 (2005), pp. 217–235. DOI: `10.1016/j.nima.2004.10.009`. arXiv: `physics/0408075` (cited on pages 101, 136, 138).

[152] M. A. Unland Elorrieta. 'Studies on dark rates induced by radioactive decays of the multi-PMT digital optical module for future IceCube extensions'. Master Thesis. University of Münster, Dec. 2017. DOI: `10.5281/zenodo.6611735` (cited on pages 106, 110, 112, 171, 173, 174, 181, 182, 185, 203).

[153] IceCube Collaboration. *South Pole Ice Temperature*. 2020. DOI: `10.21234/SP-ICE-TEMPERATURE` (cited on pages 107, 159, 160).

[154] H. O. Meyer. 'Spontaneous electron emission from a cold surface'. In: *EPL (Europhysics Letters)* 89.5 (2010), p. 58001. DOI: `10.1209/0295-5075/89/58001` (cited on page 110).

[155] Lasse Halve. Private communication. (cited on pages 112, 124).

[156] S. Aiello et al. 'Characterization of the 80-mm diameter Hamamatsu PMTs for the KM3NeT project'. In: *AIP Conf. Proc.* (2014). DOI: `10.1063/1.4902786` (cited on page 113).

[157] T. DeYoung. 'IceTray: A software framework for IceCube'. In: *14th International Conference on Computing in High-Energy and Nuclear Physics*. 2005, pp. 463–466. URL: `https://cds.cern.ch/record/865626/files/p463.pdf` (cited on page 113).

[158] K. J. Ma et al. 'Time and Amplitude of Afterpulse Measured with a Large Size Photomultiplier Tube'. In: *Nucl. Instrum. Meth. A* 629 (2011), pp. 93–100. DOI: `10.1016/j.nima.2010.11.095`. arXiv: `0911.5336 [physics.ins-det]` (cited on page 122).

[159] R. V. Poleshchuk et al. ‘An Observation of a new class of afterpulses with delay time in the range of 70-200 microseconds in classical vacuum photomultipliers’. In: *Nucl. Instrum. Meth. A* 695 (2012), pp. 362–364. DOI: `10.1016/j.nima.2011.11.030`. arXiv: `1202.6198 [physics.ins-det]` (cited on page 124).

[160] J Haser et al. ‘Afterpulse measurements of R7081 photomultipliers for the Double Chooz experiment’. In: *Journal of Instrumentation* 8.04 (Apr. 2013), P04029–P04029. DOI: `10.1088/1748-0221/8/04/p04029`. arXiv: `1301.2508` (cited on page 126).

[161] Anthony P. Gies. ‘Chapter 9 - Mass spectrometry of polymers’. In: *Molecular Characterization of Polymers*. Elsevier, 2021, pp. 305–368. ISBN: 978-0-12-819768-4. DOI: `https://doi.org/10.1016/B978-0-12-819768-4.00006-3` (cited on page 126).

[162] Michael. Karas and Franz. Hillenkamp. ‘Laser desorption ionization of proteins with molecular masses exceeding 10,000 daltons’. In: *Analytical Chemistry* 60.20 (1988), pp. 2299–2301. DOI: `10.1021/ac00171a028` (cited on page 126).

[163] Anna Katharina Steuer. ‘Cascade type identification in IceCube and an application in a search for new physics’. PhD thesis. 2018. DOI: `10.25358/OPENSCIENCE-4463` (cited on page 126).

[164] J. Allison et al. ‘Recent developments in Geant4’. In: *Nucl. Instrum. Meth. A* 835 (2016), pp. 186–225. DOI: `10.1016/j.nima.2016.06.125` (cited on page 128).

[165] S. Agostinelli et al. ‘GEANT4–a simulation toolkit’. In: *Nucl. Instrum. Meth. A* 506 (2003), pp. 250–303. DOI: `10.1016/S0168-9002(03)01368-8` (cited on pages 128, 129).

[166] Björn Herold. ‘Simulation and Measurement of Optical Background in the Deep Sea Using a Multi-PMT Optical Module’. PhD Thesis. Friedrich-Alexander-Universität Erlangen-Nürnberg (FAU), 2017 (cited on page 128).

[167] Geant4 Collaboration. *Geant4 User Guide for Toolkit Developers — Release 11.0*. 2021. URL: `https://geant4-userdoc.web.cern.ch/UsersGuides/ForToolkitDeveloper/fo/BookForToolkitDevelopers.pdf` (cited on page 129).

[168] Ankit Rohatgi. *Webplotdigitizer: Version 4.5*. 2021. URL: `https://automeris.io/WebPlotDigitizer` (cited on page 130).

[169] MKS Instruments, Inc. *Spectralon Diverging Beam Integrating Spheres — 819D Series*. 2020. URL: `https://www.newport.com/mam/celum/celum_assets/resources/DS-050720_819D_Series_Spectralon_Diverging_Spheres.pdf` (visited on 09/06/2022) (cited on page 132).

[170] A. Levin and C. Moisan. ‘A more physical approach to model the surface treatment of scintillation counters and its implementation into DETECT’. In: *1996 IEEE Nuclear Science Symposium. Conference Record*. Vol. 2. 1996, 702–706 vol.2. DOI: `10.1109/NSSMIC.1996.591410` (cited on page 133).

[171] Geant4 Collaboration. *Book For Application Developers — Release 11.0*. 2021. URL: `https://geant4-userdoc.web.cern.ch/UsersGuides/ForApplicationDeveloper/fo/BookForApplicationDevelopers.pdf` (cited on page 133).

[172] C. M. Poole et al. ‘A CAD Interface for GEANT4’. In: *Australasian Physical & Engineering Science in Medicine* (2012). DOI: `10.1007/s13246-012-0159-8` (cited on page 137).

[173] S. Schmiemann. ‘Squark Annihilation Contributions to Neutralino Dark Matter in NLO SUSY-QCD’. PhD thesis. Munster U., ITP, 2019 (cited on pages 137, 163, 164).

[174] *Refractiveindex.info*. URL: `https://refractiveindex.info/?shelf=glass&book=BK7&page=SCHOTT` (visited on 07/12/2022) (cited on page 137).

[175] E. Hecht. *Optics*. Pearson education. Addison-Wesley, 2002. ISBN: 9780805385663 (cited on page 137).

[176] R. Brun and F. Rademakers. 'ROOT: An object oriented data analysis framework'. In: *Nucl. Instrum. Meth. A* 389 (1997), pp. 81–86. DOI: `10.1016/S0168-9002(97)00048-X` (cited on page 141).

[177] Alexander Kappes. *mDOM Pressure Test (presentation)*. mDOM-dev Call (only accessible for IceCube members). Apr. 7, 2022 (cited on page 151).

[178] SimScale GmbH. *SimScale: Simulation Software Engineering in the Cloud*. 2020. URL: `https://simscale.com` (cited on page 153).

[179] W. H. Yang. 'A Generalized von Mises Criterion for Yield and Fracture'. In: *Journal of Applied Mechanics* 47.2 (June 1980), pp. 297–300. DOI: `10.1115/1.3153658` (cited on page 153).

[180] Philipp Laurens Rosendahl. 'From bulk to structural failure: fracture of hyperelastic materials'. PhD thesis. Darmstadt: Technische Universität Darmstadt, 2020. DOI: `https://doi.org/10.25534/tuprints-00008693` (cited on page 154).

[181] P. Bagley et al. 'KM3NeT: Technical Design Report for a Deep-Sea Research Infrastructure in the Mediterranean Sea Incorporating a Very Large Volume Neutrino Telescope'. In: (2009) (cited on page 160).

[182] Louis Lavoie. 'Photomultiplier Cathode Poisoning'. In: *Rev. Sci. Instrum.* 38.6 (1967), pp. 833–834. DOI: `10.1063/1.1720903` (cited on page 168).

[183] H Mehrer, A W Imre, and E Tanguep-Nijokep. 'Diffusion and ionic conduction in oxide glasses'. In: *J. Phys. Conf. Ser.* 106 (2008), p. 012001. DOI: `10.1088/1742-6596/106/1/012001` (cited on page 168).

[184] Markus Dittmer. 'Characterisation of scintillation light induced by radioactive excitation in the mDOM glass pressure vessel'. Master Thesis. University of Münster, Apr. 2020. URL: `https://www.uni-muenster.de/imperia/md/content/physik_kp/agkappes/abschlussarbeiten/masterarbeiten/dittmer.pdf` (cited on pages 171, 173, 185, 203).

[185] P. Lecoq. 'Scintillation Detectors for Charged Particles and Photons'. In: *Particle Physics Reference Library: Volume 2: Detectors for Particles and Radiation*. Cham: Springer, 2020, pp. 45–89. DOI: `10.1007/978-3-030-35318-6_3` (cited on page 171).

[186] P. Lecoq et al. *Inorganic Scintillators for Detector Systems*. Particle Acceleration and Detection. Berlin: Springer, 2006. ISBN: 978-3-540-27766-8, 978-3-540-27768-2. DOI: `10.1007/3-540-27768-4` (cited on page 171).

[187] Cornelis R. Ronda, ed. *Luminescence: From Theory to Applications*. Wiley-VCH, 2007. ISBN: 9783527314024 (cited on pages 171, 173).

[188] B. G. Yacobi and D. B. Holt. *Cathodoluminescence Microscopy of Inorganic Solids*. Springer US, 1990. DOI: `10.1007/978-1-4757-9595-0` (cited on page 172).

[189] Glenn Knoll. *Radiation detection and measurement*. Hoboken, N.J: John Wiley, 2010. ISBN: 978-0-470-13148-0 (cited on pages 173, 187).

[190] M.S. Basunia. 'Nuclear Data Sheets for A = 237'. In: *Nuclear Data Sheets* 107.8 (2006), pp. 2323–2422. ISSN: 0090-3752. DOI: `https://doi.org/10.1016/j.nds.2006.07.001` (cited on page 174).

[191] Hans Dembinski and Piti Ongmongkolkul et al. 'scikit-hep/iminuit'. In: (Dec. 2020). DOI: `10.5281/zenodo.3949207` (cited on pages 181, 200, 225).

[192] F. James and M. Roos. 'Minuit: A System for Function Minimization and Analysis of the Parameter Errors and Correlations'. In: *Comput. Phys. Commun.* 10 (1975), pp. 343–367. DOI: `10.1016/0010-4655(75)90039-9` (cited on pages 181, 200, 225).

[193] Joseph R. Lakowicz, ed. *Principles of Fluorescence Spectroscopy*. Springer US, 2006. DOI: `10.1007/978-0-387-46312-4` (cited on page 181).

[194] Lutz Köpke. 'Improved Detection of Supernovae with the IceCube Observatory'. In: *J. Phys. Conf. Ser.* 1029.1 (2018), p. 012001. DOI: `10.1088/1742-6596/1029/1/012001`. arXiv: `1704.03823 [astro-ph.HE]` (cited on page 186).

[195] M.J. Martin. 'Nuclear Data Sheets for A = 208'. In: *Nuclear Data Sheets* 108.8 (2007), pp. 1583–1806. ISSN: 0090-3752. DOI: `https://doi.org/10.1016/j.nds.2007.07.001` (cited on page 187).

[196] Krzysztof W Fornalski. 'Simple empirical correction functions to cross sections of the photoelectric effect, Compton scattering, pair and triplet production for carbon radiation shields for intermediate and high photon energies'. In: *Journal of Physics Communications* 2.3 (Mar. 2018), p. 035038. DOI: `10.1088/2399-6528/aab408` (cited on page 187).

[197] The PyNE Development Team. *PyNE: The Nuclear Engineering Toolkit*. 2014. URL: `http://pyne.io` (cited on page 188).

[198] Jonas Reubelt. 'Hardware studies, in-situ prototype calibration and data analysis of the novel multi-PMT digital optical module for the KM3NeT neutrino telescope'. PhD thesis. Friedrich-Alexander-Universität Erlangen-Nürnberg (FAU), 2019 (cited on page 195).

[199] T. M. Eder. 'Studies on an in-situ calibration method for the IceCube multi-PMT optical module using radioactive decays'. Master Thesis. University of Münster, 2019. URL: `https://www.uni-muenster.de/imperia/md/content/physik_kp/agkappes/abschlussarbeiten/masterarbeiten/master_thesis_eder.pdf` (cited on pages 195, 197).

[200] A. Tenbruck. 'Implementation von LEDs in eine Geant4-Simulation des mDOM-Sensors für das IceCube Upgrade und Simulationsstudien zu deren Emissionsprofil'. Bachelor Thesis. University of Münster, 2022. URL: `https://www.uni-muenster.de/imperia/md/content/physik_kp/agkappes/abschlussarbeiten/bachelorarbeiten/ba_tenbruck.pdf` (cited on page 202).

[201] Daniel Zwillinger. *Table of Integrals, Series, and Products*. Elsevier, 2015. DOI: `10.1016/c2010-0-64839-5` (cited on page 220).

[202] Enrico Masina. *Useful review on the Exponential-Integral special function*. 2019. DOI: `10.48550/ARXIV.1907.12373` (cited on page 222).

[203] Matthew A. Lazzara et al. 'Fifty-year Amundsen–Scott South Pole station surface climatology'. In: *Atmospheric Research* 118 (2012), pp. 240–259. ISSN: 0169-8095. DOI: `https://doi.org/10.1016/j.atmosres.2012.06.027` (cited on page 227).

[204] J. M. Solano-Altamirano, John D. Malcolm, and Saul Goldman. 'Gas bubble dynamics in soft materials'. In: *Soft Matter* 11 (1 2015), pp. 202–210. DOI: `10.1039/C4SM02037E` (cited on page 227).

[205] Alexander Kappes. *Bubble Dynamics in Gel (presentation)*. mDOM-dev Call (only accessible for IceCube members). June 11, 2021 (cited on page 227).

[206] Göran Flodberg, Henrik Pettersson, and Li Yang. 'Pore analysis and mechanical performance of selective laser sintered objects'. In: *Additive Manufacturing* 24 (2018), pp. 307–315. ISSN: 2214-8604. DOI: `https://doi.org/10.1016/j.addma.2018.10.001` (cited on page 227).

APPENDIX

A Solving Bellamy's convolution

In the following, the charge distribution of a PMT is calculated following the Ansatz of [121] (see Section 5.5).

The ideal response of a PMT is:

$$\begin{aligned} S_{\text{ideal}}(q) &= P(n,\mu) \otimes G_n(q) \\ &= \frac{\mu^n e^{-\mu}}{n!} \otimes \frac{1}{\sqrt{2\pi n}\sigma_1} \exp(-\frac{(q-nQ_1)^2}{2n\sigma_1^2}) \\ &= \sum_{n=0}^{\infty} \frac{\mu^n e^{-\mu}}{n!} \frac{1}{\sqrt{2\pi n}\sigma_1} \exp(-\frac{(q-nQ_1)^2}{2n\sigma_1^2}), \end{aligned} \tag{A.1}$$

Where $G_n(q)$ is a Gaussian of the form $G(q, nQ_1, \sqrt{n}\sigma_1) = \frac{1}{\sqrt{2\pi n}\sigma_1} \exp(-\frac{(q-nQ_1)^2}{2n\sigma_1^2})$.

The background function is:

$$B(q) = \underbrace{\frac{(1-P_u)}{\sigma_0\sqrt{2\pi}} \exp(-\frac{(q-Q_0)^2}{2\sigma_0^2})}_{B_1(q)} + \underbrace{P_u \cdot \Theta(q-Q_0) \cdot \lambda \cdot \exp\left(-\lambda\,(q-Q_0)\right)}_{B_2(q)}, \tag{A.2}$$

The convolution of both functions yields the realistic response of a PMT:

$$\begin{aligned} S_{\text{real}}(q) &= \int_{-\infty}^{\infty} S_{\text{ideal}}(q')B(q-q')dq' \\ &= \sum_{n=0}^{\infty} \frac{\mu^n e^{-\mu}}{n!} \left[\int_{-\infty}^{\infty} G_n(q')B_1(q-q')\,dq' + \int_{-\infty}^{\infty} G_n(q')B_2(q-q')\,dq' \right] \end{aligned} \tag{A.3}$$

Solving the first integral:

$$\begin{aligned} \int_{-\infty}^{\infty} G_n(q')B_1(q-q')\,dq' &= \int_{-\infty}^{\infty} \frac{1}{\sqrt{2\pi n}\sigma_1} \exp(-\frac{(q'-nQ_1)^2}{2n\sigma_1^2}) \cdot \frac{(1-P_u)}{\sigma_0\sqrt{2\pi}} \exp(-\frac{(q-q'-Q_0)^2}{2\sigma_0^2}) \cdot dq' \\ &= \frac{1}{\sqrt{2\pi n}\sigma_1} \frac{(1-P_u)}{\sigma_0\sqrt{2\pi}} \int_{-\infty}^{\infty} \exp(-\frac{(q'-nQ_1)^2}{2n\sigma_1^2} - \frac{-(q-q'-Q_0)^2}{2\sigma_0^2}) \cdot dq'. \end{aligned} \tag{A.4}$$

After expanding and rearranging the terms inside the exponential to a quadratic equation, one can solve the integration with [201, p. 108]

$$\int \exp\left(-(ax^2+2bx+c)\right)\,dx = \frac{1}{2}\sqrt{\frac{\pi}{a}} \exp(\frac{b^2-ac}{a}) \operatorname{erf}(\sqrt{a}x + \frac{b}{\sqrt{a}}). \tag{A.5}$$

With $\lim_{x\to\pm\infty}\operatorname{erf}(x) = \pm 1$, Equation A.4 can be expressed as

$$\begin{aligned}
&= \frac{1}{\sqrt{2\pi n}\sigma_1}\frac{(1-P_u)}{\sigma_0\sqrt{2\pi}}\left[\frac{\sqrt{\pi n}\sigma_0\sigma_1}{\sqrt{2\cdot(n\sigma_1^2+\sigma_0^2)}}\exp\left(-\frac{(Q_0+nQ_1-q)^2}{2(\sigma_0^2+n\sigma_1^2)}\right)\operatorname{erf}\left(\frac{nQ_1\sigma_0^2-Q_0n\sigma_1^2+qn\sigma_1^2-q'(\sigma_0^2+n\sigma_1^2)}{\sqrt{2n}\sigma_1\sigma_0\sqrt{n\sigma_1^2+\sigma_0^2}}\right)\Bigg|_{-\infty}^{\infty}\right]\\
&= \frac{(1-P_u)}{2\sqrt{2\pi\cdot(n\sigma_1^2+\sigma_0^2)}}\exp\left(-\frac{(Q_0+nQ_1-x)^2}{2(\sigma_0^2+n\sigma_1^2)}\right)\cdot 2\\
&= \frac{(1-P_u)}{\sqrt{2\pi}\sigma_n}\exp(-\frac{(Q_n-x)^2}{2\sigma_n^2})\\
&= (1-P_u)\cdot G(q,Q_n,\sigma_n),
\end{aligned} \tag{A.6}$$

where $Q_n = Q_0 + nQ_1$ and $\sigma_n^2 = \sigma_0^2 + n\sigma_1^2$.

The second integral of Equation A.3 is solved as follows, using $\Theta(q-q'-Q_0) = 0$ if $q' > q - Q_0$:

$$\begin{aligned}
\int_{-\infty}^{\infty} G_n(q')B_2(q-q')\,dq' &= \int_{-\infty}^{\infty}\frac{1}{\sqrt{2\pi n}\sigma_1}\exp\left(-\frac{(q'-nQ_1)^2}{2n\sigma_1^2}\right)P_u\Theta(q-q'-Q_0)\lambda\exp\left(-\lambda(q-q'-Q_0)\right)\,dq'\\
&= \frac{\lambda\cdot P_u}{\sqrt{2\pi n}\sigma_1}\int_{-\infty}^{q-Q_0}\exp\left(-\frac{(q'-nQ_1)^2}{2n\sigma_1^2}-\lambda(q-q'-Q_0)\right)\,dq'.
\end{aligned} \tag{A.7}$$

Following the same strategy as before using Equation A.5, we get

$$\begin{aligned}
\int_{-\infty}^{\infty} G_n(q')B_2(q-q')\,dq' &= \frac{\lambda\cdot P_u}{\sqrt{2\pi n}\sigma_1}\frac{\sqrt{\pi n}}{\sqrt{2}}\sigma_1\exp\left(\frac{n\lambda^2\sigma_1^2}{2}+\lambda(nQ_1+Q_0-q)\right)\operatorname{erf}\left(\frac{q'-\lambda n\sigma_1^2-nQ_1}{\sqrt{2n}\sigma_1}\right)\Bigg|_{-\infty}^{q-Q_0}\\
&= \frac{\lambda\cdot P_u}{2}\exp\left(\frac{n\lambda^2\sigma_1^2}{2}+\lambda(nQ_1+Q_0-q)\right)\left[1-\operatorname{erf}\left(\frac{\lambda n\sigma_1^2+nQ_1+Q_0-q}{\sqrt{2n}\sigma_1}\right)\right]\\
&= \frac{\lambda\cdot P_u}{2}\exp\left(-\lambda(q-\frac{1}{2}\lambda n\sigma_1^2-Q_n)\right)\left[1-\operatorname{erf}\left(\frac{\lambda n\sigma_1^2+Q_n-q}{\sqrt{2n}\sigma_1}\right)\right].
\end{aligned} \tag{A.8}$$

Thus:

$$S_{\mathrm{real}}(q) = \sum_{n=0}^{\infty}\frac{\mu^n\cdot \mathrm{e}^{-\mu}}{n!}\left[(1-P_u)\cdot G(q,Q_n,\sigma_n)+P_u\cdot\frac{\lambda}{2}\cdot\mathrm{e}^{-\lambda\cdot(q-Q_n-\frac{1}{2}\lambda n\sigma_1^2)}\cdot\left[1-\operatorname{erf}\left(\frac{Q_n-q+\lambda\cdot n\cdot\sigma_1^2}{\sqrt{2n}\sigma_1}\right)\right]\right]. \tag{A.9}$$

The SPE fitter used in this thesis has been implemented in Python and is available at [122].

B Derivation of Equation 6.12

In the following, the complete derivation of Equation 6.12 is given. For clarity, the pdf of the transit time (Equation 6.11) is repeated here:

$$f(t) = \frac{1}{N} \cdot \sum_{n=1}^{\infty} P(n,\mu) \cdot G(t, \mathrm{TT}, \sigma/\sqrt{n}). \tag{B.1}$$

The variance of this distribution can be determined analytically with

$$\begin{aligned} \sigma_\mu^2 &= \mathrm{Var}[f(t)] = \mathrm{E}[t^2] - \mathrm{E}[t]^2 \\ &= \int_{-\infty}^{\infty} t^2 \cdot f(t)\, dt - \left[\int_{-\infty}^{\infty} t \cdot f(t)\, dt\right]^2 \end{aligned} \tag{B.2}$$

As $f(t)$ is a sum of Gaussians with the same mean TT, the expected value $\mathrm{E}[t] = \int_{-\infty}^{\infty} t \cdot f(t)\, dt$ is just equal to TT, and thus

$$\begin{aligned} \sigma_\mu^2 &= -\mathrm{TT}^2 + \int_{-\infty}^{\infty} t^2 \cdot f(t)\, dt \\ &= -\mathrm{TT}^2 + \frac{1}{N} \sum_{n=1}^{\infty} P(n,\mu) \cdot \int_{-\infty}^{\infty} t^2 \cdot G(t, \mathrm{TT}, \sigma/\sqrt{n})\, dt \end{aligned} \tag{B.3}$$

As the variance of a Gaussian $G(x,\mu,\sigma)$ is $\mathrm{E}[x^2] - \mathrm{E}[x]^2 = \sigma^2$, we know that $\int_{-\infty}^{\infty} x^2 \cdot G(x,\mu,\sigma)\, dx = \sigma^2 + \mathrm{E}[x]^2 = \sigma^2 + \mu^2$. Thus, the last integral of Equation B.3 simplifies to

$$\begin{aligned} \sigma_\mu^2 &= -\mathrm{TT}^2 + \frac{1}{N} \sum_{n=1}^{\infty} P(n,\mu) \cdot (\mathrm{TT}^2 + \frac{\sigma^2}{n}) \\ &= -\mathrm{TT}^2 + \mathrm{TT}^2 \frac{1}{N} \sum_{n=1}^{\infty} P(n,\mu) + \frac{1}{N} \sum_{n=1}^{\infty} P(n,\mu) \cdot \frac{\sigma^2}{n} \\ &= \frac{\sigma^2}{N} \sum_{n=1}^{\infty} \frac{P(n,\mu)}{n} \end{aligned} \tag{B.4}$$

The last step stems from $\sum_{n=1}^{\infty} P(n,\mu) = 1 - e^{\mu} = N$. At this point one can use the expression of the exponential integral $\mathrm{Ei}(x)$ for a real argument [202, p. 9]

$$\mathrm{Ei}(x) = \gamma + \ln(x) + \sum_{k=1}^{\infty} \frac{(x)^k}{k \cdot k!}, \tag{B.5}$$

where γ is the Euler-Mascheroni constant. This is advantageous as $\mathrm{Ei}(x)$ and γ can be calculated quickly with Python packages (for example scipy.special.expi and np.euler_gamma). Thus, the infinite sum of Equation B.4 is simplified as

$$\begin{aligned} \sigma_\mu^2 = \frac{\sigma^2}{N} \sum_{n=1}^{\infty} \frac{\mu^n \cdot e^{-\mu}}{n \cdot n!} &= \sigma^2 \cdot \frac{e^{-\mu}}{1 - e^{-\mu}} [\mathrm{Ei}(\mu) - \gamma - \ln(\mu)] \\ &= \frac{\sigma^2}{e^{\mu} - 1} [\mathrm{Ei}(\mu) - \gamma - \ln(\mu)]. \end{aligned} \tag{B.6}$$

C Tables of best fit parameters

The following tables list the best fit parameters of various studies. Tables C.1 and C.2 show the fit results for the delayed pulse (as described in Section 8.2.2) and AP2 time histogram (Section 8.2.3) studies conducted for calculating IceTray mDOM PMT parameters.

Table C.3 list the parameters obtained from the scintillation lifetime fit, conducted at different temperatures (as described in Section 11.2.3).

Table C.1: Fit parameters of the sum of Fisher-Tippett distributions (see Equation 6.9) that model delayed pulses in Figure 8.25. As the fit is only an effective model for random sampling in IceTray, the uncertainties were omitted.

Amplitude	μ (ns)	σ (ns)	Peak type
$1.13 \cdot 10^7$	0	1.11	Regular pulses
$9.57 \cdot 10^4$	23.0	4.60	Inelastic
$8.69 \cdot 10^4$	9.0	3.79	Inelastic
$6.99 \cdot 10^4$	15.5	3.08	Inelastic
$6.29 \cdot 10^4$	28.6	1.71	Elastic
1699	49.4	5.34	Inelastic
1323	58.1	-4.38	Elastic

Table C.2: Fit parameters of the sum of Gaussians modelling the afterpulses type II. Fit was performed on the mean waveform of the PMT response to a very bright LED pulse shown in Figure 8.28. As the fit is only an effective model for random sampling in IceTray, the uncertainties were omitted.

Amplitude (mV)	μ (ns)	σ (ns)
39.9	517	27.7
21.8	576	72.0
41.0	885	564
18.3	1886	226
24.3	2402	242
27.0	3087	423
16.9	3658	694
15.0	5980	1253

Table C.3: Fit parameters of the scintillation lifetime of VITROVEX glass. As only an effective model was sought, the model with best goodness of fit was used (i.e. the model with most free parameters). The uncertainties are large due to the large number of fit parameters. See Section 11.2.3. The lifetimes τ_i where bounded to have a maximal value of 3 ms; τ_8 reached this value at certain temperatures, and the uncertainty is underestimated (and thus was omitted in the table).

	0 °C	−10 °C	−20 °C	−30 °C	−40 °C	−50 °C
R_{dr} ($\cdot 10^6$)	2.43 ± 0.06	1.50 ± 0.11	1.02 ± 0.08	1.43 ± 0.05	1.67 ± 0.07	1.50 ± 0.05
α'_1	0.176 ± 0.006	0.170 ± 0.007	0.166 ± 0.005	0.145 ± 0.007	0.153 ± 0.004	0.139 ± 0.007
τ_1 (0.1 µs)	2.92 ± 0.12	3.17 ± 0.14	3.20 ± 0.13	3.03 ± 0.16	3.28 ± 0.12	3.30 ± 0.16
α'_2	0.322 ± 0.020	0.27 ± 0.18	0.329 ± 0.011	0.24 ± 0.10	0.298 ± 0.011	0.23 ± 0.04
τ_2 (µs)	1.89 ± 0.11	1.95 ± 0.35	2.20 ± 0.09	1.9 ± 0.4	2.30 ± 0.09	1.99 ± 0.25
α'_3	0.209 ± 0.015	0.10 ± 0.17	0.210 ± 0.032	0.16 ± 0.07	0.065 ± 0.028	0.17 ± 0.08
τ_3 (µs)	6.3 ± 0.8	3.1 ± 2.0	9.1 ± 0.9	4.3 ± 2.1	8.7 ± 3.5	5.9 ± 2.7
α'_4	0.11 ± 0.04	0.183 ± 0.027	0.001 ± 0.03	0.177 ± 0.032	0.129 ± 0.028	0.12 ± 0.08
τ_4 (µs)	25 ± 9	9.6 ± 2.0	10 ± 9	13.6 ± 3.3	8.6 ± 1.8	14 ± 9
α'_5	0.05 ± 0.04	0.111 ± 0.015	0.124 ± 0.011	0.116 ± 0.015	0.151 ± 0.010	0.142 ± 0.029
τ_5 (10 µs)	6 ± 5	3.3 ± 0.9	3.4 ± 0.5	4.9 ± 1.1	3.14 ± 0.31	4.5 ± 1.1
α'_6	0.047 ± 0.017	0.067 ± 0.015	0.075 ± 0.009	0.064 ± 0.012	0.095 ± 0.008	0.083 ± 0.015
τ_6 (ms)	0.21 ± 0.11	0.111 ± 0.032	0.123 ± 0.020	0.18 ± 0.05	0.124 ± 0.016	0.154 ± 0.034
α'_7	0.036 ± 0.014	0.053 ± 0.006	0.050 ± 0.007	0.049 ± 0.010	0.053 ± 0.007	0.064 ± 0.008
τ_7 (ms)	0.68 ± 0.23	0.50 ± 0.12	0.58 ± 0.14	0.61 ± 0.11	0.47 ± 0.10	0.59 ± 0.08
α'_8	0.043 ± 0.006	0.046 ± 0.004	0.046 ± 0.006	0.050 ± 0.005	0.055 ± 0.006	0.055 ± 0.005
τ_8 (ms)	3.0	2.6 ± 0.7	2.5 ± 0.7	3.0	2.01 ± 0.32	3.0

D Fit of simulated collection efficiency

The weights were calculated by fitting the relative detection efficiency against the distance to the PMT centre from Section 7.3.4. Figure D.1 shows the data to be fitted, which was calculated by averaging the five curves presented in Figure 7.24. The fit model was constructed as follows:

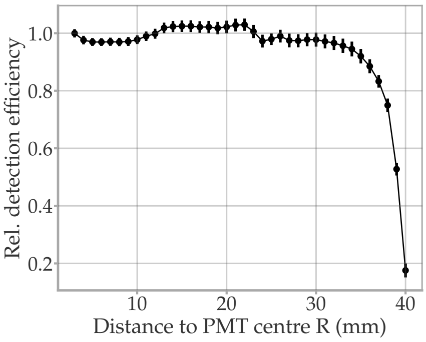

Figure D.1: The mean relative detection efficiency against the distance to the PMT centre of the measurements presented in Section 7.3.4. The data were used to estimate the weights for the absorbed photons in the photocathode layer.

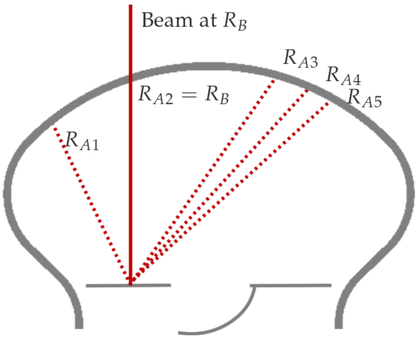

Figure D.2: Sketch of the cross section of a PMT being illuminated by a beam at R_B relative to the PMT centre and detecting photons at different photocathode locations R_{Ai}.

- A scan was simulated, where the photocathode positions of photon absorptions was recorded at each beam location.
- Assuming radial symmetry, only the distance to the PMT centre of the absorption location R_A was used. In addition, although a 2D-scan across the entire photocathode was simulated, the position of the beam was parameterised in one dimension with R_B, the distance of the beam to the PMT centre. [1] Figure D.2 illustrates the difference between R_A and R_B. As a beam positioned at R_B can be reflected diffusely on internal structures, photons can be detected on several locations on the photocathode R_{Ai}.
- The beam positions were binned from 0 mm to 41 mm with a bin width of 0.25 mm. For each of these bins, a histogram of the absorbed locations $h_{R_B}(R_A)$ was also calculated with bins of width 0.25 mm. All histograms are shown in Figure D.3.
- A set of weights (w_{R_A}) were created to model the collection efficiency of the photocathode. There is one w_{R_A} for each bin of the histograms h_{R_B}. The simulated PMT response ϵ_{R_B} at the beam position R_B is the sum of the histogram h_{R_B} weighted by w_{R_A}:

  $$\epsilon_{R_B} = \sum_{R_A} h_{R_B}(R_A) \cdot w_{R_A},$$

  where $h_{R_B}(R_A)$ is the counts at the bin corresponding to R_A. Once the complete curve is calculated, it is normalised by the average ϵ_{R_B} of the central region $R_B < 25$ mm.[2]
- The fit was performed minimising with Minuit [191, 192] following chi-square statistics.

The direct fitting of the weights, which were bounded within the interval $[0, 1]$, resulted in zigzag patterns between the weights in the region $R_A < 20$ mm, likely due to the high number of fit parameters. To enforce monotonicity, the difference from the neighbouring weight $\delta_r = w_{r-1} - w_r$ was used as the fit parameter, starting from the centre of the PMT towards the edges. The weight in the centre ($R_A = 0$ mm) was set to 1, and the fit parameters for $R_A < 20$ mm were restricted to be positive, ensuring a monotonic decrease of the weights. Weights larger than unity would artificially increase the simulated efficiency, since the sum of the weights should represent the number of detected photons in the simulation. At the edges, which were less affected by the zigzag behaviour, negative values of δ_r were allowed within the interval $[-0.05, 0.1]$ to prevent the results from fluctuating excessively.

[1] Here the distance to PMT centre considers only the x-y-plane, ignoring the photocathode curvature, following the coordinates of Figure 7.5.

[2] This is the same region as defined for the measurement data in Section 7.3.4.

[191]: Dembinski et al. (2020), *scikit-hep/iminuit*

[192]: James et al. (1975), *Minuit: A System for Function Minimization and Analysis of the Parameter Errors and Correlations*

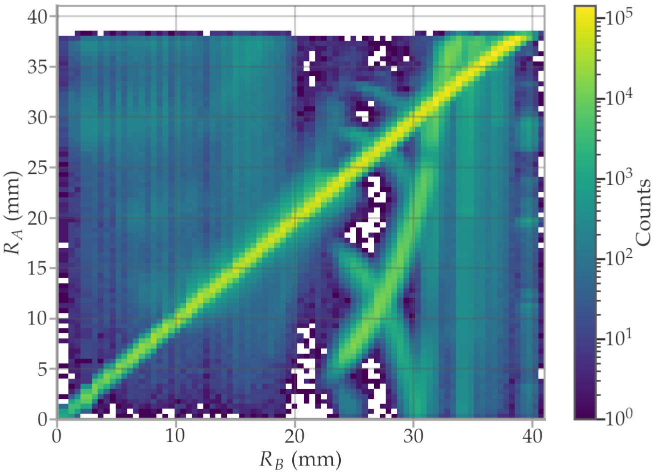

Figure D.3: The Geant4 PMT model was scanned with a beam in a grid covering the entire photocathode. The position on the photocathode layer where the photons were absorbed was saved. The figure shows the location of the absorption in dependence on the position of the beam, both parameterised as distance to the photocathode centre.

E Expansion of air bubbles inside cured gel

During production, the mDOM is sealed after the *wedding* of the two half-modules, where the cables from the top half-module are connected to the mainboard on the bottom half-module. The pressure vessels are placed in their final position inside a vacuum bell for sealing. The bell is pumped to 480 mBar and purged with nitrogen five times and pumped one last time to the same pressure, which is the internal end pressure of the module. Thus, both pressure vessels are held together by the pressure difference with respect to the outside. 480 mBar is required to ensure that the module does not open at the South Pole Station, where the lowest recorded ambient pressure was 642 mBar [203].

[203]: Lazzara et al. (2012), *Fifty-year Amundsen–Scott South Pole station surface climatology*

After sealing the first DVT at DESY by IceCube collaborators, several of the modules were observed to begin developing air bubbles inside the gel layer, which increased with time (see Figure E.1). This was hypothesised to be due to the expansion of initially tiny air bubbles, invisible to the eye, which, after the gel cures, freeze in their position.

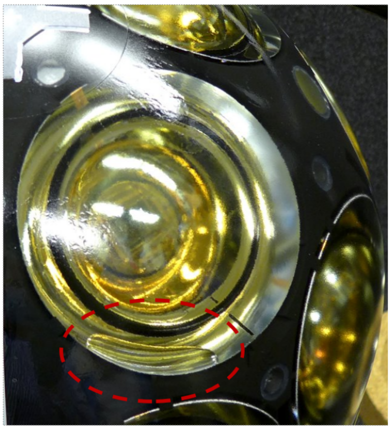

Figure E.1: Photograph of a bubble on one of the reflectors of DVT 03. Picture courtesy of the DESY IceCube group.

An introduction to the dynamic of gas bubbles inside soft materials can be found in [204]. In the cited work, a theoretical framework is introduced that describes the change of the bubble radius in time once the soft material is placed in a higher- or lower-pressure environment. The gas bubble can grow or shrink as a result of the diffusion of solved gas into or out of the bubble, caused by a concentration gradient between the bubble and the environment outside the soft material. Several studies and measurements were performed by Münster's IceCube group following this theoretical framework. It was estimated that after setting the internal pressure of the modules at 480 mBar, any bubble inside the gel larger than ~3 µm would increase in time, while smaller bubbles would collapse at some point [205]. Although this number has to be taken with caution since several gel parameters needed for the model had to be roughly estimated, this points to a very strict constraint on the number and size of bubbles allowable after curing.

[204]: Solano-Altamirano et al. (2015), *Gas bubble dynamics in soft materials*

[205]: Kappes (2021), *Bubble Dynamics in Gel (presentation)*

During the evacuation of the half-modules after gel pouring in DESY Zeuthen, collaborators observed that the air bubbles tended to appear from very specific places of the support structure. For example, components with sharp edges, such as reflector pins, hardly ever stop producing bubbles during evacuation. Another region prone to release bubbles was the contact area between the reflectors and the copper tape of the PMTs, which connects the reflectors to the cathode pin.

PA12 objects printed with SLS are very porous [206], with small grains of the order of magnitude of a few micrometres, and painting the surface does not reduce this porosity by a significant factor.

[206]: Flodberg et al. (2018), *Pore analysis and mechanical performance of selective laser sintered objects*

To test whether this porosity could be a source of the observed bubbles, a setup was constructed in the scope of this thesis in which a PA12 sample was held inside a recipient with liquid gel, but without being immersed in the gel. The sample and the recipient were inside a vacuum chamber. The sample could be moved externally without having to vent the chamber. The vacuum chamber was pumped to 10 mBar, and after ten minutes, the sample was slowly immersed in the gel without changing the internal pressure of the chamber. Once one side of the sample was submerged, bubbles formed on the surface of the sample (see Figure E.2). These bubbles could be explained by two possible sources. On the one hand, the air trapped on the surface of the samples needs a very long time to completely evacuate, and therefore 10 mBar for ten minutes was not enough to extract all of it. On the other hand, the sample itself could be outgassing, which is known to happen to several materials under low pressure. This latter possibility was found to be improbable or of lesser importance, since no difference could be seen between the painted and unpainted samples, and as was mentioned earlier, the bubble formation during the pouring of half-modules is very localised. In this context, regions such as the reflector pins could trap air in the contact area between the reflector and the support structure due to the porosity of the PA12 surface.

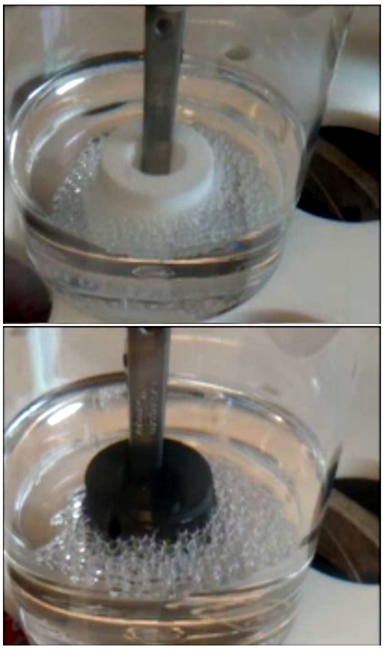

Figure E.2: Picture of bubble formation under samples that were evacuated over ten minutes at 10 mBar. The photograph on the top is of a plain PA12 sample, and the bottom is of a painted one.

These observations led to the removal of all sharp edges in the design of the support structure (see Figure E.3) and the addition of a production step of *chemical smoothing*, which the manufacturer performs after printing. This step reduces the porosity of the PA12 surface, leaving a smoother finish.

The bubbles from the copper tape can be explained in large part by a similar effect, but in this case, there is air trapped between the glue of the tape and the reflectors. However, an outgassing of the glue itself has not been completely excluded as a possible source. A reduction in the amount of air released from this region was achieved by evacuating the half-module for two days at 2 mBar before pouring. Subsequently, without venting to atmospheric pressure, the first gel shot is poured at 200 mBar, and then a schema similar to that described in Section 10.2.3 is followed. However, these production steps are still being optimised and may change for the final mDOM production.

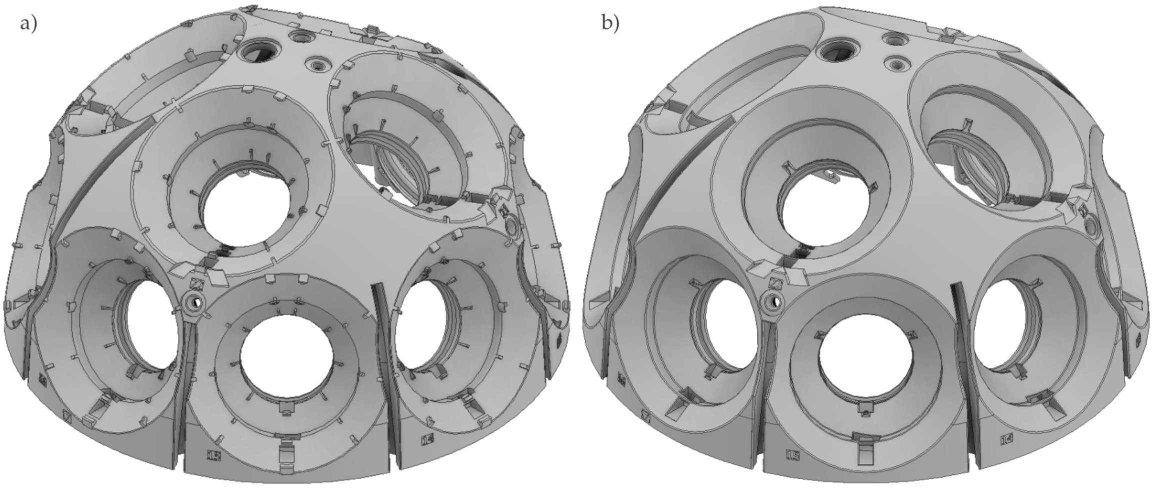

Figure E.3: Top view of the support structure of the mDOM's bottom half before (a) and after (b) applying the changes to reduce the amount of air bubbles. The reflector holders were removed and the number of PMT spacers was reduced from nine to three thicker ones.

F Dark rate of DVT 04

The raw data of the dark rate of DVT 04, measured at temperatures of −10 °C, −20 °C, −30 °C, and −40 °C, are presented in the following two pages. Figure F.1 shows the rates for PMT channels 0 to 11, and Figure F.2 displays the results for channels 12 to 23. See Section 11.3 for details.

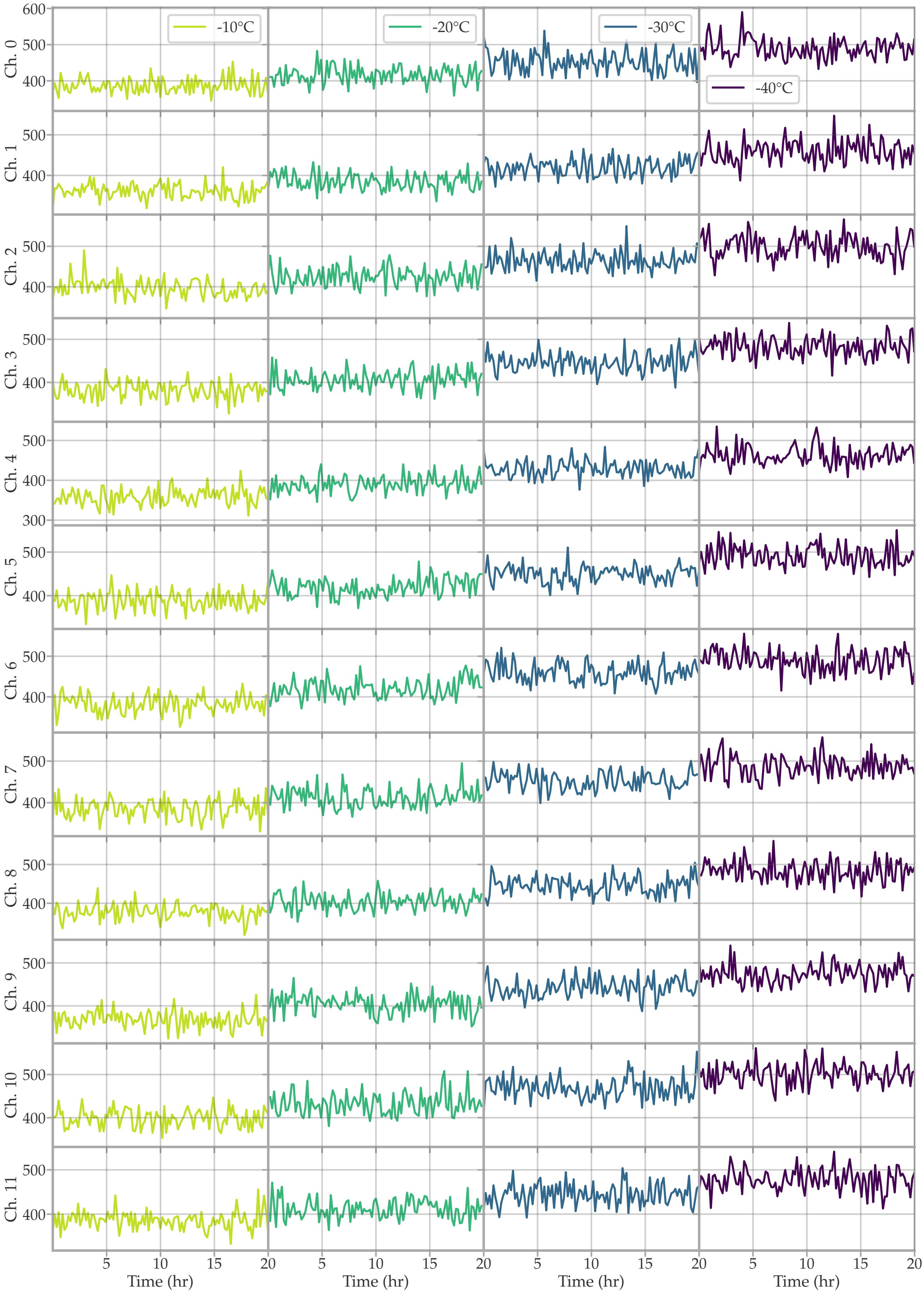

Figure F.1: The dark rate of channels 0 to 11 in DVT 04 plotted against time. Columns from left to right display the rate measured at temperatures of −10 °C to −40 °C.

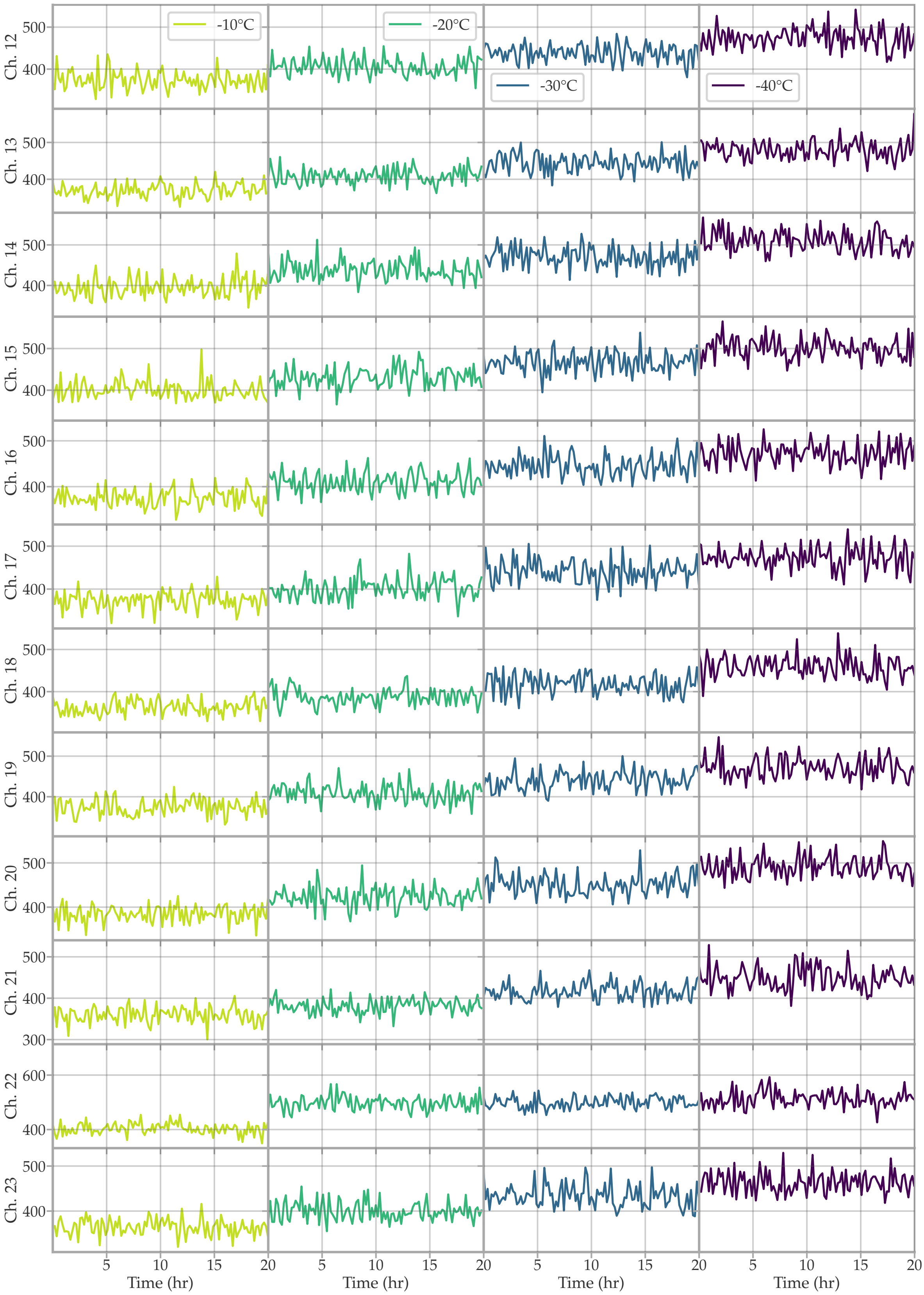

Figure F.2: The dark rate of channels 12 to 23 in DVT 04 plotted against time. Columns from left to right display the rate measured at temperatures of −10 °C to −40 °C.

G Numbering of PMTs and AFE channels

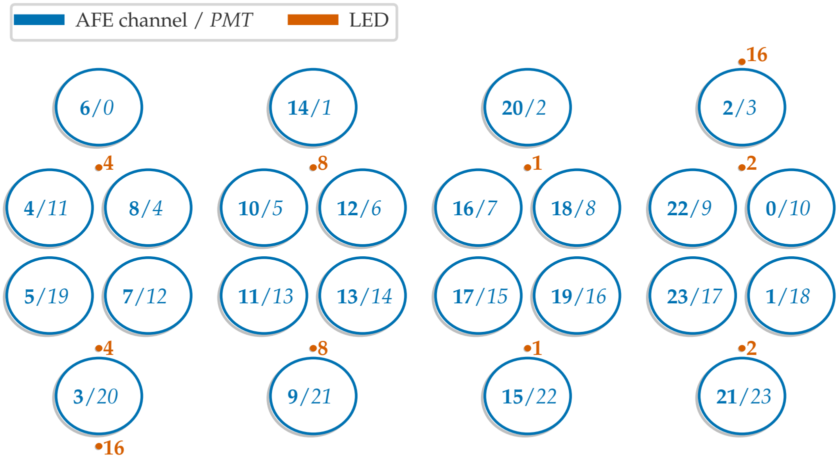

Figure G.1: Projection of the PMT and LED positions of an mDOM with their corresponding numbers. The AFE channel number corresponding to each PMT is also given.

Acknowledgements

I would like to express my heartfelt gratitude to my advisor, Alexander Kappes, for providing me with the opportunity to work in his amazing research group and pursue a very exciting topic. His constant support, guidance, and infinite patience have been invaluable to me. I would also like to extend my thanks to my second supervisor, Alfons Khoukaz, for his unwavering support and for his valuable advice throughout my F-Praktikum duties.

My experience in the AG Kappes has been enriched by the many incredible people I have met. I am immensely grateful to Lew Classen for his invaluable help, particularly during my rookie years. Raffi Busse, thank you for your insightful plant tips, the many meetups and for the TV ;). I would also like to acknowledge the contributions of Willhelm Achtermann, Lew Classen, Markus Dittmer, Daniel Guderian, Javier Vara, and Berit Schlüter in correcting my thesis. Last but not least, I am deeply grateful to my colleague, roommate and friend, Cristian Lozano, for everything; I would not have finished without him.

I am aware that there are many others who have helped me over the past five years, and it is difficult to name them all without risking forgetting someone. Nevertheless, I extend my sincere thanks to all of them.

Finally, I would like to thank my family: my parents, Ana Maria and Bernhard, for their constant support throughout my life, and my sister Tania for designing the most amazing title page for my thesis. I would also like to express my gratitude to Ani, Martín, and Pilar for always being by my side despite the distance, and my uncle Franz for the regular pizza visits :)